VERSLAGEN EN VERHANDELINGEN

REPORTS AND TRANSACTIONS

NATIONAAL LUCHTVAARTLABORATORIUM

NATIONAL AERONAUTICAL RESEARCH INSTITUTE

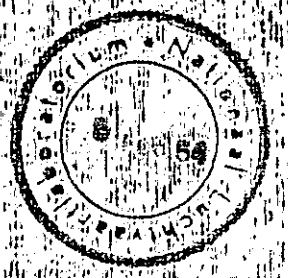

AMSTERDAM

XVI — 1952

VERSLAGEN EN VERHANDELINGEN

REPORTS AND TRANSACTIONS

NATIONAAL LUCHTVAARTLABORATORIUM

NATIONAL AERONAUTICAL RESEARCH INSTITUTE

AMSTERDAM

XVI — 1952

Preface

This volume of "Verslagen en Verhandelingen" contains a selection of reports, which were released for publication in 1950, 1951 and 1952. Two extensive reports (F. 100 and S. 402) have been published separately in Vol. XVII, which was issued some time ago.

Predominance has been given in this volume to reports dealing with various aspects of the research work, including measuring methods, of the Aerodynamics Section, since the intensive engagement of this section in ad-hoc research and the development of modern experimental equipment, prevented the preparation of publications for the previous post-war volumes.

As usual, the reports contained in this volume form only part of the publications issued in the period covered. A list of other papers, published in typescript form or in scientific journals, is given on the following pages. A complete list of publications (1920 to 1952) is available upon request.

Homage should be paid in this preface to the memory of Ir C. Koning, former scientific director of the N. L. L. By his death in July 1952, the institute was bereft of his outstanding scientific abilities, particularly as a theoretical aerodynamicist. He also will be remembered by many of his colleagues abroad and by his collaborators in all ranks, a. o. for his keen and broad interest in their technical as well as personal affairs and his sense of humour and proportion. A glance at the list of publications of Ir Koning on pp. v to vii will show his important contribution to the national and international appreciation of the research work of this institute.

C. ZWIKKER

Director.

December 1952.

Contents

List of Publications of Ir C. Koning.

Pigeaud, F. D. Koning, C.	Les méthodes logarithmiques Eiffel appliquées à quelques cas spéciaux.	Rapports premier Congr. Intern. de la Navigation Aérienne Paris, Tome II, p. 18–25.	1921
von Baumhauer, A. G. Koning, C.	On the stability of the oscillations of an aeroplane wing.	Report Intern. Air Congress, London, pp. 221–238.	1923
von Baumhauer, A. G. Koning, C.	Unstable oscillations of a wing aileron system. (In Dutch).	Rep. A. 48. Also in Vol. II V. en V.	1923
Koning, C.	Einige Bemerkungen über nicht-stationäre Strömungen von Tragflügeln.	Proc. first intern. Congr. Appl. Mech. p. 414–417.	1924
Wolff, E. B. Koning, C.	Essais tendant à déterminer l'influence d'un cylindre rotatif, adopté à un profile d'aile.	IIIe Congr. intern. de la Navig. aérienne, Bruxelles. Tome II, pp. 477–492.	1925
Wolff, E. B. Koning, C.	Further experiments on the influence of a rotating cylinder accomodated in a wing section. (In Dutch).	Rep. A. 105. Also in Vol. IV V. en V.	1925
Koning, C.	Theory of the "Flettner" Rotortowers. (In Dutch).	"Het Schip", no. 1.	1925
Biezeno, C. B. Koch, J. J. Koning, C.	The influence of the ribs on the strength of the main plane spars. I. (In Dutch).	Rep. V. 175. Also in Vol. IV V. en V.	1926
Biezeno, C. B. Koch, J. J. Koning, C.	Ueber die Berechnung von freitragenden Flugzeugflügeln.	ZAMM VI, pp. 97–105.	1926
Koning, C. v. d. Maas, H. J.	Experiments on the action of the ailerons of a thick tapered wing. (In Dutch).	Rep. A. 32. Also in Vol. IV V. en V.	1926
Wolff, E. B. Koning, C.	Discussion of the results of the tests on the boundary layer of the aerofoil with rotating cylinder. (In Dutch).	Rep. A. 130. Also in Vol. IV. V. en V.	1926
Koning, C.	The influence of the ribs on the strength of aeroplane wings. II. (In Dutch).	Rep. V. 284. Also in Vol. VI V. en V.	1928
Koning, C.	The influence of the ribs on the strength of aeroplane wings. III. (In Dutch).	Rep. V. 285. Also in Vol. VI V. en V.	1928
Koning, C.	Experiments with two models of airscrews with bodies placed behind them. (In Dutch).	Rep. A. 180. Also in Vol. VI V. en V.	1928
Koning, C.	About the scale effect. (In Dutch).	Rep. A. 210. "Vliegveld", no. 6.	1928
Koning, C.	The influence of the ribs on the strength of aeroplane wings. IV. (In Dutch).	Rep. V. 357. Also in Vol. VI V. en V.	1930
Koning, C. v. d. Maas, H. J.	Some experiments on nacelles with Townend-rings.	Ve Congrès Intern. de la Navigation Aérienne, Bull. séparé, no. 3, The Hague.	1930

Koning, C.	The influence of the ribs and wing covering on the strength of aeroplane wings.	Ve Congrès Intern. de la Navigation Aérienne, Bull. séparé, no. 4, The Hague.	1930
Koning, C.	The influence of the ribs and wing covering on the strength of aeroplane wings. I. (In Dutch).	Rep. V. 358. Also in Vol. VI V. en V.	1931
Koning, C.	Nomograms for the determination of the roots of biquadratic equations. (In Dutch).	Rep. A. 321. Also in Vol. VI V. en V.	1931
Koning, C. Boelen, A.	The influence of the aeroplane on the action of the tail plane. (In Dutch).	Rep. A. 363. Also in Vol. VI V. en V.	1931
Koning, C. de Haas, T. P.	The critical velocity of a body towed by an aeroplane. (In Dutch).	Rep. A. 367. Also in Vol. VII V. en V.	1931
	Translated into English as:	NACA Tech. Memo. 832.	1937
Koning, C.	Aerofoil-theory. (In Dutch).	"Physica, Ned. Tijdschrift voor Natuurkunde", Vol. 11, no.3, pp. 73–82.	1931
Koning, C.	The indication of thermometers in moving air. (In Dutch).	Rep. A. 322. Also in Vol. VII V. en V.	1932
Koning, C. Boelen, A.	Aerodynamische Eigenschaften der Quasi-Trapezflügel mit verschiedener Breite des prismatischen Teiles.	Rep. A. 390. Reprint from "Zeitschrift für Motorluftschiffahrt", Heft 2. Also in Vol. VII V. en V.	1933
Koning, C. Boelen, A.	Separation of the flow at large angles of incidence. (In Dutch).	Rep. A. 426. Also in Vol. VII V. en V.	1933
Koning, C. Taub, J.	Stoszartige Knickbeanspruchung schlanker Stäbe im elastischen Bereich bei beiderseits gelenkiger Lagerung.	Rep. S. 83. Also in Vol. VII V. en V. and in "Luftfahrtforschung", Band 10, Heft 2.	1933
Koning, C.	Zuschrift zum Aufsatz: "Korrektur für das Quermoment von Tragflügeln bei Untersuchungen im Windkanal mit Kreisquerschnitt". M. Biot, Pasadena, ZFM, S. 410.	Zeitschr. Flugtechn. u. Motorluftschiffahrt Vol. 24 nr. 22, S. 614.	1933
Koning, C.	The aerodynamical properties of airscrews, the blade width and (or) number of blades being changed. (In Dutch).	Rep. A. 511. Also in Vol. VII V. en V.	1934
Koning, C. v. d. Neut, A.	The influence of the ribs and wing covering on the strength of aeroplane wings, III. (In Dutch).	Rep. S. 68. Also in Vol. VII V. en V.	1934
Wolff, E. B. Koning, C.	The technical importance of large wind tunnels. (In Dutch).	Rep. A. 544. Also in Vol. VIII V. en V.	1935
Koning, C.	The influence of wing warping on the drag. (In Dutch).	Rep. A. 557. Also in Vol. VIII V. en V.	1935
Koning, C.	Influence of the propeller on other parts of the airplane structure.	Aerodynamic Theory - W. F. Durand, Vol. IV. Div. M. p. 361.	1935

Koning, C.	A problem of probability, relating to the occurrence of engine failure. (In Dutch).	Rep. A. 558. Also in Vol. VIII V. en V.	1936
Koning, C.	The wall interference for a propeller in a mixed wind tunnel. (In Dutch).	Rep. A. 589. Also in Vol. VIII V. en V.	1936
Koning, C.	A probability problem relating to operating troubles. (In Dutch).	"De Ingenieur" Vol. 51 - 17 April. p. A 142–145.	1936
Koning, C.	Dreikomponentenmessung an Tragflügeln im RSL-Windkanal.		1936
Koning, C.	The motion of an oscillating system with one degree of freedom under the action of an arbitrary external force. (In Dutch).	Rep. A. 649. Also in Vol. VIII V. en V.	1937
Koning, C.	Considerations on explosion phenomenae; I. Stationary flat shock wave. (In Dutch).	Rep. A. 650.	1937
Koning, C. Boelen, A.	Comparison of the measured and calculated load distribution for a tapered wing. (In Dutch).	Rep. A. 676. Also in Vol. VIII V. en V.	1938
Koning, C.	Diagram for the determination of the critical velocity of a body towed by an aeroplane. (In Dutch).	Rep. A. 635. Also in Vol. VIII V. en V.	1939
Koning, C.	Wind tunnel research for non-aeronautical transportation. (In Dutch).	Lecture, delivered on 25th June 1941 for Transport Engineering Section of Royal Inst. of Engineers.	1941
Koning, C.	In memoriam Dr Ir E. B. Wolff. (In Dutch).	"Het Vliegveld", Vol. 25 nr. 2. Febr.	1941
Koning, C.	About some interference problems.	To be published.	

List of Publications Issued in Typescript or Published in Scientific Journals between 1st January 1950 and 1st January 1953.

N.B. These reports are in English, unless indicated otherwise.

A. 985:	Slotboom, J. G.	Thrust augmentation by means of an ejector	1950
A. 1198:	Benthem, J. P.	Investigation of turbulence by hotwire measurements. (In Dutch)	1951
A. 1231:	Zwaaneveld, J.	About a vortex-indicator and the possible development of a vortex intensity gauge. (In Dutch)	1950
A. 1263:	Wijker, H.	Experiments on the Two-Dimensional Flow over a NACA 0018 Profile at High Angles of Attack	1952
A. 1266:	Loos, H. G.	Theoretical considerations on the interference occurring at the connection of a wing to a wall resulting from boundary layer effects. Part I. (In Dutch)	1952
A. 1267:	Wijker, H.	Experiments on disturbed regions in the laminar boundary layer behind isolated surface excrescences for two- and three-dimensional flow	1952
A. 1282:	Loos, H. G.	Theoretical considerations on the interference occurring at the connection of a wing to a wall resulting from boundary layer effects. Part II. (In Dutch)	1952
F. 52:	v. d. Vooren, A. I. and Hofsommer, D. J.	Binary aileron-tab flutter	1949
F. 55:	van Heemert, A.	On the numerical evaluation of certain types of integrals	1949
F. 56:	Zaat, J. A.	A profile catalogue with 36 symmetrical profiles for profile calculation. (In Dutch)	1949
F. 57:	Zaat, J. A. and Timman, R.	Methods of calculation for profiles in subsonic compressible flow. (In Dutch)	1949
F. 58:	van Heemert, A.	The calculation of the down wash at the surface of a lifting plane in steady flow. Tables, graphs and some simple checks.	
F. 59:	van Heemert, A.	Application of a method in lifting surface theory to a rectangular plane wing of aspect ratio 6	1950
F. 61:	Hofsommer, D. J.	Systematic representation of aerodynamic coefficients of an oscillating aerofoil in two dimensional incompressible flow	1950
F. 62:	Timman, R.	La méthode des caractéristiques et la calculation de la couche limite laminaire en écoulement tridimensionel	1950
F. 64:	Greidanus, J. H. and de Kock, A. C.	Catalogue of Aerodynamic Measurements	1950
F. 65:	Hofsommer, D. J.	Stability criteria. (In Dutch)	1951
F. 70:	Zaat, J. A.	A method of calculation for closed profiles with prescribed discontinuous velocity distribution. (In Dutch)	1951
F. 71:	v. d. Vooren, A. I. and Muller, W.H. (Fokker)	Flutter calculation for a modern aeroplane with an appendix on the use of punched-card machines. (In Dutch)	1951
F. 73:	van Heemert, A.	The calculation of the downwash of swept-back wings in the region of the tail unit	1950
F. 74:	Timman, R.	The potentional flow about a yawed ellipsoid at zero incidence	1951
F. 77:	van Heemert, A.	Application of the generalized Prandtl equation to an elliptic plane wing under yaw	1951
F. 78:	Greidanus, J. H. and van Heemert, A.	Chordwise downwash distribution of an infinite wing of constant chord with a periodic spanwise distribution of vorticity in oblique flow	1951
F. 86:	v. d. Vooren, A. I.	Ternary wing bending-aileron-tab flutter	1951

M. 1575:	Hartman, A.	Mechanical properties of glued metal-to-metal joints. III. (In Dutch)	1950
M. 1627:	Hartman, A.	Fatigue tests of 24 S-T alclad single lap joints glued with Redux, including some comparative tests with riveted joints. (In Dutch)	1951
M. 1713:	Hartman, A.	Comparative investigation of the corrosion resistance of some types of wrought aluminium alloys in different corrosive solutions. (In Dutch).	1951
M. 1819:	Hartman, A.	Investigation of notch sensitivities of clad 24 ST and 75 ST aluminium alloys under fluctuating tension. (In Dutch)	1952
M. 1839:	Hartman, A.	Shear- and peeling tests on 0.8 mm austenitic stainless steel glued with Redux. (In Dutch)	1952
M. 1883:	Hartman, A.	Results of ageing tests on wood specimens glued with cold setting resin glue. (In Dutch)	1952
V. 1439b:	—	Operating instructions for an apparatus for determining the resistance and volume of pipelines of aeroplane pitot systems. (In Dutch)	1950
V. 1509a:	de Boer, I.	Report on the determination of the c_L–c_D relation of the aeroplane PH-NLL. Siebel 204 D-1 in flight (2nd series). (In Dutch)	1949
V. 1575:	v. d. Linden, J. C.	Properties of the N.L.L. resistance thermometer. (In Dutch)	1951
V. 1583:	Roskam, P. and van Munster, G.	Report on the exhibition of instruments developed by the National Aeronautical Research Institute. (In Dutch)	1949
V. 1595:	Kalkman, C. M.	Investigation of the possibilities of lateral control in the presence of fullspan landing flaps. (In Dutch)	1951
V. 1599:	Wynia, S. and Buhrman, J.	Summary of the results of flight testing the aeroplane FT-404, North-American "Harvard II B". (In Dutch)	1951
V. 1609:	v. d. Linden, J. C.	Calibration of the pedal force indicator of the Fokker S 13 aeroplane. (In Dutch)	1951
V. 1610:	—	Development and testing of a stagnation temperature probe. (In Dutch)	1951
V. 1622:	Pool, A.	Measurement of the recovery factor of the NARI stagnation temperature probe in a wind tunnel. (In Dutch)	1951
V. 1624:	Pool, A.	Report of a number of tests in non-steady flight with the aeroplane PH-NLL. (In Dutch)	1952
MP. 40:	Warsen, W. and v. d. Linden, J. C.	Measuring instruments of Netherlands origin. (In Dutch). Polyt. Tijdschrift 5, no. 1—2, 10 Jan. 1950, pp. 13a—17a.	
MP. 41:	Sanders, W. G.	A high-precision force-measuring instrument. (In Dutch). TNO-Nieuws 5, no. 46, p. 52, Febr. 1950.	
MP. 42:	Greidanus, J. H. and v. d. Vooren, A. I.	Station functions in flutter analysis. J. Aero. Sci., 17, no. 3. p. 178. March 1950.	
MP. 43:	—	An instrument for calibrating extensometers at the NLL. (In Dutch). TNO-Nieuws 5, no. 48, p. 121. April 1950.	
MP. 44:	Plantema, F. J.	The new 150-tons compression machine of the NLL. (In Dutch). TNO-Nieuws 5, no. 48, p. 122—123. April 1950. De Ingenieur 62, no. 16, p. A. 203—204. 21 April 1950.	
MP. 45:	Palm, J. H.	The theoretical background and interpretation of the Schnadt impact test. Metalen 4, nos. 9, 10, 11; pp. 177—184; 213—217; 231—236. May, June, July 1950.	
MP. 46:	Greidanus, J. H. and v. d. Vooren, A. I.	Complementary energy method in vibration analysis. J. Aero. Sci., 17, no. 7, pp. 454, 455, July 1950.	
MP. 47:	Lucassen, L. R. and Marx, A. J.	Rational performance requirements. (In Dutch). De Ingenieur 62, no. 39, pp. L. 47, L. 48, 29 Sept. 1950.	
MP. 48:	Palm, J. H.	Considerations on the relationship between stress and strain in plastic metals. Metalen 5, no. 1, pp. 9—14, Sept. 1950.	
MP. 49:	v. d. Linden, J. C.	The desynn system for electrical remote indication. (In Dutch). Polyt. Tijdschrift 5, no. 49/50, pp. 855a—860a. 12 Dec. 1950.	
MP. 50:	Hartman, A.	Mechanical testing of wood and metal glues, methods and test results. (In Dutch). De Ingenieur 26, no. 50, pp. Mk. 108—115, 15 Dec. 1950.	

MP. 51:	Slotboom, J. G.	Jet-propelled aircraft and related problems. (In Dutch). Voordrachten Kon. Inst. v. Ingenieurs, no. 42, 1951; Marineblad 60, *no. 7, pp. 1038—1051; Dec. 1950.*
MP. 52:	Zwaaneveld, J.	Aerodynamic properties of circular-sheet profiles (in Dutch). Polyt. Tijdschr. nr. 9/10, p. 149a, 6 March 1951.
MP. 53:	Rondeel, J. H.	Some investigations on mechanical properties of sandwich core materials. (In Dutch). Plastica, Febr. and March 1951.
MP. 54:	Greidanus, J. H.	A review of aeroelasticity. Appl. Mech. Reviews, Vol. 4, no. 3, p. 138. March 1951.
MP. 55:	Meijer Drees, J. and Hendal, W. P.	Airflow patterns in the neighbourhood of helicopter rotors. Aircraft Engng., 33, no. 226, p. 107, April 1951.
MP. 56:	Rondeel, J. H.	The 150-tons compression machine of the N.L.L. (in Dutch). Polyt. Tijdschr. 6, no. 17/18, p. 289a. 1 May 1951.
MP. 57:	Plantema, F. J.	A note on the buckling of struts. J. Roy. Aero. Soc., July 1951, pp. 454–455.
MP. 58:	Wijker, H.	Aerodynamic investigations at the Nationaal Luchtvaartlaboratorium (in Dutch). Ver. v. luchtbehandeling. *Communication no. 6,* July 1951.
MP. 59:	Erdmann, S. F.	A new simple interferometer to obtain a quantitative analysis of flow patterns (in German). Appl. Sci. Research Vol. B 2, nr. 3, p. 149, 1951.
MP. 60:	Floor, W. K. G.	An interferometer for calibrating extensometers. (Abstract of report S. 359). J. Sci. Instrum. Vol. 29, no. 6, p. 200, June 1952.
MP. 61:	Timman, R.	The aerodynamic forces on an oscillating aerofoil between two parellel walls. Appl. Sci. Research, Vol. A 3, 1951.
MP. 62:	Timman, R.	Aerodynamic coefficients of an oscillating airfoil in two-dimensional subsonic flow. J. Aero. Sci. 1951.
MP. 63:	Slotboom, J. G.	Some considerations on the fundamentals of aircraft propulsion (in Dutch). "De Ingenieur", Vol. 63, no. 42, p. L 49–L 56, 19 Oct. 1951.
MP. 66:	Greidanus, J. H. and de Kock, A. C.	Note on a card-index system of bibliographic control of published results of aerodynamic measurements. FID XVIIIth Conf. 1951.
MP. 67:	Timman, R.	La méthode des caractéristiques et le calcul de la couche limite laminaire en écoulement tridimensionnel. Extrait des Actes du Colloque International de Mécanique. Poitiers 1950 — Tome II. (Voir publications Scientifiques et Techniques du Ministère de l'Air no. 250).
MP. 68:	Greidanus, J. H.	Elementary considerations on one-dimensional compressible flows. (In Dutch). Ingenieur Vol. 63 nr. 28, pp. L 39–48. 13 July 1951.
MP. 69:	Timman, R.	La théorie des profiles minces en écoulement non-stationnaire en fluide incompressible ou compressible.
MP. 70:	Floor, W. K. G.	Some directions for measurements by means of resistance strain gauges in strength investigations, especially on aircraft constructions. Lecture "Ned. Ver. v. Luchtvaarttechniek", 15 March 1951. (In Dutch).
MP. 71:	Schering, D. C. and Scherpenhuijsen Rom, G.	An electronic resistance strain gauge stick force indicator developed at the Nationaal Luchtvaartlaboratorium. "TNO-Nieuws", July 1952. (In Dutch).
MP. 72:	Erdmann, S. F.	The activity on the supersonic range in Sweden. (Dutch with English summary). Lectures "Kon. Inst. v. Ingenieurs", no. 41, 1951.
MP. 73:	v. d. Vooren, A. I.	Generalization of the Theodorsen function to stable oscillations. J. Aero. Sci., Vol. 19, no. 3, March 1952.
MP. 76:	Erdmann, S. F.	Experimental research in the transsonic and supersonic range. "De Ingenieur", Vol. 64, 1 Aug. 1952.
MP. 77:	Timman, R., Greidanus, J. H. and v. d. Vooren, A. I.	Aerodynamic coefficients of an oscillating airfoil in two-dimensional subsonic flow. A reply to Mr Fettis' Comments. J. Aero. Sci. 19, Nov. 1952.
MP. 79:	v. d. Vooren, A. I.	Theory of the Erdmann interferometer for investigation of compressible flows. Appl. Sci. Res. A.3, Dec. 1952.

C. C. L. Class. D 93: D 94: D 24: D 25

CAM
ACF

REPORT A. 1241.

Methods for Windtunnel Measurements on Models of Vehicles, Vessels and Constructions

by

A. DE LATHOUDER.

Contents.

1 General considerations concerning the mounting of the models.

Carrying out measurements in the windtunnel to determine the aerodynamic forces acting on vehicles, vessels or constructions, we distinguish objects which are either moving or at rest with respect to the ground or any other supporting plane. The plane mentioned has to be represented in the windtunnel by installing a flat plate. In several cases the influence of the supporting plane, such as the road for a motor-car and the water-level for a ship, may be imitated in a sufficiently exact way by applying a dummy or image-model, so that it will not be necessary to install the plate referred to in the tunnel.

The supporting plane (further also called "base plate") being installed in the tunnel, it will depend on the kind of the measurements and the model, whether the model has to be fixed to the plate or not. For carrying out pressure-distribution measurements there is, from the point of view of measuring technics, no objection to fix the model to the supporting plane in case model and plate do not move with respect to one another. In this report we will not enter into the pressure measurements, but consider the case of force measurements which are as a rule less simple. The mounting of the model can be carried out in the following ways:

a fixed to the base plate,
b free from the base plate.

In case *a* one can fix the base plate to the balances with wires or rods, but this should be done in such a way, that these suspension-parts do not give a disturbing influence on the model. The model forces are then determined as a difference between measurements of the plate with and without the model being fastened to it. This method is however only recommendable if the mutual influence between plate and model is small or anyhow if it can be determined easily. A further condition is that the model forces are not too small with respect to the aerodynamic forces acting on base plate and model as a whole. This method is for instance preferable in case of measuring a number of similar models in succession. The models can be mounted on the base plate successively, in order to avoid suspending each model separately to the balances. Further, this way of measuring will be called the method "plate with and without model".

In case *b* the model itself is suspended to the balance whereas the base plate is fixed separately to the bottom of the tunnel. Then the model forces are determined from the difference between the measurements of the suspension-parts, such as wires or rods, both with and without the model. Using a well chosen wire suspension, the mutual influence between model and wires will in general be small. Often, this method is preferred to the way of mounting and measuring, mentioned under *a*. The way of measuring models, being mounted separately from the plate, is called the method "model without plate".

With regard to the model measurements here mentioned, one has to consider first, whether the body to be examined moves with respect to the supporting plane or not on full scale.

If the object does not move (for instance a building or a floating dock) and one has to deal with the case of forces as a result of the natural wind only, the ground (water-level) has to be imitated by a plate *at rest*, consequently not

moving with respect to the model. The plate has to achieve the right variation of the wind velocity as a function of the height above the ground. As a result of the restricted length of the base plate, the slowing down of the airflow along the plate will often be too small. Therefore, if required, one can use a retouch or smoothing screen, which has to be placed upstream of the model in order to obtain the right distribution of the wind velocity above the ground. In chapter 3 we will enter further into the mounting of bodies at rest.

The other case is that where the object does move with respect to the supporting plane (a car, train, ship). Leaving the natural wind out of consideration, the base plate and the air in the tunnel have to *move* with the same velocity with respect to the model. Then, in accordance with the fullscale situation, the same velocity distribution with respect to the model occurs in every point in front of the model. Going against or down the wind, the base plate velocity has to be slowed down or accelerated in the right proportion to the air velocity in the tunnel, to imitate the velocity of the natural wind varying with the distance to the ground. As the construction of the moving base plate leads to a rather complicated mounting, this fundamentally correct method is usually replaced by approximate methods, where the model is either suspended above (eventually attached to) a plate at rest or built together with an image model, thus forming a double-model. In the following, the designation "plane of symmetry" will be used for the hypothetical supporting plane, which is supposed to lie between the bottoms of the two parts of a double-model. Chapter 2 goes into the subject of the moving objects.

Apart from the question whether the body moves with respect to the supporting plane, one has to distinguish between objects which touch the supporting plane in some points only (wheels of a car or train, supporting points of an open frame-work construction) and bodies which contact the supporting plane fully (base of a building, water-line of a ship). In the first case there will be an air flow between the object and the ground which of course will be present on model-scale too. In the second case there is no air flow along the bottom of the body, so on model scale no flow is permitted between model and base plate. The slit between model and plate has to be sealed for instance with a labyrinth seal, in case of measuring the model free from the plate. Of course there are other methods to avoid "slit flow", for instance by connecting model and plate to each other by means of a flexible rubber strip.

Fig. 1. Mountings for objects which are moving with respect to the ground.

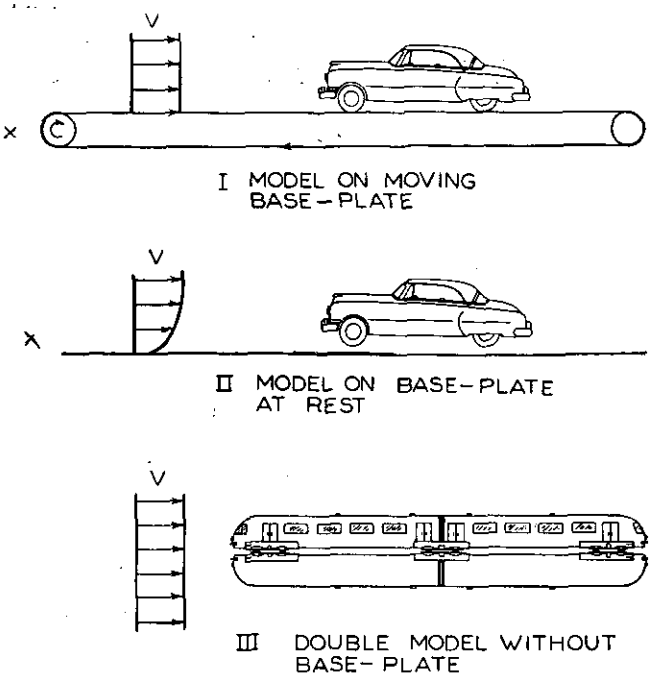

Situation *with* flow between model and supporting-plane.

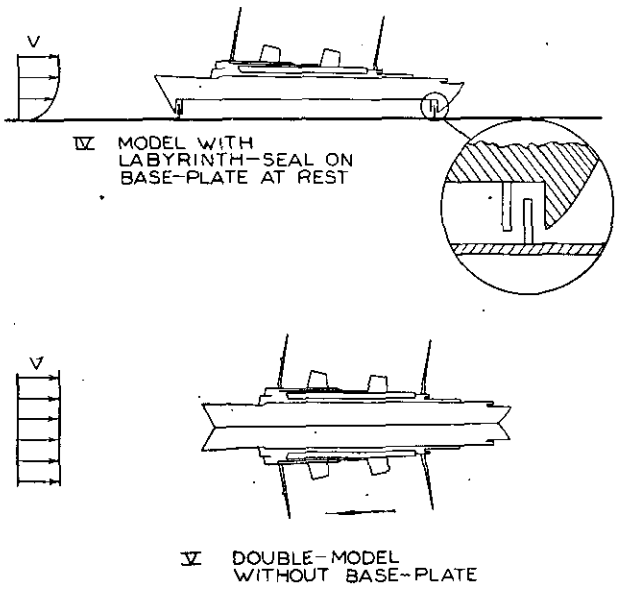

Situation *without* flow between model and supporting-plane.

2 Models of objects which are moving with respect to the ground (see fig. 1).

2.1 *Situation with flow between model and supporting plane.*

In fig. 1a the following three mountings are given for objects belonging to this category.

I The base plate exists of a moving conveyor which can be adjusted at the right velocity for conditions either with or without wind. Applying this method it will be possible to get a nearly correct velocity distribution in front of the model, but a rather complicated special apparatus is required. This method is recommendable if this type of measurements is carried out regularly (for instance for automobile works).

II In this case the base plate does not move with respect to the model. The wind is slowed

down in the neighbourhood of the plate and the velocity distribution in front of the model is no more constant. However, if the model represents a situation without natural wind, the velocity in front of the model has to be constant and equal the moving speed of the object on model-scale. So, in this case we have to reckon with an error in the velocity distribution. Applying a small base plate which extends just a short distance upstream of the model, this error can be kept within reasonable limits. Measuring a situation of head wind (then the natural wind is slowed down along the ground), it will be clear that some slackening action of the base plate is desirable. Apart from that it will always be possible to correct the velocity distribution upstream by artificial means (for instance with a screen). Making use of this method, the results will mostly be sufficiently accurate, even without special means to correct the flow. In this connection one has to consider that a limit is already put to the accuracy for other reasons, such as the influence of Reynolds number and suspension-parts. If no special precautions are taken, the measured resistance is somewhat lower than the real resistance, as a result of the slowed down air stream along the lowest parts of the model. This statement, of course, only holds in case there is no natural wind, for otherwise the air has just to be slackened more or less in the neighbourhood of the plate, as stated before.

As noticed already in chapter 1 the measurement itself could be done by measuring the plate both with and without model. Attention is drawn to the necessity of imitating the influence of the model on the plate, during the measurement of the plate without model. Therefore the model is not taken away, but removed slightly upwards from the base plate, in order to measure the plate, being just free from the model.

III In case a double-model is applied, the slowing down influence of the base plate on the air moving along its surface will be eliminated. The condition, prescribing a flow pattern where no velocity components perpendicular to the supporting plane occur, is satisfied with a good approximation by the presence of the plane of symmetry of the double-model which replaces the base plate in this respect. Considering a situation without natural wind, this method gives an improvement with respect to the method mentioned under II, because of the constant velocity distribution in front of the model. Here too, however, the flow in the plane of symmetry between model and image is slowed down more than in reality. In case II the relative velocity on ground level (with respect to the vehicle) was zero both in front and at the back of the model. In case III the relative velocity in the plane of symmetry (hypothetical base plane) is correct in front of the model, but too small at the rear of the model. This can be seen at once, considering that a correct representation of the full-scale situation can be achieved only by moving the base plate back in the plane of symmetry between the two models with a speed equal to the driving velocity of the vehicle. Then the full driving velocity with respect to the model does not exist in front of the model only, but also behind the model in the plane of symmetry. In case III this velocity is so much slowed down by friction along the bottom and the projecting parts of model and dummy model, that it will have but a low value, especially behind long models having a narrow slit in between. So in general, one can expect here too the measured resistance coefficient to be somewhat smaller than the full-scale drag coefficient, though the difference will be smaller than in case II. It may be stated here that the Reynolds number mostly has an opposite influence on the drag coefficient, which might compensate the differences more or less.

Concerning the flow in the plane of symmetry it may be pointed out that acute angled projecting parts at the bottom of a vehicle, causing separation of the flow, often form periodically detached vortices which go through the plane of symmetry. Of course this will not take place on full scale because of the presence of the supporting plane, such as road, railroad, etc. This difficulty makes itself felt to a smaller extent as the parts in the neighbourhood of the ground are better streamlined. In case the phenomenon should be troublesome (vibrations), it might be helpfull to mount locally (i. e. at the spot where the vortices occur) a small thin plate in the plane of symmetry.

Only, if forces and moments parallel to the plane of symmetry have to be measured, it will be allowed to connect the models immovably. If it is, however, necessary to determine the centre of the aerodynamic forces above the ground or forces perpendicular to the ground, one model has to be fixed to the balances, whereas the image model has to be fixed in the tunnel.

2.2 *Situation without flow between model and supporting plane.*

If there is now flow between the object and supporting plane, such as in case of a ship, it will be clear that slits between model and supporting plane or in the plane of symmetry must be avoided on model-scale too. Two usual ways of mounting the models are given in fig. 1b, IV and V.

IV Using a base plate for measurements without natural wind, the difficulty of the slowed down flow in the neighbourhood of the water-level arises here too. However, the error will be smaller than in case II, for the slit flow, being too slow and therefore responsible for the greater part of the difference, does not exist here.

A labyrinth seal provides for the sealing of the clearance between model and plate. With regard to the question whether the measurement has to be carried out either "with and without" or "without", the model being fixed to the plate, the following remarks can be made. At first sight there might be some preference to measure the

"plate with and without model", to avoid the labyrinth seal which would in any case be necessary for the method "model without plate". But if one would determine the model forces for case IV by measuring the plate both "with and without model", yet it would be necessary to mount the model in the latter case (measuring the plate without model) with a labyrinth seal above the plate in order to imitate correctly the influence of the model on the plate. From this it is evident that a labyrinth seal which is the very thing that asks for the greatest attention, cannot be avoided by applying mounting IV, the model being measured either separately or in combination with the plate.

In order to ascertain undesirable contacts in the labyrinth seal, this can be made of brass strip which forms part of an electrical circuit, giving a signal in case of contact.

For ships the resistance of the natural wind often contributes to a large extent to the total air resistance. In that case there is an advantage in using a base plate, as the velocity distribution in front of the model will be in better accordance with the reality as a result of the presence of the plate.

V To avoid the difficulties of mountings having a labyrinth seal (compare with case III), a double-model can be applied. Considering a condition of calm weather, the right velocity will occur in front of the model. Since we have nothing to do with (incorrect) flow through slits and no periodically detached vortices can be expected in case of good streamlining, this method may be recommended. The influence of the natural wind can eventually be imitated by mounting a free plate in the plane of symmetry in front of the model.

Here too, the models have to be mounted separately if one wants to determine for instance the height of the centre of the aerodynamic forces above the water-level. But then there will of course be the difficulty of the labyrinth seal between model and image model.

3 Models of objects which are at rest with respect to the ground (see fig. 2).

3.1 *Situation with flow between model and supporting plane.*

For objects at rest a base plate has to be applied to obtain the disired velocity distribution of the natural wind.

VI If there is an air flow between the object and the supporting plane (see fig. 2a), the model can be measured in a simple way by suspending it just free from the base plate to the balances. If there is any preference to do so for some reason (for instance to measure a number of models), the method of measuring the "plate both with and without model" can be applied just like in case II.

Fig. 2. Mountings for objects which are at rest with respect to the ground.

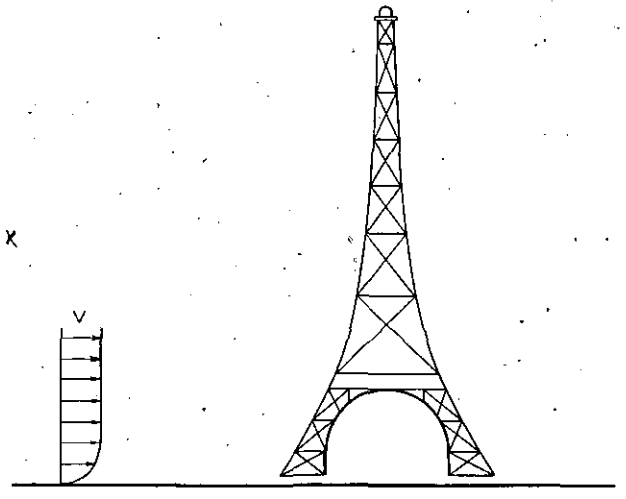

Situation *with* flow between model and supporting-plane.

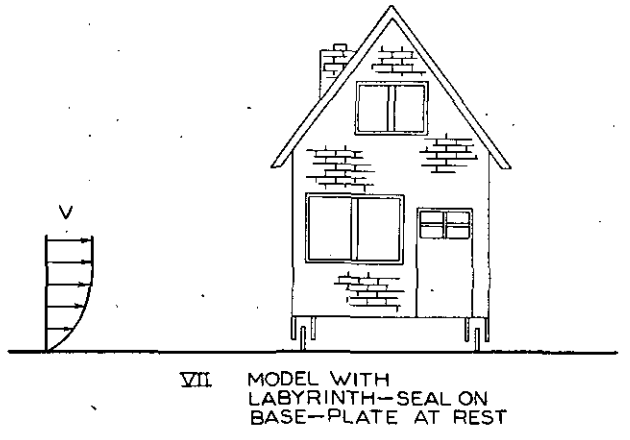

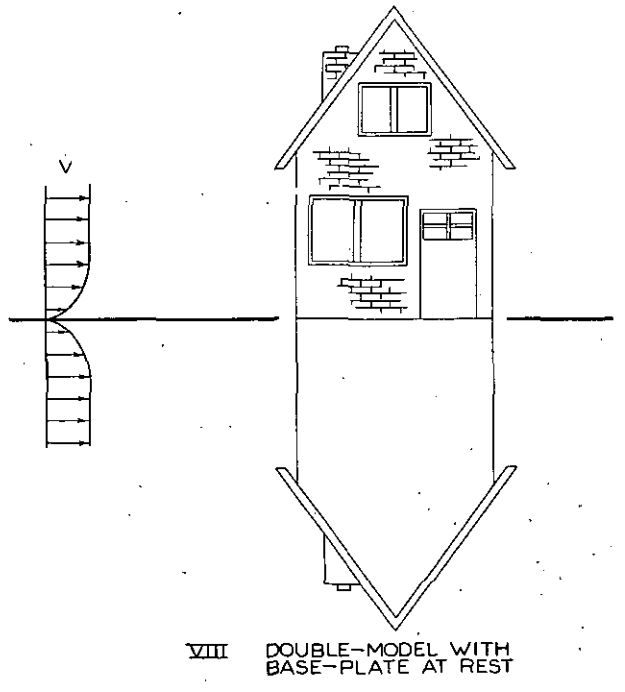

Situation *without* flow between model and supporting-plane.

3.2 *Situation without flow between model and supporting plane.*

In this case too a base plate is applied, but here we encounter the complication to prevent the air from flowing through a slit between model and base plate (see fig. 2b). Therefore we use either a model with labyrinth seal (VII) or a double-model (VIII).

VII In order to reduce the slit flow as much as possible, the space between model and plate has to be sealed with a labyrinth seal.

VIII In many cases, it will be possible to avoid the application of a labyrinth seal by making use of a double-model. The base plate (provided with a gap) is located in the plane of symmetry, but is mounted free from the model. In this case too, the model could be fixed to the plate if there is any preference to follow the method of measuring the "plate with and without the model".

4 Conclusion and summary.

It is not possible to give a clear-cut scheme which is generally holding for the application of measuring methods for windtunnel research on models of vehicles, vessels, constructions etc. The choice of the mounting depends among other things on the answer to the following questions:

a Does the object on full scale move with respect to the supporting plane?

b Does the object touch the supporting plane in some points only (car: slit flow), or does it make full contact with this plane (ship: no slit)?

c Are there certain advantages in measuring the base plate together with the model (model forces not too small with respect to the aerodynamic forces acting on the plate, a number of models or model configurations)?

d Has a high accuracy to be pursued?

A general view is given of a number of useful methods, classified according to the conditions mentioned under *a* and *b*. The advantages and disadvantages of the various methods are considered. At the same time items *c* and *d* are raised, so far as this might be of any importance.

Completed: November 1950.

REPORT A. 1210.

On the Determination of the Transition Point from Measurements of the Static Pressure along a Surface

by

Drs H. WIJKER.

Summary.

In this report a calculation has been carried out of the difference $p(\delta) - p(0)$ between the static pressure at the edge of the boundary layer and at the surface of a flat plate, placed at zero angle of attack in a parallel flow, for the laminar as well as for the turbulent boundary layer. These calculations can make clear the apparent discrepancy between the experimental results of FAGE and PFENNIGER both using a corner point in the pressure distribution along the surface for the determination of the transition point. It has been made evident, that this method is not always suitable for the determination of the transition point.

In connection with these calculations it has been shown (see appendix III) that the law of resistance of the turbulent boundary layer, given by FALKNER, has to be preferred to PRANDTL's one, for the latter has been derived with the aid of an inaccurate supposition. Then it appears, that objections, raised against the condition $\delta_2 =$ constant at transition, are not valid any longer.

Contents.

1 Introduction.

In 1928 FAGE (Ref. 1) perceived a *corner point* in the p-s-line (fig. 1a) when doing pressure measurements on a circular cylinder ($p =$ static pressure, $s =$ distance to the stagnation point measured along the surface). Later measurements (Ref. 2, 3) confirmed this. FAGE pointed out, that this corner point should indicate the transition point. PFENNIGER also used this method for determining the transition point (Ref. 4). However the deflection in the p-s-line he found (fig. 1b) is just to the other side as that found by FAGE. In this article the author wishes to

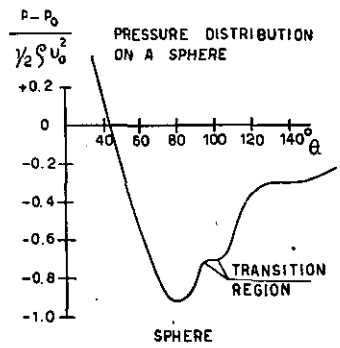

Fig. 1a (from ref. 3)

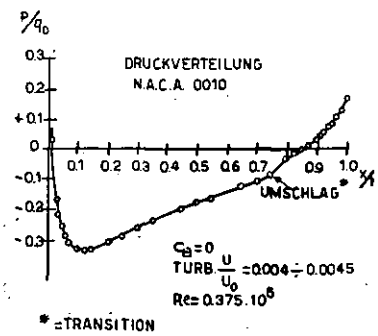

Fig. 1b (from ref. 4)

show, theoretically, that both the measurements of FAGE and PFENNIGER may be correct: the p-s-line may deflect to one side or the other depending on the circumstances. Only the simplified case of a flat plate placed with zero angle of attack in an

incompressible parallel flow will be considered and it will be shown that in this case the direction of the deflection only depends on the REYNOLDS number of the transition point. The author has not tried to solve the problem for other cases: these are much more complicated and the author does not expect them to give new points of view.

2 The pressure difference across the laminar boundary layer.

The equations of continuity and of motion for stationary flow in the laminar boundary layer (Ref. 5, p. 81), may be written as follows:

$$u_x + v_y = 0 \qquad (2.1a)$$

$$uu_x + vu_y = -p_x + \alpha u_{xx} + \alpha u_{yy} \qquad (2.2a)$$

$$uv_x + vv_y = -p_y + \alpha v_{xx} + \alpha v_{yy} \qquad (2.3a)$$

where $u = U/U_\infty$, $v = V/U_\infty$, $p = P/\rho U_\infty^2$, $\alpha = \nu/U_\infty$; U = velocity-component parallel to the plate, V ditto normal to the plate, U_∞ = the velocity of the undisturbed flow, P = static pressure, ρ = density and ν = kinematic viscosity. A suffix denotes partial derivation. Following PRANDTL, the second terms of the right hand sides of the equations (2.2a) and (2.3a) may be neglected in the boundary layer, for they are small compared with the other terms.

Moreover p_x is supposed to be zero in our problem so that the equations can be simplified to

$$u_x + v_y = 0 \qquad (2.1b)$$

$$uu_x + vu_y = \alpha u_{yy} \qquad (2.2b)$$

$$uv_x + vv_y = -p_y + \alpha v_{yy} \qquad (2.3b)$$

From (2.1b) and (2.2b) one can find the approximate values of u and v in the well known way. Using these values in (2.3b) one can calculate p_y and by integrating one gets the pressure profile in the direction normal to the surface.

All terms of (2.3b) are very small compared with the terms of the other equations and therefore usually neglected. In our case, however, we have to take (2.3b) into consideration, for the very cause of the corner point in the p-s-line is the difference between the pressure profiles of the laminar and the turbulent boundary layers. As p, found in this way, will be a function of both x and y, p_x will not be zero as assumed beforehand. The variations in p however will be so small, that the values of u and v, calculated from (2.1b) and (2.2b), will be very good approximations. It seems not necessary to recalculate them and to use the new values in (2.3b) in order to get a better approximation of p.

Introducing $Re_x = xU_\infty/\nu$ *), $z = Re_x^{1/2}\, y/x$, the solution of (2.1b) and (2.2b) is (Ref. 5, p. 85) $u = f_z$, $v = \frac{1}{2} Re_x^{-1/2}\,(zf_z - f)$ where f is the solution of the differential equation $2f_{zzz} + ff_{zz} = 0$ with the boundary conditions $f(0) = 0$, $f_z(0) = 0$ and $f_z(\infty) = 1$.

*) A suffix of Re does not denote partial derivation, but the length which Re is related to.

f may be written in the form (Ref. 5, p. 87) $f = z - \beta + \varphi(z)$ in which $\varphi(\infty) = 0$, $\varphi_z(\infty) = 0$ and $\lim_{z\to\infty} z^n\varphi_z = 0$ for arbitrary n, $\beta = Re_{\delta_1}/Re_x^{1/2} = 1.73$ (Ref. 5, p. 89),

$$Re_{\delta_1} = \delta_1 U_\infty/\nu, \qquad \delta_1 = \int_0^\infty (1-u)\,dy.$$

Integrating (2.3b) from $y = 0$ to $y = \infty$ one gets

$$p(\infty) - p(0) = -\int_0^\infty uv_x dy - \tfrac{1}{2} v^2(\infty) + \alpha v_y(\infty)$$

and as computation carried out in appendix I gives $v(\infty) = \frac{1}{2}\beta\, Re_x^{-1/2}$,

$$v_y(\infty) = 0$$

and

$$-\int_0^\infty uv_x dy = \tfrac{1}{8}\, Re_x^{-1} \lim_{z\to\infty} .\, \beta\,(2z - \beta)$$

we can write

$$p(\infty) - p(0) = \tfrac{1}{4}\, Re_x^{-1}\,(-\beta^2 + \beta \lim_{z\to\infty} .\, z) =$$

$$= -0.75\, Re_x^{-1} + 0.43\, Re_x^{-1} \lim_{z\to\infty} .\, z = \infty .$$

This result, surprising at first sight, can be explained as follows: the stream lines are bent towards the plate, as known. This means, that the flow direction of the mass between two streamlines changes. Therefore a pressure gradient in y-direction is indispensable.

As in the outlines, commonly used in the boundary layer theory, the mass of the bulk of flow to be changed is infinite, one needs an infinite pressure difference. In these outlines namely $v(\infty) \neq 0$ as is the case in reality.

For our purpose, the exact solution of the boundary layer equations cannot be used and we shall use the well known approximate solutions found with the method of VON KÁRMÁN, POHLHAUSEN and others, in which method is introduced a boundary layer thickness δ well defined by the impuls equation of the boundary layer

$$\frac{d}{dx}\int_0^\delta U^2 dy - U_\infty \frac{d}{dx}\int_0^\delta U dy =$$

$$-\frac{\delta}{\rho}\,\frac{dP}{dx} - \nu\left(\frac{dU}{dy}\right)_{y=0}$$

or ,as in our case $dP/dx = 0$

$$(\overline{u^2} - \overline{u})\,\delta_x = -\alpha u_y(0) \qquad (2.4)$$

with $\overline{u^2} = \int_0^1 u^2 d\eta$, $\overline{u} = \int_0^1 u\, d\eta$ and $\eta = y/\delta$.

Introducing the new independent variables η and δ instead of x and y with the aid of the equations $\delta = \delta(x)$ and $\eta = y/\delta$, one gets

$$dy = \eta d\delta + \delta d\eta \qquad (2.5a)$$

and equation (2.4) can be written (see appendix II)

$$dx = B\delta d\delta \text{ with } B = (\bar{u} - \bar{u^2})/\alpha u_\eta(0) \quad (2.5b)$$

In the new coordinates, the continuity equation can be written as (see appendix II for calculations)

$$v_\eta = \eta u_\eta / B\delta. \quad (2.6)$$

v can be found by integrating (2.6) and can be substituted in equation (2.7), derived from (2.3b) by integrating:

$$p(\delta) - p(0) = = -\int_0^\delta uv_x dy - \tfrac{1}{2} v^2(\delta) + \alpha v_y(\delta) \quad (2.7)$$

Introducing the momentum thickness $\delta_2 = (\bar{u} - \bar{u^2})\delta$, so that $Re_{\delta_2} = (\bar{u} - \bar{u^2}) Re_\delta$, (2.8a) becomes

$$\Delta_l p = Re_{\delta_2}^{-2} [u_\eta^2(0) \,.\, (\bar{u} - \bar{u^2}) + + u_\eta(0) \,.\, u_\eta(1) \,.\, (\bar{u} - \bar{u^2})] \,. \quad (2.8c)$$

Results of calculations for several velocity profiles are given in table 1. For all chosen profiles $u_\eta(1) = 0$ except for the roughest approximation $u = \eta$. Though the agreement of the results of the approximate velocity profiles is not very good, it is sufficient for our purposes. An impression of the accuracy of the approximate method by comparison with the exact one, may be got from the last column, in which $Re_x \{ p(0) - p_a(0) \}$ is given.

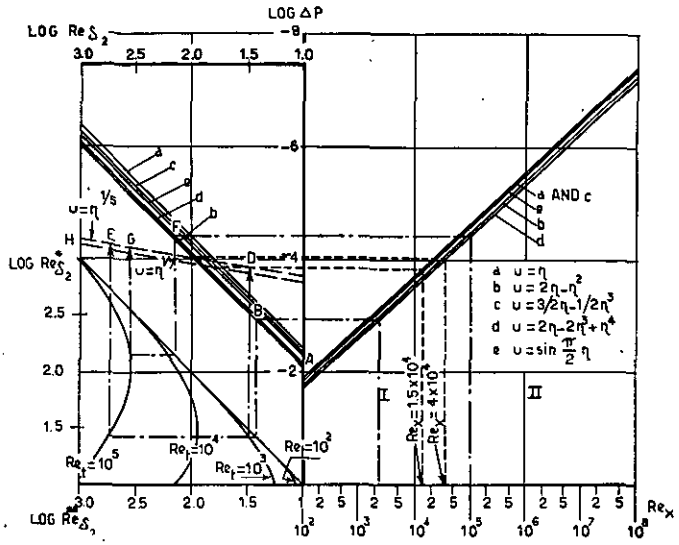

Fig. 2

I Transition starts at $Re_x = 2.3 \times 10^5$. For $Re_t = 10^3$, the pressure follows the line *ABDII* (sharp bend upwards), for $Re_t = 10^5$ the line *ABEII* (gradual bend, from which the determination of the transition region is very inaccurate if not impossible).

II Transition starts at $Re_x = 10^6$; $Re_t = 10^5$. The pressure follows the line *AFGII* (bend downwards).

After substitution of the coordinates δ and η, (2.7) will give

$$\Delta_l p = p(\delta) - p(0) = \doteq Re_\delta^{-2} [u_\eta^2(0) \,.\, \{\bar{u} - \bar{u^2}\}^{-2} \{\bar{u} - \bar{u}^2\} + + u_\eta(0) \,.\, u_\eta(1) \,.\, \{\bar{u} - \bar{u^2}\}^{-1}] \,. \quad (2.8a)$$

The suffix l indicates "laminar".

From (2.4):

$$(\bar{u} - \bar{u^2}) d\, Re_\delta / d\, Re_x = + u_\eta(0)/Re_\delta$$

or

$$(\bar{u} - \bar{u^2})\, Re_\delta^2 = 2\, u_\eta(0) \,.\, Re_x$$

so that in the coordinates Re_x and η equation (2.8a) can be written as

$$\Delta_l p = Re_x^{-1} [\tfrac{1}{2} u_\eta(0) \,.\, (\bar{u} - \bar{u^2})^{-1} (\bar{u} - \bar{u}^2) + + \tfrac{1}{2} u_\eta(1)]. \quad (2.8b)$$

$p_a(0)$ is the pressure indicated by the point where the asymptote intersects the p-axis (see appendix I).

The linear connection between $\log \Delta_l p$ and $\log Re_{\delta_2}$ is given in fig. 2 as well as that between $\log \Delta_l p$ and $\log Re_x$.

3 The pressure difference across the turbulent boundary layer.

Choosing again from experiments an adequate velocity profile $u = u(\eta)$, v can be calculated with the help of the equations

$$u_x + v_y = 0 \quad \text{(equation of continuity)}, \quad (3.1)$$

$$(\bar{u} - \bar{u^2})\delta_x = \tau(0) \quad \text{(impuls equation)}. \quad (3.2)$$

$\tau(0)$ is defined by $\tau(0) = T(0)/\rho U_\infty^2$ in which $T(0)$, the shearing stress for $y = 0$, is known from experiments. In the case of a wholly turbulent boundary layer $\tau(0)$ can be written in the form

$$\tau(0) = A\, Re_x^m \quad (3.3)$$

in which A and m are constants and X denotes the distance from the stagnation point to the considered point in a boundary layer, turbulent from the very beginning.

In the case of a boundary layer flow partly laminar, partly turbulent, Re_X can, if required, be expressed in Re_x and $Re_{x,tr}$, the REYNOLDS number of the transition point (see appendix III).

Once v is known, p can be calculated from an equation, analogical to (2.3b), namely (Ref. 6, p. 610)

$$uv_x + vv_y = -p_y + \\ + \alpha v_{yy} - \overline{(\Delta u \,.\, \Delta v)}_x - \overline{(\Delta v \,.\, \Delta v)}_y \,, \quad (3.5)$$

in which Δu and Δv are fluctuations of u and v and the bars denote mean values in time.

In the turbulent boundary layer the molecular contribution to the shearing stress can be neglected compared with the convectional contribution:

$$\tau = -\overline{\Delta u \,.\, \Delta v}. \quad (3.6)$$

For τ we can use the formula of FEDIAEVSKY (Ref. 7), for $p_x = 0$ well confirmed by the experiments of DRYDEN (Ref. 8, fig. 11)

$$\tau/\tau(0) = 1 - 4\,\eta^3 + 3\,\eta^4. \quad (3.7)$$

Calculations, carried out in appendix IV, give the formula

$$\Delta_t p = 0.1\, A^2 (\overline{u} - \overline{u^2})^{-2} \{ 10(\mu - 1)\overline{\eta u^2} + \\ 6(\mu - 1)\overline{u^2} - 5(\mu + 1)\overline{u}^2 + (16 - 6\,\mu)\overline{u} \}\, Re_X^{2m} \quad (3.8)$$

with $\mu = -m/(m+1)$.

The suffix "t" denotes "turbulent".

$\Delta_t p$ can be connected with the momentum thickness of the boundary layer $\delta_2 = (\overline{u} - \overline{u^2})\delta$ or with Re_{δ_2} instead of with Re_X:

$$\Delta_t p = 0.1(m+1)^{-2\mu} A^{2(1+\mu)} (\overline{u} - \overline{u^2})^{-2} \cdot \\ \{ 10(\mu - 1)\overline{\eta u^2} + 6(\mu - 1)\overline{u^2} - 5(\mu + 1)\overline{u}^2 + \\ + (16 - 6\,\mu)\overline{u} \}\, Re_{\delta_2}^{-2\mu}. \quad (3.9)$$

The velocity profile can approximately be written in the form

$$u = \eta^{1/N} \quad (3.10)$$

so that (3.9) becomes

$$\Delta_t p = (m+1)^{-2\mu} A^{2(1+\mu)} Re_{\delta_2}^{-2\mu} (N+2) \cdot \\ \{ 11\,N + 16 - (N-4)\mu \}/N. \quad (3.11)$$

According to FALKNER $A = 0.0131$ and $m = -1/7$ (see also the discussion in appendix III). As for N, some investigators assume $N = 7$, others $N = 5$ (see the discussion in appendix III).

With the given values of A and m, (3.11) becomes

$$\Delta_t p = 0.00051\, Re_{\delta_2}^{-1/3} \text{ for } N = 7$$

and

$$\Delta_t p = 0.00042\, Re_{\delta_2}^{-1/3} \text{ for } N = 5.$$

In fig. 2 the linear connection between $\log \Delta_t p$ and $\log Re_{\delta_2}$ is given for both cases.

4 The pressure difference connected with transition; conclusions.

Assuming, that the laminar velocity profile suddenly changes into the turbulent one in a definite point, the transition point, with $x = x_{tr}$, $\log \Delta p$ will, independently of the chosen velocity profiles, decrease for $\log Re_{\delta_2,tr} < 1.75$ and increase for $\log Re_{\delta_2,tr} > 2.0$ (see fig. 2), as δ_2 will be the same in the transition point both for the laminar and the turbulent velocity profile (see appendix III).

According to fig. 2 the values $Re_{\delta_2} = 1.75$ and 2.0 agree with the values $Re_x = 1.5 \times 10^4$ and 4×10^4.

As $p(0) = p(\delta) - \Delta p$ and we assumed *), that the pressure outside the boundary layer is constant $= p(\delta)$, we can draw the following conclusion:

The pressure on the wall just behind the transition point will be lower than that just before it, if transition takes place in a point with $R_{x,tr} > 4 \times 10^4$, and it will be higher, if $Re_{x,tr} < 1.5 \times 10^4$.

The value of x_{tr} depends on the turbulence of the bulk of the stream; it is smaller if the turbulence is greater. In reality transition does not take place suddenly in one point, but in a region, so that we can conclude:

Depending on the turbulence of the bulk of the stream the p-x-line will bend either upwards or downwards in the transition region.

However the length of the transition region plays some part in this phenomenon. If the length t of the transition region is given and $\tau(0)$ in this region as well, it is possible to calculate Re_{δ_2} at the end of the region (which will be indicated as $Re_{\delta_2}^{**}$) for a given value of Re_{δ_2} at the beginning of it (indicated as $Re_{\delta_2}^{*}$).

These calculations have been carried out in appendix III and the results are given in the graph down at the left of fig. 2. The use of this graph can be explained with the following example.

Transition may start at $Re_x = 2.3 \times 10^5$ and the REYNOLDS number, based on the length t, will be $Re_t = 10^3$. Using lines "d" of fig. 2 for the laminar flow, $\log \Delta p$ is known at the beginning of the transition (see line I), and consequently $\log Re_{\delta_2}$ (see point B). The vertical line through B intersects the 135°-line in the point for which the ordinate equals $\log Re_{\delta_2}^{*}$ $(= \log Re_{\delta_2}$ for $B)$.

From this point going to the left till the line for $Re_t = 10^3$, we find $\log Re_{\delta_2}^{**}$, and the vertical line gives the point D, the ordinate of which is $\log \Delta p$ at the end of the transition region. So $\log \Delta p$ follows the line $ABDH$ and the p-x-line will have the same character.

In fig. 2 more examples are given, from which may be seen, that the p-x-line may bend down-

*) Some remarks on this assumption are given at the end of appendix III.

wards, sharply upwards or will not show any marked transition.

The same may be expected if $p_x \neq 0$; for the essential part of the discussion is the difference of the slopes of the log Re_{δ_2} - log Δp-lines in fig. 2 for the laminar and the turbulent boundary layer and this is caused by the different values of the exponent in the expression $\tau(0) = A\, Re_x^m$. Therefore the method of determining the transition point from the p-x-line seems to be somewhat inadequate: there will exist cases in which it cannot be used at all.

5 Nomenclature.

A = constant in eq. $\tau(0) = A\, Re_x^m$

B = $(\overline{u} - \overline{u^2})/\alpha\, u_\eta(0)$

C = $A^{-1-\mu}(m+1)^\mu (\overline{u} - \overline{u^2})^{1+\mu} \alpha^{-\mu}$

c_D = local drag coefficient $(T(0)/\frac{1}{2}\rho U_\infty^2)$

C_D = drag coefficient $\left(= \frac{1}{L}\int_0^L c_D dX\right)$

D = $C\alpha^\mu$

L = length of a plate

m = exponent in $\tau(0) = A\, Re_x^m$

n = exponent in $u = \eta^n$

N = $1/n$

P = pressure

p = $P/\rho\, U_\infty^2$

Δp = $p(\delta) - p(0)$

Re = Reynolds number

s = distance to the stagnation point, measured along the surface

t = length of the transition region

T = shearing stress

U = velocity component parallel to the plate

U_∞ = velocity of the undisturbed flow

u = U/U_∞

$\overline{u}$ = $\int_0^1 u\, d\eta$

Δu = fluctuation of u

$\overline{\Delta u \,.\, \Delta v}$ = average in time of the product of the fluctuations Δu and Δv

V = velocity component normal to the plate

v = V/U_∞

Δv = fluctuation of v

x = abscis; distance from a point of the plate to the leading edge

X = x for a shortened plate with a wholly turbulent boundary layer

y = ordinate; distance from a point to the plate

z = $Re_x^{1/2} y/x$

α = ν/U_∞

δ = boundary layer thickness

δ_1 = displacement thickness = $\int_0^\infty (1-u)dy$

δ_2 = momentum thickness = $\int_0^\infty u(1-u)dy$

η = y/δ

μ = $-m/(m+1)$

ν = kinematic viscosity

ρ = density

τ = $T/\rho\, U_\infty^2$

Indices: a = asymptote
l = laminar
t = turbulent, except in Re_t (see below)
tr = transition

The other indices denote either partial derivations or lengths (if used for Re).

Asterisks:
one asterisk indicates: at the beginning of the transition region
two asterisks indicate: at the end of the transition region.

6 References.

1. Fage, A. The Airflow around a Circular Cylinder in the Region where the Boundary Layer separates from the Surface. A. R. C. Rep. and Mem. 1179.
2. Fage, A. and Falkner, V. M. The Flow around a Circular Cylinder. A. R. C. Rep. and Mem. 1369.
3. Fage, A. Experiments on a Sphere at Critical Reynolds Numbers. A. R. C. Rep. and Mem. 1766.
4. Pfenniger, W. Untersuchungen über Reibungsverminderungen an Tragflügeln, ins besondere mit Hilfe von Grenzschichtabsaugung. Mitt. Inst. f. Aerod., Eidg. Techn. Hochschule, Zürich, nr. 13.
5. Durand, W. F. Aerodynamic Theory Vol. III (Julius Springer, 1935).
6. Bairstow, L. Applied Aerodynamics (1939).
7. Fediaevsky, K. Turbulent Boundary Layer of an Aerofoil. J. Aer. Sci. 1937, p. 491.
8. Dryden, H. L. Some Recent Contributions to the Study of Transition and Turbulent Boundary Layers. N. A. C. A. Techn. Note 1168.
9. Wieselsberger, C. Untersuchungen über den Reibungswiderstand von stoffbespannten Flächen. Ergebn. Aerod. Versuchsanst. Göttingen, I. 1921, p. 121.
10. Prandtl, L. *Ueber den Reibungswiderstand strömender Luft.* Ergebn. Aerod. Versuchsanst. Göttingen, III, 1927, p. 1.
11. Goldstein, S. Modern Developments in Fluid Dynamics (Oxford 1938).
12. Hegge Zijnen, B. G. van der. Measurements of the Velocity Distribution in the Boundary Layer along a Plane Surface. Mededeling no. 6, Thesis, Delft, 1924.
13. Kármán, Th. v. Ueber laminare und turbulente Reibung. Zeitschr. f. Angew. Math. und Mech. 1921, p. 233.
14. Hansen, M. Die Geschwindigkeitsverteilung in der Grenzschicht an einer eingetauchten Platte. Abh. Aerod. Inst. Techn. Hochschule Aachen, Heft 8, 1928, p. 31.
15. Falkner, V. M. A New Law for Calculating Drag. Aircraft Eng. 1943, p. 65.
16. Squire, H. B. and Young, A. D. The Calculation of the Profile Drag of Aerofoils. A. R. C. Rep. and Mem. 1838.
17. Pretsch, J. Zur theoretischen Berechnung des Profilwiderstandes. Jahrb. d. Deutschen Luftfahrtforschung 1938, I, p. 60.
18. Helmbold, H. B. Zur Berechnung des Profilwiderstandes. Ing. Archiv XVII, 4, 1949, p. 273.
19. Pohlhausen, K. Zur naherungsweisen Integration der Differentialgleichung der laminaren Grenzschicht. Zeitschrift f. Angew. Math. und Mech. 1921, p. 252.
20. Lamb, H. Hydrodynamics (Cambridge 1932).

APPENDIX I.

Calculations in the case of the exact laminar velocity profile.

By integration of equation (2.3b), $uv_x + vv_y = -p_y + \alpha v_{yy}$, from $y=0$ to $y=\infty$ one gets, as $v(0)=0$:

$$p(\infty) - p(0) = -\int_0^\infty uv_x dy - \tfrac{1}{2} v^2(\infty) + \alpha v_y(\infty) - \alpha v_y(0).$$

As $u(0)=0$ also $u_x(0)=0$ and thus from equation of continuity $v_y(0)=0$.

Further

$$v(\infty) = \lim_{z\to\infty} \tfrac{1}{2} Re_x^{-1/2}(zf_z - f) =$$

$$= \tfrac{1}{2} Re_x^{-1/2} \lim_{z\to\infty} (z + z\varphi_z - z + \beta - \varphi) = \tfrac{1}{2}\beta Re_x^{-1/2}$$

and

$$v_y(\infty) = \lim_{y\to\infty} v_z z_y =$$

$$\lim_{z\to\infty} \tfrac{1}{2} Re_x^{-1/2}(f_z + zf_{zz} - f_z)\, Re_x^{1/2}/x =$$

$$= \frac{1}{2x} \lim_{z\to\infty} z\varphi_{zz} = \frac{1}{2x} \lim_{z\to\infty} \{ (z\varphi_z)_z - \varphi_z \} = 0.$$

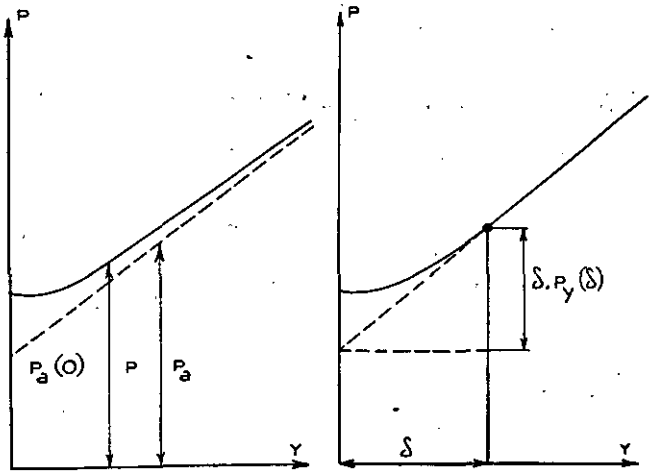

Fig. 3

Exact solution Approximate solution

The first term on the right hand side can be evaluated as follows

$$-\int_0^\infty uv_x dy = -\int_0^\infty f_z \{ -\tfrac{1}{4} Re_x^{-1/2} x^{-1}(z^2 f_{zz} + zf_z - f) \}\, d(x\, Re_x^{-1/2} z) =$$

$$= \tfrac{1}{4} Re_x^{-1} \int_0^\infty zf_z(zf_{zz} + f_z)dz - \tfrac{1}{4} Re_x^{-1} \int_0^\infty ff_z dz =$$

$$= \tfrac{1}{4} Re_x^{-1} \int_0^\infty zf_z(zf_z)_z dz - \tfrac{1}{4} Re_x^{-1} \int_0^\infty f df =$$

$$= \tfrac{1}{8} Re_x^{-1} [\, z^2 f_z^2 - f^2 \,]_0^\infty = \tfrac{1}{8} Re_x^{-1} \lim_{z\to\infty} (zf_z - f)(zf_z + f) = \tfrac{1}{8} Re_x^{-1} \lim_{z\to\infty} (z\varphi_z + \beta - \varphi)(2z - \beta + z\varphi_z + \varphi) = \tfrac{1}{8} Re_x^{-1} \lim_{z\to\infty} \beta(2z - \beta).$$

So $p(\infty) - p(0) = \tfrac{1}{4} Re_x^{-1} \lim_{z\to\infty} \beta z - \tfrac{1}{8} Re_x^{-1}\beta^2 - \tfrac{1}{2}\cdot\tfrac{1}{4}\beta^2 Re_x^{-1} = \tfrac{1}{4} Re_x^{-1}(-\beta^2 + \beta \lim_{z\to\infty} z)$.

The asymptote (fig. 3) is

$$p_a = p(0) - \tfrac{1}{4} Re_x^{-1}\beta^2 + \tfrac{1}{4} Re_x^{-1}\beta z$$

and intersects the axis $z=0$ in a point with

$$p_a(0) = p(0) - \tfrac{1}{4}\beta^2 Re_x^{-1},$$

or with $\beta = 1.73$:

$$Re_x \{ p(0) - p_a(0) \} = 0.75.$$

APPENDIX II.

Calculations in the case of approximate laminar velocity profiles.

In the following the velocity profile $u = u(\eta)$ with $\eta = y/\delta$ is assumed. Differentiating $y = \eta\delta$, one gets

$$dy = \eta d\delta + \delta d\eta$$

and as $u_y(0) = \{ u_y(0) \}_{x=\text{const.}} = \{ u_y(0) \}_{\delta=\text{const.}} = u_\eta(0) \cdot (\eta_y)_{\delta=\text{const.}} = u_\eta(0)/\delta$, equation (2.4) becomes

$$dx = B\delta d\delta \text{ with } B = \{ \bar{u} - \overline{u^2} \} / \{ \alpha\, u_\eta(0) \}.$$

v_y can be evaluated as follows:

$$v_y = (\partial v/\partial y)_{x=\text{const.}} = (\partial v/\partial y)_{\delta=\text{const.}} = (1/\delta)(\partial v/\partial\eta)_{\delta=\text{const.}} = v_\eta/\delta$$

and as

$$u_x = (\partial u/\partial x)_{y=\text{const.}} = (1/B\delta)(\partial u/\partial\delta)_{y=\text{const.}} = (1/B\delta)[(\partial u/\partial\delta)_{\eta=\text{const.}} + (\partial u/\partial\eta)_{\delta=\text{const.}} (\partial\eta/\partial\delta)_{y=\text{const.}}] = -B^{-1}\delta^{-2} u_\eta \eta,$$

the equation of continuity $u_x + v_y = 0$ can be written as

$$v_\eta = B^{-1}\delta^{-1}\eta\, u_\eta.$$

From this

$$v = \int_0^\eta B^{-1}\delta^{-1}\eta\, u_\eta d\eta \;^*) =$$

$$= B^{-1}\delta^{-1}\int_0^\eta \eta du = B^{-1}\delta^{-1}(\eta u - \int_0^\eta u d\eta),$$

so that

$$v_x = (\partial v/\partial x)_{y=\text{const.}} = (1/B\delta)(\partial v/\partial\delta)_{y=\text{const.}} = (1/B\delta)[(\partial v/\partial\delta)_{\eta=\text{const.}} + (\partial v/\partial\eta)_{\delta=\text{const.}} (\partial\eta/\partial\delta)_{y=\text{const.}}] = B^{-1}\delta^{-1}[v_\delta + v_\eta(-\eta/\delta)] =$$

$$-B^{-2}\delta^{-3}(\eta u - \int_0^\eta u d\eta + \eta^2 u_\eta).$$

*) As there is no fear of confusion, the same letter is used above and behind the integral sign.

Introducing $I = \int_0^\eta u d\eta$ and a bar for the mean value of a function f according to $\overline{f} = \int_0^1 f d\eta$, so that for instance

$$\overline{uI} = \int_0^1 u\, I\, d\eta = \int_0^1 I dI = \tfrac{1}{2}\{ I^2(1) - I^2(0) \} = \tfrac{1}{2}\overline{u}^2,$$

one can evaluate the integral in (2.7), taken at constant x and thus at constant δ, as follows:

$$-\int_0^\delta uv_x dy = -\int_0^1 u B^{-2}\delta^{-3}(\eta u - \int_0^\eta u d\eta +$$

$$+ \eta^2 u_\eta)\delta d\eta = B^{-2}\delta^{-2}(\overline{\eta u^2} - \overline{uI} + \tfrac{1}{2}\int_0^1 \eta^2 du^2) =$$

$$= B^{-2}\delta^{-2}(\overline{\eta u^2} - \tfrac{1}{2}\overline{u}^2 + \tfrac{1}{2} - \overline{\eta u^2}) =$$

$$= \tfrac{1}{2} B^{-2}\delta^{-2}(1 - \overline{u}^2).$$

With the aid of this formula and of the formulas

$$v_y(\delta) = v_\eta(1)/\delta = B^{-1}\delta^{-2} u_\eta(1)$$

and

$$v(\delta) = v_{y=\delta} = v_{\eta=1} = v(1) = B^{-1}\delta^{-1}(1 - \overline{u}),$$

equation (2.7) becomes

$$\Delta_l p = B^{-2}\delta^{-2}(\overline{u} - \overline{u}^2) + \alpha B^{-1}\delta^{-2} u_\eta(1)$$

and as

$$B^{-2}\delta^{-2} = \alpha^2 u_\eta^2(0) \,.\, (\overline{u} - \overline{u^2})^{-2}\delta^{-2} =$$

$$= Re_\delta^{-2} u_\eta^2(0) \,.\, (\overline{u} - \overline{u^2})^{-2}$$

and

$$\alpha B^{-1}\delta^{-2} = \alpha^2 u_\eta(0) \,.\, (\overline{u} - \overline{u^2})^{-1}\delta^{-2} =$$

$$= Re_\delta^{-2} u_\eta(0)(\overline{u} - \overline{u^2})^{-1}$$

one gets (2.8a).

APPENDIX III.

On the conditions at transition and the resistance of the turbulent boundary layer.

As $(\overline{u} - \overline{u^2})\delta_x = \tau(0)$ or $(\overline{u} - \overline{u^2}) d Re_\delta / d Re_x = \tau(0)$ and $\delta_2 = (\overline{u} - \overline{u^2})\delta$ or $Re_{\delta_2} = (\overline{u} - \overline{u^2}) Re_\delta$, one gets

$$d Re_{\delta_2} = \tau(0) d Re_x. \qquad \text{(III, 1)}$$

Assuming that transition occurs in an infinitesimal small region with the length dx, $d Re_{\delta_2}$ will approach to 0 if dx and consequently $d Re_x$ approaches to 0, for $\tau(0)$ is finite in this region. So, if transition occurs in a point $x = x_{tr}$, δ_2 will be the same for the laminar boundary layer just before x_{tr} and for the turbulent layer just behind it.

In order to calculate the turbulent boundary layer, one can replace the part of the plate with the laminar boundary layer (length $= x_{tr}$) by a shorter part, length $= X_{tr}$, where the boundary layer is turbulent from the very beginning, $Re_{\delta_2,t}$ for $x = x_{tr}$ in the laminar layer being the same as $Re_{\delta_2,t}$ for $X = X_{tr}$ in the turbulent layer (see fig. 4).

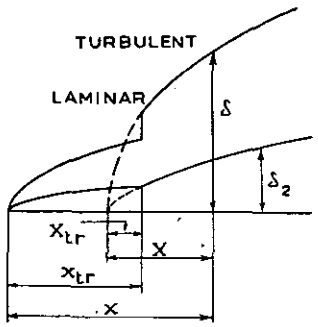

Fig. 4

$Re_{\delta_2,l}$ can be calculated as follows:

$$Re_{\delta_2,l} = \int_0^\infty u(1-u) d Re_y = \text{(using the exact velocity profile)} Re_x^{1/2}\int_0^\infty f_z(1-f_z)dz = Re_x^{1/2}\int_0^\infty (1-f_z) df =$$

$$Re_x^{1/2}\left\{ \left[f - f_z f \right] + \int_0^\infty f f_{zz} dz \right\} = \text{(see differential equation for } f\text{)} - Re_x^{1/2}\int_0^\infty 2 f_{zzz} dz = 2 f_{zz}(0) \,.\, Re_x^{1/2} =$$

$0.664\, Re_x^{1/2}$ (see ref. 5, p. 86 and 88, where $\alpha = A_2 = f_{zz}(0) = 0.332$).

As $X - X_{tr} = x - x_{tr}$ or $Re_X - Re_{X,tr} = Re_x - Re_{x,tr}$ and $\tau_t(0) = A\, Re_X^m$, $Re_{\delta_2,t}$ can be calculated from (III, 1) as follows:

$$Re_{\delta_2,t} = \int_0^X \tau(0)\, d Re_X = \int_0^X A\, Re_X^m\, d Re_X =$$

$$= \frac{A}{m+1} Re_X^{m+1}.$$

In the transition point $Re_{\delta_2,t} = Re_{\delta_2,t}$ so that

$$\frac{A}{m+1} Re_{X,tr}^{m+1} = 0.664\, Re_{x,tr}^{1/2}$$

or

$$Re_{X,tr} = \{ 0.664(m+1)/A \}^{1/(m+1)} \,.\, Re_{x,tr}^{1/(2m+2)}$$

and

$$Re_X = Re_x - Re_{x,tr} + \{ 0.664(m+1)/A \}^{1/(m+1)} Re_{x,tr}^{1/(2m+2)}. \qquad \text{(III, 2)}$$

So from $\tau_t(0) = A\, Re_X^m$:

$$\log \tau_t(0) = \log A + m \log [Re_x - Re_{x,tr} + \{ 0.664(m+1)/A \}^{1/(m+1)} Re_{x,tr}^{1/(2m+2)}] \qquad \text{(III, 3)}$$

and in the transition point

$$\log \tau_{t,tr}(0) = \frac{1}{m+1} \log A + \frac{m}{m+1} \log 0.664(m+1) + \frac{m}{2(m+1)} \log Re_{x,tr} \quad \text{(III, 4)}$$

For the laminar layer $\tau_l(0) = \alpha u_y(0) = \alpha u_z(0)$. $\therefore Re_x^{1/2}/x = f_{zz}(0)$. $Re_x^{-1/2} = 0.332 Re_x^{-1/2}$ so that

$$\log \tau_l(0) = \log 0.332 - \tfrac{1}{2} \log Re_x \quad \text{(III, 5)}$$

and, for the transition point

$$\log \tau_{l,tr}(0) = \log 0.332 - \tfrac{1}{2} \log Re_{x,tr} \quad \text{(III, 6)}.$$

(III, 6) is given as line 1 in fig. 5.

ence in local resistance in case of transition. The difference found in this way is greater than that found by experiments. Therefore PRANDTL proposed to cancel the condition $Re_{\delta_2,l} = Re_{\delta_2,t}$ in the transition point and to replace it by the condition $X = x$.

In that case $\tau_t(0) = 0.0296\, Re_x^{-1/5}$ or $\log \tau_t(0) = \log 0.0296 - {}^1/_5 \log Re_x$, which equation is represented by line 3 of fig. 5.

The difference in local resistance at the transition point, found in this way, agrees much better with experimental values and PRANDTL's proposi-

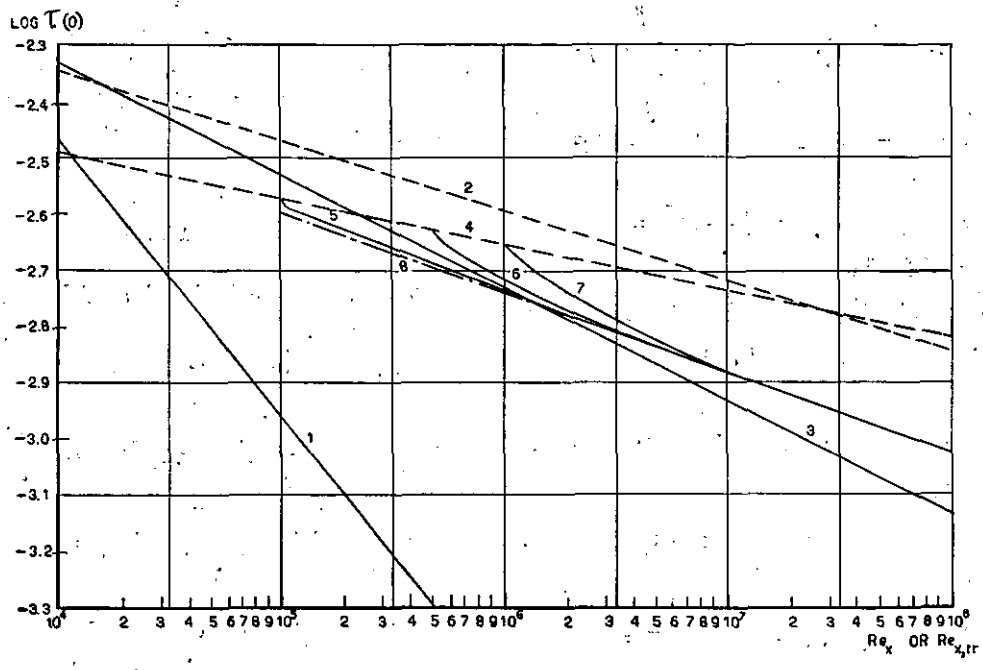

Fig. 5. Wall shearing stress along a flat plate in parallel flow.

From the experiments of WIESELSBERGER (ref. 9) PRANDTL deduced the following formula for the drag coefficient $C_{D,t}$ of a plate, length L with turbulent boundary layer (ref. 10)

$$C_{D,t} = 0.074\, Re_L^{-1/5}. \quad \text{(III, 7)}$$

The local drag coefficient c_D is connected with C_D by the equation

$$L C_D = \int_0^L c_D dX$$

so that

$$c_D = d(Re_X C_D(X))/d\, Re_X = 0.0592\, Re_X^{-1/5}.$$

As $T(0) = c_D \cdot \frac{1}{2} \rho U_\infty^2$ and $\tau(0) = T(0)/\rho U_\infty^2$ one gets $\tau(0) = \frac{1}{2} c_D$ so that, following PRANDTL

$$\tau_t(0) = 0.0296\, Re_X^{-1/5}.$$

Using the values $A = 0.0296$ and $m = -{}^1/_5$, equation (III, 4) can be represented by line 2 in fig. 5.

The vertical distance between line 1 and 2 for a given value of $Re_{x,tr}$ is a measure of the differ-

tions are accepted in several handbooks (ref. 5, p. 152; ref. 11, p. 329).

However, PRANDTL's suggestion $X = x$ instead of $Re_{\delta_2,t} = Re_{\delta_2,l}$ in the transition point must be rejected, as the discrepancy between theory and experiment, found by him, is the result of an inaccurate supposition in his derivation of formula III, 7 from WIESELSBERGER's experiments.

PRANDTL's derivation of the formula $C_{D,t} = 0.074\, Re_L^{-1/5}$ is based on

1 boundary layer measurements of VAN DER HEGGE ZIJNEN (ref. 12), who found the velocity profile $u = \eta^{1/7}$ for the turbulent boundary layer of a flat plate.

2 dimensional analyses of VON KÁRMÁN (ref. 13), who derived for the turbulent flow through a pipe $m = -2n/(3n+1)$ in which n is defined by $u = \eta^n$. Using this expression for the flow along the flat plate too, PRANDTL suggested $C_{D,t} = \text{constant} \cdot Re_L^{-1/5}$.

3 resistance measurements of WIESELSBERGER, from which the constant of the formula above was found to be 0.074.

The following objections against PRANDTL's derivation can be raised:

1 HANSEN experimentally found $u = \eta^{1/5}$ instead of $u = \eta^{1/7}$ (ref. 14). He showed that the existance of a small pressure gradient in the direction of the flow in VAN DER HEGGE ZIJNEN's experiments has been very probable, which pressure gradient may account for the difference in the exponent. The exponent $n = 1/5$, or in accordance with this $H = \delta_1/\delta_2 = 1.4$, is also accepted by others e. g. FALKNER (ref. 15) and SQUIRE and YOUNG (ref. 16).

2 The formula $m = -2n/(3n+1)$ does not apply for the flow along a flat plate, as FALKNER (ref. 15) pointed out. VON KÁRMÁN's analysis applies only in case the velocity profile is independent of x. So m is not fixed by the choice of n and must be derived independently from the experiments.

The best equation to fit the measurements of WIESELSBERGER, is $C_{D,t} = 0.0375\, Re_L^{-0.15}$. By these measurements Re_L had a range from 2×10^5 to 8×10^6. FALKNER sorted out and correlated a great number of measurements, known to him from several papers. The range of Re_L was from 10^6 to 4×10^8. He found $C_{D,t} = 0.0306\, Re_L^{-1/7}$, a formula which agrees very well with the formula, fitting WIESELSBERGER's measurements best. FALKNER's formula will be used in this report. From this formula one derives $\tau_t(0) = 0.0131\, Re_x^{-1/7}$ so that (III, 4) can be written $\log \tau_{t,tr}(0) = -2.156 - 1/12 \log Re_{x,tr}$, a formula, represented by the line 4 in fig. 5. The difference between $\tau_{t,tr}(0)$ and $\tau_{t,tr}(0)$ is less in this case than when taking $\delta_2 =$ constant and $C_{D,t} = 0.074\, Re_L^{-1/5}$. For $Re_{x,tr} \approx 2 \times 10^5$ it agrees with the difference found by PRANDTL when using $C_{D,t} = 0.074\, Re_L^{-1/5}$ and $x = X$.

So one can conclude, that $\delta_{2,l} = \delta_{2,t}$ at the transition point can be used in connection with the right formula for the resistance of the turbulent boundary layer. In modern calculations they do indeed (ref. 16, 17, 18).

In fig. 5 also lines are drawn representing $\log \tau_t(0)$ as function of Re_x following (III, 3) with $m = -1/7$ and $A = 0.0131$ for $Re_{x,tr} = 10^5$ (line 5), 5×10^5 (line 6) and 10^6 (line 7). Line 8 is the asymptote

$$\log \tau_t(0) = \log 0.0131 - \\ - 1/7 \log Re_x \text{ for } Re_x \gg Re_{x,tr}.$$

Up to here, we have assumed, that transition takes place suddenly. But this involves, that the displacement thickness δ_1 is discontinuous in the transition point, a fact, that is difficult to bring in accordance with the assumption of constant velocity at the outer edge of the boundary layer. One can avoid this difficulty by introducing a transition region, in which the velocity profile gradually changes from the laminar one into the turbulent one. The region may have a length t and outer points $x = x^*$ and $x = x^{**}$; asterisks denote values in these points.

From (III, 1) it follows, that

$$Re_{\delta_2}^{**} - Re_{\delta_2}^{*} = \int_{x^*}^{x^{**}} \tau(0)\, .\, d\, Re_x. \qquad \text{(III, 8)}$$

$\tau(0)$ versus x will be approximated by a linear function in this region.

Then $\int_{x^*}^{x^{**}} \tau(0) d\, Re_x = \frac{1}{2} \{ \tau^{**}(0) + \tau^{*}(0) \}\, Re_t$.

Now

$$\tau^{**}(0) = A\, Re_X^m \text{ and } Re_{\delta_2}^{**} = \frac{A}{m+1} Re_X^{m+1},$$

so that

$$\tau^{**}(0) = A^{\frac{1}{m+1}} (m+1)^{\frac{m}{m+1}} (Re_{\delta_2}^{**})^{\frac{m}{m+1}}.$$

Moreover

$$\tau^{*}(0) = C\, Re_x^{-1/2} \text{ and } Re_{\delta_2}^{*} = 2\, C (Re_x^{*})^{1/2}$$

so that

$$\tau^{*}(0) = 2\, C^2 / Re_{\delta_2}^{*}.$$

Therefore (III, 8) leads to

$$Re_{\delta_2}^{**} - \tfrac{1}{2} A^{\frac{1}{m+1}} (m+1)^{\frac{m}{m+1}} Re_t (Re_{\delta_2}^{**})^{\frac{m}{m+1}} = \\ = Re_{\delta_2}^{*} + C^2\, Re_t / Re_{\delta_2}^{*}. \qquad \text{(III, 9)}$$

Using $A = 0.0131$, $m = -1/7$ (ref. 15) and $C = 0.332$ (exact velocity profile of laminar flow) one finds,

$$Re_{\delta_2}^{**} - 0.00371\, Re_t (Re_{\delta_2}^{**})^{-1/6} = \\ = Re_{\delta_2}^{*} + 0.110\, Re_t / Re_{\delta_2}^{*} \qquad \text{(III, 9a)}$$

Log $Re_{\delta_2}^{**}$ versus $\log Re_{\delta_2}^{*}$ for a number of values of Re_t is given in fig. 2 (in the corner left down).

If assuming another velocity profile for the laminar boundary layer than the exact one, C will change somewhat, but the changes in the lines $\log Re_{\delta_2}^{**}$ versus $\log Re_{\delta_2}^{*}$ will not be of any importance. Therefore no calculations have been carried out for other velocity profiles.

APPENDIX IV.

Calculations in the case of a turbulent boundary layer.

Using the boundary conditions $v(0) = 0$, $v_y(0) = -u_x(0) = 0$ and in connection with the first of these, $\{\overline{\Delta v(0)}\}^2 = 0$ one gets by integrating (3.5)

$$p(\delta) - p(0) = \Delta_t p = -\int_0^{\delta} u\, v_x\, dy - \tfrac{1}{2} v^2(\delta) + \\ + \alpha v_y(\delta) + \int_0^{\delta} \overline{(\Delta u\, .\, \Delta v)}_x + \{\overline{\Delta v(\delta)}\}^2. \qquad \text{(IV, 1)}$$

The last term on the right hand side will be omitted: it depends on the turbulence outside the boundary layer and by not introducing this term in the calculations of the laminar boundary layer, we tacitly assumed that there is no turbulence in the bulk of the stream. If however some degree of turbulence does exist outside the boundary layer, the term

$$\{\overline{\Delta v(\delta)}\}^2$$

will be found in the expression for $\Delta_t p$ as well as in that for $\Delta_l p$ and these will cancel each other out in $\Delta_t p - \Delta_l p$. Therefore we can omit this term without limitating our conclusions only to a bulk of stream free of turbulence.

The fourth term on the right hand side of (IV, 1) can be evaluated as follows:

$$-\int_0^\delta \overline{(\Delta u \,.\, \Delta v)}_x\, dy = \text{(see 3.6)} \int_0^\delta \tau_x dy =$$

$$= \int_0^\delta \tau_X dy = \text{(see 3.7 and 3.3)}$$

$$\int_0^\delta [A\, Re_X^m (1 - 4\eta^3 + 3\eta^4)]_X\, dy =$$

$$= mA\, Re_X^{m-1} (U_\infty/\nu) \int_0^\delta (1 - 4\eta^3 + 3\eta^4) dy +$$

$$+ A\, Re_X^m \int_0^\delta (1 - 4\eta^3 + 3\eta^4)_\eta \,.\, \eta_\delta \,.\, \delta_X dy.$$

As the integration has to be carried out at constant X or at constant δ, one gets from (2.5a) $dy = \delta d\eta$. The expression η_δ has to be taken at constant y and will be $= -\eta/\delta$ (see 2.5a).

So $-\int_0^\delta \overline{(\Delta u \,.\, \Delta v)}_x dy = mA\, Re_X^{m-1} (U_\infty/\nu)\delta \cdot \int_0^1 (1 - 4\eta^3 + 3\eta^4) d\eta + A\, Re_X^m \delta_X \int_0^1 (-12\eta^2 + 12\eta^3)(-\eta) d\eta =$ (see 3.2 and 3.3) $= \frac{3}{5} mA Re_X^{m-1} Re_\delta + \frac{3}{5} A^2 (\bar{u} - \overline{u^2})^{-1} Re_X^{2m} = \frac{3}{5} A^2 (\bar{u} - \overline{u^2})^{-1} \frac{1+2m}{1+m} Re_X^{2m}$

as $Re_\delta = A(\bar{u} - \overline{u^2})^{-1} \frac{1}{1+m} \,.\, Re_X^{m+1}$ (from integrating 3.2 after substituting $\tau(0)$ from 3.3). The other terms of (IV, 1) can be evaluated in a way, analogical to that used in appendix II.

The only difference is that (2.5b) has to be replaced by $dX = dx = C\delta^\mu d\delta$ with $\mu = -m/(1+m)$ and $C = A^{-1-\mu}(m+1)^\mu (\bar{u} - \overline{u^2})^{1+\mu} U_\infty^\mu \nu^{-\mu}$, for instead of (2.4) we have to write (3.2) combined with (3.3). Now the calculations are carried out as follows:

$$u_x = u_\eta \eta_\delta \delta_x = u_\eta (-\eta/\delta) C^{-1} \delta^{-\mu} =$$

$$- C^{-1} \delta^{-\mu-1} u_\eta \eta;\ v_y = v_\eta \eta_y = v_\eta/\delta.$$

So from the equation of continuity $u_x + v_y = 0$ one gets $v_\eta = C^{-1}\delta^{-\mu}\eta u_\eta$.

Integrating this:

$$v = C^{-1}\delta^{-\mu}(\eta u - \int_0^\eta u d\eta)\ *).$$

From this

$$v_x = C^{-1}\delta^{-\mu} v_\delta = C^{-1}\delta^{-\mu}\Big[-\mu C^{-1}\delta^{-\mu-1}(\eta u - \int_0^\eta u d\eta) + C^{-1}\delta^{-\mu}(u + \eta u_\eta - u)(-\eta/\delta)\Big] =$$

$$= -C^{-2}\delta^{-2\mu-1}\Big[\mu\eta u - \mu\int_0^\eta u d\eta + \eta^2 u_\eta\Big],$$

so that $-\int_0^\delta u v_x dy = \int_0^1 C^{-2}\delta^{-2\mu-1}(\mu\eta u^2 - \mu u\int_0^\eta u d\eta + u\eta^2 u_\eta)\,\delta d\eta = C^{-2}\delta^{-2\mu}(\mu\overline{\eta u^2} - \mu\overline{uI} + \frac{1}{2}\int_0^1 \eta^2 du^2) = \frac{1}{2} C^{-2}\delta^{-2\mu}\{1 - \mu\bar{u}^2 + 2(\mu-1)\overline{\eta u^2}\}.$

For $CU_\infty^{-\mu}\nu^\mu = D$, say, equation (VI, 1) becomes

$$\Delta_t p = \tfrac{1}{2} D^{-2} Re_\delta^{-2\mu}\{1 - \mu\bar{u}^2 + 2(\mu-1)\overline{\eta u^2}\} - \tfrac{1}{2} D^{-2} Re_\delta^{-2\mu}(1-\bar{u})^2 + D^{-1} Re_\delta^{-\mu-1} u_\eta(1) + \tfrac{3}{5} A^2(\bar{u} - \overline{u^2})^{-1} \frac{1+2m}{1+m} Re_X^{2m} =$$

$$= A^2 Re_X^{2m}(\bar{u} - \overline{u^2})^2 [(\mu-1)\overline{\eta u^2} + \bar{u} - \tfrac{1}{2}(1+\mu)\bar{u}^2 + \tfrac{3}{5}(1-\mu)(\bar{u} - \overline{u^2})] + u_\eta(1)(m+1) Re_X^{-1}.$$

For a well chosen velocity profile $u_\eta(1) = 0$ and the second term of the expression is cancelled out.

And even for an in this point less well chosen velocity profile, e. g. for the velocity profile $u = \eta^n$, this term may be omitted.

For, as $m > -\frac{1}{2}$ for the turbulent boundary layer the second term will be negligeably small compared with the first term in the case of a not too small Re_X. So

$$\Delta_t p = 0.1\, A^2(\bar{u} - \overline{u^2})^{-2}\{10(\mu-1)\overline{\eta u^2} + (16 - 6\mu)\bar{u} - 5(1+\mu)\bar{u}^2 + 6(\mu-1)\overline{u^2}\} Re_X^{2m}$$

and as

$$Re_{\delta_2} = (\bar{u} - \overline{u^2}) Re_\delta = A(m+1)^{-1} Re_X^{m+1}$$

or $Re_X^{2m} = A^{2\mu}(m+1)^{-2\mu} Re_{\delta_2}^{-2\mu}$.

---

*) See note on page A 12.

$$\Delta_l p = 0.1\, A^{2(\mu+1)} (m+1)^{-2\mu} (\bar{u} - \overline{u^2})^{-2} \{ 10\,(\mu - 1)\overline{\eta u^2} + (16 - 6\,\mu)\,\bar{u} - 5\,(1+\mu)\overline{u}^2 + 6\,(\mu-1)\overline{u^2} \}\, Re_{\delta_2}^{-2\mu}.$$

For the velocity profile $u = \eta^{1/N}$ is $\bar{u} = N/(N+1)$; $\overline{u^2} = N/(N+2)$; $\overline{\eta u^2} = N/2(N+1)$ so that

$$(\bar{u} - \overline{u^2})^{-2} \{ 10\,(\mu-1)\overline{\eta u^2} + (16 - 6\mu)\,\bar{u} - 5\,(1+\mu)\overline{u}^2 + 6\,(\mu-1)\overline{u^2} \} = (N+2)\,\{(4-N)\mu + 11\,N + 16\}/N.$$

Completed: March 1952.

TABLE 1.

Results of calculations for the laminar boundary layer.

velocity profile	See	$\tau(0) \cdot Re_x^{1/2}$	$Re_x \Delta_l p$	$Re_{\delta_2}^2 \cdot \Delta_l p$	$Re_x \{ p(0) - p_a(0) \}$
exact: $u = f_x$	Ref. 5	0.332			0.75
$u = \eta$	Ref. 19	0.289	1.25	0.416	
$u = 2\,\eta - \eta^2$	„	0.365	1.67	0.889	
$u = \frac{3}{2}\,\eta - \frac{1}{2}\,\eta^3$	„	0.323	1.26	0.527	
$u = 2\,\eta - 2\,\eta^3 + \eta^4$	„	0.343	1.79	0.840	0.77
$u = \sin \frac{\pi}{2}\,\eta$	Ref. 20, p. 686	0.328	1.33	0.571	0.76

C.C.L. Class. D 931 : D 328

REPORT A. 1204

Tunnelwall Interference for Aerofoils and Aerofoil-Fuselage Combinations in a Tunnel with an Octagonal Section for Incompressible Flow

by

H. G. LOOS.

Summary.

The interference between tip vortices and the walls of an octagonal tunnel is calculated by replacing the oblique walls by quadrupoles with a suitably chosen strength.

An approximate image method is applied to calculate a simple correction for the interaction of a cylindrical fuselage, the aerofoil and the tunnel.

Contents.

1 Introduction.

The tunnelwall influence on models in a rectangular working-section can be determined in a well known way by the method of images.

With the octagonal tunnel the walls cannot be represented exclusively by a set of image-vortices, as the image-method fails for walls enclosing an obtuse angle. This method gives rise to singularities at places where they do not exist in reality.

G. K. BATCHELOR (refs. 1 and 2) has solved this difficulty by replacing the oblique tunnelwalls by a row of vortices with a strength varying linearly with distance along the wall.

The linear vortex distributions on the oblique walls are chosen so that the oblique walls become approximately streamlines. One can obtain a further simplification by replacing the vortex distribution on the oblique side by a discrete vortex, introducing however again a small error. The image-method gives rise to a square round each angular point of the rectangle described on the tunnel, with 4 discrete vortices on the sides (see fig. 1).

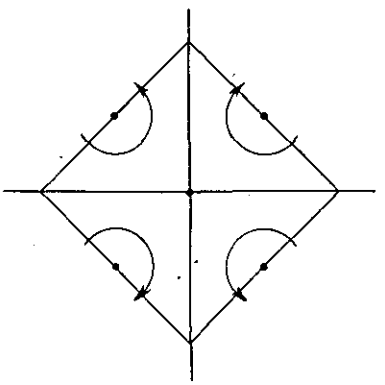

Fig. 1

In this report it is proposed to replace the vortex distribution not by 4 discrete vortices but by a quadrupole. The calculation becomes simpler whilst the boundary condition on the oblique side can be fulfilled more satisfactorily.

2 The perturbation field of the tip vortices in a rectangular tunnel.

2.1 *Aerofoils with small aspect ratio.*

For aerofoils with small aspect ratio the trailing vortices can be approximated by a dipole μ. The image-method gives rise to a set of dipoles as shown in fig. 2. Indexes n and m are introduced to denote the dipoles, the dipole (n, m) being in the n^{th} column and in the m^{th} row; the dipole representing the trailing vortices of the aerofoil will be indicated by $(0, 0)$.

The velocity field corresponding to the half infinite dipole (n, m) *) can be written in complex form as

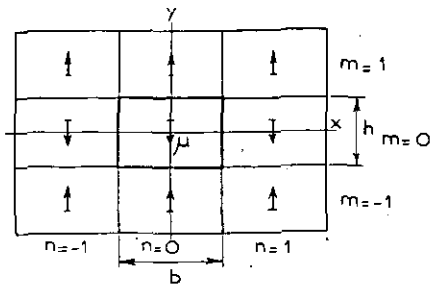

Fig. 2

$$\overline{V}_{n,m} = \frac{-i\mu(-1)^m}{4\pi(z - imh - nb)^2}.$$

The resulting field of all dipoles can be obtained by suming over n and m

$$\overline{V} = \frac{-i\mu}{4\pi} \sum_{n,m} \frac{(-1)^m}{(z - imh - nb)^2}, \quad (2.1.1)$$

n, m being integer numbers. The double sum $\sum_{n,m}$ can be simplified with the aid of the relation

$$\sum_n \frac{1}{(z - imh - nb)^2} = \left(\frac{\pi}{b}\right)^2 \frac{1}{\sin^2 \frac{\pi}{b}(z - imh)},$$

(2.1.1) changing into

$$\overline{V} = \frac{-i\mu}{4\pi} \sum_m (-1)^m \left(\frac{\pi}{b}\right)^2 \frac{1}{\sin^2 \frac{\pi}{b}(z - imh)} \quad (2.1.2)$$

The perturbation field V^* due to the tunnelwalls is equal to the field of all dipoles, the field of the central dipole $(0, 0)$ being substracted

$$\overline{V^*}(z) = \frac{i\mu}{4\pi}\left\{\frac{1}{z^2} - \sum_m (-1)^m \left(\frac{\pi}{b}\right)^2 \frac{1}{\sin^2 \frac{\pi}{b}(z - imh)}\right\}. \quad (2.1.3)$$

The expression (2.1.3) is indeterminate for $z = 0$; however, continuity conditions lead to

$$\overline{V^*}(0) = \lim_{z \to 0} \overline{V^*}(z) = \frac{-i\mu}{4\pi}\left(\frac{\pi}{b}\right)^2 \left\{\frac{1}{3} + \sum_{m \neq 0} (-1)^m \frac{1}{\sin^2 \frac{\pi}{b} imh}\right\}. \quad (2.1.4)$$

For the points on the X-axis of the tunnel (fig. 2) $\overline{V^*}$ is purely imaginary, with $\overline{V^*} = V_x^* - iV_y^*$ follows

$$V_y^*(x) = \frac{-u}{4\pi}\left\{\frac{1}{x^2} - \sum_m (-1)^m \left(\frac{\pi}{b}\right)^2 \frac{1}{\sin^2 \frac{\pi}{b}(x - imh)}\right\}$$

and (2.1.5)

$$V_y^*(0) = -\frac{u}{4\pi}\left(\frac{\pi}{b}\right)^2 \left\{\frac{1}{3} + \sum_{m \neq 0} (-1)^m \frac{1}{\sin^2 \frac{\pi}{b} imh}\right\}. \quad (2.1.6)$$

The dipole-strength μ can be expressed in the lift A

$$\mu = \frac{A}{\rho U} \qquad \text{(see 2.2.7)} \quad (2.1.7)$$

U representing the free-stream-velocity.

With $A = \frac{1}{2}\rho U^2 c_a F$ (F = wing area) and $0 = bh$ (0 = area of working section) (2.1.5) and (2.1.6) reduce to

$$V_{\mu y}^* = \delta_1(x) \cdot U c_a \frac{F}{0} \quad (2.1.8)$$

from which follows for the correction of the angle of incidence

$$\Delta_1\alpha = \frac{V_{\mu y}^*}{U} = \delta_1(x) c_a \frac{F}{0}. \quad (2.1.9)$$

The dimensionless coefficient $\delta_1(x)$ is given by

$$\delta_1(x) = \frac{-h}{8\pi b}\left\{\left(\frac{b}{x}\right)^2 - \pi^2 \sum_m \frac{(-1)^m}{\sin^2 \frac{\pi}{b}(x - imh)}\right\}$$

and (2.1.10)

$$\delta_1(0) = \frac{\pi h}{8b}\left\{\frac{1}{3} + \sum_{m \neq 0} \frac{(-1)^m}{\sin^2 \frac{\pi}{b} imh}\right\} \quad (2.1.11)$$

The tunnelwall influence gives an upwash angle $\Delta\alpha$ at the aerofoil, so that a lift coefficient in the tunnel with geometrical angle of incidence α_T corresponds to a lift coefficient in free flight with a geometrical angle of incidence

$$\alpha_V = \alpha_T + \Delta\alpha. \quad (2.1.12)$$

2.2 *Aerofoils with large aspect ratio.*

For aerofoils with not too large aspect ratio the trailing vortex section can be replaced by a discrete vortex pair. In order to investigate the optimum representation of the vortex section we consider the vortex pairs (0), (1) and (2) represented in fig. 3.

We want to determine the pair (0) so that its field agrees as much as possible with the resutling field of the vortex pairs (1) and (2). The fields of the pair (0) and of the sum of (1) and (2),

*) All velocities are in the plane perpendicular to the tunnel centre line and through the lifting vortex of the model.

$$\overline{V}_0 = \frac{\Gamma_0}{2\pi i}\left(\frac{1}{z-z_0} - \frac{1}{z+z_0}\right),$$

$$\overline{V}_{1+2} = \frac{\Gamma_1}{2\pi i}\left(\frac{1}{z-z_1} - \frac{1}{z+z_1}\right) + \frac{\Gamma}{2\pi i}\left(\frac{1}{z-z_2} - \frac{1}{z+z_2}\right)$$

can be developed in power series of $1/z$,

$$\overline{V}_0 = \frac{1}{\pi i}\left(\frac{\Gamma_0 z_0}{z^2} + \frac{\Gamma_0 z_0^3}{z^4} + \ldots\ldots\right),$$

$$\overline{V}_{1+2} = \frac{1}{\pi i}\left(\frac{\Gamma_1 z_1 + \Gamma_2 z_2}{z^2} + \frac{\Gamma_1 z_1^3 + \Gamma_2 z_2^3}{z^4} + \ldots\ldots\right).$$

The two unknowns Γ_0 and z_0 will be determined by two independent equations.

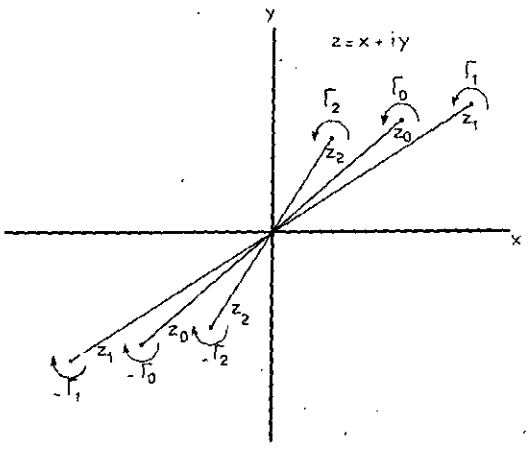

Fig. 3

The best agreement between $\overline{V}_0$ and $\overline{V}_{1+2}$ is therefore obtained if the first two terms of the series for $\overline{V}_0$ and $\overline{V}_{1+2}$ agree,

$$\Gamma_0 z_0 = \Gamma_1 z_1 + \Gamma_2 z_2,$$
$$\Gamma_0 z_0^3 = \Gamma_1 z_1^3 + \Gamma_2 z_2^3.$$

Extension to n vortex pairs gives

$$\Gamma_0 z_0 = \sum_{k=1}^{n} \Gamma_k z_k, \qquad (2.2.1)$$

$$\Gamma_0 z_0^3 = \sum_{k=1}^{n} \Gamma_k z_k^3. \qquad (2.2.2)$$

These relations are now used to calculate the vortex pair that represents as closely as possible the field of the trailing vortex sheet AB (see fig. 4).

Calling the strength of these vortices Γ and $-\Gamma$ and their locations $x = c$ and $x = -c$ respectively, and indicating the vortex strength per unit length of the distribution AB by $\gamma(x)$, then (2.2.1) and (2.2.2) yield

$$\Gamma c = \int_0^{s/2} \gamma(x)\, x\, dx, \qquad (2.2.3)$$

$$\Gamma c^3 = \int_0^{s/2} \gamma(x)\, x^3 dx. \qquad (2.2.4)$$

From (2.2.3) and (2.2.4) follows

$$c^2 = \frac{\int_0^{s/2} \gamma(x) x^3 dx}{\int_0^{s/2} \gamma(x) x dx}. \qquad (2.25)$$

Hence for an aerofoil with an elliptical distribution of circulation

$$c = \tfrac{1}{2}\sqrt{3}\cdot\frac{s}{2}. \qquad (2.2.6)$$

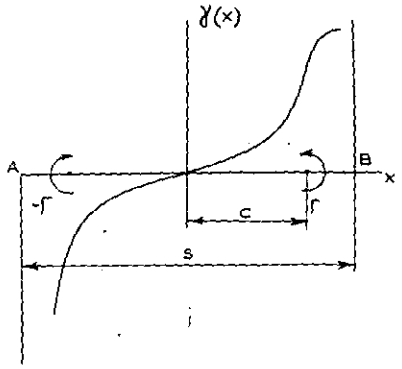

Fig. 4

This formula for the location of the substituting vortices will also be used when the circulation-distribution over the aerofoil is unknown. In general, the real distributions will not diverge much from the elliptical distribution.

Whereas the value of c depends upon the circulation-distribution round the aerofoil, the product Γc can obviously be expressed, independent of the circulation-distribution, in the lift A, the free stream velocity U and the density ρ.

Calling the circulation around the aerofoil $\Gamma'(x)$ then $\gamma(x) = -\frac{d\Gamma'}{dx}$ so that partial integration of (2.2.3) leads to

$$\Gamma c = \int_0^{s/2} \gamma(x) x dx = -\left[\Gamma'(x)\cdot x\right]_0^{s/2} + \int_0^{s/2} \Gamma'(x) dx,$$

$$\Gamma c = \int_0^{s/2} \Gamma'(x) dx.$$

For symmetrical circulation-distributions $\Gamma'(x)$ is given by

$$\int_0^{s/2} \Gamma'(x) dx = \frac{A}{2\rho U},$$

so that

$$2\Gamma c = \frac{A}{\rho U}. \qquad (2.2.7)$$

After replacing the trailing vortices in the above mentioned way by a discrete vortex pair the latter is reflected against the horizontal and vertical tunnel walls. This gives rise to a vortex configuration as represented in fig. 5.

Each vortex pair is indicated by the indexes n and m, n determining the column and m the row.

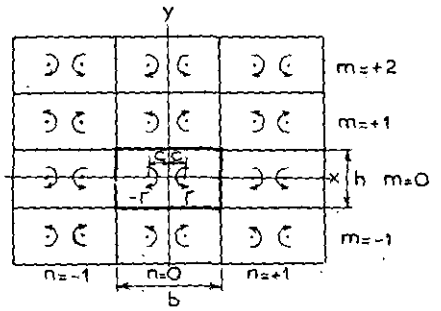

Fig. 5

The field of the half infinite vortex pair (n, m) can be expressed by

$$\overline{V}_{n,m} = \frac{\Gamma}{4\pi i}(-1)^m \left\{ \frac{1}{z-(nb+ihm+c)} - \frac{1}{z-(nb+imh-c)} \right\}.$$

Hence the field of all vortex pairs becomes

$$\overline{V}(z) = \frac{\Gamma}{4\pi i} \sum_{n,m} (-1)^m \left\{ \frac{1}{z-(nb+ihm+c)} - \frac{1}{z-(nb+imh-c)} \right\}. \quad (2.2.8)$$

With the aid of the relation

$$\sum_n \frac{1}{z-imh-c-nb} = \frac{\pi}{b} \operatorname{cotg} \frac{\pi}{b}(z-imh-c),$$

$\overline{V}(z)$ can be simplified to

$$\overline{V}(z) = \frac{\Gamma}{4\pi i} \cdot \frac{\pi}{b} \sum_m (-1)^m \left\{ \operatorname{cotg} \frac{\pi}{b}(z-imh-c) - \operatorname{cotg} \frac{\pi}{b}(z-imh+c) \right\}. \quad (2.2.9)$$

The perturbation field due to the tunnel walls is equal to the field of all image vortices,

$$\overline{V}^*(z) = \frac{\Gamma}{4\pi i} \cdot \frac{\pi}{b} \sum_m (-1)^m \left\{ \operatorname{cotg} \frac{\pi}{b}(z-imh-c) - \operatorname{cotg} \frac{\pi}{b}(z-ihm+c) \right\} - \frac{\Gamma}{4\pi i}\left(\frac{1}{z-c} - \frac{1}{z+c}\right). \quad (2.2.10)$$

In the same way as shown in section 2.1 (2.2.10) can be written as

$$V^*_{\Gamma_y}(x) = \delta_1(x) \cdot U c_a \frac{F}{0}, \quad (2.2.11)$$

with

$$\delta_1(x) = \frac{h}{16c} \sum_m (-1)^m \left\{ \operatorname{cotg} \frac{\pi}{b}(x-imh-c) - \operatorname{cotg} \frac{\pi}{b}(x-imh+c) \right\} - \frac{hb}{16\pi c}\left(\frac{1}{x-c} - \frac{1}{x+c}\right), \quad (2.2.12)$$

an expression which is purely real as a result of symmetry. The correction angle follows from

$$\Delta_1\alpha = \delta_1(x) c_a \frac{F}{0}. \quad (2.2.13)$$

3 The disturbance due to the oblique walls in an octagonal tunnel.

3.1 *Aerofoils with small aspect ratio.*

The flow field of a dipole μ in a rectangular tunnel has been found in (2.1.2) to be

$$\overline{V}(z) = \frac{-i\mu}{4\pi} \frac{\pi^2}{b^2} \sum_m (-1)^m \frac{1}{\sin^2 \frac{\pi}{b}(z-imh)}. \quad (3.1.1)$$

We now want to determine the velocities normal to the oblique wall CD of fig. 6. Along the line CD we assume a parameter t, which is zero at C and is equal to 1 at D.

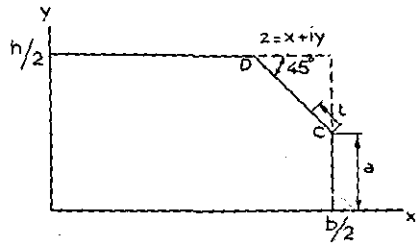

Fig. 6

The points on the wall are given by

$$z = \frac{b}{2} + ia + t(i-1)\left(\frac{h}{2} - a\right). \quad (3.1.2)$$

The velocity normal to CD,

$$V_{\mu n} = \tfrac{1}{2}\sqrt{2}\,(V_x(t) + V_y(t))$$

can now be determined.

With $\overline{V} = V_x - iV_y$ follows from (3.1.1)

$$V_x(t) = Re\left\{ \frac{-i\mu}{4\pi}\left(\frac{\pi}{b}\right)^2 \sum_m (-1)^m \frac{1}{\sin^2 \frac{\pi}{b}(z-imh)} \right\},$$

$$V_y(t) = Im\left\{ \frac{i\mu}{4\pi}\left(\frac{\pi}{b}\right)^2 \sum_m (-1)^m \frac{1}{\sin^2 \frac{\pi}{b}(z-imh)} \right\}, \quad (3.1.3)$$

in which the expression (3.1.2) has to be substituted for z. As an example, the velocity $V_{\mu n}$ normal to the oblique walls was computed for the working section of tunnel 3 of the N.L.L., for which $b = 300$ cm, $h = 10$ cm and $a = 55$ cm. The results are represented in fig. 7.

It is seen that the distribution of $V_{\mu n}$ is antisymmetrical with respect to $t = \frac{1}{2}$ and roughly linear. The square generated by reflecting the oblique wall is drawn in fig. 8; on the sides the normal velocities are schematically indicated. We

now seek a flow with a singularity in the angular point E, which neutralizes the normal velocities on the sides of the square. Approximately this is satisfied by the flow of a quadrupole with a suitably strength Q.

To a half infinite quadrupole which lies in the origin and is orientated as indicated in fig. 9, belongs a velocity field

$$\overline{V} = \frac{-Q}{4\pi z^3}.$$

The quadrupole (m, n) with a strength $-(-1)^m.Q$ at

$$z = \frac{b}{2} + i\,\frac{h}{2} + nb + imh$$

consequently has a velocity-field

$$\overline{V}_{m,n} = \frac{-(-1)^m Q}{4\pi\left(z - \frac{b}{2} - i\,\frac{h}{2} - nb - imh\right)^3}.$$

The influence of all quadrupoles together

$$\overline{V}_q = \frac{-Q}{4\pi} \sum_{m,n} \frac{(-1)^m}{\left(z - \frac{b}{2} - i\,\frac{h}{2} - nb - imh\right)^3}$$

can be calculated by first summing over n, making use of

$$\sum_n \frac{1}{(z - n\pi)^3} = \frac{\cos z}{\sin^3 z}.$$

Then

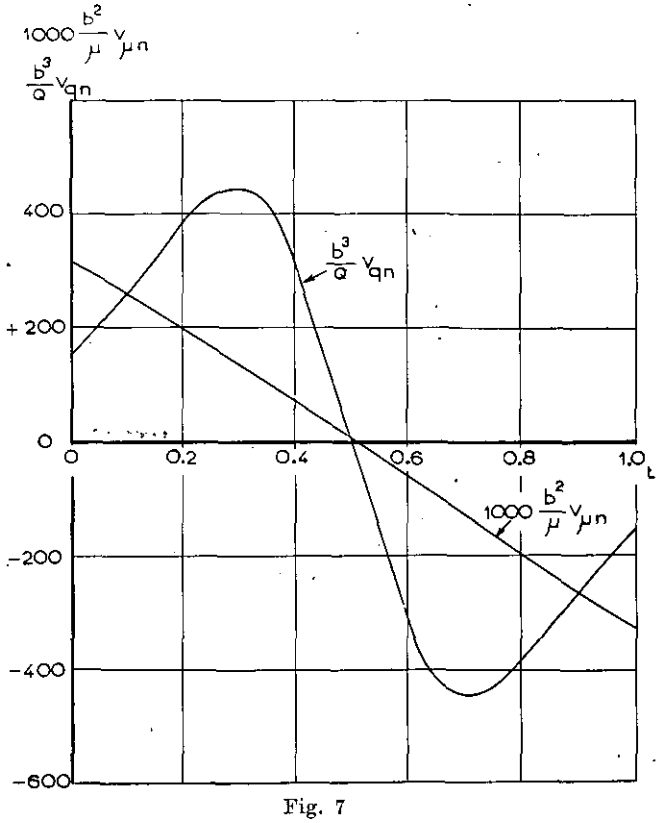

Fig. 7

$$\overline{V}_q = \frac{-Q}{4\pi} \sum_m (-1)^m \left(\frac{\pi}{b}\right)^3 \frac{\cos\frac{\pi}{b}\left(z - \frac{b}{2} - i\,\frac{h}{2} - imh\right)}{\sin^3\frac{\pi}{b}\left(z - \frac{b}{2} - i\,\frac{h}{2} - imh\right)} \tag{3.1.4}$$

is obtained.

For the points along the oblique wall CD

$$z = \frac{b}{2} + ia + t(i-1)\left(\frac{h}{2} - a\right)$$

according to (3.1.2), so that the velocity components are given by

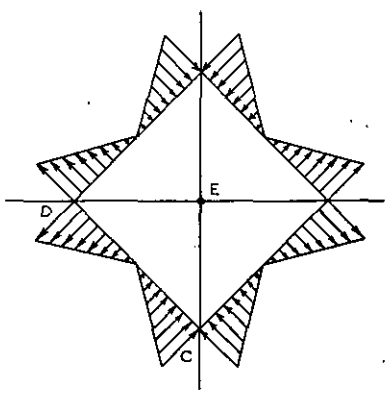

Fig. 8

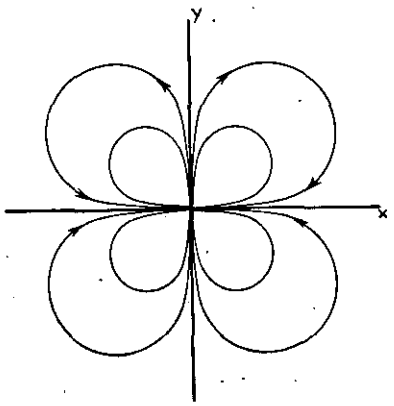

Fig. 9

$$\left.\begin{aligned} V_{qx}(t) &= Re\left\{\frac{-Q}{4\pi}\left(\frac{\pi}{b}\right)^3 \sum_m (-1)^m \frac{\cos\frac{\pi}{b}\left[ia - ih(\tfrac{1}{2}+m) + t(i-1)(h/2-a)\right]}{\sin^3\frac{\pi}{b}\left[ia - ih(\tfrac{1}{2}+m) + t(i-1)(h/2-a)\right]}\right\} \\ V_{qy}(t) &= Im\left\{\frac{Q}{4\pi}\left(\frac{\pi}{b}\right)^3 \sum_m (-1)^m \frac{\cos\frac{\pi}{b}\left[ia - ih(\tfrac{1}{2}+m) + t(i-1)(h/2-a)\right]}{\sin^3\frac{\pi}{b}\left[ia - ih(\tfrac{1}{2}+m) + t(i-1)(h/2-a)\right]}\right\} \end{aligned}\right\} \tag{3.1.5}$$

The velocity normal to the wall CD is given by

$$V_{qn}(t) = \tfrac{1}{2}\sqrt{2}\,(V_{qx}(t) + V_{qy}(t)). \tag{3.1.6}$$

For the tunnel mentioned under 3.1 $V_{qn}(t)$ is plotted together with $V_{\mu n}(t)$ in fig. 7.

The choice of Q has to be so that the average velocity normal to the wall CD is a small as possible. This happens when the transport through the half wall (from $t=0$ till $t=\frac{1}{2}$) is zero. Thus, the strength Q of the quadrupole is determined from the equation

$$\int_0^{1/2} (V_{\mu n} + V_{qn})dt = 0. \qquad (3.1.7)$$

The field (3.1.4) of the quadrupoles now gives only vertical perturbation velocities along the X-axis of the tunnel

$$V_{qy} = \frac{Q}{4\pi} \sum_m (-1)^m \left(\frac{\pi}{b}\right)^3 \frac{\cos \frac{\pi}{b}(x - \frac{b}{2} - i\frac{h}{2} - imh)}{\sin^3 \frac{\pi}{b}(x - \frac{b}{2} - i\frac{h}{2} - imh)}. \qquad (3.1.8)$$

Analogous to 2.1 and 2.2, (3.1.8) can be written as

$$V_{qy}(x) = \delta_2(x) U c_a \frac{F}{0}, \qquad (3.1.9)$$

with

$$\delta_2(x) = \frac{\pi^2}{8} \frac{Q}{\mu b}\left(\frac{h}{b}\right) \sum_m (-1)^m \frac{\cos \frac{\pi}{b}(x - \frac{b}{2} - i\frac{h}{2} - imh)}{\sin^3 \frac{\pi}{b}(x - \frac{b}{2} - i\frac{h}{2} - imh)}. \qquad (3.1.10)$$

Hence the correction angle due to the oblique tunnelwalls is

$$\Delta_2\alpha = \delta_2(x) c_a \frac{F}{0}. \qquad (3.1.11)$$

3.2 *Aerofoils with large aspect ratio.*

For aerofoils with large aspect ratio the calculation of the perturbation field and of the factor $\delta_2(x)$ as a result of the presence of the oblique tunnelwalls is about the same as for aerofoils with small aspect ratio.

The only difference appears in the formula (3.1.7) where the normal velocity $V_{\mu n}$ has to be replaced by $V_{\Gamma n}$ which corresponds with an aerofoil with finite aspect ratio.

From (2.2.9), the component normal to the oblique side is obtained as

$$V_{\Gamma n}(t) = \tfrac{1}{2}\left(\sqrt{2}\,(V_{\Gamma x}(t) + V_{\Gamma y}(t)\right). \qquad (3.2.1)$$

$$\left.\begin{aligned} V_{\Gamma x}(t) &= Re\left\{\frac{\Gamma}{4\pi i}\frac{\pi}{b}\sum_m (-1)^m \left[\operatorname{cotg}\frac{\pi}{b}(z - ihm - c) - \operatorname{cotg}\frac{\pi}{b}(z - imh + c)\right]\right\} \\ V_{\Gamma y}(t) &= Im\left\{\frac{-\Gamma}{4\pi i}\frac{\pi}{b}\sum_m (-1)^m \left[\operatorname{cotg}\frac{\pi}{b}(z - ihm - c) - \operatorname{cotg}\frac{\pi}{b}(z - imh + c)\right]\right\} \end{aligned}\right\} \qquad (3.2.2)$$

The dimensionless quantity $\frac{Q}{2\Gamma cb}$ can be determined from

$$\int_0^{t/2} (V_{\Gamma n} + V_{qn})dt = 0. \qquad (3.2.3)$$

V_{qn} being given by (3.1.6).

The perturbation-velocities along the X-axis of the tunnel, induced by the oblique walls and directed vertically because of the symmetry, are now given by

$$V_{qy}(x) = \delta_2(x) U c_a \frac{F}{0} \qquad (3.2.4)$$

with

$$\left.\begin{aligned} \delta_2(x) = \frac{\pi^2}{8} \frac{Q}{2\Gamma cb}\left(\frac{h}{b}\right) \sum_m (-1)^m \\ \frac{\cos \frac{\pi}{b}(x - \frac{b}{2} - i\frac{h}{2} - imh)}{\sin^3 \frac{\pi}{b}(x - \frac{b}{2} - i\frac{h}{2} - imh)} \end{aligned}\right\} \qquad (3.2.5)$$

The correction angle can be determined from

$$\Delta_2\alpha = \delta_2(x) c_a \frac{F}{0}. \qquad (3.2.6)$$

4 Aerofoil-fuselage-tunnel interference.

With an aerofoil-fuselage combination placed in a rectangular tunnel the flow has to satisfy two boundary conditions; both on the tunnelwall and on the fuselage the normal velocity has to disappear.

When the fuselage is long enough it can be substituted in first approximation by an infinitely long cylinder. The normal velocity can be made zero both on the tunnelwalls and on the cylindrical fuselage by applying a twofold image-process consisting of the reflecting with respect to the tunnelwalls, discussed earlier, and moreover a reflecting against the cylinder. The principle of the images with respect to a circular cylinder is dealt with in Appendix A; we will restrict ourselves to such cylinders.

The complete image-process is as follows:

The trailing vortices are reflected with respect to the rectangular tunnelwalls (linear reflection). The so generated virtual vortex pairs are now taken as dipoles and reflected with respect to the cylinder (circular reflection), through which a set of virtual dipoles are obtained within the cylinder. In a plane perpendicular to the undisturbed flow

this set of dipoles has the centre of the fuselage circle as a limit point; with small relative fuselage-diameter all these virtual dipoles can be thought in the centre of the circle, giving rise to a single dipole in this point. This dipole is now reflected linearly, the generated images being reflected circularly afterwards. With unlimited continuation of this image-process the virtual dipole within the circle converges to a limit dipole, with the aid of which the aerofoil-fuselage-tunnel-wall interference can be determined in first approximation.

In fig. 10 the aerofoil-fuselage combination in

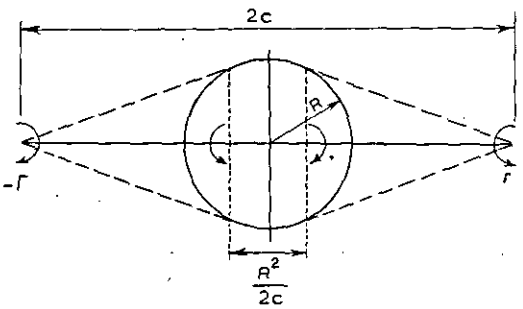

Fig. 10

free flight is represented. In first approximation the trailing vortex section can be seen as a vortex pair with strength $\pm \Gamma$ and distance $2c$.

The aerofoil-fuselage interference can now be expressed by the field of the vortex images represented in fig. 10 (within the circle) with strength $\pm \Gamma$ and distance $\frac{R^2}{2c}$, R representing the radius of the fuselage circle.

The resulting dipole strength of the two vortex-pairs together is given by

$$\mu = 2c\Gamma - \frac{R^2}{2c}\Gamma = \left(2c - \frac{R^2}{2c}\right)\Gamma. \quad (4.1)$$

attaching to the down-pointed dipole-vector a positive strength. Considering now this aerofoil-fuselage combination in a rectangular tunnel, the

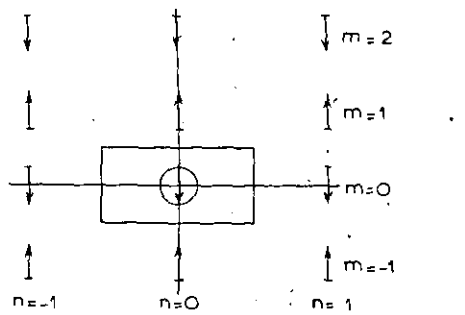

Fig. 11

first linear reflecting will have to be carried out with a dipole with strength μ (4.1). The result of this reflection is represented in fig. 11, the dipole in the n^{th} column and on the m^{th} row having a complex strength $M_{n,m} = -i\mu(-)^m$. The virtual dipoles have now to be reflected with respect to the circle.

According to Appendix A the image of the dipole (n, m) with complex strength $M_{n,m} = -i\mu(-1)^m$ and lying in the point $z = nb + imh$ is a virtual dipole with complex strength

$$-(-1)^m i\mu e^{i\alpha_{n,m}} \frac{R^2}{(mh^2) + (nb)^2}, \quad (4.2)$$

where $\alpha_{n,m} = bg\ tg\ \frac{mh}{nb}$.

Thinking all virtual dipoles in 0 and reflecting all dipoles generated by linear reflecting a virtual dipole with complex strength

$$M' = \sum_{m,n}{}' -(-1)^m i\mu e^{2i\alpha_{n,m}} \frac{R^2}{(mh)^2 + (nb)^2}, \quad (4.3)$$

is generated, the dash at the sum indicating that the term with $n = m = 0$ has to be excluded.

Out of considerations of symmetry M' is purely imaginary (resulting dipole-vector in Y-direction).

The ratio

$$\varepsilon = \frac{M'}{M_0} = \sum_{m,n}{}' (-1)^m e^{2i\alpha_{n,m}} \frac{R^2}{(mh)^2 + (nb)^2}, \quad (4.4)$$

$M_0 = -i\mu$ representing the complex notation for the "initial" dipole, is consequently real.

The extra dipole $M' = \varepsilon M_0$ generates by linear reflecting a row of image dipoles as in fig. 11, however, the strength of the dipoles now is ε times as large. Circularly reflecting the latter dipole set generates in 0 a new image dipole with strength $\varepsilon M' = \varepsilon^2 M_0$. Unlimited continuation of the linear and circular reflections gives in 0 a dipole with a complex strength

$$M^* = M_0(1 + \varepsilon + \varepsilon^2 + \ldots\ldots) = \frac{M_0}{1 - \varepsilon}.$$

As ε is real, the strength of this dipole is given by

$$\mu^* = \frac{\mu}{1 - \varepsilon}. \quad (4.5)$$

Supposing that the trailing tipvortex has the same strength Γ in both the free-flight situation and the tunnel situation the aerofoil-fuselage-tunnel interference has the following consequences:

1 the lift in free-flight is $A = \mu U\mu$, μ representing the resulting dipole strength of the trailing vortices plus the image-vortices.
The lift in the tunnel at the same strength Γ of the trailing vortices is $A^* = \rho U\mu^*$, where

$$\mu^* = \frac{\mu}{1 - \varepsilon}$$

Between the quantities A en A^* there exists the relation

$$\frac{A}{A^*} = \frac{\mu}{\mu^*} = 1 - \varepsilon. \quad (4.6)$$

2 The velocity $V_{\mu y}{}^*$ due to the tunnelwall influence has to be calculated with the aid of the dipole strength $\mu^* = \frac{A^*}{\rho U}$.

Consequently the *measured* lift coefficient $c_a{}^*$ has to be used in (2.1.9).

3 Compared to the free-flight situation, an extra dipole with a strength $\mu^* - \mu = \mu^*(1-(1-\varepsilon)) = \varepsilon\mu^*$ is located in 0.

This dipole induces a field which generates an extra induced velocity variation

$$\Delta_3\alpha = \frac{\varepsilon\mu^*}{4\pi x^2 U} = \frac{\varepsilon A^*}{4\pi\rho U^2}\,\frac{1}{x^2}.$$

With

$$A^* = \tfrac{1}{2}\rho U^2 c_a{}^* F$$

$$\Delta_3\alpha = \delta_3(x) c_a{}^*\,\frac{F}{0}. \qquad (4.7)$$

$$\delta_3(x) = \frac{\varepsilon}{8\pi}\left(\frac{h}{b}\right)\left(\frac{b}{x}\right)^2. \qquad (4.8)$$

5 List of symbols.

x, y	cartesian coordinates
$z = x + iy$	complex coordinate
b	tunnel width
h	tunnel height
a	vertical distance between tunnelaxis and intersecting line of the oblique wall with vertical tunnelwall
s	wing-span
$2c$	distance between the substituted vortices
R	radius of the fuselage
F	wing area
O	tunnel cross sectional area
v_x, v_y	velocity-components in X- and Y-directions
$\bar{v} = v_x - iv_y$	conjugated complex velocity
U	free-stream velocity
Γ	vortex strength
μ	dipole strength
M	complex dipole strength
Q	quadrupole strength
A	lift
ρ	density
t	parameter along the oblique tunnelwall
c_a	liftcoefficient
ε	interference factor
$\delta_1(x)$	tunnelwall influence factor in rectangular tunnel
$\delta_2(x)$	tunnelwall influence factor due to the oblique walls
$\delta_3(x)$	influence factor due to the aerofoil-fuselage-tunnel interference

6 References.

1. Batchelor, G. K. Interference in a wind tunnel of octagonal section. Report ACA — 1.
2. Batchelor, G. K. Interference on wings, bodies and airscrews in a closed tunnel of octagonal section. Report ACA — 5.
3. Knopp, K. Theory of functions II, page 278. Dover publications New York 1947.

Completed: March 1950.

APPENDIX A.

Reflecting with respect to a circle.

In a flowfield with complex potential $F(z)$ a circle C is drawn with radius R and centre 0.

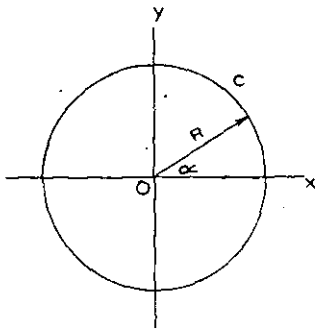

Fig. 12

We now look for a correction flow which neutralizes the normal velocities on the circle, C becoming a streamline in the resulting flow.

We shall prove that a correction flow with complex potential function $\overline{F}\left(\frac{R^2}{z}\right)$ satisfies this requirement.

The complex potential of the resulting flow is equal to

$$\varphi + i\psi = F(z) + \overline{F}\left(\frac{R^2}{z}\right);$$

For points on the circle $z = Re^{i\alpha}$, so

$$\varphi + i\psi = F(Re^{i\alpha}) + \overline{F}(Re^{-i\alpha}).$$

The two quantities in the right-hand side are conjugated complex, the sum therefore is real. Hence the flow function $\psi = 0$ vanishes on the circle and the circle is a streamline.

We shall apply this theorem to the flow of a dipole with strength μ and orientation β lying at the point $re^{i\alpha}$ (see fig. 13). This dipole has a flow-field

$$\bar{v}_1 = \frac{\mu e^{i\beta}}{2\pi(z - re^{i\alpha})^2}$$

and a complex potential

$$F(z) = \frac{-\mu e^{i\beta}}{2\pi(z - re^{i\alpha})}. \qquad (A.1)$$

The correction flow which has to be superposed to make the circle coincide with a streamline, consequently has a complex potential

$$\overline{F}\left(\frac{R^2}{z}\right) = \frac{-\mu e^{-i\beta}}{2\pi\left(\frac{R^2}{z} - re^{-i\alpha}\right)}$$

and a velocity field

$$\bar{v}_2 = \frac{-\mu R^2 e^{-i\beta}}{2\pi(R^2 - zre^{-i\alpha})^2} = \frac{\mu\frac{R^2}{r^2}e^{i(\pi+2\alpha-\beta)}}{2\pi(z - \frac{R^2}{r}e^{i\alpha})^2}. \qquad (9.2)$$

This flow field corresponds to a dipole with a strength $\mu \frac{R^2}{r^2}$ and a direction $(\pi + 2\alpha - \beta)$, situated at the point $z = \frac{R^2}{r^2} e^{i\alpha}$, being the inversion-point of $re^{i\alpha}$ with respect to the circle.

Reflecting a dipole with respect to a circle thus gives rise to a virtual dipole in the image-point,

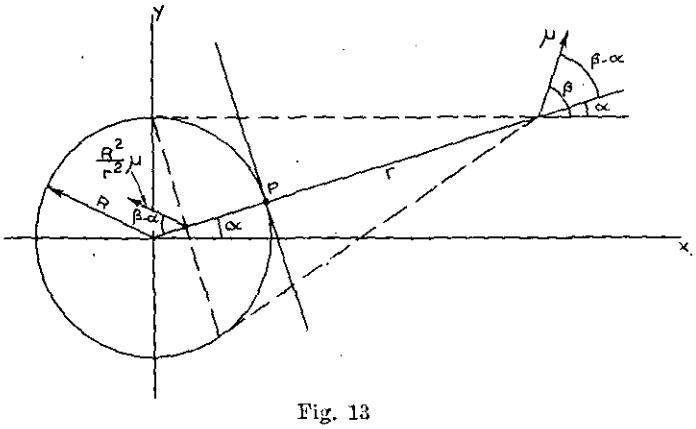

Fig. 13

the direction being reflected with respect to the tangent of the circle in P (see fig. 13) and the strength being multiplied with a factor $\frac{R^2}{r^2}$.

APPENDIX B.

The number of poles and stagnation-points in the octagonal tunnel.

Reflecting in the horizontal and vertical tunnel-walls gives rise to a doubly periodical flow field. The conjugated complex velocity then is an elliptic function, of which the period-parallelogram is the rectangle which can be described on the octagonal tunnel, doubled in height (see fig. 14). The fat drawn parts of the contour belong to the parallelogram. the dotted parts do not.

Now, according to the third theorem of LIOUVILLE (ref. 3), the number of zero-points of an elliptic function within the period-parallelogram is equal to the number of poles lying within it (a pole of the m^{th} order is counted m-fold).

Counting the number of zero-points of the conjugated complex velocity i. e. the number of stagnation-points within the period-parallelogram ,this number appears to be at least ten in the presence of one trailing vortex pair (see the numbered

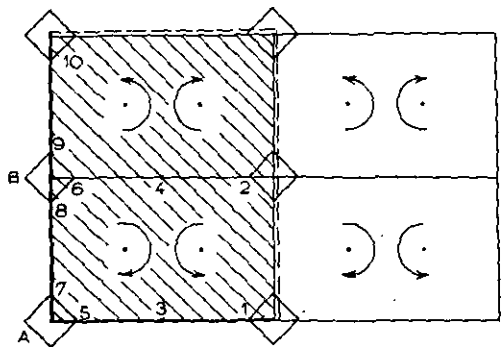

Fig. 14

points in fig. 14). Except the 4 vortices shown in fig. 14 at least six other poles are distributed in the period-parallelogram.

As the flow field in the tunnel is free from singularities, except for the drawn vortices, the remaining six poles can only be situated in the squares described on the oblique tunnelwalls. We now place the poles in the centres of these squares, i. e. in the angular points A and B of the rectangle, which can be described on the tunnel.

Because of anti-symmetry the six poles have to be distributed anti-symmetrically over A and B, so that at least a pole of the 3rd order at A and a reversed pole of the 3rd order at B have to be situated.

Formerly we have called a pole of the 3rd order of the velocity-function a quadrupole (as this can be formed out of 4 vortices). So it has been proved that the oblique wall of the tunnel can be represented by quadrupoles, if no more stagnation-points are present than indicated in fig. 14.

When there exist still other stagnation-points, poles of still higher order will be situated in the angular-points of the rectangle.

C.C.L. Class. D 982 : D.502

CAM
CH

REPORT A. 1269.

Survey of Transition Point Measurements at the N.L.L., Mainly for Two-Dimensional Flow over a N.A.C.A. 0018 Profile

by

Drs H. WIJKER.

Summary.

This report contains some remarks on experiences in the determination of the transition point. Results following various techniques are compared. Transition points on a N.A.C.A. 0018 profile are given for an angle of incidence between $-6°$ and $+10°$ and REYNOLDS numbers between 0.4×10^6 and 2.9×10^6.

Contents.

1 Some remarks on the mechanism of transition.

During the last four years some experiments have been carried out at the N. L. L. in order to get acquainted with the technique of the determination of the transition point, i. e. the point where the boundary layer flow changes from laminar into turbulent.

The experiments were carried out partly in wind tunnel nr 3, in which $Re_{cr} = 3.5 \times 10^5$ for a sphere of 150 mm diameter (*ref.* 1) and the intensity of turbulence $I \simeq 3\frac{1}{2}\,{}^0/_{00}$ (from hot-wire measurements), and partly, viz. smoke experiments, in tunnel nr 4 ($Re_{cr} = 3.1 \times 10^5$; $I \simeq 4\frac{1}{2}\,{}^0/_{00}$).

For these values of I, the fluctuations of the pressure in the flow outside the boundary layer will play a part in the transition phenomena (*ref.* 2). It is believed, that in this case transition always is preceded by laminar separation(*refs.* 3, 4, 5). As the pressures and pressure gradients fluctuate with time, the separation point will also fluctuate with time. The distance between the separation point and the point of reattachment may be rather large, especially at low REYNOLDS numbers. The separation and the sudden outburst into a turbulent jet can be seen very clearly in fig. 1b (see p. A 41). A smoke generator (fig. 2), developed at the N. L. L. (*ref.* 6), was placed in front of the model. This generator has the advantage that the smoke generation can be started and stopped very suddenly by switching an electric current on and off. Fig. 1a (see p. A 41) was taken shortly after the current had been switched on. The dead region between the separated flow

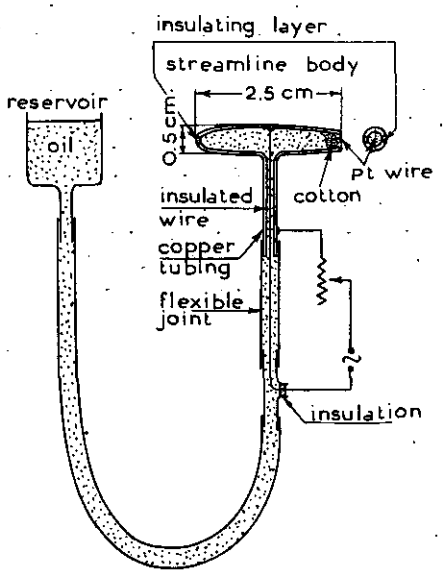

Fig. 2. Hot-wire smoke generator.

and the model has not yet been filled up with smoke. Before this occurred the current was switched off. The smoke will stay longest near the surface, where the velocity is lowest. Though at the edge of the dead region the velocity is not zero, it is low enough (see appendix I) to enable the smoke to stay there for a rather long time (see fig. 1b, p. A 41).

The distance between the separation point and the point of reattachment decreases rapidly with increasing REYNOLDS numbers. If this distance has become smaller than the segment swept over by the fluctuating separation point, it will be difficult to discern separation at all. When using the H_2S-method (*ref.* 7) on a cylindrical model with N.A.C.A. 0018 profile at rather high velocity and REYNOLDS number ($v = 41$ m/sec, $Re = 1.7 \times 10^6$), it once happened, however, that after a long time *) only a brown spot appeared round the hole out of which the gas was flowing. (The 4th hole from below in the lead-white layer of fig. 3, see p. A 41). With the China-clay method (*ref.* 8) it could be shown, that the hole just happened to be on the transition line.

This result strengthened our opinion, that even at high velocities transition commonly is preceded by laminar separation, provided that the turbulence of the main flow is not too low.

2 Some remarks on methods used.

2.1 *The China-clay method.*

Although using (lacquered) plastic models, we encountered difficulties similar to those found by other investigators in the case of wooden models (*ref.* 9). Therefore it may be useful to describe, how we have overcome these difficulties, thanks to kind information of Dr R. C. Pankhurst of the National Physical Laboratory, Teddington. They found their origin in the fact, that the liquids, used in this technique, have a great penetrating power and partly dissolved the lacquer. Therefore it is necessary to use a special lacquer of great hardness. A suitable lacquer is "Phenoglaze" which can be ordered from the "Phenoglaze Limited", 466 London Road, Croydon, Surrey.

The lacquer is sprayed in three layers. The drying time between the spraying of two successive layers is 1 day, after the third layer 1 week. These times may be reduced considerably by using infra-red drying, which however generally will not be allowed with wooden models. As for polishing, it is recommended to use waterproof emery paper (nr 600 for finishing) and water.

2.2 *The H_2S-method.*

From the chemical methods, described in *ref.* 7, we choose the H_2S-method as it is possible to regenerate the layer in this case with the aid of 30 % H_2O_2 (hydrogen peroxide). This is based on the well known equation

$$PbS + 4\,H_2O_2 \rightarrow PbSO_4 + 4\,H_2O\,.$$

The white $PbSO_4$ will react with H_2S in a similar way as the original $PbCO_3$, and will then give the brown or black PbS too.

The advantage of the method is, that it is possible to make a lead-white layer of the same smoothness as the best lacquer layer.

2.3 *Transition indication with smoke.*

At low air velocities it is possible to find the transition point with the aid of a smoke generator. PRESTON and SWEETING (*ref.* 10) described a method, where smoke was introduced into the boundary layer from a small hole in the surface. In the turbulent boundary layer the smoke will be diffused much more rapidly than in the laminar boundary layer, so that the visual smoke line ends at the transition point. With the smoke technique, used at the N. L. L., similar photos were obtained by taking them just a moment after having switched off the electric current (**1**). It may be pointed out, that originally we always found a smoke spot at the end of a line (fig. 4). Such a spot which could be very well reproduced, was caused by the small amount of turbulence introduced into the stream by the streamline body of the generator. By the liquid film technique (*ref.* 11) it could be shown, that this turbulence gives transition sooner (bend in the transition line of fig. 5). Comparison of the extension of the bends with the corresponding smoke spots showed, that they coincided entirely.

It is suggested, that only near the surface is the turbulence somewhat stronger at these spots, but that in the outer regions of the boundary layer the flow is laminar. Then the diffusion may be stronger than in the entirely laminar boundary layer, so that the liquid there evaporates more rapidly. However diffusion at this spot will be slower than in the entirely turbulent boundary layer, so that the smoke disappears later than it does further on over the surface.

The bend could be made smaller by increasing the distance between the leading edge of the model and the smoke generator. In this way we have taken smoke photos in flow, where the influence of the generator has been reduced to a negligible amount.

The smoke technique, used at the N. L. L. has several advantages compared with the technique of *ref.* 10, viz. (1): hole and tube in the model are not required; (2): with the same amount of disturbance, introduced into the flow by the mere fact that smoke has to be introduced, the smoke density is appreciably higher; (3): as a consequence of (2), the exposure time is appreciably smaller (0.05 sec. for the N. L. L. measurements, 30 sec. at those of *ref.* 10).

Another method of indicating transition points with the aid of smoke gives photos like fig. 6 (see p. A 42). The generator is placed so high, that a small part of the laminar boundary layer near

*) About the same time as the line in the turbulent boundary layer behind the 5th hole from below had been produced.

the surface is not filled with smoke. As soon as the flow becomes turbulent, the smoke diffuses to the surface and the black line, which can be observed in the laminar boundary layer between the smoke and its image, reflected by the smooth black lacquer, disappears.

3 Some remarks on obtainable results.

3.1 *The* H_2S*-method.*

When using the H_2S-method for transition indication, it is necessary to be sure that the reactive gas enters the flow in the laminar boundary layer. If, however, the H_2S enters the flow in the turbulent boundary layer, it will also draw a dark line behind the hole (in fig. 3 the line behind the 5th hole from below). It only requires more gas, before the line becomes visible.

The nearer these lines are together, the higher is the velocity between them. The curved lines in fig. 7b are streamlines. The product of the velocity and the distance between a line and its neighbour has been thought constant. So the smaller the area of the segment, the higher the velocity over it. The diagram below gives a survey of possible transitions (in the direction of the arrows). If such a transition can give a line of demarcation between wet and dry surfaces, the arrow is drawn; if this is not the case the arrow is dotted. In some cases (line 1) the latter is the usual one, though the former may occur for another drying time.

The regions of separation are divided into closed and open regions. Behind the former, the boundary layer reattaches to the surface, behind the latter it does not do so. Furthermore weak and strong separations are distinguished (fig. 8). In

Diagram of regions and transitions

(for further explanation: see below)

Wet	I	Laminar boundary layer
	II	Closed region of laminar separation
	III	Final part of the turbulent boundary layer
	IV	Open region of weak separation
	V	Front part of an open region of strong separation
Dry	VI	Front part of the laminar boundary layer
	VII	Turbulent boundary layer
	VIII	Open region of strong separation
	IX	Final part of an open region of strong separation

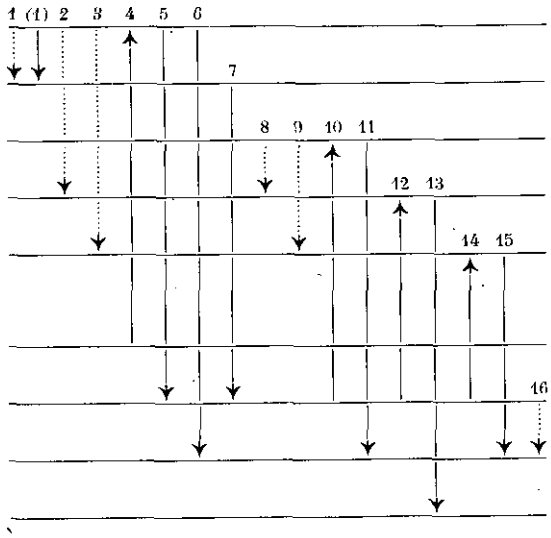

It may occur that one gets a line in a direction opposite to that of the main flow. This indicates reversed flow, which may be detected when for instance transition is preceded by a somewhat extended region of laminar separation. In this case a line starting from a hole in front of the laminar separation point will end at the separation point and not at the transition point.

3.2 *Evaporation methods (China-clay (ref. 8), liquid film (ref. 11)).*

Evaporation methods often give more than one line between wet and dry surface, as may be seen from fig. 7a (see p. A 42). The possible explanation is given in fig. 7b. The vertical lines on the fuselage are lines of constant pressure, if the wing would have been removed (simplified outline). These would have to be changed somewhat for the wing-fuselage combination. But for a rough insight this is unnecessary and is therefore omitted.

the former the speed of evaporation is very low, in the latter it is high at the trailing edge of the

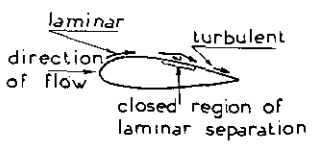

Fig. 8a.
Laminar separation (closed region).

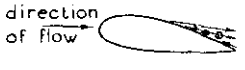

Fig. 8b.
Weak separation.

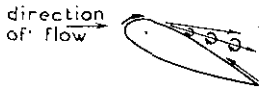

Fig. 8c.
Strong separation.

model and slows down in the direction of the leading edge. So drying up starts at the trailing edge.

The speed of evaporation and the wall shearing stress (τ_w) are closely related; qualitatively they may be given by the same line (fig. 9). The drying time is inversely proportionate to the speed of evaporation, provided that the amount of liquid per unit of area is constant at the start. In what follows this proviso is assumed.

Between the laminar and the turbulent layer there exists a transition region in which the velocity profiles gradually change from typically laminar profiles into typically turbulent ones (fig. 9). After the running time t_1 the surface

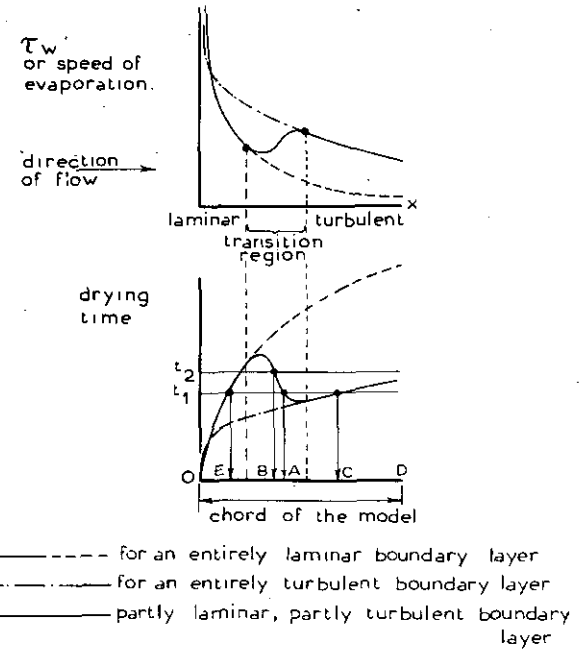

Fig. 9. Shearing stress, speed of evaporation and drying time along the surface.

will be dry along OE (front part of the laminar boundary layer) and AC and still wet along EB and CD (final part of the turbulent boundary layer). From the measurements one would conclude, that the transition "point" moves from A to B between the times t_1 and t_2. The transition region is smaller for large pressure gradients in the direction of flow than for small ones. At high, and even at moderate angles of attack, the extent of the transition region is negligibly small.

Fig. 10 gives somewhat idealized drying time curves for some flow conditions. The positions of the demarcation lines between wet and dry for several running times are given by the intersections of the drying-time line and the horizontal dotted lines. The numbers refer to the arrows in the "diagram of regions and transitions" on page A 31.

3.3 *Turbulence measurements in the boundary layer.*

Turbulence measurements without compensating for the time constant of the hot wire have been carried out in the boundary layer for two-dimensional flow over a N.A.C.A. 0018 profile with chord-length = 0.6 m, at an angle of incidence $\alpha = 0°$ and velocities $v = 29$ and 63 m/sec. The results for $v = 63$ m/sec are given in fig. 11a

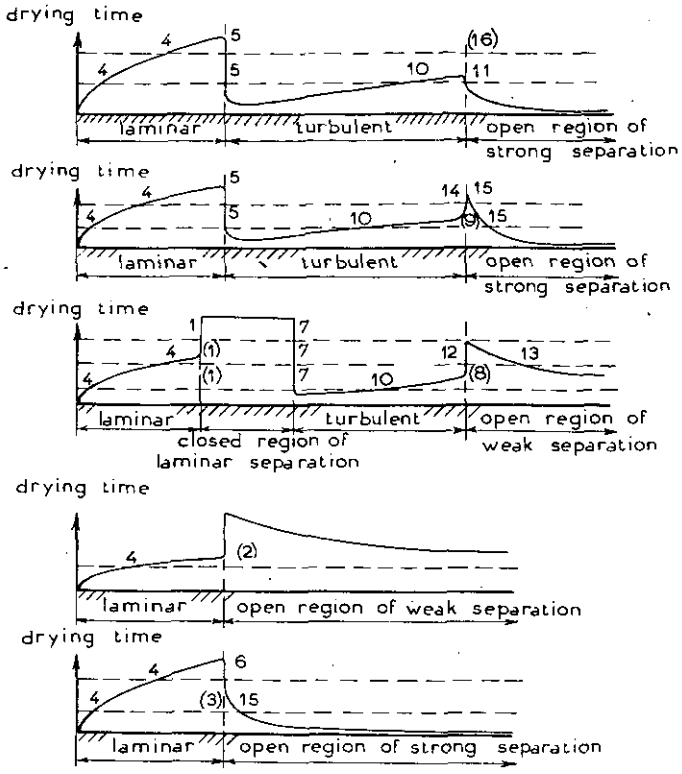

Fig. 10. Drying time *vs* place.

Figures refer to the diagram on page 4.
Figures in parenthesis = invisible transitions.

and 11b. The x, corresponding with the maximal values of $\sqrt{\overline{u^2}}/U$ in fig. 11a only varies 3 % chord with y. This nearly constant value is in accordance with experimental results of MICHEL and MÉNARD (*ref.* 12) and corroborates the basis of MICHEL's method of finding the transition point for drag calculations (*ref.* 13). Fig. 11b was derived from fig. 11a, omitting the points with question marks. From the measurements of MICHEL and MÉNARD one can derive a similar pattern for lines of constant turbulence viz. a maximum and a saddle surface behind it. The following explanation is suggested: —

After the laminar separation a turbulent jet originates (fig. 1b) in which, starting at a point not too far from the apex, the mean square root of the velocity fluctuations in the direction of the main flow, u', may decrease in the direction of flow (compare *ref.* 13). The mean velocity U decreases as well but we believe, that in our case this decrement will be far less than in the case of a jet in free air. In the latter u'/U becomes nearly constant (*ref.* 14, fig. 16); so in the former u'/U may decrease. After the flow has reattached to the surface, u' may stay nearly constant in the direction of flow, (e. g. *ref.* 15, fig. 8 for x between 17 and 20 ft), U however decreases, so that u'/U will increase.

It is surprising that very similar patterns are

obtained in the turbulent boundary layer just before separation (*ref.* 15, fig. 8).

Whether the points with question marks in fig. 11a are blunders or not is difficult to decide. It seems improbable that the same mistake could

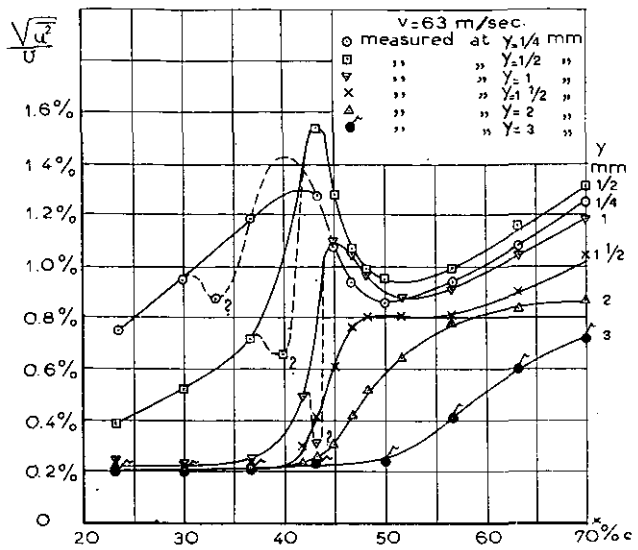

Fig. 11a. $\frac{\sqrt{\overline{u^2}}}{U}$ *vs* x for a NACA 0018 profile at $\alpha = 0°$ and $v = 63$ m/sec.

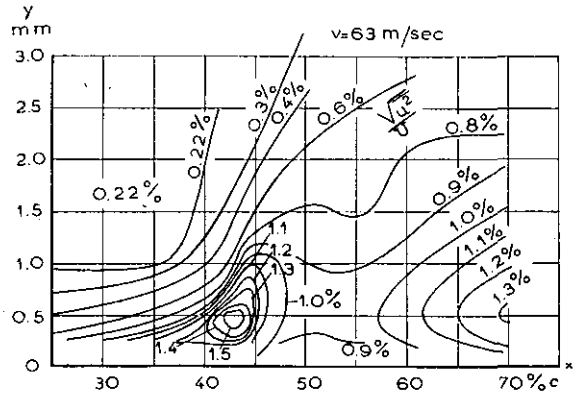

Fig. 11b. Lines of constant turbulence component $\frac{\sqrt{\overline{u^2}}}{U}$ in the boundary layer of a NACA 0018 profile at $\alpha = 0°$ and $v = 63$ m/sec.

be made three times at different positions. May be the minimum is a reality, whose existence is due to the laminar separation. On the other hand however we did not find similar minima at $v = 29$ m/sec.

3.4 *Measurement of the transition region with a total head tube.*

When moving a total head tube parallel to the surface from leading edge to trailing edge, the total head will first decrease, then increase and finely decrease again. Usually one considers the region between the minimum and the maximum for a line near the surface as the transition region. In reality the transition region extends from a point in front of the minimum to a point somewhat behind the maximum as is demonstrated in fig. 12. In this figure the caluated values of the pressure coefficient $\pi = (h - p)/\frac{1}{2}\rho V^2$ ($h =$ total head, $p =$ static pressure, $\frac{1}{2}\rho V^2 =$ dynamic

Fig. 12a

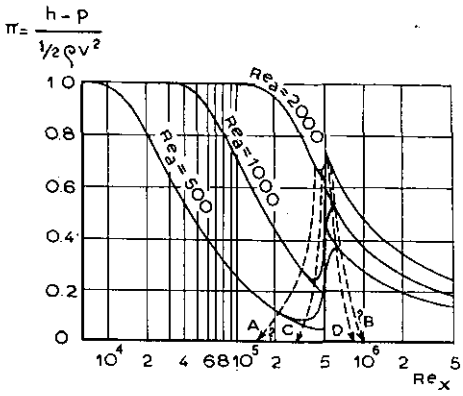

Fig. 12b

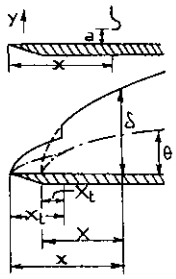

Fig. 12c

Fig. 12. Pressure coefficient $\pi = \frac{h-p}{\frac{1}{2}\rho V^2}$ *vs* $Re_x = Vx/\nu$ and $Re_a = Va/\nu$ for flow over a flat plate with $dp/dx = 0$.

pressure outside the boundary layer) for flow over a flat plate are given as a function of the position of the total head tube (fig. 12b). The following assumptions were made: —

1) the velocity profile in the laminar boundary layer can be represented by POHLHAUSEN's formula $U = V(2\eta - 2\eta^3 + \eta^4)$, $\eta = y/\delta$, $\delta =$ boundary layer thickness, $U =$ velocity component in x-direction, $V =$ velocity at the edge of the boundary layer $=$ constant. With this velocity profile one finds (when using VON KÁRMÁN's integral equation for the boundary layer) that $\delta/x = 5.83/Re_x^{1/2}$ with $Re_x = Vx/\nu$ (*ref.* 16).

2) the velocity profile of the turbulent boundary layer can be represented by the formula $U = V(y/\delta)^{1/5}$ *). This leads to the formula $\delta/X = 0.1285/Re_X^{1/5}$ with $Re_X = VX/\nu$ (*ref.* 18) for a boundary layer, turbulent from the very beginning. (For X see below and fig. 12c).

3) Transition occurs suddenly for $Re_x = 5.10^5$. At the transition point the momentum thickness

$$\theta = \int_0^\delta (U/V)(1 - U/V)\,dy$$

is the same for the laminar and the turbulent velocity profile. This implies a discontinuity in δ. After having calculated $\theta = \theta_t$ for the transition point, one can replace the first part of the plate

*) In this formula the exponent 1/7 is often used instead of 1/5. The exponent 1/7 was theoretically found by VON KÁRMÁN for turbulent pipe flow, for which $dp/dx < 0$. This derivation however does not hold for the flow along a flat plate with $dp/dx = 0$ (*ref.* 18) and, as HANSEN (*ref.* 17) pointed out, VAN DER HEGGE ZIJNEN's (*ref.* 19) experimental verification of the exponent 1/7 seems to be disputable. The exponent 1/5 leads to a value $H = \delta^*/\vartheta = 1.4$, which is generally accepted ($\delta^* =$ displacement thickness; $\vartheta =$ momentum thickness).

with length x_t by a part with length X_t, so that a boundary layer, turbulent from the very beginning, has the momentum thickness θ_t for $X = X_t$. Then $x - X = x_t - X_t$ (fig. 12c).

Hereafter, the δ of the turbulent boundary layer can be calculated.

Starting with the assumptions mentioned above one will get lines π versus Re_x for constant $Re_a = Va/\nu$ (a = distance between centre line of the total head tube and the surface), which lines have discontinuities at the transition point (fig. 12a).

In reality however the velocity profile will gradually change from the laminar one into the turbulent one, so that the discontinuous rises of π at the transition point must be replaced by continuous π-lines, as sketched in fig. 12a. The points, where these lines depart from and rejoin the original lines, can be connected, and by extrapolation to the surface ($Re_a = 0$) one gets the region AB in fig. 12a which ought to be defined as the transition region instead of CD (fig. 12a).

This has recently been confirmed by the measurements of MALOTAUX, DENIER VAN DER GON and YAP KIE JAN (*ref.* 20, p. 18). They determined the value of Re_x, at which transition starts, with the aid of a hot wire, placed in a static pressure hole just below the surface of the aerofoil. This value of Re_x appeared to be somewhat lower than the value of Re_x, at which the pressure coefficient π had its minimum (π was measured with a total head tube, the axis of which was situated about 0.2 mm above the surface c. i. 0.013 $^0/_{00}$ of the chord; Re_a was about 750).

In practice however it will be impossible to determine AB by measurements with a total head tube, so that, using this method, one has to be satisfied with CD as a first approximation. Along the same lines one can argue that the transition region is larger than the distance between the relative maximum and minimum of drying time (fig. 9).

3.5 *Measurements with a transition wire.*

A transition wire, placed on the surface in the laminar boundary layer normal to the direction of flow, increases the resistance of the model, for the part of the boundary layer between the wire and the transition point of the undisturbed flow has been made turbulent by it. So when moving a transition wire from the leading edge backwards, this part will decrease and the resistance will decrease as well. Once the transition point has been passed the resistance will not change appreciably any more (*ref.* 21). Fig. 13 gives a typical result of the measurements at the N. L. L. which differs somewhat from those of RICHARDS and BROWN (*ref.* 21), who did not find a minimum or relative maximum. This may be due to the small number of their points with the wire in the turbulent boundary layer. By using an integrating manometer (*ref.* 22) developed at the N. L. L., for the determination of the resistance from the total head measurements in the wake, we could measure a great number in a reasonable time (half an hour for the series of points given in fig. 13).

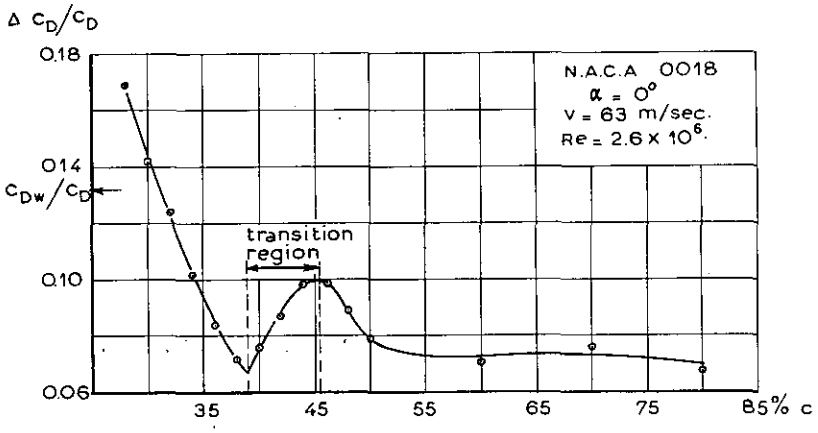

Fig. 13. Increase of drag, caused by a transition wire on the surface, ΔC_D, compared with the drag of the model without transition wire, C_D, versus the situation of the wire (0.5 mm ϕ). C_{Dw} = wire drag if placed in flow with $v = 63$ m/sec.

The drag coefficient of the model without transition wire is

$$C_D = \int_0^c \tau dx / \tfrac{1}{2}\rho v^2 c$$

(c = chord, $\frac{1}{2}\rho v^2$ = dynamic pressure, τ = shearing stress given by $ABHDE$ in fig. 14b. This value is given by the ordinate of the horizontal part of line a of fig. 14d).

For the model with transition wire the drag coefficient will be

$$C_D + \Delta C_D = \left(\int_0^c \tau dx + D_w \right) / \tfrac{1}{2}\rho v^2 c,$$

in which D_w = drag of the wire per unit length and τ is represented by $ABCDE$ (fig. 14b) for a

wire in P_1 (fig. 14a), by *ABHKDE* for a wire in P_2. Line *a* of fig. 14d gives $\int_0^c \tau dx / \frac{1}{2}\rho v^2 c$ versus the position of the wire.

D_w depends on the position and the diameter of the wire for a given value of V. The average value of the velocity U over the height of the wire decreases in the laminar boundary layer, when moving the wire backwards, increases in the transition region and decreases again in the turbulent layer, but much more slowly now.

D_w is closely related to this average speed, so the curve $D_w/\frac{1}{2}\rho v^2 c$ versus x of the wire has a similar character (fig. 14c). By adding the coordinates of curve *a* of fig. 14d and the curve of fig. 14c, curve *b* of fig. 14d was obtained. For a thinner wire a curve of type *c* (fig. 14d) may be obtained. Then the end of the transition region cannot be estimated any more.

From these considerations it follows that there is no contradiction in the results of RICHARDS' and and BROWN's measurements and ours.

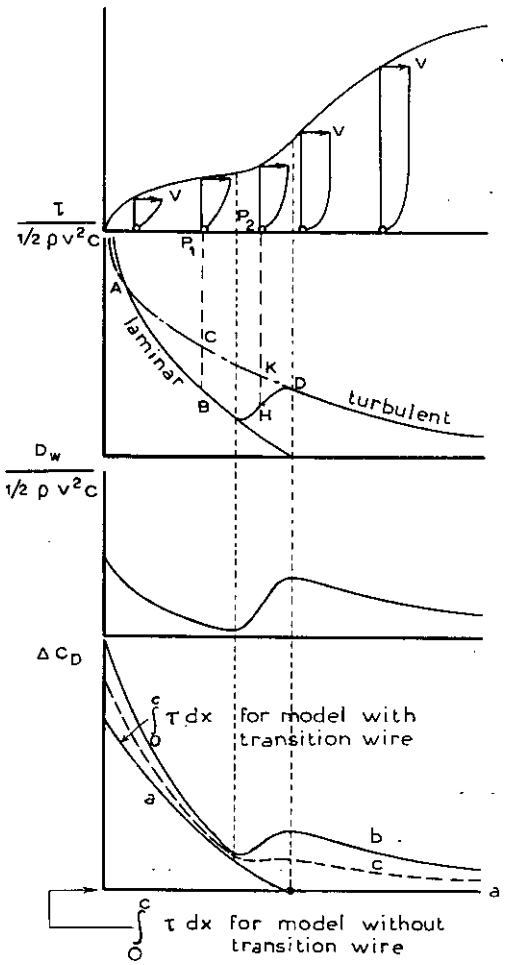

Fig. 14a.

Boundary layer thickness and velocity profiles.

Fig. 14b.

Local skin friction coefficient per cm width of the model.

Fig. 14c.

Drag contribution of the wire versus situation of the wire.

Fig. 14d

line a: drag of the model itself versus situation of the transition wire.

line b: drag of the model plus drag contribution of the wire.

line c: the same as curve b for a thinner wire.

4 Transition on a cylindrical model with N.A.C.A. 0018 profile.

4.1 *Comparison of results at $\alpha = 0°$, obtained by various techniques.*

The transition region at an angle of incidence $\alpha = 0°$ was determined by the following techniques:

a turbulence (4.3)
b total head tube (4.4)
c transition wire (4.5)
d stethoscope (The noise, heard in a stethoscope connected with a total head tube, is a measure of the pressure fluctuations).

The results are given in fig. 15 *). They show a great deal of scatter. Fig. 15 gives also a comparison with results given in *ref.* 23 which are obtained from the measurement of the velocity with hot wires along a line at 0.14 $^0/_{00}$ chord from the surface. The transition regions given in *ref.* 22 are much larger than those found with the total head tube at the N. L. L. There are two reasons for this. In the first place the centre of the hole of the total head tube was at a distance of 0.84 $^0/_{00}$ chord from the surface (e. i. 6 times as much as in *ref.* 23), in the second place the tube was moved along a straight line instead of parallel to the surface, which also results in a smaller distance between minimum and maximum. Furthermore the "transition points" obtained with the H_2S, the China-clay and the liquid film technique are given in fig. 15.

Their average values for constant speed lay as a mean about 1 % chord from the average starting points of the measured transition regions, which have an average length of 5 % chord.

*) For total head tube and transition wire measurements the distance between minimum and maximum has been taken as transition region instead of the region described in 3.4.

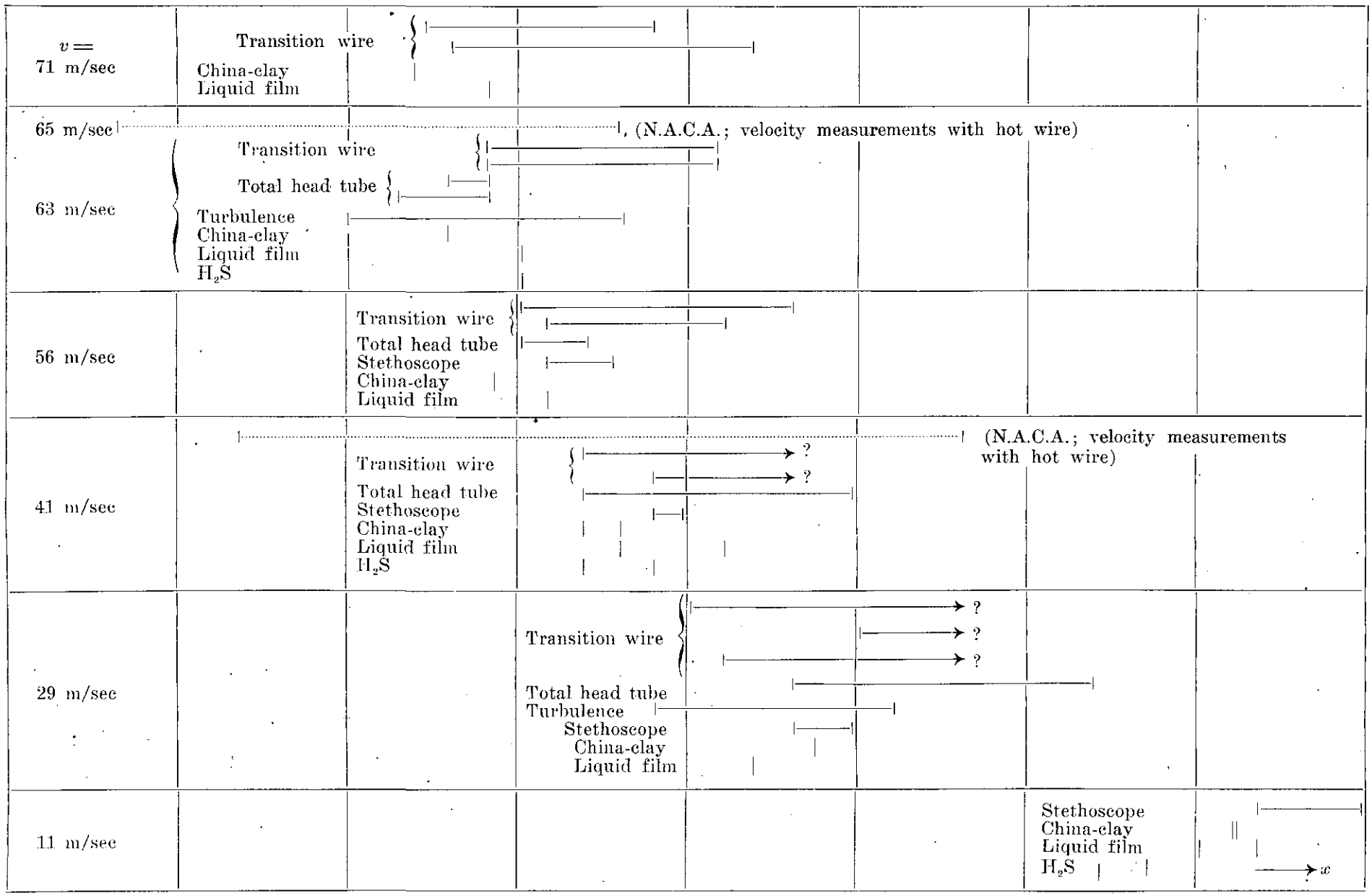

Fig. 15. Comparison of transition regions and transition points measured following various techniques for a N. A. C. A. 0018 profile (chord 0,6 m) at $\alpha = 0°$.

4.2 *Measurements at various angles of incidence.*

Results of the measurements of the transition points with the H_2S, the China-clay and the liquid film technique at various angles of incidence α and velocities are given in table 1, p. A 40. A negative angle means, that the surface is the pressure side of the model. Only occasionally is the scatter more than 2 % chord, and if so, this occurs chiefly for negative values of α, in which case the transition regions are rather large.

With the aid of the mean values, fig. 16 and 17 are plotted, giving the position of the transition point versus α and v and versus C_L and Re. From fig. 17 the values of x_t could be obtained at values of C_L and Re, at which measurements were carried out in the N.A.C.A. full scale tunnel, which has nearly the same turbulence characteristics as the N.L.L. tunnel.

From table 2 one can see, that the points found at the N.L.L. lay in the regions, found in the full scale tunnel (*ref.* 23), except one point, which lays only 1 % before the starting point of the region. This result is very satisfactory.

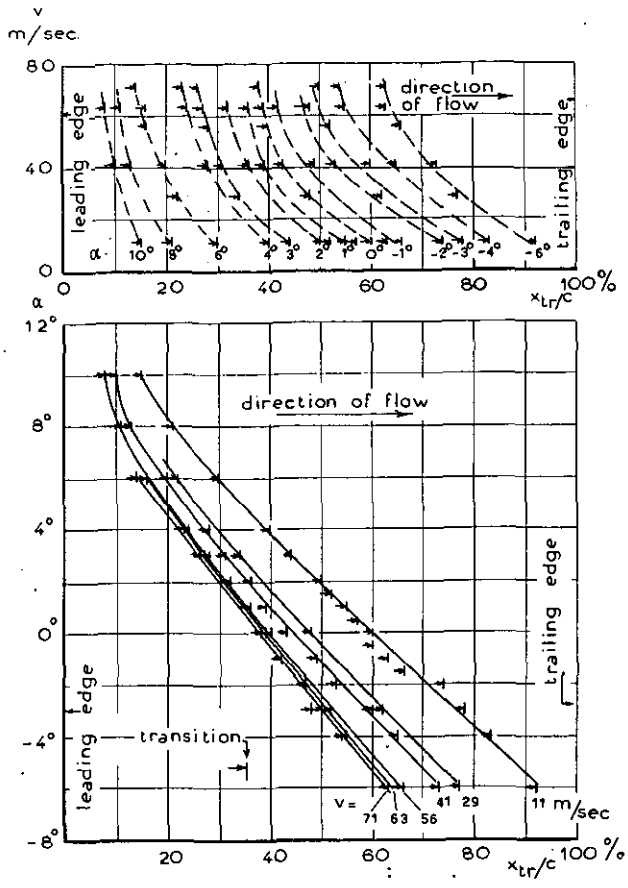

Fig. 16. Transition points for N.A.C.A. 0018 profile (chord 0.6 m).

Fig. 16a. Transition point versus velocity for various values of the angle of attack.

Fig. 16b. Transition point versus angle of attack for various values of the velocity v of the undisturbed flow.

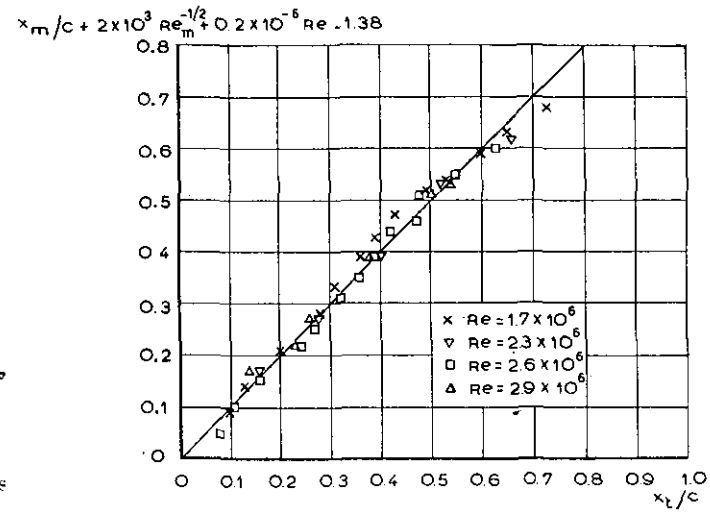

Fig. 18. Correlation of transition point measurements for a N.A.C.A. 0018 profile.

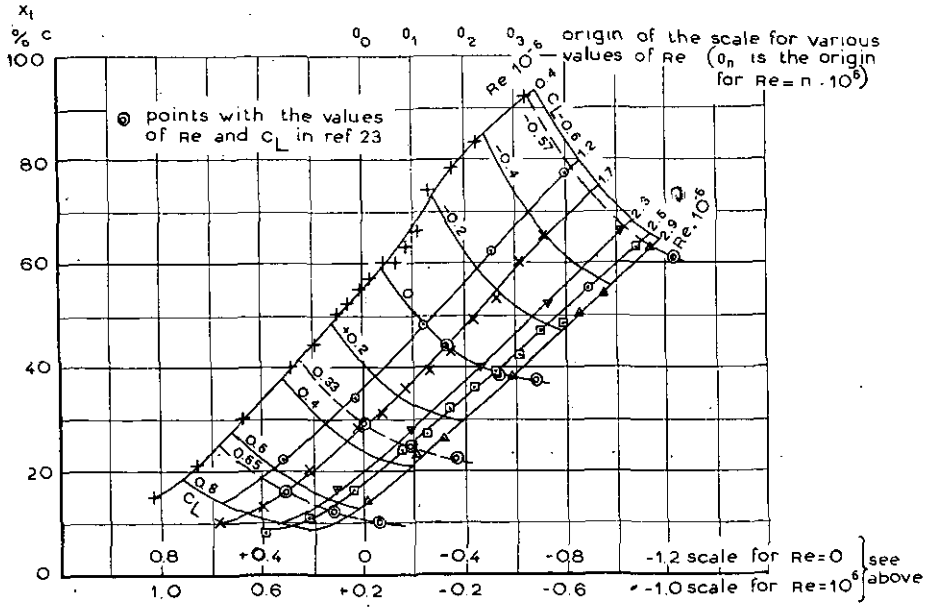

Fig. 17. Transition point on N.A.C.A. 0018 profile vs lift coefficient and Reynolds number of the undisturbed flow.

BECKER (*ref.* 24) found, that for the N.A.C.A. 0012 and N.A.C.A. 23012 profiles the transition points t for various speeds and angles of attack could be related with x_m, the abscissa of the position of maximum speed v_m, following the formula

$$(x_t - x_m)/c = 584\, Re_m^{-1/2} - 0.08$$
$$\text{with } Re_m = v_m c/\nu.$$

The results obtained at the N.L.L. with the N.A.C.A. 0018 profile did not fit this formula; they could be correlated by the formula

$$(x_t - x_m)/c = 2 \cdot 10^3\, Re_m^{-1/2} +$$
$$+ 0.2 \cdot 10^{-6}\, Re - 1.38 \text{ with } Re = vc/\nu.$$

as can be seen in fig. 18: the deviations from the 45° line are only small.

Completed: January 1952.

5 References.

1. WISELIUS, S. I. Drag and Pressure Measurements with Plaster Spheres in Wind Tunnel 3 and 4 of the National Aeronautical Research Institute. N. L. L. Report A. 950. Reports and Transactions Vol. XIII, 1947, p. A 1.
2. DRYDEN, H. L. Mechanics of Boundary Layer Flow. R. v. Mises, Th. v. Kármán, Advances in Applied Mechanics, Vol. 1 (1948).
3. TAYLOR, G. I. Statistical Theory of Turbulence. Part I—IV. Proc. Roy. Soc. A 151 (1935); Part V, ibid. A 156 (1936).
4. JACOBS, E. N. and VON DOENHOFF, A. E. Transition as it Occurs Associated with and Following Laminar Separation. Proc. Vth Intern. Congress of Appl. Mech., 1938, p. 311.
5. DROUGGE, G. Undersökning av Turbulensens Inverkan på Omslagspunktens Läge på en Vingprofil. Flygtekniska Försöksanstalten, Medd. Nr 20.
6. MEIJER DREES, J. and HENDAL, W. P. The Field of Flow through a Helicopter Rotor, Obtained from Wind Tunnel Smoke Tests. N. L. L. Report A. 1205; Aircr. Eng. Apr. 1951, p. 107.
7. PRESTON, J. H. and SWEETING, N. E. Experiments on the Measurements of Transition Position by Chemical Methods. R & M 2014.
8. RICHARDS, E. J. and BURSTALL, F. H. The "China-clay" Method of Indicating Transition. R & M 2126.
9. JAŇOUR, Z. Experimentální Vyšetřování Vývoje Mezní Vrstvy na Profilu (Experimental Investigation of the Development of the Boundary Layer on an Airfoil Section). Letecký Výzkumný Ústav, Praha, Zpráva čís 6 (1949).
10. PRESTON, J. H. and SWEETING, N. E. Wood Smoke as a Means of Visualising Boundary Layer Flow at High Reynolds Numbers. J. Roy. Aer. Soc., March 1943, No. 37, XLVII, p. 93.
11. GRAY, W. E. A Simple Visual Method of Recording Boundary Layer Transition (Liquid Film). Royal Aircraft Establishment, Techn. Note no. Aero 1816.
12. MICHEL, R. et MÉNARD, M. Transition et Turbulence de Couche Limite. O.N.E.R.A. Publ. No. 33.
13. MICHEL, R. Détermination du Point de Transition et Calcul de la Trainée des Profils d'Ailes en Incompressible. La Recherche Aéronautique No. 24, 1951, p. 41.
14. CORRSIN, S. and UBEROI, M. S. Further Experiments on the Flow and Heat Transfer in a Heated Turbulent Air Jet. N.A.C.A. T. N. 1865.
15. SCHUBAUER, G. B. and KLEBANOFF, P. S. Investigation of Separation of the Turbulent Boundary Layer. N. A. C. A. T. N. 2133.
16. POHLHAUSEN, K. Zur näherungsweisen Integration der Differentialgleichung der laminaren Grenzschicht. Z. A. M. M., 1921, S 252.
17. HANSEN, M. Die Geschwindigkeitsverteilung in der Grenzschicht an einer eingetauchten Platte. Abh. Aerod. Inst. Techn. Hochschule, Aachen, 8, 1928, S 31.
18. FALKNER, V. M. F. A New Law for Calculating Drag. Aircr. Eng. March 1943, p. 65.
19. HEGGE ZIJNEN, B. G. VAN DER Measurement of the Velocity Distribution in the Boundary Layer along a Plane Surface. Mededeling No. 6, Thesis, Delft.
20. MALOTAUX, P. C. A.; DENIER VAN DER GON, J. J. and YAP KIE JAN Methode voor kwalitatief grenslaagonderzoek met behulp van gloeidraden zonder beinvloeding van de stroming. Rapport VTH-45, Technische Hogeschool, Delft.
21. RICHARDS, E. J. and BROWN, T. W. Note on Methods of Determining Transition on an Aerofoil in a Wind Tunnel. A. R. C. Rep. and Mem. 2053.
22. DORBINGA, E. Opmerkingen over de meetmethoden voor de bepaling van de weerstand uit impulsmetingen in een windtunnel. N. L. L. Rapport A. 984.
23. SILVERSTEIN, A. and BECKER, J. V. Determination of Boundary Transition on three Symmetrical Airfoils in the N. A. C. A. Full-Scale Wind Tunnel. N. A. C. A. Report 637.
24. BECKER, J. V. Boundary-Layer Transition on the N. A. C. A. 0012 and 23012 Airfoils in the 8-foot High-Speed Wind Tunnel. N. A. C. A. Wartime Report L-682.
25. TIMMAN, R. A One Parameter Method for the Calculation of Laminar Boundary Layer. N. L. L. Report F. 35.
26. KÁRMÁN, TH. VON and MILLIKAN, C. B. On the Theory of Laminar Layers Involving Separation. N. A. C. A. Report 504.

APPENDIX.

Calculation of the velocity at the edge of the dead region.

For the calculation of the laminar boundary layer in retarded flow, TIMMAN (*ref.* 25) introduced the following velocity profile, having the asymptotic behaviour derived by VON KÁRMÁN and MILLIKAN (*ref.* 26):

$$U/V = 1 -$$
$$- \int_\eta^\infty e^{-\eta^2} (A_1 + B_1\eta + C_1\eta^2 + D_1\eta^3 + \ldots\ldots)\, d\eta$$

which, when satisfying boundary conditions at the wall, leads to

$$U/V = B\,(1 - e^{-\eta^2}) - D\eta^2 e^{-\eta^2} +$$
$$+ \frac{4(1-B)}{3\sqrt{\pi}} \int_0^\eta e^{-\eta^2} (1 + \eta^2)\, d\eta.$$

Here B and D are constants and $\eta = \alpha y$ with $\alpha^2 = -(dV/dx)/2\,\nu(B - D)$.

TIMMAN shows, that at the separation point $B = 2\,D$. When adopting this relation for the whole retarded boundary layer flow, he gets very good results.

In the following we shall assume that the formula for the velocity distribution, given above, also holds behind the separation point. We shall calculate the velocity at the edge of the dead region (fig. 19).

Developing $e^{-\eta^2}$ in a series, one finds

$$U/V = \frac{4}{3\sqrt{\pi}} (1 - B)\eta + (B - D)\eta^2 -$$
$$- \tfrac{1}{2}\,(B - 2D)\eta^4 - \frac{2}{15\sqrt{\pi}} (1 - B)\eta^5 \ldots\ldots$$

At the separation point, $B - 2D = 0$. So the 3rd term on the right hand side disappears. As the 5th term is 4 % of the first for $\eta = 0.8$ and we only want to study the flow for rather small

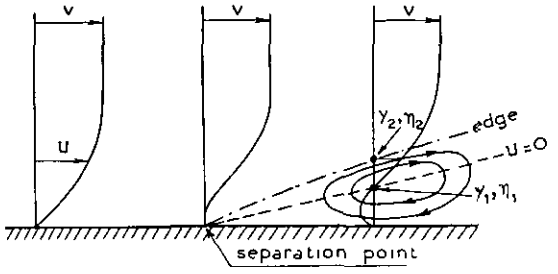

Fig. 19. Velocity profiles and dead-water region in the case of laminar separation.

values of η, we shall omit all terms except the first two.

So

$$U/V = \frac{4}{3\sqrt{\pi}} (1 - B)\eta + (B - D)\eta^2.$$

From this

$$U = 0 \text{ for } \eta = 0 \text{ and for } \eta = \eta_1 = \frac{4}{3\sqrt{\pi}} \frac{B - 1}{B - D}.$$

If there is no exchange of fluid between the main flow and the dead region, the amount of fluid going to the left between $\eta = 0$ and $\eta = \eta_1$ must be the same as that going to the right between $\eta = \eta_1$ and $\eta = \eta_2$ (fig. 19).

So

$$\int_0^{\eta_2} (U/V) d\eta = 0.$$

One finds

$$\eta_2 = \frac{2}{\sqrt{\pi}} \frac{B - 1}{B - D}$$

$$U(\eta_2)/V = \frac{4}{3\pi} \frac{(B-1)^2}{B - D}.$$

The assumption, that $B = 2D$ holds for the separated flow as well, leads to absurdities for somewhat larger distances behind the separation point (for $x - x_s > 4$ mm in the case of fig. 1). Therefore it seems better to connect B and D by an experimental result instead of using $B = 2D$. We choose instead the relation $y_2 = m(x - x_s)$, expressing that the edge of the dead region is a straight line. See fig. 1b and *ref.* 4.

Then

$$\eta_2^2 = \alpha^2 m^2 (x - x_s)^2 = \frac{-m^2 (x - x_s)^2 dV/dx}{2\nu (B - D)}$$

and with $\eta_2^2 = 4(B-1)^2/\pi(B-D)^2$ we find

$$4(B-1)^2/\pi(B-D) = -m^2(x-x_s)^2(dV/dx)/2\nu,$$

so that

$$U(\eta_2)/V = -m^2(x - x_s)^2(dV/dx)/6\nu.$$

For the case, given in fig. 1 (chord of the model $c = 0.30$ m; $V = 3$ m/sec), $dV/dx = -7.4$/sec and $m \simeq 0.1$, so that with $\nu = 15.10^{-6}$ m²/sec, $U(\eta_2)/V = 0.02$; 0.08 and 0.18 for $x - x_s = 0.5$; 1.0 and 1.5 cm respectively.

TABLE 1.

Transition point in % chord from the leading edge.

v(m/sec)	11			29		41			56		63			71	
Method / α	CC	H_2S	LF	CC	LF	CC	H_2S	LF	CC	LF	CC	H_2S	LF	CC	LF
— 6°	93	(76)	92	78	77	74		73	67	65	65		62	60	66
— 4°	82		83			64		66			53		56	53	55
— 3°	79		77	63	60	60		60	52	52	45		51	48	52
— 2°	76		72			51	52	52			46		48		
— 1.5°			66												
— 1°			63			49	48	51			42		43		
— 0.5°			60												
0°	61	58	60 *)	49	47	42	42	43 *)	39	41	38	40	40	37	39
	61	56	62			43	44	46							
+ 0.5°		58	57												
+ 1°		54	56			39	38	40			35		37		
+ 1.5°		51	52												
						36	35	36 *)							
+ 2°	51	50	49	34	34	35	33	38			31		33		
						30		32 *)							
+ 3°	45	43	45			29		32	27	29	26		29	24	27
+ 4°	40		40			27		29			23		24	22	24
+ 6°	30		30	22	22	19		20	15	17	15		17	14	14
+ 8°		22	21			13		14			11		11		
+10°			15			10		10			8		8		

*) Tests at different sides of the model in order to check symmetry conditions.

TABLE 2.

Position of the transition point on a N. A. C. A. 0018 profile, measured in the N. L. L. tunnel, in comparison with the transition region, measured in the N. A. C. A. full scale tunnel.

10^{-6} Re	Tunnel	Method	$C_L = -0.57$	$C_L = 0$	$C_L = 0.33$	$C_L = 0.65$
1.7	N.A.C.A. N. L. L.	Velocity measurements with a hot wire		32—53 44	25—35 29	15—28 16
2.7	N.A.C.A. N. L. L.	Velocity measurements with a hot wire		28—43 38	22—31 25	13—26 12
3.3_5	N.A.C.A. N.A.C.A. N.A.C.A. N. L. L.	Velocity measurements with a hot wire Total head measurements Velocity profiles	55—81 (?) 61	25—39 26—39 37	20—28 22	10—27 14—20 10

$\alpha = 4.3°$
$v = 3$ m/sec.

Direction of flow

Fig. 1a. Photo taken a short time after the smoke generator had been switched on and just before it will be switched off.
The dead region has not yet been filled up with smoke.

Fig. 1b. Some time after the smoke generator had been switched off. The smoke has not yet disappeared from regions with small velocities.

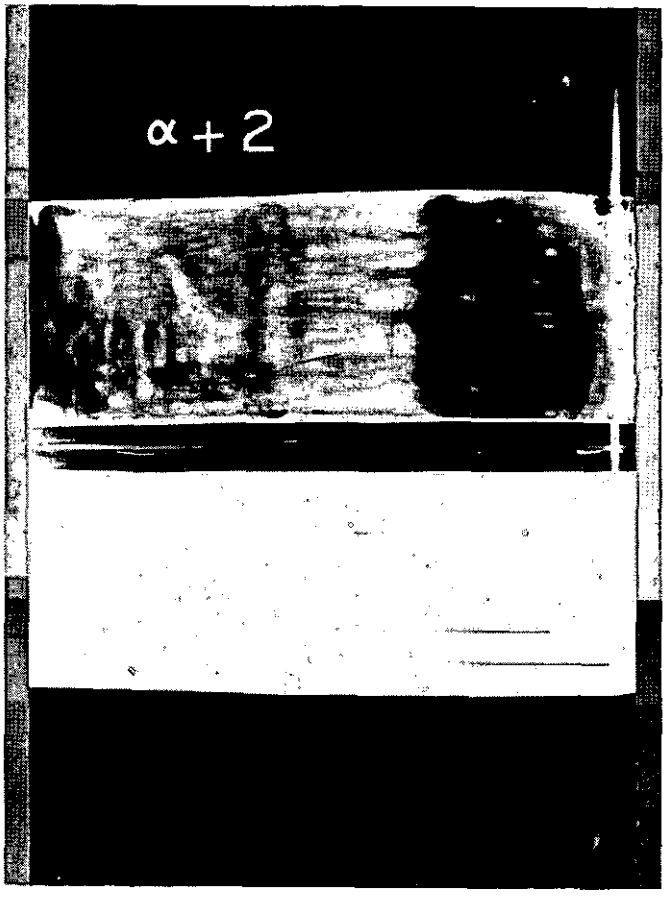

$v = 41$ m/sec.

Direction of flow

Fig. 3. China-clay method gives transition line.
Lead-white layer has reacted with hydrogen sulfur flowing from the 1st, 2nd, 4th and 5th hole from below; from the 4th and 5th hole during a comparatively long time. Spot round the 4th hole indicates separation.

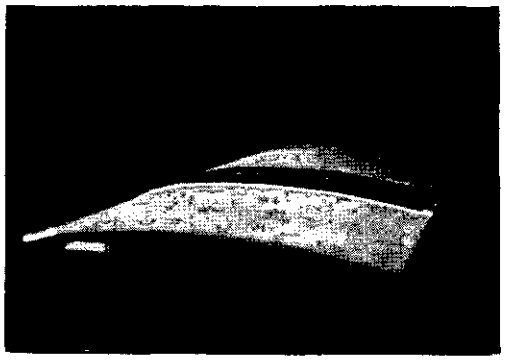

$\alpha = 0°$
$v = 5$ m/sec

Direction of flow

Fig. 4
Smoke spot at the end of the smoke line is caused by preliminar transition on account of the influence of the streamline body of the smoke generator.

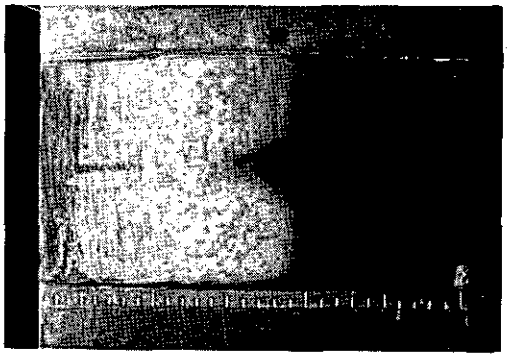

$\alpha = 4.2°$
$v = 5$ m/sec

Direction of flow

Fig. 5
Bend in the transition line is caused by the somewhat increased turbulence in the streamlines bordering the streamline body of the smoke generator.

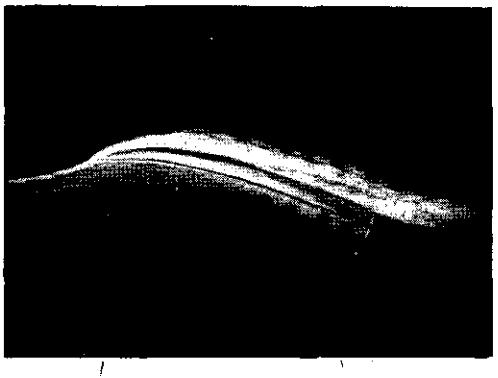

$\alpha = 9°$
$v = 3$ m/sec

Direction of flow

Fig. 6
Transition indication with smoke test. Diffusion of the smoke to the surface of the model in the turbulent boundary layer makes the black line between the smoke and its image disappear.

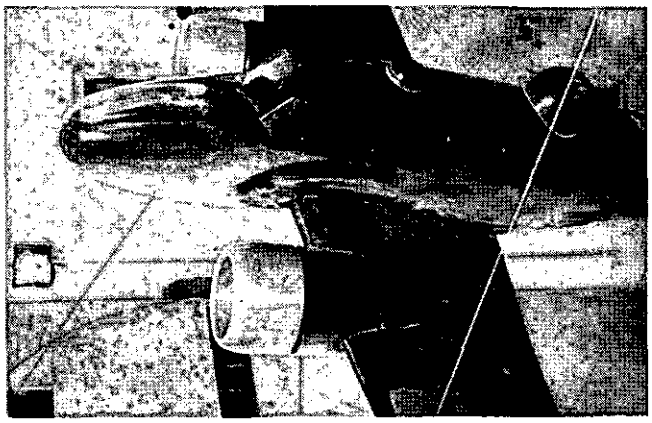

Direction

of flow

Fig. 7a.
Results, obtained with the liquid film technique, and their explanation.

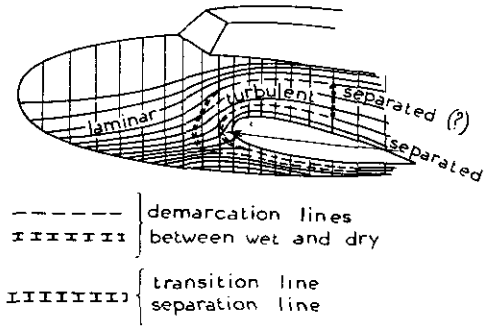

Fig. 7b. Results, obtained with the liquid film technique, and their explanation.

C.C.L. Class. E 012

CAM
044

REPORT A. 1238

Ditching Tests on a 1/8 . Size Model of the Fokker S-13 Crew Trainer

by

Ir J. F. HENGEVELD.

Summary.

A dynamically similar model of the Fokker S-13 (1/8 size) was subjected to a number of ditching tests at the NLL open air ditching station.

Conclusions were drawn on the effect of the attitude of the plane, on the character of the run, and on the influence of minor variables as flaps, propellers, landing gear, etc.

Several measures are proposed for the case of emergency.

Contents.

1 Introduction.

A series of tests were made at the request of the Netherlands Aeronautical Development Board with the object to determine the best way to make a forced landing with the Fokker S-13 aeroplane and to determine its probable behaviour. As no suitable installation for these tests was available, a launching catapult was built at the edge of the small harbour adjacent to the N.L.L. site.

Testing in the open involves a disadvantage viz. that a variable wind velocity is added to the launching speed obtained with the catapult. Windless days are very seldom in Holland, so that it is no use in postponing a test because of a slight or medium wind. The necessity of observation excludes working at night, when the atmosphere is more calm.

The nature of the wind is gusty, owing to the height of the surrounding buildings. During the tests it was attempted to start the model at the moment the wind appeared to be at a minimum. Also the tests were repeated several times under such conditions as were thought to have a chance of being succesful.

An eyewitness's estimation of all launchings was recorded, as well as the indication of the deceleration gauges. Those tests from which good results were expected were filmed as well.

From the films were obtained the length of the run of the model on the water, the attitude of the model during the run and at the time of first contact with the water and the effect of the immersion of the nacelles.

Although the tests do not give absolute certainty of the behaviour during a full size ditching, a number of rules are proposed to improve the chance of success.

2 Description of the model.

The model is a reproduction of the Fokker S-13 crew trainer, scale 1:8 (fig. 1, 2) with several simplifications: no separate ailerons or rudder, no landing gear, no gunturret, astrodome or wireless antennae are reproduced. These parts are of little or no consequence in case of ditching.

The hinge axis of the elevators was put 1 cm forward in the model, to augment the elevator capacity. Lateron, additional surface was added to the elevators, with the same object in view.

The apparent failing strength of the landing flaps can be adjusted by changing the amount of friction in the flap hinges. It was found that even a small amount of flap "strength" impaired the behaviour of the model after contact with the water. More friction in the hinges was not used for that reason.

On top of the fuselage and parallel to its longitudinal axis was fixed a wooden strip painted black and white, from which the attitude of the model could be measured on the films. Fig. 3 shows the deceleration gauges mounted between the boards by which the model is suspended from the catapult.

In order to maintain dynamic similarity the total weight of the model should be $(1/8)^3$ of the full size total weight. So that the model is 11,4 kg for 5775 kg full size. The centre of gravity was

brought to 25 % MAC by means of lead in the nose of the fuselage.

The model wing was constructed of balsa wood and light plywood frames and skin. The fuselage and nacelles were carved from balsa and hollowed out.

Model propellors shaped from aluminium sheet could be fitted.

The deceleration gauges are simple and able to operate under the conditions prevailing during ditching tests (rough usage and wetness). Each gauge has a weighted arm, retained in a near vertical position against a back-stop by an adjustable spring at the base. The weight and the spring-tension are adjusted on a whirling-arm, so that the deceleration at which the arm will move over is known. As several gauges are fitted, each adjusted to its own deceleration value, it is possible to judge the maximum value during the test from the indications.

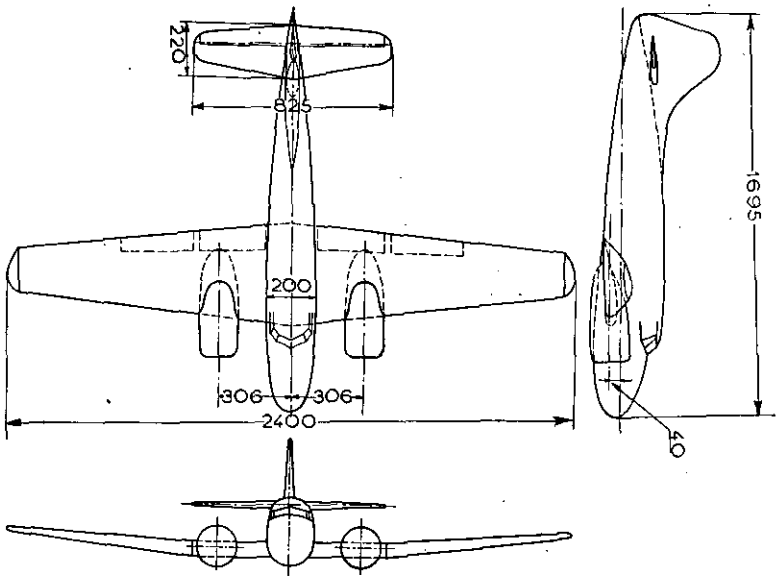

Fig. 1. Dimensions of S-13 Ditching-model.
Dimensions of model in mm.

3 Description of the launching gear.

The main components are:

a. the rail;
b. the carriage;
c. the dropweight, winch, etc.

The rail is an I beam 12 m (40 feet) long and suspended from two frames. It is adjustable in height and inclination. During all tests the inclination was 3°. The lowest position of the beam just allowed the model to clear the edge of the harbour. In this way the height above water at which the model began its free light was rather great, except with a very high water level.

Of the total length of the rail, about 10 m (32 feet) was available for acceleration of the model, the rest was taken up by the brake and by the length of the carriage.

The carriage runs on rubber covered wheels along the lower flange of the rail. The model is carried in two open hooks at the front of the carriage, and rests with its tail against a light frame which is adjustable in height for setting the angle of incidence of the model. Wooden strips on the carriage work the brake at the end of the run, so that it comes to a stop.

The dropweight hangs in a tower 3 m (10 feet) high from a rope, connected at one end to the carriage and at the other end to the winch. A system of pulleys is provided so that the speed of the carriage is four times the speed of the weight.

Additional weights of 10 or 20 kg (22 or 44 lbs) can be added as desired to the basic weight of 50 kg (110 lbs).

A certain *launching speed* can be obtained through the use of an appropriate weight. If we put: (change in potential energy) × (efficiency of the installation) = (change in kinetic energy), we find that:

$$\left(B \,.\, \frac{10}{4}\ \text{kgm}\right) \times 0.90 = \frac{A}{2\,g} \,.\, V^2 + \frac{B}{2\,g} \,.\, \left(\frac{V}{4}\right)^2 ;$$

where: A = weight of carriage, model and part of the rope;
B = total weight in tower;
g = acceleration of gravity;
V = launching speed.

When the carriage travels 10 m, the weight in the tower descends $\frac{10}{4}$ m. Also if the final speed of the carriage $= V$, that of the weight $= \frac{V}{4}$.

For these tests $A = 18.5$ kg $= 5$ kg (carriage) +

+ 11.4 kg (model) + 2.1 kg (rope). The efficiency was put at 0.90.

From this formula the value of B can be calculated for any launching speed V. The airspeed of the model is the vector sum of the launching speed and the negative windvelocity.

In fig. 4 curves are given for:

Launching speed (V) *vs* weight in tower (B).

Lift coefficient C_L *vs* airspeed.

These curves are only applicable to this model.

The centre of gravity was brought to 25 % of the mean aerodynamic chord with the aid of lead in the nose. The total weight had a value of 5835 kg (full size). During some tests with the ballast removed, the c. g. was at 39 % MAC and the equivalent full size weight was 5375 kg.

As a result of the numerous immersions the weight was augmented by water absorption, so that in the end the weight (with ballast) increased to: 6560 kg (full size) with c. g. at 30 % MAC and without ballast to 6100 kg with c. g. at 43 % MAC.

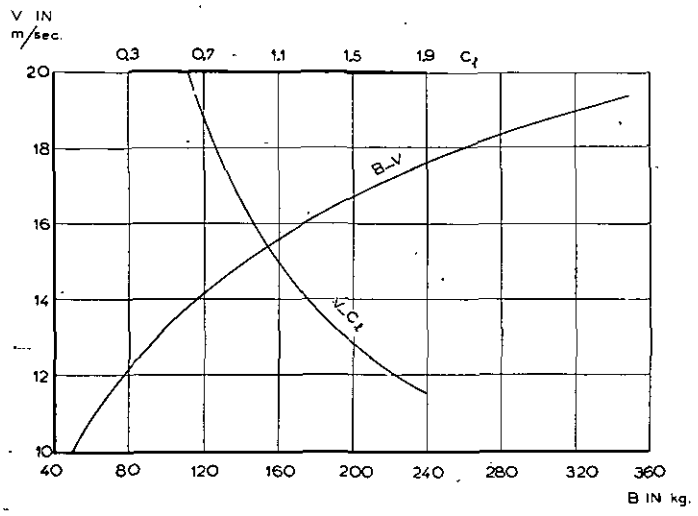

Fig. 4. Lauching speed V vs weight in tower B for S-13-model.
Liftcoefficient C_L vs air speed for S-13-model.

4 Test method and conditions.

Variables are:

Launching speed;
Elevator angle;
Landing flap angle;
Centre of gravity;
(these can be chosen at will).
Windforce and direction;
Height of rail above water level;
(these are outside influences and must be taken as they come).
Vertical speed and
Position of the model at the moment of contact with the water (these are a result of all variables mentioned before).

The launching speed had a value between 12 and 16 m/sec (120 and 160 km/h or 75 and 100 mph equivalent full size speed) although at first higher speeds up to 18 m/sec (184 km/ or 114 mph full size speed) were used.

The elevator was used to trim the model in a tail-down position till it touched the surface of the water. Owing to ground effect the original elevators were too small to be effective ,they were enlarged to obtain a better trim.

The landing flaps were either "up" or 60° "down". The friction in the hinges was adjusted so that the flaps returned to the "up" position as soon as they touched the water. Even so there is a bad effect on the behaviour of the model, and no larger amount of friction in the hinges was therefore used with flaps "down".

The wind velocity varied considerably during the tests. As far as possible the periods of low velocity were chosen for the tests but these were rather few at that time of the year.

The wind velocity at the moment of launching was estimated. It was usually in the range of 1—2 m/sec (2—4.5 mph) but speeds of 4 m/sec (9 mph) also occurred.

The direction of the wind was usually the opposite of the direction in which the model was launched. This is comparable to the full scale situation.

The height at which the model is set free could be varied. In practice the model always just passed over the edge of the bank, with the launching gear in the lowest position. The effective height is also influenced by the level of the water itself; variations of 0.20 m (8 ″) are possible. A high level improved the behaviour of the model (fig. 11) as it reduced the length of free flight.

The angle of incidence at the moment of first contact with the water is obtained from the film. The attitude at this moment is very important for the subsequent run.

The vertical velocity was 5 % of the launching speed at the beginning of the free flight. However, it was largely influenced by the peculiarities of the free flight.

It was not attempted to try out all combinations of the different variables. The elevator setting

was changed systematically, for different launching speeds and attitudes of the model, also with and without ballast, and with flaps up or flaps 60° *down*.

Films were made of those tests from which reasonable results were expected.

From each film was obtained:

a. the attitude of the model at the moment of contact with the water;
b. the length of the run;
c. the attitude at the time the nacelles began to dig in.

The range of maximum deceleration for each test was obtained (at that time) from the deceleration gauges on the model. It was not thought worthwhile to analyse the films in order to obtain the speeds and decelerations as the background in the film did not allow a sufficiently accurate measurement of the exact movement of the model.

During the tests the gauges were set to indicate decelerations of 2 g, 2.5 g and 3 g respectively. These values were chosen according to the evaluation of the run as *satisfactory* if the deceleration was below 2 g (no indication) as *unsatisfactory* when it was more than 3 g (three indications), and passable with one or two indications.

The quality of the run is also shown by its length. A bad landing has a run of only 2 lengths, a medium one of about 4 lengths and a good run may be up to 6 lengths of the model.

All these values are valid for the S-13 plane only.

5 Results.

A number of enlargements of the films of several runs are reproduced in figs. 7—12. Starting at the moment of first contact with the water, the equivalent full size time is given for each picture, as well as the length of the run, the approximate *maximum of the deceleration, the airspeed* and the windvelocity.

The runs depicted in figs. 7, 8, 9 are unsatisfactory. Very soon the nacelles dig in, as can be observed from the mass of water thrown up in a nearly perpendicular direction, with a dive as result as well as a high deceleration.

The run on fig. 10 is somewhat better although a certain amount of diving is visible towards the end. It is important that the tail of the model first touches the water.

The best run of all is that in fig. 11. The attitude during approach is definitely tail-down, and this is maintained during the run. The nose of the cockpit keeps above water all the time until the model is at rest when it floats on an even keel. The maximum deceleration is low (< 2 g) so that the gauges give no indication.

It is curious that by coincidence another satisfactory run was obtained (fig. 12) when the model approached tail-down and touched water *initially* with the starboard wing tip. As can be seen in fig. 12 the cockpit-nose stays out of the water all the time. The longitudinal deceleration was over 2,5 g, but nothing is known of the radial acceleration due to the angular speed. A similar ditching in tail-up position resulted in a serious dive.

6 Conclusions.

The only way to ditch the S-13 succesfully is to bring it down so that the tail touches the water first. Compare fig. 5, the attitude for $\alpha = 12°$. Otherwise the nacelles will dig in and a dive is the result.

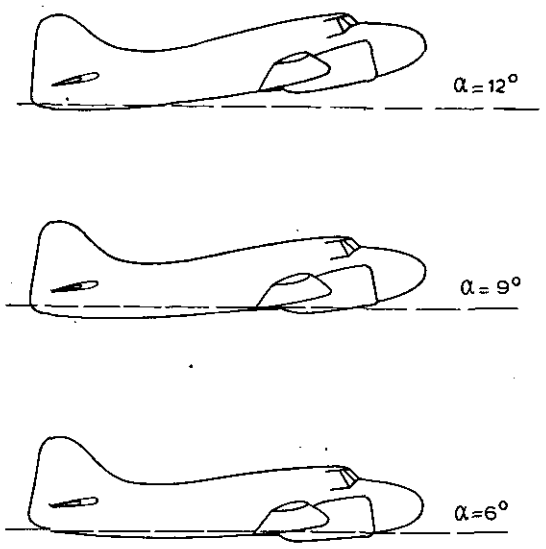

Fig. 5. Attitude of model on surface of water at different angles ($\alpha = 12°$, 9° or 6°).

The bottom of the fuselage aft of the wing is flat and wide so that the normal tendency of the pressure of the water on the model is to reduce the angle of incidence. It can be seen from fig. 6 that at $\alpha = 7°$ the nacelles will start to dig themselves in. This has to be avoided with all possible means.

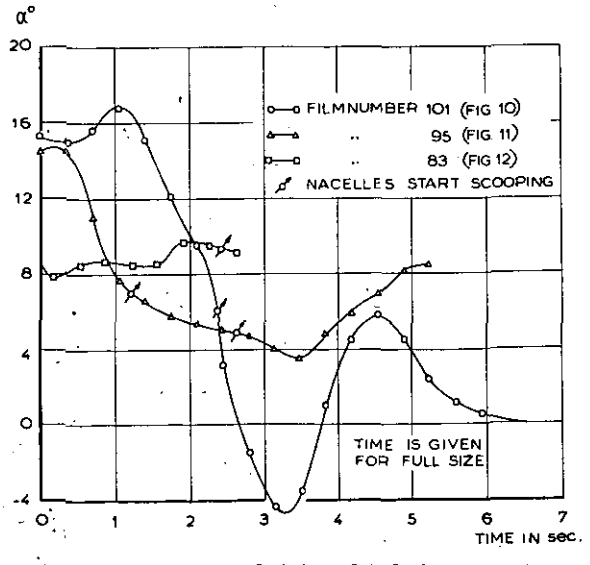

Fig. 6. Change of attitude of model during several runs, *obtained from films.*

In general, it is advisable to reduce the landing speed as much as possible, as well as the vertical

speed. The attitude should be with the tail down. To reduce the tendency of the nose going down, flaps and landing gear should be retracted, and propellers feathered. The centre of gravity should be as far aft as possible and ditching stations for the crew should be in the rear compartment. This is also advisable in connection with the risk to the occupants of the nose cockpit if the plane should dive.

The tests give no indication of the effect of waves. It is felt that in a regular swell the best chances are for a ditching along a wave.

Should a wingtip touch the water first, a rather violent swing is to be expected. As long as the tail is kept well down, this should not be specially dangerous.

If no major damage occurs, the attitude of the plane, when at rest on the water, should be about level (fig. 11). It will probably fill up more or less quickly after that. So long as no dive takes place, there is not much damage to be expected. As a result of diving, however, considerably damage will occur to the front of the fuselage, for instance to the bomb-aimers compartment and to the nose-wheel covers. This will reduce the buoyancy of the fuselage as well as the longitudinal stability on the water.

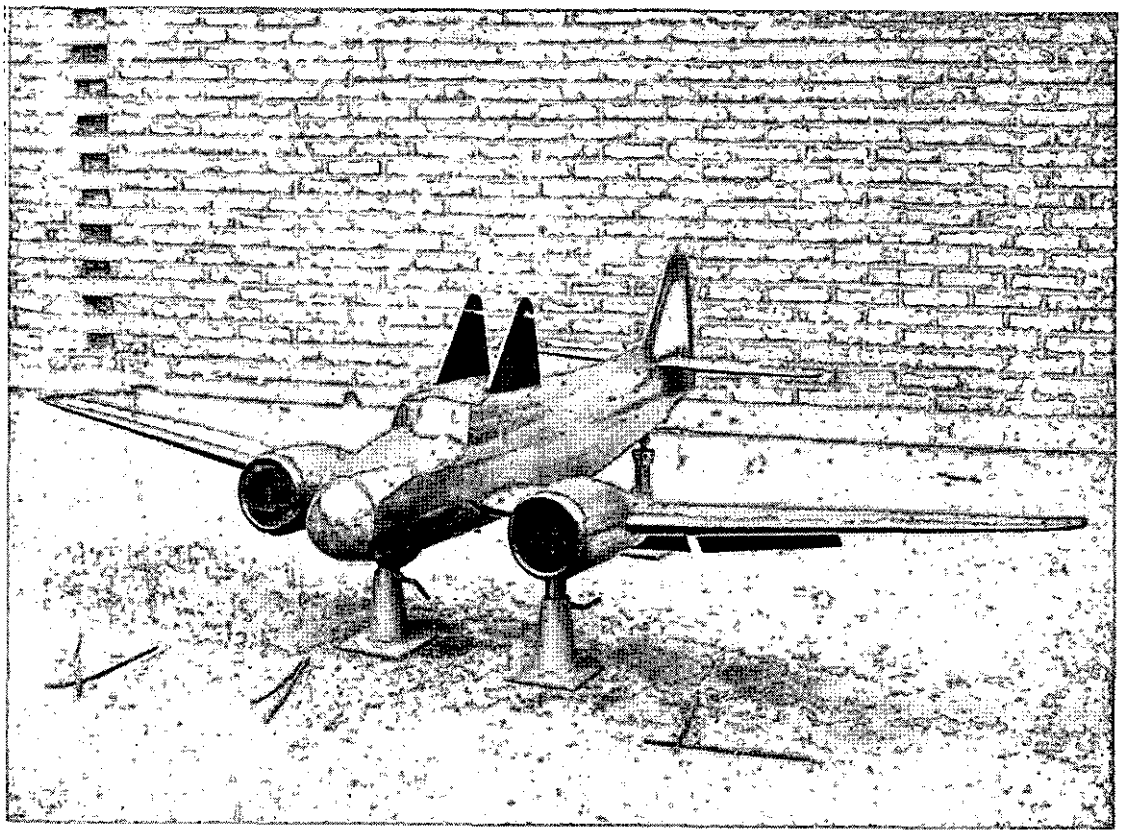

Fig. 2. a. Ditching-model, 1/8 th size. 3/4 Front view.

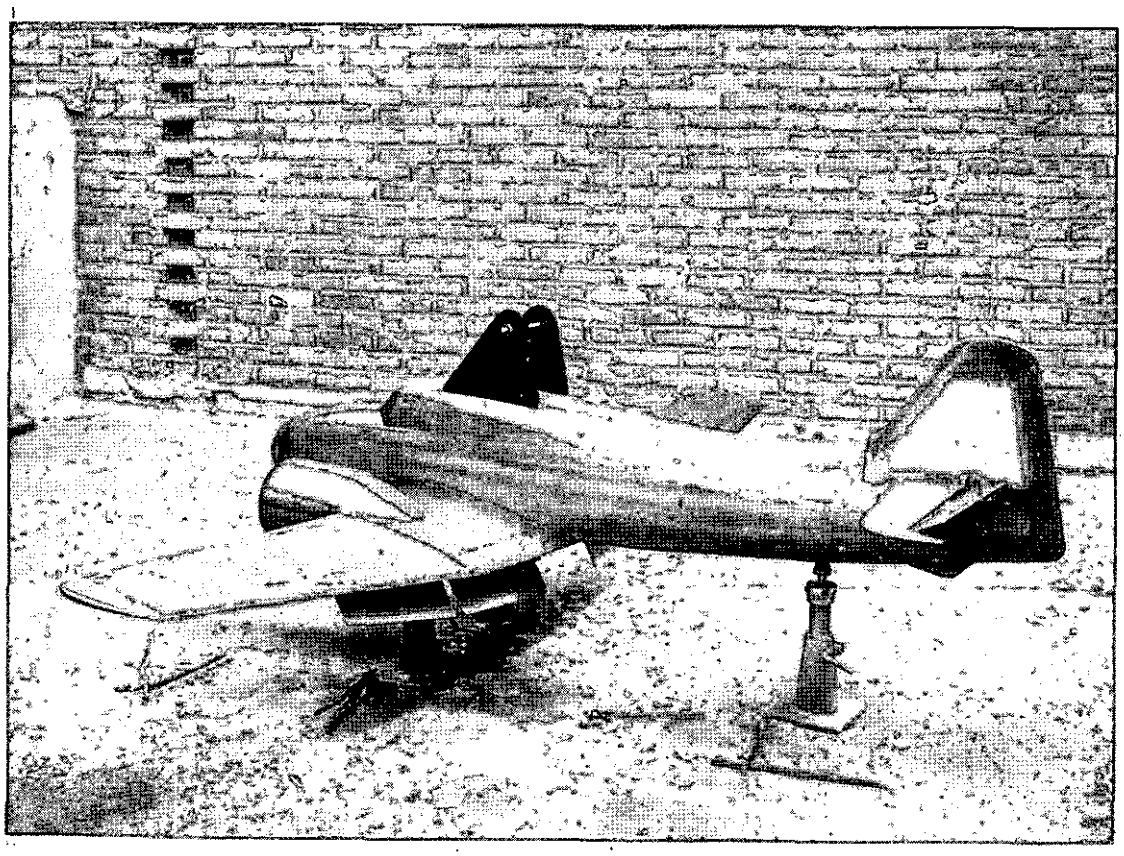

Fig. 2. b. Ditching-model, 1/8 th size. 3/4 Rear view.

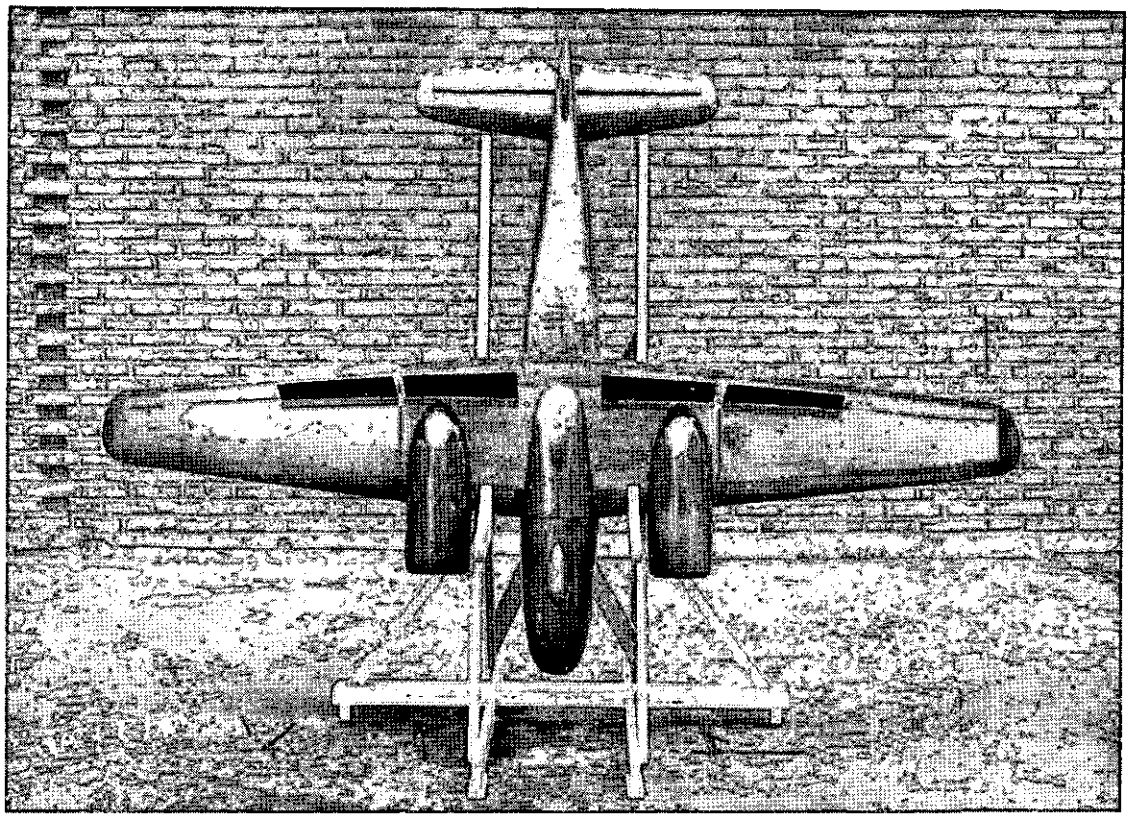

Fig. 2. c. Ditching-model, 1/8 th size. Under side with flaps down.

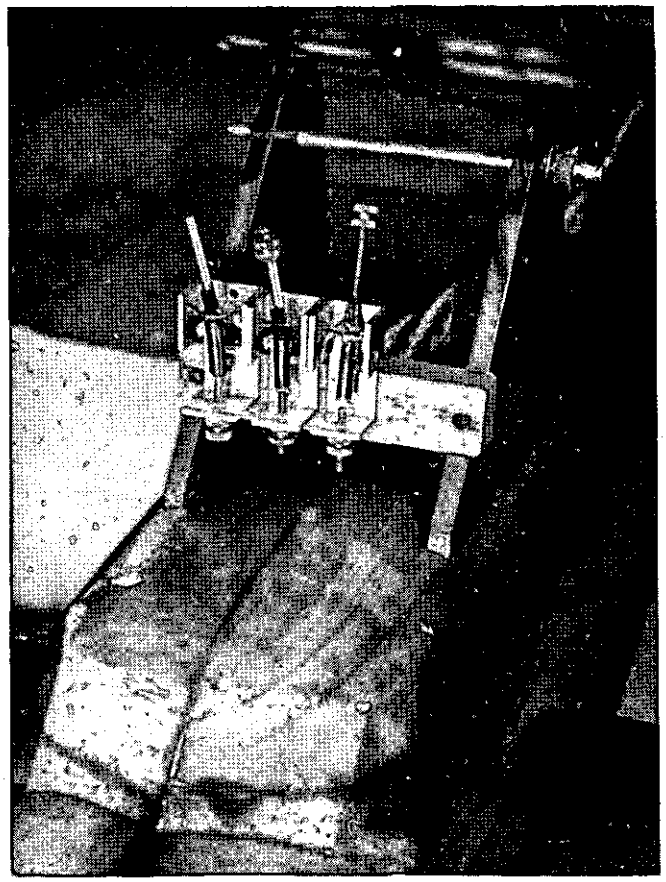

Fig. 3. Three maximum deceleration gauges located on the S-13 ditching model.
The gauges on the left and in the middle indicate certain decelerations, the arm of the right hand gauge is still in the original position.
The gauges are adjusted by screwing a small mass up or down the arm, or by varying the tension of the retaining spring with a screw at the bottom.

$t =$ 0 0.35 0.70 1.05 sec.

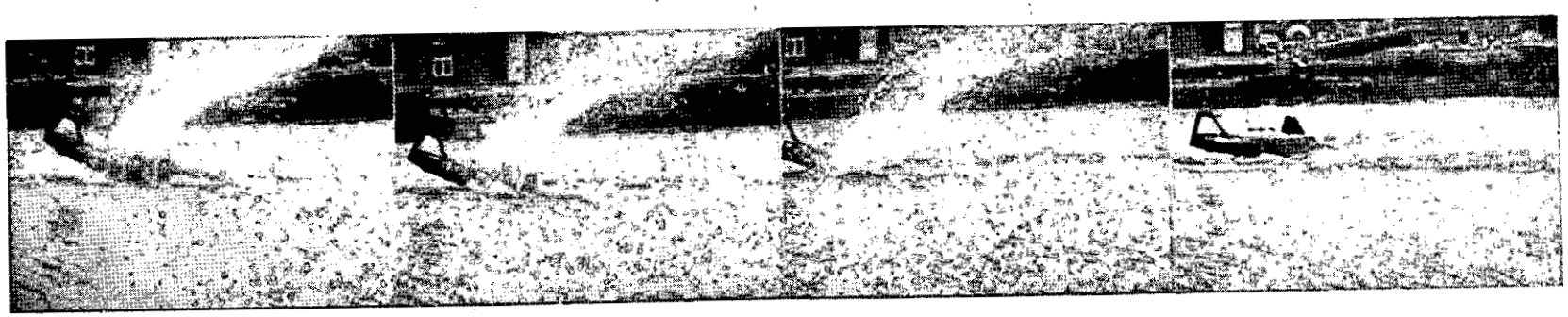

$t =$ 1.40 1.75 2.10 4.20 sec.

Fig. 7.

Film Nr. 70

Airspeed = 140 km/h (87 mph)
Windvelocity = 5 km/h (3 mph)

Length of run = 25 m = 1.9 × length of fuselage
Max. deceleration = > 3 g

All values given for full size

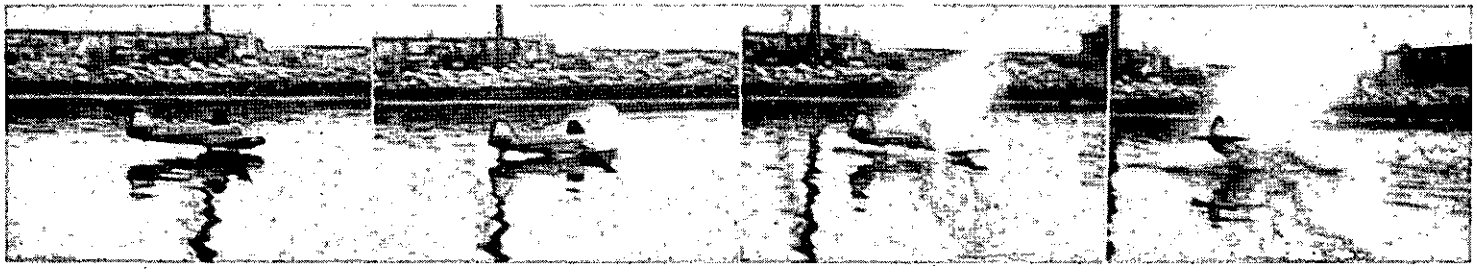

$t =$ 0 0.35 0.70 1.05 sec.

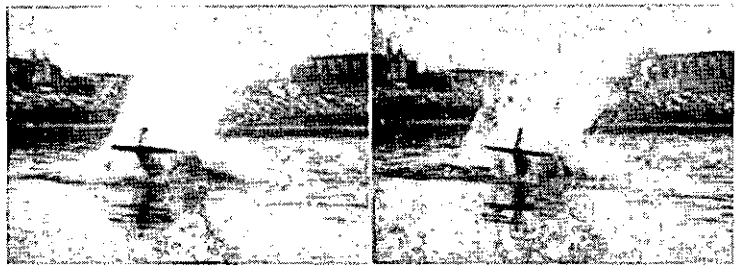

$t =$ 1.40 1.75 sec.

Fig. 8.

Film Nr. 45

Airspeed = 160 km/h (100 mph)
Windvelocity = 15 km/h (10 mph)

Length of run = 23 m = 1.7 × length of fuselage
Max. deceleration = > 4 g

All values given for full size

$t =$ 0 0.20 0.35 0.70 sec.

$t =$ 1.05 1.40 1.75 2.10 sec.

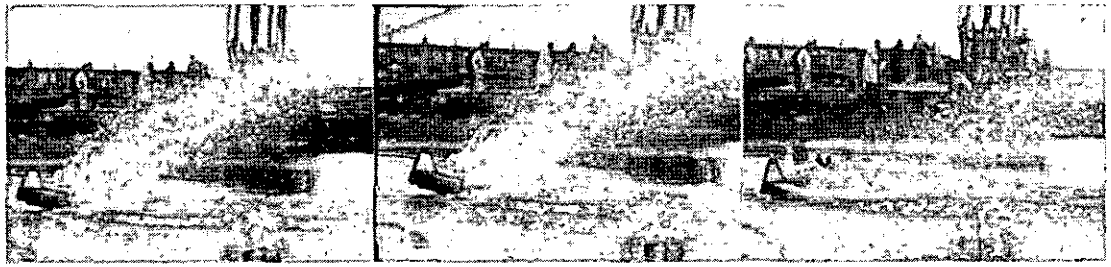

$t =$ 2.45 2.80 3.15 sec.

Film Nr. 68

Fig. 9.

Airspeed = 160 km/h (100 mph)
Windvelocity = 10 km/h (6 mph)

Length of run = 34 m = 2.5 × length of fuselage
Max. deceleration = > 4 g.

All values given for full size

$t =$ 0 0.35 0.70 1.05 1.40 1.75 sec.

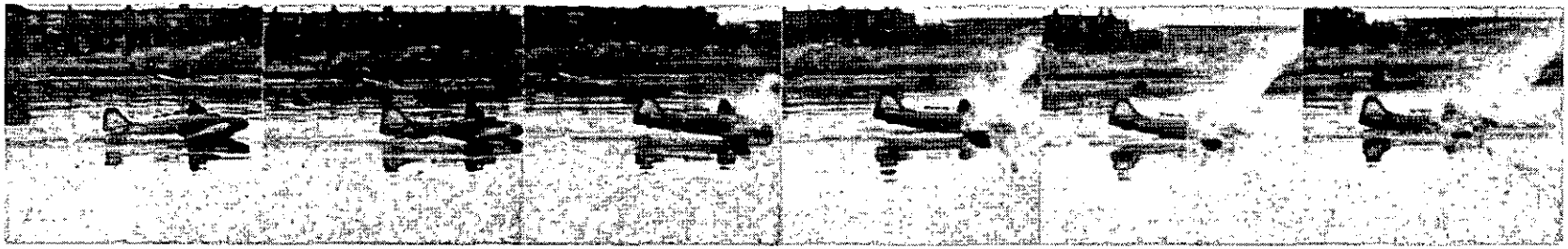

$t =$ 2.10 2.45 2.80 3.15 3.50 3.85 sec.

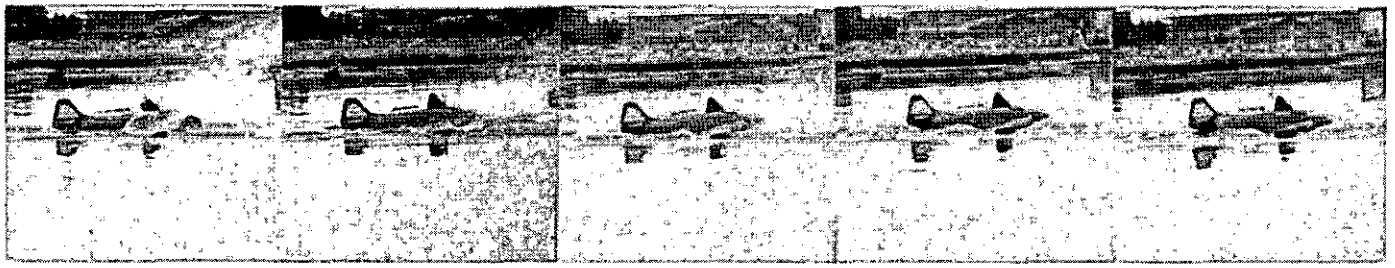

$t =$ 4.20 4.55 4.90 5.25 5.60 sec.

Film Nr. 101

Fig. 10.

Airspeed = 140 km/h (87 mph)
Windvelocity = 0 km/h (0 mph)

Length of run = 85 m = 6.4 × length of fuselage
Max. deceleration < 2 g

All values given for full size

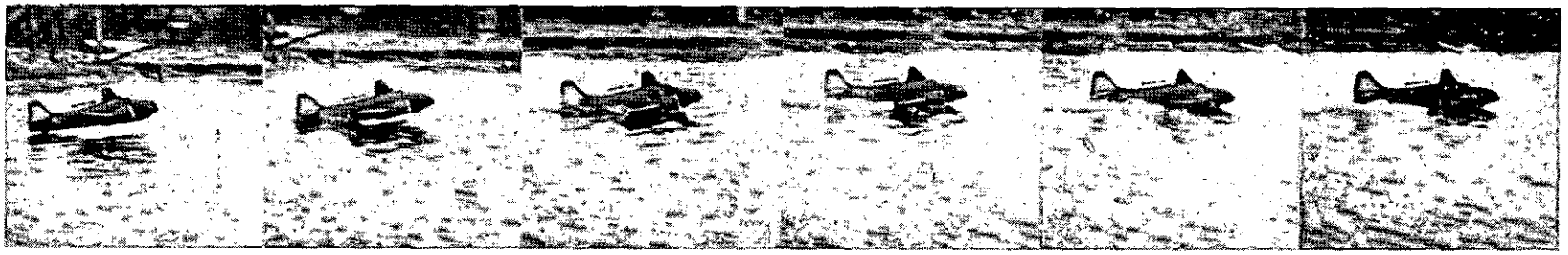

$t =$ 0 0.35 0.70 1.05 1.40 1.75 sec.

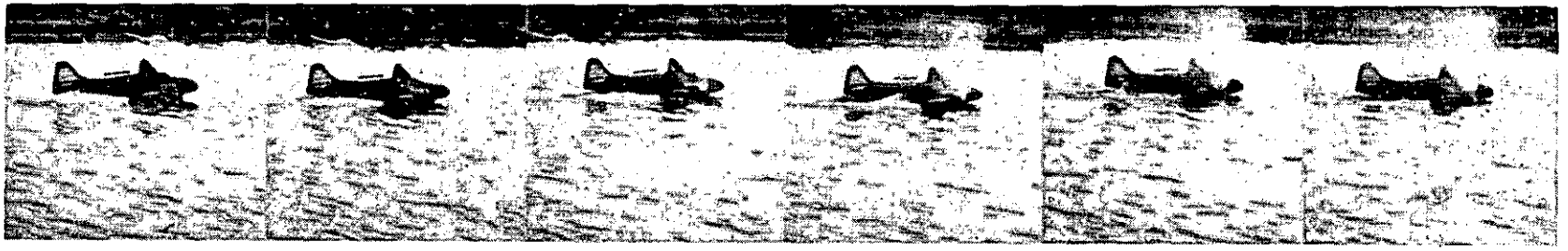

$t =$ 2.10 2.45 2.80 3.15 3.50 3.85 sec.

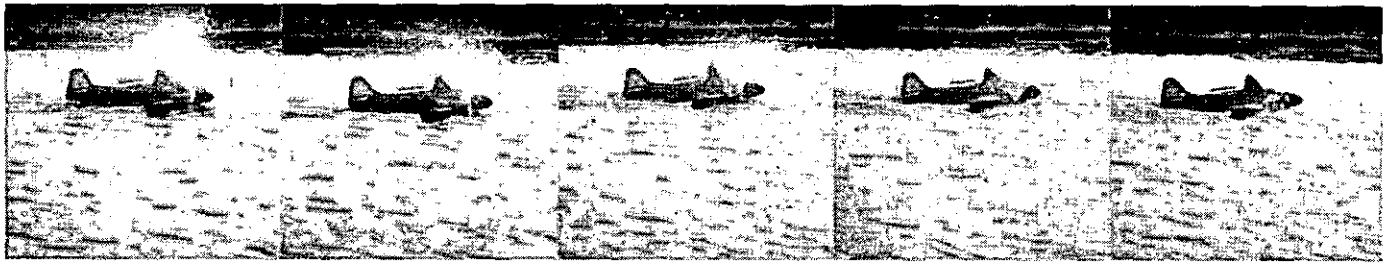

$t =$ 4.20 4.55 4.90 5.25 5.60 sec.

Film Nr. 95

Fig. 11.

Airspeed = 160 km/h (100 mph)
Windvelocity = 25 km/h (15 mph)

Length of run = 80 m = 6 × length of fuselage
Max. deceleration = $< 2\,g$

All values given for full size

$t =$ 0 0.35 0.70 1.05 1.40 1.75 sec.

$t =$ 2.10 2.45 2.80 3.15 3.50 3.85 sec.

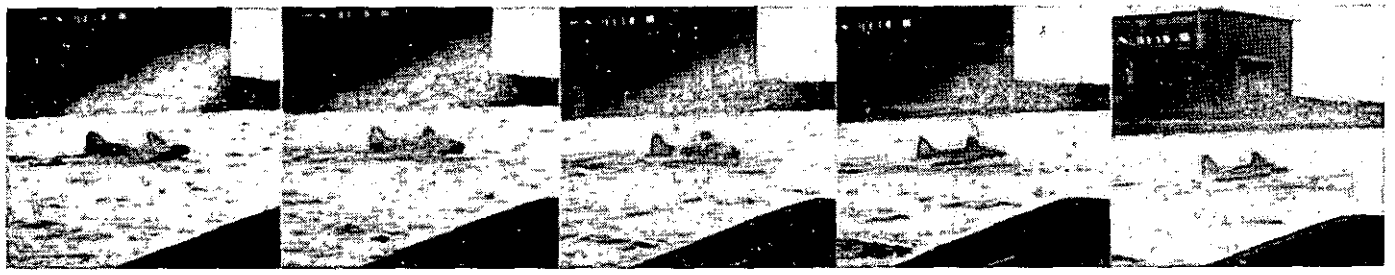

$t =$ 4.20 4.55 5.25 4.90 5.60 sec.

Film Nr. 83

Fig. 12.

Airspeed = 160 km/h (100 mph)
Windvelocity = 10 km/h (6 mph)

Length of run = 62 m = 4.6 × length of fuselage
Max. deceleration = 2.5 à 3 g

All values given for full size

CCL Class. D 300

REPORT F. 16.

The Direct and the Inverse Problem of Aerofoil Theory. A method, to obtain numerical solutions

by

Dr. R. TIMMAN.

Contents.

Preface.

Early in 1947 the Netherlands Aircraft Development Board (N. I. V.) ordered the National Aeronautical Research Institute to make a theoretical investigation of the design of laminar flow and high speed aerofoils. At that time results obtained in Britain and America during and after the war were not yet known in this country and hence the investigation started from prewar papers by BETZ (ref. 1) and MANGLER (ref. 2).

The method developed appeared afterwards to be closely related to LIGHTHILL's method (ref. 3), which again involves the same basic idea's as MANGLER's. Also PEEBLE's method is based on the same principles. Essentially, all main differences concern to the principles applied in the numerical application and evaluation.

The present report gives a complete review of all work done in the National Aeronautical Research Institute on the theory of incompressible two-dimensional potential flow about aerofoils and thus covers all results published previously (refs. 5 to 11 incl.) including latest improvements. Moreover an attempt has been made to give at the same time a modern account of the whole basic theory.

Reference is made to important contributions of Dr. J. A. ZAAT to the perfectioning and facilitations of the involved methods of numerical computation (refs. 10 and 11).

PART I.

General theory.

1 General theory of two dimensional, steady, irrotational flow of an incompressible fluid.

1.1 *The field equations.*

EULER's equations of motion for two-dimensional, steady, irrotational flow of an incompressible, non-viscous fluid are (referred to cartesian coordinates x, y)

$$\begin{aligned} v_x \frac{\partial v_x}{\partial x} + v_y \frac{\partial v_x}{\partial y} &= -\frac{1}{\rho}\frac{\partial p}{\partial x}, \\ v_x \frac{\partial v_y}{\partial x} + v_y \frac{\partial v_y}{\partial y} &= -\frac{1}{\rho}\frac{\partial p}{\partial y}. \end{aligned} \tag{1.1}$$

Together with the equation of continuity

$$\frac{\partial v_x}{\partial x} + \frac{\partial v_y}{\partial y} = 0 \tag{1.2}$$

they represent the relations between the components v_x and v_y of the velocity and the pressure p in any point of the field.

In view of (1.2) a function $\omega(x, y)$, known as the stream function, can be introduced by putting

$$\begin{aligned} v_x &= \frac{\partial \omega}{\partial y}, \\ v_y &= \frac{-\partial \omega}{\partial x}. \end{aligned} \tag{1.3}$$

If the flow is irrotational,

$$\frac{\partial v_x}{\partial y} - \frac{\partial v_y}{\partial x} = 0, \tag{1.4}$$

a similar function can be introduced, the velocity potential $\chi(x, y)$, such that

$$\begin{aligned} v_x &= \frac{\partial \chi}{\partial x}, \\ v_y &= \frac{\partial \chi}{\partial y}. \end{aligned} \tag{1.5}$$

In this case eq. (1.1) can at once be integrated, yielding BERNOULLI's equation

$$\frac{1}{2}\left(v_x^2 + v_y^2\right) + \frac{p}{\rho} = \text{const.} = \frac{p_0}{\rho}, \tag{1.6}$$

where p_0 is the pressure in stagnation points of the flow.

By substituting (1.3) in (1.4) and (1.5) in (1.2), the functions ω and χ are both seen to satisfy LAPLACE's equation

$$\begin{aligned} \frac{\partial^2 \omega}{\partial x^2} + \frac{\partial^2 \omega}{\partial y^2} &= 0, \\ \frac{\partial^2 \chi}{\partial x^2} + \frac{\partial^2 \chi}{\partial y^2} &= 0. \end{aligned} \tag{1.7}$$

From (1.3) and (1.5) the relations

$$\begin{aligned} \frac{\partial \chi}{\partial x} &= \frac{\partial \omega}{\partial y}, \\ \frac{\partial \chi}{\partial y} &= -\frac{\partial \omega}{\partial x}, \end{aligned} \tag{1.8}$$

identical with the CAUCHY-RIEMANN equations for the real and imaginary parts of an analytic function of the complex variable $z = x + iy$, are obtained.

Hence the function

$$F(z) = F(x+iy) = \chi(x, y) + i\omega(x, y) \tag{1.9}$$

is analytic in the whole region of the complex z plane, where equations (1.8) hold.

The derivative

$$\frac{dF}{dz} = \frac{\partial \chi}{\partial x} + i\frac{\partial \omega}{\partial x} = -i\frac{\partial \chi}{\partial y} + \frac{\partial \omega}{\partial y} =$$

$$= \frac{\partial \chi}{\partial x} - i\frac{\partial \chi}{\partial y} = i\frac{\partial \omega}{\partial x} + \frac{\partial \omega}{\partial y} \qquad (1.10)$$

yields, in view of (1.3) and (1.5)

$$F'(z) = \frac{dF}{dz} = v_x - iv_y = \bar{v}, \qquad (1.11)$$

where $\bar{v}$ is the conjugate of the complex velocity vector v.

In the case of steady twodimensional flow about a cylindrical aerofoil, the contour of the section is a streamline of the flow, i. e. a line $\omega = \text{const.}$ The flow is further known to be irrotational. If the field has, apart of the surface of the aerofoil, no boundaries, neither discontinuities nor infinities of the velocity components occur anywhere in the field outside of the contour. So the function $F(z)$, representing the flow must be regular everywhere in the corresponding part of the complex z plane and

$$\oint F'(z)dz = 0 \qquad (1.12)$$

for any reducible contour in this part of the plane. If, however, the contour encloses the image of the aerofoil, it is irreducible and

$$\oint F'(z)dz = \Gamma = \text{const.} \qquad (1.13)$$

independent of the special choice of the contour [1]). The value Γ of these integrals is called the circulation (about the aerofoil).

If the complex velocity v is regular even on the contour representing the aerofoil itself (which applies if this contour is a regular arc), the path of integration in (1.13) can be identified with this contour. Then, since $\omega = \text{const.}$ on this line

$$\frac{\partial \omega}{\partial x}dx + \frac{\partial \omega}{\partial y}dy = 0 \qquad (1.14)$$

on this line and, by (1.10) and (1.14)

$$\Gamma = \oint F'(z)dz = \oint \left(i\frac{\partial \omega}{\partial x} + \frac{\partial \omega}{\partial y}\right)(dx + idy) =$$

$$= \oint \left(\frac{\partial \omega}{\partial y}dx - \frac{\partial \omega}{\partial x}dy\right) + i\oint \left(\frac{\partial \omega}{\partial x}dx + \frac{\partial \omega}{\partial y}dy\right) =$$

$$= \oint \left(\frac{\partial \omega}{\partial y}dx - \frac{\partial \omega}{\partial x}dy\right), \qquad (1.15)$$

which shows that the constant Γ is real.

[1]) A contour is always assumed to be a single loop, i. e. to have no double points.

1.2 Mapping of fields of flow.

Let

$$\zeta = f(z) \qquad (1.16)$$

be a functional relation mapping the complex z plane on a complex ζ plane. Define, in this plane, a complex potential $\Phi(\zeta)$ connected with $F(z)$ by identifying the values of both functions in corresponding points,

$$\Phi\{f(z)\} = F(z), \qquad (1.17)$$

or, denoting the inverse transformation of (1.16) by

$$z = g(\zeta), \qquad (1.18)$$

$$\Phi(\zeta) = F\{g(\zeta)\}. \qquad (1.19)$$

If $f(z)$ is an analytic function, the transformation is known to be conformal except at zeroes or singularities of $f'(z)$. A closed contour in the z plane, not passing through one of those points, is mapped into a closed contour in the ζ plane. If

$$\zeta = \xi + i\eta \qquad (1.20)$$

the function Φ defines a flow in a physical ξ, η plane with a complex velocity, whose conjugate is equal to

$$\frac{d\Phi}{d\zeta} = \frac{dF}{dz}\cdot\frac{dz}{d\zeta} = F'(z)\cdot g'(\zeta) = \frac{F'(z)}{f'(z)}. \qquad (1.21)$$

Hence the ratio of the complex velocities in corresponding points of the z and ζ planes is completely determined by the derivative of the mapping function.

If $f'(z)$ is non-vanishing and regular in the whole part of the z plane and, moreover, tends to a non-vanishing constant c at infinity, the flow around the aerofoil in the z plane is transformed into a flow in the ζ plane, about the corresponding contour, which is again free of double points, and the flow patterns in infinity are similar.

For such transformations, the circulation, being defined in exactly the same way, is evidently invariant.

2 The flow about a circle.

The mapping of fields of flow, considered in the preceding section, can be used to analyse the field of flow about an arbitrary profile by reducing it to the well-known flow about a circle.

This field is determined by the following properties:

a) for large values of z the complex velocity converges to a constant value $v_\infty e^{i\alpha}$, representing a parallel flow with velocity v_∞ under an angle α with the X axis.

b) The complex potential function $F(z)$ is regular everywhere outside and on the circle.

c) The circle is a streamline.

Taking the circle to have its centre in the origin and radius R, the only function, which satisfies these three conditions can be shown to be

$$F(z) = v_\infty \left[e^{-i\alpha} z + \frac{R^2 e^{i\alpha}}{z} \right] - i \frac{\Gamma}{2\pi} \ln z, \quad (2.1)$$

where Γ is an arbitrary constant, which represents the circulation.

The velocity function is

$$\bar{v} = v_x - i v_y = \frac{dF}{dz} = v_\infty \left(e^{-i\alpha} - \frac{R^2 e^{i\alpha}}{z^2} \right) - \frac{i\Gamma}{2\pi z}, \quad (2.2)$$

whence, on the circle,

$$\bar{v} = v_\infty \cdot i e^{-i\varphi} \left\{ 2 \sin(\varphi - \alpha) - \frac{\Gamma}{2\pi v_\infty R} \right\}, \quad (2.3)$$

showing that the velocity vector is tangential to the circle and that it has the magnitude

$$|v_c| = 2 v_\infty \cdot \left| \sin(\varphi - \alpha) - \frac{\Gamma}{4\pi v_\infty R} \right|. \quad (2.4)$$

If

$$\frac{\Gamma}{4\pi v_\infty R} < 1 \quad (2.5)$$

the velocity vanishes in two points on the circle. If one of these points is denoted by $\varphi = -\beta$, the circulation Γ is equal to

$$\Gamma = -4\pi R v_\infty \sin(\alpha + \beta) \quad (2.6)$$

and

$$\frac{v_c}{v_\infty} = e^{i(\varphi - \pi/2)} \cdot 2 \{ \sin(\varphi - \alpha) + \sin(\alpha + \beta) \}. \quad (2.7)$$

3 The conformal transformation of the flow about a circle into the flow about an aerofoil.

3.1 RIEMANN's *theorem.*

The existence of a mapping function $f(z)$, transforming the flow about an aerofoil into the flow about a circle results from RIEMANN's fundamental theorem on conformal transformation (ref. 19, p. 398).

Any simply-connected region G with at least one boundary point can be mapped uniquely by an analytic function on the region inside a given circle. The mapping function is uniquely determined by specifying one pair of conjugated points and one pair of corresponding directions in these points.

In the application, considered here, where the field of flow outside an aerofoil is mapped into the field of flow outside a circle, the corresponding points are taken to be the points at infinity of the planes of the aerofoil and the circle, both considered as internal points of the mapped regions, while the region inside the circle to which the theorem refers is mapped on the region outside by a simple inversion. The corresponding directions in the point of infinity are the directions of the undisturbed flow in both planes.

If the boundary consists of parts of analytic curves, i. e. curves, on which the coordinates can be represented as analytic functions of a parameter, the mapping function is not only analytic in the whole region outside the circle, but can be continued analytically over the contour of the circle (ref. 19, p. 400).

The singularities of the mapping function are all located either at the inside of the circle or on its contour, where different analytical arcs join, as is e. g. the case at a sharp trailing edge of an aerofoil.

The mapping of the regions being unique, the mapping function is one-valued in the region outside the circle.

Denoting the plane of the circle as the z plane and the plane of the aerofoil as the ζ plane, the *mapping function can, outside the circle, be* represented by a Laurent series

$$\zeta(z) = \ldots + c_{-2} z^2 + c_{-1} z + c_0 + \frac{c_1}{z} + \frac{c_2}{z^2} + \ldots \quad (3.1)$$

because it is, in this region, regular and single-valued.

The behaviour of the function in infinity is determined by the condition, that the points at infinity correspond and that the directions of flow in these points correspond. This means that

$$c_{-2} = c_{-3} = \ldots\ldots\ldots = 0 \quad (3.2)$$

and that c_{-1} is a real positive constant.

If, moreover, the condition is imposed, that the ζ and z planes shall coincide at infinite, $c_{-1} = 1$ and the mapping function has an expansion, valid in the whole region outside the circle:

$$f(z) = \zeta = c_0 + z + \frac{c_1}{z} + \frac{c_2}{z^2} + \ldots\ldots \quad (3.3)$$

The derivative has the expansion

$$f'(z) = \frac{d\zeta}{dz} = 1 - \frac{c_1}{z^2} - \frac{2c_2}{z^3} - \frac{3c_3}{z^4} \ldots\ldots \quad (3.4)$$

3.2 *The relation between the velocities and the mapping function.*

According to (1.21) the derivatives $\frac{d\Phi}{d\zeta}$ and $\frac{dF}{dz}$ of the complex potential functions, which are equal to the conjugates $\bar{v}_p$ and $\bar{v}_c$ of the velocities in the flow fields, are related by the equation

$$\frac{\bar{v}_c}{\bar{v}_p} = \frac{\overline{\frac{dF}{dz}}}{\overline{\frac{d\Phi}{d\zeta}}} = \frac{d\zeta}{dz} = f'(z) \quad (3.5)$$

which holds also on the contour of the circle and the aerofoil in non-singular points.

This formula represents the basic relation of the following theory. It will prove to be adequate to represent the mapping function by two real functions $\sigma(x, y)$ and $\tau(x, y)$, defined by

$$\sigma(x, y) + i\tau(x, y) = \ln f'(z) = \ln f'(x + iy). \quad (3.6)$$

Then

$$\sigma = Re\{\ln f'(z)\} = \ln|f'(z)| = \ln\left|\frac{v_c}{v_p}\right| \quad (3.7)$$

and

$$\tau = Im\{\ln f'(z)\} = \arg f'(z) = \arg v_p - \arg v_c. \quad (3.8)$$

σ represents the logarithm of the ratio of the velocities in corresponding points of the fields of flow and τ represents the difference in direction of these velocities.

Since $f'(z)$ is, outside the circle, nowhere singular nor zero, the function $\ln f'(z)$ is regular everywhere in this region, including infinity and so its real and imaginary parts, σ and τ are conjugate regular harmonic functions in this region, including the parts of the circumference, corresponding to the regular arcs of the profile. In the singular points of the aerofoil contour, the functions have singularities to be considered separately.

From a practical point of view, the values of the velocities on the aerofoil contour are of particular importance, for they determine the pressure on the aerofoil and thus its fundamental aerodynamic characteristics. Hence, the relation between σ and τ on the circumference of the circle merits closer investigation.

4 The relation between the conjugate functions on the circle.

4.1 Poisson's *integral.*

Let

$$z = x + iy = re^{i\psi};\ r > R \quad (4.1)$$

be a point outside the circle representing the image of the contour of the aerofoil, and let

$$h(z) = \sigma + i\tau, \quad (4.2)$$

where σ and τ are the functions, defined in section 3.2. Then, since $h(z)$ is analytic and regular

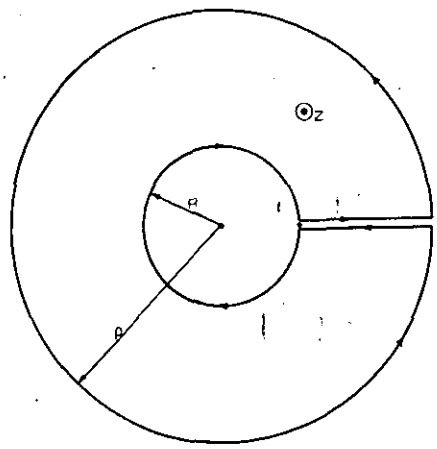

Fig. 1. The derivation of the Poisson integral.

in the part of the plane outside the circle, by Cauchy's theorem applied to the region, bounded by the circle and a circle with large radius ρ (fig. 1),

$$h(z) = \frac{1}{2\pi i}\int_C \frac{h(t)}{t-z}\,dt =$$

$$= -\frac{1}{2\pi}\int_0^{2\pi} h(Re^{i\varphi})\cdot\frac{Re^{i\varphi}}{Re^{i\varphi} - re^{i\psi}}\,d\varphi +$$

$$+\frac{1}{2\pi}\int_0^{2\pi} h(\rho e^{i\varphi})\cdot\frac{\rho e^{i\varphi}}{\rho e^{i\varphi} - re^{i\psi}}\,d\varphi. \quad (4.3)$$

If $\rho \to \infty$, the function $h(\rho e^{i\varphi})$ tends to a constant value, say α_0, according to the suppositions made about $f'(z)$, and the expression becomes:

$$h(z) = -\frac{1}{2\pi}\int_0^{2\pi} h(Re^{i\varphi})\frac{Re^{i\varphi}}{Re^{i\varphi} - re^{i\psi}}\,d\varphi + \alpha_0. \quad (4.4)$$

If z^* is the image of z with respect to the circle, i. e.

$$z^* = \frac{R^2}{z} = \frac{R^2}{r}e^{i\psi}, \quad (4.5)$$

then $\frac{h(z)}{t - z^*}$ is regular in the same region considered above and its integral over a closed contour in this region vanishes, whence

$$0 = \frac{1}{2\pi i}\int_C \frac{h(t)}{t - z^*}\,dt =$$

$$-\frac{1}{2\pi}\int_0^{2\pi} h(Re^{i\varphi})\cdot\frac{re^{i\varphi}}{re^{i\varphi} - Re^{i\psi}}\,d\varphi + \alpha_0, \quad (4.6)$$

the integration along the circle at infinity yielding the same result as above.

Subtraction of (4.4) and (4.6) gives:

$$h(z) = \sigma + i\tau =$$

$$= \frac{-1}{2\pi}\int_0^{2\pi} h(Re^{i\varphi})\cdot\frac{R^2 - r^2}{R^2 - 2Rr\cos(\psi - \varphi) + r^2}\,d\varphi, \quad (4.7)$$

whence

$$\sigma(r,\psi) =$$

$$-\frac{1}{2\pi}\int_0^{2\pi} \sigma(R,\varphi)\cdot\frac{R^2 - r^2}{R^2 - 2Rr\cos(\psi - \varphi) + r^2}\,d\varphi, \quad (4.8)$$

$$\tau(r,\psi) =$$

$$-\frac{1}{2\pi}\int_0^{2\pi} \tau(R,\varphi)\cdot\frac{R^2 - r^2}{R^2 - 2Rr\cos(\psi - \varphi) + r^2}\,d\varphi. \quad (4.9)$$

These formulae express the values of the functions σ and τ in a point outside the circle in their boundary values on the circle. Formula (4.7) is known as Poisson's integral.

4.2 *Relations between the functions σ and τ on the circle.*

Addition of (4.4) and (4.6) yields:

$$h(z) = \sigma + i\tau =$$

$$= -\frac{1}{2\pi}\int_0^{2\pi} h(Re^{i\varphi})\,d\varphi + 2\,\alpha_0 -$$

$$-\frac{i}{2\pi}\int_0^{2\pi} \frac{h(Re^{i\varphi})\,.\,2\,Rr\sin(\psi-\varphi)}{R^2-2\,Rr\cos(\psi-\varphi)+r^2}\,.\,d\varphi. \quad (4.10)$$

For $r\to\infty$,

$$h(z) = \alpha_0 = -\frac{1}{2\pi}\int_0^{2\pi} h(Re^{i\varphi})\,d\varphi + 2\,\alpha_0 \quad (4.11)$$

and so

$$\sigma + i\tau =$$

$$-\frac{iRr}{\pi}\int_0^{2\pi} \frac{\sin(\psi-\varphi)\,.\,(\sigma+i\tau)}{R^2-2\,Rr\cos(\psi-\varphi)+r^2}\,.\,d\varphi + \alpha_0\,. \quad (4.12)$$

Putting

$$\alpha_0 = a_0 + i\,b_0, \quad (4.13)$$

separation of real and imaginary parts in (4.12) yields

$$\sigma(r,\psi) = a_0 +$$

$$+\frac{Rr}{\pi}\int_0^{2\pi} \frac{\tau(R,\varphi)\sin(\psi-\varphi)}{R^2-2\,Rr\cos(\psi-\varphi)+r^2}\,.\,d\varphi, \quad (4.14)$$

$$\tau(r,\psi) = b_0 -$$

$$-\frac{Rr}{\pi}\int_0^{2\pi} \frac{\sigma(R,\varphi)\sin(\psi-\varphi)}{R^2-2\,Rr\cos(\psi-\varphi)+r^2}\,.\,d\varphi. \quad (4.15)$$

In the limit $r\to R$ the integrals become improper. Defining their values as principal values in the sense of CAUCHY, the corresponding formulae for σ and τ, which on the circle are denoted by $\sigma(\varphi)$ and $\tau(\varphi)$, become:

$$\sigma(\psi) = a_0 + \frac{1}{2\pi}\int_0^{2\pi} \tau(\varphi)\,.\,\operatorname{cotg}\tfrac{1}{2}(\psi-\varphi)\,d\varphi, \quad (4.16)$$

$$\tau(\psi) = b_0 - \frac{1}{2\pi}\int_0^{2\pi} \sigma(\varphi)\,.\,\operatorname{cotg}\tfrac{1}{2}(\psi-\varphi)\,d\varphi, \quad (4.17)$$

as can be shown by elementary reduction.

These formulae, relating conjugate functions on the circumference of the circle, are a main tool for the solution of problems of aerofoil theory.

4.3 *Fourier series expansions of the fundations σ and τ.*

According to (4.8) and (4.15):

$$\sigma(re^{i\psi}) + i\tau(re^{i\psi}) = ib_0 -$$

$$-\frac{1}{2\pi}\int_0^{2\pi} \sigma(Re^{i\varphi})\,.\,\frac{R^2-r^2+2\,iRr\sin(\psi-\varphi)}{R^2-2\,Rr\cos(\psi-\varphi)+r^2}\,d\varphi =$$

$$= ib_0 -$$

$$-\frac{1}{2\pi}\int_0^{2\pi} \sigma(Re^{i\varphi})\,.\,\frac{(Re^{i\varphi}+re^{i\psi})(Re^{-i\varphi}-re^{-i\psi})}{(Re^{i\varphi}-re^{i\psi})(Re^{-i\varphi}-re^{-i\psi})}\,d\varphi =$$

$$= ib_0 - \frac{1}{2\pi}\int_0^{2\pi} \sigma(Re^{i\varphi})\,\frac{t+z}{t-z}\,d\varphi. \quad (4.18)$$

Expanding $\frac{t+z}{t-z}$, $|z|>|t|$, in a uniformly convergent series,

$$\frac{t+z}{t-z} = -1-2\sum_{n=1}^{\infty}\left(\frac{t}{z}\right)^n =$$

$$= -1-2\sum_{n=1}^{\infty}\left(\frac{R}{r}\right)^n\,.\,e^{in(\varphi-\psi)}, \quad (4.19)$$

formula (4.18) is transformed into

$$\sigma(re^{i\psi}) + i\tau(re^{i\psi}) = ib_0 + \alpha_0 +$$

$$+\sum_{n=1}^{\infty}\left(\frac{R}{r}\right)^n\,.\,\alpha_n\,.\,e^{-in\psi} =$$

$$= ib_0 + \alpha_0 + \sum_{n=1}^{\infty}\frac{\alpha_n R^n}{z^n}\,. \quad (4.20)$$

where α_0 is defined by (4.11), and

$$\alpha_n = \frac{1}{\pi}\int_0^{2\pi} \sigma(\varphi)\,e^{in\varphi}\,d\varphi = a_n + ib_n. \quad (n=1;\ldots) \quad (4.21)$$

Separating real and imaginary parts, the following Fourier expansions of the conjugate functions are obtained:

$$\sigma(re^{i\psi}) =$$

$$= +\,a_0 + \sum_{n=1}^{\infty}\left(\frac{R}{r}\right)^n(a_n\cos n\psi + b_n\sin n\psi) \quad (4.22)$$

$$\tau(re^{i\psi}) =$$

$$= +\,2\,b_0 - \sum_{n=1}^{\infty}\left(\frac{R}{r}\right)^n(a_n\sin n\psi - b_n\cos n\psi) \quad (4.23)$$

4.4 *Conditions for the Fourier coëfficiënts.*

In section 3.1 the derivative of the mapping function has been argued to admit the expansion

$$f'(z) = \frac{d\zeta}{dz} = 1 - \frac{c_1}{z^2} - \frac{2\,c_2}{z^3} - \frac{3\,c_3}{z^4} \ldots, \quad (4.24)$$

valid in the whole region outside the circle.

Hence, for the function $h(z) = ln\, f'(z)$, the expansion

$$h(z) = -\frac{c_1}{z^2} - \frac{2c_2}{z^3} - \frac{3c_3 + \frac{1}{2}c_1^2}{z^4} \ldots \quad (4.25)$$

holds. Comparing this with (4.21), it is seen that

$$\alpha_0 = a_0 = b_0 = 0 \quad (4.26)$$

and

$$\alpha_1 = a_1 = b_1 = 0, \quad (4.27)$$

or

$$\int_0^{2\pi} \sigma(\varphi)d\varphi = \int_0^{2\pi} \tau(\varphi)d\varphi = 0 \quad (4.28)$$

and

$$\int_0^{2\pi} \sigma(\varphi)\cos\varphi \,.\, d\varphi = \int_0^{2\pi} \sigma(\varphi)\sin\varphi \,.\, d\varphi =$$

$$\int_0^{2\pi} \tau(\varphi)\cos\varphi \,.\, d\varphi = \int_0^{2\pi} \tau(\varphi)\sin\varphi \,.\, d\varphi = 0. \quad (4.29)$$

4.5 *The case of singularities on the contour.*

The case, where the function $h(z)$ has singularities on the contour needs separate consideration.

As the formulae of the preceding section are based on CAUCHY's theorem, it is seen, that a pole on the contour of the circle introduces half of the residue of the function in that pole into formula (4.2). This case is, however, of little practical importance and can thus be waived.

The case of a branch point of the function $h(z)$ is of much more importance. In this case, formula (4.2) holds, if the contour of integration is wholly situated on one blade of the Riemann surface. pertaining to the function. The function $h(z)$ being regular in the whole plane outside the circle, the branch line, starting at the branch point on the contour extends into the inner region of the circle and the condition is, thus, satisfied.

Hence, all results of the preceding sections also hold in the case of the branch points of the function $h(z)$ on the contour of the circle.

5 The singularity of the mapping function, due to a sharp trailing edge of the aerofoil.

5.1 *The singularity at the trailing edge.*

Usually aerofoils have a sharp trailing edge, which causes the mapping function to be singular in the corresponding point on the circle.

Denoting the tail angle by δ (fig. 2) the mapping function must transform, in this point, an angle $2\pi - \delta$ in the ζ plane into an angle π in the z plane.

Hence, in a sufficiently small neighbourhood of this point (to be represented by $z_0 = Re^{-i\beta}$), the mapping function admits the expansion

$$\zeta - \zeta_0 = (z - z_0)^{\frac{2\pi-\delta}{\pi}} \{a_0 + a_1(z - z_0) + a_2(z - z_0)^2 + \ldots\}. \quad (5.1)$$

Putting

$$k = \frac{2\pi - \delta}{\pi} = 2 - \frac{\delta}{\pi} \quad (5.2)$$

the derivative has the expansion

$$\frac{d\zeta}{dz} = (z - z_0)^{k-1}\{ka_0 + (k+1)a_1(z - z_0) + \ldots\}, \quad (5.3)$$

If $\delta < \pi$, $k > 1$, by (5.3),

$$\left(\frac{d\zeta}{dz}\right)_{z=z_0} = \left(\frac{\bar{v}_c}{\bar{v}_p}\right)_{z=z_0} = 0. \quad (5.4)$$

Now, the Kutta conditios requires $\bar{v}_p$ to remain finite at the trailing edge. Obviously, this condition can be satisfied only by taking $(\bar{v}_c)_{z=0}$ zero, i. e. the velocity on the circle in the point $z_0 = Re^{-i\beta}$ corresponding to the trailing edge must vanish.

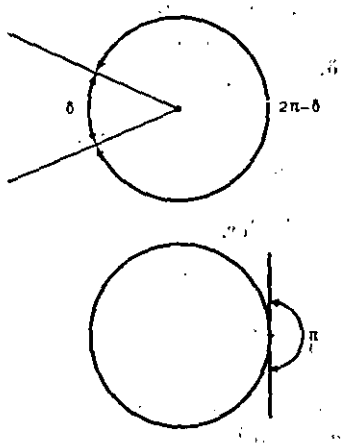

Fig. 2. The mapping of the tail angle.

According to (2.6) this condition determines the value Γ of the circulation.

From (5.3) it follows that,

$$\sigma + i\tau = ln\,\frac{d\zeta}{dz} = (k-1)\,ln\,(z - z_0) + g(z). \quad (5.5)$$

where $g(z)$ is regular in the point z_0, and, if the aerofoil contour has no other singularities, in all points on and outside the circle.

Elimination of the singularity at the trailing edge.

On the circle $z = Re^{i\varphi}$ and (5.5) reduces to

$$(\sigma + i\tau)_{circle} = (k-1)\,ln\,(Re^{i\varphi} - Re^{i\beta}) + g(\varphi) =$$

$$= (k-1)\,ln\left\{2R\sin\frac{\varphi+\beta}{2}\right\} +$$

$$+ (k-1)i\,\frac{\pi + \varphi - \beta}{2} + g(\varphi). \quad (5.6)$$

Hence, the function $\sigma(\varphi)$ has a logarithmic singularity at the trailing edge and the function τ is discontinuous at $\varphi = -\beta$, its value increasing with $(k-1)\pi$ at each revolution round the circle.

The functions

$$\sigma_1(\varphi) = \sigma(\varphi) - (k-1)\, ln\, 2 \sin \tfrac{1}{2}(\varphi + \beta) \qquad (5.7)$$

$$\tau_1(\varphi) = \tau(\varphi) - (k-1)\left\{\frac{\pi}{2} + \frac{\varphi - \beta}{2}\right\} \qquad (5.8)$$

are the real and imaginary parts on the contour of an analytic function of φ and hence are also related by POISSON's integral, when the integrand has no singularities. It should be remarked, however, that it is not strictly necessary to use the particular functions, involved in (5.7) and (5.8) in order to eliminate the singularity. Any pair of conjugate functions, having the proper singularity, may be subtracted from σ and τ to obtain a pair of non-singular conjugate functions. Use of this remark will be made later on by assuming these functions to be generated by a known aerofoil with tail angle δ.

6 Formulae for the contour and the radius of curvature of the aerofoil.

6.1 *The coordinates.*

Integrating the relation

$$\frac{d\zeta}{dz} = f'(z) = e^{h(z)} = \exp.\{\sigma(z) + i\tau(z)\} \qquad (6.1)$$

along the circle from any point z_0 to another point z the formula

$$\zeta - \zeta_0 = \int_{z_0}^{z} e^{\sigma(z) + i\tau(z)} \, dz \qquad (6.2)$$

is obtained.

Substituting $z = Re^{i\varphi}$ and taking $z_0 = R$ to correspond to $\zeta = 0$, the formula

$$\xi + i\eta = Ri \int_0^{\psi} e^{\sigma(\varphi) + i\tau(\varphi) + i\varphi} \, d\varphi \qquad (6.3)$$

is obtained, or

$$\frac{\xi}{R} = -\int_0^{\psi} e^{\sigma(\varphi)} \sin(\tau + \varphi) \, d\varphi, \qquad (6.4)$$

$$\frac{\eta}{R} = \int_0^{\psi} e^{\sigma(\varphi)} \cos(\tau + \varphi) \, d\varphi. \qquad (6.5)$$

From the expansion (3.4) it is seen, that

$$\oint e^{\sigma(z) + i\tau(z)} \, dz = 0 \qquad (6.6)$$

along the circle. So, the aerofoil connects up to a closed contour, provided σ and τ satisfy conditions (4.28) and (4.29).

6.2 *The radius of curvature.*

A useful formula for the radius of curvature of the contour of the aerofoil can be obtained as follows (fig. 3). By definition

$$\rho = \lim_{\Delta s \to 0} \frac{\Delta s}{\Delta \alpha} = \lim_{\Delta \zeta \to 0} \left| \frac{\Delta \zeta}{\Delta \alpha} \right| = \left| \frac{d\zeta}{d\alpha} \right|, \qquad (6.7)$$

where α is the angle between the normal at the aerofoil and the X-axis.

Now, in the plane of the circle, the tangent in

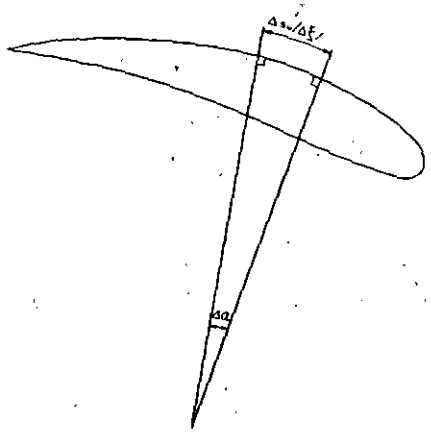

Fig. 3. The radius of curvature.

the point $re^{i\varphi}$, corresponding to the point of the aerofoil considered, makes an angle $\varphi + \frac{\pi}{2}$ with the X-axis. It is, by the transformation, turned over an angle

$$\arg \frac{d\zeta}{dz} = \arg e^{\sigma + i\tau} = \tau \qquad (6.8)$$

and so the tangent of the aerofoil contour makes an angle

$$\varphi + \frac{\pi}{2} + \tau$$

with the X-axis. Hence,

$$\alpha = \varphi + \tau \qquad (6.9)$$

and

$$\rho = \left| \frac{d\zeta}{d\alpha} \right| = \frac{\left| \frac{d\zeta}{dz} \right| \cdot \left| \frac{dz}{d\varphi} \right|}{\left| \frac{d\alpha}{d\varphi} \right|} = \frac{e^{\sigma} R}{1 + \frac{d\tau}{d\varphi}}, \qquad (6.10)$$

for, on the circle

$$\left| \frac{dz}{d\varphi} \right| = |iRe^{i\varphi}| = R, \qquad (6.11)$$

$$\frac{d\alpha}{d\varphi} = 1 + \frac{d\tau}{d\varphi}, \qquad (6.12)$$

$$\left| \frac{d\zeta}{dz} \right| = e^{\sigma}. \qquad (6.13)$$

7 The velocity and pressure distribution on the aerofoil.

7.1 *Velocity and pressure distribution.*

Since

$$\frac{\bar{v}_c}{v_p} = e^{\sigma + i\tau} \qquad (3.5)$$

and

$$\frac{\bar{v}_c}{v_\infty} = ie^{-i\varphi}\left\{2\sin(\varphi-\alpha) - \frac{\Gamma}{2\pi v_\infty R}\right\}, \quad (2.3)$$

the velocity distribution on the aerofoil contour is given by

$$\frac{\bar{v}_p}{v_\infty} = e^{-\sigma(\varphi)}\cdot\left\{2\sin(\varphi-\alpha) - \frac{\Gamma}{2\pi v_\infty R}\right\} e^{-i\tau(\varphi) - i\varphi + i\pi/2}, \quad (7.1)$$

the velocities in infinity being equal in the two planes.

If the circulation is fixed by the KUTTA-condition, this formula reduces to

$$\frac{\bar{v}_p}{v_\infty} = \left\{\right.$$

$$= e^{-\sigma(\varphi)}\cdot 2\{\sin(\varphi-\alpha) + \sin(\alpha+\beta)\}\cdot e^{-i\{\tau+\varphi-\pi/2\}} \quad (7.2)$$

The pressure is related to the velocity by BERNOULLI's law

$$p = p_0 - \tfrac{1}{2}\rho\,\bar{v}_p\,v_p, \quad (1.6)$$

or

$$p_p - p_0 = -2\rho v^2_\infty\{\sin(\varphi-\alpha) + \sin(\alpha+\beta)\}^2\cdot e^{-2\sigma(\varphi)}. \quad (7.3)$$

According to BLASIUS the formula for the complex force is (e.g. ref. 12)

$$\bar{P} = P_\xi - iP_\eta = -i\oint p\,d\bar{\zeta} = \tfrac{1}{2}i\rho\oint \bar{v}_p^2\,d\zeta. \quad (7.4)$$

If the integral is evaluated by means of the theory of residues the formula

$$\bar{P} = \rho v_\infty\,\Gamma\cdot ie^{-i\alpha} = -4\pi\rho v^2_\infty R\cdot\sin(\alpha+\beta)\cdot e^{(\pi/2-\alpha)i} \quad (7.5)$$

results, showing that

$$c_L = \frac{8\pi R}{l}\cdot\sin(\alpha+\beta). \quad (7.6)$$

BLASIUS' formula for the moment about the origin

$$M_0 = -\frac{\rho}{2}\,Re\oint \bar{v}_p^2\,\zeta\,d\zeta \quad (7.7)$$

can be evaluated in the same way. It is apt to show, in combination with (7.5), that a point exists about which the moment is independent of the angle of incidence α. For the same point, the real value

$$M = 2\pi\rho v^2_\infty\, b^2R^2\cdot\sin 2(\gamma+\beta), \quad (7.8)$$

is obtained, where b^2 and γ are defined by

$$a_2 = a_2 + ib_2 = b^2e^{2i\gamma}. \quad (7.9)$$

If $\gamma = -\beta$, the moment M about this point is zero, independent of α, which means that the resulting lift force passes invariantly through a fixed point, the *centre of pressure.*

If, in particular, the reference axes are so chosen that $\beta = 0$, this condition yields

$$b_2 = \int_0^{2\pi}\sigma(\varphi)\cdot\sin 2\varphi\,d\varphi = 0. \quad (7.10)$$

8 The principal problems of aerofoil theory.

8.1 *Formulation of the principal problems.*

The two principal problems of aerofoil theory are:

I The calculation of the velocities in the two-dimensional incompressible flow about an aerofoil of given shape, and in particular the velocities on its contour, the magnitude and direction of the velocity in infinity being given (the *direct* problem).

II The calculation of the coordinates of the contour of an aerofoil, which generates, for a given magnitude and direction of the flow in infinity, a given distribution of the velocity along its contour (the *inverse* problem).

The first problem has been solved long ago (ref. 12). The second has been attacked during the war and has been solved approximately by GOLDSTEIN (ref. 20) and exactly by LIGHTHILL (ref. 3). The method, presented here, is fundamentally the same as LIGHTHILL's solution, but, being established independently, differences of some importance do occur. Moreover, it enables the establishment of an alternative solution of problem I.

8.2 *Mathematical formulae to be used for the solution.*

Mathematically the solution of both problems depends on the following equations, for the coordinates of the aerofoil established previously:

a) eqs (6.4) and (6.5),

$$\frac{\xi}{R} = -\int_0^\psi e^{\sigma(\varphi)}\sin(\tau+\varphi)\,d\varphi, \quad (8.1)$$

$$\frac{\eta}{R} = \int_0^\psi e^{\sigma(\varphi)}\cos(\tau+\varphi)\,d\varphi, \quad (8.2)$$

φ being the angular variable on the circle with radius R, on which the aerofoil is supposed to be mapped.

b) equations (4.16) and (4.17), representing POISSON's integral

$$\sigma(\psi) = \frac{1}{2\pi}\int_0^{2\pi}\tau(\varphi)\,\operatorname{cotg}\frac{1}{2}(\psi-\varphi)\,d\varphi, \quad (8.3)$$

$$\tau(\psi) = -\frac{1}{2\pi}\int_0^{2\pi}\sigma(\varphi)\,\operatorname{cotg}\frac{1}{2}(\psi-\varphi)\,d\varphi. \quad (8.4)$$

c) equation (7.2) for the velocity distribution on the aerofoil,

$$\frac{\bar{v}_p}{v_\infty} = e^{-\sigma(\varphi)}\cdot 2\{\sin(\varphi-\alpha) + \sin\alpha\}\cdot e^{i(\pi/2-\varphi-\tau)}, \quad (8.5)$$

assuming $\varphi = 0$ to represent the trailing edge.

The solutions of both problems will be established by aid of iteration methods.

8.3 *Iterative solution of the direct problem.*

To obtain the solution of the direct problem assume a reference system with origin somewhere in the interior of the aerofoil, the X-axis passing through the trailing edge. The velocity distribution can be calculated if the coordinates ξ, η and the functions σ and τ are all known as functions of the angle φ on the circle. The angle between a tangent to the contour and the X-axis in the point $x = \xi$ is a given function of ξ. In section 6.2 this angle was shown to be equal to $\varphi + \tau(\varphi) + \frac{\pi}{2}$, so that the given shape of the aerofoil induces a relation

$$\varphi + \tau(\varphi) = \lambda(\xi), \tag{8.6}$$

where $\lambda(\xi)$ is a known function of ξ.

The unknown functions $\sigma(\varphi)$, $\tau(\varphi)$, $\xi(\varphi)$ and $\eta(\varphi)$ are determined by an iteration process.

Assume a suitable zero-order approximation

$$\xi = \xi_0(\varphi). \tag{8.7}$$

Then, the iteration formulae run as follows

a) from (8.6)

$$\tau_n(\varphi) = \lambda\{\xi_{n-1}(\varphi)\} - \varphi, \tag{8.8}$$

b) from (8.3)

$$\sigma_n(\varphi) = \frac{1}{2\pi}\int_0^{2\pi} \tau_n(\psi)\,\operatorname{cotg}\,\frac{1}{2}(\varphi - \psi)d\psi \tag{8.9}$$

and

c) from (8.1)

$$\xi_n(\varphi) = -R\int_0^{\varphi} e^{\sigma_n(\psi)}\,\sin(\tau_n + \psi)d\psi. \tag{8.10}$$

Having obtained

$$\sigma = \lim_{n\to\infty}\sigma_n, \qquad \tau = \lim_{n\to\infty}\tau_n, \tag{8.11}$$

the velocity distribution follows from (8.5).

8.4 *Iterative solution of the inverse problem.*

In the inverse problem the velocity distribution v_p cannot be given along the contour, which, initially, is unknown, but it is supposed to be given as a function of the coordinate ξ along the chord. Further, this function cannot be chosen arbitrarily, as the function σ, which is derived from it, has to satisfy the conditions (4.28), (4.29), and, in the case of an aerofoil with fixed centre of pressure, (7.10).

In order to be able to satisfy these conditions, the velocity distribution is introduced as a function $v_p(\xi, \kappa^1, \kappa^2, \kappa^3, \kappa^4)$, containing four parameters.

According to (8.5) the function $\sigma(\varphi)$ is related to $|v_p|$ by the formula

$$\sigma(\varphi) = -\ln\left|\frac{v_p}{v}\right| + \ln 2\{\sin(\varphi - \alpha) + \sin\alpha\}. \tag{8.12}$$

From the known function $v_p(\xi, \kappa^1, \kappa^2, \kappa^3, \kappa^4)$ follows the relation

$$\sigma(\varphi) = \mu(\xi, \varphi, \kappa^1, \kappa^2, \kappa^3, \kappa^4). \tag{8.13}$$

Assuming a zero-order approximation,

$$\xi = \xi_0(\varphi), \tag{8.14}$$

the iteration formulae run as follows

a) $$\sigma_{n-1}(\varphi) = \mu\{\xi_{n-1}(\varphi), \varphi, \kappa^1_{n-1}, \kappa^2_{n-1}, \kappa^3_{n-1}, \kappa^4_{n-1}\}, \tag{8.15}$$

where $\kappa^1_{n-1}, \ldots \kappa^4_{n-1}$ are to be determined by the relations

$$\int_0^{2\pi}\sigma_{n-1}(\varphi)d\varphi = \oint_0^{2\pi}\sigma_{n-1}(\varphi)\cdot\cos\varphi d\varphi =$$

$$= \int_0^{2\pi}\sigma_{n-1}(\varphi)\sin\varphi d\varphi =$$

$$= \int_0^{2\pi}\sigma_{n-1}(\varphi)\sin 2\varphi d\varphi = 0, \tag{8.16}$$

b) $$\tau_{n-1}(\varphi) =$$

$$-\frac{1}{2\pi}\int_0^{2\pi}\sigma_{n-1}(\psi)\,\operatorname{cotg}\,\frac{1}{2}(\varphi - \psi)d\psi, \tag{8.17}$$

and

c) $$\xi_n(\varphi) = -R\int_0^{\varphi} e^{\sigma_{n-1}(\psi)}\sin(\tau_{n-1} + \psi)d\psi. \tag{8.18}$$

If

$$\lim_{n\to\infty}\sigma_n = \sigma, \qquad \lim_{n\to\infty}\tau_n = \tau$$

are known, the coordinates follow from (8.1) and (8.2) and the velocity distributions at other angles of attack from (8.5).

8.5 *Choice of initial approximations.*

In both cases suitable initial relations can be drawn from an "intermediate aerofoil" with known properties. This aerofoil should be adapted, with respect to geometrical shape, to the aerofoil considered (Problem I) or to the aerofoil expected to result from the calculation (Problem II).

It could be chosen from a sufficiently extensive family of aerofoils, depending on a limited number of parameters, which admit a simple analytical treatment.

A point of particular importance is the coincidence of the tail angles of the intermediate aerofoil and the aerofoil considered or requested. This precaution removes the tail-point singularity in the differences $\sigma - \sigma_0$ and $\tau - \tau_0$ and, hence, simplifies the numerical calculation of the Poisson integral to a great extent.

9 Convergence of the iteration procedure.

9.1 *Preliminary considerations.*

The convergence of the iteration procedures, described in section 8 should, of course, be demonstrated. The first process is essentially the conformal mapping of the aerofoil on the circle. The proof of the convergence can be given in a way, resembling more or less WARSCHAWSKI's proof of the convergence of the Theodorsen-Garrick process (ref. 21). It will be omitted here. The convergence of second process, the computation of an aerofoil, having a required velocity distribution along the chord, will be considered somewhat more closely.

A simplified case is taken, where the imposed velocity distribution contains only one parameter κ, in a very simple way. No account has been taken of a branch point of the mapping function. Such a point is, as already mentioned, eliminated in practice by taking a zero approximation with the same singularity, the difference functions being regular everywhere on the contour of the circle.

9.2 *Two lemmas.*

Lemma 1.

If $Re\, z > Re\, t$, then

$$|e^z - e^t| < |z - t| \cdot e^{Re\, z}. \tag{9.1}$$

The proof is easy.

Lemma 2.

If the function

$$h(z) = \sigma(z) + i\tau(z) \tag{9.2}$$

is regular on and outside the circle $z = Re^{i\varphi}$, and if

$$\oint \frac{h(z)}{z}\, dz = 0 \tag{9.3}$$

along the circle, then

$$\int_0^{2\pi} \sigma^2(\varphi) d\varphi = \int_0^{2\pi} \tau^2(\varphi) d\varphi \tag{9.4}$$

and

$$\oint_0^{2\pi} \sigma(\varphi) \cdot \tau(\varphi) d\varphi = 0. \tag{9.5}$$

This lemma is proved by expanding the function into a Laurant series $h(z) = \sum_{\nu=1}^{\infty} \frac{a_\nu}{z^\nu}$ and considering the expansion of $h^2(z)$.

9.3 *Convergence of the second process.*

The convergence of the design procedure of an aerofoil with given velocity distribution along the chord is, in a simple case, established by the following theorem.

If

a) $\mu(\theta)$ is a regular, periodic function of θ with period 2π;

b) $\sigma_0(\varphi)$ and $\tau_0(\varphi)$ are the real and imaginary parts on the circle $z = Re^{i\varphi}$ of a function $h(z)$, analytic on and outside the circle, satisfying the condition

$$\int_0^{2\pi} \sigma_0(\varphi) d\varphi = 0; \tag{9.6}$$

c) the functions $\sigma_n(\varphi)$, $\tau_n(\varphi)$ and $\xi_n(\varphi)$ are defined by

$$\sigma_n(\varphi) = \mu(\theta_{n-1}) - \kappa_{n-1}, \tag{9.7}$$

$$\frac{1}{2} c_{n-1} (1 - \cos\theta_{n-1}) = \xi_{n-1}, \tag{9.8}$$

$$\xi_n = \int_0^{\varphi} e^{\sigma_n(\psi)} \sin(\tau_n + \psi) d\psi, \tag{9.9}$$

$$c_{n-1} = \max \int_0^{\varphi} e^{\sigma_n(\psi)} \sin(\tau_n + \psi) d\psi, \tag{9.10}$$

$$\tau_n(\varphi) = \frac{1}{2\pi} \int_0^{2\pi} \sigma_n(\psi) \operatorname{cotg} \frac{1}{2}(\varphi - \psi) d\psi, \tag{9.11}$$

the constant κ_{n-1} being determined by the condition

$$\int_0^{2\pi} \sigma_n(\varphi) d\varphi = 0; \tag{9.12}$$

then numbers M and m exist independent of n, so that

$$\sigma_n < 2m,$$

$$|\mu\{\xi_n(\varphi)\} - \mu\{\xi_{n-1}(\varphi)\}| < M |\xi_n(\varphi) - \xi_{n-1}(\varphi)| \tag{9.13}$$

and

$$|\sigma_{n+1} - \sigma_n|^2 \leqq 2 (e^{4m} \cdot 4\pi M^2)^{n-1} \cdot \left| \int_0^{2\pi} (\sigma_1 - \sigma_0)^2 d\varphi \right|. \tag{9.14}$$

To prove the theorem, let

$$\zeta_n = \xi_n + i\eta_n = \int_R^z e^{h_n(z)} dz, \tag{9.15}$$

taking the path of integration along the circumference of the circle $z = Re^{i\varphi}$.

Then

$$|\xi_n - \xi_{n-1}|^2 \leqq |\zeta_n - \zeta_{n-1}|^2 = \left| \int_R^z (e^{h_n} - e^{h_{n-1}})\, dz \right|^2 \leqq$$

$$\leqq \left\{ \int_R^z \left| e^{h_n} - e^{h_{n-1}} \right| \cdot \left| dz \right| \right\}^2 =$$

$$= R^2 \left\{ \int_0^{\varphi} \left| e^{h_n} - e^{h_{n-1}} \right| d\psi \right\}^2 \tag{9.16}$$

By SCHWARTZ' inequality

$$\left\{ \int_0^{\varphi} \left| e^{h_n} - e^{h_{n-1}} \right| d\psi \right\}^2 \leqq$$

$$\leqq \varphi \int_0^{\varphi} \left| e^{h_n} - e^{h_{n-1}} \right|^2 d\psi. \qquad (9.17)$$

Further, being regular for $0 \leqq \varphi \leqq 2\pi$, μ is bounded in the closed interval; hence

$$\mu < m.$$

For k_{n-1}, defined by

$$2\pi k_{n-1} = \int_0^{2\pi} \mu \{ \xi_{n-1}(\varphi) \} d\varphi, \qquad (9.18)$$

the estimate

$$| k_{n-1} | < m$$

holds.

Hence

$$| \sigma_n | < | \mu | + | k_{n-1} | < 2m.$$

Now, as

$$| e^{h_n} | = e^{\sigma_n} < e^{2m},$$

$$| e^{h_{n-1}} | = e^{\sigma_{n-1}} < e^{2m},$$

by lemma 1,

$$| e^{h_n} - e^{h_{n-1}} | \leqq e^{2m} . | h_n - h_{n-1} |,$$

$$\int_0^{\varphi} \left| e^{h_n} - e^{h_{n-1}} \right|^2 d\psi \leqq e^{4m} \int_0^{\varphi} \left| h_n - h_{n-1} \right|^2 d\psi \leqq$$

$$\leqq e^{4m} \int_0^{2\pi} \left| h_n - h_{n-1} \right|^2 d\psi. \qquad (9.19)$$

As κ_n is adjusted so that $\oint \frac{h_n(z)}{z} dz = 0$, along the circle, application of Lemma 2 yields

$$\int_0^{2\pi} \left| h_n - h_{n-1} \right|^2 d\psi =$$

$$= \int_0^{2\pi} \{ (\sigma_n - \sigma_{n-1})^2 + (\tau_n - \tau_{n-1})^2 \} d\psi =$$

$$= 2 \int_0^{2\pi} (\sigma_n - \sigma_{n-1})^2 d\psi. \qquad (9.20)$$

As, further, $\mu(\theta)$ is regular, it satisfies a Lipschitz condition

$$| \mu(\theta_1) - \mu(\theta_2) | < M_1 | \theta_1 - \theta_2 | \qquad (9.21)$$

for any pair of values θ_1 and θ_2. Hence, there is a number M, so that

$$| \sigma_{n+1}(\varphi) - \sigma_n(\varphi) |^2 \leqq M^2 | \xi_n - \xi_{n-1} |^2 \leqq$$

$$\leqq 2 M^2 e^{4m} . \int_0^{2\pi} (\sigma_n - \sigma_{n-1})^2 d\psi . \leqq$$

$$\leqq (4\pi M^2 e^{4m})^{n-1} \int_0^{2\pi} (\sigma_1 - \sigma_0)^2 d\psi. \qquad (9.22)$$

This completes the proof of the theorem.

This theorem shows, that the process converges for sufficiently small values of m and M, yielding a limit set of values σ, τ and ξ, from which η can be found easily. In practice, a satisfactory result will generally be obtained after the first step, as will be shown in the chapter on numerical methods.

10 Approximate theory.

10.1 *General formulae.*

From the set of exact formulae, relating the velocity distribution with the geometrical properties of the aerofoil, a simple approximative theory, valid only for thin aerofoils, can be obtained.

This approximation allows a rapid conversion of geometrical specifications of the aerofoil into specifications of the velocity distribution and conversely and may thus facilitate considerably the design of aerofoils.

For a flat plate at zero incidence the transformation formula into a circle is

$$\zeta = z + \frac{R^2}{z} \qquad (10.1)$$

and

$$\frac{d\zeta}{dz} = 1 - \frac{R^2}{z^2} = e^{\sigma_0 + i\tau_0}. \qquad (10.2)$$

Hence, the functions $\sigma_0(\varphi)$ and $\tau_0(\varphi)$ take on the circle

$$z = Re^{i\varphi} \qquad (10.3)$$

the value

$$\sigma_0 = ln\, 2 \sin \varphi, \qquad (10.4)$$

$$\tau_0 = \pi/2 - \varphi. \qquad (10.5)$$

Now, assume for a thin aerofoil

$$\sigma = \sigma_0 + \Delta\sigma = ln\, 2 \sin \varphi + \Delta\sigma, \qquad (10.6)$$

$$\tau = \tau_0 + \Delta\tau = \pi/2 - \varphi + \Delta\tau, \qquad (10.7)$$

where $\Delta\sigma$ and $\Delta\tau$ are relatively small corrections.

Then, the formulae for the coordinates become

$$\frac{\xi}{R} = 2 \int_0^{\varphi} \sin\varphi . e^{\Delta\sigma} . \cos\Delta\tau . d\varphi \approx 2 (1 - \cos\varphi) -$$

$$- 2 \int_0^{\varphi} \Delta\sigma\, d\cos\varphi \approx 2 (1 - \cos\varphi) \qquad (10.8)$$

$$\frac{\eta}{R} = 2 \int_0^{\varphi} \sin\varphi . e^{\Delta\sigma} . \sin\Delta\tau . d\varphi \approx -2 \int_0^{\varphi} \Delta\tau\, d\cos\varphi,$$

and (10.9)

$$\frac{d\eta}{d\xi} = \operatorname{tg} \Delta\tau \approx \Delta\tau. \qquad (10.10)$$

Hence $\Delta\tau$ is the slope of the tangent to the aerofoil contour (except near the nose).

The function $\Delta\sigma$ is related to the velocity distribution v_{p_α} at angle of incidence α.

From

$$\sigma = \sigma_0 + \Delta\sigma = ln \left| \frac{v_{c_\alpha}}{v_{p_\alpha}} \right| = ln \left| \frac{v_{c_0}}{v_{p_0}} \right| =$$

$$= - ln \left| \frac{v_{p_0}}{v_\infty} \right| + ln \{ 2 \sin \varphi \} \qquad (10.11)$$

it follows that

$$\Delta\sigma = - ln \left| \frac{v_{p_0}}{v_\infty} \right|, \qquad (10.12)$$

where v_{p_0} is the velocity distribution at zero incidence.

Further, introducing the function (excess velocity at zero incidence)

$$\lambda_0(\varphi) = \frac{(v_{p_0}) - v_\infty}{v_\infty}, \qquad (10.13)$$

which is easily found from the distribution at incidence α,

$$\Delta\sigma = - \lambda_0(\varphi). \qquad (10.14)$$

Now $\Delta\sigma$ and $\Delta\tau$ are conjugate functions and, hence, related by POISSON's integral.

The formula

$$\Delta\sigma(\varphi) = \frac{1}{2\pi} \int_0^{2\pi} \Delta\tau(\psi) \, . \operatorname{cotg} \frac{1}{2} (\varphi - \psi) d\psi, \quad (10.15)$$

or

$$- \lambda_0(\varphi) = \frac{1}{2\pi} \int_0^{2\pi} \left(\frac{d\eta}{d\xi} \right) . \operatorname{cotg} \frac{1}{2} (\varphi - \psi) d\psi \quad (10.16)$$

admits the estimation of $\lambda_0(\varphi)$ (or the velocity distribution) from the shape of the aerofoil, as, by (10.8), the derivative, which initially is given as a function of ξ can be expressed as a function of ψ.

Hence (10.8) and (10.16) solve problem I in first order approximation.

Conversely

$$\Delta\tau(\varphi) = - \frac{1}{2\pi} \int_0^{2\pi} \Delta\sigma(\psi) \, . \operatorname{cotg} \frac{1}{2} (\varphi - \psi) d\psi, \quad (10.17)$$

or

$$\Delta\tau(\varphi) = \frac{1}{2\pi} \int_0^{2\pi} \lambda_0(\psi) \, . \operatorname{cotg} \frac{1}{2} (\varphi - \psi) d\psi. \quad (10.18)$$

Substitution into (10.9) yields

$$\frac{\eta(\varphi)}{R} = \frac{1}{\pi} \int_0^{\varphi} \int_0^{2\pi} \lambda_0(\psi) \, . \operatorname{cotg} \frac{1}{2} (\theta - \psi) d\psi \, . \sin \theta d\theta.$$

As the conjugate of the integral of a function is equal to the integral of the conjugate function this can be transformed into

$$\frac{\eta(\varphi)}{R} = \frac{1}{\pi} \int_0^{2\pi} \int_0^{\psi} \lambda_0(\theta) \sin \theta d\theta \operatorname{cotg} \frac{1}{2} (\varphi - \psi) d\psi. \qquad (10.19)$$

Together with (10.8) this formula derives the shape of the aerofoil from $\lambda(\varphi)$, which is itself derived from the prescribed velocity distribution at angle of incidence α. Hence (10.8), (10.9) and (10.19) solve problem II in first approximation.

Note that the conditions, imposed on the velocity distribution in the exact theory do not occur here. They refer to the requirement, that the aerofoil should have a closed contour. As the approximation formulae developed here, are no longer valid near the nose, it cannot be decided in this approximation whether the aerofoil contour will be closed or not.

10.2 *Symmetrical aerofoils.*

In the case of a symmetrical aerofoil $\sigma(\varphi)$ is an even and $\tau(\varphi)$ an old function of φ and the formulae can be somewhat simplified.

$$\Delta\sigma(\varphi) = \frac{1}{\pi} \int_0^{\pi} \Delta\tau(\psi) \, . \frac{\sin \psi d\psi}{\cos \psi - \cos \varphi}. \quad (10.20)$$

So, by (10.8) and (10.10), the well known formula

$$\lambda_0(\xi_1) = \frac{1}{\pi} \int_0^{4R} \frac{d\eta}{d\xi} \, . \frac{d\xi}{\xi - \xi_1}. \qquad (10.21)$$

is obtained, where

$$\xi_1 = 2R(1 - \cos \varphi), \; \xi = 2R(1 - \cos \psi). \qquad (10.22)$$

This formula expresses the excess velocity in first approximation at zero incidence.

In the same approximation, the velocity distribution at other angles of incidence is given by

$$\left| \frac{v_{p_\alpha}}{v_{p_0}} \right| = \frac{\cos (\frac{1}{2} \varphi - \alpha)}{\cos \frac{1}{2} \varphi} =$$

$$= \cos \alpha + \sin \alpha \, . \operatorname{tg} \frac{1}{2} \varphi \approx 1 + \alpha \, . \operatorname{tg} \tfrac{1}{2} \varphi. \quad (10.23)$$

Hence, the excess velocity at incidence α is

$$\lambda_\alpha = (1 + \alpha \operatorname{tg} \frac{1}{2} \varphi) (1 + \lambda_0) -$$

$$- 1 = 1 + \lambda_0 + \alpha \sqrt{\frac{\xi_1}{4R - \xi_1}}, \qquad (10.24)$$

a formula, which does not hold near the leading edge $\xi = 4R$.

In the case of a symmetrical aerofoil $\lambda_0(\varphi)$ is an even function of φ and likewise

$$\int_0^{\varphi} \lambda_0(\theta) \sin\theta d\theta.$$

Hence the formula for the coordinates becomes

$$\frac{\eta(\varphi)}{R} = \frac{-2\sin\varphi}{\pi} \int_0^{\pi} \frac{\int_0^{\psi} \lambda_0(\theta)\sin\theta d\theta}{\cos\varphi - \cos\psi} d\psi, \quad (10.25)$$

from which the shape of the aerofoil can be derived to first approximation.

PART II.

Numerical methods.

11 Basic properties of numerical methods.

11.1 *Preliminary considerations.*

Disregarding the few special cases where problem I and II can be solved analytically, the analytical operations involved in the iteration procedures developed must be approximated by purely numerical methods.

Aside from simple operations like differentiation or integration of analytic functions, adequately soluble by aid of conventional numerical methods, the numerical evaluation of the principal value of POISSON's integral

$$\tau(\varphi) = -\frac{1}{2\pi} \int_0^{2\pi} \sigma(\psi) \operatorname{cotg} \frac{1}{2}(\varphi - \psi) d\psi \quad (11.1)$$

is a more complicated problem occurring in every iteration step. The function $\sigma(\psi)$ is approximated by interpolation polynomials, through the values of $\sigma(\psi)$ in $4n$ equidistant points (lattice points)

$$\varphi_m = m \cdot \frac{\pi}{2n}; \quad m = 0,1, \quad 4n-1. \quad (11.2)$$

The choice of this interpolation formula is governed by a practical consideration, viz. the fact, that waviness of the aerofoil contour deteriorates the aerodynamic properties and hence, that any waviness merely resulting from inaccuracies of the numerical design procedure is to be prevented as much as possible. So the numerical procedures should not affect properties of the functions σ and τ referring to continuous differentiability and non-oscillatory variation. It is not so easy to specify accurately the conditions involved (applying to the methods of numerical evaluation), but the following proposition may be satisfactory.

Any interpolatory function must be continuously differentiable and non-oscillatory (i. e. its graph must not contain waves of order $10^{-4} \times$ max. value of the function with a wave length comparable to or smaller than $\frac{\pi}{2n}$).

If the function considered shows either discontinuities, or discontinuities of its first derivatve, these must be treated separately by subtracting from the function a suitable simple function with the same discontinuities, apt to be treated analytically. This condition should not be considered to imply that cases of a steep gradient along a distance of one or two intervals are excluded.

Under these circumstances, the Poisson integral can be evaluated numerically with the help of interpolation formulae. Two different methods have found extensive application. The first proceeds from THEODORSEN and GARRICK (ref. 12) and is based, not only on the $4n$ lattice point values of the function itself, but also on the values of the derivative in these points, which gives rise to inaccuracies if the function is not defined by an analytical expression.

The second method has been developed by RIEGELS and WITTICH (ref. 14) and, independently by GERMAIN (ref. 15). It makes use of trigonometric interpolation polynomials and results, by a skilful use of the properties of the coefficients of these polynomials, in a simple matrix-multiplication operation. The method is entirely satisfactory in many cases. Difficulties, however, emerge in cases, where a steep gradient is present, as referred to and definitely admitted above. If the interpolatory function used is a trigonometric polynomial, it obtains, in such cases, a larger waviness than is acceptable. At the spot, where the gradient is steep, the interpolating function shows GIBBS' phenomena, commonly encountered in approximating Fourier polynomials for a function with a discontinuity. The resulting values will show the same waviness in the lattice points. Even if this feature is only slight, it may be inacceptable, for it may, e. g. in the calculation of laminar flow aerofoils, lead to waviness in the contour. For this reason, a new method has been developed, based on algebraic interpolation polynomials of a special kind, established by SCHOENBERG (ref. 17) and apt to avoid irregularities of any unacceptable type as much as possible.

11.2 *Interpolation polynomials.*

Introducing the variable

$$p = \frac{\psi - \frac{m\pi}{2n}}{\pi/2n}, \quad (11.3)$$

whence

$$\psi = \frac{(m+p)\pi}{2n}, \quad (11.4)$$

the interpolation will be required to represent a function, whose values are given in the lattice points, determined by integer values of the abscissae.

Now, any interpolation formula can be repre-

sented by a "basic function" $L(x)$ with the property

$$L(0)=1;\quad L(n)=0,\quad n=\text{integer}\neq 0, \tag{11.5}$$

the interpolatory function being represented by the expression

$$F(p)=\sum_{\nu=-\infty}^{\infty}\lambda_\nu L(p-\nu), \tag{11.6}$$

where λ_0 is the sequence of values of the function in the lattice points. In the cases considered the function is periodic and the sequence is infinite [1]). Taking the Lagrange interpolation as an example of interpolation with a central difference formula of the second order, the interpolation polynomial is

$$\begin{aligned}F(p)=&\lambda_{-2}\frac{p(p-1)(p+1)(p-2)}{24}-\\&-\lambda_{-1}\frac{p(p-1)(p+2)(p-2)}{6}+\\&+\lambda_0\frac{(p+1)(p-1)(p+2)(p-2)}{4}-\\&-\lambda_1\frac{p(p+1)(p+2)(p-2)}{6}+\\&+\lambda_2\frac{p(p-1)(p+1)(p+2)}{24}.\end{aligned} \tag{11.7}$$

Hence, $L(p)$ is defined by the formulae:

$$L(p)=\begin{cases}0, & p<-5/2,\\ \dfrac{(p+2)(p+1)(p+3)(p+4)}{24}, & -5/2<p<-3/2,\\ -\dfrac{(p+1)(p+2)(p+3)(p-1)}{6}, & -3/2\leq p<-1/2,\\ \dfrac{(p+1)(p-1)(p+2)(p-2)}{4}, & -1/2<p<+1/2,\end{cases} \tag{11.8}$$

and

$$L(-p)=L(p).$$

This function is reproduced in fig. 4. It is discontinuous in the points $p=\text{integer}+\frac{1}{2}$. In the special case, where the values λ_ν belong to a function of the second degree, its values are reproduced exactly by the interpolation formula (11.6) and the discontinuities cancel in the addition of the successive terms in (11.6). In all other cases these discontinuities of the interpolatory function do not cancel and may cause considerable errors, e. g. when, as mentioned above, a local steep gradient of the function $\lambda(x)$, causing large differences in successive values of λ_ν, is present. They have proved to affect the conjugate function in the calculation of the Poisson integral, derived from a σ function, interpolated by Lagrange interpolation, in a quite unsatisfactory way.

These difficulties can be avoided by the application of interpolation by one of the basic functions, introduced by SCHOENBERG. This basic function L has the following properties:

(I) it is continuous, together with its first derivative.

(II) any function of the second degree is reproduced exactly.

(III) it has the same "span" as the Langrangian basic function defined by (11.8).

(IV) it is composed of arcs of at most the third degree.

From these conditions, the function can be deduced to be

$$L(p)=\begin{cases}0, & p\leqq -5/2,\\ -\dfrac{1}{8}(p+2)^3-\dfrac{1}{8}(p+2)^2-\dfrac{1}{32}(p+2), & -5/2\leqq p\leqq -3/2,\\ \dfrac{1}{4}(p+1)^3+(p+1)^2+\dfrac{9}{16}(p+1), & -3/2\leqq p\leqq -1/2,\\ -\dfrac{7}{4}p^2+1, & -1/2\leqq p\leqq +1/2\end{cases} \tag{11.9}$$

and

$$L(-p)=-L(p).$$

Its graph is given in fig. 5. The general method indicated by SCHOENBERG, to generate such interpolation functions will not be considered here, as the function (11.9) can be deduced from the properties (I) to (IV) mentioned above by quite elementary reasoning.

[1]) The practical interpolation in finite sequences may call for modifications of the interpolation function L near the end points of the interval, or for extrapolation at both sides of the interval.

The interpolation formula ,valid in the interval $-\frac{1}{2} \leqq p \leqq \frac{1}{2}$, belonging to (11.9), is

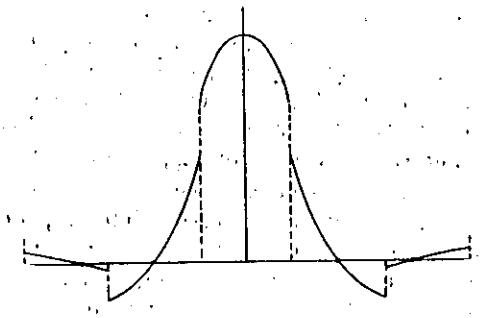

Fig. 4. The Lagrange interpolation.

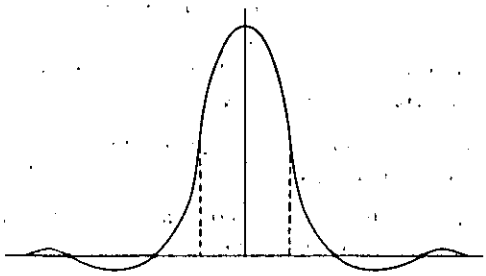

Fig. 5. The Schoenberg interpolation.

$$F(p) = \lambda_{-2}\left(\frac{1}{8}p^3 - \frac{1}{8}p^2 + \frac{1}{32}p\right) + \lambda_{-1}\left(-\frac{1}{4}p^3 + p^2 - \frac{9}{16}p\right) + \lambda_0\left(1 - \frac{7}{4}p^2\right) + \lambda_1\left(\frac{1}{4}p^3 + p^2 + \frac{9}{16}p\right) + \lambda_2\left(-\frac{1}{8}p^3 - \frac{1}{8}p^2 - \frac{1}{32}p\right), \quad (11.10)$$

which will be used to evaluate the Poisson integral.

11.3 *Reduction of the Poisson integral.*

The Poisson integral (11.1) is, for the present purpose, written in the form

$$\tau(\varphi) = + \frac{1}{2\pi}\sum_{m=0}^{4n-1}\int_{\varphi_m - \varepsilon}^{\varphi_m + \varepsilon} \sigma(\psi) \,.\, \operatorname{cotg}\frac{\psi - \varphi}{2}\, d\psi, \quad (11.11)$$

with

$$\varphi_m = m\frac{\pi}{2n}; \qquad \varepsilon = \frac{\pi}{4n}.$$

It is evaluated by substituting in each partial integral an interpolation approximation for σ

$$\sigma(\psi) = \sigma\left(\varphi_m + p\frac{\pi}{2n}\right) = F_m(p), \quad -\tfrac{1}{2} \leqq p \leqq +\tfrac{1}{2}, \quad (11.12)$$

where $F_m(p)$ is taken from (11.10) with $\lambda = \sigma_{m+\nu}$.

$$F_m(p) = \sum_{\nu=-\infty}^{\nu=+\infty} \sigma_{m+\nu}\, L(p-\nu). \quad [1]) \quad (11.13)$$

In the interval $-\frac{1}{2} \leqq p \leqq +\frac{1}{2}$ the expression for $F_m(p)$ is.

$$F_m(p) = \sigma_{m-2}\left(\frac{1}{8}p^3 - \frac{1}{8}p^2 + \frac{1}{32}p\right) + \sigma_{m-1}\left(-\frac{1}{4}p^3 + p^2 - \frac{9}{16}p\right) + \sigma_m\left(1 - \frac{7}{4}p^2\right) + \sigma_{m+1}\left(\frac{1}{4}p^3 + p^2 + \frac{9}{16}p\right) + \sigma_{m+2}\left(-\frac{1}{8}p^3 - \frac{1}{8}p^2 - \frac{1}{32}p\right). \quad (11.14)$$

Substitution of (11.12) yields

$$\tau(\varphi) = + \frac{1}{4n}\sum_{m=0}^{4n-1}\int_{-\frac{1}{2}}^{+\frac{1}{2}} F_m(p) \,.\, \operatorname{cotg}\frac{1}{2}\left\{(\varphi_m - \varphi) + p\frac{\pi}{2n}\right\}. dp. \quad (11.15)$$

If it is sufficient to determine the values of $\tau(\varphi)$ in the lattice points $\varphi_k = k\frac{\pi}{2n}$, substitution of (11.14) leads to integrals of the form

$$p_{k,\nu} = \frac{\pi}{2n}\int_{-\frac{1}{2}}^{+\frac{1}{2}} p^\nu \,.\, \operatorname{cotg}\frac{(k+p)\pi}{4n}\,.\, dp, \quad (11.16)$$

$$k = m - l = 0,1, \ldots\ldots 4n-1.$$

11.4 *Calculation of the integrals* $p_{k,\nu}$.

For small k, the ratio $\frac{k+p}{4n}$ is small, and use is made of the expansion

$$\operatorname{cotg} x = \frac{1}{x} - \frac{1}{3}x - \frac{1}{45}x^3 - \frac{2}{945}x^5 - \theta_1 \cdot \frac{x7}{4725}. \quad (11.17)$$

$$0 < \theta_1 < 1.$$

Putting

$$T_\nu^\mu(k) = \int_{-\frac{1}{2}}^{+\frac{1}{2}} p^\nu \,.\, (k+p)^\mu\, dp, \quad (11.18)$$

it is found that

$$p_{k,\nu} = \frac{\pi}{2n}\left\{\frac{4n}{\pi}T_\nu^{-1}(k) - \frac{1}{3}\cdot\frac{\pi}{4n}T_\nu^1(k) - \frac{1}{45}\left(\frac{\pi}{4n}\right)^3 T_\nu^3(k) - \frac{2}{945}\cdot\left(\frac{\pi}{4n}\right)^5 T_\nu^5(k) - \theta_2\cdot\frac{1}{4725}\left(\frac{\pi}{4n}\right)^7 \cdot T_\nu^7(k).\right\}$$

$$0 < \theta_2 < 1$$

[1]) Taking account of the definition (11.12) of $Fm(p)$ the expression (11.13) is seen to represent the same function of φ, independent of m.

The $T_\nu^\mu(k)$ are calculated from

$$T_\nu^0(k) = \int_{-1/2}^{+1/2} p^\nu \, dp = \begin{cases} 0 & , \quad \nu = 2\lambda + 1 \\ \dfrac{2^{-2\lambda}}{2\lambda+1}, & \nu = 2\lambda \end{cases} \tag{11.20}$$

and the recursion formulae

$$T_\nu^\mu(k) = \sum_{\rho=0}^{\mu} \binom{\mu}{\rho} T_{\nu+\rho}^0(k) \cdot k^{\mu-\rho}, \quad \mu > 0 \tag{11.21}$$

$$T_\nu^{-1}(k) = \sum_{\rho=0}^{n-1} T_\rho^0 \, (-k)^{n-1-\rho} - k \, ln \left| \frac{k+1/2}{k-1/2} \right|,$$

replacing the integral by its principal value for $k=0$ and $\mu=-1$.

For small values of k these methods are sufficiently accurate as can, if desired, be inferred from the error term.

For large values of k the function

$$\operatorname{cotg}\left\{\frac{k\pi}{4n} + p \cdot \frac{\pi}{4n}\right\}$$

is expanded in a Taylor series. Putting

$$\operatorname{cotg}\frac{k\pi}{4n} = t \tag{11.22}$$

elementary calculations yield

$$\operatorname{cotg}\left\{\frac{k\pi}{4n} + p \cdot \frac{\pi}{4n}\right\} = t - (1+t^2) \cdot \frac{p\pi}{4n} + (t+t^3) \cdot \left(\frac{p\pi}{4n}\right)^2 - \left(\frac{1+4t^2+3t^4}{3}\right) \cdot \left(\frac{p\pi}{4n}\right)^3 + \left(\frac{2t+5t^3+3t^5}{3}\right) \cdot \left(\frac{p\pi}{4n}\right)^4 - \frac{2+17t^2+30t^4+15t^6}{15} \left(\frac{p\pi}{4n}\right)^5 + O\left(\frac{p\pi}{4n}\right)^6. \tag{11.23}$$

Substitution into the integral gives

$$P_{k,2\mu} = \frac{\pi}{8n} \cdot \frac{1}{2^{2\mu-2}} \cdot \frac{1}{2\mu+1} \left\{ t + t(1+t^2) \cdot \frac{2\mu+1}{2\mu+3} \cdot \left(\frac{\pi}{8n}\right)^2 + \frac{2t+5t^3+3t^5}{3} \cdot \frac{2\mu+1}{2\mu+5} \left(\frac{\pi}{8n}\right)^4 \right\} + O\left(\frac{\pi t}{8n}\right)^6, \tag{11.24}$$

$$P_{k,2\mu+1} = -\left(\frac{\pi}{8n}\right)^2 \cdot \frac{1}{2^{2\mu-1}} \cdot \frac{1}{2\mu+3} \left\{ 1 + t^2 + \frac{2\mu+3}{2\mu+5} \cdot \frac{(1+t^2)(1+3t^2)}{3} \left(\frac{\pi}{8n}\right)^2 + \frac{2\mu+3}{2\mu+7} \cdot \frac{2+17t^2+30t^4+15t^6}{15} \left(\frac{\pi}{8n}\right)^4 \right\} + O\left(\frac{\pi t}{8n}\right)^7. \tag{11.25}$$

The coefficiënts $P_{k,\nu}$ are calculated in the case $n=9$, corresponding to a division of the circle in arcs of 10°. The first method is used for $k=0, 1, 2, 3$, the second for $k=3, \ldots 18$. For $k=3$, agreement of the results up to 6 decimal places has been obtained.

For values of $k > 2n$, the functions $P_{k,n}$ are related by

$$P_{-k,\nu} = P_{4n-k,\nu} = (-1)^{\nu+1} P_{k,\nu}, \tag{11.26}$$

as can be shown as follows

$$P_{-k,\nu} = P_{4n-k,\nu} =$$

$$= \frac{\pi}{2n} \int_{-1/2}^{+1/2} p^\nu \cdot \operatorname{cotg}\left\{\frac{(4n-k)\pi}{4n} + \frac{p\pi}{4n}\right\} dp =$$

$$= \frac{\pi}{2n} \int_{-1/2}^{+1/2} p^\nu \cdot \operatorname{cotg}\left\{\pi - \frac{k\pi}{4n} + \frac{p\pi}{4n}\right\} dp =$$

$$= -\frac{\pi}{2n} \int_{-1/2}^{+1/2} p^\nu \cdot \operatorname{cotg}\left\{\frac{k\pi}{4n} - \frac{p\pi}{4n}\right\} dp =$$

$$= \frac{\pi}{2n}(-1)^{\nu-1} \int_{-1/2}^{+1/2} p^\nu \operatorname{cotg}\left\{\frac{k\pi}{4n} + \frac{p\pi}{4n}\right\} dp =$$

$$= (-1)^{\nu+1} \cdot P_{k,\nu}. \tag{11.27}$$

11.5 *Calculation of the Poisson integral.*

Introducing

$$A_{m-l}^{-2} = \frac{1}{32}(4P_{m-l,3} - 4P_{m-l,2} + P_{m-l,1}),$$

$$A_{m-l}^{-1} = \frac{1}{16}(-4P_{m-l,3} + 16P_{m-l,2} - 9P_{m-l,1}),$$

$$A_{m-l}^{0} = P_{m-l,0} - \frac{7}{4}P_{m-l,2}, \tag{11.28}$$

$$A_{m-l}^{1} = \frac{1}{16}(4P_{m-l,3} + 16P_{m-l,2} + 9P_{m-l,1}),$$

$$A_{m-l}^{2} = \frac{1}{32}(-4P_{m-l,3} - 4P_{m-l,2} - P_{m-l,1}),$$

the integral (11.15) can be written as

$$\tau(\varphi_l) = +\frac{1}{2\pi} \sum_{m=0}^{4n-1} \cdot \sum_{\nu=-2}^{+2} \sigma_{m+\nu} \cdot A_{m-l}^{\nu} = \tag{11.29}$$

$$= +\frac{1}{2\pi} \sum_{m=0}^{4n-1} \sigma_m \cdot \sum_{\nu=-2}^{+2} A^{\nu}{}_{m-l-\nu} =$$

$$= +2 \sum_{m=0}^{4n-1} \sigma_m \cdot C_{m-l},$$

where

$$C_{m-l} = \frac{1}{4\pi} \sum_{\nu=-2}^{+2} A^{\nu}{}_{m-l-\nu}. \tag{11.30}$$

The symmetry properties (11.26) prove, that

$$A_{4n-k}^{\nu} = -A_k^{-\nu} \tag{11.31}$$

and hence

$$C_{4n-k} = -C_k. \tag{11.32}$$

Introducing the symbols

$$s_0 = \sigma_0 \quad , \quad d_0 = 0$$
$$s_m = \sigma_m + \sigma_{4n-m} \quad , \quad d_m = \sigma_m - \sigma_{4n-m} \quad ,$$
$$s_{2n} = \sigma_{2n} \quad , \quad d_{2n} = 0 \qquad (11.33)$$

and

$$\alpha_{ml} = C_{m-l} + C_{4n-m-l} = C_{m-l} - C_{m+l} \, ,$$
$$\beta_{ml} = C_{m-l} - C_{4n-m-l} = C_{m-l} + C_{m+l} \, , \qquad (11.34)$$

formula (11.29) can be reduced to

$$\tau(\varphi_l) = + \sum_{m=0}^{2n} \alpha_{ml} s_m + \sum_{m=0}^{2n} \beta_{ml} d_m . \qquad (11.35)$$

Restricting also the values of l to $0 \leqq l \leqq 2n$, the coefficients α_{ml} and β_{ml} can be recollected in two matrices of order $2n$ and the column $\tau(\varphi_l)$ $(0 \leqq l \leqq 2n)$ is the sum of two columns, the first, D_l, resulting from a multiplication of the α matrix with the row s_m, the second S_l, from a multiplication of the β matrix with the row d_m.

$$\tau(\varphi_l) = S_l + D_l \qquad 0 \leqq l \leqq 2n. \qquad (11.36)$$

To find the values of $\tau(\varphi_l)$ for $2n \leqq l \leqq 4n-1$, note that

$$\alpha_{m,4n-l} = C_{-4n+m+l} - C_{4n+m-l} =$$
$$= C_{m+l} - C_{m-l} = -\alpha_{ml} \, , \qquad (11.37)$$

$$\beta_{m,4n-l} = C_{-4n+m+l} + C_{4n+m-l} =$$
$$= C_{m+l} + C_{m-l} = + \beta_{ml} \, ,$$

whence

$$\tau(\varphi_{4n-l}) = S_l - D_l \, . \quad 0 \leqq l \leqq 2n. \qquad (11.38)$$

If $\sigma(\varphi)$ is an even function of φ, $d_m = 0$ and $S_l = 0$, τ is an odd function, and if $\sigma(\varphi)$ is an odd function, τ is even.

Finally, a number of relations between the matrix elements can be established

$$\alpha_{ml} = C_{m-l} - C_{m+l} =$$
$$= -(C_{l-m} + C_{l+m}) = -\beta_{lm} \, , \qquad (11.39)$$

$$\alpha_{2n-m,2n-l} = C_{l-m} - C_{4n-l-m} =$$
$$= -C_{m-l} + C_{l+m} = -\alpha_{ml} \, , \qquad (11.40)$$

$$\beta_{2n-m,2n-l} = C_{l-m} + C_{4n-l-m} =$$
$$= -C_{m-l} - C_{m+l} = -\beta_{ml} \, . \qquad (11.41)$$

So the β matrix is the transposed of the α matrix with a negative sign.

For $n = 9$ the α matrix is given in table I.

11.6 *Calculation of the derivative of the conjugate function.*

In certain cases, especially for the calculation of the radius of curvature in any point of the aerofoil, it is convenient to dispose of the values of the derivative of the conjugate function.

Now $\frac{d\tau}{d\varphi}$ is the conjugate of $\frac{d\sigma}{d\varphi}$ and,

$$\frac{d\tau}{d\psi} = -\frac{1}{2\pi} \int_0^{2\pi} \frac{d\sigma}{d\varphi} \cdot \operatorname{cotg} \frac{\psi - \varphi}{2} \cdot d\varphi. \qquad (11.42)$$

Using the interpolation polynomial (11.14) for σ, the formula for $\frac{d\tau}{d\psi}$ becomes

$$\frac{d\tau}{d\psi} = + \frac{1}{4n} \cdot \frac{2n}{\pi} \cdot \sum_{m=0}^{4n-1} \int_{-1/2}^{+1/2} \frac{dF_m(p)}{dp} \cdot$$
$$\cdot \operatorname{cotg} \frac{1}{2} \left\{ (\varphi_m - \varphi) + p \, \frac{\pi}{2n} \right\} \cdot dp. \qquad (11.43)$$

Now, from (11.14)

$$\frac{dF_m(p)}{dp} = \sigma_{m-2} \left(\frac{3}{8} p^2 - \frac{1}{4} p + \frac{1}{32} \right) +$$
$$+ \sigma_{m-1} \left(-\frac{3}{4} p^2 + 2p - \frac{9}{16} \right) - \frac{7}{2} p \cdot \sigma_m +$$
$$+ \sigma_{m+1} \left(\frac{3}{4} p^2 + 2p + \frac{9}{16} \right) +$$
$$+ \sigma_{m+2} \left(-\frac{3}{8} p^2 - \frac{1}{4} p - \frac{1}{32} \right) . \qquad (11.44)$$

Introducing

$$B^{-2}_{m-l} = \frac{1}{32} (12 P_{m-l,2} - 8 P_{m-l,1} + P_{m-l,0}) \, ,$$
$$B^{-1}_{m-l} = \frac{1}{16} (-12 P_{m-l,2} + 32 P_{m-l,1} - 9 P_{m-l,0}) \, ,$$
$$B^{0}_{m-l} = -\frac{7}{2} P_{m-l,1} \, ,$$
$$B^{1}_{m-l} = \frac{1}{16} (12 P_{m-l,2} + 32 P_{m-l,1} + 9 P_{m-l,0}) \, ,$$
$$B^{2}_{m-l} = \frac{1}{32} (-12 P_{m-l,2} - 8 P_{m-l,1} - P_{m-l,0}) \, , \qquad (11.45)$$

the integral formula for $\frac{d\tau}{d\varphi}$ can be written as

$$\frac{d\tau(\varphi_l)}{d\varphi} = + \frac{2n}{\pi} \cdot \frac{1}{2\pi} \sum_{m=0}^{4n-1} \sum_{\nu=-2}^{+2} \sigma_{m+\nu} \cdot B^{\nu}_{m-l} = \qquad (11.46)$$
$$= + \frac{n}{\pi^2} \cdot \sum_{m=0}^{4n-1} \sigma_m \cdot \sum_{\nu=-2}^{+2} B^{\nu}_{m-l-\nu} \, ,$$

or, of

$$D_{m-l} = \frac{1}{4\pi} \sum_{\nu=-2}^{+2} B^{\nu}_{m-l-\nu} \, , \qquad (11.47)$$

$$\frac{d\tau(\varphi_l)}{d\varphi} = + \frac{4n}{\pi} \sum_{m=0}^{4n-1} \sigma_m \cdot D_{m-l} \, . \qquad (11.48)$$

Again the symmetry properties of the $P_{m-l,\nu}$ show that

$$B^{\nu}_{4n-k} = + B^{-\nu}_{k} \qquad (11.49)$$

and hence

$$D_{4n-k} = D_k \, . \qquad (11.50)$$

With the symbols s_m, d_m of (11.33) and

$$\gamma_{ml} = D_{m-l} + D_{4n-m-l} = D_{m-l} + D_{m+l}, \quad (11.51)$$
$$\delta_{ml} = D_{m-l} - D_{4n-m-l} = D_{m-l} - D_{m+l},$$

formula (11.48) can be reduced to

$$\frac{\pi}{2n}\frac{d\tau(\varphi_l)}{d\varphi} = + \sum_{m=0}^{2n} \gamma_{ml}\, s_m + \sum_{m=0}^{2n} \delta_{ml}\, d_m . \quad (11.52)$$

12 A class of intermediate aerofoils.

12.1 *Preliminary considerations.*

In the general theory of part I, the desirability to choose an adequate intermediate aerofoil was emphasized. This intermediate aerofoil, serving as zero-order approximation in the iteration procedures, must be so chosen that the differences $\sigma - \sigma_0$ and $\tau - \tau_0$ are, everywhere on the circle, analytic in order to realize the conditions necessary for a successful application of the numerical procedure of chapter 1 for the Poisson integral.

Moreover, with a suitable choice of the intermediate aerofoil already the first step in the iteration procedure yields a sufficiently accurate result.

A suitable family of intermediate aerofoils has, for practical purposes, to satisfy two conditions

(i) It must be possible to represent its coordinates as well as its functions σ and τ by simple analytic formulae.

(ii) these formulae must involve a few parameters so as to give a fair variety of shapes, in order to secure a satisfactory adaptability to a required shape or velocity distribution.

Initially, Karman-Trefftz aerofoils have been used for this purpose (ref. 7), but ZAAT (ref. 10) has developed a new family of aerofoils, which involve simpler calculations. Of course, however, other well known aerofoil families, like those of PIERCY (ref. 22) or ROSSNER (ref. 23) could be used for the same purpose.

12.2 *The mapping function.*

It follows from 1.5 that a very simple mapping function transforming an aerofoil with tail angle δ in the ζ plane in a regular, closed analytic curve in the z-plane, the point $z = \alpha$ corresponding to the trailing edge $\zeta = 0$, is giving by

$$\zeta = z\left(1 - \frac{\alpha}{z}\right)^k . \quad (12.1)$$

This function is seen to satisfy the additional requirements for the mapping function, i. e. identity of the ζ and z plane in infinity and regularity throughout the outer part of any contour, enclosing the origin.

The derivative is

$$\frac{d\zeta}{dz} = k\left(1 - \frac{\alpha}{z}\right)^{k-1} - (k-1)\left(1 - \frac{\alpha}{z}\right)^k . \quad (12.2)$$

By mapping a circle in the z-plane with the origin as centre a one-parameter family of aerofoils is obtained.

In order to obtain a greater variety ZAAT considers an ellipse in the z-plane, with centre in the point $a(\varepsilon + i\nu\gamma)$.

$$z = x + iy = a\{\varepsilon + \cos\varphi + i\nu(\gamma + \sin\varphi)\}, \quad (12.3)$$

which results from a circle

$$\frac{Z}{a} = \frac{1+\nu}{2} . e^{i\varphi} \quad (12.4)$$

in a Z-plane by the transformation

$$z = a(\varepsilon + i\nu\gamma) + Z + \frac{1-\nu^2}{4} . \frac{a^2}{Z} . \quad (12.5)$$

The coordinates of the aerofoil are found by substitution of (12.3) into (12.1), choosing for α, the point in the z-plane corresponding to the trailing edge, the intersection of the ellipse with the x axis,

$$\alpha = a(\varepsilon + \sqrt{1-\gamma^2}). \quad (12.6)$$

The calculation is simplified by introducing auxiliary functions λ and μ, defined by

$$e^{\lambda + i\mu} = 1 - \frac{\alpha}{z} = 1 - \frac{\varepsilon + \sqrt{1-\gamma^2}}{\varepsilon + \cos\varphi + i\nu(\gamma + \sin\varphi)}$$

or (12.7)

$$e^{2\lambda} = 1 + \frac{(\varepsilon + \sqrt{1-\gamma^2})(\sqrt{1-\gamma^2} - \varepsilon - 2\cos\varphi)}{(\varepsilon + \cos\varphi)^2 + \nu^2(\gamma + \sin\varphi)^2}, \quad (12.8)$$

$$\operatorname{tg}\mu = \frac{\nu(\varepsilon + \sqrt{1-\gamma^2})(\gamma + \sin\varphi)}{(\varepsilon + \cos\varphi)(\cos\varphi - \sqrt{1-\gamma^2}) + \nu^2(\gamma + \sin\varphi)^2} . \quad (12.9)$$

Thus the coordinates of the aerofoil can be calculated from

$$\zeta = \xi + i\eta = a\{(\varepsilon + \cos\varphi) + i\nu(\gamma + \sin\varphi)\}e^{k\lambda + ik\mu}, \quad (12.10)$$

or

$$\frac{\xi}{a} = e^{k\lambda}[(\varepsilon + \cos\varphi)\cos k\mu - \nu(\gamma + \sin\varphi)\sin k\mu], \quad (12.11)$$

$$\frac{\eta}{a} = e^{k\lambda}[(\varepsilon + \cos\varphi)\sin k\mu + \nu(\gamma + \sin\varphi)\cos k\mu]. \quad (12.12)$$

The functions σ and τ, which are defined by

$$e^{\sigma + i\tau} = \frac{d\zeta}{dZ} = \frac{d\zeta}{dz} . \frac{dz}{dZ} \quad (12.13)$$

can, on the circle, be found from (12.2) and (12.5)

$$e^{\sigma(\varphi) + i\tau(\varphi)} = \{k . e^{(k-1)(\lambda + i\mu)} - (k-1) . e^{k(\lambda + i\mu)}\} . \left(1 - \frac{1-\nu}{1+\nu} . e^{-2i\varphi}\right) =$$
$$= \left(e^{i\varphi} + \frac{\nu - 1}{\nu + 1} . e^{-i\varphi}\right)\{k . e^{-1/2(\lambda + i\mu)} - (k-1)e^{1/2(\lambda + i\mu)}\} . e^{(k-1/2)(\lambda + i\mu) - i\varphi} . \quad (12.14)$$

Introducing functions λ_1 and μ_1 by putting

$$e^{\lambda_1 + i\mu_1} = e^{i\varphi} + \frac{\nu - 1}{\nu + 1} e^{-i\varphi}, \qquad (12.15)$$

or

$$\left.\begin{aligned} e^{2\lambda_1} &= 2\,\frac{\nu^2 + 1}{(\nu+1)^2} + 2\,\frac{\nu - 1}{\nu + 1}\cos 2\varphi, \\ \operatorname{tg}\mu_1 &= \frac{1}{\nu}\operatorname{tg}\varphi \end{aligned}\right\} \qquad (12.16)$$

and functions λ_2 and μ_2 by putting

$$e^{\lambda_2 + i\mu_2} = ke^{-1/2(\lambda + i\mu)} - (k-1)e^{1/2(\lambda + i\mu)}, \qquad (12.17)$$

or

$$\left.\begin{aligned} e^{2\lambda_2} &= k^2 e^{-\lambda} + (k-1)^2 e^{\lambda} - \\ &\quad - 2k(k-1)\cos\mu, \\ \operatorname{tg}\mu_2 &= -\frac{k + (k-1)e^{\lambda}}{k - (k-1)e^{\lambda}}\operatorname{tg}\frac{1}{2}\mu, \end{aligned}\right\} \qquad (12.18)$$

the functions $\sigma(\varphi)$ and $\tau(\varphi)$ can be written as

$$\sigma = (k - 1/2)\lambda + \lambda_1 + \lambda_2, \qquad (12.19)$$

$$\tau = (k - 1/2)\mu + \mu_1 + \mu_2 - \varphi. \qquad (12.20)$$

From $\sigma(\varphi)$ the velocity distribution round the aerofoil can be calculated

$$\left|\frac{v_p}{v_\infty}\right| = e^{-\sigma}\left[\sin(\varphi - \alpha) + \sin(\alpha - \beta)\right]. \qquad (12.21)$$

where β is the point on the circle, corresponding to the trailing edge of the aerofoil. From (12.6) it follows that

$$\sin\beta = -\gamma. \qquad (12.22)$$

Any intermediate aerofoil of this family can easily be calculated and the parameters can easily be adapted to the specification of the aerofoil to be considered, either in problem I or problem II.

12.3 *First-order approximation for the intermediate aerofoil.*

By using the approximate theory for small values of $\nu - 1$, ε, γ and putting $\delta = 0$, the formulae for the coordinates become

$$\xi = -2(1 - \cos\varphi), \qquad (12.23)$$

$$\eta = 2\varepsilon\sin\varphi - \varepsilon\sin 2\varphi - (1 - \cos 2\varphi)\gamma - (\nu - 1)\sin\varphi(1 - \cos 2\varphi), \qquad (12.24)$$

from which it is seen, that the camber line is

$$\eta(+\varphi) + \eta(-\varphi) = -2(1 - \cos 2\varphi)\gamma. \qquad (12.25)$$

Hence, the camber is determined by γ.

Further, the thickness distribution is

$$\begin{aligned} t &= \frac{\eta(+\varphi) - \eta(-\varphi)}{4} = \\ &= \frac{1}{2}\{2\varepsilon\sin\varphi(1 - \cos\varphi) - \\ &\quad - (\nu - 1)\sin\varphi(1 - \cos 2\varphi)\} = \\ &= \sin\varphi(1 - \cos\varphi)\{\varepsilon - (\nu - 1)(1 + \cos\varphi)\}. \end{aligned} \qquad (12.26)$$

If $\varepsilon = 0$ and $\nu < 1$ the maximum thickness is equal to $1 - \nu$, and occurs at $\varphi = \frac{1}{2}\pi$, if $\varepsilon > 0$ and $\nu = 1$ it is equal to ε and is located at $\varphi = {}^2/_3\,\pi$, for $\varepsilon > 0$ and $\nu < 1$ it lies in between these points.

Hence it is easy to estimate values of ε and ν, which will yield a given value and location of maximum thickness.

13 The design of aerofoils with specified velocity distributions.

13.1 *General considerations.*

Problem II, stated in section 8 of part I, refers to the design of aerofoils with velocity distributions specified along the chord. It can be solved by means of the iteration process, indicated in the same section.

In the practical design of laminar-flow or high-speed aerofoils it is generally not necessary to keep rigorously to a given velocity distribution along the chord, generally the velocity distribution at a certain angle of incidence has only to show certain properties, e. g. to involve a non-decreasing velocity on the forward part with a given maximum value down to a certain point.

Generally, it is possible to specify the velocity distribution as a function of the image angle φ, as the relation between chordwise coordinate and φ is approximately known (compare I, 10). This function can serve as a first approximation for the iteration process, if a closer agreement with a chordwise specified-velocity distribution is required, which, usually, is not the case.

The velocity distribution as a function of φ, however, cannot be chosen arbitrarily, but has to satisfy the conditions, derived from the relations (5.27) and (5.28)

$$\int_0^{2\pi}\sigma(\varphi)\,d\varphi = 0, \qquad (13.1)$$

$$\int_0^{2\pi}\sigma(\varphi)\cos\varphi\,d\varphi = 0, \qquad (13.2)$$

$$\int_0^{2\pi}\sigma(\varphi)\sin\varphi\,d\varphi = 0, \qquad (13.3)$$

to which, in the case of aerofoils with fixed centre of pressure the condition

$$\int_0^{2\pi}\sigma(\varphi)\sin 2\varphi\,d\varphi = 0 \qquad (13.4)$$

is to be added.

This function $\sigma(\varphi)$ is completely determined by the specified velocity distribution $v_p(\varphi)$, at an angle of incidence α, as

$$\sigma(\varphi) = ln\left|\frac{v_c}{v_p}\right| = ln\left|\frac{2\{\sin(\varphi - \alpha) + \sin\alpha\}}{v_p/v_\infty}\right| \qquad (13.5)$$

if the sharp trailing edge of the aerofoil is transformed into the point $\varphi = 0$.

The conjugate function $\tau(\varphi)$ is derived from $\sigma(\varphi)$ by using POISSON's integral and the coordinates of the aerofoil then fellow from

$$-\frac{\xi}{R} = \int_0^{\varphi} e^{\sigma(\psi)} \sin(\tau + \psi) d\psi, \qquad (13.6)$$

$$\frac{\eta}{R} = \int_0^{\varphi} e^{\sigma(\psi)} \cos(\tau + \psi) d\psi, \qquad (13.7)$$

by numerical integration.

Since, in the case of a sharp trailing edge, the function $\sigma(\varphi)$ becomes infinite for $\varphi = 0$, the matrix method cannot be used. Hence, use is made of an intermediate aerofoil as explained earlier and the matrix method is applied to the difference $\sigma(\varphi) - \sigma_i(\varphi)$, which is nowhere infinite in the interval $0 \leqq \varphi < 2\pi$.

In principle any velocity distribution $v_{p\alpha}(\varphi)$, delivering a function $\sigma(\varphi)$ satisfying the conditions (13.1), (13.2), (13.3) and perhaps (13.4) yields a closed aerofoil contour. In order to obtain a surveyable, suitably organized system of aerofoils, certain general properties of form are imposed on the velocity distributions to be considered. These restrictions, however, leave a sufficient margin to design aerofoils with considerably varying properties. It is, moreover, easily possible to vary the calculation method to meet other requirements, e. g. the design of suction aerofoils with a prescribed jump in the velocity at the suction slot.

The velocity distributions to be considered are all of the so called "roof top" type.

At a certain angle of incidence the logarithm of the velocity along the forward part of the upper side is assumed to be a constant up to a certain point and then to decrease linearly with φ

$$ln\left|\frac{v_p}{v_\infty}\right| = a + b(\varphi - \varphi_2) \quad 0 < \varphi < \varphi_2 \qquad (13.8)$$

$$ln\left|\frac{v_p}{v_\infty}\right| = a \qquad \varphi_2 < \varphi < \pi \qquad (13.9)$$

In the case of a symmetrical aerofoil the velocity distribution at the lower side ($\pi \leqq \varphi < 2\pi$) is then completely determined, $\sigma(\varphi)$ being a symmetrical function. In the case of an asymmetrical aerofoil, however, the velocity at the lower part must be specified by an analoguous distribution, pertaining to another (negative) angle of incidence.

A rigorous compliance with persistence of these distributions in the vicinity of the leading edge and of a sharp trailing edge, however, is not possible; at the sharp trailing edge $\varphi = 0$ the velocity must go down to zero and near the nose it also falls off, because of the presence of a stagnation point at $\varphi = \pi + 2\alpha$, which, at least for angles of incidence α, occurring in practice, is quite near the nose, just at the opposite of the side to which the distribution (13.8) refers. This means, that in the small region $\pi \lesseqgtr \varphi \lesseqgtr \pi + 2a$ the velocity distribution must fall off very steeply causing irregularities in the contour. A better contour can be obtained by designing the velocity distribution in the neighbourhood of the nose and the tail by special parameters, to be adjusted during the calculation in order to meet the special conditions necessary to obtain a closed contour.

13.2 *First-order approximation.*

Usually, in aerofoil design, the imposed conditions apply to geometrical as well as to velocity-distribution properties and it is, for this reason, very useful to dispose of a set of formulae, giving at least approximative relations between the parameters involved.

Such formulae are furnished by the first-order approximation method, derived in section I, 10. Assume for a symmetrical aerofoil the excess velocity distribution on the upper side at angle of incidence α to be given by

$$\left.\begin{aligned} \lambda_\alpha(\varphi) &= \frac{(v_p) - v_\infty}{v_\infty} = \\ &= a + b(\cos\varphi_2 - \cos\varphi), \quad 0 < \varphi < \varphi_2 \\ \lambda_\alpha(\varphi) &= \frac{(v_p) - v_\infty}{v_\infty} = a \quad , \varphi_2 < \varphi < \pi \end{aligned}\right\} \qquad (13.10)$$

As

$$\lambda_0(\varphi) = \lambda_\alpha(\varphi) - \alpha \,.\, \mathrm{tg}\,\tfrac{1}{2}\varphi,$$

$\Delta\sigma(\varphi)$ is given by

$$\left.\begin{aligned} \Delta\sigma(\varphi) &= -\lambda_0(\varphi), \qquad 0 < \varphi < \pi \\ \Delta\sigma(\varphi) &= \Delta\sigma(2\pi - \varphi), \qquad \pi < \varphi < 2\pi \end{aligned}\right\} \qquad (13.11)$$

and the coordinates of the aerofoil are found from the formula

$$\frac{\eta}{R} = -\frac{\alpha\xi}{R} + \frac{2\sin\varphi}{\pi} \int_0^{\pi} \frac{\int_0^{\psi} \lambda_\alpha(\theta) \sin\theta d\theta}{\cos\varphi - \cos\psi} d\psi. \qquad (13.12)$$

Now, with the simple assumptions (13.10)

$$\left.\begin{aligned} \int_0^{\psi} \lambda_\alpha(\theta) \sin\theta d\theta &= a(1 - \cos\psi) + \\ &+ b\{\cos\varphi_2(1 - \cos\psi) - \\ &- \tfrac{1}{2}\sin^2\psi\} \qquad 0 < \psi < \varphi_2 \\ &= a(1 - \cos\psi) + b\{\cos\varphi_2 - \\ &- 1 + \tfrac{1}{2}\sin^2\varphi_2\} \qquad \varphi_2 < \varphi < \pi \end{aligned}\right\} \qquad (13.13)$$

and the ordinates can be found from (13.12).

$$\frac{\eta}{R} = -\frac{\alpha\xi}{R} + \frac{2a\sin\varphi}{\pi} \int_0^{\pi} \frac{1 - \cos\psi}{\cos\varphi - \cos\psi} d\psi +$$

$$+ \frac{2b\sin\varphi}{\pi} \left[\int_0^{\varphi_2} \frac{\cos\varphi_2(1 - \cos\psi) - \frac{1}{2}\sin^2\psi}{\cos\varphi - \cos\psi} d\psi + \right.$$

$$\left. + (\cos\varphi_2 - 1 + \tfrac{1}{2}\sin^2\varphi_2) \int_{\varphi_2}^{\pi} \frac{d\psi}{\cos\varphi - \cos\psi} \right]. \qquad (13.14)$$

Since

$$\int_0^{\varphi_2} \frac{d\psi}{\cos\varphi - \cos\psi} = -\int_{\varphi_2}^{\pi} \frac{d\psi}{\cos\varphi - \cos\psi} =$$

$$= \frac{1}{\sin\varphi} \ln \left| \frac{\operatorname{tg} \tfrac{1}{2}\varphi_2 - \operatorname{tg} \tfrac{1}{2}\varphi}{\operatorname{tg} \tfrac{1}{2}\varphi_2 + \operatorname{tg} \tfrac{1}{2}\varphi} \right|, \quad (13.15)$$

this formula can be reduced to

$$\frac{\eta}{R} = -\frac{\alpha\xi}{R} + 2a\sin\varphi +$$

$$+ \frac{2b\sin\varphi}{\pi}\left[\frac{(\cos\varphi - \cos\varphi_2)^2}{2\sin\varphi} \ln \left|\frac{\operatorname{tg} \tfrac{1}{2}\varphi_2 - \operatorname{tg} \tfrac{1}{2}\varphi}{\operatorname{tg} \tfrac{1}{2}\varphi_2 + \operatorname{tg} \tfrac{1}{2}\varphi}\right| + \right.$$

$$\left. + \varphi_2 \cdot \cos\varphi_2 - \tfrac{1}{2}\sin\varphi_2 - \tfrac{1}{2}\varphi_2\cos\varphi\right]. \quad (13.16)$$

For any given value of a, b, φ_2 and α the shape of the aerofoil and the maximum thickness and location of maximum thickness can be calculated.

Strictly, b is not independent from the other constants it has to satisfy the conditions securing closing of the aerofoil contour. Usually, the ratio b/a is small and to a very rough approximation, for aerofoils having the maximum thickness near the middle of the chord,

$$\frac{\xi_m}{R} \approx (1 - \cos\varphi_2), \quad (13.17)$$

$$\frac{\eta_{max}}{R} = -\frac{\alpha\xi_m}{R} + 2a\sin\varphi_2, \quad (13.18)$$

from which rough estimates for φ_2 and α, for a given thickness ratio and given position of maximum thickness, can be obtained.

13.4 *The design of aerofoils with prescribed velocity distributions of a certain type.*

The velocity distributions of the "roof top" type, mentioned in section 13.1, are, in principle, used for the design of a very general class of aerofoils to be used either as laminar-flow or as high-speed aerofoils.

Owing to the occurrence of stagnation points near the leading and trailing edges of the aerofoil it is not convenient to extend the roof top type of velocity distribution to these regions, but to specify the velocity in these regions separately.

The interval $0 \leqq \varphi \leqq 2\pi$ is therefore divided into 8 parts by the points φ_i $(i, \ldots\ldots 6)$ and, of course, the tail $\varphi = 0$ and the nose $\varphi = \pi$, separating the upper and lower side.

In the regions $\varphi_1 < \varphi < \varphi_3$ and $\varphi_4 < \varphi < \varphi_6$ the roof-top velocity distribution is used, near the tail, in the regions $0 < \varphi < \varphi_1$ and $\varphi_6 < \varphi < 2\pi$, the velocity is adjusted so that the singularity, corresponding to the prescribed tail angle, is properly represented and that the velocity passes continuously and with a continuous derivative into the values, prescribed over the middle part. Near the nose, the velocity is determined by its values in a certain number of lattice points and intermediate values are assumed to be provided by Schoenberg interpolation polynomials.

If the index i refers to the intermediate aerofoil the functions $\sigma(\varphi)$ and $\tau(\varphi)$ are put equal to

$$\sigma(\varphi) = \sigma_i(\varphi) + \sigma_2(\varphi), \quad (13.19)$$

$$\tau(\varphi) = \tau_i(\varphi) + \tau_2(\varphi).$$

Then, if $v_{p\alpha}$, $v_{i\alpha}$ refer to the velocity distributions of the aerofoil and of the intermediate aerofoil, and $v_{c\alpha}$ to the velocity distribution round the circle at incidence α, the relations

$$\sigma_2(\varphi) = \ln\left|\frac{v_{p\alpha}}{v_{i\alpha}}\right| = \ln\left|\frac{v_{p\alpha}}{v_\infty}\right| - \ln\left|\frac{v_{i\alpha}}{v_\infty}\right| =$$

$$= \ln\left|\frac{v_{c\alpha}}{v_{i\alpha}}\right| - \ln\left|\frac{v_{c\alpha}}{v_{p\alpha}}\right| \quad (13.20)$$

hold, which are alternatively used.

The values of $\sigma_2(\varphi)$ now are given by the following table, (comp. fig. 6) taking $\varphi_1 = \pi/9$, $\varphi_3 = \pi - \pi/9$, $\varphi_4 = \pi + \pi/9$, $\varphi_6 = 2\pi - \pi/9$ (which means that the excluded regions near the nose and the tail extend over $2\frac{\pi}{9}$).

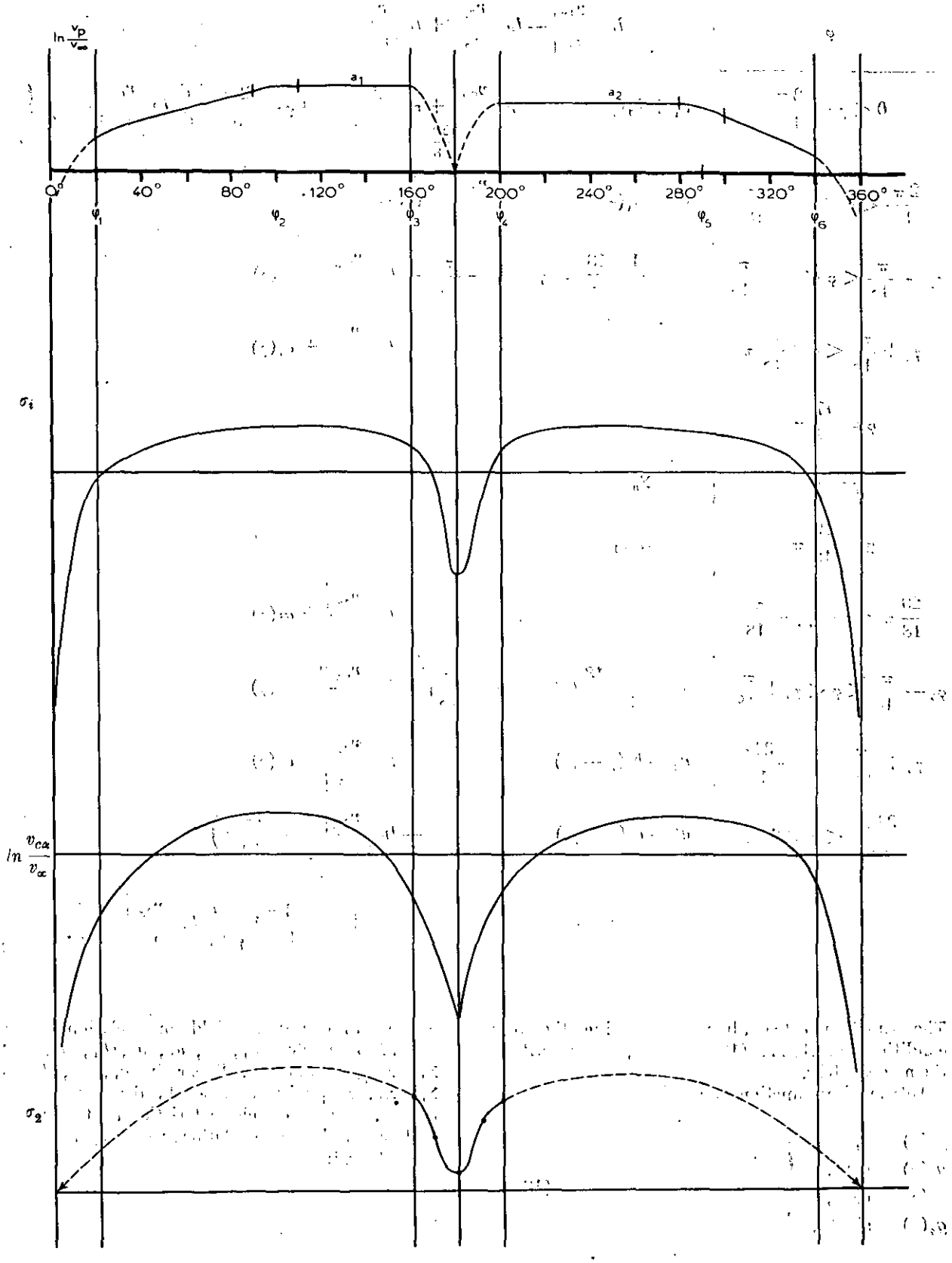

Fig. 6. The velocity distributions.
Dotted curves derived values; drawn curves initially given.

φ	$\sigma_2(\varphi) =$ $ln\left\lvert\frac{v_{n\alpha}}{v_\infty}\right\rvert - ln\left\lvert\frac{v_{c\alpha}}{v_\infty}\right\rvert + ln\left\lvert\frac{v_c}{v_i}\right\rvert =$
$0 < \varphi < \frac{2\pi}{18}$	$a_1 + b_1(\varphi - \varphi_2) - ln\left\lvert\frac{v_{c\alpha_1}}{v_\infty}\right\rvert_{\frac{2\pi}{18}} + \sigma_i\left(\frac{2\pi}{18}\right) - \left(\varphi - \frac{2\pi}{18}\right)\left\{\frac{d}{d\varphi} ln\left\lvert\frac{v_{c\alpha_1}}{v_\infty}\right\rvert - \frac{d\sigma_i}{d\varphi}\right\}_{\varphi\ \frac{2\pi}{18}}$
$\frac{2\pi}{18} < \varphi < \varphi_2 - \frac{\pi}{18}$	$a_1 + b_1(\varphi - \varphi_2) - ln\left\lvert\frac{v_{c\alpha_1}}{v_\infty}\right\rvert + \sigma_i(\varphi)$
$\varphi_2 - \frac{\pi}{18} < \varphi < \varphi_2 + \frac{\pi}{18}$	$a_1 - \frac{1}{4}\cdot\frac{18}{\pi} b_1\left(\varphi - \varphi_2 - \frac{\pi}{18}\right)^2 - ln\left\lvert\frac{v_{c\alpha_1}}{v_\infty}\right\rvert + \sigma_i(\varphi)$
$\varphi_2 + \frac{\pi}{18} < \varphi < \frac{16}{18}\pi$	$a_1 - ln\left\lvert\frac{v_{c\alpha_1}}{v_\infty}\right\rvert + \sigma_i(\varphi)$
$\varphi = \frac{17}{18}\pi$	Σ_1
$\varphi = \pi$	Σ_0
$\varphi = \frac{19}{18}\pi$	Σ_{-1}
$\frac{20}{18}\pi < \varphi < \varphi_5 - \frac{\pi}{18}$	$a_2 - ln\left\lvert\frac{v_{c\alpha_2}}{v_\infty}\right\rvert + \sigma_i(\varphi)$
$\varphi_5 - \frac{\pi}{18} < \varphi < \varphi_5 + \frac{\pi}{18}$	$a_2 - \frac{1}{4}\cdot\frac{18}{\pi} b_2\left(\varphi - \varphi_5 + \frac{\pi}{18}\right)^2 - ln\left\lvert\frac{v_{c\alpha_2}}{v_\infty}\right\rvert + \sigma_i(\varphi)$
$\varphi_5 + \frac{\pi}{18} < \varphi < \frac{34\pi}{18}$	$a_2 - b_2(\varphi - \varphi_5) - ln\left\lvert\frac{v_{c\alpha_2}}{v_\infty}\right\rvert + \sigma_i(\varphi)$
$\frac{34\pi}{18} < \varphi < 2\pi$	$a_2 - b_2(\varphi - \varphi_5) - ln\left\lvert\frac{v_{c\alpha_2}}{v_\infty}\right\rvert + \sigma_i\left(\frac{34}{18}\pi\right) - \left(\varphi - \frac{34\pi}{18}\right)\left\{\frac{d}{d\varphi} ln\left\lvert\frac{v_{c\alpha_2}}{v_\infty}\right\rvert - \frac{d\sigma_i}{d\varphi}\right\}_{\varphi = \frac{34\pi}{18}}$

The function $\sigma_i(\varphi)$ already satisfying the four conditions (13.1) ... (13.4), $\sigma_2(\varphi)$, has to satisfy them separately.

Introducing functions $g_k(\varphi)$ by

$$\left.\begin{aligned} g_1(\varphi) &= 1, \\ g_2(\varphi) &= \sin\varphi, \\ g_3(\varphi) &= \cos\varphi, \\ g_4(\varphi) &= \sin 2\varphi, \end{aligned}\right\} \qquad (13.21)$$

they can be written as

$$\int_0^{2\pi} \sigma_2(\varphi) g_k(\varphi) d\varphi = 0, \qquad k = 1, \ldots, 4. \qquad (13.22)$$

These four conditions yield four relations between the 12 parameters α_1, α_2, a_1, a_2, b_1, b_2, δ, Σ_0, Σ_1, Σ_{-1}, φ_2 and φ_5, linear in a_1, a_2, b_1, b_2, Σ_0, Σ_1, Σ_{-1} with coefficients depending on α_1, α_2, φ_2, φ_5 and on characteristics of the intermediate aerofoil. These relations result by performing the integrations

$$\left\{a_1 + (-1)^{k+1}a_2\right\}\int_0^{\frac{16}{18}\pi} g_k(\varphi)\,.\,d\varphi + b_1\left\{\int_0^{\varphi_2-\pi/18}(\varphi-\varphi_2)g_k(\varphi)d\varphi - \frac{18}{4\pi}\int_{\varphi_2-\pi/18}^{\varphi_2+\pi/18}\left(\varphi-\varphi_2-\frac{\pi}{18}\right)^2 g_k(\varphi)d\varphi\right\} +$$

$$-b_2\left\{\int_{\varphi_5+\pi/18}^{2\pi}(\varphi-\varphi_5)g_k(\varphi)d\varphi - \frac{18}{4\pi}\int_{\varphi_5-\pi/18}^{\varphi_5+\pi/18}\left(\varphi-\varphi_5+\frac{\pi}{18}\right)^2 g_k(\varphi)d\varphi\right\} +$$

$$-\left\{ln\left|\frac{v_{c\alpha_1}}{v_\infty}\right|_{\frac{2\pi}{18}} - \sigma_i\left(\frac{2\pi}{18}\right)\right\}\cdot\int_0^{2\pi/18} g_k(\varphi)d\varphi - \left\{\frac{d}{d\varphi}ln\left|\frac{v_{c\alpha_1}}{v_\infty}\right| - \frac{d\sigma_i}{d\varphi}\right\}_{\frac{2\pi}{18}}\cdot\int_0^{2\pi/18} g_k(\varphi)\,.\left(\varphi-\frac{2\pi}{18}\right).d\varphi +$$

$$-\left\{ln\left|\frac{v_{c\alpha_2}}{v_\infty}\right|_{\frac{34\pi}{18}} - \sigma_i\left(\frac{34}{18}\pi\right)\right\}\cdot\int_{\frac{34\pi}{18}}^{2\pi} g_k(\varphi)d\varphi - \left\{\frac{d}{d\varphi}ln\left|\frac{v_{c\alpha_2}}{v_\infty}\right| - \frac{d\sigma_i}{d\varphi}\right\}_{\frac{34\pi}{18}}\cdot\int_{\frac{34\pi}{18}}^{2\pi} g_k(\varphi)\,.\left(\varphi-\frac{34\pi}{18}\right).d\varphi +$$

$$+\left\{1+(-1)^{k+1}\right\}\int_{\frac{2\pi}{18}}^{16/18\pi}\sigma_i(\varphi)g_k(\varphi)d\varphi - \int_{\frac{2\pi}{18}}^{16/18\pi} ln\left|\frac{v_{c\alpha_1}}{v_\infty}\right| g_k(\varphi)d\varphi - \int_{\frac{20\pi}{18}}^{34/18\pi} ln\left|\frac{v_{c\alpha_2}}{v_\infty}\right| g_k(\varphi)d\varphi +$$

$$+\int_{\frac{16}{18}\pi}^{\frac{20}{18}\pi}\sigma_2(\varphi)g_k(\varphi)d\varphi = 0. \tag{13.23}$$

In view of the interpolation by the Schoenberg polynomial in the interval $\frac{16}{18}\pi < \varphi < \frac{20}{18}\pi$,

$$\frac{18}{\pi}\int_{\frac{16}{18}\pi}^{\frac{20}{18}\pi}\sigma_2(\varphi)\,.\,g_k(\varphi)d\varphi =$$

$$= +\frac{1}{1536}\left[g_k\left(\frac{14}{18}\pi\right)\left\{a_1 - ln\left|\frac{v_{c\alpha_1}}{v_\infty}\right|_{\frac{14}{18}\pi} + \sigma_i\left(\frac{14}{18}\pi\right)\right\} + g_k\left(\frac{22}{18}\pi\right)\left\{a_2 - ln\left|\frac{v_{c\alpha_2}}{v_\infty}\right|_{\frac{22}{18}\pi} + \sigma_i\left(\frac{22}{18}\pi\right)\right\}\right] -$$

$$-\frac{11}{256}\left[g_k\left(\frac{15}{18}\pi\right)\left\{a_1 - ln\left|\frac{v_{c\alpha_1}}{v_\infty}\right|_{\frac{15}{18}\pi} + \sigma_i\left(\frac{15}{18}\pi\right)\right\} + g_k\left(\frac{21}{18}\pi\right)\left\{a_2 - ln\left|\frac{v_{c\alpha_2}}{v_\infty}\right|_{\frac{21}{18}\pi} + \sigma_i\left(\frac{21}{18}\pi\right)\right\}\right] +$$

$$+\frac{1}{2}\left[g_k\left(\frac{16}{18}\pi\right)\left\{a_1 - ln\left|\frac{v_{c\alpha_1}}{v_\infty}\right|_{\frac{16}{18}\pi} + \sigma_i\left(\frac{16}{18}\pi\right)\right\} + g_k\left(\frac{20}{18}\pi\right)\left\{a_2 - ln\left|\frac{v_{c\alpha_2}}{v_\infty}\right|_{\frac{20}{18}\pi} + \sigma_i\left(\frac{20}{18}\pi\right)\right\}\right] +$$

$$+1\frac{11}{256}\left\{\Sigma_1 + \Sigma_{-1}(-1)^{k+1}\right\} g_k\left(\frac{17}{18}\pi\right) + \frac{767}{768}\Sigma_0\,.\,g_k(\pi). \tag{13.24}$$

Now, introduce the following abbreviations:

$$\frac{18}{\pi}\left[\int_0^{\varphi_2-\pi/18}(\varphi-\varphi_2)g_k(\varphi)d\varphi - \frac{18}{4\pi}\int_{\varphi_2-\pi 18}^{\varphi_2+\pi/18}\left(\varphi-\varphi_2-\frac{\pi}{18}\right)^2 g_k(\varphi)d\varphi\right] = F_k(\varphi_2), \tag{13.25}$$

$$\left\{\begin{array}{l} \left\{\dfrac{18}{\pi}\displaystyle\int_0^{\frac{16\pi}{18}} g_k(\varphi)\,d\varphi + \dfrac{1}{1536}\,g_k\left(\dfrac{14}{18}\,\pi\right) - \dfrac{11}{256}\,g_k\left(\dfrac{15}{18}\,\pi\right) + \dfrac{1}{2}\,g_k\left(\dfrac{16}{18}\,\pi\right)\right\} = p_k, \\ \dfrac{18}{\pi}\displaystyle\int_0^{2\pi/18} g_k(\varphi)\,d\varphi = q_k, \quad \dfrac{18}{\pi}\int_0^{2\pi/18} g_k(\varphi)\left(\varphi - \dfrac{2\pi}{18}\right)d\varphi = r_k, \end{array}\right. \tag{13.26}$$

$$\frac{18}{\pi}\int_{\frac{2\pi}{18}}^{\frac{16\pi}{18}} ln\left|\frac{v_{c\alpha}}{v_\infty}\right| g_k(\varphi)\,d\varphi = B_k(\alpha), \tag{13.27}$$

$$\frac{18}{\pi}\int_{\frac{2\pi}{18}}^{\frac{16\pi}{18}} \sigma_i(\varphi)\,g_k(\varphi)\,d\varphi = A_k, \tag{13.28}$$

which are used to build up the following functions of the angle α

$$P_k(\alpha) = -B_k(\alpha) - \left\{q_k\,.\,ln\left|\frac{v_{c\alpha}}{v_\infty}\right| + r_k\,\frac{d}{d\varphi}\,.\,ln\left|\frac{v_{c\alpha}}{v_\infty}\right|\right\}_{\frac{2\pi}{18}} -$$

$$- \left\{+\frac{1}{1536}\,g_k\left(\frac{14}{18}\,\pi\right) ln\left|\frac{v_{c\alpha}}{v_\infty}\right|_{\frac{14}{18}\pi} - \frac{11}{256}\,ln\left|\frac{v_{c\alpha}}{v_\infty}\right|_{\frac{15}{18}\pi} g_k\left(\frac{15}{18}\,\pi\right) + \frac{1}{2}\,ln\left|\frac{v_{c\alpha}}{v_\infty}\right|_{\frac{16}{18}\pi} g_k\left(\frac{16}{18}\,\pi\right)\right\} \tag{13.29}$$

and the following functions of the intermediate acrofoil

$$\frac{1}{2}\,Q_k = A_k + q_k\,.\,\sigma_i\left(\frac{2\pi}{18}\right) + r_k\,.\,\frac{d\sigma_i}{d\varphi}\left(\frac{2\pi}{18}\right) +$$

$$+ \left\{+\frac{1}{1536}\,\sigma_i\left(\frac{14}{18}\,\pi\right).\,g_k\left(\frac{14}{18}\,\pi\right) - \frac{11}{256}\,.\,\sigma_i\left(\frac{15}{18}\,\pi\right) g_k\left(\frac{15}{18}\,\pi\right) + \frac{1}{2}\,\sigma_i\left(\frac{16}{18}\,\pi\right) g_k\left(\frac{16}{18}\,\pi\right)\right\}, \tag{13.30}$$

Then the 4 relations between a_1, a_2, b_1, b_2, Σ_0, Σ_1 and Σ_{-1} become

$$\left\{a_1 + (-1)^{k+1} a_2\right\} p_k + b_1 F_k(\varphi_2) + b_2 F_k(2\pi - \varphi_5)\,(-1)^{k+1} +$$

$$+ \frac{267}{256}\,g_k\left(\frac{17}{18}\,\pi\right)\left\{\Sigma_1 + (-1)^{k+1}\,\Sigma_{-1}\right\} + \frac{767}{768}\,g_k(\pi)\,.\,\Sigma_0 + P_k(\alpha_1) + (-1)^{k+1} P_k(-\alpha_2) +$$

$$+ Q_k\left\{\frac{1 + (-1)^{k+1}}{2}\right\} = 0, \tag{13.31}$$

or explicitly

$$16{,}45768\,(a_1 + a_2) + b_1 F_1(\varphi_2) + b_2 F_1(2\pi - \varphi_5) +$$

$$- 1{,}027124\,(\Sigma_1 + \Sigma_{-1}) -$$

$$+ 0{,}998698\,\Sigma_0 + P_1(\alpha_1) + P_1(-\alpha_2) + Q_1 = 0, \tag{13.32}$$

$$1{,}526497\,(a_1 + a_2) + b_1 F_3(\varphi_2) + b_2 F_3(2\pi - \varphi_5) -$$

$$+ 1{,}027124\,(\Sigma_1 + \Sigma_{-1}) +$$

$$- 0{,}998698\,\Sigma_0 + P_3(\alpha_1) + P_3(-\alpha_2) + Q_3 = 0, \tag{13.33}$$

$$0{,}181110\,(\Sigma_1 - \Sigma_{-1}) + b_1 F_2(\varphi_2) - b_2 F_2(2\pi - \varphi_5) +$$

$$+ P_2(\alpha_1) + P_2(-\alpha_2) + 11{,}26356\,(a_1 - a_2) = 0, \tag{13.34}$$

$$0{,}3556716\,(\Sigma_1 - \Sigma_{-1}) - b_1 F_4(\varphi_2) + b_2 F_4(2\pi - \varphi_5) -$$

$$- P_4(\alpha_1) + P_4(-\alpha_2) - 0{,}385410\,(a_1 - a_2) = 0. \tag{13.35}$$

For a symmetrical acrofoil only two conditions remain, $(k = 1, 3)$ the other two being identically satisfied. The four conditions (13.22) do not determine the 5 parameters unambiguously; hence one more relation can be imposed, e. g. the radius of curvature of the nose.

This radius of curvature is given by

$$\frac{\rho}{R} = \frac{e^\sigma}{1 + \dfrac{d\tau}{d\varphi}}, \tag{13.36}$$

its value at $\varphi = \pi$ can be expressed into Σ_0 and Σ_1, using the value of the derivative of the conjugate

function $\frac{d\tau}{d\varphi}$ expressed into the values of $\sigma(\varphi)$ as provided by the matrix of section 11.6

$$\frac{d\tau}{d\varphi} = \frac{d\tau_i}{d\varphi} - 1{,}6554\,\Sigma_0 + 0{,}6692\,(\Sigma_1 + \Sigma_{-1}) + \ldots\ldots, \quad (13.37)$$

where the dots stand for terms with small coefficients, which are neglected for the present purpose.

Then a prescribed value of ρ/R at the nose provides a fifth relation

$$\frac{\rho}{R} = \frac{e^{-\Sigma_0 + \sigma_i}}{1 + \frac{d\tau_i}{d\varphi} + 1{,}6554\,\Sigma_0 + 0{,}6692\,(\Sigma_1 + \Sigma_{-1})}, \quad (13.38)$$

which finally determines the values of the constants unambiguously.

In order to obtain acceptable velocity distributions, however, certain inequalities must also be satisfied, warranting a monotonic non-decreasing velocity over the forward part of the aerofoil at the angle of incidence for which the velocity distribution is prescribed.

$$\left.\begin{aligned}
&\Sigma_0 < a_1 + \sigma_i(\pi) - \left\{ ln \left| \frac{v_{c\alpha_1}}{v_\infty} \right| \right\}_\pi \\
&\Sigma_0 < a_2 + \sigma_i(\pi) - \left\{ ln \left| \frac{v_{c,-\alpha_2}}{v_\infty} \right| \right\}_\pi \\
&\Sigma_1 < a_1 + \sigma_i\left(\frac{17}{18}\pi\right) - \left\{ ln \left| \frac{v_{c\alpha_1}}{v_\infty} \right| \right\}_{\frac{17}{18}\pi} \\
&\Sigma_{-1} < a_2 + \sigma_i\left(\frac{17}{18}\pi\right) - \left\{ ln \left| \frac{v_{c,-\alpha_2}}{v_\infty} \right| \right\}_{\frac{17}{18}\pi} \\
&\Sigma_0 - \Sigma_1 < \sigma_i(\pi) - \sigma_i\left(\frac{17}{18}\pi\right) + \\
&\qquad + \left\{ ln \left| \frac{v_{c\alpha_1}}{v_\infty} \right| \right\}_{\frac{17}{18}\pi} - \left\{ ln \left| \frac{v_{c/\alpha_2}}{v_\infty} \right| \right\}_\pi \\
&\Sigma_0 - \Sigma_{-1} < \sigma_i(\pi) - \sigma_i\left(\frac{17}{18}\pi\right) + \\
&\qquad + \left\{ ln \left| \frac{v_{c,-\alpha_2}}{v_\infty} \right| \right\}_{\frac{17}{18}\pi} - \left\{ ln \left| \frac{v_{c/\alpha_1}}{v_\infty} \right| \right\}_\pi
\end{aligned}\right\} \quad (13.39)$$

If all parameters are determined, the 36 values of the function $\sigma_2(\varphi)$ in the lattice points can be calculated and the conjugate function $\tau_2(\varphi)$ is to be determined by the *matrix method of section 11*.

Thus the coordinates of the aerofoil contour follow from

$$\left.\begin{aligned}
-\frac{\xi}{R} &= \int_0^\varphi e^{\sigma_i(\varphi) - \sigma_2(\varphi)} \sin(\tau_i - \tau_2 + \varphi)\, d\varphi, \\
\frac{\eta}{R} &= \int_0^\varphi e^{\sigma_i(\varphi) - \sigma_2(\varphi)} \cos(\tau_i - \tau_2 + \varphi)\, d\varphi
\end{aligned}\right\} \quad (13.40)$$

by numerical integration.

Here again the introduction of the intermediate aerofoil improves the accuracy of the calculation. As the coordinates ξ_i and η_i are known and

$$\left.\begin{aligned}
-\frac{\xi_i}{R} &= \int_0^\varphi e^{\sigma_i(\varphi)} \sin(\tau_i + \varphi)\, d\varphi, \\
\frac{\eta_i}{R} &= \int_0^\varphi e^{\sigma_i(\varphi)} \cos(\tau_i + \varphi)\, d\varphi;
\end{aligned}\right\} \quad (13.41)$$

formulae (13.40) can be replaced by

$$\begin{aligned}
-\frac{\xi}{R} &= -\frac{\xi_i}{R} + \\
&+ \int_0^\varphi e^{\sigma_i} \left\{ e^{-\sigma_2} \sin(\tau_i - \tau_2 + \varphi) - \sin(\tau_i + \varphi) \right\} d\varphi, \\
\frac{\eta}{R} &= \frac{\eta_i}{R} + \\
&+ \int_0^\varphi e^{\sigma_i} \left\{ e^{-\sigma_2} \cos(\tau_i - \tau_2 + \varphi) - \cos(\tau_i + \varphi) \right\} d\varphi.
\end{aligned} \quad (13.42)$$

Here the integrands are small and the errors involved in the numerical computation affect the results less than in the case of a direct numerical integration of the formulae (13.40).

13.4 *An alternative method: the design of asymmetric aerofoils from symmetrical aerofoils.*

Owing to the fact that symmetrical aerofoils of the family depend on 6 parameters α, a, b, Σ_0, Σ_1 and δ only, interconnected by two relations, the design of symmetrical aerofoils is considerably more simple than the design of asymmetrical aerofoils, especially as it appears to be easier to satisfy the additional inequalities for the velocity parameters near the nose.

For a symmetrical aerofoil the function $\sigma_s(\varphi)$ is an even function

$$\sigma_s(2\pi - \varphi) = \sigma_s(\varphi) \qquad 0 < \varphi < \pi \quad (13.43)$$

and the values on the lower side are thus known if the values at the upper side are given by the velocity distribution at a certain angle of incidence α.

From a symmetrical aerofoil an asymmetrical aerofoil can be obtained with a velocity distribution at the upper side which retains, for the angle of incidence α, its original characteristics by preserving the function $\sigma(\varphi)$ at the upper side (except for an additive constant) and adding an asymmetric function at the lower side

$$\begin{aligned}
\sigma(\varphi) &= \sigma_s(\varphi) + \lambda_0 \qquad\qquad , \quad 0 \leqq \varphi < \pi \\
\sigma(\varphi) &= \sigma_s(\varphi) + \lambda_0 + \sum_{\nu=1}^{\infty} \lambda_\nu \sin \nu\varphi, \quad \pi \leqq \varphi < 2\pi
\end{aligned} \quad (13.44)$$

where $\sigma_s(\varphi)$ is the function for the symmetrical aerofoil. The three conditions for a closed aerofoil then yield

$$2\pi \cdot \lambda_0 + \sum_{\nu=1}^{\infty} \lambda_\nu \int_{\pi}^{2\pi} \sin \nu\varphi d\varphi = 2\pi \cdot \lambda_0 + \sum_{\nu=1}^{\infty} \lambda_\nu \frac{1-(-1)^\nu}{\nu} = 0, \quad (13.45)$$

$$\sum_{\nu=1}^{\infty} \lambda_\nu \int_{\pi}^{2\pi} \sin \nu\varphi \cdot \sin \varphi d\varphi = \frac{1}{2}\pi\lambda_1 = 0; \quad (13.46)$$

$$\sum_{\nu=1}^{\infty} \lambda_\nu \int_{\pi}^{2\pi} \sin \nu\varphi \cdot \cos \varphi d\varphi = \sum_{\nu=2}^{\infty} \lambda_\nu \frac{1-(-1)^{\nu+1}}{\nu^2-1} = 0, \quad (13.47)$$

to which, for an aerofoil with fixed centre of pressure, the condition

$$\sum_{\nu=1}^{\infty} \lambda_\nu \int_{\pi}^{2\pi} \sin \nu\varphi \cdot \sin 2\varphi d\varphi = \frac{1}{2}\pi\lambda_2 = 0 \quad (13.48)$$

is to be added.

The value of $\sigma(\varphi)$ being defined by a suitable choice of the constants λ_ν, the conjugate function $\tau(\varphi)$ is

$$\tau(\psi) = \tau_s(\psi) + \sum_{\nu=3}^{\infty} \lambda_\nu \int_{\pi}^{2\pi} \sin \nu\varphi \operatorname{cotg} \frac{1}{2}(\varphi - \psi) d\varphi; \quad (13.49)$$

while $\tau_s(\psi)$ is already known, being the conjugate function for the symmetrical aerofoil.

The integrals can be evaluated analytically.

$$\int_{0}^{2\pi} \sin \nu\varphi \cdot \operatorname{cotg} \tfrac{1}{2}(\varphi - \psi) d\varphi =$$

$$\begin{cases} \pi \cdot \cos 2\mu\psi + 2 \sin 2\mu\psi \cdot ln\,|\operatorname{tg} \frac{1}{2}\psi| + \\ + 4 \sum_{p=1}^{\mu} \frac{1}{2p+1} \cdot \sin (2\mu - 2p + 1)\psi, \quad \nu = 2\mu \end{cases} \quad (13.50)$$

$$\begin{cases} \pi \cdot \cos (2\mu + 1)\psi + 2 \sin (2\mu + 1)\psi \cdot ln\,|\operatorname{tg} \frac{1}{2}\psi| + \\ + 4 \sum_{p=0}^{\mu-1} \frac{1}{2p+1} \cdot \sin (2\mu - 2p)\psi. \quad \nu = 2\mu + 1 \end{cases}$$

The coordinates of the asymmetrical aerofoil can be calculated by numerical integration from

$$\frac{\xi}{R} = \frac{\xi_s}{R} + \int_{0}^{\varphi} e^{\sigma_s} \{ e^{\sigma - \sigma_s} \sin (\tau_a + \varphi) - \sin (\tau_s + \varphi) \} d\varphi, \quad (13.51)$$

$$\frac{\eta}{R} = \frac{\eta_s}{R} + \int_{0}^{\varphi} e^{\sigma_s} \{ e^{\sigma - \sigma_s} \cos (\tau_a + \varphi) - \cos (\tau_s + \varphi) \} d\varphi.$$

Two simple classes of asymmetrical aerofoils result by taking

$$\sigma = \sigma_s + \frac{\lambda}{3\pi}, \quad 0 < \varphi < \pi$$
$$\sigma = \sigma_s + \lambda \left(\frac{1}{3\pi} + \sin 3\varphi \right), \quad \pi < \varphi < 2\pi \quad (13.52)$$

or

$$\sigma = \sigma_s, \quad 0 < \varphi < \pi$$
$$\sigma = \sigma_s + \lambda (\sin 3\varphi - \frac{5}{3} \sin 5\varphi). \quad \pi < \varphi < 2\pi \quad (13.53)$$

Insertion of higher-order terms will cause undesirable waviness in the aerofoil contour. The indicated classes already contain a large variety of useful aerofoils. If the condition of fixed centre of pressure is dropped, another class of asymmetrical aerofoils is obtained by putting

$$\sigma = \sigma_s, \quad 0 < \varphi < \pi$$
$$\sigma = \sigma_s + \lambda (\sin 2\varphi - \frac{5}{2} \sin 4\varphi). \quad \pi < \varphi < 2\pi \quad (13.54)$$

14 Calculation of the velocity distribution about a given aerofoil.

The numerical evaluation of the iterative solution to the direct problem of aerofoil theory, as described in part I, can be performed with the same aids as used in the preceding sections.

The intermediate aerofoil is so adjusted that the tail angle is the same as for the given aerofoil in order to avoid the singularity in the calculation of the conjugate function by the matrix method.

Moreover, it is convenient to adjust the nose radius of the intermediate aerofoil to the given aerofoil in order to make the difference function $\sigma(\varphi) - \sigma_i(\varphi)$ small. The coordinate in each successive step in the iteration process must be normed so that the interval for ξ always remains the same. Hence the ξ-axis must be so chosen that it passes through the tail and that the tangent to the contour in the nose is orthogonal to it. Then the slope $\lambda(\xi)$ of the tangent to the aerofoil as a function of ξ can be determined by analytical operations if the coordinates are given by analytical formulae (e. g. the NACA form and five digit aerofoils) or by numerical (or graphical) methods.

For the as yet unknown functions $\tau(\varphi)$ and $\xi(\varphi)$, satisfying the relation

$$\varphi + \tau(\varphi) = \lambda \{ \xi(\varphi) \} - \frac{\pi}{2}, \quad (14.1)$$

an initial approximation is taken $\xi = \xi^{(1)}(\varphi)$, pertaining to the intermediate aerofoil and

$$\tau^{(1)}(\varphi) = \lambda \{ \xi^{(1)}(\varphi) \} - \varphi - \frac{\pi}{2}. \quad (14.2)$$

The intermediate aerofoil, which, for simplicity, is taken symmetrical, is so adjusted, that its nose and tail coincide with those of the given aerofoil and its symmetry axis with the ξ axis.

For the calculation of the conjugate function $\sigma^{(1)}(\varphi)$ it is convenient to introduce

$$\tau_2^{(1)}(\varphi) = \tau^{(1)}(\varphi) - \tau_i(\varphi)$$

and to calculate the conjugate $\sigma^{(1)}(\varphi)$ from

$$\sigma^{(1)}(\varphi) = \sigma_2^{(1)}(\varphi) + \sigma_i(\varphi).$$

Because of the jump of $\tau^{(1)}(\varphi)$ at the trailing edge and the fact $\sigma_i(\varphi)$ has the same discontinuity, the difference function $\tau_2^{(1)}(\varphi)$ is continuous and the matrix method yields the conjugate function $\tau_2^{(1)}(\varphi)$ accurately.

The next step in the iteration process is to establish a new approximation for $\xi(\varphi)$

$$\xi^{(2)}(\varphi) = 1 - \frac{\int_0^{\varphi} e^{\sigma^{(1)}} \sin(\tau^{(1)} + \varphi)\, d\varphi}{\int_0^{\varphi^{(1)}} e^{\sigma^{(1)}} \sin(\tau^{(1)} + \varphi)\, d\varphi},$$

where $\varphi^{(1)}$ denotes the nose, i.e. the value of φ, where the tangent is vertical. It is useful to calculate the integrals numerically by introduction of the preceding approximation

$$\int_0^{\varphi} e^{\sigma^{(n)}} \sin(\tau^{(n)} + \varphi)\, d\varphi =$$

$$= \int_0^{\varphi} e^{\sigma^{(n-1)}} \sin(\tau^{(n-1)} + \varphi)\, d\varphi +$$

$$+ \int_0^{\varphi} e^{\sigma^{(n-1)}} \left\{ e^{\sigma^{(n)} - \sigma^{(n-1)}} \sin(\tau^{(n)} + \varphi) - \sin(\tau^{(n-1)} + \varphi) \right\} d\varphi.$$

The numerical integrations can be carried out by central difference formulae.

A few examples for the application of this method are given in ref. 11.

15 Recapitulation.

The methods explained in part I of this report are based on the representation of two-dimensional irrotational fields of flow of an incompressible fluid by analytic functions of a complex variable, which reduces the solving of a flow problem involving a complicated contour to the determination of a conformal transformation and the solving of a flow problem for a simple contour (usually a circle). Chapter 1 contains a brief account of these foundations and Chapter 2 a discussion of the potential flow about a circle.

The obviously very important general properties of the conformal transformations encountered in aerofoil theory (RIEMANN's theorem) are discussed in Chapter 3. The well known theorem reducing the ratio of the complex velocities in corresponding points of the planes of the aerofoil and of the circle to the complex derivative of the mapping function is established. Separating real and imaginary parts of the logarithm of this derivative, a set of conjugate potential functions is obtained, which, in particular on the circle, can be represented by conjugate Fourier series in the angular variable on the circle. The first of these functions evidently determines the magnitude of the velocity in the plane of the aerofoil and the second the direction (given, in both cases, the flow about the circle). These functions are the adequate representation of the mapping function in this mathematical theory of aerofoil sections. Their relation is discussed in Chapter 4, dealing with the Poisson integral and with the Fourier expansions of conjugate functions.

In Chapter 5 the singularity of the mapping function caused by the sharp trailing edge of the aerofoil and its consequences with regard to the methods of calculation are discussed.

In Chapters 6 and 7 formulae expressing the coordinates of the aerofoil contour, the radius of curvature in any point of the contour and the velocity and pressure distributions into the real and imaginary part of the logarithm of the derivative of the mapping function are established.

Defining, in Chapter 8, as principal problems of aerofoil theory:

I The calculation of the velocity distribution at the contour of a given aerofoil.

II The design of an aerofoil which generates, at its surface, a given chordwise velocity distribution at a given angle of attack, the general theory is easily seen to lead to an iteration procedure for the solution of each of these problems. The procedures are to some extent related to each other and the convergence of both depends critically upon the choice of the initial approximation. If a suitable intermediate aerofoil with known properties is taken, satisfactory results can be obtained after one iteration step. The mathematical proof of the convergence of the second procedure is outlined in Chapter 9. The first procedure requires in this respect, a somewhat more lenghty consideration, which has been omitted.

In Part II, containing numerical methods, the evaluation of the Poisson integral, which forms the basis of all numerical work on aerofoil theory, is discussed at length in Chapter 11. All existing methods (THEODORSEN-GARRICK (ref. 12), MANGLER (ref. 13), RIEGELS-WITTICH (ref. 14) and its Anglo-French counterparts (refs. 15, 16) to perform this operation have (at least by this author) been found to imply imperfections and so a new method has been developed.

This method makes use of matrices ,essentially like those of refs. 14—16, but the trigonometric polynomial approximations of the basic conjugate functions used there, have been replaced by approximations by aid of interpolation polynomials of a type, established recently by SCHOENBERG (ref. 17). In this way the occasional introduction of quite unacceptable waviness resulting from trigometric approximations is avoided.

The conjugate function is finally obtained by simple matrix multiplications, the transforming matrix being given in table I.

In chapter 12 of Part II a useful class of intermediary aerofoils with very simple analytical properties, developed by ZAAT (ref. 10) is presented. In principle, all kinds of "mathematical" aerofoil families (KARMAN-TREFFTZ, PIERCY and numerous others) can be used for the same purpose, but the family presented is at the same time sufficiently adaptable and numerically quite easily manageable. For this class extensive preparations and auxiliary tables for the application of the general procedures discussed in this report have been made available (ref. 18).

In chapter 13 detailed rules and procedures are given for the design, by the preceding methods, of an extensive class of laminar-flow or high-velocity profiles, having at a certain angle of incidence constant velocity along a forward part of the upper side of the contour, followed by a linear decrease backward and an analoguous distribution at the lower side at a negative angle of incidence (whose absolute value may differ from the value of the above-mentioned "positive angle). In the nose and tail regions the velocities are to be adjusted so as to lead to a suitable nose radius and to secure continuity of the velocity distribution.

In the final, fourteenth Chapter the numerical evaluation of the velocity distribution round a given aerofoil by the iteration method, indicated in chapter I, 8 is discussed.

16 References.

1. BETZ, A. Änderung eines Profils zur Erziehlung einer vorgegebenen Änderung der Druckverteilung. Luftfahrtforschung, Vol. 11, 1934, p. 158—164.
2. MANGLER, W. Die Berechnung eines Tragflügelprofils mit vorgeschriebener Druckverteilung. Jahrbuch 1938 der Deutschen Luftfahrtforschung, S I 46—I 53.
3. LIGHTHILL, M. J. A new method for aerodynamic design. Reports and Memoranda 2112, 1945.
4. PEEBLES, GLENN H. A method for calculating airfoil sections from specifications of the pressure distributions. Journal of the Aeronautical Sciences, Vol. 14, 1947, p. 451—456.
5. GREIDANUS, J. H. en TIMMAN, R. Inleidende beschouwing over actuele vraagstukken uit de profieltheorie. Report F. 10 of the National Aeronautical Research Institute.
6. TIMMAN, R. Mathematische grondslagen van een berekeningsmethode voor profielen met voorgeschreven drukverdeling. Report F. 11 of the National Aeronautical Research Institute 1947.
7. TIMMAN, R. Numerieke berekening van profielen bij voorgeschreven drukverdeling. Deel I: Symmetrische profielen, Report F. 12, 1947; Deel II. Asymmetrische profielen, Report F. 13, 1948, National Aeronautical Research Inst.
8. COHEN, J. Investigation into the application of the method of Theodorsen-Garrick for the calculation of the pressure distribution of an aerofoil. Report F. 14, National Aeronautical Research Institute.
9. TIMMAN, R. The numerical evaluation of the Poisson integral. Report F. 32, 1948, National Aeronautical Research Institute.
10. ZAAT, J. A. Een klasse van profielen met eenvoudige analytische eigenschappen. Report F. 42, 1946, National Aeronautical Research Institute.
11. ZAAT, J. A. Een nieuwe berekeningsmethode voor de snelheidsverdeling langs een gegeven profiel in het incompressibele stromingsveld. Report F. 15, 1949, National Aeronautical Research Institute.
12. THEODORSEN, TH. and GARRICK, I. E. General potential theory of arbitrary wing sections. NACA-report 452, 1933.
13. MANGLER, W. Zur numerischen Auswertung des Poissonschen Integrals. Z.A.M.M. (18), 1938.
14. RIEGELS, F.—WITTICH, H. Zur Berechnung der Druckverteilung von Profilen. Jahrbuch 1942 der Deutschen Luftfahrtforschung I 120—I 132.
15. GERMAIN, P. Sur le calcul numérique de certains operateurs linéaires. C. R. Acad. Sci., Paris, Vol. 220, 1945, p. 765—768.
16. WATSON, E. J. Formulae for the computation of the functions employed for calculating the velocity distribution about a given aerofoil. R. and M. 2176, 1945.
17. SCHOENBERG, I. J. Contributions to the problem of approximation of equidistant data by analytic functions. Quarterly of Applied Mathematics (4), 1946. A, p. 45—99, B. p. 112—141.
18. ZAAT, J. A. Een profielcatalogus met 36 symmetrische profielen ten dienste van profielberekening en profielconstructie. Report F. 56, 1950, National Aeronautical Research Institute.
19. HURWITZ, A.—COURANT, R. Vorlesungen über Allgemeine Funktionentheorie und elliptische Funktionen. Berlin, 1929. Reprint 1944, Interscience Publishes.
20. GOLDSTEIN. A theory of aerofoils of small thickness. Part I ....V, A.R.C. Reports 5004, 6156, 6225, 8548, 8549.
21. GOLDSTEIN, S. Low-Drag and suction Aerofoils. Journal of the Aeronautical Sciences, Vol. 15, 1948, p. 189—214.
22. WARSCHAWSKI, S. On Theodorsen's method of conformal mapping of nearly circular regions. Quarterly of Applied Mathematics, Vol. 3, 1945, p. 12—28.
23. PIERCY, N. A. V. Aerodynamics, 2nd Edition. The English University Press, London, 1947.
24. ROSSNER, G. Über eine Klasse von theoretischen Profilen mit vier frei wählbaren geometrischen Parameter. S. I 141—I 159.
Jahrbuch 1942 der Deutschen Luftfahrtforschung.

Completed: April 1950.

Matrix $\alpha_{.\,k,l}$

$\alpha_{k,1}$	$\alpha_{k,2}$	$\alpha_{k,3}$	$\alpha_{k,4}$	$\alpha_{k,5}$	$\alpha_{k,6}$	$\alpha_{k,7}$	$\alpha_{k,8}$	$\alpha_{k,9}$	$\alpha_{k,10}$	$\alpha_{k,11}$	$\alpha_{k,12}$	$\alpha_{k,13}$	$\alpha_{k,14}$	$\alpha_{k,15}$	$\alpha_{k,16}$	$\alpha_{k,17}$	$\alpha_{k,18}$
0,501786	0,146940	0,103222	0,076224	0,059540	0,048100	0,039666	0,033102	0,027776	0,023308	0,019450	0,016038	0,012952	0,010110	0,007442	0,004898	0,002430	0
0,073470	0,302504	0,111582	0,081381	0,062162	0,049603	0,040601	0,033721	0,028205	0,023613	0,019673	0,016201	0,013074	0,010197	0,007504	0,004936	0,002449	0
−0,199282	+ 0,038112	0,280663	0,097520	0,071444	0,054663	0,043658	0,035704	0,029558	0,024570	0,020364	0,016709	0,013446	0,010468	0,007691	0,005055	0,002506	0
−0,035358	— 0,221123	+ 0,024050	0,270726	0,090021	0,065499	0,049766	0,039495	0,032069	0,026309	0,021606	0,017609	0,014103	0,010940	0,008019	0,005261	0,002606	0
−0,021841	— 0,049420	— 0,231060	+ 0,016551	0,264781	0,085124	0,061336	0,046131	0,036246	0,029105	0,023554	0,019000	0,015103	0,011654	0,008510	0,005570	0,002755	0
−0,014062	— 0,031778	— 0,056919	— 0,237005	+ 0,011654	0,260618	0,081489	0,058087	0,043167	0,033491	0,026499	0,021048	0,016551	0,012673	0,009205	0,006004	0,002964	0
−0,009937	— 0,021561	— 0,037723	— 0,061816	— 0,241168	+ 0,008019	0,257369	0,078525	0,055332	0,040561	0,030985	0,024050	0,018618	0,014102	0,010168	0,006599	0,003249	0
0,007499	— 0,015882	— 0,026458	— 0,041886	— 0,065453	— 0,244417	+ 0,005055	0,254614	0,075919	0,052826	0,038112	0,028555	0,021601	0,016112	0,011496	0,007412	0,003635	0
−0,005945	— 0,012396	— 0,020045	— 0,030093	— 0,045135	— 0,068415	— 0,247172	+ 0,002449	+ 0,252208	0,073470	0,050396	0,035663	0,026049	0,018995	0,013357	0,008532	0,004163	0
−0,004897	— 0,010108	— 0,016031	— 0,023294	— 0,033057	— 0,047890	— 0,071021	— 0,249578	0	+ 0,249578	0,071021	0,047890	0,033057	0,023294	0,016031	0,010108	0,004897	0
−0,004163	— 0,008532	— 0,013357	— 0,018995	— 0,026049	— 0,035663	— 0,050396	— 0,073470	— 0,252208	— 0,002449	+ 0,247172	0,068415	0,045135	0,030093	0,020045	0,012396	0,005945	0
−0,003635	— 0,007412	— 0,011496	— 0,016112	— 0,021601	— 0,028555	— 0,038112	— 0,052826	— 0,075919	— 0,254614	— 0,005055	+ 0,244417	0,065453	0,041886	0,026458	0,015882	0,007499	0
−0,003249	— 0,006599	— 0,010167	— 0,014102	— 0,018618	— 0,024050	— 0,030985	— 0,040561	— 0,055332	— 0,078525	— 0,257369	— 0,008019	+ 0,241168	0,061816	0,037723	0,021561	0,009937	0
−0,002964	— 0,006004	— 0,009205	— 0,012673	— 0,016551	— 0,021048	— 0,026499	— 0,033491	— 0,043167	— 0,058087	— 0,081489	— 0,260618	— 0,011654	+ 0,237005	0,056919	0,031778	0,014062	0
−0,002755	— 0,005570	— 0,008510	— 0,011654	— 0,015103	— 0,019000	— 0,023554	— 0,029105	— 0,036246	— 0,046131	— 0,061336	— 0,085124	— 0,264781	— 0,016551	+ 0,231060	0,049420	0,021841	0
−0,002606	— 0,005261	— 0,008019	— 0,010940	— 0,014103	— 0,017609	— 0,021606	— 0,026309	— 0,032069	— 0,039495	— 0,049766	— 0,065499	— 0,090021	— 0,270726	— 0,024050	+ 0,221123	0,035358	0
−0,002506	— 0,005055	— 0,007691	— 0,010468	— 0,013446	— 0,016709	— 0,020364	— 0,024570	— 0,029558	— 0,035704	— 0,043658	— 0,054663	— 0,071444	— 0,097520	— 0,280663	— 0,038112	+ 0,199282	0
−0,002449	— 0,004936	— 0,007504	— 0,010197	— 0,013074	— 0,016201	— 0,019673	— 0,023613	— 0,028205	— 0,033721	— 0,040601	— 0,049603	— 0,062162	— 0,081381	— 0,111582	— 0,302504	— 0,073470	0
−0,002430	— 0,004898	— 0,007442	— 0,010110	— 0,012952	— 0,016038	— 0,019450	— 0,023308	— 0,027776	— 0,033102	— 0,039666	— 0,048100	— 0,059540	— 0,076224	— 0,103222	— 0,146940	— 0,501786	0

CCL Class. D 050

REPORT F. 66

A Calculation Method for Threedimensional Laminar Boundary Layers*)

by

Dr. R. TIMMAN.

Summary.

The momentum equation, which in the case of two-dimensional flow leads to an approximative method for the calculation of laminar boundary layers is extended to the case of three-dimensional flow. By introducing velocity profiles, depending on a thickness parameter and a parameter, which indicates the deviation of the boundary layer velocity from the free stream direction, a set of quasi-linear first order partial differential equations is obtained. These can be solved numerically by the method of characteristics.

Contents.

1 Introduction.

The calculation of laminar boundary layers in the case of three-dimensional flow has as yet received very little attention in the literature.

Aside from a small report by PRANDTL (ref. 1), which outlines a possible method for really three dimensional calculations, the papers known to the author refer only to the formulation of general equations of motion (ref. 2) or to the infinite yawed wing, which is essentially a two-dimensional case (refs. 3 and 4).

In this paper an attempt will be made to treat the general three-dimensional case and to develop a general method to solve the equations.

The set of boundary layer equations, together with the boundary conditions at the wall and in infinity can be replaced by the momentum equation (ref. 5), completed by a, in principle infinite, number of boundary conditions at the wall and in infinity.

In the usual approximate calculation method, the velocity profile in the boundary layer is represented by a function, depending on one paramteer. By choosing this function so, that it approximates the free stream velocity in a proper way, as can be inferred from an asymptotic solution of the boundary layer equations, and by satisfying a number of boundary conditions at the wall, it is possible to replace the boundary layer equations by a single non-linear first order ordinary differential equation. Here a practical limit is posed on the number of boundary conditions at the wall, which can be satisfied, as the first three yield only an algebraic condition on the velocity profile, while the higher boundary conditions require the additional solution of differential equations and so greatly complicate the calculations (comp. ref. 6). If the initial conditions at the stagnation point are known, this equation can be solved numerically. This initial condition is obtained by requiring the solution in the stagnation point, which is a singular point for the differential equation, to be regular. Substituting the power series expression the initial values and the higher coefficients of the power series can be obtained, thus providing a start for the numerical calculations.

A similar procedure, applied to the boundary layer equations in three-dimensional flow would replace the set of partial differential equations in the three velocity components by a set of two non-linear first order partial differential equations in two unknown functions. These functions are two parameters, characterizing the velocity profiles in the direction of the free stream at the outer edge of the boundary layer and the deviation of the boundary layer flow in a direction parallel to the surface and normal to this free stream direction.

In boundary layer calculations the free stream flow is assumed to be known. In the case of irrotational motion it can be described by a velocity potential $\varphi(y^l)$ where the y^l are Euclidean coordinates in ordinary space.

This velocity potential φ must satisfy the condition that on the surface of the body grad φ is tangential to this surface. With this condition in view a new set of curvilinear coordinates in space is introduced, formed by a set of Gaussian

*) This report was prepared by order of the N. I. V. (Netherlands Aircraft Development Board).

coordinates $x^\alpha (\alpha = 1,2)$ on the surface and a coordinate x^0, which expresses the Euclidean distance of a point in space to the body. If the body is convex and the surface is regular, the coordinates describe the space round the body uniquely *).

The boundary layer equations acquire a simpler form if the Gaussian coordinates on the surface are so specified, that the coordinate lines are the equipotential lines and the stream lines on the surface. These coordinates $\xi^\lambda (\xi^0 = x^0, \xi^1 = \varphi, \xi^2 = \psi)$ will be called "free stream-line" coordinates.

The momentum equations are derived from the boundary layer equations. Introducing a displacement thickness vector and a momentum thickness tensor they can be written as simple differential relations between these quantities.

The general equations can be solved approximately by the introduction of special velocity profiles, which are chosen according to the same principles as in the two dimensional case (ref. 6); viz. a set of profiles having the asymptotic behaviour at the outer edge of the boundary layer as derived by VON KARMAN and MILLIKAN (ref. 7) and satisfying only those boundary conditions at the wall that do not involve additional differentiations with respect to the variables ψ and φ. In each of the two velocity profiles (in free stream direction and perpendicular to it) one parameter is left free, which serves as the unknown function in the resulting first order partial differential equations.

These partial differential equations are quasi-linear and can be solved numerially by the method of characteristics, wellknown from the theory of supersonic flow.

The circumstances here are somewhat more complicated as in the case of plane supersonic flow, owing to the fact, that in the coefficients of the partial differential equations the coordinates occur explicitly, which makes it impossible to use a fixed set of characteristics.

The initial conditions are found from a consideration of the conditions at the stagnation point. As the singularity of the equations in this point is rather complicated, at first an approximate expression for the streamlines in the neigbourhood of this point is derived, which is used to describe the behaviour of the coefficients in the partial differential equations.

The stagnation point is a so called "nodal" point for the equations of the streamlines and these streamlines behave as a set of higher order parabola's touching one line through the stagnation point. Then it can be shown that all boundary layer quantities in the stagnation point are, approximately, only dependent on the coordinate in the direction of that particular line. Using this approximation the partial differential equations can be replaced by a set of two simultaneous ordinary differential equations of the same character as in the two-dimensional theory. The initial values then are determined in the same way by the substitution of power series expressions.

*) For the purpose of boundary layer calculations, where only a small layer round the body is considered, the condition of convexity can in practical cases be relaxed.

2 Three-dimensional potential flow about a body of arbitrary shape.

The potential flow about a body in a three-dimensional Euclidean space with coordinates y^i $(i = 1, 2, 3)$ is fully determined by its potential $\varphi (y^i)$, which satisfies the condition, that in any point of the surface the gradient $\frac{\partial \varphi}{\partial y^i}$ is tangential to this surface. Suppose, on the surface, a set of Gaussian coordinates to be introduced, so that its equations are

$$y^i = y^i(x^\alpha). \quad i = 1, 2, 3; \; \alpha = 1,2. \tag{1}$$

Then the line element on the surface is given by: (comp. ref. 8, p. 88, ref. 9)

$$ds^2 = g_{\alpha\beta}\, dx^\alpha dx^\beta, \; *) \tag{2}$$

where

$$g_{\alpha\beta} = \frac{\partial y_i}{\partial x^\alpha} \cdot \frac{\partial y^i}{\partial x^\beta}. \tag{3}$$

Introduce now in the complete space a new set of coordinates x^0, x^1 and x^2, x^1 and x^2 being the coordinates on the surface and x^0 the Euclidean distance from a point in space to the surface measured along the normal to the surface through this point. If the surface is convex, these coordinates can be unambiguously defined. Then the line element in space is

$$ds_j^2 = g_{\alpha\beta} dx^\alpha dx^\beta + (dx^0)^2. \tag{4}$$

The components of the velocity vector in Euclidean coordinates are

$$U_i = U^i = \frac{\partial \varphi}{\partial y_i} = \frac{\partial \varphi}{\partial y^i}, \tag{5}$$

as in Euclidean coordinates there is no difference between co- and contravariant components.

In the new coordinates the covariant components of the velocity vector are

$$\begin{aligned} U_\alpha = U_i \frac{\partial y^i}{\partial x^\alpha} &= \frac{\partial \varphi}{\partial y^i} \frac{\partial y^i}{\partial x^\alpha} = \\ &= \frac{\partial \varphi(x^1, x^2, x^0)}{\partial x^\alpha}, \; \alpha = 1,2 \\ U_0 = U_i \frac{\partial y^i}{\partial x^0} &= \frac{\partial \varphi}{\partial y^i} \frac{\partial y^i}{\partial x^0} = \frac{\partial \varphi}{\partial x^0}. \end{aligned} \tag{6}$$

The condition that the vector is tangential to the surface then requires $U_0 = 0$ for $x^0 = 0$;

$$\frac{\partial \varphi}{\partial x^0} = \frac{\partial \varphi}{\partial y^i} \cdot \frac{\partial y^i}{\partial x^0} = 0; \; x^0 = 0. \tag{7}$$

Hence, on the surface, the velocity vector is completely determined by its two components U_α or U^α in the Gaussian system $x^\alpha (\alpha = 1,2)$. Now,

*) In this report the summation convention is used throughout, so that for any tensor equation, as:

$$A_\alpha^{\beta\gamma} B_{\delta\varepsilon}^{\alpha} = \sum_{\alpha=1}^{2} A_\alpha^{\beta\gamma} B_{\delta\varepsilon}^{\alpha}.$$

a new system of orthogonal curvilinear coordinates $\xi^\lambda(\lambda=1,2)$, is introduced on the surface defined by requiring the covariant components of the velocity vector to assume the simple form

$$\overline{U}_1=1,\ \overline{U}_2=0. \tag{8}$$

The transformation formulae then read

$$U_\alpha=\frac{\partial\xi^\lambda}{\partial x^\alpha}\,\overline{U}_\lambda, \tag{9}$$

or

$$\begin{cases} U_1=\dfrac{\partial\xi^1}{\partial x^1}, \\ U_2=\dfrac{\partial\xi^1}{\partial x^2}. \end{cases} \tag{10}$$

The formulae (6) and (10) show that

$$\xi^1=\varphi(x\ ), \tag{11}$$

taking the value of the constant of integration to be zero.

The second coordinate ξ^2 is to be determined from the orthogonality conditions.

Denoting the new metric tensor by $\gamma_{\lambda\mu}$ the line element is

$$ds^2=g_{\alpha\beta}dx^\alpha dx^\beta=\gamma_{\lambda\mu}\,d\xi^\lambda d\xi^\mu. \tag{12}$$

If the new coordinates are orthogonal

$$\gamma_{12}=\gamma_{21}=0. \tag{13}$$

The contravariant components $\gamma^{\lambda\mu}$ are

$$\gamma^{11}=\frac{\gamma_{22}}{\gamma}\ ;\ \gamma^{12}=\gamma^{21}=-\frac{\gamma_{12}}{\gamma}\ ;\ \gamma^{22}=\frac{\gamma_{11}}{\gamma}, \tag{14}$$

where

$$\gamma=|\det\gamma_{\lambda\mu}|=\gamma_{11}\cdot\gamma_{22}. \tag{15}$$

Then it follows that

$$\gamma^{11}=\frac{1}{\gamma_{11}}\ ;\ \gamma^{12}=\gamma^{21}=0;\ \gamma^{22}=\frac{1}{\gamma_{22}}. \tag{16}$$

From the conditions $\gamma^{12}=\gamma^{21}=0$ an equation for ξ^2 can be derived

$$\gamma^{12}=\gamma^{21}=g^{\alpha\beta}\,\frac{\partial\xi^1}{\partial x^\alpha}\cdot\frac{\partial\xi^2}{\partial x^\beta}=$$

$$=g^{\alpha\beta}\cdot U_\alpha\cdot\frac{\partial\xi^2}{\partial x^\beta}=U^\beta\,\frac{\partial\xi^2}{\partial x^\beta}=0, \tag{17}$$

or explicitly

$$U^1\,\frac{\partial\xi^2}{\partial x^1}+U^2\,\frac{\partial\xi^2}{\partial x^2}=0. \tag{18}$$

Denoting from now on ξ^2 by ψ, the partial differential equation is solved by putting

$$\begin{aligned} \frac{\partial\psi}{\partial x^2}&=\frac{\partial\xi^2}{\partial x^2}=-\sqrt{\rho g}\,U^1, \\ \frac{\partial\psi}{\partial x^1}&=\frac{\partial\xi^2}{\partial x^1}=+\sqrt{\rho g}\,U^2, \end{aligned} \tag{19}$$

where g is $|\det.g_{\alpha\beta}|$ and ρ is a function, which must satisfy the equation obtained from (19) by equating $\dfrac{\partial^2\psi}{\partial x^2\partial x^1}$ to $\dfrac{\partial^2\psi}{\partial x^1\partial x^2}$:

$$\frac{\partial\sqrt{\rho g}\,U^1}{\partial x^1}+\frac{\partial\sqrt{\rho g}\,U^2}{\partial x^2}=0. \tag{20}$$

Further

$$\gamma^{11}=g^{\alpha\beta}\,\frac{\partial\xi^1}{\partial x^\alpha}\cdot\frac{\partial\xi^1}{\partial x^\beta}=g^{\alpha\beta}\ U_\alpha U_\beta=T$$

is the square of the modulus of the velocity vector, denoted by T and

$$\gamma^{22}=g^{\alpha\beta}\,\frac{\partial\psi}{\partial x^\alpha}\ \frac{\partial\psi}{\partial x^\beta}=$$

$$=\rho g\ \{\ g^{11}(U^2)^2-2\,g^{12}U^1U^2+\ g^{22}(U^1)^2\ \}=$$

$$=\rho\ \{\ g_{\alpha\beta}U^\alpha U^\beta\}=\rho T, \tag{23}$$

because of the relations

$$g^{11}=\frac{g_{22}}{g}\ ,\ g^{12}=g^{21}=-\ \frac{g_{12}}{g}=$$

$$=-\frac{g_{21}}{g},\ g^{22}=\frac{g_{11}}{g}\ . \tag{24}$$

Then the line element in the new coordinates is, because of (17), (23) and (16)

$$ds^2=\frac{1}{T}\cdot\left\{d\varphi^2+\frac{1}{\rho}\ d\psi^2\right\}. \tag{25}$$

In dealing with an arbitrary vector u^α the Riemann-Christoffel symbols for the line-element (25) are needed.

$$\begin{aligned} \Gamma_{11}{}^1&=\frac{1}{2}\ \gamma^{11}\left(\frac{\partial\gamma_{11}}{\partial\xi^1}+\frac{\partial\gamma_{11}}{\partial\xi^1}-\frac{\partial\gamma_{11}}{\partial\xi^1}\right)=-\frac{T_\varphi}{2\,T}\ , \\ \Gamma_{12}{}^1&=\Gamma_{21}{}^1= \\ &=\frac{1}{2}\ \gamma^{11}\left(\frac{\partial\gamma_{21}}{\partial\xi^1}+\frac{\partial\gamma_{11}}{\partial\xi^2}-\frac{\partial\gamma_{12}}{\partial\xi^1}\right)=-\frac{T_\psi}{2\,T}\ , \\ \Gamma_{22}{}^1&=\frac{1}{2}\ \gamma^{11}\left(\frac{\partial\gamma_{12}}{\partial\xi^2}+\frac{\partial\gamma_{21}}{\partial\xi^2}-\frac{\partial\gamma_{22}}{\partial\xi^1}\right)= \\ &=\frac{1}{2\,\rho}\left(\frac{T_\varphi}{T}+\frac{\rho_\varphi}{\rho}\right), \\ \Gamma_{11}{}^2&=\frac{1}{2}\ \gamma^{22}\left(\frac{\partial\gamma_{21}}{\partial\xi^1}+\frac{\partial\gamma_{12}}{\partial\xi^1}-\frac{\partial\gamma_{11}}{\partial\xi^2}\right)=\frac{\rho}{2}\ \frac{T_\psi}{T}\ , \\ \Gamma_{12}{}^2&=\frac{1}{2}\ \gamma^{22}\left(\frac{\partial\gamma_{22}}{\partial\xi^1}+\frac{\partial\gamma_{12}}{\partial\xi^2}-\frac{\partial\gamma_{12}}{\partial\xi^2}\right)= \\ &=-\frac{1}{2}\left(\frac{T_\varphi}{T}+\frac{\rho_\varphi}{\rho}\right), \\ \Gamma_{22}{}^2&=\frac{1}{2}\ \gamma^{22}\left(\frac{\partial\gamma_{22}}{\partial\xi^2}+\frac{\partial\gamma_{22}}{\partial\xi^2}-\frac{\partial\gamma_{22}}{\partial\xi^2}\right)= \\ &=-\frac{1}{2}\left(\frac{T_\psi}{T}+\frac{\rho_\psi}{\rho}\right). \end{aligned} \tag{26}$$

3 The momentum equation in curvilinear coordinates.

If in the coordinates x^0, x^1, x^2 of the preceding section a new variable ζ normal to the surface is introduced by putting

$$\zeta = \frac{x^0}{\sqrt{\nu}} \tag{1}$$

and for the velocity component U^0 in this direction is put

$$W = \frac{U_0}{\sqrt{\nu}}, \tag{2}$$

then, according to LIN (ref. 9), the boundary layer equations assume the form

$$\begin{cases} U^\beta U_{\alpha,\beta} + W \dfrac{\partial U_\alpha}{\partial \zeta} = -\dfrac{\partial \pi}{\partial x^\alpha} + \dfrac{\partial^2 U_\alpha}{\partial \zeta^2}, \quad \alpha = 1,2 & (3) \\ 0 = \dfrac{\partial \pi}{\partial \zeta}, & (4) \\ U^\beta{}_{,\beta} + \dfrac{\partial W}{\partial \zeta} = 0. & (5) \end{cases}$$

Here $U\beta$ denote the contravariant components of the velocity in the boundary layer and π denotes the pressure, divided by the density of the air.

The comma's denote covariant differentiation in the coordinates x^α ($\alpha = 1,2$), so that

$$U_{\alpha,\beta} = \frac{\partial U_\alpha}{\partial x^\beta} - \Gamma^\lambda_{\alpha\beta} U_\lambda, \tag{6}$$

$$U^\beta{}_{,\alpha} = \frac{\partial U^\beta}{\partial x^\alpha} + \Gamma^\beta_{\alpha\lambda} U^\lambda. \tag{7}$$

The boundary conditions imposed on the solution U^α of these equations, require that for $\zeta \to \infty$ the flow passes into the free stream with velocity U^α.

$$\begin{aligned} u^\alpha &\to U^\alpha, \\ \pi &\to \Pi, \end{aligned} \tag{8}$$

while

$$U^\beta U_{\alpha,\beta} = -\frac{\partial \Pi}{\partial x^\alpha}. \tag{9}$$

Regarding the fact that according to (4) π is independent of ζ, the equations become

$$U^\beta U_{\alpha,\beta} - u^\beta u_{\alpha,\beta} + \frac{\partial^2 u_\alpha}{\partial \zeta^2} - W \frac{\partial u_\alpha}{\partial \zeta} = 0, \tag{10}$$

$$U^\beta{}_{,\beta} \frac{\partial W}{\partial \zeta} = 0. \tag{11}$$

From this pair of equations the momentum equation is found by integration with respect to ζ from 0 to ∞. By partial integration and application of (11) the result is

$$\int_0^\infty (U^\beta U_{\alpha,\beta} - u^\beta u_{\alpha,\beta})\, d\zeta - \left[\frac{\partial u_\alpha}{\partial \zeta}\right]_0 + \int_0^\infty (U_\alpha - u_\alpha)\, u^\beta{}_{,\beta}\, d\zeta = 0, \tag{12}$$

which can be written as

$$U_{\alpha,\beta} \int_0^\infty (U^\beta - u^\beta)\, d\zeta + \int_0^\infty \{(U_\alpha - u_\alpha)_{,\beta}\, u^\beta + (U_\alpha - u_\alpha)\, u^\beta{}_{,\beta}\}\, d\zeta = \left[\frac{\partial u_\alpha}{d\zeta}\right]_0. \tag{13}$$

Introduction of the displacement length *vector*

$$\delta^\beta = \int_0^\infty (U^\beta - u^\beta)\, d\zeta \tag{14}$$

and the momentum length *tensor*

$$\vartheta^\beta_\alpha = \int_0^\infty (U_\alpha - u_\alpha)\, u^\beta\, d\zeta \tag{15}$$

gives to the equations the form

$$U_{\alpha,\beta}\, \delta^\beta + \vartheta^\beta_{\alpha,\beta} = \left[\frac{\partial u_\alpha}{\partial \zeta}\right]_0. \tag{16}$$

Now, in the streamline coordinates φ and ψ of the preceding section the covariant components of the free stream velocity are

$$\begin{aligned} U_1 &= 1, \\ U_2 &= 0 \end{aligned} \tag{17}$$

and the covariant derivatives $U_{\alpha,\beta}$ in (16) become

$$\begin{aligned} U_{1,1} &= -\Gamma_{11}{}^1 = \frac{T_\varphi}{2T}, \\ U_{1,2} &= -\Gamma_{12}{}^1 = \frac{T_\psi}{2T}, \\ U_{2,1} &= -\Gamma_{21}{}^1 = \frac{T_\psi}{2T}, \\ U_{2,2} &= -\Gamma_{22}{}^1 = -\frac{1}{2\rho}\left(\frac{T_\varphi}{T} + \frac{\rho_\varphi}{\rho}\right). \end{aligned} \tag{18}$$

Using the covariant components

$$\begin{aligned} \delta_1 &= \int_0^\infty (1 - u_1) d\zeta, \\ \delta_2 &= -\int_0^\infty u_2 d\zeta, \\ \vartheta_{11} &= \int_0^\infty (1 - u_1) u_1 d\zeta, \\ \vartheta_{12} &= \int_0^\infty (1 - u_1) u_2 d\zeta, \end{aligned} \tag{19}$$

$$\vartheta_{21} = -\int_0^\infty u_2 u_1 d\zeta = +\delta_2 + \vartheta_{12},$$

$$\vartheta_{22} = -\int_0^\infty u_2^2 d\zeta, \tag{19}$$

which have only the dimension of the coordinate ζ (T), the equations (16) are transformed into

$$U_{\alpha,\beta} \cdot \gamma^{\beta\varepsilon}\delta_\varepsilon + \gamma^{\beta\varepsilon}\vartheta_{\alpha\varepsilon,\beta} = \left[\frac{\partial u_\alpha}{\partial\zeta}\right]_0 \tag{20}$$

or explicitly, taking account of the values

$$\gamma^{11} = T,\ \gamma^{12} = \gamma^{21} = 0,\quad \gamma^{22} = \rho T,$$

$$\begin{aligned} U_{1,1}\delta_1 + \rho U_{1,2}\delta_2 + \vartheta_{11,1} + \rho\vartheta_{12,2} &= \frac{1}{T}\left[\frac{\partial u_1}{\delta\zeta}\right]_0, \\ U_{2,1}\delta_1 + \rho U_{2,2}\delta_2 + \vartheta_{21,1} + \rho\vartheta_{22,2} &= \frac{1}{T}\left[\frac{\partial u_2}{\partial\zeta}\right]_0. \end{aligned} \tag{21}$$

The covariant derivatives $\vartheta_{\alpha\beta,\gamma}$ are

$$\begin{aligned} \vartheta_{11,1} &= \frac{\partial\vartheta_{11}}{\partial\varphi} - \Gamma_{11}^1\vartheta_{11} - \Gamma_{11}^2\vartheta_{12} - \Gamma_{11}^1\vartheta_{11} - \\ &- \Gamma_{11}^2\vartheta_{21} = \frac{\partial\vartheta_{11}}{\partial\varphi} + \frac{T_\varphi}{T}\vartheta_{11} - \frac{\rho}{2}\frac{T_\psi}{T}(\vartheta_{12} + \vartheta_{21}), \\ \vartheta_{12,2} &= \frac{\partial\vartheta_{12}}{\partial\psi} - \Gamma_{22}^1\vartheta_{11} - \Gamma_{22}^2\vartheta_{12} - \\ &- \Gamma_{12}^1\vartheta_{12} - \Gamma_{12}^2\vartheta_{22} = \\ &= \frac{\partial\vartheta_{12}}{\partial\psi} - \frac{1}{2\rho}\left(\frac{T_\varphi}{T} + \frac{\rho_\varphi}{\rho}\right)\vartheta_{11} + \\ &+ \frac{1}{2}\left(2\frac{T_\psi}{T} + \frac{\rho_\psi}{\rho}\right)\vartheta_{12} + \\ &+ \frac{1}{2}\left(\frac{T_\varphi}{T} + \frac{\rho_\varphi}{\rho}\right)\vartheta_{22}, \\ \vartheta_{21,1} &= \frac{\partial\vartheta_{21}}{\partial\varphi} - \Gamma_{11}^1\vartheta_{21} - \Gamma_{11}^2\vartheta_{22} - \\ &- \Gamma_{21}^1\vartheta_{11} - \Gamma_{21}^2\vartheta_{21} = \\ &= \frac{\partial\vartheta_{21}}{\partial\varphi} + \left(\frac{T_\varphi}{T} + \frac{1}{2}\frac{\rho_\varphi}{\rho}\right)\vartheta_{21} + \\ &+ \frac{1}{2}\cdot\frac{T_\psi}{T}\cdot(\vartheta_{11} - \rho\vartheta_{22}), \\ \vartheta_{22,2} &= \frac{\partial\vartheta_{22}}{\partial\psi} - \Gamma_{22}^1\vartheta_{21} - \Gamma_{22}^2\vartheta_{22} - \\ &- \Gamma_{22}^1\vartheta_{12} - \Gamma_{22}^2\vartheta_{22} = \\ &= \frac{\partial\vartheta_{22}}{\partial\psi} - \frac{1}{2\rho}\left(\frac{T_\varphi}{T} + \frac{\rho_\varphi}{\rho}\right)(\vartheta_{21} + \vartheta_{12}) + \\ &+ \left(\frac{T_\psi}{T} + \frac{\rho_\psi}{\rho}\right)\vartheta_{22}. \end{aligned} \tag{21}$$

Then, finally, the equations become:

$$\begin{aligned} &\frac{\partial\vartheta_{11}}{\partial\varphi} + \rho\frac{\partial\vartheta_{12}}{\partial\psi} + \frac{T_\varphi}{2T}(\delta_1 + \vartheta_{11} + \rho\vartheta_{22}) + \\ &+ \frac{\rho_\varphi}{2\rho}(-\vartheta_{11} + \rho\vartheta_{22}) + \frac{\rho_\psi}{2}\vartheta_{12} = \frac{1}{T}\left[\frac{\partial u_1}{\partial\zeta}\right]_0, \end{aligned} \tag{22}$$

$$\begin{aligned} &\frac{\partial\vartheta_{21}}{\partial\varphi} + \rho\frac{\partial\vartheta_{22}}{\partial\psi} + \frac{T_\psi}{2T}(\delta_1 + \vartheta_{11} + \rho\vartheta_{22}) - \\ &- \frac{\rho_\varphi}{2\rho}\vartheta_{21} + \rho_\psi\vartheta_{22} = \frac{1}{T}\left[\frac{\partial u_2}{\partial\zeta}\right]_0. \end{aligned}$$

4 Reduction to a set of partial differential equations in two unknown functions.

The momentum equations, derived in the preceding section are not sufficient to determine completely the boundary layer flow. In fact, the boundary value problem formed by the boundary layer equations together with the boundary conditions at the wall and in infinity is equivalent to the momentum equation and a set of infinitely many boundary conditions for $\zeta = 0$ and $\zeta = \infty$, obtained from (3.10) by differentiation with respect to ξ and putting $\zeta = 0$. The first of these equations reads:

$$-U^\beta U_{\alpha,\beta} = \left[\frac{\partial^2 u_\alpha}{\partial\zeta^2}\right]_{\zeta=0}. \tag{1}$$

Unfortunately the following boundary conditions contain already derivatives of unknown functions, as is seen by differentiating (3.10) once with respect to ζ and putting $\zeta = 0$,

$$\frac{\partial^3 u_\alpha}{\partial\zeta^3} - U_{\alpha,\beta}\frac{\partial u^\beta}{\partial\zeta} + u_\beta^\beta\frac{\partial u_\alpha}{\partial\zeta} = 0, \tag{2}$$

and hence cannot be taken into account without greatly complicating the calculations.

In the streamline coordinates (1) becomes

$$\begin{aligned} -\frac{1}{2}T_\varphi &= \left[\frac{\partial^2 u_1}{\partial\zeta^2}\right]_{\zeta=0}, \\ -\frac{1}{2}T_\Psi &= \left[\frac{\partial^2 u_2}{\partial\zeta^2}\right]_{\zeta=0}. \end{aligned} \tag{3}$$

In order to specify the velocity profiles in the boundary layer the covariant components of the velocity profiles, which are dimensionless quantities, are considered.

For $\zeta \to \infty$ these covariant components tend to the components of the free stream velocity $U_1 = 1$, $U_2 = 0$. The velocity profiles are introduced as functions of a dimensionless variable

$$\eta = \zeta \cdot \sigma^{-1/2}, \tag{4}$$

where $\sigma^{1/2}$ is a measure for the boundary layer thickness. These functions have to satisfy, besides (3), the following boundary conditions.

For $\eta = 0$,

$$u_1 = u_2 = 0, \tag{5}$$

and for $\eta \to \infty$,

$$u_1 \to 1,\ u_2 \to 0,$$
$$u_1' \to u_2' \to u_1'' \to u_2'' \ldots\ldots \to 0. \tag{6}$$

Assume, that u_1 and u_2 are linearly composed from three basic functions $f(\eta)$, $g(\eta)$ and $h(\eta)$, which satisfy the conditions

$$\begin{aligned} &f(0) = 0,\ f''(0) = 0, \\ &f(\infty) = 1,\ f'(\infty) = f''(\infty) = \ldots = 0, \end{aligned} \tag{7}$$

$$\begin{aligned} &g(0) = 0,\ g''(0) = 1, \\ &g(\infty) = g'(\infty) = g''(\infty) = \ldots = 0, \end{aligned} \tag{8}$$

$$\begin{aligned} &h(0) = 0,\ h'(0) = 1,\ h''(0) = 0, \\ &h(\infty) = h'(\infty) = h''(\infty) = \ldots = 0. \end{aligned} \tag{9}$$

Putting

$$u_1 = f(\eta) - \Lambda\, g(\eta),$$
$$u_2 = \sqrt{\rho}\,\{ Nh(\eta) - Mg(\eta) \}, \qquad (10)$$

where ρ is defined in the preceding section and Λ, M and N are functions of φ and ψ.

Then the conditions (3) yield

$$\Lambda = \frac{1}{2} T_\varphi \,.\, \sigma,$$
$$M = \frac{1}{2} \sqrt{\rho}\, T_\psi \,.\, \sigma, \qquad (11)$$

so that Λ and M can be expressed into the parameter σ, which also is a function of φ and ψ. In this way only two unknown functions $\sigma(\varphi, \psi)$ and $N(\varphi, \psi)$ remain.

As the covariant components of the displacement thickness vector and the momentum thickness tensor have the dimension of the coordinate ζ, it is convenient to introduce new quantities by putting (compare (4))

$$\Delta_1 = \sigma^{-1/2}\delta_1\,,\quad \Delta_2 = \rho^{1/2}\,\delta^{-1/2}\delta_2\,, \qquad (12)$$

and

$$\Theta_{11} = \sigma^{-1/2}\,\vartheta_{11}\,,\quad \Theta_{12} = \rho^{1/2}\sigma^{-1/2}\,\vartheta_{12}\,,$$
$$\Theta_{21} = \rho^{1/2}\sigma^{-1/2}\,\vartheta_{21}\,,\quad \Theta_{22} = \rho\sigma^{-1/2}\,\vartheta_{22}\,. \qquad (13)$$

Then the equations (3.22) pass into

$$2\sigma\frac{\partial\Theta_{11}}{\partial\varphi} + \Theta_{11}\frac{\partial\sigma}{\partial\varphi} + 2\sigma\sqrt{\rho}\,\frac{\partial\Theta_{12}}{\partial\psi} + \Theta_{12}\sqrt{\rho}\,\frac{\partial\sigma}{\partial\psi} + \sigma\frac{T_\varphi}{T}(\Delta_1 + \Theta_{11} + \Theta_{22}) + \frac{\sigma\rho_\varphi}{\rho}(-\Theta_{11} + \Theta_{22}) = \frac{2}{T}\left[\frac{\partial u_1}{\partial\eta}\right]_0, \qquad (14)$$

$$2\sigma\frac{\partial\Theta_{21}}{\partial\varphi} + \Theta_{21}\frac{\partial\sigma}{\partial\varphi} + 2\sigma\sqrt{\rho}\,\frac{\partial\Theta_{22}}{\partial\psi} + \Theta_{22}\sqrt{\rho}\,\frac{\partial\sigma}{\partial\psi} + \sigma\sqrt{\rho}\,\frac{T_\psi}{T}(\Delta_1 + \Theta_{11} + \Theta_{22}) - \frac{\sigma\rho_\varphi}{\rho}\Theta_{21} = \frac{2\sqrt{\rho}}{T}\left[\frac{\partial u_2}{\partial\eta}\right]_0. \qquad (15)$$

Here the quantities Θ_{ik} and Δ_i contain only the parameters Λ, M and N and their differential quotients contain the derivatives of these functions. As the unknown functions are only σ and N, the functions Λ and M being related with σ by (11), it is more conveniant to write the differential equations explicitly in the form of relations between the derivatives of σ and N only. From the definition of Λ and M by (11) follow the relations

$$2\sigma\Lambda_\varphi = \sigma^2 T_{\varphi\varphi} + \sigma\sigma_\varphi T_\varphi = 2\Lambda\sigma_\varphi + \sigma^2 T_{\varphi\varphi},$$
$$2\sigma\Lambda_\psi = \sigma^2 T_{\varphi\psi} + \sigma\sigma_\psi T_\varphi = 2\Lambda\sigma_\psi + \sigma^2 T_{\varphi\psi},$$
$$2\sigma M_\varphi = \sigma^2\sqrt{\rho}\,T_{\psi\varphi} + \sigma\sigma_\varphi\sqrt{\rho}\,T_\psi + \frac{\sigma^2}{2\sqrt{\rho}}\rho_\varphi T_\psi = 2M\sigma_\varphi + \sigma^2\frac{\partial}{\partial\varphi}(\sqrt{\rho}\,T_\psi), \qquad (16)$$
$$2\sigma M_\psi = \sigma^2(\sqrt{\rho}\,T_\psi)_\psi + \sigma\sqrt{\rho}\,T_\psi\sigma_\psi = 2M\sigma_\psi + \sigma^2(\sqrt{\rho}\,T_\psi)_\psi.$$

Substitution into eqs. (14) and (15) yields the differential equations for σ and N.

$$(2\Lambda\Theta_{11\Lambda} + \Theta_{11})\sigma_\varphi + (2M\Theta_{12M} + 2\Lambda\Theta_{12\Lambda} + \Theta_{12})\sqrt{\rho}\sigma_\psi + 2\sigma\Theta_{12N}\sqrt{\rho}N_\psi = \frac{2}{T}\left[\left(\frac{\partial u_1}{\partial\eta}\right)_{\eta=0} - \Lambda(\Delta_1 + \Theta_{11} + \Theta_{22})\right] - \sigma^2 T_{\varphi\varphi}\Theta_{11\Lambda} - \sigma^2\Theta_{12\Lambda}\sqrt{\rho}T_{\varphi\psi} - \sigma^2\sqrt{\rho}\,\frac{\partial}{\partial\psi}(\sqrt{\rho}T_\psi)\Theta_{12M} + \frac{\sigma\rho_\varphi}{\rho}(\Theta_{11} - \Theta_{12}), \qquad (17)$$

$$(2\Lambda\Theta_{21\Lambda} + 2M\Theta_{21M} + \Theta_{21})\sigma_\varphi + (2M\Theta_{22M} + \Theta_{22})\sqrt{\rho}\sigma_\psi + 2\sigma\Theta_{21N}N_\varphi + 2\sigma\Theta_{22N}\sqrt{\rho}\,N_\psi = \frac{2}{T}\left[\left(\frac{\partial u_2}{\partial\eta}\right)_{\eta=0}\sqrt{\rho} - M(\Delta_1 + \Theta_{11} + \Theta_{22})\right] - \sigma^2 T_{\varphi\varphi}\Theta_{21\Lambda} - \sigma^2\Theta_{21M}(\sqrt{\rho}T_\psi)_\varphi - \sigma^2\Theta_{22M}\sqrt{\rho}(\sqrt{\rho}T_\psi)_\psi + \frac{2\sigma\rho_\varphi}{\rho}\Theta_{21}. \qquad (18)$$

5 The velocity profiles.

The velocity profiles are determined by the choice of the functions f, g and h. The form of these functions is suggested by an earlier report (ref. 6), referring to the case of two-dimensional flow. In that report a method, similar to POHLHAUSEN's method for two-dimensional case is developed, which does not use polynomials but functions, which have the asymptotic behaviour as derived by VON KARMAN and MILLIKAN (ref. 7).

The velocity components u_1 and u_2 are introduced in the general form

$$u_1 = 1 - a_1\int_\eta^\infty e^{-y^2}dy - e^{-\eta^2}(b_1 + c_1\eta + d_1\eta^2 + \ldots\ldots),$$
$$u_2 = a_2\int_\eta^\infty e^{-y^2}dy - e^{-\eta^2}(b_2 + c_2\eta + d_2\eta^2 + \ldots\ldots). \qquad (1)$$

A set of functions $f(\eta)$, $g(\eta)$, $h(\eta)$ of the form (1), which satisfies the conditions, imposed in section 4 is

$$f(\eta) = \frac{4}{3\sqrt{\pi}}\int_0^\eta e^{-y^2}(1 + y^2)dy,$$
$$g(\eta) = \frac{2}{3\sqrt{\pi}}\int_\eta^\infty e^{-y^2}(1 + y^2)dy - \frac{1}{2}e^{-\eta^2}, \qquad (2)$$
$$h(\eta) = \eta e^{-\eta^2}.$$

Then the velocity profiles are

$$u_1 = f(\eta) - \Lambda g(\eta),$$
$$\sqrt{\rho}\, u_2 = Nh(\eta) - Mg(\eta), \qquad (3)$$

and the formulae for the displacement thickness vector and momentum thickness tensor are

$$\Delta_1 = \int_0^\infty (1-f)d\eta + \Lambda \int_0^\infty g d\eta,$$
$$\Delta_2 = -N \int_0^\infty h d\eta + M \int_0^\infty g d\eta, \qquad (4)$$

and

$$\Theta_{11} = \int_0^\infty (1-f)f d\eta - \Lambda \int_0^\infty (1-2f) g d\eta - \Lambda^2 \int_0^\infty g^2 d\eta,$$
$$\Theta_{12} = N \int_0^\infty (1-f) h d\eta - M \int_0^\infty (1-f) g d\eta + \Lambda N \int_0^\infty gh d\eta - \Lambda M \int_0^\infty g^2 d\eta, \qquad (5)$$
$$\Theta_{21} = \Theta_{12} + \Delta_2,$$
$$\Theta_{22} = -N^2 \int_0^\infty h^2 d\eta + 2MN \int_0^\infty gh d\eta - M^2 \int_0^\infty g^2 d\eta.$$

The integrals are evaluated in the appendix. The results are

$$\Delta_1 = 0.752\,253 - 0.066\,987\,\Lambda, \qquad (6)$$
$$\Delta_2 = -0.5\,N - 0.066\,987\,M,$$
$$\Theta_{11} = 0.289\,430 + 0.007\,335\,\Lambda - 0.003\,798\,\Lambda^2,$$
$$\Theta_{12} = 0.205\,372\,N + 0.037\,161\,M - 0.022319\,\Lambda N - 0.003\,798\,\Lambda M, \qquad (7)$$
$$\Theta_{21} = -0.294\,628\,N - 0.029\,826\,M - 0.022\,319\,\Lambda N - 0.003\,798\,\Lambda M,$$
$$\Theta_{22} = -0.156\,664\,N^2 - 0.044\,638\,MN - 0.003798\,M^2.$$

Further

$$\left[\frac{\partial u_1}{\partial \eta}\right]_{\eta=0} = \frac{2}{3\sqrt{\pi}}(2+\Lambda) = 0.376\,127\,(2+\Lambda), \qquad (8)$$
$$\sqrt{\rho}\left[\frac{\partial u_2}{\partial \eta}\right]_{\eta=0} = N + \frac{2}{3\sqrt{\pi}} M = N + 0.376\,127\,M.$$

Then the final form for the differential equations (4.17) and (4.18) is

$$T[a^1\sigma_\varphi + a^2\sqrt{\rho}\sigma_\psi + b^1 N_\varphi + b^2\sqrt{\rho}N_\psi] = c + c^1\frac{\rho_\varphi T}{\rho} - c^{11}TT_{\varphi\varphi} - c^{12}T\sqrt{\rho}T_{\varphi\psi} - c^{22}T\sqrt{\rho}(\sqrt{\rho}T_\psi)_\psi, \qquad (9)$$

$$T[A^1\sigma_\varphi + A^2\sqrt{\rho}\sigma_\psi + B^1 N_\varphi + B^2\sqrt{\rho}N_\varphi] = C + C^1\frac{\rho_\varphi T}{\rho} - C^{11}TT_{\varphi\varphi} - C^{21}T(\sqrt{\rho}T_\psi)_\varphi - C^{22}T\sqrt{\rho}(\sqrt{\rho}T_\varphi)_\psi, \qquad (10)$$

where

$a^1 = 0.289\,430 + 0.022\,005\,\Lambda - 0.018\,990\,\Lambda^2,$
$a^2 = 0.205\,372\,N + 0.111\,483\,M - 0.066\,957\,\Lambda N - 0.018\,990\,\Lambda M,$
$b^1 = 0,$
$b^2 = \sigma(0.410\,744 - 0.044\,638\,\Lambda),$
$c = 2\,(0.752\,254 - 0.665\,556\,\Lambda + 0.059\,652\,\Lambda^2 + 0.003\,798\,\Lambda^3 + 0.156\,664\,N^2\,\Lambda + 0.044\,638\,\Lambda MN + 0.003\,798\,\Lambda M^2),$
$c^1 = (0.289\,430 + 0.007\,335\,\Lambda - 0.003\,798\,\Lambda^2 + 0.156\,664\,N^2 + 0.044\,638\,MN + 0.003\,798\,M^2)\sigma,$
$c^{11} = (0.007\,335 - 0.007\,596\,\Lambda)\sigma^2,$
$c^{12} = (-0.022\,319\,N - 0.003\,798\,M)\sigma^2,$
$c^{22} = (0.037\,161 - 0.003\,798\,\Lambda)\sigma^2,$

and

$A^1 = -0.066\,957\,\Lambda N - 0.018\,990\,\Lambda M - 0.089\,478\,M - 0.294\,628\,N,$
$A^2 = -0.156\,664\,N^2 - 0.133\,914\,MN - 0.018\,990\,M^2,$
$B^1 = \sigma(-0.589\,256 - 0.044\,638\,\Lambda),$
$B^2 = \sigma(-0.626\,656\,N - 0.089\,276\,M),$
$C = 2\,(N - 0.665\,556\,M + 0.059\,652\,\Lambda M + 0.003\,798\,\Lambda^2 M + 0.156\,664\,MN^2 + 0.044\,638\,M^2N + 0.003\,798\,M^3),$
$C^1 = 2\,\sigma(-0.294\,628\,N - 0.029\,826\,M - 0.022\,319\,\Lambda N - 0.003\,798\,\Lambda M),$
$C^{11} = \sigma^2\,(-0.022\,319\,N - 0.003\,798\,M),$
$C^{21} = \sigma^2\,(-0.029\,826 - 0.003\,798\,\Lambda),$
$C^{22} = \sigma^2\,(-0.044\,638\,N - 0.007\,596\,M).$

6 The conditions in a stagnation point.

In a stagnation point the velocity components u_α are both zero. Assuming this stagnation point to be the origin of the system of coordinates x^α and the velocity potential to be regular, its value on the surface can be expanded into a power series,

$$\varphi = a_{\alpha\beta}x^\alpha x^\beta + a_{\alpha\beta\gamma}x^\alpha x^\beta x^\gamma + \ldots\ldots, \quad \alpha,\beta = 1,2 \qquad (1)$$

since the terms of the first degree vanish because of the condition

$$U_\alpha \frac{\partial\varphi}{\partial x^\alpha} = \varphi_{,\alpha} = 0. \qquad (2)$$

The quantities $a_{\alpha\beta}$ are the values in the origin of the tensor

$$\varphi_{,\alpha,\beta} = \left(\frac{\partial\varphi}{\partial x^\alpha}\right)_{,\beta} = \frac{\partial^2\varphi}{\partial x^\alpha \partial x^\beta} + \Gamma^\lambda_{\alpha\beta}\frac{\partial\varphi}{\partial x^\lambda}, \quad (3)$$

as the second terms on the right hand side vanish in the origin because of (2) and similarly for the $a_{\alpha\beta\gamma}$.

The line element in the origin is given by the equation

$$ds^2 = g_{\alpha\beta}(0)\,.\,dx^\alpha dx^\beta, \quad (4)$$

and the magnitude of the free stream velocity vector by

$$T = g_{\alpha\beta}(0)\,U^\alpha U^\beta = U_\beta U_\beta, \quad (5)$$

which vanishes in the origin.

Hence the origin is a singular point for the differential equations and the conditions there need a careful consideration.

At first a new system of canonical coordinates is introduced in the neighbourhood of the origin in which the two quadratic forms

$$\varphi(0) = a_{\alpha\beta}x^\alpha x^\beta \quad (6)$$

and

$$G = g_{\alpha\beta}(0)x^\alpha x^\beta,$$

assume simple representations.

$$\varphi(0) = \frac{1}{2}\,r(\chi^2 + \lambda\zeta^2),$$
$$G = \chi^2 + \zeta^2. \quad (7)$$

Then, in the neighbourhood of the origin the velocity components are

$$v_1 = v^1 = r\chi, \quad (8)$$
$$v_2 = v^2 = r\lambda\zeta,$$

and the function $T = v_1v^1 + v_2v^2$ becomes

$$T = r^2(\chi^2 + \lambda^2\zeta^2). \quad (9)$$

The streamlines are given by the equation

$$\frac{d\chi}{v^1} = \frac{d\zeta}{v^2}, \quad (10)$$

or

$$\frac{d\chi}{\chi} = \frac{d\zeta}{\lambda\zeta}, \quad (11)$$

which has the solution

$$\lambda\ln\chi - \ln\zeta = \psi, \quad (12)$$

where ψ is, in this neighbourhood a constant along the streamlines and is here equal to the "surface stream function".

Consider now the case $\lambda \gg 1$.

Then the approximation formula for the streamlines is

$$\zeta = e^{-\psi}\cdot\chi^\lambda. \quad (13)$$

The origin is a so called nodal point for the differential equation and the streamlines have all as a common tangent the line $\zeta = 0$. Because of the large value of λ the raccordance is of very high order. Then it is seen, that along a streamline the value of ζ in the neighbourhood of the origin is extremely small against χ and hence it is permitted to neglect those values of ζ against χ for all streamlines except those, where $-\psi$ is very large. It follows, that if the differential equations are solved by power series expansions, the terms containing ζ may all be neglected against the terms containing χ in the neighbourhood of the origin.

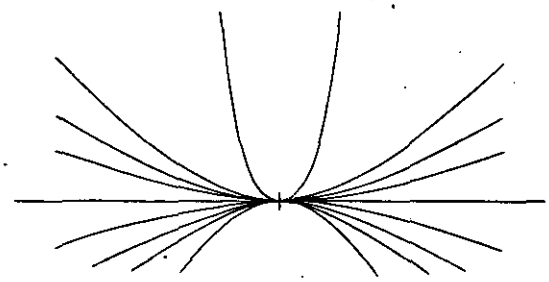

Fig. 1

But then σ and N may be considered as functions of χ only and the partial differential equations become ordinary differential equations. In order to obtain these the partial differential equations must be transformed into the coordinates χ and ζ.

From the transformation formulae

$$\varphi_\chi = r\chi, \quad \psi_\chi = \lambda/\chi,$$
$$\varphi_\zeta = \lambda r\zeta, \quad \psi_\zeta = -1/\zeta, \quad (14)$$

and the inverse formulae

$$\chi_\varphi\,\frac{r\chi}{T}\qquad, \quad \zeta_\varphi = \frac{r\lambda\zeta}{T},$$
$$\chi_\psi\,\frac{\lambda r\zeta}{T}\;.\,r\chi\zeta, \quad \zeta_\psi = -\frac{r\chi}{T}\,.\,r\chi\zeta, \quad (15)$$

it follows easily that

$$T_\varphi = \frac{2\,r(\chi^2 + \lambda^3\zeta^2)}{\chi^2 + \lambda^2\zeta^2},$$
$$T_\psi = -\frac{2\,r^2(\lambda-1)\lambda\,.\,\chi^2\zeta^2}{\chi^2 + \lambda^2\zeta^2}. \quad (16)$$

Further the form of the function ρ in the origin can be determined from the definition

$$\frac{\partial\psi}{\partial\chi} = -\sqrt{\rho g}\,\frac{\partial\varphi}{\partial\zeta},$$
$$\frac{\partial\psi}{\partial\zeta} = \sqrt{\rho g}\,\frac{\partial\varphi}{\partial\chi}, \quad (17)$$

which yields, as $g = 1$

$$\sqrt{\rho} = -\frac{1}{r\chi\zeta}. \quad (18)$$

Then

$$\sqrt{\rho}\,T_\psi = \frac{2\,r\lambda(\lambda-1)\chi\zeta}{\chi^2 + \lambda^2\zeta^2}, \quad T_\varphi = \frac{2\,r(\chi^2 + \lambda^3\zeta^2)}{\chi^2 + \lambda^2\zeta^2} \quad (19)$$

and

$$\Lambda = \frac{1}{2}\,T_\varphi\,\sigma = \frac{r(\chi^2 + \lambda^3\zeta^2)}{\chi^2 + \lambda^2\zeta^2}\,\sigma,$$
$$M = \frac{1}{2}\,\rho^{1/2}\,T_\psi\,\sigma = \frac{r\lambda(\lambda-1)\chi\zeta}{\chi^2 + \lambda^2\zeta^2}\,\sigma. \quad (20)$$

Hence it is seen, that in the origin M goes to zero like $\frac{\chi\zeta}{T}$ or $\frac{1}{T\sqrt{\rho}}$. As this denotes the order of the velocity component u_2 in the origin, a new unknown function τ is introduced by

$$\tau = \frac{T\sqrt{\rho}}{r^2} N. \tag{21}$$

Putting further

$$\mathfrak{M} = \frac{T\sqrt{\rho}}{r^2} M, \tag{22}$$

both τ and $\mathfrak{M}$ remain finite in the stagnation point.

Then the equations (5.9) and (5.10) take the form

$$f^1\sigma_\varphi + f^2\sigma_\psi + \quad + g^2\tau_\psi = d, \tag{23}$$

$$F^1\sigma_\varphi + F^2\sigma_\psi + G^1\tau_\varphi + G^2\tau_\psi = D, \tag{24}$$

where the new symbols f^1, f^2, g^1, g^2, F^1, F^2, G^1, G^2 are defined by

$$f^1(\sigma) = a^1(\Lambda) = 0.289\,430 + 0.022\,005\,\Lambda - 0.018\,990\,\Lambda^2,$$

$$f^2(\sigma,\tau) = \sqrt{\rho}\,a^2 = \frac{r^2}{T}[0.205\,372\,\tau + 0.111\,483\,\mathfrak{M} - 0.066\,957\,\Lambda\,\tau - 0.018\,990\,\Lambda\,\mathfrak{M}]; \tag{25}$$

$$g^1 = b^1 = 0,$$

$$g^2(\sigma) = b^2 = \sigma\,(0.410\,744 - 0.044\,638\,\Lambda),$$

and

$$F^1 = \frac{T\sqrt{\rho}\,A^1}{r^2} = -0.066\,957\,\Lambda\,\tau - 0.018\,990\,\Lambda\,\mathfrak{M} - 0.089\,478\,\mathfrak{M} - 0.294\,628\,\tau, \tag{26}$$

$$F^2 = \frac{T\rho\,A^2}{r^2} = -0.156\,664\,\tau^2 - 0.133\,914\,\mathfrak{M}\,\tau - 0.018\,990\,\mathfrak{M}^2,$$

$$G^1(\sigma) = B^1 = \sigma(-0.589\,256 - 0.044\,638\,\Lambda),$$

$$G^2(\sigma,\tau) = \sqrt{\rho}\,B^2 = \sigma(-0.626\,656\,\tau - 0.089\,276\,\mathfrak{M}),$$

where Λ, $\mathfrak{M}$ and σ are related by

$$\Lambda = \frac{1}{2} T_\varphi\,\sigma, \tag{27}$$

$$\mathfrak{M} = \frac{1}{2}\frac{\rho T_\psi}{r^2}\sigma. \tag{28}$$

The right hand sides of the equation are:

$$d = \frac{\gamma}{T} + \gamma^1\frac{\rho_\varphi}{\rho} - \gamma^{11}T_{\varphi\varphi} - \gamma^{12}\sqrt{\rho}\,T_{\varphi\psi} - \gamma^{22}\sqrt{\rho}\,(\sqrt{\rho}\,T_\psi)_\psi + g^2\frac{r^2}{T}\tau\left\{\frac{T_\psi}{T} + \frac{\rho_\psi}{2\rho}\right\}, \tag{29}$$

$$D = \frac{\Gamma}{T} + \Gamma^1\frac{\rho_\varphi}{\rho} - \Gamma^{11}T_{\varphi\varphi} - \Gamma^{21}(\sqrt{\rho}\,T_\psi)_\varphi - \Gamma^{22}\sqrt{\rho}\,(\sqrt{\rho}\,T_\psi)_\psi + G^1\tau\left\{\frac{T_\varphi}{T} + \frac{\rho_\varphi}{2\rho}\right\} + \frac{r^2G^2}{T}\tau\left\{\frac{T_\psi}{T} + \frac{\rho_\psi}{2\rho}\right\}, \tag{30}$$

where

$$\gamma = 2\left[0.752\,254 - 0.665\,556\,\Lambda + 0.059\,652\,\Lambda^2 + 0.003\,798\,\Lambda^3 + \{0.156\,664\,\tau^2\Lambda + 0.044\,638\,\Lambda\,\mathfrak{M}\,\tau + 0.003\,798\,\Lambda\,\mathfrak{M}^2\}\cdot\frac{r^2}{T^2\rho}\right],$$

$$\gamma^1 = \left[0.289\,430 + 0.007\,335\,\Lambda - 0.003\,798\,\Lambda^2 + \{0.156\,664\,\tau^2 + 0.044\,638\,\mathfrak{M}\,\tau + 0.003\,798\,\mathfrak{M}^2\}\frac{r^2}{T^2\rho}\right]\sigma, \tag{31}$$

$$\gamma^{11} = (0.007\,335 - 0.007\,596\,\Lambda)\sigma^2,$$

$$\gamma^{12} = (-0.022\,319\,\tau - 0.003\,798\,\mathfrak{M})\sigma^2\,\frac{r}{T\sqrt{\rho}},$$

$$\gamma^{22} = (0.037\,161 - 0.003\,798\,\Lambda)\sigma^2,$$

$$\Gamma = 2\left[\tau - 0.665\,556\,\mathfrak{M} + 0.059\,652\,\Lambda\,\mathfrak{M} + 0.003\,798\,\Lambda^2\mathfrak{M} + \{0.156\,664\,\mathfrak{M}\,\tau^2 + 0.044\,638\,\mathfrak{M}^2\tau + 0.003\,798\,\tau^3\}\frac{r^2}{T^2\rho}\right].$$

$$\Gamma^1 = 2\,\sigma(-0.294\,628\,\tau - 0.029\,826\,\mathfrak{M} - 0.022\,319\,\Lambda\,\tau - 0.003\,798\,\Lambda\,\mathfrak{M}), \tag{32}$$

$$\Gamma^{11} = \sigma^2(-0.022\,319\,\tau - 0.003\,798\,\mathfrak{M}),$$

$$\Gamma^{21} = \sigma^2(-0.029\,826 - 0.003\,798\,\Lambda),$$

$$\Gamma^{22} = \sigma^2(-0.044\,638\,\tau - 0.007\,596\,\mathfrak{M}).$$

The initial values of σ and τ now are obtained by requiring that the solutions on the streamlines in the neighbourhood of the origin are regular in χ and ζ, so that the derivatives in the stagnation point σ_χ, σ_ζ and τ_χ τ_ζ are finite. Then,

$$\sigma_\psi = \sigma_\chi\cdot r_{\chi\zeta}\cdot\frac{\lambda r\zeta}{T} - \sigma_\zeta\cdot\frac{r_\chi}{T}\,r_{\chi\zeta}; \tag{33}$$

$$\tau_\psi = \tau_\chi\cdot r_{\chi\zeta}\cdot\frac{\lambda r\zeta}{T} - \tau_\zeta\cdot\frac{r_\chi}{T}\cdot r_{\chi\zeta}. \tag{34}$$

These derivatives are of order ζ and can, on the streamlines with moderate values of ψ be negleted. Then the system reduces to a system of ordinary differential equations for $\sigma(\varphi)$ and $\tau(\varphi)$ which can be integrated numerically in the ordinary way.

$$\begin{cases} f^1\sigma_\varphi = d, & (35)\\ F^1\sigma_\varphi + G^1\tau_\varphi = D. & (36)\end{cases}$$

The numerical integration starts with assuming a power series expansion

$$\sigma = \sigma_0 + \sigma_1\varphi + \sigma_2\varphi^2 + \ldots\ldots,$$

$$\tau = \tau_0 + \tau_1\varphi + \tau_2\varphi^2 + \ldots\ldots, \tag{37}$$

the coefficients in which can be determined by substitution into the equations and, using the known expansions of the functions on the right hand side, equation of equal powers of φ. (In actual calculations, it is somewhat more convenient to use χ instead of φ as a variable. This will be discussed in the numerical example, to be discussed in a subsequent report). The solution of this

equation yields the value of σ and τ in a region, where the approximation is valid and hence these values on a certain curve in this region enclosing the stagnation point can be taken as initial values.

7 The method of characteristics.

The set of partial differential equations

$$l \equiv f^1\sigma_\varphi + f^2\sigma_\psi + g^1\tau_\varphi + g^2\tau_\psi = d, \quad (1)$$

$$L \equiv F^1\sigma_\varphi + F^2\sigma_\psi + G_1\tau_\varphi + G^2\tau_\psi = D. \quad (2)$$

where f^1, f^2, ... d and D are functions of σ and τ can be solved by the method of characteristics (ref. 10 Ch. V, ref. 11 Ch. II). Assume the values of σ and τ to be known on a curve $c\,\varphi(t), \psi(t)$. Then, denoting differentiation with respect to t by dots, along this curve

$$\dot{\sigma} = \sigma_\varphi\dot{\varphi} + \sigma_\psi\dot{\psi}, \quad (3)$$

$$\dot{\tau} = \tau_\varphi\dot{\varphi} + \tau_\psi\dot{\psi}. \quad (4)$$

The four equations (1) ... (4) generally determine the values of the derivatives σ_φ, σ_ψ, τ_φ and τ_ψ.

Now, following COURANT and FRIEDRICHS, introduce the characteristics as a new set of coordinates along C, so that the equations for the derivatives σ_α, σ_β, τ_α and τ_β assume a simpler form. Determine a set of multipliers λ and Λ, so that in

$$\lambda l + \Lambda L \equiv (\lambda f^1 + \Lambda F^1)\sigma_\varphi + (\lambda f^2 + \Lambda F^2)\sigma_\psi + (\lambda g^1 + \Lambda G^1)\tau_\varphi + (\lambda g^2 + \Lambda G^2)\tau_\psi$$

the derivatives of σ and τ are taken in the same direction α. Then

$$(\lambda f^1 + \Lambda F^1) : (\lambda f^2 + \Lambda F^2) = (\lambda g^1 + \Lambda G^1) : (\lambda g^2 + \Lambda G^2) = \varphi_\alpha : \psi_\alpha, \quad (5)$$

or

$$\lambda(f^1\psi_\alpha - f^2\varphi_\alpha) + \Lambda(F^1\psi_\alpha - F^2\varphi_\alpha) = 0,$$
$$\lambda(g^1\psi_\alpha - g^2\varphi_\alpha) + \Lambda(G^1\psi_\alpha - G^2\varphi_\alpha) = 0, \quad (6)$$

which admits only a solution for $\lambda : \Lambda$, if

$$\begin{vmatrix} f^1\psi_\alpha - f^2\varphi_\alpha & F^1\psi_\alpha - F^2\varphi_\alpha \\ g^1\psi_\alpha - g^2\varphi_\alpha & G^1\psi_\alpha - G^2\varphi_\alpha \end{vmatrix} = 0, \quad (7)$$

or

$$(f^2G^2 - F^2g^2)\varphi^2{}_\alpha - (f^1G^2 + f^2G^1 - F^2g^1 - F^1g^2)\varphi_\alpha\psi_\alpha + (f^1G^1 - F^1g^1)\psi^2{}_\alpha = 0. \quad (8)$$

Then the characteristic directions α and β are found from

$$\psi_\alpha = \rho_\alpha\varphi_\alpha,$$
$$\psi_\beta = \rho_\beta\varphi_\beta, \quad (9)$$

where ρ_α and ρ_β are the roots of the quadratic equation

$$(f^1G^1 - F^1g^1)\rho^2 - (f^1G^2 + f^2G^1 - F^2g^1 - F^1g^2)\rho + (f^2G^2 - F^2g^2) = 0. \quad (10)$$

From (6) then follows the ratio λ/Λ along the α and β characteristics and the differential equations become

$$(\lambda_\alpha f^1 + \Lambda_\alpha F^1)(\varphi_\alpha\sigma_\varphi + \sigma_\psi\psi_\alpha) + (\lambda_\alpha g^1 + \Lambda_\alpha G^1)(\tau_\varphi\varphi_\alpha + \tau_\psi\psi_\alpha) = (\lambda_\alpha d + \Lambda_\alpha D)\varphi_\alpha,$$

and similarly for the β equation. These equations then finally become

$$(f^1F^2 - f^2F^1)\sigma_\alpha + \{(f^1G^1 - F^1g^1)\rho_\alpha + g^1F^2 - f^2G^1\}\tau_\alpha = \{(f^1D - F^1d)\rho_\alpha + (F^2d - f^2D)\}\varphi_\alpha, \quad (11)$$

$$(f^1F^2 - f^2F^1)\sigma_\beta + \{(f^1G^1 - F^1g^1)\rho_\beta + g^1F^2 - f^2G^1\}\tau_\beta = \{(f^1D - F^1d)\rho_\beta + (F^2d - f^2D)\}\varphi_\beta. \quad (12)$$

Now, it is shown in ref. 10, Ch. V, that in the coordinates α and β the boundary value problem with given values of σ and τ along a curve in the α, β plane is uniquely solvable.

This fact being established, a finite difference method can be derived which enables a stepwise, approximative solution of the boundary value problem.

Assume, that along a curve in the φ, ψ plane in a row of points $P_{n,m}$ $(\varphi_{n,m}, \psi_{n,m})$, $m = \text{const.}$ the values of α, β, σ and τ are known. Then the coefficients in the equations are known and the characteristic directions can be calculated from (10).

The next row of points is then determined as

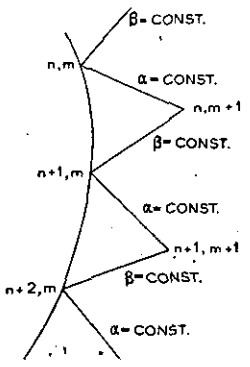

Fig. 2

the intersection of characteristic lines $\alpha = \text{const.}$, $\beta = \text{const.}$ from successive points

$$P_{n,m},\ P_{n+1,m}.$$

Using only first order finite difference approximation the equations for the point $P_{n,m+1}$ become

$$\frac{\psi_{n,m+1} - \psi_{n,m}}{\varphi_{n,m+1} - \varphi_{n,m}} = \rho_\beta\ (\sigma, \tau, \varphi, \psi)_{n,m},$$
$$\frac{\psi_{n,m+1} - \psi_{n+1,m}}{\varphi_{n,m+1} - \varphi_{n,m}} = \rho_\alpha\ (\sigma, \tau, \varphi, \psi)_{n,m}, \quad (13)$$

and the increments of φ and ψ can be solved, using the known values of the differences $\varphi_{n,m} - \varphi_{n+1,m}$ and $\psi_{n,m} - \psi_{n+1,m}$.

$$\varphi_{n,m+1} - \varphi_{n,m} = \frac{\psi_{n+1,m} - \psi_{n,m}}{\rho_\beta - \rho_\alpha} - \frac{\rho_\alpha}{\rho_\beta - \rho_\alpha} \cdot (\varphi_{n+1,m} - \varphi_{n,m}),$$

$$\psi_{n,m+1} - \psi_{n,m} = \frac{\rho_\beta}{\rho_\beta - \rho_\alpha} (\psi_{n+1,m} - \psi_{n,m}) - \frac{\rho_\alpha \rho_\beta}{\rho_\beta - \rho_\alpha} (\varphi_{n+1,m} - \varphi_{n,m}). \quad (14)$$

Then the values of $\sigma_{n,m+1}$ and $\tau_{n,m+1}$ can be determined by the use of eqs (11) and (12)

$$(f^1F^2 - f^2F^1)(\sigma_{n,m+1} - \sigma_{n+1,m}) + \{(f^1G^1 - F^1g^1)\rho_\alpha + g^1F^2 - f^2G^1\}(\tau_{n,m+1} - \tau_{n+1,m}) = \{(f^1D - F^1d)\rho_\alpha + (F^2d - f^2D)\}(\varphi_{n,m+1} - \varphi_{n+1,m}), \quad (15)$$

$$(f^1F^2 - f^2F^1)(\sigma_{n,m+1} - \sigma_{n,m}) + \{(f^1G^1 - F^1g^1)\rho_\beta + g^1F^2 - f^2G^1\}(\tau_{n,m+1} - \tau_{n,m}) = \{(f^1D - F^1d)\rho_\beta + (F^2d - f^2D)\}(\varphi_{n,m+1} - \varphi_{n,m}). \quad (16)$$

In actual calculations, the free stream flow is only given in terms of the curvilinear coordinates x^1, x^2 on the surface and hence these coordinates must also be expressed into the values of ψ and φ in order to calculate the new values of the coefficients in the following row of points. ψ is defined by the differential equation

$$U^1 \frac{\partial \psi}{\partial x^1} + U^2 \frac{\partial \psi}{\partial x^2} = 0, \quad (16a)$$

which also has to be solved.

Suppose, along a curve $x^1(s), x^2(s)$ the values of $\psi(s)$ and $\varphi(s)$ are known (this curve is later on identified with the m^{th} row of points).

Then:

$$\frac{\partial \psi}{\partial s} = \frac{\partial \psi}{\partial x^1} \cdot \frac{\partial x^1}{\partial s} + \frac{\partial \psi}{\partial x^2} \cdot \frac{\partial x^2}{\partial s}, \quad (17)$$

which serves together with (16a) to determine the differential quotients $\frac{\partial \psi}{\partial x^1}$ and $\frac{\partial \psi}{\partial x^2}$ along the curve.

Introducing $\Delta_1 = U^2 \frac{\partial x^1}{\partial s} - U^1 \frac{\partial x^2}{\partial s}$ the result is

$$\frac{\partial \psi}{\partial x^1} = \frac{U^2}{U^2 \frac{\partial x^1}{\partial s} - U^1 \frac{\partial x^2}{\partial s}} \cdot \frac{\partial \psi}{\partial s} = \frac{U^2}{\Delta_1} \cdot \frac{\partial \psi}{\partial s},$$

$$\frac{\partial \psi}{\partial x^2} = \frac{-U^1}{U^2 \frac{\partial x^1}{\partial s} - U^1 \frac{\partial x^2}{\partial s}} \cdot \frac{\partial \psi}{\partial s} = \frac{-U^1}{\Delta_1} \cdot \frac{\partial \psi}{\partial s}. \quad (18)$$

supposing that $\Delta_1 = U^2 \frac{\partial x^1}{\partial s} - U^1 \frac{\partial x^2}{\partial s} \neq 0$, which means that the initial curve does not touch a streamline. Then, proceeding in another direction the increments of φ and ψ are related to the increments of x^1 and x^2 by

$$\delta x^1 = \frac{\partial x^1}{\partial \varphi} \cdot \delta\varphi + \frac{\partial x^1}{\partial \psi} \cdot \delta\psi,$$

$$\delta x^2 = \frac{\partial x^2}{\partial \varphi} \cdot \delta\varphi + \frac{\partial x^2}{\partial \psi} \cdot \delta\psi, \quad (19)$$

where $\frac{\partial x^1}{\partial \varphi}$, $\frac{\partial x^1}{\partial \psi}$, $\frac{\partial x^2}{\partial \varphi}$ and $\frac{\partial x^2}{\partial \psi}$ can be expressed into $U_1 = \frac{\partial \varphi}{\partial x^1}$, $U_2 = \frac{\partial \varphi}{\partial x^2}$, U^1, U^2 and the known derivatives with respect to s.

$$\frac{\partial x^1}{\partial \varphi} = \frac{1}{\Delta_2} \cdot \frac{\partial \psi}{\partial x^2}, \qquad \frac{\partial x^1}{\partial \psi} = -\frac{U^2}{\Delta_2},$$

$$\frac{\partial x^2}{\partial \varphi} = -\frac{1}{\Delta_2} \cdot \frac{\partial \psi}{\partial x^1}; \qquad \frac{\partial x^2}{\partial \psi} = \frac{U_1}{\Delta_2}, \quad (20)$$

where

$$\Delta_2 = U_1 \frac{\partial \psi}{\partial x^2} - U_2 \frac{\partial \psi}{\partial x^1} = -\frac{U_1U^1 + U_2U^2}{\Delta_1} \cdot \frac{\partial \psi}{\partial s} = -\frac{T}{\Delta_1} \cdot \frac{\partial \psi}{\partial s}. \quad (21)$$

Then the increments are

$$\delta x^1 = \frac{\partial x^1}{\partial \varphi} \cdot \delta\varphi + \frac{\partial x^1}{\partial \psi} \delta\psi = \frac{1}{\Delta_2}\left[-\frac{U^1}{\Delta_1} \cdot \frac{\partial \psi}{\partial s} \cdot \delta\varphi - U_2 \cdot \delta\psi\right],$$

$$\delta x_2 = \frac{\partial x^2}{\partial \varphi} \cdot \delta\varphi + \frac{\partial x^2}{\partial \psi} \delta\psi = \frac{1}{\Delta_2}\left[-\frac{U^2}{\Delta_1} \cdot \frac{\partial \psi}{\partial s} \cdot \delta\varphi + U_1 \cdot \delta\psi\right]. \quad (22)$$

Applying these formulae to the case, considered here, the parameter s is to be replaced by the index n and the formulae for the new values of the coordinates x^1 and x^2 become:

$$x^1_{n,m+1} - x^1_{n,m} = \frac{1}{T}\left[U^1(\varphi_{n,m+1} - \varphi_{n,m}) + U_2(\psi_{n,m+1} - \psi_{n,m}) \cdot \frac{U^2(x^1_{n+1,m} - x^1_{n,m}) - U^1(x^2_{n+1,m} - x^1_{n,m})}{\psi_{n+1,m} - \psi_{n,m}}\right],$$

$$x^2_{n,m+1} - x^2_{n,m} = \frac{1}{T}\left[U^2(\varphi_{n,m+1} - \varphi_{n,m}) - U_1(\psi_{n,m+1} - \psi_{n,m}) \cdot \frac{U^2(x^1_{n+1,m} - x^1_{n,m}) - U^1(x^2_{n+1,m} - x^1_{n,m})}{\psi_{n+1,m} - \psi_{n,m}}\right]. \quad (23)$$

For the new values of x^1 and x^2 on the row $m+1$ the values of the coefficients in the equation can be determined and the calculation can proceed. It lies at hand, that second order difference formulae deliver more accurate results, but for a first calculation these formulae are sufficient.

Appendix.

Calculation of some integrals.

$$f=\frac{4}{3\sqrt{\pi}}\int_0^{\eta} e^{-y^2}(1+y^2)dy,$$

$$1-f=\frac{4}{3\sqrt{\pi}}\int_{\eta}^{\infty} e^{-y^2}(1+y^2)dy,$$

$$g=\frac{2}{3\sqrt{\pi}}\int_{\eta}^{\infty} e^{-y^2}(1+y^2)dy-\frac{1}{2}e^{-\eta^2}=$$

$$=\frac{1}{2}(1-f-e^{-\eta^2}),$$

$$h=\eta e^{-\eta^2}.$$

$$\int_0^{\infty}(1-f)d\eta=\frac{4}{3\sqrt{\pi}}\int_0^{\infty}d\eta\int_{\eta}^{\infty}e^{-y^2}(1+y^2)dy=$$

$$=\frac{4}{3\sqrt{\pi}}=0.752\,253.$$

$$\int_0^{\infty} g d\eta=\frac{1}{2}\int_0^{\infty}(1-f)d\eta-\frac{1}{2}\int_0^{\infty}e^{-\eta^2}d\eta=\frac{2}{3\sqrt{\pi}}-$$

$$-\frac{1}{4}\sqrt{\pi}=-0.0669871.$$

$$\int_0^{\infty} h d\eta=\int_0^{\infty}e^{-\eta^2}\,\eta d\eta=\frac{1}{2}=0.5.$$

$$\int_0^{\infty}(1-f)f d\eta=$$

$$=\frac{16}{9\pi}\int_0^{\infty}d\eta\int_{\eta}^{\infty}e^{-y^2}(1+y^2)dy.$$

$$\int_0^{\eta}e^{-z^2}(1+z^2)dz=\frac{16}{9\pi}\left\{\int_0^{\infty}e^{-\eta^2}(1+\eta^2)\eta d\eta\cdot\right.$$

$$\int_0^{\eta}e^{-z^2}(1+z^2)dz-$$

$$\left.-\int_0^{\infty}e^{-\eta^2}(1+\eta^2)\eta d\eta\int_{\eta}^{\infty}e^{-y^2}(1+y^2)dy\right\}.$$

introduce polar coordinates

$$z \text{ or } y=r\cos\theta,\ \eta=r\sin\theta.$$

Then

$$\frac{9\pi}{16}\cdot\int_0^{\infty}(1-f)f d\eta=$$

$$=\int_0^{\infty}\int_{\pi/4}^{\pi/2}e^{-r^2}(1+r^2+r^4\cos^2\theta\sin^2\theta)\cdot$$

$$\cdot r^2\sin\theta\,dr d\theta-$$

$$-\int_0^{\infty}\int_0^{\pi/4}e^{-r^2}(1+r^2+r^4\cos^2\theta\sin^2\theta)\cdot$$

$$\cdot r^2\sin\theta\,dr d\theta=$$

$$=\frac{5}{8}\sqrt{\pi}\cdot\frac{1}{2}\sqrt{2}+\frac{15}{16}\sqrt{\pi}\,\frac{7}{60\sqrt{2}}-$$

$$-\frac{5}{8}\sqrt{\pi}\cdot\left(1-\frac{1}{\sqrt{2}}\right)-$$

$$-\frac{15}{16}\sqrt{\pi}\cdot\left(\frac{2}{15}-\frac{7}{60\sqrt{2}}\right)=$$

$$=\frac{47-24\sqrt{2}}{32}\sqrt{\frac{\pi}{2}}.$$

$$\int_0^{\infty}(1-f)f d\eta=\frac{47-24\sqrt{2}}{18\sqrt{2\pi}}=0.289\,430.$$

$$\int_0^{\infty}(1-2f)g d\eta=\frac{1}{2}\int_0^{\infty}(1-2f)\,(1-f-e^{-\eta^2})\,d\eta=$$

$$=\frac{1}{2}\int_0^{\infty}(1-f)d\eta-\int_0^{\infty}(1-f)f d\eta-$$

$$-\int_0^{\infty}(1-f)e^{-\eta^2}\,d\eta+\frac{1}{2}\int_0^{\infty}e^{-\eta^2}d\eta.$$

Now

$$\int_0^{\infty}(1-f)e^{-\eta^2}d\eta=$$

$$=\frac{4}{3\sqrt{\pi}}\int_0^{\infty}e^{-\eta^2}d\eta\int_{\eta}^{\infty}e^{-y^2}(1+y^2)dy=$$

$$=\frac{4}{3\sqrt{\pi}}\int_0^{\infty}\int_0^{\pi/4}e^{-r^2}(1+r^2\cos^2\theta)\cdot r dr d\theta=$$

$$=\frac{4}{3\sqrt{\pi}}\left(\frac{\pi}{8}+\frac{\pi}{16}+\frac{1}{8}\right)=\frac{3\pi+2}{12\sqrt{\pi}},$$

and

$$\int_0^{\infty}(1-2f)g d\eta=\frac{2}{3\sqrt{\pi}}-\frac{(47-24\sqrt{2})}{18\sqrt{2\pi}}-$$

$$-\frac{3\pi+2}{12\sqrt{\pi}}+\frac{1}{4}\sqrt{\pi}=$$

$$=\frac{-94+66\sqrt{\pi}}{36\sqrt{2\pi}}=-0.007.335.$$

$$\int_0^{\infty}g^2 d\eta=\frac{1}{4}\int_0^{\infty}(1-f)^2 d\eta-$$

$$-\frac{1}{2}\int_0^{\infty}(1-f)e^{-\eta^2}d\eta+\frac{1}{4}\int_0^{\infty}e^{-2\eta^2}d\eta=$$

$$=\frac{1}{4}\int_0^{\infty}(1-f)d\eta-\frac{1}{4}\int_0^{\infty}(1-f)f d\eta-$$

$$-\frac{1}{2}\int_0^{\infty}(1-f)e^{-\eta^2}d\eta+\frac{1}{4}\int_0^{\infty}e^{-2\eta^2}d\eta=$$

$$=\frac{1}{3\sqrt{\pi}}-\frac{47-24\sqrt{2}}{72\sqrt{2\pi}}-\frac{3\pi+2}{24\sqrt{\pi}}+$$

$$+\frac{1}{8}\sqrt{\frac{\pi}{2}}=\frac{84-47\sqrt{2}}{144\sqrt{\pi}}-\frac{2-\sqrt{2}}{16}\sqrt{\pi}=$$

$$=0.0037975.$$

$$\int_0^\infty (1-f)h\,d\eta = $$

$$= \frac{4}{3\sqrt{\pi}} \int_0^\infty \eta e^{-\eta^2}\,d\eta \int_\eta^\infty e^{-y^2}\,(1+y^2)\,dy =$$

$$= \frac{4}{3\sqrt{\pi}} \int_0^\infty \int_0^{\pi/4} e^{-r^2}(1 + r^2\cos^2\theta) r^2 \sin\theta\, dr\, d\theta =$$

$$= \frac{4}{3\sqrt{\pi}} \left\{ \frac{1}{4}\sqrt{\pi}\cdot\left(1-\frac{1}{2}\sqrt{2}\right) + \right.$$

$$\left. + \frac{3}{8}\sqrt{\pi}\cdot\frac{1}{3}\left(1-\frac{1}{4}\sqrt{2}\right)\right\} =$$

$$= \frac{12-5\sqrt{2}}{24} = 0.205\,372.$$

$$\int_0^\infty (1-f)g\,.\,d\eta = \frac{1}{2}\int_0^\infty (1-f)^2 d\eta -$$

$$- \frac{1}{2}\int_0^\infty (1-f)e^{-\eta^2}\,d\eta = \frac{1}{2}\int_0^\infty (1-f)\,d\eta -$$

$$- \frac{1}{2}\int_0^\infty (1-f)f\,d\eta - \frac{1}{2}\int_0^\infty (1-f)e^{-\eta^2}\,d\eta =$$

$$= \frac{2}{3\sqrt{\pi}} - \frac{47-24\sqrt{2}}{36\sqrt{2\pi}} - \frac{3\pi+2}{24\sqrt{\pi}} =$$

$$= \frac{90\sqrt{2}-94-9\pi\sqrt{2}}{72\sqrt{2\pi}} = -0.037\,161.$$

$$\int_0^\infty gh\,d\eta = \frac{1}{2}\int_0^\infty (1-f)h\,d\eta - \frac{1}{2}\int_0^\infty e^{-2\eta^2}\,\eta\,d\eta =$$

$$= \frac{12-5\sqrt{2}}{48} - \frac{1}{8} = \frac{6-5\sqrt{2}}{48} = -0.022\,314.$$

$$\int_0^\infty h^2 d\eta = \int_0^\infty e^{-2\eta^2}\,\eta^2 d\eta = \frac{1}{8}\sqrt{\frac{\pi}{2}} = 0.156\,664.$$

References.

1. Prandtl, L. On boundary layers in threedimensional flow. M. A. P. Völkenrode, P. B. 39652, 6 August 1946. Also: Festschrift: Albert Betz zum 60. Geburtstag, 25-12-1945, *Gattingen*, p. 134.
2. Tetervin, N. Boundary-layer *momentum equations for* threedimensional flow. N. A. C. A. Tech. Note 1479, 1947.
3. Sears, W. R. The *boundary layer of yawed cylinders.* Journal of the Aeron. Sciences, Vol. 15, 1948, p. 49—52.
4. Wild, J. M. The Boundary layer of a yawed infinite wing. Journal Aeron. Sciences, 1949, Vol. 16, p. 41.
5. Von Karman, T. Ueber laminare und turbulente Reibung. Z. A. M. M., Vol. 1, 1921, p. 235.
6. Timman, R. A one parameter method for the calculation of laminar boundary layers. Report F 35. Nat. Aeron. Res. Lab., Amsterdam, 1948.
7. Von Karman, T. and Millikan, C. B. On the theory of laminar boundary layers involving separation. N. A. C. A. Report 504, 1934.
8. Levi Civita, T. The absolute differential calculus. English translation, Blackie and Son, 1947.
9. Michael, A. D. Matrix and Tensor Calculus. Galcit Aeron. Series. John Wiley, 1948.
10. Courant, R. and Hilbert, D. Methoden der Mathematischen Physik, Band II, Springer, 1937.
11. Courant, R. and Friedrichs, K. O. Supersonic flow and shock waves. Interscience Publishers, 1947.

Completed, 24th Aug. 1950.

REPORT F. 76.

A Generalization of Prandtl's Equation

by

Dr. A. VAN HEEMERT.

Contents.

1 Introduction.

In a previous report [1] a method has been given for the solution of problems concerning lifting surfaces. This method, whose practical application (compare [2]) involves fairly elaborate calculations, may have value for a final investigation of a given wing design, however, more convenient, simplified, procedures are urgently needed. Such procedures are, actually, available in the case of straight wings of large aspect ratio. They are incorporated in Prandtl's lifting line theory. For straight wings in oblique flow as well as for swept-back wings, this theory is known to be inadequate. It will be shown in the present report that the famous Prandtl equation can be generalized so that, in its generalized form, it becomes applicable to these important cases.

It is remarked, that the reader is assumed to be acquainted with the results of [1] from which the present analysis starts.

The reductions, required to obtain the final results, being very tedious, the next chapter will contain a survey of the basic principles and the results, using a minimum of mathematical formulae.

As to the adequacy of the generalized Prandtl equation, some results have been acquired which seem very promising. They refer to

(i) a wing of infinite span in oblique flow with periodic vorticity distribution in spanwise direction (compare [3]),

(ii) a plane elliptic wing under yaw; here a comparison with the results of Krienes [11], is possible (compare [4]).

2 Survey of principles and results.

2.1 *The fundamental formulae of linearized lifting surface theory.*

In linearized lifting surface theory for steady flow the region of the (thin) wing and that of the corresponding wake vortex sheet is replaced by two regions A and A' lying in a plane, the ξ, η plane. They bear a vorticity distribution $\vec{\Gamma}(\xi, \eta)$ with components $\Gamma_\xi(\xi, \eta)$ and $\Gamma_\eta(\xi, \eta)$ (compare fig. 1) inducing in the points of A a

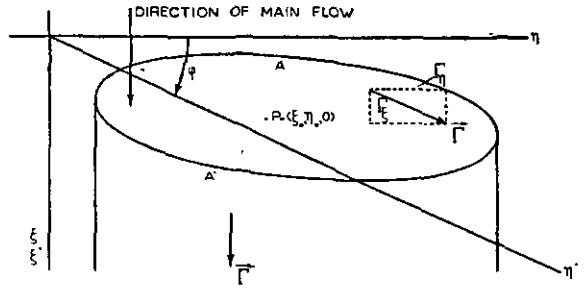

Figure 1.

downwash, v_ζ, which must be equal to the component of the main velocity normal to actual wing, hence,

$$v_\zeta = v_0 \,.\, \tan\alpha \approx v_0 \,.\, \alpha \qquad (2.1)$$

where α is the slope of the wing surface and v_0 is the magnitude of the main velocity.

The following conditions must be fulfilled:

(i) $\Gamma_\eta = 0$ on A',

(ii) $\dfrac{d\Gamma_\xi}{d\xi} + \dfrac{d\Gamma_\eta}{d\eta} = 0$ on $A + A'$ (expressing the fact that vortex lines are either closed or extend to infinity),

(iii) Γ_ξ is independent of ξ on A' (follows from (i) and (ii)),

(iv) a condition on the behaviour of $\vec{\Gamma}$ near the trailing (Kutta-Joukowski condition) and the leading edge, to be introduced later on by a suitable choice of the series representing Γ_η.

By the wellknown law of Biot and Savart (compare [1], [2])

$$4\pi v_\zeta(\xi_0, \eta_0, 0) = -$$

$$-\iint_A \frac{\xi-\xi_0}{r^3}\,\Gamma_\eta\,d\xi d\eta + \iint_{A+A'} \frac{\eta-\eta_0}{r^3}\,\Gamma_\xi\,d\xi d\eta \qquad (2.2)$$

where

$$r^2 = (\xi-\xi_0)^2 + (\eta-\eta_0)^2. \qquad (2.3)$$

The integrals are improper and, as explained in [1], the principal value in Cauchy's sense has to be taken (if necessary).

An alternative formula, which holds in the oblique reference system (ξ^*, η^*, ζ) (compare fig. 1), is

$$\frac{4\pi v_\zeta(\xi_0^*, \eta_0^*, 0)}{\cos^2\varphi} = -\iint_A \frac{\xi^*-\xi_0^*}{r^3}\,\Gamma_{\eta^*}d\xi^* d\eta^* +$$

$$+\iint_{A+A'} \frac{\eta^*-\eta_0^*}{r^3}\,\Gamma_{\xi^*}d\xi^* d\eta^*, \qquad (2.4)$$

where Γ_{η^*} and Γ_{ξ^*} are the components of $\vec{\Gamma}$ in the oblique system (compare [1]).

Finally, the pressure difference is, then, given by

$$\Pi = \rho v_0 \Gamma_\eta \qquad (2.5)$$

in rectangular, or

$$\Pi = \rho v_0 \Gamma_{\eta^*} \cos\varphi \qquad (2.6)$$

in oblique coordinates.

It is observed that (ii) implies

$$\Gamma_\xi(\xi,\eta) = -\frac{\partial}{\partial\eta}\int_{\xi_l(\eta)}^{\xi} \Gamma_\eta(\xi_1,\eta)\,d\xi_1 \qquad (2.7)$$

where

$$\xi = \xi_l(\eta)$$

is the equation of the leading edge.

2.2 *The Prandtl approximation for straight wings of large aspect ratio under zero yaw.*

In this case, considering the downwash in $P = (\xi_0, \eta_0, 0)$ (see figure 2), the vorticity components are decomposed

$$\Gamma_\eta(\xi,\eta) = \Gamma_\eta^{(1)}(\xi,\eta) + \Gamma_\eta^{(2)}(\xi,\eta),$$

$$\Gamma_\eta^{(1)}(\xi,\eta) = \Gamma_\eta(\xi,\eta_0) + (\eta-\eta_0)\frac{\partial\Gamma_\eta(\xi,\eta_0)}{\partial\eta}, \qquad (2.8)$$

$$\Gamma_\xi(\xi,\eta) = -\frac{d\Gamma(\eta)}{d\eta} + \left\{\Gamma_\xi(\xi,\eta) + \frac{d\Gamma(\eta)}{d\eta}\right\},$$

$$\Gamma(\eta) = \int_{\xi_l(\eta)}^{\xi_t(\eta)} \Gamma_\eta(\xi,\eta)\,d\xi, \qquad (2.9)$$

where $\xi = \xi_l(\eta)$ and $\xi = \xi_t(\eta)$ are the equations of the leading and trailing edges respectively. $\Gamma(\eta)$ is the circulation round the wing at section η, hence

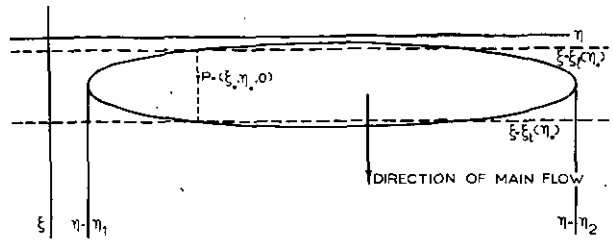

Figure 2.

$$-\frac{d\Gamma(\eta)}{d\eta} = \Gamma_{\xi,\ \text{wake}}. \qquad (2.10)$$

It is pointed out that $\Gamma_\eta^{(1)}(\xi,\eta)$ is assumed to be defined in the strip bounded by the dashed lines (fig. 2), elsewhere it is taken zero.

It will be shown that the downwash induced in P by Γ_η is approximately equal to the downwash of $\Gamma_\eta^{(1)}$, where $\Gamma_\eta^{(1)}$ is to be considered as defined on the whole strip mentioned above (from $\eta = -\infty$ to $\eta = +\infty$). It is, thereby, assumed that P does not lie near one of the wing tips. Indeed, considering the first integral of (2.2), substituting $\Gamma_\eta^{(2)}$ instead of Γ_η and integrating over the whole region where $\Gamma_\eta^{(2)}$ is, now, defined, this integral will be small: the integrand is, apart from a small subregion, of order $(\eta-\eta_0)^2$ near $\eta=\eta_0$ and of order $(\eta-\eta_0)^{-2}$ far from this chord. At least a first order term is, hence, obtained by replacing Γ_η by the distribution $\Gamma_\eta^{(1)}$ defined on the infinite strip between $\xi=\xi_l(\eta_0)$ and $\xi=\xi_t(\eta_0)$.

Now the antisymmetric part (with respect to $\eta=\eta_0$) of $\Gamma_\eta^{(1)}$ can, obviously, be cancelled at once, because the contributions of it due to the subregions at both sides of $\eta=\eta_0$ compensate each other. Hence, the downwash induced by the distribution Γ_η on A can approximately be represented by that induced by the two-dimensional distribution $\Gamma_\eta(\xi,\eta_0)$, i.e. by

$$-\frac{1}{4\pi}\int_{\xi_l(\eta_0)}^{\xi_t(\eta_0)}\int_{-\infty}^{\infty} \frac{\xi-\xi_0}{r^3}\,\Gamma_\eta(\xi,\eta_0)\,d\eta d\xi =$$

$$-\frac{1}{2\pi}\,\text{⨍}\!\!\!\!-\!\!\!\!\!\!\int_{\xi_l(\eta_0)}^{\xi_t(\eta_0)} \frac{\Gamma_\eta(\xi,\eta_0)}{\xi-\xi_0}\,d\xi$$

where $\text{⨍}\!\!\!\!-\!\!\!\!\!\!\int$ denotes the principal value of the considered integral.

It will, now, be shown that the second integral in (2.2) is, approximately, independent of the situation of P on the chord $\eta=\eta_0$. Indeed, substituting (2.9) and integrating with respect to ξ, where possible, this integral reduces to

$$-\oint_{SPAN}\frac{d\Gamma}{d\eta}\cdot\frac{d\eta}{\eta-\eta_0}+\oint_{SPAN}\frac{d\Gamma}{d\eta}\cdot\frac{\xi_l-\xi_0}{r_l(\eta-\eta_0)}\,d\eta+$$

$$+\iint_A\frac{\eta-\eta_0}{r^3}\left\{\Gamma_\xi+\frac{d\Gamma}{d\eta}\right\}d\xi d\eta. \quad (2.11)$$

The last two terms in this result are negligible with respect to the first. Actually, in all three integrals the regions near and at both sides of $\eta=\eta_0$ yield contributions which compensate each other, at least approximately, but for $|\eta-\eta_0|$ large (assuming, for the moment, $\frac{d\Gamma}{d\eta}$ and Γ_ξ to be bounded, which actually is not true, but which does not invalidate the result) the contributions to these integrals in the last two of them are small as compared with that in the first one. In fact, the integrand in the second integral is, in this case, of order $(\eta-\eta_0)^{-2}$ and so is that in the single integral emerging from the third one bij integrating first over ξ.

The first integral in (2.11) is retained. Its integrand is only of order $(\eta-\eta_0)^{-1}$ for $|\eta-\eta_0|$ large. It is hence large with respect to the integrands of all integrals which have, up till now, been cancelled. In fact the considered term is, except for a constant factor, the term of Prandtl's equation which contains an integral and which represents the induced downwash.

By the previous heuristic arguments the following result has, hence, been obtained:

$$4\pi v\zeta=-2\oint_{CHORD}\frac{\Gamma_\eta(\xi,\eta_0)}{\xi-\xi_0}\,d\xi-\oint_{SPAN}\frac{d\Gamma}{d\eta}\cdot\frac{d\eta}{\eta-\eta_0}, \quad (2.12)$$

which is simply Prandtl's equation. Assuming the expansion

$$\Gamma_\eta(\xi,\eta)=\frac{2}{l(\eta)}\left\{c_0(\eta)\cot\frac{\vartheta}{2}+\sum_{n=1}^{\infty}c_n(\eta)\sin n\vartheta\right\} \quad (2.13)$$

(compare the first part of appendix 3),

where $l(\eta)$ is the chord at the section η and ϑ the familiar chordwise parameter defined by

$$\xi-\xi_l(\eta)=\frac{l(\eta)}{2}(1-\cos\vartheta), \quad (2.14)$$

it follows that

$$\Gamma(\eta)=\pi\{c_0(\eta)+\tfrac{1}{2}c_1(\eta)\} \quad (2.15)$$

and

$$4\pi v\zeta=\frac{4\pi}{l(\eta_0)}\cdot\left\{c_0(\eta_0)-\sum_{n=1}^{\infty}c_n(\eta_0)\cos n\vartheta_0\right\}-$$

$$-\oint_{SPAN}\frac{d\Gamma}{d\eta}\cdot\frac{d\eta}{\eta-\eta_0}. \quad (2.16)$$

It is pointed out, that, though it might be expected that the applicability is restricted to points P far from the tips it is proved by practice, that no difficulties arise here. In fact the Prandtl equation is commonly used in a slightly other form, not to be given here, which contains only the complete circulation Γ as unknown. For the solution of that form of Prandtl's equation the wellknown Multhopp method uses sections lying very near to the tip (dependent upon the number of sections chosen).

2.3 *Generalization to straight wings under yaw.*

In the case of the straight wing in oblique flow heuristic arguments analogous to those used above

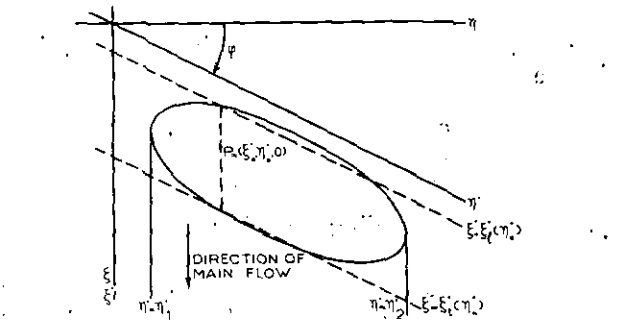

Figure 3.

will be employed. It is profitable to start from (2.4). A similar substitution as (2.8), viz.

$$\Gamma_{\eta^*}(\xi^*,\eta^*)=\Gamma_{\eta^*}{}^{(1)}(\xi^*,\eta_0{}^*)+\Gamma_{\eta^*}{}^{(2)}(\xi^*,\eta^*),$$

$$\Gamma_{\eta^*}{}^{(1)}=\Gamma_{\eta^*}(\xi^*,\eta_0{}^*)+(\eta^*-\eta^*)\frac{\partial\Gamma_{\eta^*}(\xi^*,\eta_0{}^*)}{\partial\eta^*} \quad (2.17)$$

in the first integral of (2.4) yields again the result that this integral can be approximated by replacing Γ_{η^*} simply by $\Gamma_{\eta^*}{}^{(1)}$, which depends linearly on the spanwise coordinate, and to integrate over the strip bounded by the dashed lines in figure 3. However, now the contribution of the part containing the spanwise gradient of Γ_{η^*} viz.

$$(\eta^*-\eta_0{}^*)\frac{\partial\Gamma_{\eta^*}(\xi^*,\eta_0{}^*)}{\partial\eta^*}$$

is not zero and must be determined and taken into account.

For the contribution yielded by the second integral in (2.4) a similar reduction can be given as for the corresponding integral in the case of zero yaw. Here also, no compensating effects due to the vorticity near and on both sides of the considered chord or its prolongation can be taken into account explicitly. Hence, here also an estimate for the effect due to this lack of compensation is necessary. Though, for the chordwise vorticity components, the situation is much more complicated than for the spanwise components, it may, here, already be stated that an acceptable approximation will be to deduce this estimate from the vorticity distribution $\Gamma_{\eta^*}{}^{(1)}$ on the above mentioned strip (extended at both sides to $\eta=\eta_0+\delta$ and $\eta=\eta_0-\delta$ respectively, where $\delta\gg l(\eta_0)$). How this can be done will be explained below. The final result is an equation very similar to Prandtl's equation (2.16) for zero yaw viz., with the same notations as above (and expressed in rectangular coordinates ξ,η),

$$4\pi v_\zeta = \frac{4\pi \sec\varphi}{l(\eta_0)}\left\{c_0(\eta_0) - \sum_{n=1}^{\infty} c_n(\eta_0)\cos n\vartheta_0\right\} + 2\pi\sin\varphi \sum_{n=1}^{\infty} e_n(\eta_0)\cos n\vartheta_0 - \pi\{c_0'(\eta_0) + \tfrac{1}{2}c_1'(\eta_0)\}\Phi(\varphi) - \int_{SPAN} K(\eta,\eta_0)\cdot\frac{d\Gamma}{d\eta}\,d\eta, \qquad (2.18)$$

where the $e_n(\eta_0)$ are simple linear expressions in the

$$c_n'(\eta_0) = \left[\frac{dc_n(y)}{dy}\right]_{y=y_0},$$

$\Phi(\varphi)$ is an elementary function of the angle of yaw φ (not depending on wing plan form) and $K(\eta,\eta_0)$ is a function of very simple structure, which contains only φ as parameter. In fact, different alternatives for this kernel will be considered below. This equation has to be considered as a genuine generalization of Prandtl's equation in the form (2.16). It contains, indeed, a line integral only and, as will be shown below, it reduces for $\varphi = 0$ to Prandtl's equation for the straight unyawed wing.

2.4 *Generalization to swept back wings.*

In this report only swept back wings of symmetrical plan form consisting of two straight parts, which join in the plane of symmetry, are considered. It is assumed that each of the mentioned parts has a large "aspect ratio".

In this case, practically the same reductions as used heuristically for a straight wing in oblique flow remain valid if the point P lies not near the root section. The main change in the previous result (2.18) is a replacement of $K(\eta,\eta_0)$ by another kernel which is nearly equally simple. Moreover, the influence of the spanwise components of the vorticity distribution on the wing-half on which P doesn't lie, must be taken into account. In fact, this influence, now, becomes of the same order as the contribution of the trailing vortices. It will be clear that it can be accounted for, approximately, by concentrating these components along e. g. the ¼ chord line and taking P also on this line (on the other wing-half). This, at least, will give a first estimate of the considered effect. Hence a corresponding term has to be added to the equation which expresses the downwash in P in the intensity of the vorticity distribution. Besides this, only the case of P lying on the root chord will be considered. Here the situation is much more difficult.

Assuming a development for Γ_η as given by (2.13) it is, first, necessary, to obtain an idea of the behaviour of the functions $c_n(\eta)$ near $\eta = 0$, the reference system being taken so that the root chord lies on the ξ-axis (see fig. 4). These functions must be such that Γ_ξ, which follows from Γ_η by means of (2.7), is continuous and, by virtue of the assumed symmetry, zero for $\eta = 0$.

This implies that the $c'_n(\eta)$ will, generally, be discontinuous for $\eta = 0$, as will be shown later on. The continuity of Γ_ξ for $\eta = 0$ means, geometrically, that the vortex lines on the wing cross the root chord perpendicular and have there, hence, a continuous tangent (except, perhaps, for a restricted number of singular points as e. g. the points on the leading and trailing

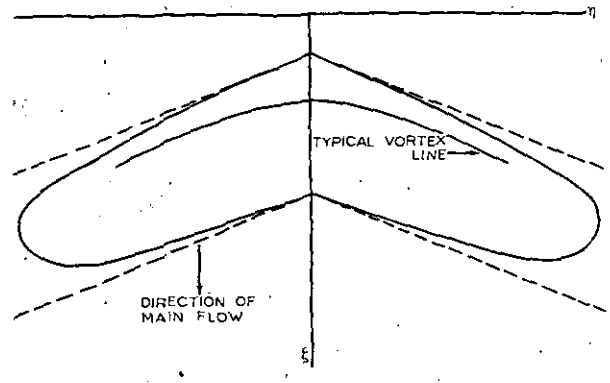

Figure 4.

edges). For the prolongation of the root chord, the condition that Γ_ξ is continuous means that

$$\left[\frac{d\Gamma(\eta)}{d\eta}\right]_{\eta=0} = \pi\{c_0'(+0) + \tfrac{1}{2}c_1'(+0)\} = 0.$$

Hence $c_0'(\eta) + \frac{1}{2}c_1'(\eta)$ must be continuous at $\eta = 0$ and its value there is zero. Finally it will appear to be necessary to impose the condition

$$c_0(0) = 0$$

in order to obtain a bounded downwash near the leading edge of the root chord.

With these conditions satisfied a similar procedure as discussed above for the straight yawed wing will be applied, viz. an estimate for the effect due to the lack of compensation present in this case is inferred from that for a vorticity distribution

$$\Gamma'_\eta(\vartheta,\eta) = \frac{2}{l(0)}\{c_0(0) + |\eta|\cdot c_0'(+0)\}\cot\frac{\vartheta}{2} + \sum_{n=1}^{\infty}\{c_n(0) + |\eta|\cdot c_n'(+0)\}\sin n\vartheta$$

and the corresponding (compare (2.7)) Γ_ξ-distribution, defined on the region bounded by the dashed lines in figure 4 (extending at both sides to some value $|\eta| = \delta$ where $\delta \gg l(0)$).

3 Prandtl's equation for straight yawed wings of large aspect ratio.

Let, figure 5, the angle of yaw be φ and let a left handed *) rectangular system of reference be given such that the x-axis points in the direction of the main stream, the z-axis points vertically downwards. Assume the following distribution for the y-components of the vorticity:

*) Erroneously this reference system has been termed "right handed" in the reports F. 51 en F. 58.

$$\Gamma_y = \frac{2}{l(y)} \left\{ c_0(y) \cot \vartheta/2 + \sum_{n=1}^{\infty} c_n(y) \sin n\vartheta \right\}, \tag{3.1}$$

so that, by (2.7) (compare [1] or [2]), on the wing,

$$\Gamma_x = -c_0'(y)(\vartheta + \sin\vartheta) - \\ - \tfrac{1}{2} c_1'(y)(\vartheta - \tfrac{1}{2}\sin 2\vartheta) - \\ - \tfrac{1}{2} \sum_{n=2}^{\infty} c_n'(y) \left\{ \frac{\sin(n-1)\vartheta}{n-1} - \frac{\sin(n+1)\vartheta}{n+1} \right\} \\ + [h'(y) - \tfrac{1}{2} l'(y) \cos\vartheta] \cdot \Gamma_y \tag{3.2}$$

where $l(y)$ represents the chord and

$$x = h(y) \tag{3.3}$$

is the equation of the mid-chord line.

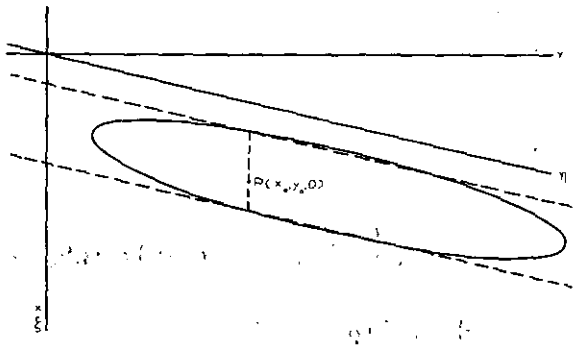

Figure 5.

In the oblique reference system (ξ, η, ζ), whose ξ- and ζ-axis coincide with the x- and z-axes respectively and whose η-axis lies in the direction of the straight wing, so that y and η-axis make an angle φ (compare figure 5),

$$\Gamma_\eta = \frac{2}{l(y)} \left\{ c_0(y) \cot \vartheta/2 + \sum_{n=1}^{\infty} c_n(y) \sin n\vartheta \right\} \sec\varphi \tag{3.4}$$

and

$$\Gamma_\xi = -c_0'(y)(\vartheta + \sin\vartheta) - \\ - \tfrac{1}{2} c_1'(y)(\vartheta - \tfrac{1}{2}\sin 2\vartheta) - \\ - \tfrac{1}{2} \sum_{n=2}^{\infty} c_n'(y) \left\{ \frac{\sin(n-1)\vartheta}{n-1} - \frac{\sin(n+1)\vartheta}{n+1} \right\} \\ + \{ h'(y) - \tfrac{1}{2} l'(y) \cos\vartheta - \tan\varphi \} \cos\varphi \cdot \Gamma_\eta. \tag{3.5}$$

The vorticity distribution in the wake is obviously given by

$$\Gamma_\eta = 0, \quad \Gamma_\xi = -\{ c_0'(y) + \tfrac{1}{2} c_1'(y) \} \pi. \tag{3.6}$$

Now, in accordance with the preliminary results of section 2.3, the following problem is discussed in Appendix I.

If a vorticity distribution on the region of the parallelogram with vertices $(0, -\delta)$, $(0, \delta)$, $(2, \delta)$ and $(2, -\delta)$ in the oblique reference system (ξ, η) (compare figure A.I.1) is given by

$$\Gamma_\eta = \bar{c}_0(\eta) \cot \vartheta/2 + \sum_{n=1}^{\infty} \bar{c}_n(\eta) \sin n\vartheta,$$

$$\bar{c}_n(\eta) = a_n + b_n\eta, \tag{3.7}$$

$$\Gamma_\xi = -b_0(\vartheta + \sin\vartheta) - \tfrac{1}{2} b_1(\vartheta - \tfrac{1}{2}\sin 2\vartheta) - \\ - \tfrac{1}{2} \sum_{n=2}^{\infty} b_n \left\{ \frac{\sin(n-1)\vartheta}{n-1} - \frac{\sin(n+1)\vartheta}{n+1} \right\} \tag{3.8}$$

and, on the corresponding wake region, by

$$\Gamma_\eta = 0 \quad \Gamma_\xi = -\pi(b_0 + \tfrac{1}{2} b_1), \tag{3.9}$$

determined the downwash distribution along the chord $\eta = 0$ provided that $\delta \gg 2$. The result proves to be

$$4\pi v_z = 2\pi \left\{ a_0 - \sum_{n=1}^{\infty} a_n \cos n\vartheta_0 \right\} + \\ + 2\pi \sin\varphi \sum_{n=1}^{\infty} e_n \cos n\vartheta_0 \\ - (b_0 + \tfrac{1}{2} b_1)\pi\Phi(\varphi) + \\ + 2\pi(b_0 + \tfrac{1}{2} b_1) \sin\varphi \ln 4\delta + O(\delta^{-2}), \tag{3.10}$$

where φ is the angle of yaw (see figure A.I.1),

$$\Phi(\varphi) = \ln \frac{1 + \sin\varphi}{1 - \sin\varphi} + 2 \sin\varphi \ln\cos\varphi - 2\sin\varphi$$

and (3.11)

$$e_1 = \tfrac{1}{2}(b_2 + 2b_0), \quad e_n = \frac{1}{2n}(b_{n+1} - b_{n-1}), \quad n \geqq 2. \tag{3.12}$$

This result is derived if the chord is 2. It is seen that, if the chord is l and if the distribution of the components Γ_η is represented by

$$\Gamma_\eta = \frac{2}{l} \left\{ \bar{c}_0(\eta) \cot\frac{\vartheta}{2} + \sum_{n=1}^{\infty} \bar{c}_n(\eta) \sin n\vartheta \right\}, \\ \bar{c}_n(\eta) = a_n + b_n\eta, \tag{3.13}$$

the distributions of Γ_η in the wake and of Γ_ξ on the wing and in the wake are, again, given by (3.8) and (3.9) and, further, that the downwash in $\eta = 0$, $\vartheta = \vartheta_0$ is, then,

$$4\pi v_z = 2\pi \cdot \frac{2}{l} \left\{ a_0 - \sum_{n=1}^{\infty} a_n \cos n\vartheta_0 \right\} + \\ + 2\pi \sin\varphi \sum_{n=1}^{\infty} e_n \cos n\vartheta_0 \\ - (b_0 + \tfrac{1}{2} b_1)\pi\Phi(\varphi) + \\ 2\pi(b_0 + \tfrac{1}{2} b_1) \sin\varphi \ln \frac{8}{l} \delta + O(\delta^{-2}). \tag{3.14}$$

The first term represents simply the two dimensional downwash for the distribution which is obtained if $\delta \to \infty$ and $b_n = 0$. The second term represents an effect which is typical for the influence of yaw. It includes induced camber. The other parts are constant along the chord.

This result is transferred to the general case considered in this chapter as follows: In accordance with chapter 2.3 all terms of the previous result (3.14) are, mutatis mutandis, retained ex-

cept for the last two. The term $O(\delta^{-2})$ is cancelled and the term

$$2 \sin \varphi \,.\, (b_0 + \tfrac{1}{2} b_1)\pi \ln \frac{8\,\delta}{l}, \qquad (3.14a)$$

which accounts, "roughly", for the influence of the trailing vortices, is first written as an integral and will, then, be transferred to the present, more general, case.

Write the considered term as

$$-(b_0 + \tfrac{1}{2} b_1)\pi \,.\, -2 \sin \varphi \,.\, \ln \frac{8\,\delta}{l}.$$

The first factor represents the vorticity intensity in the wake for the distribution determined by (3.13). The last factor is written as

$$f_{\varphi,\delta} = \int_{-\delta}^{\delta} \left(1 - \frac{\eta}{|\eta|} \sin \varphi\right) \frac{\dot{\eta} d\eta}{\eta^2 + {}^1/_{64}\, l^2}$$

or, alternatively, as

$$f_{\varphi,\delta} = \int_{-\delta}^{\delta} \left(1 - \frac{\eta}{|\eta|} \sin \varphi\right) \cdot \frac{\eta}{|\eta|} \frac{d\eta}{\sqrt{\eta^2 + {}^1/_{16}\, b^2}}$$

It is easily checked that in both cases the integrands are approximately

$$\left(1 - \frac{\eta}{|\eta|} \sin \varphi\right) \,.\, \dot{\eta}^{-1}$$

so that both integrals for bounds δ', δ'' which are either both positive or both negative and which are, further, in absolute value both $\gg l/8$ or $\gg l/4$ respectively, represent the downwash induced by the parts of the wake between $\eta = \delta'$ and $\eta = \delta''$.

In a general case, the strength of the trailing vortices is

$$-\{\, c_0'(\eta) + \tfrac{1}{2} c_1'(\eta) \,\}\, \pi,$$

and, therefore, the considered term is, writing down the results in rectangular coordinates (x, y), replaced by

$$-\pi \int_{-b}^{b} \left(1 - \frac{y - y_0}{|y - y_0|} \sin \varphi\right) \{\, c_0'(y) + \tfrac{1}{2} c_1'(y) \,\} \,.\, \frac{(y - y_0)\, dy}{(y - y_0)^2 + {}^1/_{64}\, l^2 \cos^2 \varphi} \qquad (3.15)$$

or

$$-\pi \int_{-b}^{b} \left(1 - \frac{y - y_0}{|y - y_0|} \sin \varphi\right) \{\, c_0'(y) + \tfrac{1}{2} c_1'(y) \,\} \,.\, \frac{y - y_0}{|y - y_0|} \frac{dy}{\sqrt{(y - y_0)^2 + {}^1/_{16}\, l^2 \cos^2 \varphi}} \qquad (3.16)$$

respectively. Here $y = y_0$ indicates the chord which bears the pivotal point, $l = l(y_0)$ and the wing is, further, assumed to lie between $y = +b$ and $y = -b$. It will be consistent with the approximations introduced thus far to replace the (straight) wing, considered here by a pseudo lifting line as indicated in figure 6. The final formula is obtained from the results of Appendix I by writing $\frac{2}{l(y_0)} c_n(y_0)$ for a_n, $c_n'(y_0)$ for b_n and by introducing the integral (3.15) or (3.16). Hence, if

$$e_1(y) = \tfrac{1}{2} \{\, c_2'(y) + 2\, c_0'(y) \,\},$$

$$e_n(y) = \frac{1}{2n} \{ c'_{n+1}(y) - c'_{n-1}(y) \} \quad n = 2, 3, \ldots,$$

and (3.17)

$$\Phi(\varphi) = ln \frac{1 + \sin \varphi}{1 - \sin \varphi} + 2 \sin \varphi \, ln \cos \varphi - 2 \sin \varphi, \qquad (3.18)$$

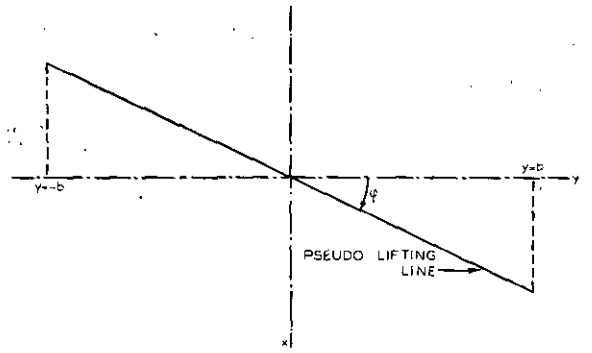

Figure 6.

$$4\pi v_z =$$

$$= 2\pi \sec \varphi \frac{2}{l(y_0)} \left\{ c_0(y_0) - \sum_{n=1}^{\infty} c_n(y_0) \cos n\vartheta_0 \right\} +$$

$$+ 2\pi \sin \varphi \sum_{n=1}^{\infty} e_n(y_0) \cos n\vartheta_0 -$$

$$- \pi \{\, c_0'(y_0) + \tfrac{1}{2} c_1'(y_0) \,\} \,.\, \Phi(\varphi)$$

$$- \pi \int_{-b}^{b} K(y, y_0) \{\, c_0'(y) + \tfrac{1}{2} c_1'(y) \,\}\, dy, \qquad (3.19)$$

where for $K(y, y_0)$ one of the kernels

$$K(y, y_0) =$$

$$= \left\{1 - \frac{y - y_0}{|y - y_0|} \sin \varphi\right\} \frac{y - y_0}{(y - y_0^2) + {}^1/_{64}\, l^2 \cos^2 \varphi} \qquad (3.20)$$

or

$$K(y, y_0) =$$

$$= \left\{\frac{y - y_0}{|y - y_0|} - \sin \varphi\right\} \frac{1}{\sqrt{(y - y_0)^2 + {}^1/_{16}\, l^2 \cos^2 \varphi}} \qquad (3.21)$$

can be taken.

If in (31.9) the Fourier expansion of v_z (which is given by the geometry of the wing) is introduced, this equation can be separated into a system of linear differential equations together with one integrodifferential equation.

Observe that if $\varphi = 0$, (3.19) reduces to

$$4\pi v_z = 2\pi \frac{2}{l(y_0)} \left\{ c_0(y_0) - \sum_{n=1}^{\infty} c_n(y_0) \cos n\vartheta_0 \right\} -$$

$$- \pi \int_{-b}^{b} K(y, y_0) \,.\, \{\, c_0'(y) + \tfrac{1}{2} c_1'(y) \,\}\, dy. \qquad (3.22)$$

It is, further, remarked that

$$\Phi(\varphi) = -\sin^3\varphi \cdot \sum_{n=1}^{\infty} \frac{1}{n(2n+1)} \sin^{2n-2}\varphi$$

as can easily be checked. Hence, as the series at the right hand side is convergent and

$$\sum_{n=1}^{\infty} \frac{1}{n(2n+1)} = 2 \sum_{n=1}^{\infty} \frac{1}{2n(2n+1)} = 2 \cdot (1 - ln\,2)$$

it follows that

$$|\Phi(\varphi)| \leqq 2\,(1 - ln\,2) \cdot \sin^3\varphi = 0.6137\ldots \cdot \sin^3\varphi$$

and especially

$$\Phi(0) = 0,$$

the last relation also being evident from the definition of $\Phi(\varphi)$.

Now, in this case ($\varphi = 0$),

$$K(y, y_0) = \frac{y - y_0}{(y - y_0)^2 + {}^1/_{64}\, l^2}$$

or

$$K(y, y_0) = \frac{y - y_0}{|y - y_0| \sqrt{(y - y_0) + {}^1/_{16}\, l^2}}$$

and it can be shown that the integral in (3.22) is an approximation of

$$\oint_{-b}^{b} \frac{c_0'(y) + \frac{1}{2} c_1'(y)}{y - y_0}\, dy,$$

which is the ordinary form of the integral which occurs in the Prandtl equation. This will be shown in more detail in Appendix 4. Another kernel will be considered in Appendix 5, which reduces exactly to the kernel of Prandtl's equation if $\varphi \to 0$.

It is pointed out, that applications of the equation (3.19) have been made (compare [3] and [4] with results which seem very satisfactory.

4 Approximative treatment of a symmetrical swept back wing.

The only case which will be considered in the present report is that of a swept back wing consisting of two straight parts which are symmetrical with respect to the median section of the complete wing. The aspect ratio of the wing is, again, assumed to be great and the chord only slowly varying along the span. Two fundamentally different positions of the pivotal point will be considered below. First the pivotal point is taken on one of the parts far from the median section and, of course, far from the tip. Afterwards the pivotal point is taken on the median section. The latter case is, as can be expected, by far the most complicated.

4.1 *Pivotal point far from median section.*

It will be obvious that, if the symmetrical parts are denoted by A_I and A_{II} (compare figure 7) the chord has, for convenience, been taken constant and the pivotal point P lies on A_I, the contribution of the vorticity on A_I and its wake to the downwash in P can be approximated in the same way as above for the straight yawed wing. The only difference comes from the contribution of the vorticity on A_{II} and its wake.

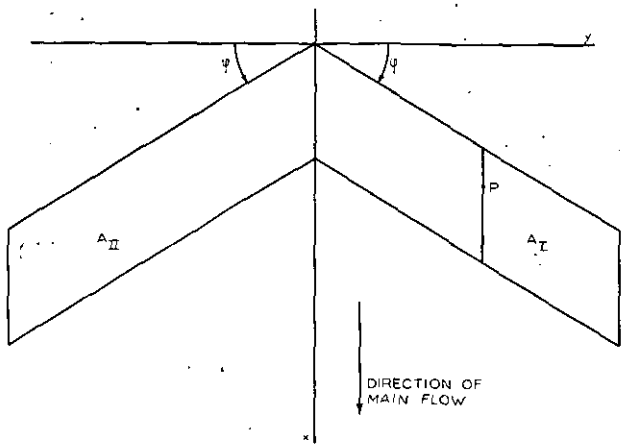

Figure 7.

Indeed, if the vorticity on A_{II} is decomposed in directions parallel to the mainstream and to the direction of the leading and trailing edges of A_{II}, it will be obvious that the contribution of the "spanwise" vortices on A_{II} to the downwash in P is of an order which cannot be neglected (compare section 2.4). In order to obtain this contribution these spanwise vortices may be concentrated in a single (singular) line vortex along (for instance) the ¼-chord line and the pivotal point P may also be taken on the ¼-chord line, as the chordwise position of P seems to be less important.

If the ¼-chord line is (figure 8)

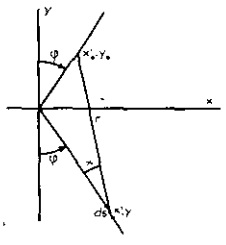

Figure 8.

$$x = y \tan\varphi \quad \text{and} \quad x = -y \tan\varphi, \qquad (4.1)$$

(where φ is the angle of sweep) for A_I and A_{II} respectively, the downwash induced at the point (x_0', y_0) corresponding to the pivotal point (x_0, y_0) is determined as follows. The strength of the line vortex is

$$\Gamma(y) = \pi \{ c_0(y) + \tfrac{1}{2} c_1(y) \} \qquad (4.2)$$

and the contribution of an element of this line vortex x', y is given by

$$\frac{1}{4\pi} \frac{\Gamma(y) \cdot \sin \cdot \chi}{r^2}\, ds,$$

where ds is the line element, χ and r are specified in fig. 8, so that

$$r^2 = (x' - x_0')^2 + (y - y_0)^2. \tag{4.3}$$

The complete result is, obviously,

$$\frac{1}{4\pi}\int_{-b}^{0} \frac{\Gamma(y)\,.\sin\chi}{r^2}\,.\,\frac{d\eta}{\cos\varphi} = \frac{\sec\varphi}{4\pi}\int_{-b}^{0}\frac{\Gamma(y)}{r^2}\sin\chi d\eta \tag{4.4}$$

if $2b$ is the span of the wing and if $y_0 > 0$. A similar result is obtained for $y_0 < 0$. It can be written as

$$\frac{\sec\varphi}{4\pi}\int_{0}^{b}\frac{\Gamma(y)}{r^2}\sin\chi d\eta. \tag{4.5}$$

It is obvious that in both cases

$$x_0' = |y_0|\,.\tan\varphi, \quad x' = |y|\tan\varphi$$

and figure (8) yields immediately

$$\sin\chi = \frac{|y_0|}{\cos\varphi}\,.\sin 2\varphi\,\frac{1}{r} = 2\sin\varphi\,\frac{|y_0|}{r}\,.$$

Hence (4.4) and (4.5) reduce to

$$2y_0\,\frac{\tan\varphi}{4\pi}\int_{-b}^{0}\frac{\Gamma(y)}{\{(y+y_0)^2\operatorname{tg}^2\varphi + (y-y_0)^2\}^{3/2}}\,dy \qquad \text{for } y_0 > 0$$

and

$$2|y_0|\,\frac{\tan\varphi}{4\pi}\int_{0}^{b}\frac{\Gamma(y)}{\{(y+y_0)^2\tan\varphi + (y-y_0)^2\}^{3/2}}\,dy \qquad \text{for } y_0 < 0$$

These integrals are elliptic if the usual development for $\Gamma(y)$ is chosen. As, however, the influence of the vorticity components near the tips is only small, the actual approximative computation of these integrals will give no difficulties.

The complete equation for a pivotal point (x_0, y_0) is, in the present case

$$\left.\begin{aligned} &4\pi v_z = \\ &= \frac{4\pi}{l(y_0)}\sec\varphi\left\{c_0(y_0) - \sum_{n=1}^{\infty} c_n(y_0)\cos n\vartheta_0\right\} \\ &+ 2\pi\sin\varphi\sum_{n=0}^{\infty} e_n(y_0)\cos n\vartheta_0 - \\ &\quad - \pi\{c_0'(y_0) + \tfrac{1}{2}c_1'(y_0)\}\,.\,\Phi(\varphi) \\ &- \pi\int_{-b}^{b} K(y,y_0)\{c_0'(y) + \tfrac{1}{2}c_1'(y)\}\,dy \\ &+ 2|y_0|\tan\varphi\,. \\ &\int_{-b}^{0}\frac{\Gamma(y)}{\{(y+y_0)^2\operatorname{tg}^2\varphi + (y-y_0)^2\}^{3/2}}\,dy \end{aligned}\right\} \tag{4.6}$$

where e_n and $\Phi(\varphi)$ are given by (3.17) and (3.18) respectively and $\Gamma(y)$ by (4.2).

It is pointed out that equation (4.6) is only valid if $|y_0|$ is not too small.

Indeed, the discontinuities in leading and trailing edges introduce additional effects which make deeper investigations necessary. This question will be discussed below in 4.2.

Finally, the kernel $K(y, y_0)$, given by (3.20) or (3.21), has to be altered in a simple way in order to account for the discontinuity in leading and trailing edge which is present here. If $y_0 > 0$ it is obvious that the original definition applies for $y > 0$. However for $y < 0$

$$K(y,y_0) = \{1 + \psi(y)\}\;\frac{y - y_0}{(y-y_0)^2 + {}^1/_{64}\,l^2\cos^2\varphi} \tag{4.8}$$

or

$$K(y,y_0) = -\{1 + \sin\psi(y)\}\;\frac{1}{\sqrt{(y-y_0)^2 + {}^1/_{16}\,l^2\cos^2\varphi}} \tag{4.9}$$

where $\psi(y)$ is specified in figure 9.

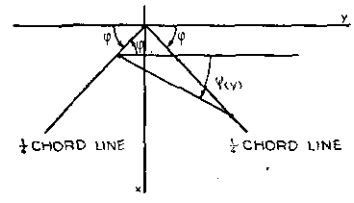

Figure 9.

These kernels are defined with respect to the ¼-chord line, which will apparently not introduce appreciable errors.

4.2 *Pivotal point on the median section.*

In this case, assume the usual development

$$\Gamma_y = \frac{2}{l(y)}\left\{c_0(y)\cot\frac{\vartheta}{2} + \sum_{n=1}^{\infty} c_n(y)\sin n\vartheta\right\} \tag{4.10}$$

in the rectangular reference system (x, y) implying the development for Γ_x given by (3.2), viz.

$$\Gamma_x = -c_0'(y)(\vartheta + \sin\vartheta) - \tfrac{1}{2}c_1'(y)(\vartheta - \tfrac{1}{2}\sin 2\vartheta) - \\ - \tfrac{1}{2}\sum_{n=2}^{\infty} c_n'(y)\left\{\frac{\sin(n-1)\vartheta}{n-1} - \frac{\sin(n+1)\vartheta}{n+1}\right\} \\ + [h'(y) - \tfrac{1}{2}l'(y)\cos\vartheta]\,.\,\Gamma_y, \tag{4.11}$$

where

$$h'(y) = \pm\tan\varphi, \tag{4.12}$$

φ being the angle of sweep. Here the + - or —- sign has to be taken for A_I and A_{II} respectively. The axis of x is taken as indicated in figure 7. Now, from the results of appendix 3, it is obvious that in general, with sufficiently regular functions $c_n(y)$, the vorticity distribution will have discontinuities at $y = 0$. These discontinuities can be avoided by assuming discontinuities in the derivatives $c_n'(y)$ at $y = 0$. The general character of the behaviour of the functions $c_n(y)$ near $y = 0$ is discussed in detail in Appendix 3 and a solution is given, there, to the problem of finding a development of the type (4.10) for

which the vorticity distribution remains continuous near $y=0$. It is, thereby, shown, that the obtained functions automatically fulfill the condition (which is also obvious from physical considerations)

$$c_0'(0) + \tfrac{1}{2} c_2'(0) = 0, \tag{4.13}$$

an equation which expresses the fact that

$$c_0'(y) + \tfrac{1}{2} c_1'(y)$$

is a continuous function of y taking the value 0 at $y=0$ (only the symmetrical case is considered in the present report). It is pointed out that $c_0'(y)$ and $c_1'(y)$ apart need to be continuous for $y=0$. In fact experimental results (compare [5], [6]) seem to indicate that the coefficient $c_0(y)$ rapidly decreases to zero for $y_0 \to 0$, in such a way that the assumption of a discontinuity in $c_0'(y)$ seems feasible. On the other hand the occurrence of a term

$$-2 \sec\varphi \, ln \, \frac{1+\sin\varphi}{1-\sin\varphi} \, \Gamma_y(0, \vartheta_0)$$

in the result (A. 2.31) of Appendix 2 indicates that $c_0(0)$ must be zero provided that the downwash will be bounded near the pointed nose of the wing. It is observed that according to the same result of Appendix 2, again, $c_0'(0) + \frac{1}{2} c_1'(0)$ must be zero provided that the downwash will remain finite at the trailing edge of the same chord.

Now, according to the arguments of section 2.4, it follows that the results of Appendix 2 can be applied immediately to the present case.

In Appendix 2 the following problem has been solved:

Determine the downwash in the points near the chord $y=0$ if a vorticity distribution on the region indicated in fig. 10 is given by

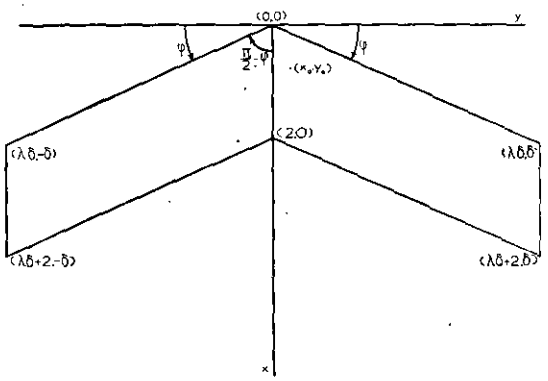

Figure 10.

$$\Gamma_y = c_0 \cot\frac{\vartheta}{2} + \sum_{n=1}^{\infty} c_n \sin n\vartheta, \quad c_n = a_n + b_n |y|, \tag{4.14}$$

and, hence,

$$\Gamma_x = \frac{|y|}{y}\left\{-b_0(\vartheta+\sin\vartheta) - \tfrac{1}{2} b_1(\vartheta - \tfrac{1}{2}\sin 2\vartheta) - \tfrac{1}{2}\sum_{n=2}^{\infty} b_n\left[\frac{\sin(n-1)\vartheta}{n-1} - \frac{\sin(n+1)\vartheta}{n+1}\right]\right\} + \lambda\frac{|y|}{y}:\Gamma_y \tag{4.15}$$

and the, usual, corresponding distribution on the "wake". Here

$$\lambda = \tan\varphi \tag{4.16}$$

and it is assumed that

$$\delta \gg 2.$$

In Appendix 2 it was shown that the downwash v_z in (x_0, y_0), y_0 small, is given by the following formula

$$\left.\begin{aligned} 4\pi v_z = {} & 2\pi\sec\varphi\left\{a_0 - \sum_{n=1}^{\infty} a_n \cos n\vartheta_0\right. \\ & - 2\sec\varphi \, ln\,\frac{1+\sin\varphi}{1-\sin\varphi}\,\Gamma_y(0,\vartheta_0) \\ & - 2\,\Gamma_{\xi'}(0,\vartheta_0)\left\{2 + \sin\varphi\, ln\,\frac{1+\sin\varphi}{1-\sin\varphi}\right\} + \\ & \left. + 2\pi\sin\varphi\sum_{n=1}^{\infty} d_n \frac{\sin n\vartheta_0}{\sin\vartheta_0}\right\} \\ & + 2\int_0^{\pi}\frac{\Gamma_x(+0,\vartheta)}{w}\sin\vartheta d\vartheta \\ & + 2\pi(b_0 + \tfrac{1}{2} b_1)\{-(1-\sin\varphi) - \\ & - (1+\sin\varphi)\, ln\,(1+\sin\varphi) + 3\, ln\, 2 + \\ & + ln\,(2-\xi_0) - (1-\sin\varphi)\, ln\, 4\delta\sec\varphi\} + \\ & + O(y_0 ln|y_0|) + O(\delta^{-2}) \end{aligned}\right\} \tag{4.17}$$

where

$$1 - \cos\vartheta_0 = x_0, \tag{4.18}$$

further

$$\Gamma_x(+0,\vartheta_0) = \lim_{\eta_0 \to +0} \Gamma_x(\eta_0, \vartheta_0), \tag{4.19}$$

next, w denotes the distance of (x_0, y_0) from a point on the chord $y=0$ characterized by its parameter ϑ, which is the variable of integration and, finally,

$$\Gamma_{\xi'}(0,\vartheta_0) = \Gamma_x(+0,\vartheta_0) - \lambda\Gamma_y(0,\vartheta_0) \tag{4.20}$$

$$= -b_0(\vartheta+\sin\vartheta) - \tfrac{1}{2} b_1(\vartheta - \tfrac{1}{2}\sin 2\vartheta) - \tfrac{1}{2}\sum_{n=2}^{\infty} b_n\left[\frac{\sin(n-1)\vartheta}{n-1} - \frac{\sin(n+1)\vartheta}{n+1}\right].$$

Now, if, as has already been remarked, $\Gamma_x(+0,\vartheta) = 0$, v_z will be finite for $0 < \vartheta_0 < \pi$ and $\eta_0 \to 0$. If, furthermore, the chord is l instead of 2, and if moreover the development of Γ_y is taken to be

$$\Gamma_y = \frac{2}{l}\left\{c_0(y)\cot\frac{\vartheta}{2} + \sum_{n=1}^{\infty} c_n(y)\sin n\vartheta\right\}, \quad c_n = a_n + b_n|y| \tag{4.21}$$

so that

$$\Gamma_x = \frac{|y|}{y}\left[-b_0(\vartheta+\sin\vartheta) - \tfrac{1}{2} b_1(\vartheta - \tfrac{1}{2}\sin 2\vartheta) - \tfrac{1}{2}\sum_{n=2}^{\infty} b_n\left\{\frac{\sin(n-1)\vartheta}{n-1} - \frac{\sin(n+1)\vartheta}{n+1}\right\}\right] + \lambda\frac{|y|}{y}\Gamma_y, \tag{4.22}$$

it follows easily that

$$
\left.
\begin{aligned}
4\pi v_z = {} & 2\pi \sec\varphi \frac{2}{l}\left\{ a_0 - \sum_{n=1}^{\infty} a_n \cos n\vartheta_0 \right\} \\
& - 2\sec\varphi \ln\frac{1+\sin\varphi}{1-\sin\varphi} \cdot \Gamma_y(0,\vartheta_0) \\
& - 2\,\Gamma_{\xi'}(0,\vartheta_0)\left\{ 2 + \sin\varphi \ln\frac{1+\sin\varphi}{1-\sin\varphi} \right\} \\
& + 2\pi\sin\varphi \sum_{n=1}^{\infty} e_n \cos n\vartheta_0 \\
& + 2\pi\,(b_0 + \tfrac{1}{2} b_1)\{ -(1-\sin\varphi) - \\
& - (1+\sin\varphi)\ln(1+\sin\varphi) + \tfrac{3}{2}\ln 2 + \\
& + \ln(2-\xi_0) - (1-\sin\varphi)\ln 4\delta\sec\varphi \} \\
& + O(y_0 \ln|y_0|) + O(\delta^{-2})
\end{aligned}
\right\} \quad (4.23)
$$

with

$$
e_1 = \tfrac{1}{2}(b_2 + 2b_0), \qquad e_n = \frac{1}{2n}(b_{n+1} - b_{n-1}), \quad n \geqq 2. \qquad (4.24)
$$

Considering this result and recalling the arguments of section 2.4, it appears that most of the terms which occur in (4.23) represent the influence of the vorticity near the root chord and are, mutatis mutandis, retained in the general case. The only alterations are the substitutions

$$
a_0 \to c_0(0) = 0,\ a_n \to c_n(0),
$$

$$
b_n \to c_n'(+0),\ b_0 + \tfrac{1}{2} b_1 \to c_0'(+0) + \tfrac{1}{2} c_1'(+0) = 0.
$$

The term $O(y_0 \ln|y_0|)$ is zero for $y_0 = 0$ and the term $O(\delta^{-2})$ is, again (compare 3), dropped.

Only one term of (4.23) must be considered separately viz. that immediately preceding the term $O(y_0 \ln|y_0|)$. The part

$$
-2\pi\,(b_0 + \tfrac{1}{2} b_1)(1-\sin\varphi)\ln 4\delta\sec\varphi
$$

which is analogous to (3.14a) will, again, be written as an integral. The remaining part of the considered term of (4.23) is dropped, because of

$$
b_0 + \tfrac{1}{2} b_1 = 0.
$$

The author is aware of the fact that this procedure is not completely unambiguous. However, no more reasonable alternative being, as yet, present, it will provisionally be adopted, though it cannot a priori be claimed to be definitve.

The, just mentioned, substitutions and reductions, now, easily lead to the following equations:

$$
\begin{aligned}
4\pi v_z = {} & -\frac{4\pi}{l(0)} \sec\varphi \sum_{n=1}^{\infty} c_n(0) \cos n\vartheta_0 - \\
& - 2\sec\varphi \ln\frac{1+\sin\varphi}{1-\sin\varphi}\,\Gamma_y(0,\vartheta_0) \\
& - 2\,\Gamma_{\xi'}(+0,\vartheta_0)\left\{ 2 + \sin\varphi \ln\frac{1+\sin\varphi}{1-\sin\varphi} \right\} + \\
& + 2\pi\sin\varphi \sum_{n=1}^{\infty} e_n(+0)\cos n\vartheta_0 \qquad (4.25) \\
& - \pi(1-\sin\varphi) \int_{-b}^{b} K^*(y,y_0)\{ c_0'(y) + \tfrac{1}{2} c_1'(y) \}\, dy
\end{aligned}
$$

with

$$
K^*(y,y_0) = \frac{y-y_0}{(y-y_0)^2 + {}^1/_{64}\, l^2(0)\cos^2\varphi} \qquad (4.26)
$$

or

$$
K^*(y,y_0) = \frac{y-y_0}{|y-y_0|} \cdot \frac{1}{\sqrt{(y-y_0)^2 + {}^1/_{16}\, l^2(0)\cos^2\varphi}} \qquad (4.27)
$$

and

$$
\begin{aligned}
\Gamma_{\xi'}(0,\vartheta_0) = {} & -c_0'(+0)(\vartheta_0 + \sin\vartheta_0) - \\
& - \tfrac{1}{2} c_1'(+0)(\vartheta_0 - \tfrac{1}{2}\sin 2\vartheta_0) - \\
& - \tfrac{1}{2} \sum_{n=2}^{\infty} c_n'(+0)\left[\frac{\sin(n-1)\vartheta_0}{n-1} - \frac{\sin(n+1)\vartheta_0}{n+1} \right],
\end{aligned} \qquad (4.28)
$$

$$
e_1(+0) = \tfrac{1}{2}\{ c_2'(+0) + 2c_0'(+0) \},\quad e_n(+0) = \frac{1}{2n}\{ c_{n+1}'(+0) - c_{n-1}'(+0) \},\ n \geqq 2. \qquad (4.29)
$$

5 Summary.

In this report generalizations of Prandtl's equation are derived applying to:

(i) straight wings of large aspect ratio under yaw;
the final result is equation (3.19),

(ii) symmetrical swept back wings with a symmetrical distribution of vorticity, the wing consisting of two straight parts, each having large "aspect ratio" when considered apart and joining, of course, in the plane of symmetry;
the final result is, in this case, given by (4.6) and (4.25).

In both cases the result is a genuine generalization of Prandtl's equation, as it expresses the downwash at the surface of the wing in the vorticity distribution associated with it and, further, as it contains only line integrals to be extended, e. g. over the ¼-chord line.

The resulting equations, mentioned above, express the downwash at the surface after assuming a suitable expansion for the spanwise components of the vorticity distribution viz. that given by (3.1). Special care has been taken (compare Appendix 3) to ensure the continuity of the vorticity distribution along the root-chord in the case of a swept back wing.

Applications, made thus far only of (3.19), indicate the adequacy of the obtained results (compare [3] and [4]).

It is remarked that throughout the present report the chordwise vorticity distribution is taken into account. This is in contrast with the wellknown Weissinger lifting line method ("Traglinienverfahren"; compare [9]) which constitutes the main method used, up till now, to calculate the distribution of the circulation for swept wings.

In connection with the results of this report the work of E. Reissner must, still, be mentioned [10]. This author has derived integro-differential equations for both the lift- and the moment-distribution along the span and has indicated a method to in-

troduce higher moment-distributions as well. In this way the chordwise vorticity distribution is not introduced directly, but in the form of certain integral quantities (as e. g. the lift- and moment-distribution).

6 References.

[1] HEEMERT, A. VAN. The calculation of downwash fields for a lifting plane in steady flow. Nat. Aer. Res. Inst. Amsterdam. Report F. 51 (1949).

[2] HEEMERT, A. VAN. The calculation of the downwash at the surface of a lifting plane in steady flow... Tables, graphs and some simple checks. Nat. Aer. Res. Inst. Amsterdam. Report F. 58 (1950).

[3] GREIDANUS, J. H. and HEEMERT, A. VAN. Chordwise downwash distributions of an infinite wing of constant chord with a periodic spanwise distribution of vorticity. Nat. Aer. Res. Inst. Amsterdam. Report F. 78 (1950).

[4] HEEMERT, A. VAN. Application of the generalized Prandtl equation to an elliptic plane wing under yaw. Nat. Aer. Res. Inst. Amsterdam. Report F. 77 (1951).

[5] SCHWENK, TH. Messungen an einem trapezförmigen Pfeilflügel. P. B. 36139, Göttingen 1943.

[6] INGELMANN—SUNDBERG, M. Experimental determination of pressure-distributions on a plane wing with 40° sweep back at low speed. K. T. H.-Aero TN8, Stockholm 1949.

[7] THEILHEIMER, F. The influence of sweep on the spanwise liftdistribution. Journ. Aer. Sc. 10 (1943), p. 101.

[8] GAIL, A. Letter to the editor. Journ. Aer. Sc. 10 (1943), p. 320; with a reply of F. THEILHEIMER on p. 320/21.

[9] WEISSINGER, J. Ueber die Auftriebsverteilung gerader und gepfeilter Flugel. Berlin 1943. Compare also N.A.C.A. T.M. 1120.

[10] REISSNER, E. Note on the theory of lifting surfaces. Proc. Nat. Ac. of Sc. 35 (1949), p. 208.

[11] KRIENES, K. Die elliptische Tragfläche auf potential-theoretischer Grundlage. Z.A.M.M. 20 (1940).

APPENDIX I.

The downwash for a "linear" vorticitydistribution on a straight yawed wing of constant chord.

In this appendix an approximation formula is derived for the downwash due to the vorticity-distribution which is defined by the following distribution of its η-components:

$$\Gamma_\eta = c_0 \cot \vartheta/2 + \sum_{n=1}^{\infty} c_n \sin n\vartheta,$$
$$c_n = a_n + b_n\eta, \quad n = 0, 1, \ldots, \qquad (A.1.1)$$

on the region (compare figure A.1.1) defined by

$$0 \leqq \xi \leqq 2, \qquad 1 - \cos\vartheta = \xi, \qquad (A.1.2)$$
$$-\delta < \eta < \delta, \qquad \delta \gg 2. \qquad (A.1.3)$$

Using the notation of [1], chapter 4, it is observed that in the considered case, taking the pivotal point on the median chord,

$$\eta_0 = 0, \quad |\xi_0 - 1| \leqq 1,$$
$$w_1^2 = (\xi - \xi_0)^2 + \delta^2 - 2(\xi - \xi_0)\,\delta \sin\varphi =$$
$$= \delta^2 \left(1 - 2\,\frac{\xi - \xi_0}{\delta}\sin\varphi + \frac{(\xi - \xi_0)^2}{\delta^2}\right), \qquad (A.1.4)$$
$$w_2^2 = (\xi - \xi_0)^2 + \delta^2 + 2(\xi - \xi_0)\,\delta \sin\varphi =$$
$$= \delta^2 \left(1 + 2\,\frac{\xi - \xi_0}{\delta}\sin\varphi + \frac{(\xi - \xi_0)^2}{\delta^2}\right). \qquad (A.1.5)$$

so that

$$\frac{1}{w_1} = \frac{1}{\delta}\left(1 + \frac{\xi - \xi_0}{\delta}\sin\varphi\right) + O\left(\frac{1}{\delta^3}\right),$$
$$\frac{1}{w_2} = \frac{1}{\delta}\left(1 - \frac{\xi - \xi_0}{\delta}\sin\varphi\right) + O\left(\frac{1}{\delta^3}\right). \qquad (A.1.6)$$

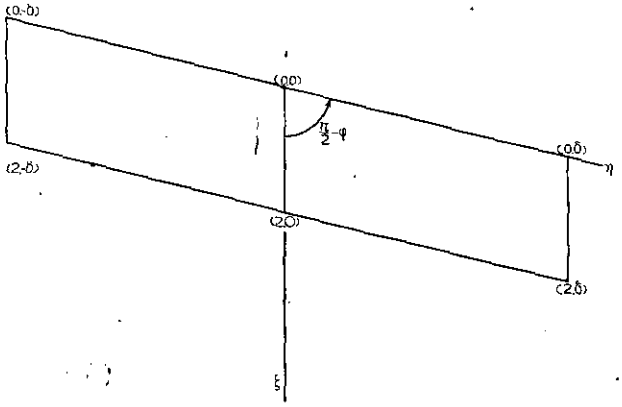

Figure A. 1. 1.

Further

$$\mu_1 = \delta, \quad \mu_2 = -\delta, \qquad (A.1.7)$$
$$\lambda_n = a_n \qquad (A.1.8)$$

and

$$\zeta_i = \frac{\sqrt{(2-\xi_0)^2 \pm 2\,\delta(2-\xi_0)\sin\varphi + \delta^2} - \delta}{2 - \xi_0}, \quad i = 1, 2, \qquad (A.1.9)$$

where the $\pm$ signs correspond to $i = \begin{matrix}2\\<\\1\end{matrix}$.

Hence

$$\zeta_i = \frac{\delta\sqrt{1 \pm 2\,\frac{2-\xi_0}{\delta}\sin\varphi + \left(\frac{2-\xi_0}{\delta}\right)^2} - \delta}{2 - \xi_0} =$$
$$\frac{\delta}{2-\xi_0}\left\{1 \pm \frac{2-\xi_0}{\delta}\sin\varphi + \right.$$
$$+ \tfrac{1}{2}\left(\frac{2-\xi_0}{\delta}\right)^2 \cos^2\varphi \mp \tfrac{1}{2}\sin\varphi\,.\cos^2\varphi\left(\frac{2-\xi_0}{\delta}\right)^3 +$$
$$\left. + O\left(\frac{1}{\delta^4}\right) - 1\right\}$$
$$= \pm\sin\varphi +$$
$$+ \tfrac{1}{2}\,\frac{2-\xi_0}{\delta}\cos^2\varphi \mp \tfrac{1}{2}\sin\varphi\cos^2\varphi\left(\frac{2-\xi_0}{\delta}\right)^2 +$$
$$+ O\left(\frac{1}{\delta^3}\right)$$

so that

$$\left.\begin{aligned}
\zeta_1 &= -\sin\varphi + \tfrac{1}{2}\frac{2-\xi_0}{\delta}\cos^2\varphi + \\
&+ \tfrac{1}{2}\sin\varphi\cos^2\varphi\left(\frac{2-\xi_0}{\delta}\right)^2 + O\left(\frac{1}{\delta^3}\right) \\
\zeta_2 &= \sin\varphi + \tfrac{1}{2}\frac{2-\xi_0}{\delta}\cos^2\varphi - \\
&- \tfrac{1}{2}\sin\varphi\cos^2\varphi\left(\frac{2-\xi_0}{\delta}\right)^2 + O\left(\frac{1}{\delta^3}\right)
\end{aligned}\right\} \quad \text{(A.1.10)}$$

and, therefore,

$$\left.\begin{aligned}
\zeta_1 + \sin\varphi &= \tfrac{1}{2}\frac{2-\xi_0}{\delta}\cos^2\varphi\left\{1 + \right. \\
&\left. + \sin\varphi\frac{2-\xi_0}{\delta} + O\left(\frac{1}{\delta^2}\right)\right\}, \\
\zeta_2 - \sin\varphi &= \tfrac{1}{2}\frac{2-\xi_0}{\delta}\cos^2\varphi\left\{1 - \right. \\
&\left. - \sin\varphi\frac{2-\xi_0}{\delta} + O\left(\frac{1}{\delta^2}\right)\right\}.
\end{aligned}\right\} \quad \text{(A.1.11)}$$

Further

$$\left.\begin{aligned}
&\frac{1+\zeta_2}{1-\zeta_2} = \frac{1+\sin\varphi}{1-\sin\varphi}\cdot \\
&\cdot\frac{1+\tfrac{1}{2}\dfrac{2-\xi_0}{\delta}(1-\sin\varphi) + O\left(\dfrac{1}{\delta^2}\right)}{1-\tfrac{1}{2}\dfrac{2-\xi_0}{\delta}(1+\sin\varphi) + O\left(\dfrac{1}{\delta^2}\right)} = \\
&\frac{1+\sin\varphi}{1-\sin\varphi}\cdot\left\{1 + \frac{2-\xi_0}{\delta} + O\left(\frac{1}{\delta^2}\right)\right\}
\end{aligned}\right\} \quad \text{(A.1.12)}$$

and, similarly

$$\frac{1-\zeta_1}{1+\zeta_1} = \frac{1+\sin\varphi}{1-\sin\varphi}\left\{1 - \frac{2-\xi_0}{\delta} + O\left(\frac{1}{\delta^2}\right)\right\}, \quad \text{(A.1.13)}$$

so that

$$\frac{1+\zeta_2}{1-\zeta_2}\cdot\frac{1-\zeta_1}{1+\zeta_1} = \left(\frac{1+\sin\varphi}{1-\sin\varphi}\right)^2\left\{1 + O\left(\frac{1}{\delta^2}\right)\right\}. \quad \text{(A.1.14)}$$

It follows from (A.1.6), (A.1.7) and (A.1.8) that (compare [1])

$$\left.\begin{aligned}
J_0 &= b_0\int_0^\pi (\xi-\xi_0)\cdot(1 + \\
&+ \cos\vartheta)\left\{2\frac{\xi-\xi_0}{\delta^2}\sin\varphi + O\left(\frac{1}{\delta^3}\right)\right\} d\vartheta \\
&+ a_0\oint_0^\pi \frac{1+\cos\vartheta}{\xi-\xi_0}\left\{2 + O\left(\frac{1}{\delta^2}\right)\right\} d\vartheta \\
&- a_0\sin\varphi\int_0^\pi (1+\cos\vartheta)\cdot \\
&\cdot\left\{2\frac{\xi-\xi_0}{\delta^2}\sin\varphi + O\left(\frac{1}{\delta^3}\right)\right\} d\vartheta \\
&- b_0\sin\varphi\int_0^\pi (1+\cos\vartheta)\cdot \\
&\cdot\left\{2 + O\left(\frac{1}{\delta^2}\right)\right\} d\vartheta \\
&= -2a_0\pi - 2b_0\pi\sin\varphi + O\left(\frac{1}{\delta^2}\right).
\end{aligned}\right\} \quad \text{(A.1.15)}$$

Similarly

$$J_1 = 2a_1\pi\cos\vartheta_0 - b_1\pi\sin\varphi + O\left(\frac{1}{\delta^2}\right) \quad \text{(A.1.16)}$$

and generally, for $n \geqq 2$,

$$J_n = 2a_n\pi\cos n\vartheta_0 + O\left(\frac{1}{\delta^2}\right) \quad \text{(A.1.17)}$$

Next, consider

$$\left.\begin{aligned}
J' &= \int_0^\pi \Gamma_\xi\sin\vartheta\cdot\left\{2\frac{\xi-\xi_0}{\delta^2}\sin\varphi + \right. \\
&\left. + O\left(\frac{1}{\delta^3}\right)\right\} d\vartheta \\
&- \oint_0^\pi \Gamma_\xi\sin\vartheta\sin\varphi\cdot\frac{1}{\xi-\xi_0} \\
&\cdot\left\{2 + O\left(\frac{1}{\delta^2}\right)\right\} d\vartheta = \\
&- 2\sin\varphi\int_0^\pi \left\{d\vartheta\sin\vartheta + \right. \\
&\left. + \sum_{n=0}^{\infty} d_n\cos n\vartheta\right\}\frac{d\vartheta}{\xi-\xi_0} + O\left(\frac{1}{\delta^2}\right) \\
&= -2\sin\varphi\cdot\left\{d\pi\,ln\,2\,|\,\xi_0 - 2\,| - \right. \\
&\left. - \pi\sum d_n\frac{\sin n\vartheta_0}{\sin\vartheta_0}\right\} + O\left(\frac{1}{\delta^2}\right)
\end{aligned}\right\} \quad \text{(A.1.18)}$$

where

$$\left.\begin{aligned}
d &= -(b_0 + \tfrac{1}{2}b_1), \\
d_0 &= -\tfrac{1}{4}(b_2 + 2b_0), \\
d_1 &= -\tfrac{1}{8}(b_3 - b_1), \\
d_2 &= \tfrac{1}{12}(6b_0 + 4b_2 - b_4)
\end{aligned}\right\} \quad \text{(A.1.19)}$$

and

$$d_n = -\tfrac{1}{4}\left(\frac{b_{n+2}}{n+1} + \frac{b_{n-2}}{n-1} - \frac{2n}{n-1}b_n\right), \quad n = 3, 4, \ldots.$$

According to

$$\frac{\sin n\vartheta_0}{\sin\vartheta_0} = \sum_{p=0}^{n-1}\cos(n-1-2p)\vartheta_0,$$

it follows that

$$\sum_{n=0}^{\infty} d_n\frac{\sin n\vartheta_0}{\sin\vartheta_0} = \sum_{n=0}^{\infty} d_n\sum_{p=0}^{n-1}\cos(n-1-2p)\vartheta_0 = \sum_{k=0}^{\infty} e_k\cos k\vartheta_0.$$

from which it can be checked that

$$e_0 = d_1 + d_3 + d_5 + \ldots = \sum_{p=0}^{\infty} d_{2p+1},$$

$$e_k = 2\,d_{k+1} + 2\,d_{k+3} + \ldots = 2\sum_{p=0}^{\infty} d_{2p+k+1}, \qquad k = 1, 2, \ldots.$$

Using, now, the definition of the d_n (A.1.19), it is easily seen that

$$\left.\begin{aligned} &e_0 = 0,\\ &e_1 = \tfrac{1}{2}\,(b_2 + 2\,b_0)\\ &\text{and}\\ &e_n = \frac{1}{2\,n}\,(b_{n+1} - b_{n-1}),\ n = 2, 3, \ldots, \end{aligned}\right\} \quad \text{(A.1.20)}$$

whence

$$\left.\begin{aligned} J' = &-\\ &-2\sin\varphi\,\Big\{-(b_0 + \tfrac{1}{2}\,b_1)\pi\,ln\,2\,|\,2 -\\ &-\xi_0\,| + \pi\sum_{n=1}^{\infty} e_n \cos n\vartheta_0\Big\} + O\left(\frac{1}{\delta^2}\right). \end{aligned}\right.$$

Considering finally J_w, it is seen that

$$\left.\begin{aligned} J_w = &-(b_0 + \tfrac{1}{2}\,b_1)\pi\left[2\,ln\,\frac{1+\sin\varphi}{1-\sin\varphi} + \right.\\ &+ ln\,\frac{1-\sin\varphi}{1+\sin\varphi} + O\left(\frac{1}{\delta^2}\right)\\ &-\sin\varphi\,\{\,ln\,(1+\sin\varphi)\,(1-\sin\varphi) -\\ &\left.-ln\,(\zeta_1 + \sin\varphi)\,(\zeta_2 - \sin\varphi)\,\}\right]\\ = &-(b_0 + \tfrac{1}{2}\,b_1)\pi\,.\left[ln\,\frac{1+\sin\varphi}{1-\sin\varphi} + \right.\\ &+ O\left(\frac{1}{\delta^2}\right) - \sin\varphi\Big\}\,.\,ln\cos^2\varphi -\\ &\left.-2\,ln\,\tfrac{1}{2}\,\frac{2-\xi_0}{\delta}\,\cos^2\varphi + O\left(\frac{1}{\delta^2}\right)\right]\\ = &-(b_0 + \tfrac{1}{2}\,b_1)\pi\left[ln\,\frac{1+\sin\varphi}{1-\sin\varphi} + \right.\\ &+ 2\sin\varphi\,ln\,|\cos\varphi| +\\ &\left.+2\sin\varphi\,ln\,|2-\xi_0| - 2\sin\varphi\,ln\,2\,\delta\right]. \end{aligned}\right\} \quad \text{(A.1.21)}$$

The final formula for the downwash is, hence, in this case given by

$$\left.\begin{aligned} 4\pi v_z = &\,2\pi\,(a_0 - \sum_{n=1}^{\infty} a_n \cos n\vartheta_0) +\\ &+ 2\,(b_0 + \tfrac{1}{2}\,b_1)\,\pi\sin\varphi\\ &-2\sin\varphi\,\Big\{-(b_0 + \tfrac{1}{2}\,b_1)\pi\,ln\,2\,|\,2 -\\ &-\xi_0\,| + \pi\sum_{n=1}^{\infty} e_n \cos n\vartheta_0\Big\}\\ &-(b_0 + \tfrac{1}{2}\,b_1)\pi\left[ln\,\frac{1+\sin\varphi}{1-\sin\varphi} + \right.\\ &+ 2\sin\varphi\,ln\,|\cos\varphi| + 2\sin\varphi\,ln\,|2 -\\ &\left.-\xi_0|- 2\sin\varphi\,ln\,2\,\delta\right] + O\left(\frac{1}{\delta^2}\right). \end{aligned}\right\} \quad \text{(A.1.22)}$$

$$\left.\begin{aligned} = &\,2\pi\left\{a_0 - \sum_{n=1}^{\infty} a_n \cos n\vartheta_0\right\} +\\ &+ 2\pi\sin\varphi\sum_{n=1}^{\infty} e_n \cos n\vartheta_0\\ &-(b_0 + \tfrac{1}{2}\,b_1)\pi\left\{ln\,\frac{1+\sin\varphi}{1-\sin\varphi} + \right.\\ &+ 2\sin\varphi\,ln\,|\cos\varphi| - 2\sin\varphi -\\ &\left.-2\sin\varphi\,ln\,4\,\delta\right\} + O\left(\frac{1}{\delta^2}\right). \end{aligned}\right\} \quad \text{(A.1.22)}$$

APPENDIX II.

The downwash for a "linear" vorticitydistribution on a swept back wing.

In this appendix an approximation formula is derived for the downwash due to the "linear" vorticity-distribution defined by the following distribution of its η-components

$$\Gamma_\eta = c_0 \cot\vartheta/2 + \sum_{n=1}^{\infty} c_n \sin n\vartheta,$$

$$c_n = a_n + b_n\,|\,\eta\,|\,,\ n = 0, 1, 2, \ldots, \qquad \text{(A.2.1)}$$

on the region (compare figure A.2.1) defined by

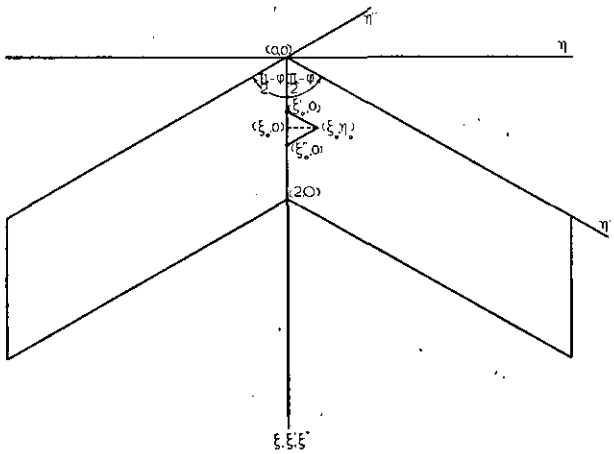

$$\lambda\,|\,\eta\,| \leqq \xi \leqq \lambda\,|\,\eta\,| + 2$$

$$1 - \cos\vartheta = \xi,\ \lambda = \tan\varphi \qquad \text{(A.2.2.)}$$

$$-\delta < \eta < \delta, \qquad \delta \gg 2 \qquad \text{(A.2.3)}$$

The distribution (A.2.1) written in the oblique reference systems (ξ', η') and $(\xi''; \eta'')$, for the right and left part respectively, reads

$$\Gamma_{\eta'} = (a_0 \sec\varphi + b_0\eta')\cot\vartheta/2 + \sum_{n=1}^{\infty}(a_n \sec\varphi + b_n\eta')\sin n\vartheta \qquad \text{(A.2.4)}$$

and

$$\Gamma_{\eta''} = (a_0 \sec\varphi - b_0\eta'')\cot\vartheta/2 + \sum_{n=1}^{\infty}(a_n \sec\varphi - b_n\eta'')\sin n\vartheta \qquad \text{(A.2.5)}$$

respectively.

Now, the downwash will be determined in (ξ_0, η_0) lying near the ξ-axis and, then, the question will be raised whether this downwash tends to a definite limit if $\eta_0 \to 0$ (compare figure A.2.1). The methods and formulae of [1] can immediately be applied if the following substitutions are introduced

$$\left.\begin{aligned} \lambda_n' &= (a_n + b_n\eta_0)\sec\varphi \\ \lambda_n'' &= (a_n - b_n\eta_0)\sec\varphi \\ \mu_1' &= \eta_0 \sec\varphi \\ \mu_2'' &= \eta_0 \sec\varphi \\ \mu_1'' &= (\delta + \eta_0)\sec\varphi \\ \mu_2' &= -(\delta - \eta_0)\sec\varphi \end{aligned}\right\} \quad (A.2.6)$$

where one or two accents are added for quantities which refer to the right and the left side respectively. This notation is used throughout the following calculations.

With (A.2.6) it is clear that (compare [1])

$$\begin{aligned} J_0' + J_0'' = b_0 \Bigg\{ & \int_0^\pi \frac{1+\cos}{w}(2\xi - \xi_0' - \xi_0'')d\vartheta - \int_0^\pi (\xi - \xi_0')\frac{1+\cos\vartheta}{w_2'}\,d\vartheta - \\ & - \int_0^\pi (\xi - \xi_0'')\frac{1+\cos\vartheta}{w_1''}\,d\vartheta \Bigg\} \\ & + (a_0 + b_0\eta_0)\sec\varphi \left\{ \eta_0 \sec\varphi \oint_0^\pi \frac{1+\cos\vartheta}{(\xi - \xi_0')w}\,d\vartheta + (\delta - \eta_0)\sec\varphi \oint_0^\pi \frac{1+\cos\vartheta}{(\xi - \xi_0')w_2'}\,d\vartheta \right\} \\ & + (a_0 - b_0\eta_0)\sec\varphi \left\{ (\delta + \eta_0)\sec\varphi \oint_0^\pi \frac{1+\cos\vartheta}{(\xi - \xi_0'')w_1''}\,d\vartheta - \eta_0 \sec\varphi \oint_0^\pi \frac{1+\cos\vartheta}{(\xi - \xi_0'')w}\,d\vartheta \right\} \\ & - (a_0 + 2b_0\eta_0)\tan\varphi \int_0^\pi \frac{1+\cos\vartheta}{w}\,d\vartheta + (a_0 + 2b_0\eta_0 - b_0\delta)\tan\varphi \int_0^\pi \frac{1+\cos\vartheta}{w_2'}\,d\vartheta \\ & - (a_0 - 2b_0\eta_0)\tan\varphi \int_0^\pi \frac{1+\cos\vartheta}{w}\,d\vartheta + (a_0 - 2b_0\eta_0 - b_0\delta)\tan\varphi \int_0^\pi \frac{1+\cos\vartheta}{w_1''}\,d\vartheta. \end{aligned} \quad (A.2.7)$$

Here w, w_1'' and w_2' denote the distances of the pivotal point (ξ_0, η_0) from a variable point on the chords $\eta = 0$, $\eta = -\delta$ and $\eta = \delta$ respectively. These distances are, for fixed (ξ_0, η_0), obviously functions of the parameter ϑ alone.

Next, the integrals occurring in this result will be estimated.

α.
$$\int_0^\pi \frac{1+\cos\vartheta}{w}(2\xi - \xi_0' - \xi_0'')d\vartheta = 2\int_0^\pi (1+\cos\vartheta)\frac{\xi - \xi_0}{w}\,d\vartheta.$$

Consider, more generally,

$$\int_0^2 f(\xi)\frac{\xi - \xi_0}{w}\,d\xi.$$

where $f(\xi)$ is an integrable function which is continuous in $0 < \xi < 2$ and let $0 < \xi_0 < 2$. It is easily seen that if $\varepsilon^2 \approx \eta_0$, $\eta_0 \ll 1$,

$$\int_0^2 f(\xi)\frac{\xi - \xi_0}{w}\,d\xi = \int_0^{\xi_0 - \varepsilon} + \int_{\xi_0+\varepsilon}^2 f(\xi)\left\{ \frac{\xi - \xi_0}{|\xi - \xi_0|} + \right.$$
$$\left. + O(\eta_0)\int_{\xi_0-\varepsilon}^{\xi_0+\varepsilon} f(\xi)\frac{\xi - \xi_0}{w}\,d\xi. \right.$$

The last integral is $O(\varepsilon)$ so that

$$\int_0^2 f(\xi)\frac{\xi - \xi_0}{w}\,d\xi = -\int_0^{\xi_0} f(\xi)\,d\xi + \int_{\xi_0}^2 f(\xi)\,d\xi + O(\eta_0^{1/2})$$
$$= \int_0^2 f(\xi)\,d\xi - 2\int_0^{\xi_0} f(\xi)\,d\xi + O(\eta_0^{1/2}).$$

Hence

$$\begin{aligned} \int_0^\pi \frac{1+\cos\vartheta}{w}(\xi - \xi_0)\,d\vartheta &= \int_0^2 \cot\vartheta/2\,\frac{\xi - \xi_0}{w}\,d\xi \\ &= \int_0^\pi \cot\vartheta/2\,d\xi - 2\int_0^{\xi_0} \cot\vartheta/2\,d\xi + O(\eta_0^{1/2}) \\ &= \pi - 2(\vartheta_0 + \sin\vartheta_0) + O(\eta_0^{1/2}). \end{aligned} \quad (A.2.8)$$

β. Remarking that according to (A.1.6) (replacing ξ_0 by ξ_0' or ξ_0'' and δ by $(\delta - \eta_0)\sec\varphi$ or $(\delta + \eta_0)\sec\varphi$ respectively)

$$\frac{1}{w_2'} = \frac{1}{(\delta - \eta_0)\sec\varphi}\left(1 - \frac{\xi - \xi_0'}{(\delta - \eta_0)\sec\varphi}\sin\varphi\right) + O(\delta^{-3}) = \frac{1}{\delta\sec\varphi}\left\{1 + \frac{\eta_0}{\delta} - \frac{\xi - \xi_0'}{\delta\sec\varphi}\sin\varphi\right\} + O(\delta^{-3}) \tag{A.2.9}$$

$$\frac{1}{w_1''} = \frac{1}{(\delta + \eta_0)\sec\varphi}\left(1 - \frac{\xi - \xi_0''}{(\delta + \eta_0)\sec\varphi}\sin\varphi\right) + O(\delta^{-3}) = \frac{1}{\delta\sec\varphi}\left\{1 - \frac{\eta_0}{\delta} - \frac{\xi - \xi_0''}{\delta\sec\varphi}\sin\varphi\right\} + O(\delta^{-3}) \tag{A.2.10}$$

it follows that

$$-\int_0^\pi (1+\cos\vartheta)\cdot\frac{\xi-\xi_0'}{w_2'}\,d\vartheta - \int_0^\pi (1+\cos\vartheta)\,\frac{\xi-\xi_0''}{w_1''}\,d\vartheta =$$

$$-\int_0^\pi (\xi-\xi_0' + \xi-\xi_0'')\quad\frac{1}{\delta\sec\varphi}\cdot(1+\cos\vartheta)d\vartheta + O(\delta^{-2}) + O(\eta_0) =$$

$$-\frac{2}{\delta\sec\varphi}\cdot\int_0^\pi (\xi-\xi_0)(1+\cos\vartheta)d\vartheta + O(\eta_0) + O(\delta^{-2}) = \frac{2\pi}{\delta\sec\varphi}(\xi_0 - \tfrac{1}{2}) + O(\eta_0) + O(\delta^{-2}),$$

the limit of which for $\eta_0 \to 0$ is

$$\frac{2\pi}{\delta\sec\varphi}(\xi_0 - \tfrac{1}{2}) + O(\delta^{-2}).$$

γ. Consider

$$\eta_0 \oint_0^\pi \frac{f(\xi)d\xi}{w(\xi - \xi_0')}$$

where $f(\xi)$ is an integrable and at least once continuous differentiable function. Then

$$f(\xi) = f(\xi_0') + (\xi - \xi_0')g(\xi)$$

with continuous and integrable $g(\xi)$, the above integral is

$$f(\xi_0')\eta_0 \oint_0^\pi \frac{d\xi}{w(\xi - \xi_0')} + \eta_0\int_0^\pi g(\xi)\,\frac{d\xi}{w} =$$

$$f(\xi_0')\eta_0\left\{\frac{1}{\eta_0\sec\varphi}ln\,\frac{1+\sin\varphi}{1-\sin\varphi} + O(\eta_0)\right\} + O(\eta_0 ln|\eta_0|) =$$

$$f(\xi_0)\cos\varphi\, ln\,\frac{1+\sin\varphi}{1-\sin\varphi} + O(\eta_0 ln|\eta_0|),$$

which converges to the first term if $\eta_0 \to 0$ and, therefore, the terms

$$(a_0 + b_0\eta_0)\eta_0\sec^2\varphi \oint_0^\pi \frac{1+\cos\vartheta}{(\xi - \xi_0')w}d\vartheta -$$

$$-\ (a_0 - b_0\eta_0)\eta_0\sec^2\varphi \oint_0^\pi \frac{1+\cos\vartheta}{(\xi - \xi_0'')w}\,d\vartheta$$

yield, if it is observed that for the second term φ has to be replaced by $-\varphi$ in the above reduction, a contribution

$$2a_0\sec\varphi\cdot\cot\frac{\vartheta_0}{2}\cdot ln\,\frac{1+\sin\varphi}{1-\sin\varphi} + O(\eta_0 ln|\eta_0|) \tag{A.2.12}$$

which, again, converges to the first term if $\eta_0 \to 0$.

δ. According to (A.2.9)

$$(\delta - \eta_0)\sec\varphi \oint_0^\pi \frac{1+\cos\vartheta}{(\xi - \xi_0')w_2'}\,d\vartheta =$$

$$= \oint_0^\pi \frac{1+\cos\vartheta}{\xi - \xi_0'}\left\{1 - \frac{\xi - \xi_0'}{(\delta - \eta_0)\sec\varphi}\sin\varphi + O(\delta^{-2})\right\}d\vartheta$$

$$= -\pi - \int_0^\pi \frac{(1+\cos\vartheta)\sin\varphi}{(\delta - \eta_0)\sec\varphi}\cdot d\vartheta + O(\delta^{-2}) +$$

$$+ O(\eta_0) = -\pi - \frac{\pi\sin\varphi}{\delta\sec\varphi} + O(\delta^{-2}) + O(\eta_0).$$

By a similar argument, which uses the development (A.2.10) for $(w_1'')^{-1}$

$$\left.\begin{aligned}&(a_0 + b_0\eta_0)(\delta - \eta_0)\sec^2\varphi \oint_0^\pi \frac{1+\cos\vartheta}{(\xi - \xi_0')w_2'}\\ &\quad + (a_0 - b_0\eta_0)(\delta + \\ &\quad + \eta_0)\sec^2\varphi \oint_0^\pi \frac{1+\cos\vartheta}{(\xi - \xi_0'')w_1''}\,d\vartheta\\ &= -2a_0\pi\sec\varphi - 2a_0\pi\,\frac{\sin\varphi}{\delta} +\\ &\quad + O(\delta^{-2}) + O(\eta_0).\end{aligned}\right\} \tag{A.2.13}$$

ε. Consider

$$\int_0^\pi \frac{f(\xi)}{w}\,d\xi.$$

This integral is, for small $|\eta_0|$, of order $ln|\eta_0|$. Hence the last four terms of (A.2.7) can be represented by

$$-2\,a_0\tan\varphi\int_0^{\pi}\frac{1+\cos\vartheta}{w}\,d\vartheta+O(\eta_0\ln|\eta_0|)+$$

$$+\frac{2\,a_0\tan\varphi}{\delta\sec\varphi}\,\pi+O(\delta^{-2})+O(\eta_0)-2\,b_0\pi\sin\varphi$$

$$-\frac{2\,\pi b_0\sin^2\varphi}{\delta\sec\varphi}(\xi_0-\tfrac{1}{2}).$$

as can easily be checked.
The result of these reductions is that for $|\eta_0|$ small

$$J_0'+J_0''=2\,b_0\{\pi-2\,(\vartheta_0+\sin\vartheta_0)\}-$$

$$-2\,a_0\pi\sec\varphi-2\,b_0\pi\sin\varphi-2\,a_0\tan\varphi\int_0^{\pi}\frac{1+\cos\vartheta}{w}\,d\vartheta$$

$$+2\,a_0\sec\varphi\cot\frac{\vartheta_0}{2}\ln\frac{1+\sin\varphi}{1-\sin\varphi}+$$

$$+\frac{2\,\pi b_0\cos^2\varphi}{\delta\sec\varphi}(\xi_0-\tfrac{1}{2})+O(\eta_0\ln|\eta_0|)+O(\delta^{-2}).\tag{A.2.14}$$

Similar reductions give

$$J_1'+J_1''=b_1\{\pi-2\,\vartheta_0+\sin 2\,\vartheta_0\}+$$

$$+2\,a_1\pi\sec\varphi-b_1\pi\sin\varphi-a_1\tan\varphi\int_0^{\pi}\frac{1-\cos 2\,\vartheta}{w}\,d\vartheta$$

$$+2\,a_1\sec\varphi\,.\sin\vartheta_0\ln\frac{1+\sin\varphi}{1-\sin\varphi}+$$

$$+\frac{\pi b_1\cos^2\varphi}{\delta\sec\varphi}(\xi_0-1)+O(\eta_0\ln|\eta_0|)+O(\delta^{-2}),\tag{A.2.15}$$

$$J_2'+J_2''=2\,b_2\left\{\frac{\sin 3\,\vartheta_0}{3}-\sin\vartheta_0\right\}+$$

$$+2\,a_2\pi\sec\varphi-a_2\tan\varphi\int_0^{\pi}\frac{\cos\vartheta-\cos 3\,\vartheta}{w}\,d\vartheta$$

$$+2\,a_2\sec\varphi\sin 2\,\vartheta_0\ln\frac{1+\sin\varphi}{1-\sin\varphi}+$$

$$+\tfrac{1}{2}\pi\frac{b_2\cos^2\varphi}{\delta\sec\varphi}+O(\eta_0\ln|\eta_0|)+O(\delta^{-2})\tag{A.2.16}$$

and generally, for $n\geqq 3$,

$$J_n'+J_n''=2\,b_n\left\{\frac{\sin(n+1)\vartheta_0}{n+1}-\frac{\sin(n-1)\vartheta_0}{n-1}\right\}$$

$$+2\,a_n\pi\sec\varphi-$$

$$-a_n\tan\varphi\int_0^{\pi}\frac{\cos(n-1)\vartheta-\cos(n+1)\vartheta}{w}\,d\vartheta$$

$$+2\,a_n\sec\varphi\sin n\vartheta_0\ln\frac{1+\sin\varphi}{1-\sin\varphi}+$$

$$+O(\eta_0\ln\eta_0)+O(\delta^{-2}).\tag{A.2.17}$$

Next the contribution of the chordwise vorticity components *on* the wing, which is given in [1], p. 17, by J', is considered. Here, again, contributions of both symmetrical parts are denoted in a similar way as above by $(J')'$ and $(J')''$.
The sum

$$J'=(J')'+(J')''\tag{A.2.18}$$

is now easily estimated on the basis of the previous results.
In an obvious notation

$$\Gamma_\xi'=-\Gamma_\xi''\tag{A.2.19}$$

and, according to [1], p. 18,

$$\Gamma_\xi'\sin\vartheta=d\vartheta\sin\vartheta+\sum_{n=0}^{\infty}d_n\cos n\vartheta\tag{A.2.20}$$

with

$$\left.\begin{aligned}
d&=-(b_0+\tfrac{1}{2}b_1),\\
d_0&=-\frac{1}{4}(b_2+2\,b_0),\\
d_1&=-\frac{1}{4}\left(\frac{b_3}{2}-\frac{b_1}{2}\right),\\
d_2&=-\frac{1}{4}\left(\frac{b_4}{3}-2\,b_0-\frac{4}{3}b_2\right),\\
d_n&=-\frac{1}{4}\left\{\frac{b_{n+2}}{n+1}+\frac{b_{n-2}}{n-1}-\frac{2n}{n^2-1}b_n\right\}\\
&\qquad\text{for } n=3,4,\ldots.
\end{aligned}\right\}\tag{A.2.21}$$

Hence, denoting $\Gamma_\xi'\sin\vartheta$ by $\Lambda(\vartheta)$ and using (5.12), (5.13) and (5.14) of [1],

$$J'=2\int_0^{\pi}\frac{\Lambda(\vartheta)}{w}\,d\vartheta-\int_0^{\pi}\Lambda(\vartheta)\left\{\frac{1}{w_2'}+\frac{1}{w_1''}\right\}d\vartheta$$

$$-\oint_0^{\pi}\Lambda(\vartheta)\eta_0\sec\varphi\sin\varphi\left\{\frac{1}{\xi-\xi_0'}-\frac{1}{\xi-\xi_0''}\right\}\frac{d\vartheta}{w}$$

$$+\oint_0^{\pi}\Lambda(\vartheta)(\eta_0-\delta)\sec\varphi\sin\varphi\,\frac{d\vartheta}{w_2'(\xi-\xi_0')}-$$

$$-\oint_0^{\pi}\Lambda(\vartheta)(\eta_0+\delta)\sec\varphi\sin\varphi\,\frac{d\vartheta}{w_1''(\xi-\xi_0'')}.\tag{A.2.22}$$

The second term, here, is $O(\delta^{-1})$.
It is, in fact given by

$$-\int_0^{\pi}\Lambda(\vartheta)\,.\left\{\frac{2}{\delta\sec\varphi}+O(\delta^{-2})\right\}d\vartheta=$$

$$-\frac{2}{\delta\sec\varphi}\int_0^{\pi}\Lambda(\vartheta)d\vartheta+O(\delta^{-2})=$$

$$-\frac{2}{\delta\sec\varphi}\int_0^{\pi}(d\vartheta\sin\vartheta+d_0)d\vartheta+O(\delta^2)=$$

$$-\frac{2\,\pi}{\delta\sec\varphi}\,.(d+d_0)+O(\delta^{-2}).$$

The third term yields, by the considerations under γ,

$$-2\,\frac{\Lambda(\vartheta_0)}{\sin\vartheta_0}\sin\varphi\,ln\,\frac{1+\sin\varphi}{1-\sin\varphi}+O(\eta_0\,ln\,|\,\eta_0\,|\,).$$

Here $\frac{\Lambda(\vartheta_0)}{\sin\vartheta_0}$ is simply the value of Γ_ξ on the right half of the wing i. e.

$$\frac{\Lambda(\vartheta_0)}{\sin\vartheta_0}=-(b_0+\tfrac{1}{2}b_1)\vartheta_0-1\tfrac{1}{2}\,b_0\sin\vartheta_0-$$
$$-\tfrac{1}{2}\sum_{n=1}^{\infty}\frac{b_{n+1}-b_{n-1}}{n}\sin n\vartheta_0. \qquad (A.2.23)$$

The last two terms of (A.2.22) yield by (A.2.9) and (A.2.10)

$$-2\sin\varphi\oint_0^{\pi}\Lambda(\vartheta)\,\frac{d\vartheta}{\xi-\xi_0}+$$
$$+2\,\frac{\sin^2\varphi}{\delta\sec\varphi}\int_0^{\pi}\Lambda\,(\vartheta)d\vartheta+O(\eta_0)+O(\delta^{-2})=$$
$$-2\sin\varphi\left\{d\pi\,ln\,2\,|\,2-\xi_0\,|-\pi\sum_{n=0}^{\infty}d_n\frac{\sin n\vartheta_0}{\sin\vartheta_0}\right\}+$$
$$+2\,\frac{\sin^2\varphi}{\delta\sec\varphi}\,.\,\pi(d+d_0)+O(\eta_0)+O(\delta^{-2}).$$

Hence, the final result is

$$\left.\begin{aligned}J'=&-2\pi\sin\varphi\left\{d\,ln\,2\,|\,2-\xi_0\,|-\right.\\&\left.-\sum_{n=0}^{\infty}d_n\,\frac{\sin n\vartheta_0}{\sin\vartheta_0}\right\}-\\&-2\sin\varphi\left\{-(b_0+\tfrac{1}{2}b_1)\vartheta-1\tfrac{1}{2}\,b_0\sin\vartheta_0\right.\\&\left.-\tfrac{1}{2}\sum_{n=1}^{\infty}\frac{b_{n+1}-b_{n-1}}{n}\sin n\vartheta_0\right\}ln\,\frac{1+\sin\varphi}{1-\sin\varphi}\\&+2\int_0^{\pi}\left\{d\vartheta\sin\vartheta+\sum_{n=0}^{\infty}d_n\cos n\vartheta\right\}\frac{d\vartheta}{w}+\\&-\frac{2\pi}{\delta\sec\varphi}(d+d_0)\cos^2\varphi+\\&+O(\eta_0\,ln\,|\,\eta_0\,|\,)+O(\delta^{-2}).\end{aligned}\right\}\qquad (A.2.24)$$

Finally, in the notation of [1], p. 19, the contribution

$$J_w=J_w'+J_w'' \qquad (A.2.25)$$

is considered. This contribution is written down in the form given in [1], formula (5.21). As no singularities arise if $\eta_0\to 0$, provided $\xi_0<2$, the value of J_w for $\eta_0=0$ will be written down immediately. It is easily shown that for some general small value of η_0 the difference is $O(\eta_0)$.

Consider, hence, first

$$-(b_0+\tfrac{1}{2}b_1)\pi\int_2^{\infty}\left(\frac{1}{w}-\frac{1}{w_2'}\right)d\xi+$$
$$+(b_0+\tfrac{1}{2}b_1)\pi\int_2^{\infty}\left(\frac{1}{w_1''}-\frac{1}{w}\right)d\xi=$$
$$-2\,(b_0+\tfrac{1}{2}b_1)\pi\int_2^{\infty}\left(\frac{1}{w}-\frac{1}{w_2'}\right)d\xi. \qquad (A.2.26)$$

In this case

$$w=\xi-\xi_0 \qquad (A.2.27)$$

and the previous integral is reduced to

$$-2(b_0+\tfrac{1}{2}b_1)\pi\lim_{A\to\infty}\int_e^{A}\left(\frac{1}{\xi-\xi_0}-\frac{1}{w_2'}\right)d\xi=$$
$$-2\,(b_0+\tfrac{1}{2}b_1)\pi\lim_{A\to\infty}\left\{ln\,\frac{A-\xi_0}{2-\xi_0}-\right.$$
$$\left.-ln\,\frac{2-\delta_2}{\delta_2'}+ln\,\frac{1+\zeta_2'}{1-\zeta_2'}\right\}$$

according to the results of [1], pag. 7. Here, for $A\gg\delta$,

$$\left.\begin{aligned}\delta_2'=&\frac{A-\xi_0-\sqrt{(A-\xi_0)^2+2\,\delta\sec\varphi(A-\xi_0)\,.\sin\varphi+\delta^2\sec^2\varphi}+\delta\sec\varphi}{A-\xi_0}\\=&\frac{\delta\sec\varphi-\delta\sec\varphi\sin\varphi}{A-\xi_0}+P\left(\frac{\delta}{A-\xi_0}\right).\frac{\delta^2}{(A-\xi_0)^2}\end{aligned}\right\}\qquad (A.2.29)$$

where P denotes some convergent power series of its arguments.

Hence, the considered integral reduces to

$$-2\,(b_0+\tfrac{1}{2}b_1)\pi\lim_{A\to\infty}\left\{-ln(2-\xi_0)-ln\,(2-\right.$$
$$\left.-\delta_2')+ln\,\frac{1+\zeta_2'}{1-\delta_2'}+ln\,\delta\sec\varphi+ln\,(1-\sin\varphi)\right.$$
$$\left.+ln\left[1+\frac{\delta}{A-\xi_0}P\left(\frac{\delta}{A-\xi_0}\right)\right]=\right.$$
$$-2\,(b_0+\tfrac{1}{2}b_1)\pi\left\{-ln\,2(2-\xi_0)+\right.$$
$$\left.+ln(1+\sin\varphi)+ln\,\delta\sec\varphi+\frac{2-\xi_0}{\delta\sec\varphi}\right\}+O(\delta^{-2})$$

according to

$$\lim_{A\to\infty}\delta_2'=0$$

and formula (A.1.12). (Observe that δ in this last formula has to be replaced by $\delta\sec\varphi$ here!)

Taking, finally, the remaining contributions emerging from the second integral of [1], (5.21), their sum, for both halves of the wing, is given by

$$
\left.
\begin{aligned}
&2\,(b_0+\tfrac{1}{2}b_1)\pi\int_2^\infty \frac{\delta\tan\varphi}{(\xi-\xi_0)w_2'}\,d\xi = \\
&2\,(b_0+\tfrac{1}{2}b_1)\pi\delta\tan\varphi\,. \\
&\quad\cdot\frac{1}{\delta\sec\varphi}\,ln\left|\frac{|\mu_2'|+\mu_2'\sin\varphi}{|\mu_2'|\,\zeta_2'+\mu_2'\sin\varphi}\right| = \\
&2\,(b_0+\tfrac{1}{2}b_1)\pi\,.\,\sin\varphi\,.\,ln\,\frac{1-\sin\varphi}{\zeta_2'-\sin\varphi} = \\
&2\,(b_0+\tfrac{1}{2}b_1)\pi\sin\varphi\,ln\left[\frac{1-\sin\varphi}{\frac{1}{2}\cdot\frac{2-\xi_0}{\delta\sec\varphi}\cos^2\varphi}\cdot\right. \\
&\quad\left.\cdot\left\{1+\sin\varphi\,\frac{2-\xi_0}{\delta\sec\varphi}+O(\delta^{-2})\right\}\right] = \\
&2\,(b_0+\tfrac{1}{2}b_1)\pi\sin\varphi\,\{-ln\,(1+ \\
&+\sin\varphi)+ln\,2\,\delta\sec\varphi-ln\,(2-\xi_0)\}+ \\
&+2\,(b_0+\tfrac{1}{2}b_1)\pi\,\frac{2-\xi_0}{\delta\sec\varphi}\sin^2\varphi+O(\delta^{-2})
\end{aligned}
\right\} \quad (A.2.30)
$$

where the results of [1], pag. 7, and (A.1.11) have been used (observe, again, the replacement of δ by $\delta\sec\varphi$!).

The complete result is, according to [1], (4.16), given by

$$
\left.
\begin{aligned}
&4\pi v_z = 2\pi\sec\varphi\left\{a_0-\sum_{n=1}^{\infty}a_n\cos n\vartheta_0\right\} \\
&\qquad -2\sec\varphi\,\Gamma_\eta(0,\vartheta_0)\,ln\,\frac{1+\sin\varphi}{1-\sin\varphi} \\
&+2\tan\varphi\int_0^\pi\frac{\Gamma_\eta(0,\vartheta)}{w}\sin\vartheta d\vartheta \\
&-4\,\Gamma_\xi\;(0,\vartheta_0)- \\
&\qquad -2\sin\varphi\,\Gamma_\xi\,(0,\vartheta_0)\,ln\,\frac{1+\sin\varphi}{1-\sin\varphi} \\
&\qquad +2\int_0^\pi\frac{\Gamma_\xi\,(0,\vartheta)}{w}\sin\vartheta d\vartheta \\
&+2\pi\sin\varphi\sum_{n=0}^{\infty}d_n\frac{\sin n\vartheta_0}{\sin\vartheta_0} \\
&+2\pi(b_0+\tfrac{1}{2}b_1)\,\{ln\,(2-\xi_0)-(1- \\
&-\sin\varphi)-[(1+\sin\varphi)\,ln\,(1+\sin\varphi)+ \\
&\quad +3\,ln\,2-(1-\sin\varphi)\,ln\,4\,\delta\sec\varphi\} \\
&+O(\eta_0\,ln\,|\eta_0|)+O(\delta^{-2}).
\end{aligned}
\right\} \quad (A.2.31)
$$

It is observed that, if Γ_x is continuous for $y=0$ (compare the developments af Appendix III) the integrals which occur in this result cancel. A finite value of the downwash is, then, obtained in each point of the chord, except probably the end points of the chord. This restriction is obvious. Only if special precautions are taken the result will yield a finite downwash over the whole considered chord.

APPENDIX III.

The condition for the continuity of the vorticity-distribution at the root section.

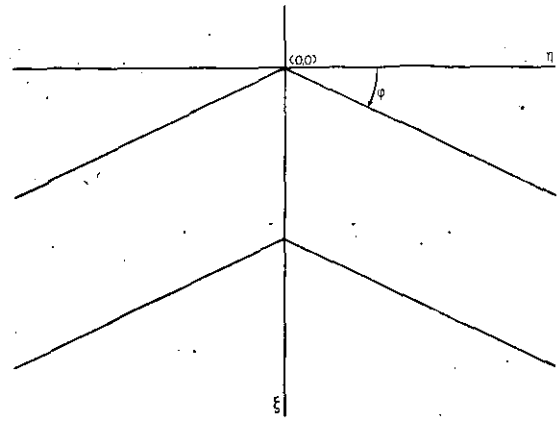

Figure A.3.1.

Let (compare fig. A.3.1) the root section be taken along the ξ-axis, the leading and trailing edges being given by

$$
\xi_l=\lambda\,|\eta| \quad\text{and}\quad \xi_t-2=\lambda\,|\eta|\,, \qquad \lambda=\tan\varphi, \qquad (A.3.1)
$$

respectively. Introduce the chordwise parameters $\bar{\xi}$ and ϑ by

$$
\bar{\xi}=\xi-\lambda\,|\eta|=1-\cos\vartheta \qquad (A.3.2)
$$

and let

$$
\mu(\xi,\eta)=-\int_{\xi_l}^{\xi}\Gamma_\eta\,(\xi_1,\eta)\,d\xi_1. \qquad (A.3.3)
$$

It is observed that $\mu(\xi_t,\eta)$ is the circulation $\Gamma(\eta)$ at the section η and that for $\xi>\xi_t$, μ depends on η only. Further

$$
\Gamma_\eta=-\frac{\partial\mu}{\partial\xi}\,,\quad \Gamma_\xi=\frac{\partial\mu}{\partial\eta}\,. \qquad (A.3.4)
$$

First, the character of μ will be investigated for a general value of η. If

$$
\bar{\mu}(\vartheta,\eta)=\mu(\xi,\eta), \qquad \xi-\lambda\,|\eta|=1-\cos\vartheta, \qquad (A.3.5)
$$

then

$$
\bar{\mu}(0,\eta)=0,\quad \bar{\mu}(\pi,\eta)=\Gamma. \qquad (A.3.6)
$$

Hence

$$
\mu^*=\bar{\mu}-\frac{\vartheta}{\pi}\Gamma \qquad (A.3.7)
$$

is zero for $\vartheta=0$ and $\vartheta=\pi$.

It is, therefore, feasible to put

$$
\mu^*=\sum_{k=1}^{\infty}\beta_k\sin k\vartheta. \qquad (A.3.8)
$$

Now, the Kutta Joukowski condition requires

$$
\Gamma_\eta=0 \quad\text{at}\quad \xi=\xi_t\,.
$$

Hence, as according to (A.3.2)

$$\left(\frac{\partial \vartheta}{\partial \xi}\right)_{\eta} = \frac{1}{\sin \vartheta}, \qquad \text{(A.3.8a)}$$

$$\frac{1}{\sin \vartheta} \cdot \left\{ \frac{\partial \mu^*}{\partial \vartheta} + \frac{1}{\pi} \Gamma \right\} = 0 \text{ for } \vartheta = \pi,$$

which implies

$$\sum_{k=1}^{\infty} (-1)^k \cdot k \cdot \beta_k + \frac{1}{\pi} \Gamma = 0 \qquad \text{(A.3.9)}$$

and thus

$$\mu = \bar{\mu} = \sum_{k=1}^{\infty} \beta_k \sin k\vartheta + \vartheta (\beta_1 - 2\beta_2 + 3\beta_3 - \ldots). \qquad \text{(A.3.10)}$$

This may be written as

$$\mu = \sum_{n=0}^{\infty} c_n \mu_n \qquad \text{(A.3.11)}$$

with

$$\mu_0 = \vartheta + \sin \vartheta, \quad \mu_1 = \tfrac{1}{2} (\vartheta - \tfrac{1}{2} \sin 2\vartheta),$$

$$\mu_n = \tfrac{1}{2} \left\{ \frac{\sin(n-1)\vartheta}{n-1} - \frac{\sin(n+1)\vartheta}{n+1} \right\}, \; n \geqq 2 \qquad \text{(A.3.12)}$$

if the condition

$$\left(\frac{\partial \mu}{\partial \vartheta}\right)_{\vartheta = 0} = -2 c_0 \qquad \text{(A.3.13)}$$

is imposed. Indeed, this condition yields

$$\begin{aligned} -2 c_0 &= (\beta_1 + 2\beta_2 + 3\beta_3 + \ldots) + \\ &\quad + (\beta_1 - 2\beta_2 + 3\beta_3 - \ldots) \\ &= 2 (\beta_1 + 3\beta_3 + 5\beta_5 + \ldots) \end{aligned}$$

and, hence,

$$c_0 = -\{ \beta_1 + 3\beta_3 + 5\beta_5 + \ldots \}. \qquad \text{(A.3.14)}$$

By comparison of coefficients,

$$\begin{aligned} -(c_0 + \tfrac{1}{2} c_1) &= \beta_1 - 2\beta_2 + 3\beta_3 - \ldots, \\ -(c_0 + \tfrac{1}{2} c_2) &= \beta_1, \\ \tfrac{1}{4} c_1 - \tfrac{1}{4} c_3 &= \beta_2, \\ \tfrac{1}{6} c_2 - \tfrac{1}{6} c_4 &= \beta_3, \\ &\text{etc.} \end{aligned}$$

Therefore,

$$\left.\begin{aligned} c_1 &= 2 \{ 2\beta_2 + 4\beta_4 + 6\beta_6 + \ldots \}, \\ c_1 &= 2 \{ 3\beta_3 + 5\beta_5 + 7\beta_7 + \ldots \}, \\ c_3 &= c_1 - 4\beta_2 = 2 \{ 4\beta_4 + 6\beta_6 + \ldots \}, \\ &\text{etc.} \end{aligned}\right\} \qquad \text{(A.3.15)}$$

It is hence shown that (A.3.11) is a feasible expansion for μ which is, moreover, adapted to the Kutta Joukowski condition. In fact, the expansion (2.13), assumed previously for Γ_η without comment, follows from it immediately by applying (A.3.4) and (A.3.8a).

Now, coming back to the problem stated in the beginning of this appendix, let the c_n's be functions of η,

$$c_n(\eta) = c_n(0) + \eta c_n'(0) + c_n^*(\eta), \; \eta \geqq 0$$

where $c_n^*(\eta)$ is of order η^2 near $\eta = 0$. Because of (A.3.2),

$$\frac{\partial \vartheta}{\partial \eta} = -\lambda \cdot \frac{|\eta|}{\eta} \cdot \frac{1}{\sin \vartheta},$$

and so, for $\eta > 0$

$$\Gamma_\xi = \frac{\partial \mu}{\partial \eta} = \frac{\partial \bar{\mu}}{\partial \eta} = -\lambda \frac{\partial \bar{\mu}}{\partial \vartheta} \cdot \frac{1}{\sin \vartheta}. \qquad \text{(A.3.16)}$$

This reduces, according to (A.3.11) and (A.3.12) to

$$\Gamma_\xi = -\sum_{n=0}^{\infty} c_n'(\eta) \mu_n + \\ + \lambda \left[c_0(\eta) \cot \frac{\vartheta}{2} + \sum_{n=1}^{\infty} c_n(\eta) \sin n\vartheta \right]. \qquad \text{(A.3.17)}$$

Now, using

$$c_0(0) = 0 \qquad \text{(A.3.18)}$$

(compare section 4.1), the condition $\Gamma_\xi = 0$ yields

$$\sum_{n=0}^{\infty} c_n'(0) \mu_n = \lambda \sum_{n=1}^{\infty} c_n(0) \sin n\vartheta$$

and, hence,

$$\mu = \bar{\mu} = -\sum_{n=1}^{\infty} c_n(0) \mu_n - \lambda \eta \sum_{n=1}^{\infty} c_n(0) \sin n\vartheta - \\ - \sum_{n=0}^{\infty} c_n^*(\eta) \mu_n. \qquad \text{(A.3.19)}$$

In order that this result is, again, expressible in the form (A.3.11), only the condition

$$\frac{\partial}{\partial \vartheta} \left\{ \sum_{n=1}^{\infty} c_n(0) \sin n\vartheta \right\} = 0 \quad \text{for} \quad \vartheta = \pi \qquad \text{(A.3.20)}$$

has to be imposed. This condition is, obviously, necessary. It is shown, now, that it is sufficient. Indeed, the condition states that

$$\sum_{n=1}^{\infty} (-1)^n n c_n(0) = 0. \qquad \text{(A.3.21)}$$

If $\sum_{n=1}^{\infty} c_n(0) \sin n\vartheta$

is to be rearranged in $\sum_{n=0}^{\infty} \alpha_n \mu_n$,

the following equations must be solved

$$\left.\begin{aligned} \alpha_0 + \tfrac{1}{2} \alpha_1 &= 0 \\ -\alpha_1 + \alpha_2 &= 2 c_1(0) \\ -\alpha_1 + \alpha_3 &= 4 c_2(0) \\ -\alpha_2 + \alpha_4 &= 6 c_3(0) \\ &\text{etc.} \end{aligned}\right\} \qquad \text{(A.3.22)}$$

If, first, a finite series

$$\sum_{n=1}^{m} c_n \sin m\vartheta$$

with

$$\sum_{n=1}^{m} (-1)^n n c_n = 0$$

is considered, the solvability of the equations (A.3.22) is easily checked. If $m \to \infty$ and (A.3.21) remains true a simple limiting process yields the solvability in the general case. The solution is

$$\left.\begin{aligned} \alpha_1 &= -2\{2c_2(0) + 4c_4(0) + \\ &\qquad + 6c_6(0) + \dots\} \\ \alpha_2 &= -2\{3c_3(0) + 5c_5(0) + \\ &\qquad + 7c_7(0) + \dots\} \\ \alpha_3 &= -2\{4c_4(0) + 6c_6(0) + \dots\} \\ &\text{etc.} \end{aligned}\right\} \quad (A.3.23)$$

and

$$\alpha_0 = 2c_2(0) + 4c_4(0) + 6c_6(0) + \dots .$$

Consequently, (A.3.19) transfers into

$$\mu = -\sum_{n=1}^{\infty} c_n(0)\mu_n - \lambda\eta \sum_{n=0}^{\infty} \alpha_n\mu_n - \sum_{n=0}^{\infty} c_n^*(\eta)\mu_n \quad (A.3.24)$$

This formula yields by (A.3.4) a vorticity distribution of the desired properties if η is replaced by $|\eta|$. Obviously no further conditions have to be imposed on the c_n^*, i. e. c_n^* is of order η^2 near $\eta = 0$.

As an example ,take

$$c_1(0) = c_2(0) = c_3(0) = 1,$$
$$c_4(0) = \tfrac{1}{2}, \quad c_n(0) = 0, \quad n \geqq 5,$$

then

$$\mu = -\mu_1 - \mu_2 - \mu_3 - \tfrac{1}{2}\mu_4 - \lambda\eta\{4\mu_0 - 8\mu_1 - 6\mu_2 - 4\mu_3\} - \sum_{n=0}^{\infty} c_n^*(\eta)\mu_n .$$

The formulae for Γ_η and Γ_ξ become, generally, by (A.3.4) and (A.3.24)

$$\Gamma_\eta = [\lambda|\eta|\alpha_0 + c_0^*(\eta)]\cot\frac{\vartheta}{2} + \sum_{n=1}^{\infty}[c_n(0) + \lambda|\eta|\alpha_n + c_n^*(\eta)]\sin n\vartheta, \quad (A.3.25)$$

$$\Gamma_\xi = -\sum_{n=0}^{\infty}\left\{\lambda\alpha_n\frac{|\eta|}{\eta} + \frac{dc_n^*(\eta)}{d\eta}\right\}\mu_n + \lambda : \frac{|\eta|}{\eta}\Gamma_\eta . \quad (A.3.26)$$

It is remarked, that the previous development automatically implies that

$$c_0'(0) + \tfrac{1}{2}c_1'(0) = 0 \quad (A.3.27)$$

(compare the first of the equations (A.3.22)). Further, as an extra condition

$$c_0(0) = 0 \quad (A.3.28)$$

has been imposed.

APPENDIX IV.

The limiting case, $\varphi = 0$.

In this appendix the differences are considered which exist between the integral in (3.19) using the kernel ($\cos\varphi = 1$)

$$K(y, y_0) = \frac{y - y_0}{(y - y_0)^2 + {}^1/_{64}\, l^2} \quad (A.4.1)$$

and the common integral of lifting line theory viz.

$$-\pi \oint_{-b}^{b} \frac{c_0'(y) + \frac{1}{2}c_1'(y)}{y - y_0},$$

the sign $\oint_{-b}^{b''}$ designates the principal value in Cauchy's sense. Hence, writing

$$-\pi\{c_0'(y) + \tfrac{1}{2}c_1'(y)\} = f(y),$$

the following integrals have to be compared:

$$I_1 = \int_{-b}^{b} f(y)\frac{y - y_0}{(y - y_0)^2 + \tau^2}\,dy \quad (A.4.2)$$

and

$$I_2 = \int_{-b}^{b}\frac{f(y)}{y - y_0}\,dy, \quad (A.4.3)$$

where

$$\tau = \frac{1}{8}l. \quad (A.4.4)$$

Put

$$f(y) = f(y_0) + (y - y_0)\frac{\chi(y)}{\sqrt{1 - y^2/b^2}},$$

$$\chi(y) \text{ bounded, } |\chi(y)| < M \text{ say,} \quad (A.4.5)$$

which agrees with the usual assumptions on the behaviour of the coefficients $c_n(y)$ for $y \to \pm b$. Then

$$I_1 = f(y_0)\int_{-b}^{b}\frac{y - y_0}{(y - y_0)^2 + \tau^2}\,dy + I_1'',$$

$$I_1'' = \int_{-b}^{b}\frac{(y - y_0)^2}{(y - y_0)^2 + \tau^2}\frac{\chi(y)}{\sqrt{1 - y^2/b^2}}\,dy \quad (A.4.6)$$

$$I_2 = f(y_0)\oint_{-b}^{b}\frac{dy}{y - y_0} + I_2'',$$

$$I_2'' = \int_{-b}^{b}\frac{\chi(y)}{\sqrt{1 - y^2/b^2}}\,dy, \quad (A.4.7)$$

Now

$$I_1' = f(y_0)\int_{-b}^{b}\frac{y-y_0}{(y-y_0)^2+\tau^2}\,dy = \tfrac{1}{2}f(y_0)\,[ln\,\{(y-y_0)^2+\tau^2\}]_{-b}^{b} = \tfrac{1}{2}f(y_0)ln\,\frac{(b-y_0)^2+\tau^2}{(b+y_0)^2+\tau^2} =$$
$$f(y_0)\,.\,ln\,\frac{b-y_0}{b+y_0} + \tfrac{1}{2}f(y_0)\left\{\frac{\tau^2}{(b-y_0)^2} - \frac{\tau^2}{(b+y_0)^2}\right\} + O(\tau^4) =$$
$$f(y_0)ln\,\frac{b-y_0}{b+y_0} + \tfrac{1}{2}f(y_0)\,\frac{\tau^2}{b^2}\,.\left\{4\frac{y_0}{b} - 6\frac{y_0^2}{b^2} + \ldots\right\} + \ldots \qquad (A.4.8)$$

and

$$I_2' = f(y_0)\oint_{-b}^{b}\frac{dy}{y-y_0} = f(y_0)\lim_{\varepsilon\to 0}\left\{\int_{-b}^{y_0-\varepsilon}\frac{dy}{y-y_0} + \int_{y_0+\varepsilon}^{b}\frac{dy}{y-y_0}\right\} = f(y_0)ln\,\frac{b-y_0}{b+y_0} \qquad (A.4.9)$$

so that if y_0 is not nearly equal to $+b$ or $-b$

$$I_1' - I_2' \approx 2f(y_0)\,\frac{\tau^2}{b^2}\,.\,\frac{y_0}{b}\,. \qquad (A.4.10)$$

Remark, further, that

$$|I_1'' - I_2''| \leqq M\,.\int_{-b}^{b}\frac{\tau^2}{(y-y_0)^2+\tau^2}\,.\,\frac{dy}{\sqrt{1-y^2/b^2}}. \qquad (A.4.11)$$

Putting

$$y = b\cos\psi, \quad y_0 = b\cos\psi_0, \qquad (A.4.12)$$

$$|I_1'' - I_2''| \leqq M\,.\,\tau^2\int_0^{\pi}\frac{b\sin\psi}{b^2(\cos\psi-\cos\psi_0)^2+\tau^2}\,.$$

$$\frac{d\psi}{\sin\psi} = \frac{M\tau^2}{b}\int_0^{\pi}\frac{d\psi}{(\cos\psi-\cos\psi_0)+\sigma^2}, \qquad (A.4.13)$$

where

$$\frac{\tau^2}{b^2} = \sigma^2. \qquad (A.4.14)$$

Now the latter integral is, as can be proved by contour integration,

$$K_0 = \int_0^{\pi}\frac{d\psi}{(\cos\psi-\cos\psi_0)+\sigma^2} = \frac{\pi}{\sigma}\,\frac{1}{\sin\psi_0} + O(\sigma) \qquad (A.4.15)$$

Hence

$$|I_1'' - I_2''| \leqq bM\,.\,\sigma^2\,.\,\frac{\pi}{\sigma}\,\frac{1}{\sin\psi_0} + O(\sigma^3) \qquad (A.4.16)$$

which is, again, small if $\left|\frac{y_0}{b}\right|$ lies *not* near 1. It is, indeed of order σ.

Hence

$$I_1 - I_2 = O(\sigma). \qquad (A.4.17)$$

Similar considerations are valid for the difference $I_3 - I_2$ where

$$I_3 = \int_{-b}^{b} f(y)\,\frac{y-y_0}{|y-y_0|}\,.\,\frac{1}{\sqrt{(y-y_0)^2+\tau^2}}\,dy.$$

One has here, however, to split the interval of integration in the parts $(\frac{1}{2}(y_0-b),\ \frac{1}{2}(y_0+b))$, $(-b, \frac{1}{2}(y_0-b))$ and $(\frac{1}{2}(y_0+b), b)$.

APPENDIX V.

An alternative form of the kernel.

In this appendix an alternative form of the kernel $K(y, y_0)$ in (3.20) and (3.21) will be discussed. Considering the term which gave rise to this integral, viz.

$$-(b_0 + \tfrac{1}{2}b_1)\pi\,.\,-2\sin\varphi\,ln\,\frac{8\delta}{l}$$

(using the notation of 3), it can be written in the following form

$$-(b_0+\tfrac{1}{2}b_1)\pi\lim_{\substack{\varepsilon_1\to 0\\ \varepsilon_2\to 0}}\left\{(1+\sin\varphi)\int_{-\delta}^{-\varepsilon_1}\frac{d\eta}{\eta} + (1-\sin\varphi)\int_{\varepsilon_2}^{\delta}\frac{d\eta}{\eta}\right\}$$

where ε_1 and ε_2 converge to zero in a way which is specified below.

Now

$$\int_{-\delta}^{-\varepsilon_1}\frac{d\eta}{\eta} = ln\,\frac{\varepsilon_1}{\delta}, \quad \int_{\varepsilon_2}^{\delta}\frac{d\eta}{\eta} = ln\,\frac{\delta}{\varepsilon_2}$$

if ε_1 and ε_2 are positive.

Hence,

$$(1+\sin\varphi)\int_{-\delta}^{-\varepsilon_1}\frac{d\eta}{\eta} + (1-\sin\varphi)\int_{\varepsilon_2}^{\delta}\frac{d\eta}{\eta} =$$
$$(1+\sin\varphi)\,.\,ln\,\frac{\varepsilon_1}{\delta} + (1-\sin\varphi)\,ln\,\frac{\delta}{\varepsilon_2} =$$
$$-2\sin\varphi\,ln\,\delta + (1+\sin\varphi)\,ln\,\varepsilon_1 - (1-\sin\varphi)\,ln\,\varepsilon_2\,.$$

This will converge to

$$-2\sin\varphi\,ln\,\frac{8\delta}{l}$$

provided that ε_1 and ε_2 converge to zero so, that the relation

$$(1+\sin\varphi)\,ln\,\varepsilon_1 - (1-\sin\varphi)\,ln\,\varepsilon_2 =$$
$$= -2\sin\varphi\,ln\,\frac{8}{l} \qquad (A.5.1)$$

holds. For an ordinary principal value in Cauchy's sense one has to take $\varepsilon_1 = \varepsilon_2 = \varepsilon$ and then $\varepsilon \to 0$. Indeed this is yielded by (A.5.1) if $\varphi = 0$. In the present case, for $\varphi \neq 0$, the generalized principal value is indicated by the scheme

$$\oint_{-b}^{b} = \lim_{\substack{\varepsilon_1 \to 0 \\ \varepsilon_2 \to 0}} \left\{ \int_{-b}^{\eta_0 - \varepsilon_1} + \int_{\eta_0 + \varepsilon_2}^{b} \right\}$$

where $\varepsilon_1, \varepsilon_2$ are both positive and related by (A.5.1). A similar generalized principal value has, previously, been introduced in the theory of swept wings in [7]. However, its use was, there, not justified from lifting plane, theory. Actually, the final elaboration proved to be in error, as was already remarked in [8].

Considering this generalized principal value more closely, observe that it is defined using oblique coordinates. If, generally, a new coordinate is introduced by

$$\eta = \lambda(\eta'),$$

also a new relation for the quantities ε_1' and ε_2' emerges ,viz. that relation which emerges if the old relation is transformed. It will be clear that it transforms into

$$(1 + \sin\varphi)\, ln \left| \varepsilon_1' \left(\frac{d\lambda}{d\eta'} \right)_{\eta = \eta_0} \right| -$$

$$-(1 - \sin\varphi)\, ln \left| \varepsilon_2' \left(\frac{d\lambda}{d\eta'} \right)_{\eta = \eta_0} \right| = -2 \sin\varphi\, ln \frac{8}{l}$$

or

$$(1 + \sin\varphi)\, ln\, |\varepsilon_1'| - (1 - \sin\varphi)\, ln\, |\varepsilon_2'| =$$

$$-2 \sin\varphi\, ln \frac{8}{l} \left(\frac{d\lambda}{d\eta'} \right)_{\eta = \eta_0}. \qquad \text{(A.5.2)}$$

It is obvious, that with this generalized principal value the equation for a yawed straight wing transforms for $\varphi \to 0$ exactly in Prandtl's equation.

The approximate equation for a yawed straight wing reads, when this generalized principal value is used, as follows:

$$4\pi v_z = 2\pi \frac{2}{l(y_0)} \left\{ c_0(y) - \sum_{n=1}^{\infty} c_n(y_0) \cos n\vartheta_0 \right\} +$$

$$+ 2\pi \sin\varphi \sum_{n=1}^{\infty} e_n(y_0) \cos n\vartheta_0$$

$$-\pi \{ c_0'(y_0) + \tfrac{1}{2} c_1'(y_0) \} \Phi(\varphi) -$$

$$-\pi \oint_{-b}^{b} \{ c_0'(y) + \tfrac{1}{2} c_1'(y) \} \frac{dy}{y - y_0}. \qquad \text{(A.5.3)}$$

Here rectangular coordinates (x, y) are used and, according to (A.5.2),

$$\oint_{-b}^{b} = \lim_{\substack{\varepsilon_1 \to 0 \\ \varepsilon_2 \to 0}} \left\{ \int_{-b}^{y_0 - \varepsilon_1} + \int_{y_0 + \varepsilon_2}^{b} \right\},$$

with

$$(1 + \sin\varphi)\, ln\, \varepsilon_1 - (1 - \sin\varphi)\, ln\, \varepsilon_2 =$$

$$-2 \sin\varphi\, ln \left(\frac{8}{l} \sec\varphi \right)$$

Similar equations can be given for swept wings. If the pivotal point lies on the root chord the integral

$$\oint_{-b}^{b}$$

can, however, immediately be replaced by

$$\oint_{-b}^{b},$$

i.e. by the ordinary principal value.

C.C.L. Class. D 050 : D 053

REPORT F. 79

Revised Methods for Routine Calculations of Laminar and Turbulent Boundary Layers of Twodimensional Incompressible Flows

by

Dr. J. A. ZAAT.

Summary.

Timman's one parameter method (ref. 1) for the calculation of laminar boundary layers is simplified by aid of a lincarization. The semi-empirical methods for the calculations of turbulent layers are modified in accordance with new experimental results of Ludwieg and Tillmann (ref. 2) for the shearing stress along the wall.

The modification implies a definite improvement, in particular with respect to the determination of the separation point. The results should be suitable for routine calculations of quite adequate accuracy.

Contents.

1 Introduction.

Conventional methods for routine calculations of laminar boundary layers are all "one parameter methods", based on the assumption that the boundary layer velocity profiles constitute a one parameter family. Using, like many others following Pohlhausen, von Karman's momentum equation, the presumably most refined elaboration of this principle has been established by Timman (ref. 1). Now, Timman's method involves a certain characteristic function of the form-parameter which appears to be representable with quite satisfactory accuracy by a straight line. Consistently using this approximation the scheme of computations appears to reduce to a residue still warranting adequate accuracy, and requiring very little work.

Conventional methods for the calculation of turbulent layers are also one parameter methods controlled by von Karman's momentum equation, in this case completed with empirical formulae for the shearing stress at the wall and for the variation of the form-parameter H (= ratio of displacement — to momentum thickness). Now, new extensive and very careful measurements of the shearing stress at the wall (actually: of the related heat transition coefficient) by Ludwieg and Tillmann (ref. 2) have revealed inaccuracies in part of the older measurements and have resulted in a new empirical formula for the shearing stress, which has the satisfactory property of yielding almost vanishing stresses in the separation point. Adopting this formula and introducing a related revision of the empirical law controlling the variation of H, a method for the calculation of turbulent boundary layers is obtained, which implies in contrast to older methods a clear indication for turbulent separation. This is an important advantage.

The location of the separation point as calculated by aid of this method will be shown to be almost independent of the selected initial value of H. This, again, is important, for this initial value is always very uncertain. At the transition point, the value of the momentum thickness is the only adequate initial datum available for the calculation of the adjacent turbulent layer.

2 A simplified method for the calculation of laminar boundary layers.

The steady twodimensional, incompressible flow in a laminar boundary layer along a flat or slightly curved wall satisfies Prandtl's classic equations

$$\rho\left(u\frac{\partial u}{\partial x}+v\frac{\partial u}{\partial y}\right)=-\frac{dp}{dx}+\mu\frac{\partial^2 u}{\partial y^2}=$$

$$=\rho U\frac{dU}{dx}+\frac{\partial \tau}{\partial y};\quad \frac{\partial u}{\partial x}+\frac{\partial v}{\partial y}=0, \qquad (2.1)$$

N.B. This report was prepared by order of the Netherlands Aircraft Development Board.

x, y: coördinates along and normal to the wall
u, v: according components of the velocity
ρ, p: density and pressure
μ, τ: dynamic viscosity and shearing stress
U : velocity just outside the boundary layer.

The first equation is the residue of the Navier-Stokes equations, the second is the equation of continuity.

The boundary conditions are

$$y = 0: \; u = 0, \; v = 0$$
$$y = \infty: \; u \sim U. \tag{2.2}$$

Von Karman's momentum equation is obtained by integrating (from $y = 0$ to ∞) the first equation (2.1). It is conventionally written as

$$\rho U \frac{dU}{dx} (\delta^* + 2\vartheta) + \rho U^2 \frac{d\vartheta}{dx} = \tau_0; \tag{2.3}$$

τ_0 (shearing stress at the wall) $= \mu \left(\frac{\partial u}{\partial y}\right)_{y=0}$.

$\delta^*(x) = \int_0^\infty \left(1 - \frac{u}{U}\right) dy$: displacement thickness.

$\vartheta(x) = \int_0^\infty \frac{u}{U}\left(1 - \frac{u}{U}\right) dy$: momentum thickness.

Since δ^* and ϑ are each in a different way dependent on the velocity profile $\frac{u(y)}{U}$ in the boundary layer, the ratio $\delta^*/\vartheta = H$ can be considered *as a characteristic of the velocity profile*. If these profiles constitute a one parameter family, the same dimensionless quantity can conveniently represent this parameter.

Adopting, from now on, this point of view, all properties depending on the velocity profile can, if expressed in a dimensionless form, be taken to be functions of H only. So, e. g., the shearing stress at the wall can be written as

$$\frac{\tau_0}{\rho U^2} = \frac{\nu}{U^2}\left(\frac{\partial u}{\partial y}\right)_0 = \frac{\nu}{U\vartheta}\left(\frac{\partial u/U}{\partial y/\vartheta}\right)_{y=0} = Re_\vartheta^{-1} \cdot T(H). \tag{2.4}$$

with ν: kinematic viscosity

$Re_\vartheta = \frac{U\vartheta}{\nu}$ Reynolds number referring to momentum thickness

$T(H)$: dimensionless function of H only.

This serves to write the momentum equation in the form (multiply by $\frac{2}{\rho U^2} Re_\vartheta$)

$$2 Re_\vartheta \frac{1}{U}\frac{dU}{dx}\vartheta(H+2) + 2 Re_\vartheta \frac{d\vartheta}{dx} = \frac{2}{\rho U^2} Re_\vartheta \tau_0 = 2 T(H):$$

This invites to the introduction of the new variable

$$\theta = \vartheta Re_\vartheta \tag{2.5}$$

with the derivative

$$\frac{d\theta}{dx} = \frac{d\vartheta}{dx} Re_\vartheta + \vartheta \frac{d}{dx}\left(\frac{U\vartheta}{\nu}\right) = 2 Re_\vartheta \frac{d\vartheta}{dx} + \frac{1}{U}\frac{dU}{dx}\vartheta Re_\vartheta. \tag{2.6}$$

The result can be written as

$$\frac{d\theta}{dx} - \theta \frac{1}{U}\frac{dU}{dx} = 2T(H) - 2(H+2)\theta \frac{1}{U}\frac{dU}{dx}. \tag{2.7}$$

The accelerations $\frac{1}{U}\frac{dU}{dx}$, however, at once generate traces in the velocity profile, for by (2.1) and (2.2)

$$\rho U \frac{dU}{dx} + \mu \left(\frac{\partial^2 u}{\partial y^2}\right)_{y=0} = 0$$

or

$$\left(\frac{\partial^2 u/U}{\partial (y/\vartheta)^2}\right)_{y=0} = -\frac{\vartheta^2}{\nu}\frac{dU}{dx} = -\vartheta Re_\vartheta \frac{1}{U}\frac{dU}{dx} = -\theta \frac{1}{U}\frac{dU}{dx}. \tag{2.8}$$

Due to the one parameter assumption, the left hand side can again be taken to be a function of H only, say (to retain agreement of symbols with (ref. 1)) $-\lambda_2(H)$. Hence (2.7) can be reduced to

$$\frac{d\theta}{dx} - \lambda_2(H) = 2T(H) - 2(H+2)\lambda_2(H) \tag{2.9}$$

in perfect agreement with formula (2.17) in (ref. 1). Now it appears that the function

$$2T(H) - \{2(H+2) - 1\}\lambda_2(H)$$

involving the velocity profile characteristics

$$T = \left(\frac{\partial u/U}{\partial y/\vartheta}\right)_{y=0}; \; H = \frac{\delta^*}{\vartheta};$$
$$\lambda_2 = -\left(\frac{\partial^2 u/U}{\partial (y/\vartheta)^2}\right)_{y=0} \tag{2.10}$$

can with satisfactory accuracy be approximated by a linear function of λ_2

$$2T - (2H+3)\lambda_2 = A - B\lambda_2 \tag{2.11}$$

with constant coefficients A en B (compare Walz, (ref. 3), and Thwaites, (ref. 4)). Suitable values of A and B can be inferred from fig. 1 in (ref. 1), taking the straight line $A - (B+1)\lambda_2 = H_2$ through the points representing the stagnation point profile and the "acceleration zero profile". They appear to be

$$A = 0{,}44 \text{ and } B = 5{,}18.$$

The resulting simplification of (2.9)

$$\frac{d\theta}{dx} = A - B\lambda_2 = A - B\theta \frac{1}{U}\frac{dU}{dx}$$

has the general solution

$$\theta = \lambda_2 \left(\frac{1}{U}\frac{dU}{dx}\right)^{-1} = \frac{A}{U^B}\left(\int_0^x U^B dx + c\right),$$

or with $c = 0$

$$\theta = \vartheta\, Re_\vartheta \frac{A}{U^B} \int_0^x U^B\, dx. \qquad (2.12)$$

Now

$$\vartheta\, Re_\vartheta = \frac{\vartheta^2 U}{\nu} = \vartheta^2 \cdot \frac{U_\infty L}{\nu} \cdot \frac{U}{U_\infty L} = \frac{\vartheta^2}{L} \cdot \frac{U}{U_\infty} Re,$$

L being a characteristic length and U_∞ a characteristic velocity, the velocity at infinity of the main flow in the case of an airfoil in a uniform parallel flow, and Re the adjoined Reynolds-number. Hence

$$\vartheta^2 = \frac{AU_\infty L}{U^{B+1}} Re^{-1} \int_0^x U^B\, dx \qquad (2.13)$$

which gives the momentum thickness by a simple integration.

Further

$$\lambda_2 = \frac{\vartheta^2}{L} \cdot \frac{1}{U_\infty} \cdot \frac{dU}{dx} \cdot Re. \qquad (2.14)$$

Other properties of the boundary layer (e.g. τ_0) cannot be deduced without recourse to an explicite specification of the velocity profiles. Using the propositions of T i m m a n, slightly different definitions are used in the regions of accelerated and retarded flow. For accelerated flow, the profile family is ($\eta = y/\delta$, δ "boundary layer thickness")

$$\frac{u}{U} = \frac{4(1-b)}{3\sqrt{\pi}} \int_0^\eta e^{-\eta^2}(1+\eta^2)d\eta + b(1-e^{-\eta^2}) \qquad (2.15)$$

and for retarded flow

$$\frac{u}{U} = \frac{4(1-b)}{3\sqrt{\pi}} \int_0^\eta e^{-\eta^2}(1+\eta^2)d\eta + b(1-e^{-\eta^2}) - \tfrac{1}{2} b\eta^2 e^{-\eta^2}. \qquad (2.16)$$

Both formulae involve one parameter, b.

Formula (2.15) yields, as shown in (ref. 1),

$$\frac{\delta^*}{\delta} = \int_0^\infty \left(1 - \frac{u}{U}\right) d\eta = 0{,}7523 + 0{,}1340\, b;$$

$$\frac{\vartheta}{\delta} = \int_0^\infty \frac{u}{U}\left(1 - \frac{u}{U}\right) d\eta = 0{,}2894 - 0{,}0147\, b - 0{,}0152\, b^2. \qquad (2.17)$$

Further, again for (2.15),

$$\left\{\frac{\partial^2 \frac{u}{U}}{\partial\left(\frac{y}{\delta}\right)^2}\right\}_{y=0} = 2b = \frac{\delta^2}{\vartheta^2}\left\{\frac{\partial^2 \frac{u}{U}}{\partial\left(\frac{y}{\vartheta}\right)^2}\right\}_{y=0} =$$

$$= (\text{comp. } (2.10)) - \lambda_2 \frac{\delta^2}{\vartheta^2} =$$

$$= \frac{-\lambda_2}{(0{,}2894 - 0{,}0147\, b - 0{,}0152\, b^2)^2}. \qquad (2.18)$$

The numerical relation between b and λ_2 is given in the following table:

b	$-1{,}0$	$-0{,}9$	$-0{,}8$	$-0{,}7$	$-0{,}6$	$-0{,}5$	$-0{,}4$	$-0{,}3$	$-0{,}2$	$-0{,}1$	0
λ_2	0,1669	0,1517	0,1359	0,1196	0,1029	0,0858	0,0686	0,0513	0,0340	0,0169	0

This formula determines b in terms of λ_2 (as given by (2.14)). The parameter H follows from

$$H^2 = \left(\frac{\delta^*}{\vartheta}\right)^2 = -\frac{2b}{\lambda_2}(0{,}7523 + 0{,}1340\, b)^2. \qquad (2.19)$$

Finally

$$\tau_0 = \rho U^2 Re_\vartheta^{-1} T = \rho U^2 Re_\vartheta^{-1} \left\{\frac{d\frac{u}{U}}{d\frac{y}{\vartheta}}\right\}_{y=0} =$$

$$= \rho U^2 Re_\vartheta^{-1} \frac{\vartheta}{\delta}\left\{\frac{d\frac{u}{U}}{d\frac{y}{\delta}}\right\}_{y=0} =$$

$$= \rho U^2 Re_\vartheta^{-1} \frac{\vartheta}{\delta} \cdot \frac{1-b}{\frac{3}{4}\sqrt{\pi}} =$$

$$= \rho U^2 Re_\vartheta^{-1} \sqrt{\frac{\lambda_2}{-2b}} \frac{1-b}{\frac{3}{4}\sqrt{\pi}}. \qquad (2.20)$$

At the pressure minimum, i. e. at the point where the acceleration vanishes $\left(\frac{dU}{dx} = 0\right)$, (2.15) must be replaced by (2.16). According to (2.8) and (2.10), $\lambda_2 = 0$ in this point, and hence (see (2.18)) $b = 0$ also. The profiles (2.15) and (2.16) are, thus, identical as required. In the region of retarded flow the last members of formulae (2.17) must, as shown in (ref. 1), be replaced by

$$0{,}7523 + 0{,}3556\, b$$
$$\text{and } 0{,}2894 + 0{,}0794\, b - 0{,}0737\, b^2 \qquad (2.21)$$

respectively. The equation (2.18) for b changes into

$$b = \frac{-\lambda_2}{(0{,}2894 + 0{,}0794\, b - 0{,}0737\, b^2)^2} \qquad (2.22)$$

and is given numerically in this table:

b	0	0,1	0,2	0,3	0,4	0,5	0,6	0,7	0,8	0,9	1,0
$-\lambda_2$	0	0,0088	0,0183	0,0282	0,0383	0,0483	0,0579	0,0668	0,0748	0,0816	0,0871

Further

$$H^2 = -\frac{b}{\lambda_2}(0{,}7523 + 0{,}3556\,b)^2 \qquad (2.23)$$

and

$$\tau_0 = \rho U^2 Re_\vartheta^{-1} \sqrt{\frac{\lambda_2}{-b}} \cdot \frac{1-b}{\frac{3}{4}\sqrt{\pi}} \qquad (2.24)$$

which shows that laminar separation occurs as soon as $b = 1$, or by (2.22), as

$$\lambda_2 = -0{,}08708.$$

The calculation, by (2.13), of ϑ should, hence, never be continued beyond the point, where (2.14) yields values of λ_2 *smaller* than $-0{,}08708$.

3 An empirical formula of Ludwieg and Tillmann for the shearing stress at the wall in the case of a turbulent boundary layer.

Turbulent boundary layers are supposed to have a *laminar sublayer which is so thin that it generally escapes observation*. Experimental results for the variation of the average velocity (on which the rapid fluctuations of turbulence are superimposed) with the distance to the wall do not take account of this sublayer. Hence the expression

$$\tau_0 = \mu \left(\frac{\partial u}{\partial y}\right)_{y=0}$$

for the shearing stress at the wall in the case of laminar flow cannot be related with empirical velocity profiles of the turbulent boundary layer, nor with theoretical propositions deduced without due reference to the alleged sublayer.

No adequate basic theory being available, the only method to predict the shearing stress at the wall in the case of a turbulent layer is to make use of suitable condensations of extensive systematic measurements. All semi-empirical methods to calculate turbulent boundary layers thus necessarily imply purely empirical data for the shearing stress at the wall, which relate this stress with appropriate properties of the velocity profile.

Measurements as required have been carried out by several investigators and a part of them is since long available. The shearing stress has, as far as known, never been measured directly; the usual procedure is to compute it by aid of von Karman's momentum equation from measured velocity profiles. For the case of a uniform main stream, both along flat plates and in cylindrical tubes, satisfactory results have been established, but most data obtained, in particular, for retarded flow outside the boundary layer are of questionable reliability. The queer point is that they suggest that the shearing stress at the wall would not vanish in the point of turbulent separation, as it yet probably does.

Exactly these problems have recently been reconsidered with great care by Ludwieg and Tillmann (ref. 2). These authors have advanced a quite plausible explanation for the imperfection of existing data referring to retarded flow; the experimental conditions are exactly such as to favour strongly the generation of so called secondary flows, that are strong disturbances originating from the *side* walls enclosing the main stream and spoiling the twodimensional character of the boundary layer on the top or bottom wall used for measurements. They claim to have found, that this undesired phenomenon can affect results for the shearing stress at the wall to over 40 %. Ludwieg and Tillmann further claim to have developed a method to measure the shearing stress which is far less sensitive to secondary flow phenomena. They do not compute the shearing stress by aid of von Karman's equation (which does not hold in cases of threedimensional flow), but they deduce it from direct *measurements of the heat transition coefficient*, with which it is very closely related. This method indeed looks very promising. Yet it must be said that Ludwieg and Tillmann's paper considered, (ref. 2), does not contain decisive and completely lucid arguments showing how they succeeded, if so, in eliminating all interferences *of secondary flow phenomena*. The results of their quite extensive measurements, however, do show the expected decrease of the shearing stress at the wall when approaching the turbulent separation point, and moreover comply satisfactorily with existing data referring to zero deceleration. They can be condensed to the following empirical formula

$$c_f = \frac{\tau_0}{\frac{\rho}{2}U^2} = \frac{\tau_0}{q} = 0{,}246 \cdot 10^{-0.678\,H} \cdot Re_\vartheta^{-0.268} \qquad (3.1)$$

with, as usual,

$H = \frac{\delta^*}{\vartheta}$ = *ratio of displacement to momentum thickness*

Re_ϑ = Reynolds number referring to momentum thickness $\left(\frac{U\vartheta}{\nu}\right)$.

The experiments of Ludwieg and Tillmann may also be said to confirm the finding of Gruschwitz, that the velocity profiles of the turbulent boundary layer constitute a one parameter family, the basic postulate of all semi-empirical calculation methods available.

Formula (3.1) will be adopted in the modified theory presented hereafter. It entails the very great advantage, that it allows a clear and practically unambiguous prediction of turbulent separation, at present a weak point in the computative treatment of turbulent boundary layers.

4 A revised semi-empirical method for the calculation of turbulent boundary layers.

The semi-empirical theories of the turbulent boundary layer have the object to establish methods for the predictive calculation of the *average* characteristics of the turbulent layer. They, thus, do not take care of the fluctuations occurring in the flow which represent its turbulence. For the *same reason*, velocity will, *in this chapter*, mean

time average of velocity, pressure time average of pressure, etc.

The basis of all semi-empirical theories of the turbulent boundary layer is formed by the assumption of Gruschwitz, that the velocity profiles constitute a one parameter family. This makes it possible, just as in the one parameter methods to determine the properties of the laminar boundary layer, to operate with suitable integrals of the differential equations of motion instead of with the differential equations themselves. The integral taken is again von Karman's momentum equation, which can be shown to hold again in the form

$$\frac{d\vartheta}{dx} + (H+2)\vartheta\,\frac{1}{U}\,\frac{dU}{dx} = \frac{\tau_0}{\rho U^2}, \quad (4.1)$$

all quantities involved being defined in exactly the same way as in the laminar case, with the proviso that, in these definitions, fluctuating quantities (u, τ_0, p, etc.) are to be replaced by the according time averages as preconcerted.

A second relation between the three quantities ϑ, H and τ_0 appearing in (4.1) is Ludwieg and Tillmann's formula for the shearing stress at the wall

$$\frac{\tau_0}{\rho U^2} = 0{,}123\,10^{-0.678\,H}\,.\,Re_\vartheta^{-0.268}. \quad (4.2)$$

What is needed in addition, is a suitable equation for the variation of the parameter H. No adequate theoretical principle being available, this relation will again have to be empirical. The same problem arises in all semi-empirical methods to treat turbulent boundary layers, and the most recent, probably best one, the method of Doenhoff and Tetervin (ref. 5), makes use of a formula

$$\vartheta\,\frac{dH}{dx} = e^{4.68(H-2.975)}\left[-\frac{\vartheta}{q}\,.\,\frac{dq}{dx}\,\frac{2\,q}{\tau_0} - \right.$$
$$\left. - 2{,}035\,(H-1{,}286)\right] \quad (4.3)$$

with $q = \frac{1}{2}\rho U^2$. This formula, however, cannot be adopted unmodified in the present case because it implies references to a predecessor of the relations (4.2) for the shearing stress(viz. to an according formula of Squire and Young) invalidated by the results of Ludwieg and Tillmann. It, yet, gives a valuable indication about the type of formula probably coming into consideration. It will, indeed, be shown that the following modified version is apt to cover quite adequately the experimental data available

$$\theta_t\,.\,\frac{dH}{dx} = f(H)\,.\,[-\Gamma - c(H-H')] \quad (4.4)$$

with

$$\theta_t = \vartheta\,Re_\vartheta^{0.268}, \quad (4.5)$$

$$\Gamma = \frac{\theta_t}{U}\,\frac{dU}{dx} = \frac{\vartheta}{U}\,\frac{dU}{dx}\,Re_\vartheta^{0.268}, \quad (4.6)$$

$f(H)$, c, H': function and constants to be determined by comparison with experimental data.

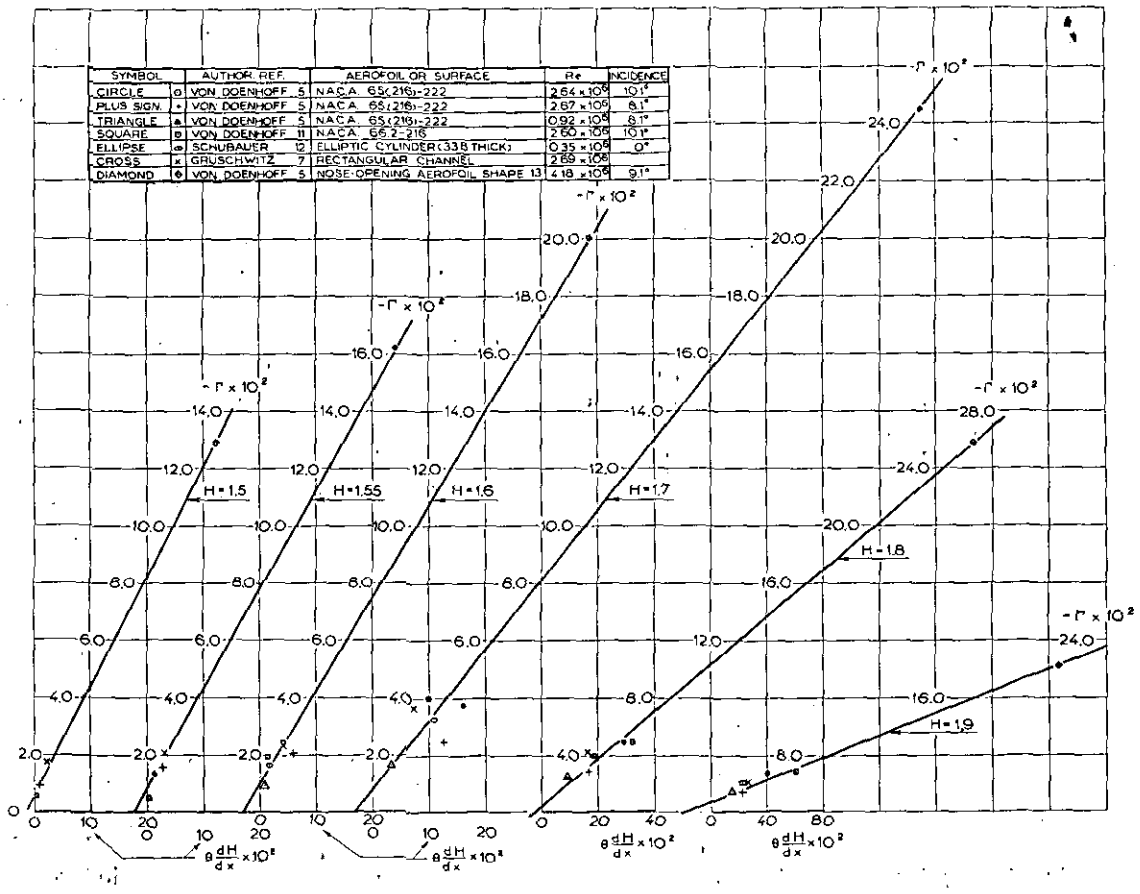

Fig. 1. $\vartheta\,\frac{dH}{dx}$ Against Γ for $H = 1{,}5$; $1{,}55$; $1{,}6$; $1{,}7$; $1{,}8$. $1{,}9$.

Considering that

$$\frac{d\theta_t}{dx} = \frac{d\vartheta}{dx} Re_\vartheta^{0.268} + 0{,}268\,\vartheta\, Re_\vartheta^{0.268}\left(\frac{1}{\vartheta}\frac{d\vartheta}{dx} + \frac{1}{U}\frac{dU}{dx}\right)$$

the following equivalent of (4.1) and (4.2), conveniently adapted to (4.6), can easily be established

$$\frac{d\theta_t}{xp} = 0{,}156\,.\,10^{-0.678\,H} - 1{,}268\,\Gamma(H + 1{,}7886). \qquad (4.7)$$

The calculation can be performed by aid of the triple (4.4), (4.6) and (4.7), starting from selected initial values of H and θ_t.

The experimental data, available for the determination of $f(H)$, c and H', have been collected by Garner (ref. 6). Denoting Garner's equivalents of Γ and θ by Γ_1 and θ_1, it is

$$\Gamma_1 = \frac{\vartheta}{U}\frac{dU}{dx} Re_\vartheta^{1/6}; \qquad \Gamma = \Gamma_1 Re_\vartheta^{0.1013}$$

$$\theta_{t,1} = \vartheta\, Re_\vartheta^{1/6} \qquad ; \qquad \theta_t = \theta_{t,1} Re_\vartheta^{0.1013}.$$

First, measured values of Γ and $\theta_t \frac{dH}{dx}$ referring to one and the same constant value of H are plotted against each other (see fig. 1 and table 1, with symbols explained in the table below), and the parameters $f(H)$ and $f(H)c(H - H')$ of the straight line represented by (4.4) are determined by aid of the method of least squares. This procedure is performed for an appropriate sequence of H values.

Next, the double logarithms of the obtained values of $f(H)$ are plotted against H (given in fig. 2A). They suggest a parabolic curve, representable by

$$\log\log f(H) = 1{,}1475\,(H - 0{,}6)\,(H - 1{,}87).$$

The resulting expression for $f(H)$ itself,

$$f(H) = 10^{10^{1.1475\,(H-0.6)\,(H-1.87)}}$$

is given in fig. 2B and can be seen to cover the calculated values quite satisfactorily.

Finally, the coefficients c and H' of the straight line $c(H - H')$ have again been determined by the method of least squares, demanding compliance with the sequence of $c(H - H')$ values obtained earlier. It is found that

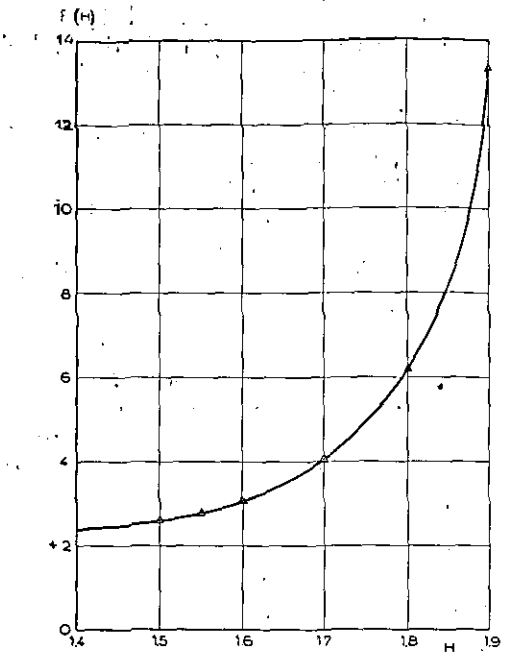

Fig. 2B. $f(H)$ against H.
The drawn line represents $f(H) = 10^{10^{1.1475\,(H-0.6)\,(H-1.87)}}$

The symbols, indicated in fig. 1 and table 1, refer to following measurements.

Symbol		Author, ref.	Aerofoil or surface	Re	Incidence
circle	⊙	von Doenhoff 5	NACA 65 (216) — 222	$2{,}64 \times 10^6$	10,1°
plus sign	+	von Doenhoff 5	NACA 65 (216) — 222	$2{,}67 \times 10^6$	8,1°
triangle	△	von Doenhoff 5	NACA 65 (216) — 222	$0{,}92 \times 10^6$	8,1°
square	□	von Doenhoff 11	NACA 66,2 — 216	$2{,}60 \times 10^6$	10,1°
ellipse	⬭	Schubauer 12	Elliptic cylinder (33/8 thick)	$0{,}35 \times 10^6$	0°
cross	×	Gruschwitz 7	Rectangular channel	$2{,}69 \times 10^6$	
diamond	◇	von Doenhoff 5	Nose-opening aerofoil shape 13	$4{,}18 \times 10^6$	9,1°

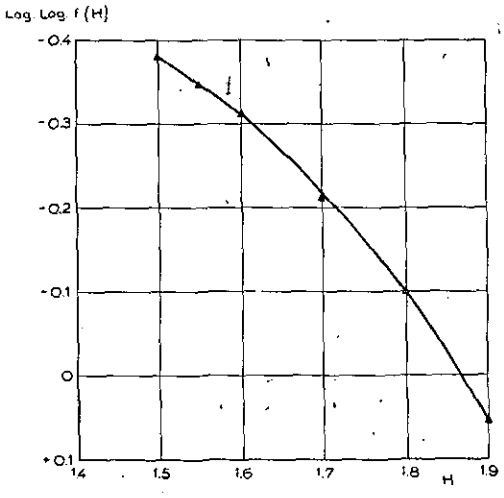

Fig. 2A. Log . log . $f(H)$ against H.
The drawn line represents the parabolic curve Log . log . $f(H) = 1.1475\,(H - 0.6)\,(H - 187)$.

$$c = 0{,}02489 \quad \text{and} \quad H' = 1{,}3025$$

but the result is, as shown in fig. 2C, not very satisfactory. It can easily be improved by adding an oscillatory term to c. Taking

$$c = 0{,}02214 + 0{,}01 \sin 14{,}8\,(H - 1{,}46) \quad (4.8)$$

the acceptable result of fig. 2C is obtained.

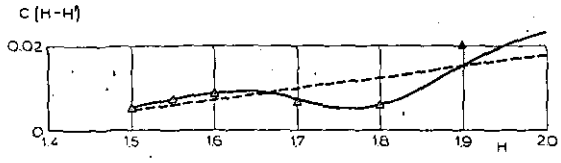

Fig. 2C. $C(H - H')$ against H.
The dotted line represents $C(H - H') = 0.02489\ (H - 1.3025)$.
The drawn line represents formula (4.8).

Thus, the final specification of the empirical relation (4.4) becomes

$$\theta_1 \frac{dH}{dx} = 10^{10^{1.1475\,(H-0.6)\,(H-1.87)}} \cdot [-\Gamma - (H - 1{,}3025) \{0{,}02214 + 0{,}01 \sin 14{,}8\,(H - 1{,}46)\}]. \quad (4.9)$$

The empirical formula (4.9) has the satisfactory property to agree in principle with a result of Tetervin and Lin (ref. 13) for the law controlling the variations of the parameter H, deduced from the energy equation.

For the flow along a flat plate, $\Gamma = 0$ and $\frac{dH}{dx} = 0$, equation (4.9) gives

$$H = 1{,}3025$$

in appropriate agreement with the value

$$H = 1{,}3037$$

following from direct measurements carried out by Nikuradse (ref. 9).

The calculation of a turbulent boundary layer by the method explained thus requires the integration of the two simultaneous non linear differential equations (4.7) and (4.9).

This integration can conveniently and accurately be performed by a modified Adam's method (see appendix).

Further the shearing stress is given by

$$\frac{\tau_0}{2q} = 0{,}123 \cdot 10^{-0.678\,H}\, Re_\vartheta^{-0.268} = \frac{\zeta\vartheta}{\theta}. \quad (4.10)$$

Denoting the initial value by the index 1

$$\frac{\vartheta}{\vartheta_1} = \left(\frac{\theta}{\theta_1}\right)^{0.78864} \left(\frac{q}{q_1}\right)^{-0.10568}, \quad (4.11)$$

$$\frac{\tau_0}{\tau_{01}} = \frac{\zeta}{\zeta_1} \cdot \frac{\vartheta}{\vartheta_1} \cdot \frac{\theta_1}{\theta} \cdot \frac{q}{q_1} = \frac{\zeta}{\zeta_1} \cdot \left(\frac{\theta}{\theta_1}\right)^{-0.21136} \left(\frac{q}{q_1}\right)^{0.89432}. \quad (4.12)$$

In the calculation of the turbulent boundary layer by means of (4.7) and (4.9) the separation is no longer, as in Doenhoff's and Tetervin's formula, connected with some more or less clearly specified values of H.

Separation occurs, if suddenly H increases so rapidly, that the numerical integration procedure breaks down. At the same time the shearing stress at the wall as given by Ludwieg and Tillmann's formula also decreases very rapidly (near the separation point).

Examples show that the computed location of the separation point is very insensitive with respect to variation of the initial value of H. If this initial value is unknown, the value $H_1 = 1{,}3$, can be selected but any other value $< 1{,}8$ will do also, if the corresponding value of $\frac{dH}{dx}$ is not too large.

5 A numerical example.

As a numerical example the momentum thickness ϑ, the form-parameter H and the shearing stress τ_0 at the wall will be calculated for an aerofoil NACA 65(216)—222 at an angle of incidence $\alpha = 10{,}1°$ and a Reynold's number $Re = 2{,}64 \times 10^6$.

The measured pressure distribution $\frac{q}{q_\infty} = \left(\frac{U}{U_\infty}\right)^2$ at the outer edge of the boundary layer, its derivative $\frac{c}{q_\infty}\frac{dq}{ds}$ (c = aerofoil chord) and the initial value of the momentum thickness ϑ/c will be taken from NACA report 772. The numerical computation according to formulae (4.7) and (4.9) will be performed by a modified Adam's method (ref. 10) for different initial values of the form-parameter H ($H = 1{,}4$; $1{,}56$; $1{,}7$).

The variation of the initial value appears to have no influence on the position of the separation point of the turbulent boundary layer. In each of the three cases the separation point is found to be located at $\frac{s}{c} = 0{,}545$. The same variation (if restricted to $H < 1{,}8$) appears to have hardly any influence on the course of the momentum thickness which is calculated from (4.11). The course of the shearing stress at the wall, however, does depend on the initial value of H. The calculation and the results are given in the table 2, and figs. 3A, 3B and 3C. If a measured value is taken as initial value for H, the graph of H against $\frac{s}{c}$ agrees well with measurements.

The method has the advantage that the calculation of the separation point is no longer connected with a badly specified value of H, as in other methods (Gruschwitz, Doenhoff and Tetervin). Separation occurs if H grows so rapidly that a further numerical calculation by Adam's method breaks down. In addition this rapid increase of H causes the wall shearing stress to decrease very rapidly.

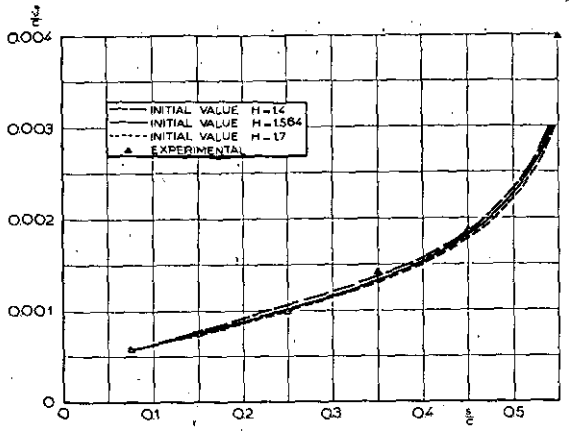

Fig. 3A. Variation of experimental and calculated value of momentum thickness $\frac{\vartheta}{c}$ with $\frac{s}{c}$.

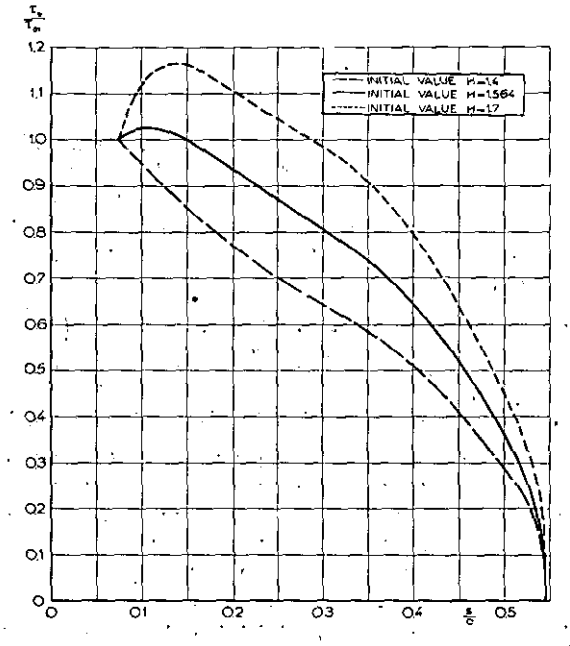

Fig. 3B. Variation of the wall shearing stress with $\frac{s}{c}$.

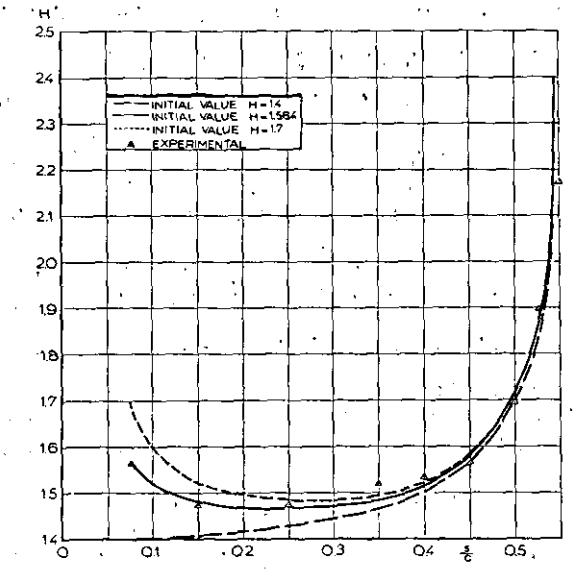

Fig. 3C. Variation of experimental and calculated value of shape parameter H with $\frac{s}{c}$.

6 References.

1. TIMMAN, R. A one Parameter Method for the Calculation of Laminar Boundary Layers. Report F. 35.
2. LUDWIEG, H. and TILLMANN, W. Untersuchungen über die Wandschubspannung in turbulenten Reibungsschichten. Ing.-Arch. 4 (1949) p. 288.
3. WALZ, A. Zur theoretischen Berechnung des Höchstauftriebsbeiwertes von Tragflügelprofilen ohne und mit Auftriebsklappen. Forschungsbericht No. 43/W/11 (1943) p. 7.
4. THWAITES, B. Approximate Calculation of the Laminar Boundary Layer. The Aeronautical Quarterly, Nov. 1949, p. 245.
5. DOENHOFF, A. VON and TETERVIN, N. Determination of General Relations for the Behaviour of Turbulent Boundary Layers. NACA Rep. No. 772 (1943).
6. GARNER, H. C. The Development of Turbulent Boundary Layers. R. and M. No. 2133 (June 1944).
7. GRUSCHWITZ, E. Die turbulente Reibungsschicht in ebener Strömung bei Druckabfall und Druckanstieg. Ing.-Arch. 3. Sept. 1931, pp. 321—346.
8. KOCK, A. C. DE en PLANTEMA, F. J. Het verwerken van waarnemingen. NLL Rep. S. 361.
9. NIKURADSE, I. Turbulente Reibungsschichten an der Platte. Zentrale Wiss. Berichtswesen der Lftf. Berlin-Adlershof. Oldenbourg, München 1942.
10. BURGERHOUT, T. J. Differentiemethoden. NLL Rep. R 7 (for internal use).
11. DOENHOFF, A. VON, and TETERVIN, N. Investigation of the Variation of Lift Coefficient with Reynolds Number at a moderate Angle of Attack on a Low-Drag Aerofoil. NACA C. B. Nov. 1942.
12. SCHUBAUER, G. B. Air Flow in the Boundary Layer of an Elliptic Cylinder. NACA Rep. No. 652 (1939).
13. TETERVIN, N. and LIN, C. A general integral Form of the Boundary-Layer Equation for Incompressible Flow with an Application to the Calculation of the Separation Point of Turbulent Boundary Layers. NACA, T. N. 2158 (1950).

APPENDIX.

Numerical integration of the ordinary differential equation $y = f(x, y)$ by aid of a modified Adams' method.

In order to integrate numerically the ordinary differential equation

$$y' = f(x, y)$$

with the initial condition

$$y = y_0 \text{ for } x = x_0,$$

introduce an appropriate small-step subdivision $x_0, x_1, x_2, \ldots\ldots$ of the interval of the x variable, taking all differences $x_{i+1} - x_i = w$ equal, and prepare the following scheme

x	y	δ^{-1}	$\delta^0 = wf$	δ^1	δ^2	δ^3	δ^4
x_0	y_0	$\delta^{-1}_{-1/2}$	δ^0_0				
				$\delta^1_{1/2}$			
x_1	y_1	$\delta^{-1}_{1/2}$	δ^0_1		δ^2_1		
				$\delta^1_{3/2}$		$\delta^3_{3/2}$	
x_2	y_2	$\delta^{-1}_{3/2}$	δ^0_2		δ^2_2		δ^4_2
				$\delta^1_{5/2}$		$\delta^3_{5/2}$	
x_3	y_3	$\delta^{-1}_{5/2}$	δ^0_3		δ^2_3		
⋮	⋮	⋮	⋮	⋮	⋮	⋮	⋮

The last four columns contain first, second, third and fourth differences of the δ^0 column, which itself contains the values

$$\delta^0_i = wf(x_i, y_i).$$

The δ^{-1} column, called sum column, contains the sum values of the δ^0 column, so that the δ^0 column on its turn contains first differences of the δ^{-1} column.

The procedure is as follows:
Insert y_0 to x_0 and put

$$\delta_0^0 = \delta_1^0 = \delta_2^0 = \delta_3^0 = \delta_4^0 = wf(x_0, y_0)$$
$$\delta_{1/2}^1 = \delta_{3/2}^1 = \delta_{5/2}^1 = \delta_{7/2}^1 = \delta_1^2 = \delta_2^2 = \delta_3^2 = \ldots\ldots = \delta_2^4 = 0.$$

Next, insert

$$\delta_{-1/2}^{-1} = y_0 - \tfrac{1}{2}\, wf(x_0, y_0)$$
$$\delta_{1/2}^{-1} = y_0 + \tfrac{1}{2}\, wf(x_0, y_0)$$
$$\delta_{3/2}^{-1} = y_0 + \tfrac{3}{2}\, wf(x_0, y_0)$$
$$\ldots\ldots\ldots\ldots\ldots\ldots$$
$$\delta_{9/2}^{-1} = y_0 + \tfrac{9}{2}\, wf(x_0, y_0)$$

and

$$y_i = \tfrac{1}{2}\,(\delta_{i-1/2}^{-1} + \delta_{i+1/2}^{-1}) = y_0 + iwf(x_0, y_0);$$
$$i = 1, 2, 3, 4.$$

Now, cross out the δ_1^0, δ_2^0, δ_3^0 and δ_4^0 values inserted previously and substitute the computed values

$$\delta_i^0 = wf(x_i, y_i);\ i = 1, 2, 3, 4.$$

Accordingly, replace the zeroes inserted in the difference columns by first, second, third and fourth differences appropriate to the δ_i^0 values.

Next, replace the $\delta_{i+1/2}^{-1}$ value for $i = 0$, by the result computed from the following general formula

$$\delta_{i+1/2}^{-1} = y_i + \tfrac{1}{2}\,\delta_i^0 + \frac{1}{24}\,(\delta_{i-1/2}^1 + \delta_{i+1/2}^1) - \frac{11}{1440}\,(\delta_{i-1/2}^3 + \delta_{i+1/2}^3) \qquad (1)$$

(using linear extrapolations in the δ columns as far as necessary). The other sum columns follows from

$$\delta_{i+1/2}^{-1} = \delta_{i-1/2}^{-1} + \delta_i^0. \qquad (2)$$

Similarly, replace y_i values inserted previously by the results of the general formula

$$y_i = \tfrac{1}{2}\,(\delta_{i-1/2}^{-1} + \delta_{i+1/2}^{-1}) - \frac{1}{24}\,(\delta_{i-1/2}^1 + \delta_{i+1/2}^1) + \frac{11}{1440}\,(\delta_{i-1/2}^3 + \delta_{i+1/2}^3) \qquad (3)$$

and go on by computing new δ^0 values from the formula

$$\delta_i^0 = wf(x_i, y_i).$$

This recurrent process is repeated untill, to the required accuracy none of the inserted values changes any more.

Subsequently, the δ^2 and the δ^4 columns are completed up to δ_4^2 and δ_4^4 (in general: up to δ_i^2 and δ_i^4 by extrapolation, and an y_5 (generally y_{i+1}) value is calculated from

$$y_{i+1} = y_{i-1} + 2\,\delta_i^0 + \frac{1}{3}\,\delta_i^2 - \frac{1}{90}\,\delta_i^4. \qquad (4)$$

Next

$$\delta_{i+1}^0 = wf(x_{i+1}, y_{i+1}) \qquad (5)$$

is inserted, and the extrapolated differences are modified so as to agree with this δ_{i+2}^0 value.

The value of y_6, generally of y_{i+2}, can now be calculated by means of (4), and the value δ_6^0, generally δ_{i+2}^0, by means of (5). The extrapolated differences can be revised accordingly. The final value of y_5, generally y_{i+1}, then follows from (3). The final value of δ_{i+1}^0 is brought in accordance with this result and the scheme of differences is revised so as to agree with δ_{i+1}^0, and so on.

The magnitude of the x steps is to be adjusted so that the next term, $-\frac{191}{60480}\,\delta_i^5$ in the expression (3) can be neglected without reduction of the accuracy decided upon. It is possible to halve, or to double, the magnitude of the steps, if desired, at some appropriate point.

The method will, in most applications, be found to work very conveniently. The convergence of the iterations is usually extremely rapid. The resulting accuracy is high.

TABLE 1.

Symbol	H	Re_ϑ	Γ	$\vartheta \frac{dH}{dx}$	H	Re_ϑ	Γ	$\vartheta \frac{dH}{dx}$	H	Re_ϑ	Γ	$\vartheta \frac{dH}{dx}$
⊙		4910	— 0,0054	0,0053		6250	— 0,0138	0,0107		7230	— 0,0246	0,0424
+		4960	— 0,0092	0,0104		5850	— 0,0156	0,0241		6430	— 0,0205	0,0608
△										1980	— 0,0092	0,0085
⊡	1,5				1,55	4330	— 0,0044	0,0019	1,6	7730	— 0,0190	0,0128
⊙										920	— 0,0162	0,0151
×		1880	— 0,0175	0,0235		2140	— 0,0206	0,0314		2370	— 0,0238	0,0411
◇		55000	— 0,1291	0,3220		59610	— 0,1626	0,4374		63600	— 0,2007	0,5865
⊙		8690	— 0,0379	0,1629		9770	— 0,0495	0,2957		10340	— 0,0560	0,4069
+		7000	— 0,0249	0,1277		7600	— 0,0283	0,1704		8350	— 0,0321	0,2242
△		2600	— 0,0166	0,0347		2990	— 0,241	0,0882		3240	— 0,0293	0,1529
⊡	1,7	10340	— 0,0400	0,0996	1,8	7860	— 0,0493	0,3178	1,9	13900	— 0,0596	0,6242
⊙		1100	— 0,0330	0,1096		1190	— 0,0400	0,1881		1270	— 0,0433	0,2372
×		3060	— 0,0371	0,0712		3780	— 0,0430	0,1613		4290	— 0,0448	0,2543
◇		70100	— 0,2444	0,9742		75800	— 0,2537	1,5356		80880	— 0,2057	2,4747

H	$f(H)$	$f(H)\,C(H-H')$	$C(H)\,(H-H')$	$\log\log f(H)$
1,5	2,6024	0,0146	0,0056	— 0,3816
1,55	2,8136	0,0211	0,0075	— 0,3475
1,6	3,0580	0,0276	0,0090	— 0,3138
1,7	4,0867	0,0277	0,0068	— 0,2137
1,8	6,2164	0,0395	0,0064	— 0,1004
1,9	13,3396	0,2721	0,0204	0,0512

TABLE 2.

Aerofoil section NACA 65(216)—222; $Re = 2{,}64 \times 10^6$ $\alpha = 10{,}1°$.
Calculation of H, ϑ and τ_0 for initial values of $H = 1{,}564$, 1,400 and 1,700.

s/c	q/q_∞	$\frac{c}{q_\infty}\frac{dq}{ds}$	$\frac{\delta}{c}\cdot 10^2$	$\Gamma\cdot 10^2 = \frac{\delta}{2q}\frac{dq}{ds}\cdot 10^2$	H	$\frac{d\delta}{ds}$	$c\frac{dH}{ds}$	s/c	$\frac{\vartheta}{c}\cdot 10^2$	$\frac{\tau_0}{\tau_{01}}$
0,075	2,550	— 2,490	0,4612	— 0,225	1,564	0,0231	— 2,249	0,095	0,0621	1,020
0,080	2,538	— 2,437	0,4729	— 0,227	1,554	0,0234	— 1,999	0,105	0,0645	1,024
0,085	2,527	— 2,385	0,4847	— 0,229	1,544	0,0237	— 1,785	0,125	0,0693	1,021
0,090	2,516	— 2,337	0,4966	— 0,231	1,536	0,0239	— 1,600	0,145	0,0743	1,005
0,095	2,506	— 2,291	0,5086	— 0,233	1,528	0,0241	— 1,441	0,265	0,1070	0,850
0,100	2,496	— 2,249	0,5207	— 0,235	1,521	0,0244	— 1,302	0,345	0,1305	0,749
0,105	2,486	— 2,209	0,5329	— 0,237	1,515	0,0246	— 1,177	0,405	0,1544	0,635
0,110	2,478	— 2,172	0,5453	— 0,239	1,509	0,0248	— 1,069	0,445	0,1770	0,536
0,115	2,470	— 2,140	0,5577	— 0,242	1,504	0,0250	— 0,971	0,485	0,2097	0,416
0,125	2,448	— 2,090	0,5829	— 0,249	1,495	0,0255	— 0,798	0,505	0,2321	0,346
0,135	2,420	— 2,065	0,6086	— 0,260	1,488	0,0261	— 0,644	0,515	0,2452	0,308
0,145	2,399	— 2,047	0,6351	— 0,271	1,483	0,0267	— 0,516	0,525	0,2598	0,264
0,155	2,380	— 2,031	0,6620	— 0,283	1,478	0,0272	— 0,407	0,530	0,2674	0,237
0,165	2,360	— 2,010	0,6894	— 0,294	1,475	0,0278	— 0,321	0,535	0,2757	0,202
0,185	2,321	— 2,003	0,7461	— 0,322	1,469	0,0290	— 0,159	0,540	0,2837	0,121
0,205	2,280	— 1,983	0,8055	— 0,350	1,467	0,0302	— 0,047			
0,225	2,240	— 1,917	0,8670	— 0,371	1,467	0,0311	+ 0,017			
0,245	2,200	— 1,823	0,9299	— 0,385	1,468	0,0317	0,051			
0,265	2,162	— 1,732	0,9936	— 0,398	1,469	0,0322	0,073			
0,285	2,131	— 1,651	1,0585	— 0,410	1,471	0,0326	0,087			
0,305	2,101	— 1,614	1,1239	— 0,432	1,473	0,0335	0,122			
0,345	2,033	— 1,845	1,2677	— 0,575	1,482	0,0393	0,354			
0,365	1,994	— 2,048	1,3510	— 0,694	1,491	0,0441	0,524			
0,405	1,899	— 2,581	1,5541	— 1,056	1,521	0,0588	0,981			
0,445	1,785	— 3,210	1,8350	— 1,650	1,572	0,0837	1,663			
0,465	1,717	— 3,546	2,0208	— 2,087	1,611	0,1026	2,180			
0,485	1,645	— 3,890	2,2507	— 2,661	1,661	0,1281	2,959			
0,490	1,625	— 3,970	2,3176	— 2,831	1,677	0,1358	3,228			
0,500	1,586	— 4,170	2,4608	— 3,235	1,713	0,1544	3,983			
0,505	1,566	— 4,222	2,5407	— 3,425	1,734	0,1634	4,435			
0,510	1,545	— 4,262	2,6242	— 3,620	1,757	0,1728	5,020			
0,515	1,525	— 4,282	2,7132	— 3,809	1,784	0,1822	5,783			
0,520	1,500	— 4,292	2,8065	— 4,015	1,816	0,1926	6,972			
0,525	1,475	— 4,290	2,9060	— 4,226	1,855	0,2038	9,055			
0,530	1,450	— 4,265	3,0107	— 4,428	1,968	0,2155	13,89			
0,535	1,431	— 4,080	3,1216	— 4,450	2,000	0,2206	37,25			
0,540	1,407	— 3,380	3,2300	— 3,880	2,310	0,2059	$9{,}10^8$			
0,545	1,390	— 3,006	3,3163	— 3,579						
0,075	2,550	— 2,490	0,4612	— 0,225	1,400	0,0266	0,055	0,095	0,0627	0,959
0,085	2,527	— 2,385	0,4878	— 0,230	1,401	0,0268	0,065	0,105	0,0653	0,940
0,095	2,506	— 2,291	0,5144	— 0,235	1,402	0,0270	0,074	0,125	0,0706	0,905
0,105	2,486	— 2,209	0,5410	— 0,240	1,403	0,0272	0,084	0,145	0,0760	0,866
0,115	2,470	— 2,140	0,5692	— 0,247	1,404	0,0274	0,096	0,265	0,1101	0,684
0,125	2,448	— 2,090	0,5967	— 0,255	1,405	0,0277	0,115	0,345	0,1341	0,594
0,135	2,420	— 2,065	0,6246	— 0,267	1,406	0,0282	0,146	0,405	0,1587	0,502
0,145	2,399	— 2,047	0,6531	— 0,279	1,407	0,0286	0,176	0,445	0,1817	0,421
0,155	2,380	— 2,031	0,6819	— 0,291	1,410	0,0291	0,189	0,485	0,2150	0,326
0,165	2,360	— 2,010	0,7117	— 0,303	1,413	0,0295	0,199	0,505	0,2379	0,272
0,185	2,321	— 2,003	0,7712	— 0,333	1,416	0,0306	0,255	0,515	0,2512	0,243
0,205	2,280	— 1,983	0,8337	— 0,363	1,422	0,0317	0,284	0,525	0,2661	0,211
0,225	2,240	— 1,917	0,8981	— 0,384	1,428	0,0325	0,287	0,530	0,2739	0,192
0,245	2,200	— 1,823	0,9634	— 0,399	1,434	0,0329	0,273	0,535	0,2822	0,170
0,265	2,162	— 1,732	1,0296	— 0,412	1,438	0,0334	0,266			
0,285	2,131	— 1,651	1,0969	— 0,425	1,444	0,0338	0,249			
0,305	2,101	— 1,614	1,1651	— 0,448	1,449	0,0346	0,260			
0,325	2,068	— 1,700	1,2356	— 0,508	1,454	0,0370	0,344			
0,365	1,994	— 2,048	1,3984	— 0,718	1,472	0,0454	0,615			
0,405	1,899	— 2,581	1,6079	— 1,093	1,505	0,0606	1,045			
0,425	1,845	— 2,885	1,7400	— 1,360	1,529	0,0715	1,331			
0,445	1,785	— 3,210	1,8966	— 1,705	1,559	0,0861	1,698			
0,465	1,717	— 3,546	2,0871	— 2,155	1,597	0,1054	2,196			
0,475	1,682	— 3,700	2,1985	— 2,418	1,622	0,1170	2,509			
0,485	1,645	— 3,890	2,3219	— 2,745	1,648	0,1315	2,937			
0,495	1,608	— 4,080	2,4628	— 3,124	1,680	0,1487	3,511			
0,500	1,586	— 4,170	2,5392	— 3,338	1,699	0,1586	3,897			
0,510	1,545	— 4,262	2,7069	— 3,734	1,742	0,1774	4,822			
0,520	1,500	— 4,292	2,8940	— 4,140	1,796	0,1976	6,421			
0,530	1,450	— 4,265	3,1032	— 4,564	1,876	0,2204	10,91			
0,535	1,431	— 4,080	3,2154	— 4,584	1,942	0,2244	18,77			
0,540	1,407	— 3,380	3,3260	— 3,995	2,080	0,2020	121,1			
0,545	1,390	— 3,000	3,4070	— 3,677	3,300					

TABLE 2 (*continued*).

Aerofoil section NACA 65(216)—222; $Re = 2{,}64 \times 10^6$, $\alpha = 10{,}1°$.
Calculation of H, ϑ and τ_0 for initial values of $H = 1{,}564$, 1,400 and 1,700.

s/c	q/q_∞	$\frac{c}{q_\infty}\frac{dq}{ds}$	$\frac{\vartheta}{c}\cdot 10^2$	$\Gamma \cdot 10^2 = \frac{\vartheta}{2q}\frac{dq}{ds}\cdot 10^2$	H	$\frac{d\vartheta}{ds}$	$c\frac{dH}{ds}$	s/c	$\frac{\delta}{c}\cdot 10^2$	$\frac{\tau_0}{\tau_{01}}$
0,075	2,550	— 2,490	0,4612	— 0,225	1,700	0,0209	— 6,004	0,095	0,0621	1,104
0,085	2,527	— 2,385	0,4826	— 0,228	1,651	0,0217	— 4,072	0,105	0,0645	1,137
0,095	2,506	— 2,291	0,5046	— 0,231	1,615	0,0225	— 3,001	0,125	0,0693	1,161
0,105	2,486	— 2,209	0,5272	— 0,234	1,586	0,0232	— 2,293	0,145	0,0733	1,168
0,115	2,470	— 2,140	0,5510	— 0,239	1,569	0,0236	— 1,890	0,265	0,1054	1,028
0,125	2,448	— 2,090	0,5746	— 0,245	1,551	0,0242	— 1,519	0,345	0,1285	0,920
0,135	2,420	— 2,065	0,5994	— 0,256	1,539	0,0249	— 1,256	0,405	0,1519	0,783
0,145	2,399	— 2,047	0,6246	— 0,267	1,525	0,0256	— 0,991	0,445	0,1743	0,661
0,155	2,380	— 2,031	0,6505	— 0,278	1,518	0,0262	— 0,831	0,485	0,2065	0,514
0,165	2,360	— 2,010	0,6773	— 0,289	1,512	0,0268	— 0,695	0,505	0,2286	0,428
0,185	2,321	— 2,003	0,7317	— 0,316	1,499	0,0282	— 0,430	0,515	0,2414	0,382
0,205	2,280	— 1,983	0,7897	— 0,343	1,493	0,0295	— 0,261	0,525	0,2558	0,331
0,225	2,240	— 1,917	0,8497	— 0,264	1,489	0,0304	— 0,153	0,535	0,2713	0,262
0,245	2,200	— 1,823	0,9110	— 0,377	1,486	0,0310	— 0,084			
0,265	2,162	— 1,732	0,9740	— 0,390	1,486	0,0315	— 0,046			
0,305	2,101	— 1,614	1,102	— 0,423	1,485	0,0329	+ 0,042			
0,345	2,033	— 1,845	1,238	— 0,562	1,490	0,0386	0,301			
0,385	1,949	— 2,297	1,415	— 0,834	1,513	0,0496	0,682			
0,425	1,845	— 2,885	1,649	— 1,289	1,548	0,0684	1,254			
0,465	1,717	— 3,546	1,979	— 2,044	1,615	0,1007	2,165			
0,475	1,682	— 3,700	2,088	— 2,297	1,638	0,1119	2,494			
0,495	1,608	— 4,080	2,340	— 2,969	1,696	0,1422	3,563			
0,515	1,525	— 4,282	2,662	— 3,737	1,784	0,1789	5,742			
0,525	1,475	— 4,292	2,849	— 4,143	1,850	0,1998	8,714			
0,535	1,431	— 4,080	3,061	— 4,364	1,970	0,2152	24,95			
0,545	1,390	— 3,000	3,280	— 3,540	2,410		10^{32}			

CCL Class. D 06 : F 41

REPORT F. 96.

Spontaneous Oscillations of an Aerofoil due to Instability of the Laminar Boundary Layer

by

Ir A. I. VAN DE VOOREN and H. BERGH *).

Summary.

Spontaneous oscillations of an aerofoil with a spanwise axis of rotation at the quarter chord point were observed in a windtunnel at Reynolds numbers for which the major part of the boundary layer was laminar. The oscillations were of small amplitude, while the frequencies coincided with natural frequencies of the model. Moreover, the frequencies were such that, according to the usual theory, they were within the range for which the laminar boundary layer is unstable. The motion of the aerofoil facilitated the occurrence of initial disturbances of the same frequency, which in the unstable region of the boundary layer were again amplified. In this way a self-exciting feed-back mechanism with its amplification in the boundary layer was realized.

Contents.

1 Introduction.

During the performance of an experimental program intended to measure the aerodynamic forces on an oscillating aerofoil, spontaneous oscillations of the model occurred under certain circumstances. The model, which had a span of 0.8 m and a chord of 0.3 m, could rotate about a spanwise axis and was kept in the position of zero angle of incidence by a couple of springs, which gave the model a natural frequency of 5 cps. The oscillations occurred in the velocity range from 4 to 13 m/sec and only if the axis of rotation coincided with the quarter-chord point. It was established by aid of the stethoscope method that for speeds below 11 m/sec the whole boundary layer was laminar, while for speeds above 11 m/sec a part of the boundary layer became turbulent. When the whole boundary layer was made turbulent, for instance by fitting disturbance wires at both sides of the aerofoil near the leading edge, no spontaneous oscillations occurred.

The oscillations are considered to be due to instability of the laminar boundary layer. This instability has first been predicted by TOLLMIEN (ref. 1) and SCHLICHTING (ref. 2) on theoretical grounds, while LIN (ref. 3) obtained more accurate results for the critical values of the important parameters. Experimental evidence has been obtained from the measurements of SCHUBAUER and SKRAMSTAD (ref. 4), while recently, MALOTAUX, V. D. GON and YAP KIE JAN (ref. 5) have found undamped oscillations in the laminar boundary layer of an aeroplane in free flight.

In the present experiments conditions in a part of the boundary layer are such that amplification of disturbances of certain frequency can occur. Such oscillations in the boundary layer will lead to periodic fluctuations in the pressure and hence, in general, a small moment will act on the model. In order that this moment will induce oscillations of the model, the two following conditions must be satisfied

(i) the model must be in a state near to indifferent equilibrium, as is the case when rotations about the quarter-chord axis are allowed. Otherwise the moment will be too small to yield any perceptable motion.

(ii) the frequency of the moment must coincide with one of the natural frequencies of the model. In fact, it was found that the frequencies of the spontaneous oscillations were the same as the natural frequencies of the elastic aerofoil (they were equal to a number of discrete values ranging from 60 to 300 cps).

An oscillation of the model, affected in this way, will, moreover easily induce new disturbances of the same frequency at points more ahead in the boundary layer and these disturbances will

*) Acknowledgement.
The authors wish to thank DR J. H. GREIDANUS and DR R. TIMMAN for valuable discussions.

again be amplified. Hence, a self exciting feedback mechanism with its amplification in the boundary layer has been realized.

This investigation has been performed by order of the Netherlands Aircraft Development Board (N. I. V.).

2 Experimental results.

An aerofoil (span 0.8 m, chord 0.3 m, maximum thickness 7.3 % at 30 % of the chord, symmetrical profile) was placed in a rectangular channel (width 0.8 m, height 1.1 m), which itself was built in a windtunnel. The purpose of the channel was to make the flow two-dimensional (channel width = aerofoil span). Moreover, this contraction gave some reduction of the turbulence in the tunnel.

The aerofoil could rotate about the quarter-chord axis and it was kept in a mean position, corresponding to a small angle of incidence by aid of weak springs (fig. 1).

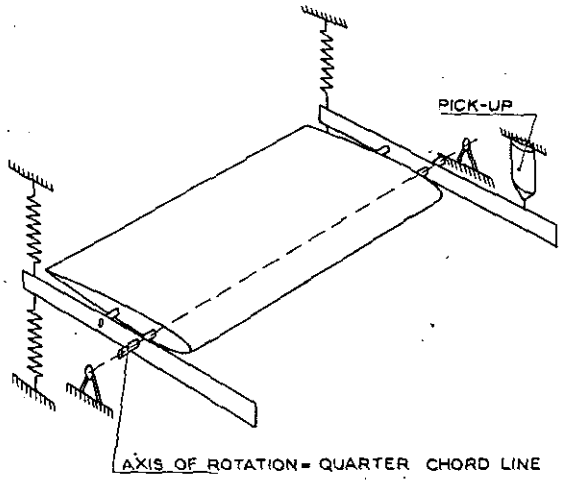

Fig. 1. The experimental set-up in the windtunnel.

When the speed in the channel was between 4 and 13 m/sec spontaneous oscillations of the model occurred. The frequency which was measured by means of a sound-analyzer, appeared to be always equal to one of the following discrete values: 60, 133, 170, 240, 288 c. p. s. The amplitude was very small, but the oscillation was clearly indicated by an electromagnetic pick-up (voltage proportional to velocity) and could be felt by hand. Moreover, the higher frequencies produced an audible tune.

It appeared that the lower frequencies were predominant at the lower speeds, while the higher frequencies were found at the higher speeds of the range. For certain speeds two or even three frequencies could be present at the same time, but usually only one of them persevered after some time. Fig. 2 shows the relation between frequency and speed for various angles of attack. The diagram is roughly symmetrical about the zero angle of attack line, as is to be expected, while an increase in the angle of attack has the effect of producing a same phenomenon at a lower speed.

Another characteristic property is that the speed range in which a certain frequency occurs, is not continuous. For special, well reproducible, values of the speed no oscillations appeared. This

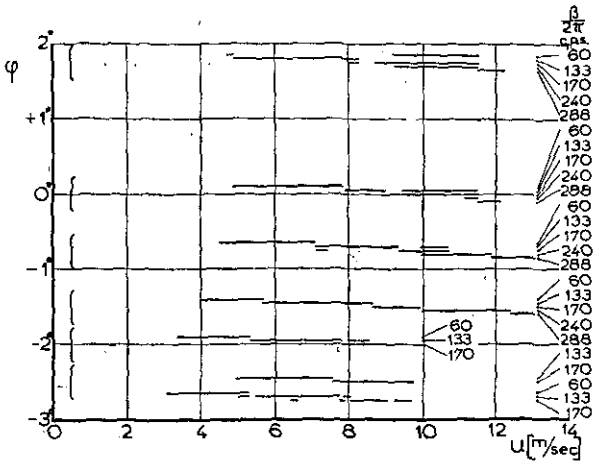

Fig. 2. Experimental results for frequency β of spontaneous oscillations, given in dependence of the speed of flow U and the angle of incidence φ.

effect was, in particular, well pronounced for the lower frequencies. With 60 c. p. s. two speeds for which no oscillations occurred differed about 0.25 m/sec.

With the stethoscope method it was established that at the trailing edge the boundary layer is laminar for speeds below 10 or 11 m/sec (zero angle of incidence), while for higher speeds it becomes turbulent. No important differences were discovered when the measurements were done with the wing completely clamped or with the wing performing spontaneous oscillations.

Neither the position nor the strength of the springs, which kept the model in its mean position, had any influence on frequency or amplitude of the spontaneous oscillations.

It was found that the frequencies of these oscillations all agreed with natural frequencies of the elastic aerofoil (chiefly torsional). To show this a very small electromagnetic exciter was held against the model and the response of the model turned out to be maximal for the same frequencies that were characteristic for the spontaneous oscillations.

When the boundary layer was made turbulent at 10 % of the chord by fitting disturbance wires to the aerofoil, the phenomenon of the spontaneous oscillations completely vanished.

3 Comparison with the stability theory of the laminar boundary layer.

Since the experiments were made with a thin profile (maximum thickness 7.3 %), it seems to be allowed to compare the measurements with zero angle of incidence with the theory for a flat plate as given by Lin (ref. 3). In section 5 the influence of the pressure gradient, introduced

by thickness and by a non-zero angle of attack will be considered.

Fig. 3 reproduces the results of LIN, the upper half of the figure presenting the frequency and the lower half the wave length, both as functions of the Reynolds number, referred to the dis-

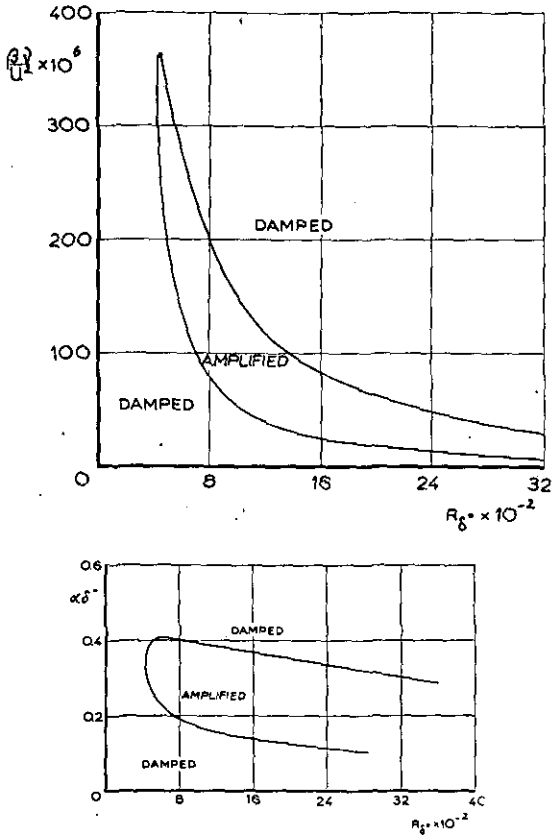

Fig. 3. Theoretical results for unstable laminar boundary layer according to LIN.

placement thickness δ^* of the boundary layer. For a flat plate δ^* is given by the Blasius formula

$$\delta^* = 1.72 \sqrt{\frac{\nu x}{u}},$$

where ν is the kinematic coefficient of viscosity, which under standard conditions is equal to $14.6 \cdot 10^{-6}$ m²/sec. x denotes the distance from the leading edge and U the speed of the undisturbed flow.

The Reynolds number R_{δ^*} is then given by

$$R_{\delta^*} = \frac{U\delta^*}{\nu}.$$

The quantity β appearing in the ordinate of the upper figure denotes the frequency in rad/sec, while α of the lower figure is given by

$$\alpha = \frac{2\pi}{\lambda},$$

where λ is the wavelength. It should be noted that the velocity by which the waves progress is not equal to U, but to $c = \beta/\alpha$, which usually lies between 0.25 U and 0.4 U and can, of course, be inferred from the two diagrams presented.

By taking special values for x, the diagrams of fig. 3 have now been transformed into the diagrams presented in figs. 4 and 5. The procedure followed is that for each value of x (not surpassing $x = 0.3$ m, which is the trailing edge) and U, δ^* can be calculated and, hence, R_{δ^*}.

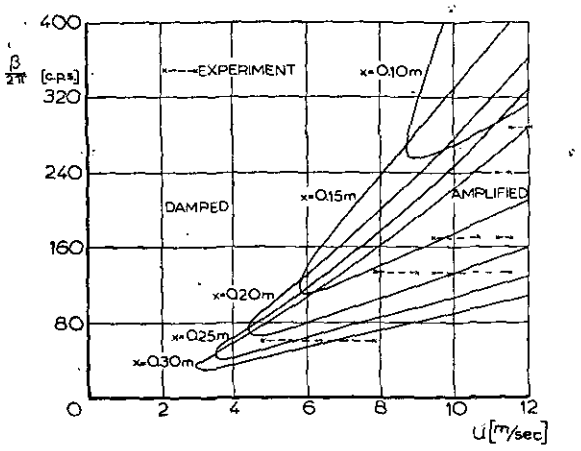

Fig. 4. Unstable frequencies as function of speed for different positions at the aerofoil. The experimental points were found with zero angle of incidence.

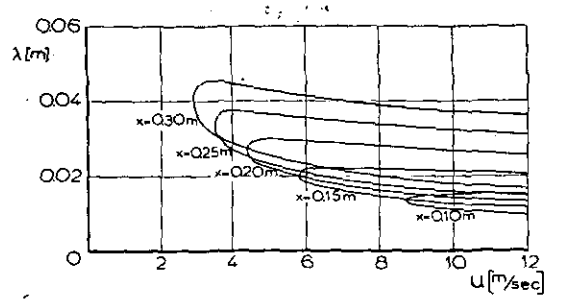

Fig. 5. Wavelength as function of speed.

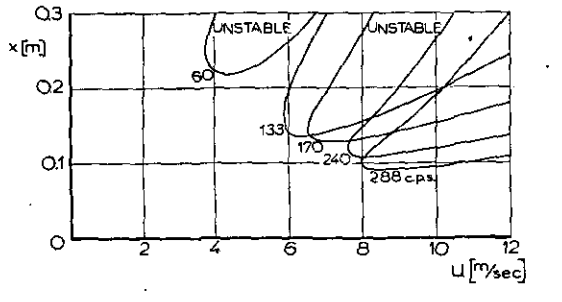

Fig. 6. Region of instability at the aerofoil as function of speed for different frequencies.

The values of β lying in the unstable region and the corresponding values of λ then can be obtained from fig. 3. Furthermore fig. 6 shows the region of the profile, where oscillations of certain specified frequencies are unstable. This diagram has been obtained as a crossplot from fig. 4.

Comparing now with the experimental results for zero angle of incidence, it is seen that the measured frequencies lie very well within the unstable region. Only the 60 c. p. s. would be expected from theory to end at 6.8 m/sec instead of at 7.8 m/sec. The higher frequencies would

probably have been observed also at speeds above 12 m/sec, if the turbulence of the tunnel would have been smaller.

4 The mechanism leading to the vibrations of the model.

While in the foregoing section ample evidence has been given that the oscillations are narrowly connected with an instability in the laminar boundary layer, it will now be explained how these oscillations lead to sustained vibrations of the model.

Though in boundary layer theory of steady flow the pressure is constant in the direction normal to the surface, this result is not retained for the pressure produced by the disturbances (ref. 4. § 2a). The reason for this difference is that in steady boundary layer theory the velocity component normal to the surface is small compared with the parallel velocity component and hence is neglected, while for the disturbances both components are of the same order of magnitude. It follows that the pressure fluctuations are of the same type as the velocity fluctuations, viz.

$$e^{\mu x}\, e^{i(\beta t - \alpha x)},$$

where the sign of μ denotes whether the oscillation in the boundary layer is damped or undamped. As a result of this varying pressure a moment about the axis of rotation will, in general, exist. This periodic moment can produce vibrations of the model if its frequency is sufficiently near to one of the resonance frequencies. In such case the motion of the model in points ahead of A ($A =$ point, where instability begins), will cause disturbances in the boundary layer, which when arrived at A, will again be amplified. These disturbances will differ 180° in phase for upper and lower side of the profile and, hence, the same phase difference exists for the pressure at both sides. This is the reason that even for a symmetrical profile at zero angle of attack a moment is built up. The fact, that the velocity fluctuations at the trailing edge are by intermediary of the aerofoil, again brought into the boundary layer at a more forward point, makes that the relatively small amplification, characteristic for the small values of R_{δ^*} (see fig. 19 in ref. 4), is sufficient for the generation of the vibrations. The direct measurement of velocity fluctuations in the boundary layer by aid of hot wire equipment requires a much larger amplification if no artificial excitation ahead of the instability region is introduced. This is the reason that SCHUBAUER and SKRAMSTAD required for their original measurements, which were done without artificial excitation, a wind tunnel set up with extremely low turbulence. However, with excitation of the boundary layer, instability could be observed for much lower R_{δ^*}. In fact, the largest value of R_{δ^*}, which occurred in the present experiments, was 900 ($U = 12$ m/sec., $x = 0.30$ m).

The pressure distribution along the chord due to the velocity fluctuations in the boundary layer will be of the type shown by fig. 7. A denotes again the point, where the instability begins. Ahead of A the pressure difference is not exactly zero since fluctuations

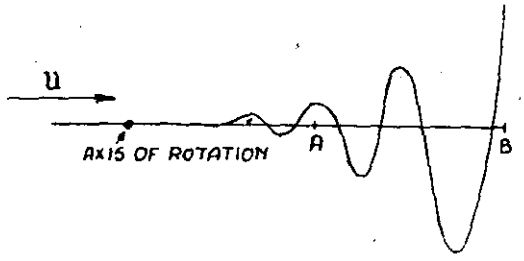

Fig. 7. Pressure distribution along the chord.

in the boundary layer are induced here by the motion of the aerofoil. However, the moment about the axis of rotation is largely due to the pressure differences aft of A. When $x = 0$ denotes the axis of rotation, the moment is given by

$$M = e^{i\beta t} \int_{x_A}^{x_B} x e^{(\mu - i\alpha)x}\, dx.$$

Now, to produce a vibration of the model a necessary condition is that the velocity fluctuations induced by the motion, arrive at A with the right phase. If this phase is exactly the opposite of the phase of the velocity fluctuations, which produced the moment, no vibration will result. This makes it probable that there are certain speeds in each range of speeds, where a specified frequency is amplified, which do not lead to a vibration of the model. Such speeds have in fact been observed. Since the phase of the moment will be roughly the same when the distance between A and B is increased by one wavelength, an estimation of the difference between two such "extinguishing" speeds can be obtained from fig. 6, noting that the wave length of the oscillations of 60 c. p. s. is about 0.03 m. The amplitude of the oscillations is probably determined by the condition that an increase in amplitude would spoil the laminar character of the boundary layer.

5 The effect of a pressure gradient.

The experiments considered have not been performed with a flat plate, but with a thin aerofoil. Hence, there will be an increasing pressure at the rear part of the aerofoil. The effect of a pressure gradient upon the stability of the laminar boundary layer has been investigated by PRETSCH (ref. 6) and SCHLICHTING (ref. 7). It can be inferred from these papers that an increasing pressure, i. e. a delayed motion, promotes instability. Hence, for the case of an aerofoil with a non-zero angle of incidence the regions of speed where the instability occurs will be shifted toward lower values of the speed as is confirmed by the experimental results shown in fig. 2.

An accurate calculation for the case of pressure gradients requires the calculation of the displacement thickness δ^* under such circumstances and, moreover, the change to which the stability curves of fig. 4 are subjected, when the boundary layer profile does not agree with the Blasius profile. It is intended to make such calculations at a later moment.

6 References.

1 TOLLMIEN, W. "Über die Entstehung der Turbulenz", Nachr. Ges. Wiss. Göttingen, 21—44 (1929).

2 SCHLICHTING, H. "Zur Entstehung der Turbulenz bei der Plattenströmung", Nachr. Ges. Wiss. Göttingen, 181—208 (1933).

3 LIN, C. C. "On the stability of two-dimensional parallel flows", Quart. Appl. Math. 3, 117—142, July 1945; 3, 218—234, Oct. 1945; 3, 277—301, Jan. 1946.

4 SCHUBAUER, G. B. and SKRAMSTAD, H. K. "Laminar-boundary-layer oscillations and transition on a flat plate", NACA Report No. 909, 1948.

5 MALOTAUX, P. C. A., DENIER VAN DER GON, J. J. and YAP KIE JAN. "A method for qualitative boundary layer investigation by means of hot wires without disturbing the flow" (in Dutch). VTH 45 Technische Hogeschool Delft.

6 PRETSCH, J. Die Stabilität einer ebenen Laminarströmung bei Druckgefälle und Druckanstieg". Jahrb. deut. Luftfahrtforschung Vol I, 58—75, (1941).

7 SCHLICHTING, H. "Über die theoretische Berechnung der kritischen Reynoldsschen Zahl einer Reibungsschicht in beschleunigter und verzögerter Strömung". Jahrb. deut. Luftf. Vol I, 97—112 (1940).

REPRINTED FROM METALEN, VOL. VII, No. 18, SEPTEMBER 1952

REPORT M. 1866 CCL Class. C 1·17-3 : G 311 : G 321

The effect of notches on the strength of aluminium alloys under static tensile loading

by Ir J. H. Palm *)

Summary.

The true fracture strength in static tensile loading of sharply notched cylindrical test bars of 24 ST and 51 SW aluminium alloys was investigated. The following factors were varied:

length of testbar;

size;

notch angle;

notch depth at constant diameter of notched section;

A notch angle of zero degrees with practically infinite sharpness was obtained by precompression.

The principle of an optical method is described, which enables to measure the change of diameter of the notched section and to observe the initation of cracks.

It may be concluded from the test data that:

the fracture strength has a slight tendency to decrease with increasing length and size of the test bar;

the fracture strength first decreases with decreasing notch angle and eventually increases again;

the fracture strength at first decreases sharply with increasing notch depth and then increases again;

the fracture strength decreases with increasing prior compressive load.

1. Introduction.

The fact that notches influence the strength and ductility of metals is known since a long time. Kirkaldy 1) already observed the effect of notches on steel bars. A more systematic investigation of the problem was started by Ludwik and Scheu 2) and especially by Kuntze 3) some 20 to 25 years ago. More recent investigations are particularly due to Mac Adam 4) and Sachs 5) 6) and their coworkers.

It is not intended here to give a theoretical consideration of the notch effect, which has already been done by several investigators. For instance Leon 7), Inglis 8) and Neuber 9), gave calculations for the stress distribution in bars with special types of notches and strained in the elastic region. Mac Adam 4) and particularly Sachs 6) treated the plastic range, for which the problem becomes extremely difficult and for which an exact quantitative or even qualitative solution can still not be given. In preliminary reports concerning tests on notched copper and steel bars the stress and strain distributions in the notched section during plastic deformation are also qualitatively treated for sharp and rounded notches 10).

We shall restrict ourselves here to a short survey of the main experiments regarding the notch strength of aluminium alloys found in the literature and to our own experiments. Experiments on aluminium alloys, the basic metals for the aircraft industry, reported in the literature are of fairly recent date and have even been partly published during the course of our own investigations 6).

2. Investigations reported in the literature.

Mac Adam, Mebs and Geill 11) used round duralumin bars of ¾ inch diameter in which notches with angles varying from 180° to 30° and notch radii varying from 0.25 to 2.0 mm were applied. The notch depth was kept almost constant, varying only between 54 and 60 % of the original diameter **). The metal was tested at room temperature, —78° C and —188° C, in the original (age hardened) condition and after 13 % prestraining. Their experiments led to the conclusion that for the ranges investigated the fracture strength and the nominal tensile strength increase with decreasing notch sharpness,

*) Formerly Head Materials Dept. National Aeronautical Research Institute, Amsterdam.

**) These authors express notch depth as $K = \frac{do^2}{D_o^2}$ in which do = diam. of notched section and Do = diameter of cylindrical part.

notch angle and temperature and increasing notch depth and prestraining.

Shapiro and North 13) investigated 14 ST, 24 ST and 75 ST aluminium alloys.

In their test on ¾ inch bars with circumferential notches the notch angle was constant (60°). The notch depth, expressed as $\frac{D_o^2 - d_o^2}{D_o^2} \cdot 100$, was 4, 7.8 and 15.3 %, the notch radii 0.5 and 0.05 mm. From their data it follows that for the range investigated the fracture strength increases with the notch sharpness and as far as 14 ST and 75 ST are concerned also with the notch depth. For 24 ST there is a very small increase of the fracture strength with the notch depth for notches of 0.05 mm radius. With notches of 0.5 mm radius the fracture strength was found to decrease with increasing notch depth.

Extensive investigations were done by Sachs, Aul and Dana 10) on ¾ inch round bars of 24 ST, 75 ST and 24 ST 86. Instead of keeping the diameter D_o of the cylindrical part of the test bars constant, as is usually done, the diameter d_o of the notched section was kept constant (at 5.4 mm) for the determination of the effect of the notch depth, like in our experiments. The effect of notch depth was investigated for notch radii varying from approx. 0.01 mm until ∞ 50 mm, the notch angle being 60° for the small radii. The length of the cylindrical part, inclusive the notched section was ∞ 25—35 mm. After complete machining the test bars were reheat-treated to obtain the desired strength and to insure a high degree of uniformity, i.e. to eliminate the effect of cold deformation in the notch due to machining.

A number of tests were made on bars with 50 % notch depth and varying notch radii, heat treated only before final machining.

The obtained fracture stresses (in kg/mm²) at constant notch radii are represented in fig. 1 as a function of the notch depth, expressed in percentage removed cross section $\left(\frac{D^2 - d^2}{D^2} \cdot 100\right)$. The following conclusions may be drawn from their data:

24 ST heat treated after machining.

(a) At constant notch radius the fracture stress at first sharply decreases for very sharp notches and then increases more slowly with increasing notch depth until the original value is reached again. For medium notch sharpness (r ∞ 0.25 mm) the initial decrease is smaller and at 50 % notch depth the original value is already exceeded in the reverse direction. For weak notches the fracture strength increases continuously and shows a weak maximum or remains constant at high notch dephts.

(b) At constant notch depth below approx. 50 %, the fracture stress increases continuously with decreasing notch sharpness.

Beyond a notch depth of approx. 50 % the fracture stress first increases with decreasing notch sharpness and then decreases again via a maximum. This maximum occurs at a greater notch sharpness the higher the notch depth.

24 ST machined after heat treatment (not represented in fig. 1).

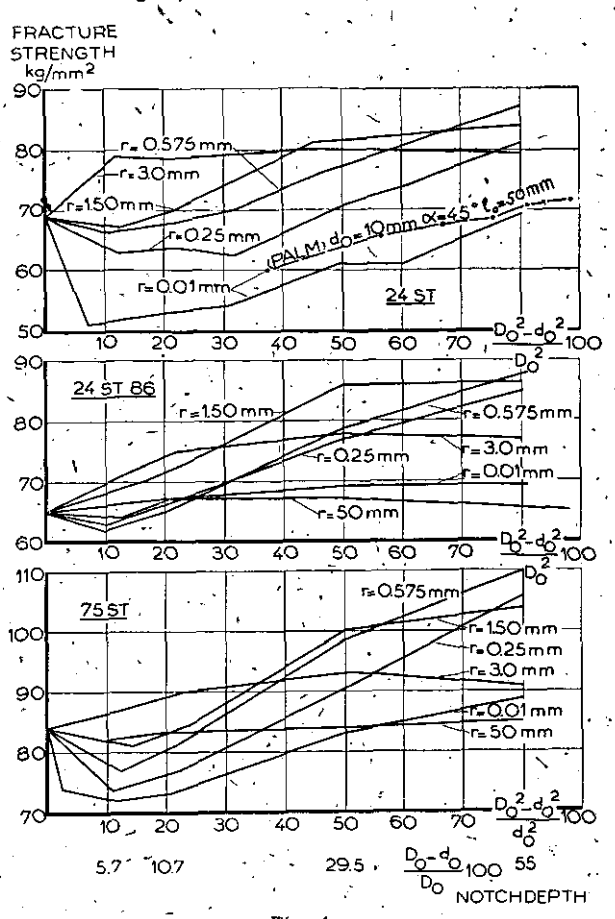

Fig. 1.

Influence of the notch depth and the notch sharpness on the fracture strength derived from data of Aul, Dana and Sachs 6).

(do = 0.212", lo = 0.75", α = 60°)

Only for fairly sharp notch notches (r < 0.3 mm) the fracture stress at a notch depth of 50 % is somewhat lower (5 %) thans for bars heat treated after machining.

24 ST 86 heat treated after machining.

The general behaviour is similar to that of 24 ST; however, the minima at low notch depth are very small.

75 ST heat treated after machining.

The general behaviour is also similar to that of 24 ST and the minima at low notch depth are also rather pronounced.

3. Materials and procedure of own investigations.

Two materials, 24 ST and 51 SW in bars of 30 mm diameter originating from one ingot each, were available for the tests. The materials were tested in the original condition and 24 ST for some tests also after softening by annealing for 2 h at 350° C followed by slow cooling.

Too late, as shown in figure 13, it became obvious that the 51 SW bar had a large inclusion over nearly the whole length. The results obtained with this bar therefore cannot be regarded as fully reliable.

The test specimens were carefully machined and provided with threaded ends. Apart from the unnotched specimens for the determination of the basic properties, all test pieces were notched with notches of the utmost sharpness (r. ∞ 0.01 mm).

Very good centric loading was obtained by using sensitive ball shackles. In some preliminary tests the specimens were loaded on a 50 tons Amsler hydraulic machine, the head of which could be moved by means of a worm wheel transmission instead of by using the oil plunger, which remained in the lowest position. In this way, this machine acted as an extremely rigid one and enabled a very slow tearing of notched metals like copper and steel. The load was measured by means of a strain-gage dynamometer.

It was tried to measure the change of diameter by means of the optical system schematically represented in fig. 2, which was first applied for the study of the effect of notches in copper and steel bars 10). With this system the change of diameter d of the notched section during loading can be measured with an accuracy of approximately 0.01 mm without touching the notch with extensometers, which may damage the notch. Moreover, it enabled an exact observation of the onset of fracture, at the notch bottom, and its proceeding up to the moment that the system of bar and testing machine becomes unstable and fracture proceeds at high speed.

Since in test pieces of the aluminium alloys with notches of 60° and less and with very sharp notches no appreciable deformation was measurable during loading, and fracture therefore occurred very suddenly, in most of the tests the usual hydraulic loading system of the machine was used. The fracture stress S_r was based on the diameter of the notched section after fracture.

4. Test scheme and test results.

Apart from the determination of the basic tensile properties of the metals on unnotched bars, the effects of the following factors on the fracture strength were investigated. All tests on notched specimens, except those for investigating the length effect, were with very few exceptions at least duplicated.

Effect of length of the cylindrical parts of the test bar.

Two series of tests with different diameters D_o were done, both with 24 ST in the state of delivery and softened.

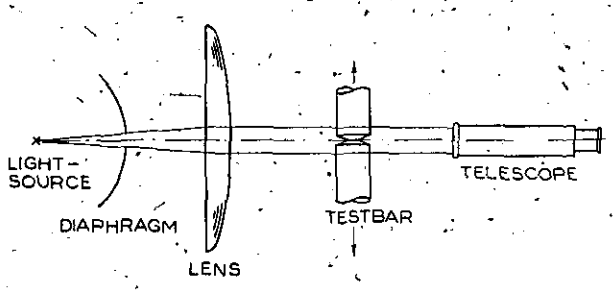

Fig. 2.
Scheme for the observation and measuring of the notched section during loading.

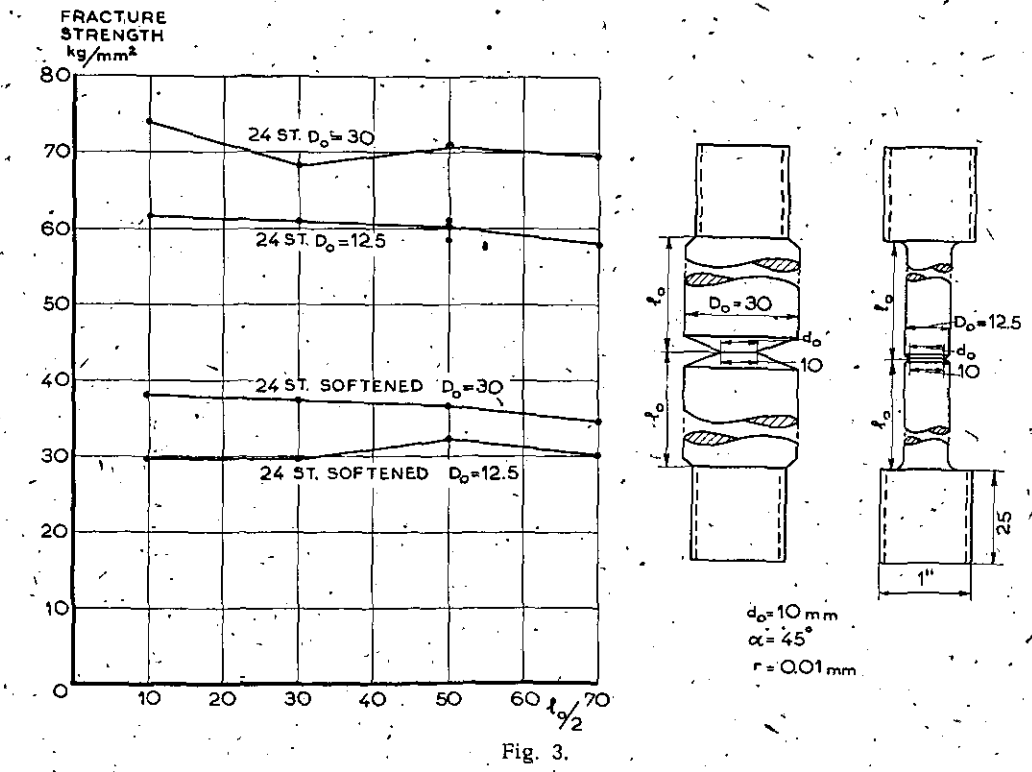

Fig. 3.
Influence of the length of the testbar on the fracture strength.

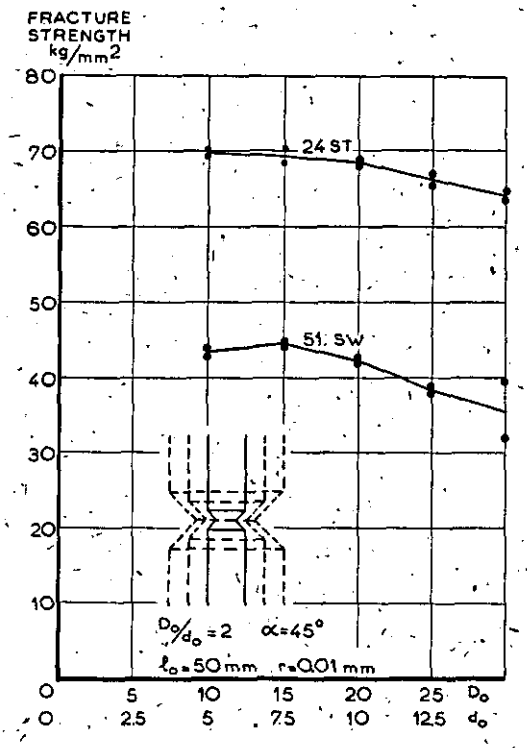

Fig. 4.
Influence of the size on the fracture strength.

In one series D_o was 30 mm, in the other series D_o was 12.5 mm. The notch angle α_o was 45°, the radius of curvature r_o of the notch was 0.01 mm and d_o was 10 mm. The length l_o of the cylindrical parts ranged from 10 to 70 mm.

Size effect.

Tests were done with 24 ST and 51 SW, both in the state of delivery. l_o was 50 mm, α_o was 45°, r_o was 0.01 mm and the ratio d_o/D_o was 0.4 d_o was varied from 5 to 15 mm.

Effect of the notch angle.

Tests were done with 24 ST and 51 SW, both in the state of delivery. D_o was 30 mm and r_o was 0.01 mm. In one series d_o was 10 mm, with l_o = 50 mm. In another series d_o was 20 mm. Due to a mistake in machining the heads, l_o had to be reduced to 10 mm.

The notch angle α_o was varied from 30° to 120°.

Effect of notch depth.

Tests were done with 24 ST and 51 SW, both in the state of delivery. l_o was 50 mm, α_o was 45°, r_o was 0.01 mm and d_o was 10 mm. D_o was varied from 10 to 30 mm.

Effect of compression prior to tension.

Tests were made only with 24 ST in the state of delivery, 51 SW being no more available. Test bars with D_o = 20 mm, d_o = 10 mm, α_o = 45°, r_o = 0.01 hh and l_o = 50 mm were preloaded in compression with loads ranging from 12 to 14 tons, corresponding to stresses ranging from 38 to 44.5 kg/mm² on the original notched area.

In figures 3 to 7 the fracture strength is plotted against the factors investigated. Figures 8 to 13 show photographs of the test bars after fracture.

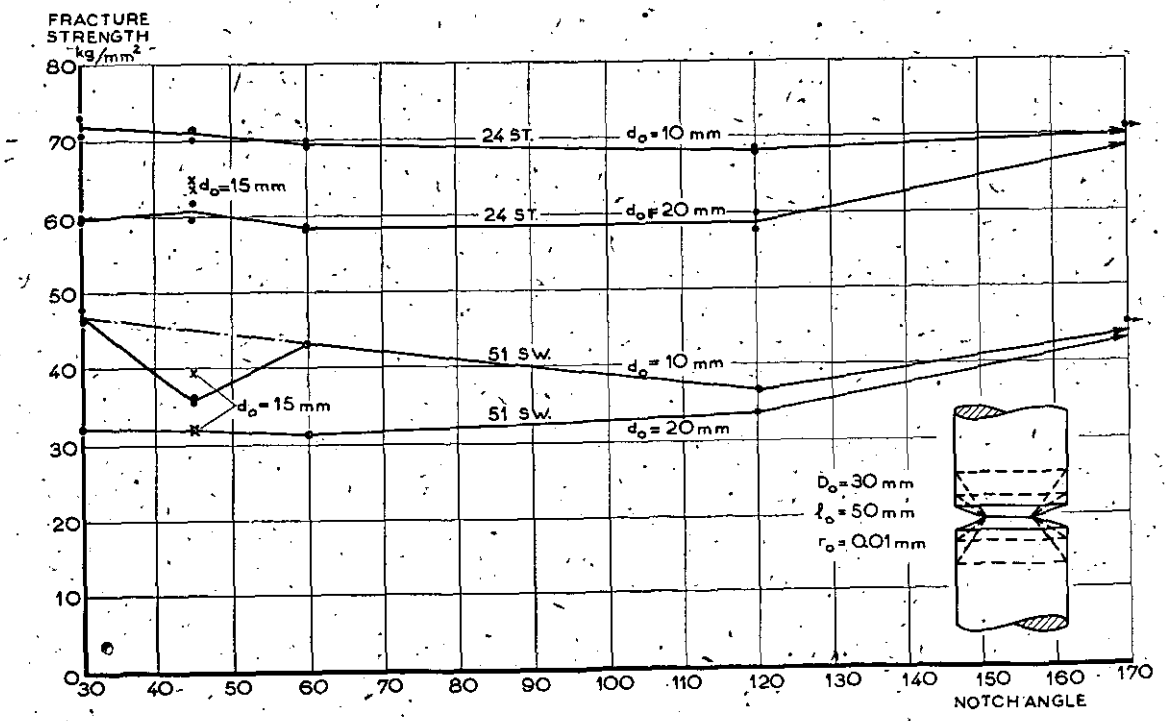

Fig. 5.
Influence of the notch angle on the fracture strength.

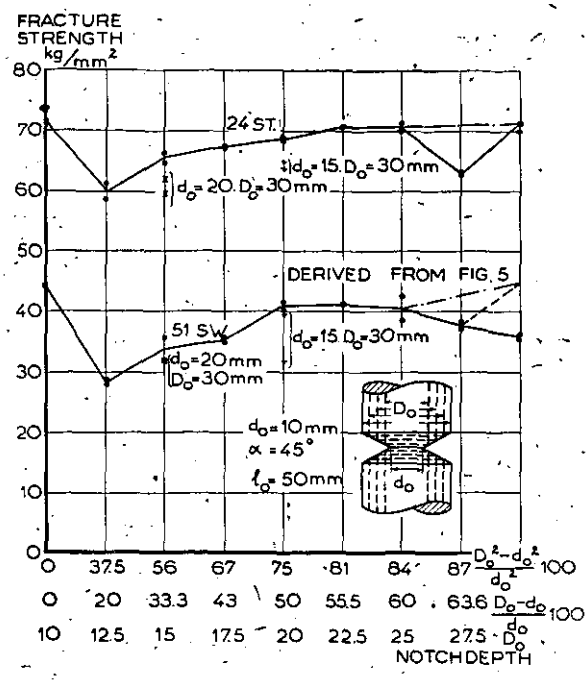

Fig. 6.
Influence of the notch depth on the fracture strength at constant diameter of the notched section.

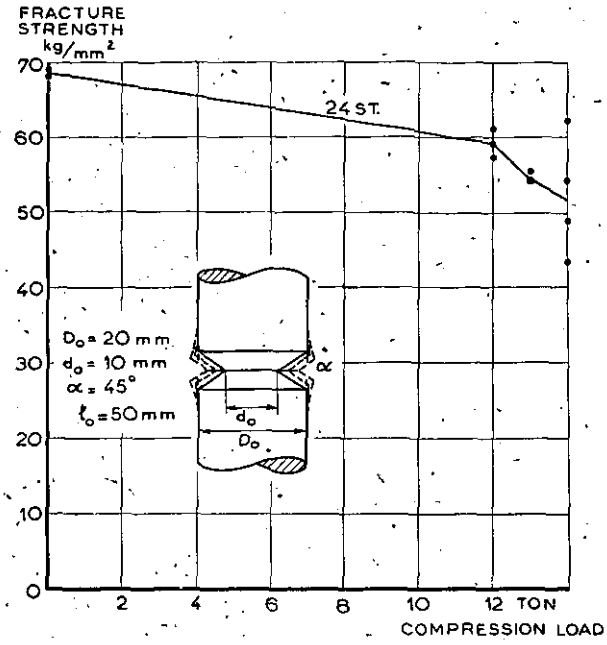

Fig. 7.
Influence of prior compression on the fracture strength.

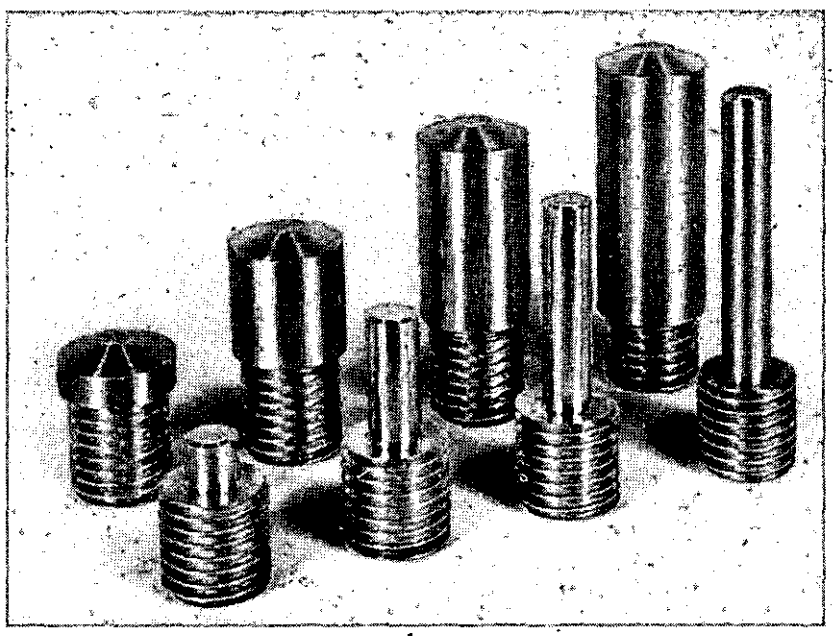

Fig. 8.
Effect of length. 24 ST

5. Discussion of results.

Effect of length of cylindrical parts (figs. 3 and 8).

Taking into account that the scatter between duplicate tests of other series in general was very small, it might be concluded that there is a slight tendency for the fracture strength to decrease with increasing length. The effect is, however, very small. To eliminate it completely l_o was taken 50 mm in the other tests, except in one series of varying notch angle, as mentioned in the preceding section.

Size effect (figs. 4 and 9).

At increasing size the fracture strength is found to decrease continuously for 24 ST; 51 SW at first shows a very slight increase and then also a monotonic decrease. Whether this really is simply a size effect becomes doubtful if we realize that the notches have in fact no infinite sharpness, but have a nearly constant finite radius. With increasing size the relative notch sharpness d_o/r_o therefore is not constant but increases as well. On the basis of Sachs' tests (fig. 1) it then follows that the decrease in fracture strength with increasing size and also the initial increase may be fully due to the change in relative notch sharpness.

Effect of notch angle (figs. 5 and 10).

Decrease of the notch angle from 180° to 30° apparently tends to decrease the fracture strength, especially for the bars with $d_o = 20$ mm, which run at a lower strength level, and then tends to increase it again. For the bars with $d_o = 10$ mm the original values are eventually reached again. For the bars with $d_o = 20$ mm the increase is very small, if present at all. The irregularity in the curve for 51 SW and $d_o = 10$ mm at an angle of 45° (too low strength) is probably due to an error, as follows also from comparison with results obtained on bars with $d_o = 15$ mm.

The general conclusion that can be drawn is that the fracture strength is governed by the stress concentration and the triaxiality in such a way that the first factor tends to decrease the fracture strength and the latter factor on the contrary tends

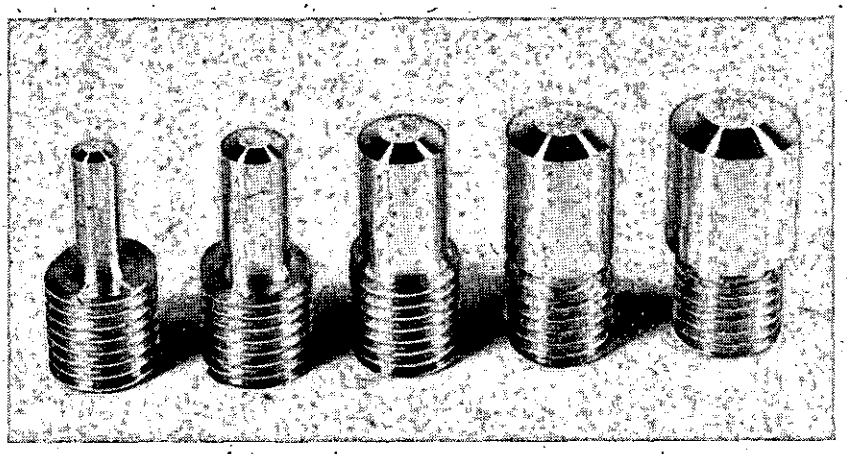

Fig. 9.
Size effect. 24 ST.

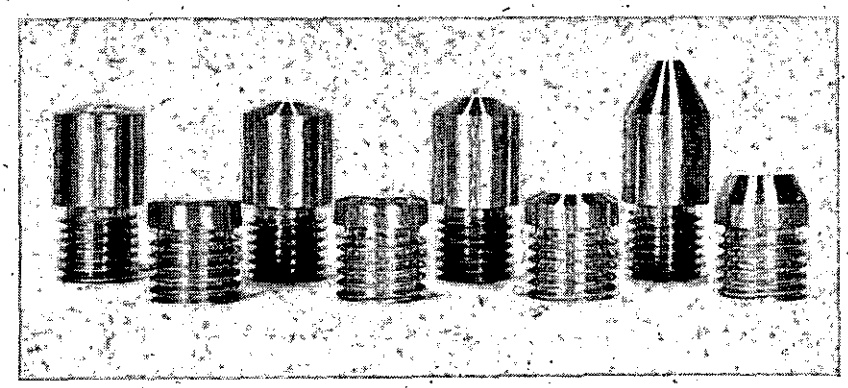

Fig. 10.
Effect of notch angle. 24 ST.

to increase this quantity. At large angles the stress concentration is predominant; however, with decreasing angle the effect of the triaxiality increases at a stronger rate.

Effect of notch depth (figs. 6 and 11).

The observed relation between fracture strength and notch depth is, at least up to about a notch depth $(D_o—d_o)/D_o$ of 55 to 60 % similar to that observed by Sachs and co-workers 6). Their curve for $r_o = 0.01$ mm only runs at a somewhat lower strength level. For very sharp notches the fracture strength at first decreases sharply, due to predomination of the stress concentration, but very soon increases again as a result of the predominant effect of increasing triaxiality. The same may also be concluded from fig. 5 concerning tests with constant D_o instead of constant d_o. However, as already pointed out in discussing the size effect, a change of d_o is accompanied by a change in the relative notch sharpness which interferes with the pure effect of notch depth. The latter effect has therefore preferably to be studied on notched bars with constant d_o. The meaning of the curves beyond 60 % notch depth is not clear. On the one hand it seems logical that the irregularity in the curve for 24 ST is due to some error in the test, though values of both test bars coincide very well. On the other hand it seems justified to conclude from fig. 5 that for 51 SW at $d_o = 10$ mm and $\alpha_o = 45°$ the fracture strength is about 45 kg/mm². This means that for 51 SW in fig. 6 the curve should show a similar irregularity as for 24 ST at a notch depth of 63.6 %. It seems, however, most probable that the curves beyond 55 to 60 % notch depth should be nearly horizontal.

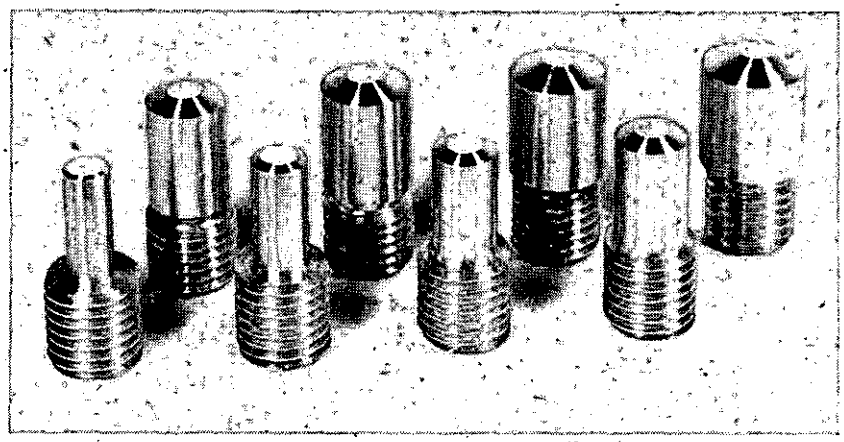

Fig. 11.
Effect of notch depth. 24 ST.

Influence of prior compression (figs. 7 and 12).

On prior compression the fracture strength apparently decreases. The notch angle decreases and the notch sharpness increases on compression. Among other factors are the increase of cross-section and the induced strain hardening and residual internal stresses. At sharp notches a decrease

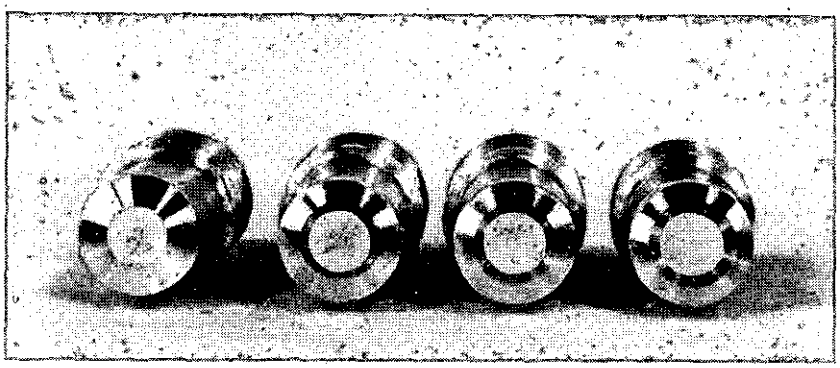

Fig. 12.
Effect of prior compression. 24 ST.

of notch angle has the tendency to increase the fracture strength. The effect is, however, very small. On the other hand it follows from the tests on the size effect and Sachs' tests on the notch sharpness that for sharp notches the fracture strength decreases at increasing notch sharpness. Obviously, the effect of notch sharpness predominates. Since at the lower compression load α_o is already practically zero, as can for instance be seen from fig. 12, showing the compression of the circumferential surface around the notch, the further decrease of fracture strength at increasing precompression load must be due to strain hardening. As a consequence of strain hardening the ductility decreases and the stress concentration in the notch therefore gets less occasion to decrease during loading, leading to a lower fracture strength. The effect of residual stresses can hardly be evaluated, but will probably also tend to decrease the fracture strength.

4. D. J. MacAdam. Reference in: Metals Technology (1948). T.P. 2296.
5. G. Sachs. Reference in: Journal Appl. Mech. 12 (1945) A 241.
6. A. W. Dana, E. L. Aul and G. Sachs. N.A.C.A. Technical Notes 1830 and 1831 March 1949.
7. A. Leon. Österr. Wochenschr. f.d. off. Baudienst 29 (1908) 524.
8. C. E. Inglis. Trans. Inst. Naval. Arch. 55 (1913) 219.
9. H. Neuber. Kerbspannungslehre Berlin 1937. Springer.
10. J. H. Palm and J. H. v. Dooyenweerd. Report Nat. Aeron. Res. Inst. M 1297. 1306. 1307 (1948) and M 1603 (1949) (in Dutch).
11. D. J. MacAdam, R. W. Mebs and G. W. Geill Reprint 27 A.S.T.M. (1944).
12. L. Schapiro and H. E. North. Journ. Aeron. Sc. 13 (1946) 391.

Completed: May 1952.

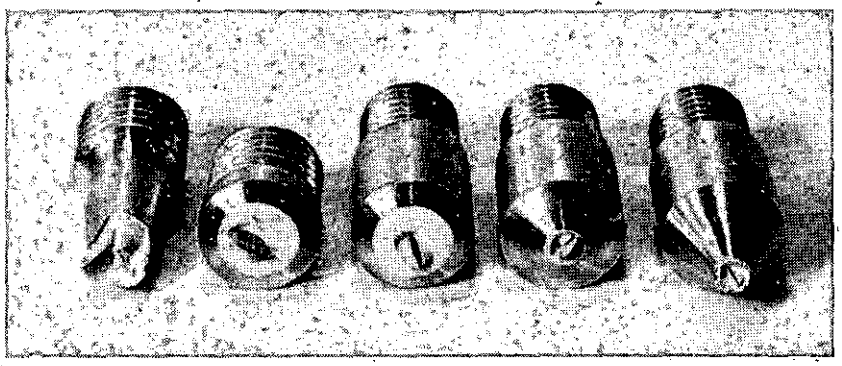

Fig. 13.
Test bars of 51 SW showing inclusion.

References.

1. D. Kirkaldy. Proc. Scot. Shipb. Ass. (1860—61) App. p. 74.
2. P. Ludwik and R. Scheu. Stahl u Eisen 43 (1923) 999.
3. W. Kuntze. Kohesionsfestigkeit. Mitt. D. Mat. Prüf. Anst. Sonderheft 20 (1932).

7. Acknowledgment.

The author wishes to express his thanks to the Nederlandsche Aluminium Pers- en Walsbedrijven at Utrecht for their kindness to present the alloys for this investigation.

C.C.L. Class. C 121–1

REPORT S. 313

Large Deflections of Semi-oval Rings[1])

by

Dr Ir A. VAN WIJNGAARDEN[2]).

Contents.

1 Introduction.

It is well-known that the distortions of a loaded elastic body are, in general, not exactly proportional to the applied load, even if the material, of which the body exists, exactly obeys HOOKE's law. On the other hand, such deviations from linearity are of importance only if the shape of the body is rather essentially changed by the deformations. So, the effect will be of interest especially for flexible bodies, like thin rods and rings, in short for springs. The principle of the determination of the deformation of a thin — eventually originally curved — rod, loaded at its ends only, is known, but nevertheless it seems worthwhile to communicate in some detail the solution of some special problems of this type, partly for the sake of the interesting results, partly because a number of other investigators, dealing with problems of the same type, either gave no theoretical solution at all (ref. 1), or overlooked the possibility of an exact solution (ref. 2) or, at last, have not followed the most suitable way (ref. 3).

The problem that we want to solve especially, deals with an originally uniformly curved rod (length πr) that we bend into a semi-oval ring by clamping both ends perpendicularly to their connecting line at a distance $2\rho r$ (fig. 1). If $\rho = 1$, the ring is semi-circular. As a matter of fact, we are interested particularly in the case $\rho > 1$. This ring is loaded at its middle A by a normal force P (positive, if it is directed inwards), and A undergoes a deflection u. This deflection will by no means be considered as small, as the most interesting phenomenae just appear if u is about half the distance AM.

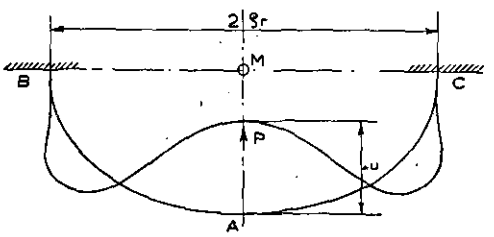

Fig. 1

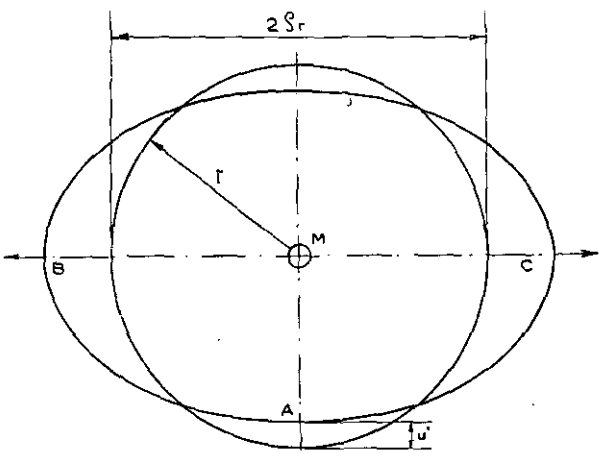

Fig. 2

First, we have to determine the shape of the ring in the unloaded condition. We therefore consider a closed circular ring (radius r), loaded by a diametral pair of forces, applied at B and C (see fig. 2), of such a magnitude as to distort the ring into an oval, the major axis of which being equal to $2\rho r$. In particular, we calculate the radial inward deflection u' of A. It is obvious that the half of this ring exactly represents our semi-oval ring.

Next, we consider the same circular ring, but now loaded by a diametral pair of forces P and

[1]) This paper has been presented at the Sixth Int. Congress of Applied Mechanics, Paris, 1946.

[2]) Now section chief Mathematical Centre, Amsterdam.

a second pair of diametral forces νP at right angles to the first one (fig. 3). For every value of P, ν is determined in such a way, as to make the major axis of the distorted ring equal to $2\rho r$. Again, we calculate the inward displacement u'' of A, and after subtracting u', we find the de-

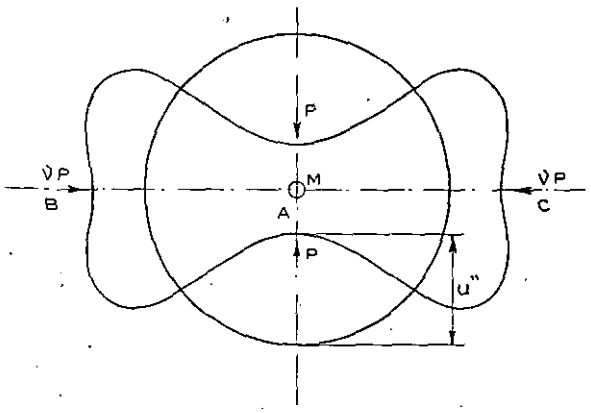

Fig. 3

flection u, measured from the unloaded semi-oval ring. As it is obvious that the calculation of u' is only a special case of that of u'', we can confine ourselves to the solution of the second problem. The formulae that we shall develop are, however, by no means restricted to the case of closed circular rings.

2 The differential equation.

We consider a thin rod that is — in the unloaded state — arbitrarily curved in a plane that contains one principal axis of inertia of each normal cross-section of the rod. The flexural rigidity may vary arbitrarily along its length. The rod is supposed to be loaded at a number of discrete points by forces and couples in the plane, so that it is bent in that plane only.

We denote by P_k the points where external forces or couples are applied, or where there is a discontinuity of either the radius of curvature R_0 (in the unloaded state) or the flexural rigidity EI themselves, or of one of their derivatives with respect to the length coordinate measured along the rod. We can confine ourselves to the study of a part P_kP_{k+1} that is, therefore, loaded only at its ends P_k and P_{k+1} and along which both R_0 and EI are continuous together with all their derivatives.

At the end P_k the load may consist of a couple M_k and a force F_k (fig. 4), and at the other end P_{k+1} of such a couple and a force as to be in equilibrium. We introduce a system of axes XY, having its origin in P_k, such that the X-axis coincides with the tangent in P_k (in the distorted state) in the direction of P_{k+1}, and the Y-axis coincides with the normal in P_k in the direction, in which (in the undistorted state) lies the centre of curvature. F_k makes an angle β with the X-axis.

The bending moment M in an arbitrary point $P(xy)$ of the rod — we give it the positive sign, if it decreases the curvature — follows from reasons of equilibrium to be:

$$M = M_k - F_k\,(x\sin\beta - y\cos\beta). \qquad (2.1)$$

On the other hand, if R is the radius of curvature in the distorted state, the differential equation of the rod, if the effects of tension and shearing are neglected, is:

$$M = EI\left(\frac{1}{R_0} - \frac{1}{R}\right). \qquad (2.2)$$

We pass from the XY-coordinates to the natural coordinates s and φ, where s is the length of the arc P_kP, and φ is the angle between the Y-axis and the normal in P. In the undistorted state $\varphi = \varphi_0$. Then $1/R = d\varphi/ds$, and $1/R_0 = d\varphi_0/ds$. Furthermore $dx/ds = \cos\varphi$, and $dy/ds = \sin\varphi$.

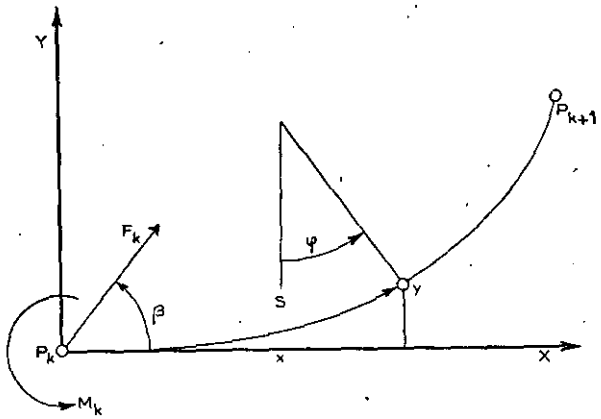

Fig. 4

From (2.1) and (2.2) we find, after differentiating with respect to s:

$$\frac{d}{ds}\left(EI\,\frac{d\varphi}{ds}\right) + F_k\sin(\varphi-\beta) = \frac{d}{ds}\left(EI\,\frac{d\varphi_0}{ds}\right). \qquad (2.3)$$

If r and EI_0 are some suitably chosen standards of length and stiffness, and if we introduce the non-dimensional quantities

$$\sigma = \frac{s}{r}\ ;\ \xi = \frac{x}{r}\ ;\ \eta = \frac{y}{r}\ ;$$

$$\rho = \frac{F_k r^2}{EI_0}\ ;\ \mu = \frac{M_k r}{EI_0}\ ;\ \omega(\sigma) = \frac{EI}{EI_0}, \qquad (2.4)$$

we can write equation (2.3) as

$$\frac{d}{d\sigma}\left(\omega\,\frac{d\varphi}{d\sigma}\right) + \rho\sin(\varphi-\beta) = \frac{d}{d\sigma}\left(\omega\,\frac{d\varphi_0}{d\sigma}\right). \qquad (2.5)$$

The initial conditions are:

$$\text{For } \sigma = 0\text{: } \varphi = 0 \text{ and } \frac{d\varphi}{d\sigma} = \frac{d\varphi_0}{d\sigma} - \mu. \qquad (2.6)$$

As both conditions hold for the same value of σ, equation (2.5) can be integrated directly either analytically or, in more complicated cases, by numerical methods. It should be mentioned, however, that those cases that we usually denote as statically determined ones, are generally not so if we deal with large deflections, so that we

mostly do not know the magnitude of F_k, β and M_k, or of ρ, β and μ. To illustrate this, we consider a horizontal straight (if unloaded) beam, clamped at one end and loaded by a vertical force P at the other end (fig. 5). Now

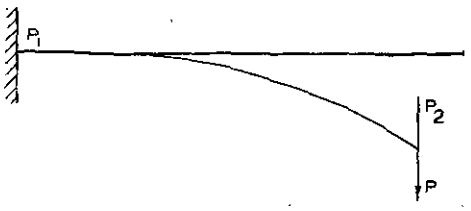

Fig. 5

the beam is distorted and so we know at the clamped end P_1 both F_1 $(=P)$ and β $(=90°)$ but not M_1, and at the free end P_2 we know M_2 $(=0)$ and F_2 $(=P)$ but not β. So, even in such a simple case, we shall have to modify the conditions (2.6) into a more practical form. Only if the relative direction of the force and the rod (β) is kept constant, we can use the conditions (2.6). An example for such a case is for instance that of a straight beam, supported at two fixed points (fig. 6), if the beam can move

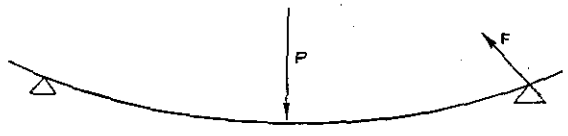

Fig. 6

freely over those supports. If this beam is loaded at its middle by a force P, we know at the support M $(=0)$ and β $(90° \pm$ angle of friction). We do not know the supporting force F, but we can assume a value for it, and find afterwards the value of P for which the result holds.

3 The solution of the differential equation in its general form.

An analytical way to solve (2.5) in its general form can be followed by expanding the known functions $\omega(\sigma)$ and $\varphi_0(\sigma)$ and the unknown function $\varphi(\sigma)$ into power series with respect to σ

$$\omega(\sigma) = \sum_0^\infty \omega_k \sigma^k;\ \varphi_0(\sigma) = \sum_1^\infty \varphi_{0k}\sigma^k;$$
$$\varphi(\sigma) = \sum_1^\infty \varphi_k \sigma^k \qquad (3.1)$$

if, at least, $\omega(\sigma)$ and $\varphi_0(\sigma)$ admit such expansions $\omega_0 \neq 0$). Now, we can also expand $\sin\varphi$ and $\cos\varphi$, first with respect to φ and then by means of (3.1) with respect to σ. If we substitute these expansions into (2.5) and (2.6), and compare the coefficients of equal powers of σ, we find the following set of equations:

$$\left.\begin{aligned}
&\omega_0\varphi_1 = \omega_0\varphi_{01} - \mu,\\
&2\,\omega_0\varphi_2 = -\omega_1\varphi_1 + 2\,\omega_0\varphi_{02} + \omega_1\varphi_{01} + \frac{\rho}{2}\sin\beta,\\
&3\,\omega_0\varphi_3 = -2\,\omega_1\varphi_2 - \omega_2\varphi_1 + 3\,\omega_0\varphi_{03} +\\
&\quad + 2\,\omega_1\varphi_{02} + \omega_0\varphi_{01} - \frac{\rho}{2}\varphi_1\cos\beta,\\
&4\,\omega_0\varphi_4 = -3\,\omega_1\varphi_3 - 2\,\omega_2\varphi_2 - \omega_3\varphi_1 +\\
&\quad + 4\,\omega_0\varphi_{04} + 3\,\omega_1\varphi_{03} + 2\,\omega_2\varphi_{02} + \omega_3\varphi_{01} -\\
&\quad - \frac{\rho}{3}\left(\tfrac{1}{2}\varphi_1^2\sin\beta + \cos\beta - \varphi_2\right),\\
&\cdots\cdots\cdots\cdots\cdots\cdots\cdots\cdots
\end{aligned}\right\} \qquad (3.2)$$

So, we can find the coefficients φ_i one by one. The restriction $\omega_0 \neq 0$ can be removed if $\mu = 0$. Then the first equation (3.2) vanishes as a whole, but also the left-hand sides of all the other equations vanish. If we bring the first terms of the right-hand side to the left-hand side, we obtain again a set of equations of the same type as (3.2).

4 The solution of the differential equation for the uniformly curved rod with constant flexural rigidity.

If the curvature of the rod is uniform in the unloaded state, and the flexural rigidity is constant $= EI_0$, then $\frac{d\varphi_0}{d\sigma} = 0$ and $\omega = 1$, so (2.5) is simplified to

$$\frac{d^2\varphi}{d\sigma^2} + \rho\sin(\varphi - \beta) = 0, \qquad (4.1)$$

which can be integrated, after multiplying by $2\,\frac{d\varphi}{d\sigma}$,

$$\left(\frac{d\varphi}{d\sigma}\right)^2 - 2\,\rho\cos(\varphi - \beta) = 2\,\rho\gamma. \qquad (4.2)$$

Here, γ is a constant of integration, and, according to (2.6)

$$\gamma = \frac{\mu^2}{2\,\rho} - \cos\beta. \qquad (4.3)$$

From (4.2) we find:

$$\frac{d\varphi}{d\sigma} = \pm\sqrt{2\,\rho}\ \sqrt{\gamma + \cos(\varphi - \beta)}. \qquad (4.4)$$

We must carefully pay attention to the ambiguous sign. If the load is small, the shape of the elastic line does not differ much from the original circular one. This means, that φ increases monotonically with σ from zero to its final value. If the load is large, it can, however, occur that the elastic line shows one or more points of inflection. In fig. 7, for instance, there are two points of inflection. Here, φ first decreases from zero to a negative minimum value φ_{min}, reached at A, that we shall denote as a "lower" point of inflection. Then φ increases to a maximum value φ_{max} at B ("upper" point of inflection), and at last φ decreases again to its final value. So, in equation (4.4), successively the minus-, plus-, and minussign should be used. We shall denote all

integrations with respect to φ by the symbol $\int ! d\varphi$, where the note of exclamation should call attention to these questions.

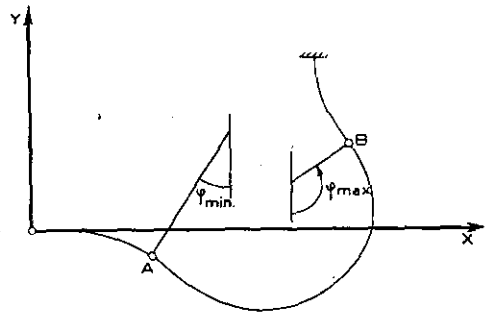

Fig. 7

Now, we can give the solution of (4.4) in the form:

$$\begin{pmatrix} \sigma \\ \xi \\ \eta \end{pmatrix} = \frac{1}{\sqrt{2\rho}} \int_0^{\varphi} ! \cdot \frac{\begin{pmatrix} 1 \\ \cos\varphi' \\ \sin\varphi' \end{pmatrix} d\varphi'}{\sqrt{\gamma + \cos(\varphi' - \beta)}} . \quad (4.5)$$

These integrals can easily be reduced to the standard elliptic integrals and elementary functions:

$$\left.\begin{aligned} &\Delta(k,\varphi) = \sqrt{1 - k^2 \sin^2\varphi}, \\ &E(k,\varphi) = \int_0^{\varphi} \Delta(k,\psi)\, d\psi\,; \; E(k) = E\left(k, \frac{\pi}{2}\right), \\ &F(k,\varphi) = \int_0^{\varphi} \frac{d\psi}{\Delta(k,\psi)}\,; \; F(k) = F\left(k, \frac{\pi}{2}\right), \end{aligned}\right\} \quad (4.6)$$

by means of the substitutions $\psi = \frac{\varphi' - \beta}{2}$ and $k = \sqrt{\frac{2}{1+\gamma}}$. If we put for abbreviation

$$\left.\begin{aligned} f_1(k,\varphi) &= kF(k,\varphi), \\ f_2(k,\varphi) &= \frac{1}{k}\{2E(k,\varphi) - (2-k^2)F(k,\varphi)\}, \\ f_3(k,\varphi) &= \frac{2}{k}\,\Delta(k,\varphi), \end{aligned}\right\} \quad (4.7)$$

we find

$$\begin{pmatrix} \sigma \\ \xi \\ \eta \end{pmatrix} = \frac{1}{\sqrt{\rho}} \left\{ \begin{pmatrix} 1 \\ 0 \\ 0 \end{pmatrix} f_1(k,\varphi) + \begin{pmatrix} 0 \\ \cos\beta \\ \sin\beta \end{pmatrix} f_2(k,\varphi) + \begin{pmatrix} 0 \\ \sin\beta \\ -\cos\beta \end{pmatrix} f_3(k,\varphi) \right\} \Bigg|_{-\beta/2}^{(\varphi-\beta)/2} \quad (4.8)$$

5 Modification of the equations (4.7).

The elliptic integrals that occur in (4.7) are tabulated for the case of real k ($= \sin\vartheta$) and $|k| \leqq 1$, and real φ and $0 \leqq \varphi \leqq \pi/2$. However, we often get values for k and φ that do not satisfy these conditions, but in those cases that are of interest to us, we can always reduce the integrals by means of simple transformations, so that the modulus and argument satisfy the said conditions.

In particular, if k is real, and $|k| > 1$, we find, by substituting $k \sin\psi = \psi'$ that, with $k^* = \sin\vartheta^* = 1/k$ and $\sin\varphi^* = k\sin\varphi$:

$$\left.\begin{aligned} f_1(k,\varphi) &= F(k^*,\varphi^*), \\ f_2(k,\varphi) &= 2E(k^*,\varphi^*) - F(k^*,\varphi^*), \\ f_3(k,\varphi) &= 2k^*\cos\varphi^*. \end{aligned}\right\} \quad (5.1)$$

If, on the other hand, k is purely imaginary, the use of the substitution $\frac{\pi}{2} - \psi = \psi'$ gives, with $k^{**} = \sin\vartheta^{**} = -ik/\sqrt{1-k^2}$ and $\varphi^{**} = \frac{\pi}{2} - \varphi$:

$$\left.\begin{aligned} f_1(k,\varphi) &= ik^{**}\{K(k^{**}) - F(k^{**},\varphi^{**})\}, \\ f_2(k,\varphi) &= \frac{-i}{k^{**}}\{2E(k^{**}) - \\ &\quad -(2-k^{**2})K(k^{**}) - 2E(k^{**},\varphi^{**}) + \\ &\quad +(2-k^{**2})F(k^{**},\varphi^{**}), \\ f_3(k,\varphi) &= \frac{-2i}{k^{**}}\Delta(k^{**},\varphi^{**}). \end{aligned}\right\} \quad (5.2)$$

If, at last, φ is real, but does not satisfy the condition $0 \leqq \varphi \leqq \pi/2$, we can use the self-evident relations,

$$\left.\begin{aligned} E(k,\varphi) &= \\ &\quad -E(k,-\varphi) = 2E(k) - E(k,\pi-\varphi), \\ F(k,\varphi) &= \\ &\quad -F(k,-\varphi) = 2K(k) - F(k,\pi-\varphi), \\ \Delta(k,\varphi) &= \Delta(k,-\varphi) = \Delta(k,\pi-\varphi). \end{aligned}\right\} \quad (5.3)$$

6 The points of inflection of the elastic line.

For the points of inflection of the elastic line $\frac{d\varphi}{d\sigma} = 0$, and from (4.4) it follows that for the extreme values φ_{ext} of φ:

$$\gamma + \cos(\varphi_{ext} - \beta) = 0. \quad (6.1)$$

Evidently, points of inflection can only occur if $|\gamma| \leqq 1$, so if $k \geqq 1$. Therefore, we better introduce ϑ^* instead of γ. Having done this, we find for the values φ_{min} and φ_{max} that correspond to the "lower" and "upper" points of inflection respectively

$$\left.\begin{aligned} \varphi_{min} &= \beta - 2\vartheta^*, \\ \varphi_{max} &= \beta + 2\vartheta^*. \end{aligned}\right\} \quad (6.2)$$

These expressions φ_{min} and φ_{max}, as defined by (6.2), are only mathematical expressions (without a physical sense), unless points of inflection really occur.

The quantity $\varphi - \beta$, that appears in the limits of integration in (4.8), takes for these values of φ the simple form:

$$\left.\begin{aligned} (\varphi_{min} - \beta)/2 &= -\vartheta^*, \\ (\varphi_{max} - \beta)/2 &= \vartheta^*. \end{aligned}\right\} \quad (6.3)$$

We must now distinguish several cases of integration, according to the number and type of points of inflection. Fig. 8 gives a survey of some simple types of an elastic line that runs from $\varphi = 0$ to $\varphi = \pi/2$. In case 0 there is no point of inflection at all. In case I_a there is a lower one, whereas in case I_b an upper one appears.

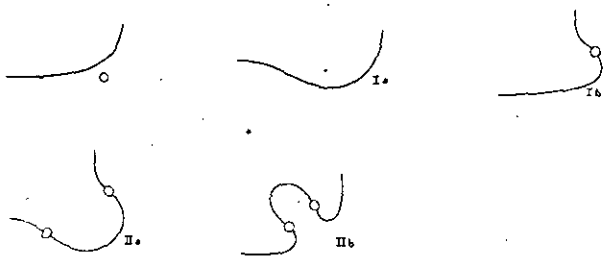

Fig. 8

In case II_a there are two, first a lower, followed by an upper one and in case II_b there are also two but first comes the upper one. Generally, in case N there are N points of inflection, to begin with a lower one in case N_a, and with an upper one in case N_b.

If we denote by G_i, H_i, I_i and J_i respectively the values of $f_i(k, \varphi)$ for the values of the argument $(\varphi - \beta)/2$, $-\beta/2$, $-\vartheta^*$ and ϑ^* respectively, then

$$f_i(k,\varphi)\left|\begin{matrix}(\varphi-\beta)/2\\ !\\ -\beta/2\end{matrix}\right. = \left\{\begin{array}{ll} G_i - H_i & \text{in case 0,}\\ G_i + H_i - 2I_i & \text{in case } I_a,\\ -G_i - H_i + 2J_i & \text{in case } I_b,\\ -G_i + H_i - 2I_i + 2J_i & \text{in case } II_a,\\ G_i - H_i - 2I_i + 2J_i & \text{in case } II_b \end{array}\right. \qquad (6.4)$$

and so on.

Moreover, I_i and J_i are simple values. As a matter of fact, we have:

$$\left.\begin{array}{l} I_1 = -J_1 = -K(k^*),\\ I_2 = -J_2 = -2E(k^*) + K(k^*),\\ I_3 = \quad J_3 = 0. \end{array}\right\} \qquad (6.5)$$

7 The closed circular ring, loaded by two orthogonal pairs of diametral forces.

We consider the special case of a closed circular ring (radius r), loaded at the points $\sigma = 0$ and $\sigma = \pi$ by a pair of normal forces P (positive, if compressive for small P), and at $\sigma = \pi/2$ and $\sigma = 3\pi/2$ by a pair of normal forces νP (fig. 3). Evidently $\beta = \pi/2 - \tan^{-1}\nu$. We shall consider only the doubly symmetrical distortions.

Instead of ρ, we use the quantity $\alpha = \dfrac{Pr^2}{EI} = \rho \cdot 2\sin\beta$. Furthermore, the deflections u'' at $\sigma = 0$ and $\sigma = \pi/2$ respectively, can be given by $u''(0)/r = \lambda''(0) = 1 - \eta(\pi/2)$, and $u''(\pi/2)/r = \lambda''(\pi/2) = 1 - \xi(\pi/2)$, respectively.

As β is a known constant, we can calculate α from the first of the equations (4.8), and $\lambda''(0)$ and $\lambda''(\pi/2)$ from the third and second equation, if we assume a certain value of k (or k^*, k^{**}) and also, if $k > 1$, the case with regard to the number and type of points of inflection. We shall illustrate this by treating in detail the case $\nu = 0$, i. e. the ring loaded only by one pair of diametral forces P.

As $\beta = 90°$, the equations (4.8) take the form:

$$\left.\begin{array}{l} \sqrt{\alpha} = \dfrac{2\sqrt{2}}{\pi} f_1(k,\varphi)\left|\begin{matrix}0\\ !\\ -\pi/4\end{matrix}\right.,\\ \lambda''(0) = 1 - \sqrt{\dfrac{2}{\alpha}}\, f_2(k,\varphi)\left|\begin{matrix}0\\ !\\ -\pi/4\end{matrix}\right.,\\ \lambda''\left(\dfrac{\pi}{2}\right) = 1 - \sqrt{\dfrac{2}{\alpha}}\, f_3(k,\varphi)\left|\begin{matrix}0\\ !\\ -\pi/4\end{matrix}\right.. \end{array}\right\} \qquad (7.1)$$

For small values of ϑ, α is small. With increasing ϑ, α increases (figs. 9, 10 and 11) to reach

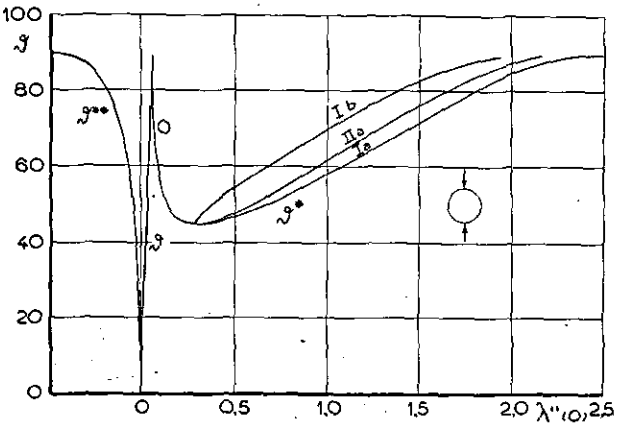

Fig. 9

the value $\alpha = 0{,}62972$ for $\vartheta = 90°$. For higher k we can make a choice out of several possibilities. If we take the case 0, we obtain, of course, that part of the $\alpha - \lambda''$-curve that suits immediately to the part that we have already obtained. The quantities φ_{min} and φ_{max} are now real, but still have no physical sense. We better express now our results in terms of ϑ^*. If k increases from 1, ϑ^* decreases from 90°, and φ_{min} increases from $-90°$ to become 0° for $\vartheta^* = 45°$. Lower values of ϑ^* are not possible, as otherwise φ_{min} should become positive. So this point ($\alpha = 2{,}7866$) is the end of case 0. Case I_a suits here, and if ϑ^* increases again to 90°, α increases indefinitely. This part of the $\alpha - \lambda''$-curve can be completed for negative values of α. Then k is purely imaginary, and we introduce k^{**} or ϑ^{**}. As ϑ^{**} increases from 0° to 90°, α decreases from zero indefinitely. In this way, we have found an $\alpha - \lambda''$-curve that runs from $\alpha = -\infty$ to $\alpha = \infty$, and that contains the point $\alpha = 0$, $\lambda'' = 0$, thus the unloaded state. But this curve does not represent all possible distortions (not even all the stable ones). As a matter of fact, we can also investigate cases I_b and II_b. If we now also take values of ϑ^* between 45° and 90°, we find another complete branch of the

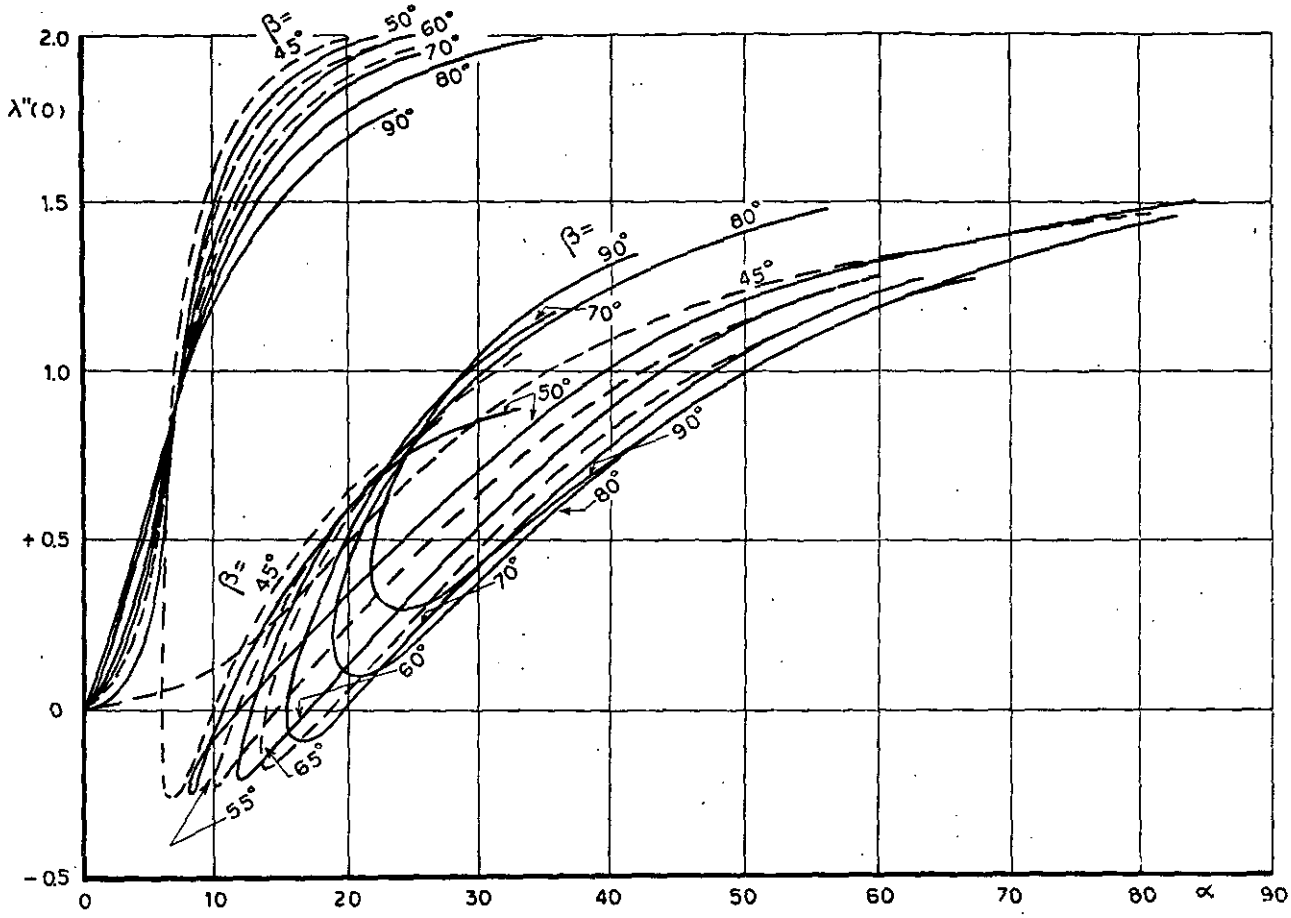
λ''(0)
2.0
1.5
1.0
+0.5
0
−0.5
0
10
20
30
40
50
60
70
80
α
90
β=
45°
50°
60°
70°
80°
90°
β=
90°
80°
45°
70°
50°
90°
80°
β=
45°
70°
60°
65°
55°

Fig. 10

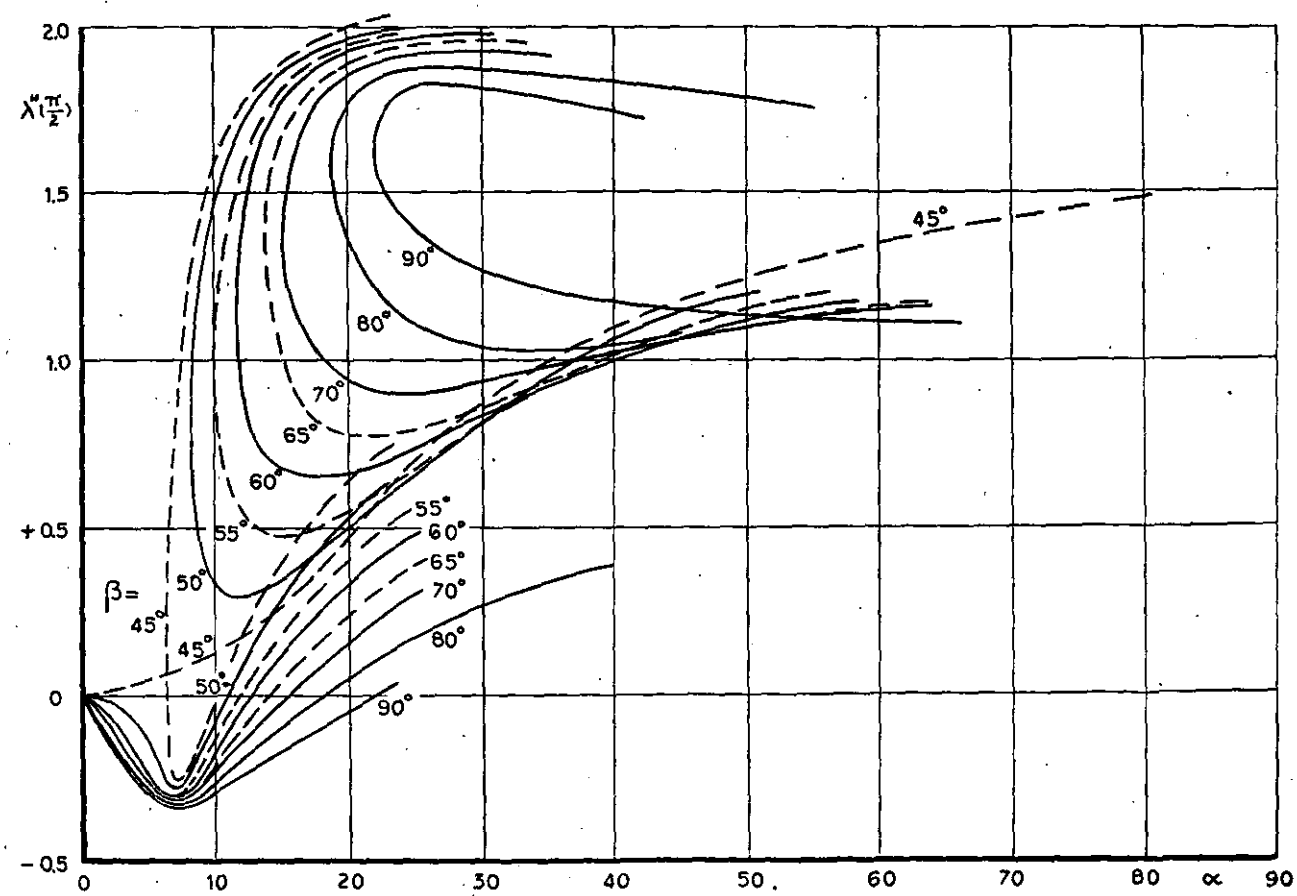
λ''(π/2)
2.0
1.5
1.0
+0.5
0
−0.5
0
10
20
30
40
50
60
70
80
α
90
45°
90°
80°
70°
65°
60°
55°
60°
65°
70°
80°
90°
β=
45°
50°
45°
50°

Fig. 11

$\alpha - \lambda''$-curve that does not contain the point $\alpha = 0$, $\lambda'' = 0$, but is completely restricted to values of $\alpha > \sim 22$. In the same way, we can find other branches of the $\alpha - \lambda''$-curve by taking into consideration cases II_b and III_a, and so on. These higher and unstable modes are, however, of no importance for our purpose. We can confine ourselves to the first two branches.

For other values of β, i. e. for the ring, loaded by two pairs of forces, similar considerations hold. As a matter of fact, we calculated the $\alpha - \lambda''$-curve for $\beta = 90°$, 80°, 70°, 65°, 60°, 55°, 50° and 45° (figs. 10 and 11). A comparison of those curves learns that the branches of the $\alpha - \lambda''$-curve approach each other with decreasing β. For $\beta = 45°$, representing the ring loaded by two equal pairs of forces, the two branches meet each other. This means that, in this case, α increasing from zero, reaches a critical value ($\alpha = 6{,}1250$, corresponding with $\lambda''(0) = \lambda''(\pi/2) = 0{,}05712$), where the $\alpha - \lambda''$-curve divides into three branches. This phenomenon is closely related to buckling. We can compare it, for instance, with the case of a straight rod, loaded at its ends by two compressive forces P, and at its middle by a lateral force νP. If we plot, for an arbitrary value of ν, a graph of the lateral deflection of the middle of the rod over the load, this curve will also consist of two separate branches (fig. 12). For a special

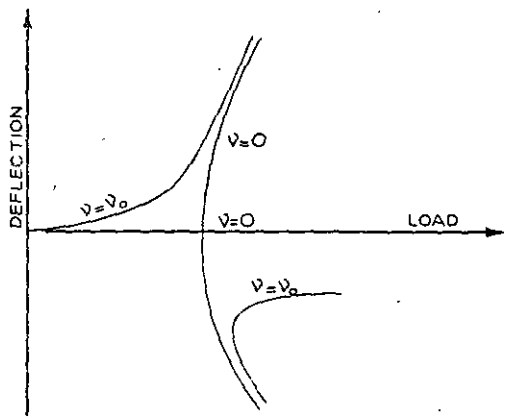

Fig. 12

value of ν (here $\nu = 0$), the branches intersect each other, corresponding to the buckling phenomenon.

8 The distortion of semi-oval rings.

From the data in figs. 10 and 11 it is now only a simple step to the load-deflection characteristics of semi-oval rings. As we have already indicated in the introduction, it is only necessary to read from the graphs for $\lambda''(\pi/2)$ in fig. 11 at the points for which $\lambda''(\pi/2) = 1 - \rho$ (where $2\rho r$ is the length of the major axis of the oval), the corresponding value of α, and from fig. 10 the corresponding values of $\lambda'(0)$. Furthermore, $\lambda'(0)$ can be found as $\lambda''(\pi/2)$ in fig. 11 for $\beta = 90°$ for that negative value of α, for which $\lambda''(0) = 1 - \rho$.

For values of $\beta < 45°$, we have only to turn the ring over 90°, and we find:

$$\left.\begin{aligned} \lambda_\beta\,(0) &= \lambda_{90-\beta}\,(\pi/2), \\ \lambda_\beta\,(\pi/2) &= \lambda_{90-\beta}\,(0), \\ \alpha_\beta &= \alpha_{90-\beta}\ .\ \mathrm{tg}\,\beta. \end{aligned}\right\} \qquad (8.1)$$

We have carried out the calculations for $\rho = 1$; 1.10; 1.20; 1.25; and 1.30. The results are plotted in fig. 13. We see that the curves for $\rho = 1.25$ have an unstable region, where α decreases if $\lambda(0)$ increases. For $\rho > 1.25$ the curve is completely stable, whereas for $\rho \sim 1.25$ the curve is partly indifferent in that there is a region where a considerable increase in deflection is not associated with a sensible increase of the load.

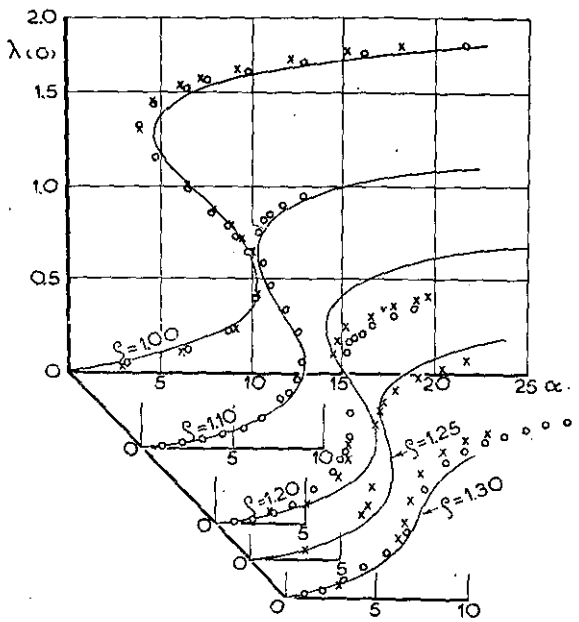

Fig. 13

In fig. 13 are also plotted some experimental results. There is a qualitatively good agreement.

As to the applicability of springs of this type, we must take into account the fact that the load that can be carried by these springs is rather small. On the other hand, the construction is extremely simple, so that they might be applied in instruments which have to combine large displacements with a constant force.

9 References.

1 Kármán, Th. von, Dunn, L. G. and Hsue-Shen Tsien, The influence of curvature on the buckling characteristics of structures, J. Aero. Sci., 7, 1940, p. 276—289.

2 Sonntag, R., Der beiderseits gestützte, symmetrisch belastete gerade Stab mit endlicher Durchbiegung und seine Stabilität, Ing. Arch., 12, 283—306 (1943).
Biezeno, C. B., On a special case of bending, Proc. Kon. Ned. Akad. v. Wet., Amsterdam, 45, 438—442 (1942).
Biezeno, C. B. and Koch, J. J., The circular ring under the combined action of compressive and bending loads, ibid., 49, 1—8 (1946).
On the non-linear deflection of a semi-circular ring, clamped at both ends, ibid., 49, 139—145 (1946).

3 Sonntag, R., Die Kreisringsfeder, Ing. Arch., 13, 389—397 (1943).

Completed: Sept. 1946.

C.C.L. Class. C 471—1

REPORT S. 370.

Evaluation of the Theory on the Post-buckling Behaviour of Stiffened, Flat, Rectangular Plates Subjected to Shear- and Normal Loads

by

Ir W. K. G. FLOOR and T. J. BURGERHOUT.

Summary.

The theory developed in N. L. L.-Report S. 295 has not been presented in such a form that it could be applied in a convenient way to the majority of practical problems. The numerical evaluation given covered only the special case of pure shear load acting upon the combination of plate and stiffeners.

Additional numerical calculations were therefore carried out, the results of which have been presented in the form of a set of diagrams.

Some numerical examples are given of the determination of the average stresses and strains or the required stiffener cross sections of specified stiffened plates subjected to specified compressive and shear loads.

The case of relatively large compressive loads acting in the plane of the plate in the lateral direction could not fully be covered because the assumed waveform of the buckles in the plate proved to be inadequate in this range.

Proposals are made for a number of additional investigations intended to increase the range of applications and the usefulness of the present diagrams.

Contents.

1 Introduction.

1.1 *Statement of the problem.*

Stiffened, flat or nearly flat plates, loaded above the buckling load by shear- and normal stresses, constitute important components in metal aircraft construction.

Thin webs of spars in wings and tailplanes are loaded mainly in pure shear provided the caps carrying the bending moments are relatively heavy.

The skin of wings and tailplanes is normally loaded in tension or compression in a spanwise direction due to bending of the construction. It may also be loaded in shear due to torsion, caused by the aerodynamical loads on the ailerons, flaps and rudders or due to landing gear reactions and dynamical loads caused by the accelerations of masses such as propulsion units during landing. In stressed skin wings and tailplanes where the skin is reinforced by relatively closely spaced stiffeners running in a spanwise direction whereas the ribs or bulkheads are widely spaced, large normal stresses are acting in a longitudinal direction upon the panels in which the skin is divided by the stiffeners and ribs.

In some constructions, however, the ribs are closely and the stiffeners widely spaced and in

certain two-spar wings, there are no stiffeners at all attached to the skin between the spars. The panels, in which the skin is divided by the rib caps, are subjected to large normal strains in their lateral direction. When the strain is compressive, they do not develop large compressive loads because of severe buckling of the plate which has mainly the character of Euler buckling, the plate behaving as a wide column. From a standpoint of structural weight efficiency these constructions must in general be considered inferior to those of the first-mentioned type.

In certain constructions such as fuselage bulkheads a stiffened plate is loaded simultaneously by longitudinal and lateral stresses as well as in shear.

In the constructions mentioned the plate has such a small ratio between thickness and width that pronounced buckling occurs at small loads. The buckles cause a marked reduction in shearing rigidity of the construction besides producing extra compressive loads in both the longitudinal and lateral stiffeners. In certain types of construction they will also load the stiffeners in bending. This applies a. o. to spar caps which can be considered as stiffeners of the spar shear web. Finally, the buckles may cause local buckling of the stiffeners, which are loaded in compression.

It is of primary importance for the aircraft industry to obtain data about the behaviour of stiffened flat plates after buckling has occurred, when they are loaded by any combination of shear stresses and longitudinal and lateral normal stresses to be expected in practice.

1.2 *Theoretical investigations.*

The theory developed by WAGNER (ref. 1) is valid for the limiting case when the bending stiffness of the plate may be neglected altogether. This means, that the buckling stress is negligible as compared with the applied stress. For practical constructions the theory usually gives a conservative but reasonable approximation of the shearing rigidity. The calculated stiffener loads, however, are nearly always extremely conservative. The need for weight efficiency therefore prohibits the application of this theory.

The theory developed by KROMM and MARGUERRE (ref. 2) gives an approximative solution of the problem. It is based upon an assumption for the form of the buckles which is reasonable only for small and moderate ratios between the applied strain or stress and the strain or stress at which the plate begins to buckle. The plate is assumed to be infinitely long and the results will in general be conservative for small length to width ratios. The evaluation deals only with constructions loaded by combinations of shear loads and longitudinal normal loads.

The theory developed by KOITER (ref. 3) is based upon an assumption for the form of the buckles which is reasonable for all ratios of applied strain or stress to buckling strain or stress, although this theory is intended in the first place for large ratios. It is in accordance with WAGNER's theory for very large ratios. For small ratios, the agreement with KROMM and MARGUERRE's theory is good. The plate is assumed to be infinitely long. Apart from the fact that it is therefore in general somewhat conservative for small length to width ratios, it must be considered the best solution of the problem hitherto available. It is also applicable to combinations of shear stresses and longitudinal and lateral normal stresses. The evaluation can be extended, if required, so as to obtain information about the internal stress distribution in a construction.

The waveform of the buckles assumed by DENKE (ref. 4) is valid for moderate ratios of stress or strain to buckling stress or strain. It is intended for stiffened plates having length to width ratios not greatly exceeding unity, e. g. not larger than two, as frequently encountered in practical aircraft constructions. For panels having much larger length to width ratios the assumed waveform of the buckles is inapplicable and it will yield unconservative results. This theory deals only with constructions loaded in shear. It contains both assumptions on the stresses and on the deformations. Two parameters are introduced which can be chosen so as to bring the results in accordance with those obtained by WAGNER for infinite ratios of stress or strain to buckling stress or strain. In the evaluation these parameters are, however, chosen in accordance with the behaviour of the plate at or slightly above the buckling load. It is not indicated how they should be chosen or determined for large but not very large ratios between the stress or strain and the buckling stress or strain. An eventual improvement in this respect would probably render the now relatively simple method of evaluation too cumbersome for practical applications. Besides, the improvement can be expected to be relatively small in all practical cases.

Ref. 5 contains a number of diagrams based upon the theory from ref. 4, enabling a rapid calculation of the stress distribution and the rigidity of stiffened flat rectangular plates loaded in pure shear.

It should be considered a definite advantage of the theory from ref. 4 and the diagrams from ref. 5 that several problems of internal load distribution have also been treated, viz. bending of the stiffeners in the plane of the plate, shear loads, bending and twisting moments in the stiffeners caused by buckling of the plate, average web stresses and web bending stresses.

In two publications by LEVY and others (refs. 6 and 7) a solution is given for square plates and rectangular plates having a length to width ratio of 2.5. All edges are assumed to be simply supported, and to remain straight. The stiffeners attached to the edges are interconnected by hinges in the corners of the panels. The constructions are loaded only in shear. An approximative solution is obtained for low stress or strain to buckling stress or strain ratios assuming a waveform described by a relatively large number of products of periodic functions of the coordinates in the plane of the plate. A very good accuracy can be obtained in this way but the amount of numerical work involved is considerable. The results

are valuable as a check on the theories assuming simpler waveforms, such as ref. 3.

The theory developed by BERGMAN (ref. 8) proceeds along the same lines as the theory from ref. 2. Actually, it assumes the same waveform as far as the infinitely long plate is concerned. In addition, square plates having different edge conditions have been investigated assuming a waveform described by no more than three products of periodic functions of the coordinates in the plane of the plate. In one case the influence of initial buckles of a similar shape as the buckles occurring in flat plates at the critical load has been investigated. The theory considers only constructions loaded in shear. It gives useful information about the stresses in the buckled plate. The results are reliable only for small and moderate ratios of stress or strain to buckling stress or strain.

Recapitulating it can be stated that KOITER's theory (ref. 3) is the only theory available hitherto which may be expected to yield reliable results for stiffened plates loaded by combinations of shear load and longitudinal and lateral normal loads at arbitrary ratios of stress or strain to buckling stress or strain.

1.3 *Experimental investigations.*

The tests by LAHDE and WAGNER (ref. 9) covered the case of the relatively long plate having clamped edges and loaded in shear. The lateral edges were rigid, the longitudinal edges were attached to heavy strips. These strips did not bend but they could be compressed so as to simulate the shortening of the stiffeners in an actual construction as a consequence of the loads exerted by the buckled plate. The results can thus be applied also when the stiffeners are relatively heavy and a small longitudinal compressive load is acting upon the construction in addition to a shear load. In general, however, they are applicable only to the case of pure shear.

The condition of clamped longitudinal edges is seldom approached in practical constructions. It is therefore inevitable when applying the diagrams from ref. 9 to introduce some correction to compensate for the difference in edge conditions.

Tests on thin-web beams having heavy spar caps and a reasonably large number of closely spaced vertical stiffeners were summarized and discussed by KUHN (ref. 10). The beams were loaded in bending and shear, the bending load being carried by the caps. The webs were thus loaded in shear combined with a small amount of bending.

The tests by LEVIN (ref. 11) were carried out by means of a construction resembling the one described in ref. 9. The plates to be tested were however, in part of the experiments attached to the heavy strips acting as longitudinal stiffeners in such a way as to simulate the edge conditions existing in actual constructions. The plates were loaded only in shear.

The tests by LEVIN and SANDLIN (ref. 12) constitute an extension of the investigation from ref. 10. Although these tests were conducted mainly with the aim of obtaining information on the ultimate loads carried by thin-web beams and stiffened plates, valuable results were also obtained for the behaviour in the elastic range.

The tests by VAN DER NEUT and others (refs. 13 and 14) were primarily intended to investigate the behaviour in the elastic range of thin-web beams subjected to combinations of a shear load and a compressive load acting in the direction of the spar caps. The panels of the web were thus loaded simultaneously in shear and in compression in the direction of the spar caps, which can be considered as the lateral stiffeners, the uprights acting as longitudinal stiffeners. A comparison is made in ref. 14 between results obtained in the experiments and results derived from the theory presented in ref. 3.

Although scatter in the experimental results is large, they seem, in general, to confirm the theory. Similar conclusions are drawn in ref. 15, giving a summary of the results from refs. 13 and 14. In ref. 16 an improved evaluation of some test results from refs. 13 and 14 was given. This led to a closer accordance between theoretical and experimental results. The conclusions drawn in this respect can thus be maintained.

1.4 *Numerical evaluation of the theory.*

Considering the fact that the scatter in the test results is large and the accordance with theoretical results reasonable it seemed worthwile to carry out a numerical evaluation of the theory from ref. 3. The results should be presented in such a way that they can easily be applied to practical problems. It is evident that they are valid only in the elastic range. For the calculation of the ultimate load a construction will sustain it is advised to apply a method of analysis developed in refs. 10 to 12, incl. and discussed in ref. 19. The aircraft industry showed much interest in the construction of diagrams representing the results of the theory from ref. 3. The Netherlands Aircraft Development Board therefore charged the National Aeronautical Research Institute with the numerical evaluation of the theory and the construction of diagrams for stiffened flat plates under combined shear load and longitudinal and lateral compressive loads. The form of the diagrams and the range of the investigation should be chosen in accordance with the requirements of the aircraft industry.

The method after which the evaluations were carried out is given in sec. 2 together with a discussion on the way to represent the results in the form of diagrams.

The diagrams are presented in sec. 3. The range covered and the method of application to practical problems are also discussed.

In sec. 4 are discussed the desirability of an extension of the investigation so as to cover the local stresses in the web, etc. and a study on the reliability of the method of calculation of the diagrams as far as combinations of small shear and large lateral compression are concerned. The conclusions which can be drawn from the investigation are summarized in sec. 5.

2 Method of evaluation.

2.1 *The form of the diagrams and the parameters of the problem.*

When an infinitely long, flat plate of thickness h and width b having hinged edges is loaded in pure longitudinal compression, it buckles at a stress σ^* and strain ε^* given by

$$\sigma^* = E\varepsilon^* = \pi^2 Eh^2/3(1-\nu^2)b^2. \qquad (2.1)$$

In the following, all stresses will be made non-dimensional by division by σ^* and all strains by division by ε^*.

In accordance with the opinion expressed by the aircraft industry it was decided to represent the results of the calculations in a series of diagrams each valid for a constant shearing stress ratio, τ/σ^*. They should contain curves of constant longitudinal and lateral normal stress ratios, σ_1/σ^* and σ_2/σ^* respectively, and curves of constant stiffness ratios, $\tau/\gamma G$. The longitudinal and lateral compressive strain ratios, $\varepsilon_1/\varepsilon^*$ and $\varepsilon_2/\varepsilon^*$, should be chosen as coordinates. It should be well understood that in a buckled plate τ, σ_1 and σ_2 represent average values of the stresses taken over the plate as a whole. Likewise, γ, ε_1 and ε_2 represent the deformations of the plate as a whole.

The diagrams thus represent the relations between $\varepsilon_1/\varepsilon^*$, $\varepsilon_2/\varepsilon^*$, σ_1/σ^*, σ_2/σ^* and $\tau/\gamma G$ for specified values of τ/σ^*.

Calculations have been based upon the theory from ref. 3, notably waveform no. 1. This assumption for the form of the buckles is intended for the case of hinged edges. It suffers from the deficiency that the nodal lines are assumed straight over the total width of the plate and do not orthogonally intersect the edges. The error introduced will in general be small, the buckling load being overestimated by no more than 6 %. Large errors can be expected only if the angles between the edges and the nodal lines become too small, which may occur at large $\varepsilon_2/\varepsilon^*$ combined with small $\varepsilon_1/\varepsilon^*$ and τ/σ^*. Leaving this case out of consideration, the unconservative error is probably approximately compensated by two causes.

The edges of the plate in an actual construction will always be restrained against rotation to some extent by the stiffeners to which they are attached. This will result in a slight underestimation of the buckling stress and the load carrying capacity. A similar effect can be expected from the fact that actual plates will always have a finite length. The assumed waveform is therefore believed to yield reasonably accurate results.

The form of the buckles is described by an expression, periodic in the longitudinal coordinate x, containing four parameters, viz. the maximum amplitude f, the half-wave length L, the cotangent of the angle between the nodal lines and the longitudinal edges m, and the ratio α as indicated in fig. 2.1. A cross section of the buckled plate parallel to the nodal lines shows a central part, wide $(1-\alpha)b\sqrt{1+m^2}$, where the amplitude is constant and two edge parts, adjacent to the edges of the plate, wide $0.5\,\alpha b\sqrt{1+m^2}$ each. Here the amplitude is given by a cosine function, vanishing at the edges, and having zero slope and the correct amplitude at the transition points to the central part.

Adequate assumptions containing the parameters f, L, m and α were also made for the displacements u and v in the X- and Y-directions respectively of an arbitrary point (x, y) of the median plane of the plate.

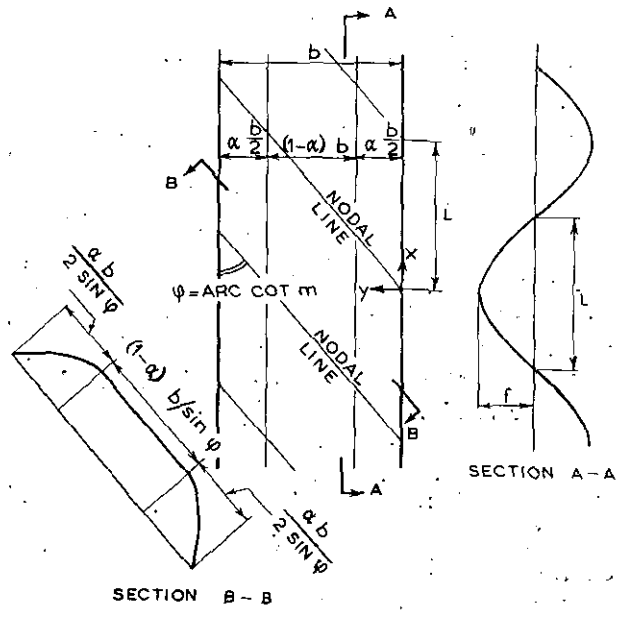

Fig. 2.1. The assumed waveform of the buckles in the plate.

In ref. 3 four equations have been given which represent the relation between the four parameters f, L, m and α on one hand and the stresses σ_1, σ_2 and τ on the other hand. These equations were obtained from the condition that the parameters should be chosen so as to render the elastic energy stored in the plate a minimum with respect to arbitrary small variations of the parameters.

Choosing three out of the seven quantities, the remaining four can be calculated. Ref. 3 also gives three relations between ε_1, ε_2, γ and the seven quantities mentioned before. All data required for the construction of the diagrams can thus be obtained by calculation.

2.2 *Range of the investigation.*

In view of the fact that fairly high compressive strains may occur in the longitudinal or lateral stiffeners, it was aimed at investigating the ranges $-100 < \varepsilon_1/\varepsilon^* < 250$ and $-100 < \varepsilon_2/\varepsilon^* < 250$.[1])

High tensile strains are not interesting, because buckling will not occur. It is not to be expected that large strains will simultaneously occur in the longitudinal and lateral stiffeners. It was thus believed sufficient to restrict the investigation in these cases roughly to the range $\varepsilon_1/\varepsilon^* + \varepsilon_2/\varepsilon^* < 250$. This could be achieved in most cases in a con-

[1]) A positive value of $\varepsilon_1/\varepsilon^*$ or $\varepsilon_2/\varepsilon^*$ corresponds to a *compressive* strain ε_1 or ε_2.

A positive value of σ_1/σ^* or σ_2/σ^* corresponds to a *tensile* stress σ_1 or σ_2.

venient way by limiting the range of the diagram by some curve of constant $\tau/\gamma G$.

Calculations were carried out for, in total, 11 diagrams, each for a constant ratio τ/σ^*. The smallest τ/σ^* was 0, the largest 50, the interval being divided in steps of 5.

The ranges of σ_1/σ^*, σ_2/σ^* and $\tau/\gamma G$ covered, followed of course from the choice of $\varepsilon_1/\varepsilon^*$, $\varepsilon_2/\varepsilon^*$ and τ/σ^*.

They can be read from figs. 2.2 to 2.4, incl.

The range where $\alpha \equiv 1$ was not investigated. This infers that the diagrams are limited to the left by a curve $\alpha = 1$ running roughly in the direction of the positive $\varepsilon_2/\varepsilon^*$-axis. For $\tau/\sigma^* \leqq 5$ all negative values of $\varepsilon_1/\varepsilon^*$ are thus excluded. The restriction becomes less serious as τ/σ^* increases. For $\tau/\sigma^* > 30$ the range $\varepsilon_1/\varepsilon^* > -100$ can be practically fully covered. It is found that $\varepsilon_1/\varepsilon^* = 0$, $\varepsilon_2/\varepsilon^* = 250$ falls outside the range $\alpha \leqq 1$ for $\tau/\sigma^* < 20$.

The range of the investigation was limited by appropriately chosen curves of constant σ_2/σ^*. Compressive stresses in the lateral (or Y-) direction have not been considered. In actual practice such stresses my arise but it is expected that they will never exceed the Euler buckling stress. This means that for infinitely long strips $\sigma_2/\sigma^* \geqq -0.25$. For plates of finite length σ_2/σ^* may be somewhat less than -0.25. It does not seem advisable, however, to apply the theory in the range of negative σ_2/σ^* (i. e. lateral compressive stress) because it does not yield the Euler buckling stress. In fact, the assumed waveform, (A.1) and (A.2), for the buckles in the plate is not adequate in this range. A principally different waveform should be assumed.

The diagrams for $\tau/\sigma^* < 15$ are limited in the direction of positive $\varepsilon_2/\varepsilon^*$ by the curve $\sigma_2/\sigma^* = 0$. This infers that $\varepsilon_2/\varepsilon^* < 10$ for $\tau/\sigma^* = 0$. The restriction becomes less serious as τ/σ^* increases.

2.3 *Derivation of the equations.*

The evaluation has been based upon the assumed waveform no. 1 from ref. 3, which is illustrated, together with the choice of the coordinate system, in fig. 2.1. Displacements of an arbitrary point (x, y) of the median plane of the plate in the X- and Y-directions are called u and v, respectively. The displacement in the Z-direction, normal to the plane of the plate prior to buckling, is called w. It is assumed that any straight line running in the Z-direction prior to buckling will remain straight and perpendicular to the median plane of the plate during buckling.

The longitudinal edges of the infinitely long plate remain straight and parallel during buckling. In the longitudinal or X-direction the mean compressive strain amounts to ε_1 and the mean tensile stress is σ_1. In the lateral or Y-direction the mean compressive strain amounts to ε_2 and the mean tensile stress is σ_2. The plate carries a mean shear stress τ and is subjected to a mean shearing strain γ. Detailed information on the waveform equations and the expression for the elastic energy, are given in Appendix A. These equations contain the four waveform parameters f, L, m and α (c.f. fig. 2.1).

The solution of the problem of the behaviour of a buckled plate consists in finding values for the elastic energy stored in the plate that are stationary with respect to small variations of the form of the buckles, the edges being held in fixed positions. Introducing assumptions for the form of the buckles containing a limited number of parameters, such as (A.1) and (A.2), the best approximation for the elastic energy is obtained by finding values for this energy (or for η after (A.4)) that are stationary with respect to small but otherwise arbitrary variations of the parameters. The four equations following from this procedure are given in Appendix B.

The set of 7 equations (A.5) and (B.5) to (B.8) incl. contain the 10 quantities (σ_1/σ^*), (σ_2/σ^*), (τ/σ^*), $(\varepsilon_1/\varepsilon^*)$, $(\varepsilon_2/\varepsilon^*)$; (γ/ε^*), (F/ε^*), D, m and α.

Three of these quantities being chosen, the others can be solved from the equations.

It should be pointed out that, for physical reasons, F/ε^*, m and D will never become negative, while $0 \leqq \alpha \leqq 1$. As has already been discussed (sec. 2.1), m should not be too large. It does not seem advisable to use the present theory for values of m far in excess of 2.

2.4 *Methods of solution.*

It was assumed in evaluating the system of equations (A.5) and (B.5) to (B.8) incl. that the solutions obtained by the methods discussed hereafter represent stable conditions of equilibrium of the buckled plate. In refs. 17 and 18 a method of evaluation is proposed by means of which a check on the stability of the buckled plate is easily obtained. This method was not used in the present investigation.

Should more than one solution be found for which the equilibrium of the buckled plate is stable with respect to small variations of the form of the buckles, then the soltuion for which the elastic energy stored in the plate is lowest has to be considered as the correct one. There has been found no evidence, however, that such ambiguities occur for the problem considered.

In ref. 3 it was proposed to specify a number of sets of values for the parameters D, m and α. The ratios $\sigma_1\sigma^*$, σ_2/σ^*, τ/σ^*, $\varepsilon_1/\varepsilon^*$, $\varepsilon_2/\varepsilon^*$ and γ/ε^* as well as F/ε^* can then be solved easily from the set of seven linear equations, (A.5) and (B.5) to (B.8) incl.

This method of evaluation proved to be extremely cumbersome because of the threefold interpolation (viz. towards D, m and α) when used to construct diagrams of the type proposed in sec. 2.1. In certain regions of these diagrams a small variation of one of the parameters causes relatively large variations in some of the other quantities. The method proved to be very useful, however, for obtaining a first approximation in the methods of solution discussed hereafter.

In the *first method of solution* succesfully used, sets of values of σ_1/σ^*, σ_2/σ^* and α were specified, because the final diagrams should contain curves of constant σ_1/σ^* and σ_2/σ^*. Besides, it was believed that curves of constant α would be con-

venient in the final evaluation. At any rate, the curve $\alpha = 1$ has to be determined which separates the diagrams in a range where $\alpha \leqq 1$ and a range $\alpha \equiv 1$.

Values for m and D were estimated either by considering results obtained as proposed in ref. 3 (see above) or by extrapolation. Improved values for m and D were obtained by an iteration process, after which the other parameters can be calculated.

The details of this method of solution are discussed in Appendix C.

This method failed for large ratios $\varepsilon_2/\varepsilon^*$ because of the fact that the curves of constant α on one hand and those of constant σ_1/σ^* and σ_2/σ^* on the other hand in the final diagrams intersected each other at small angles. Small deviations in the assumed ratios α, σ_1/σ^* and σ_2/σ^* caused therefore large changes in $\varepsilon_1/\varepsilon^*$ and $\varepsilon_2/\varepsilon^*$. No reasonable convergence of the calculation procedure could be obtained unless the first approximations for m and D were nearly equal to the correct values.

With the *second method of solution* the difficulties encountered when applying the first method of solution in the range of large $\varepsilon_2/\varepsilon^*$ were avoided as described hereafter [1]).

Sets of values of σ_1/σ^*, σ_2/σ^* and τ/σ^* were assumed corresponding to the intersections of the curves of constant σ_1/σ^* and σ_2/σ^* in the final diagrams of constant τ/σ^* proposed in sec. 2.1.

Values for m and α were estimated either by considering results obtained with the first method or by extrapolation. Improved values for m and α were obtained by an iteration process. The details of this method are described in Appendix D.

The second method requires more numerical calculations than the first one but has the important advantage of requiring no interpolations in the construction of the final diagrams of the type proposed in sec. 2.1.

It was found that the second method did not converge unless the first approximations of m and α were very close to the correct values in the range of large negative $\varepsilon_2/\varepsilon^*$ where the first method proved to be convenient. Both methods were thus applied in constructing the final diagrams.

For the *special case* $\tau/\sigma^* = 0$ a diagram was also constructed with the aim of enabling the interpolation towards τ/σ^* in the range $0 < \tau/\sigma^* < 5$.

The method of solution for this special case is fully described in Appendix E.

3 Numerical results.

3.1 *Discussion of the diagrams.*

As a result of calculations carried out after the methods discussed in sec. 2.4 the diagrams figs. 3.1 to 3.11 incl. have been constructed. According to the proposal from sec. 2.1, they are valid for a constant ratio τ/σ^* and contain curves of constant σ_1/σ^*, σ_2/σ^* and $\tau/\gamma G$ corresponding to the coordinates $\varepsilon_1/\varepsilon^*$ and $\varepsilon_2/\varepsilon^*$. For a general survey of the range covered reference may be made to figs. 2.2 to 2.4, incl.

All diagrams are limited in the direction of negative $\varepsilon_2/\varepsilon^*$ by a curve of constant σ_2/σ^* and in the direction of positive $\varepsilon_1/\varepsilon^*$ by a curve of constant σ_1/σ^*.

In the direction of positive $\varepsilon_2/\varepsilon^*$ fig. 3.1 is bounded by the curve $\tau/\gamma G = 0$, but it seems advisable not to use this diagram for $\sigma_2/\sigma^* < 0$ for the reasons mentioned in sec. 2.2. The other diagrams are, therefore, bounded partly (in general for small $\varepsilon_1/\varepsilon^*$) by curves of constant $\sigma_2/\sigma^* \geqq 0$ and partly (for large $\varepsilon_1/\varepsilon^*$) by curves of constant $\tau/\gamma G$, because these coincided reasonably well with the limit proposed in sec. 2.2, viz. $\varepsilon_1/\varepsilon^* + \varepsilon_2/\varepsilon^* = 250$.

The rapid divergence of the curves of constant σ_2/σ^* for decreasing σ_2/σ^* in the range $\sigma_2/\sigma^* < 10$ is very pronounced in figs. 3.2 to 3.5 and gives rise to some doubt as to the reliability of the assumed waveform of the buckles in the plate, (A.1) and (A.2) and hence the accuracy of the results in this range of loads and strains.

For $\tau/\sigma^* > 10$ the curve $\sigma_2/\sigma^* = 0$ falls far outside the range of the diagrams.

In the direction of negative $\varepsilon_1/\varepsilon^*$ all diagrams are bounded by the curve $\alpha = 1$, which for negative $\varepsilon_2/\varepsilon^*$ practically coincides with the buckling curve $F/\varepsilon^* = 0$ or $\tau/\gamma G = 1$.

It is observed that, as soon as $\varepsilon_2/\varepsilon^*$ exceeds a certain value, the curves $\alpha = 1$ and $F/\varepsilon^* = 0$ diverge to such an extent that they must be represented as separate curves in the diagrams. When $\varepsilon_2/\varepsilon^*$ increases above these values the curves $F/\varepsilon^* = 0$ will gradually bend away in the direction of negative $\varepsilon_1/\varepsilon^*$. The curves $\alpha = 1$ will bend relatively sharply in the direction of positive $\varepsilon_2/\varepsilon^*$ and then gradually in the direction of positive $\varepsilon_1/\varepsilon^*$, as shown in figs. 3.1 to 3.5 incl. The remaining diagrams do not extend to such large ratios of negative $\varepsilon_1/\varepsilon^*$ that this part of the curve $\alpha = 1$ is shown. In figs. 3.8 to 3.11 incl. even the first bending of the curve in the direction of positive $\varepsilon_2/\varepsilon^*$ is barely visible. These diagrams can, if so required, be extended in the direction of negative $\varepsilon_1/\varepsilon^*$ without serious difficulties (sec. 2.2).

In sec. 2.1 it was stated that large errors could eventually be expected if m would be large. Near the part of the curve $\alpha = 1$ running roughly parallel to the positive axis of $\varepsilon_2/\varepsilon^*$, figs. 3.1 to 3.5 incl. where σ_2/σ^* is small, it is found that $m > 2$. This should be considered as a second indication that in this range and for decreasing $\varepsilon_1/\varepsilon^*$ and increasing $\varepsilon_2/\varepsilon^*$ an assumption for the waveform of the buckles in the plate should be introduced having nodal lines which intersect the longitudinal edges of the plate perpendicularly. As such, waveform nr. 2, developed in ref. 3, should be mentioned. A different type of waveform having the required characteristics was proposed by MICHIELSEN (ref. 17).

3.2 *Application of the diagrams.*

3.2.1 *Introduction.*

Several types of problems can easily be solved by applying the diagrams figs. 3.1 to 3.11 incl.

*) A similar method had been recommended by the Fokker aeroplane company.

This will be evident from some numerical examples discussed hereafter (sec. 3.2.2).

The length, width and thickness of the rectangular panels considered are a, b and h, respectively. The edges remain straight and parallel. The panels are reinforced by longitudinal and lateral stiffeners along the edges having total cross sections A_b and A_a respectively as shown in fig. 3.12. The longitudinal reinforcing ratio thus is A_b/bh and the lateral reinforcing ratio A_a/ah. When two adjacent panels have a common stiffener, half the cross section of this stiffener should be attributed to each of the panels.

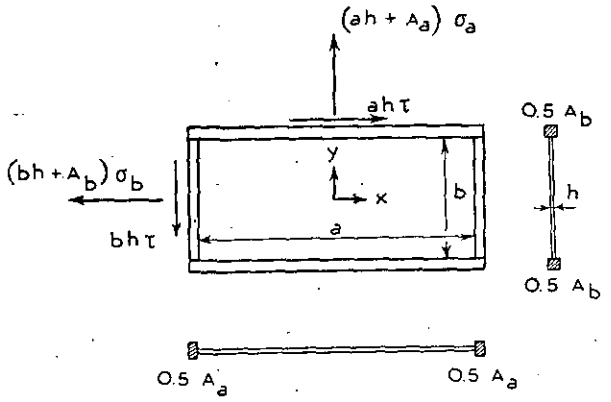

Fig. 3.12. Loading and dimensions of a stiffened panel.

The construction is loaded in tension by forces $(ah + A_a)\sigma_a$ in the lateral (or Y-) and $(bh + A_b)\sigma_b$ in the longitudinal (or X-) direction. The shear loads τah and τbh are carried by the plate because the stiffeners are interconnected by hinges. It follows from conditions of equilibrium that

$$(1+A_a/ah)\sigma_a/\sigma^* = \sigma_2/\sigma^* - (A_a/ah)\varepsilon_2/\varepsilon^*, \quad (3.1)$$

$$(1+A_b/bh)\sigma_b/\sigma^* = \sigma_1/\sigma^* - (A_b/bh)\varepsilon_1/\varepsilon^*, \quad (3.2)$$

the minus sign being caused by the fact that positive σ's are tensile stresses and positive ε's are compressive strains.

3.2.2 *Numerical examples.*

The influence of the shearing stress upon the stresses and strains in constructions of the type represented in fig. 3.12 is investigated. In the first example the construction is specified by the stiffening ratios $A_a/ah = 0.5$ and $A_b/bh = 1$. The loading is specified by the ratios $\sigma_a/\sigma^* = 0$ and $\sigma_b/\sigma^* = -100$. In this, as well as in the second, example the stiffening ratios and the external loads are given and the problem is to determine the stresses and strains. A constant external compressive load in the longitudinal direction is here acting upon the construction. In each of the diagrams figs. 3.1 to 3.11 incl. (3.1) represents a curve $\varepsilon_2/\varepsilon^* = 2\,\sigma_2/\sigma^*$ roughly parallel to the $\varepsilon_1/\varepsilon^*$-axis and (3.2) a curve $\varepsilon_1/\varepsilon^* = 200 + \sigma_1/\sigma^*$ roughly parallel to the $\varepsilon_2/\varepsilon^*$-axis. The construction of these curves is easily carried out.

The coordinates of the point of intersection of these two curves represent $\varepsilon_1/\varepsilon^*$ and $\varepsilon_2/\varepsilon^*$ for the specified value of τ/σ^*. $\tau/\gamma G$, σ_1/σ^* and σ_2/σ^* are also easily read. For $\tau/\sigma^* = 0$, 40, 45 and 50 the point of intersection fell outside the range investigated. In this respect it is remarked that it seems rather unlikely that a combination of $\sigma_b/\sigma^* = -100$ and τ/σ^* as large as 40 will ever occur in practice.

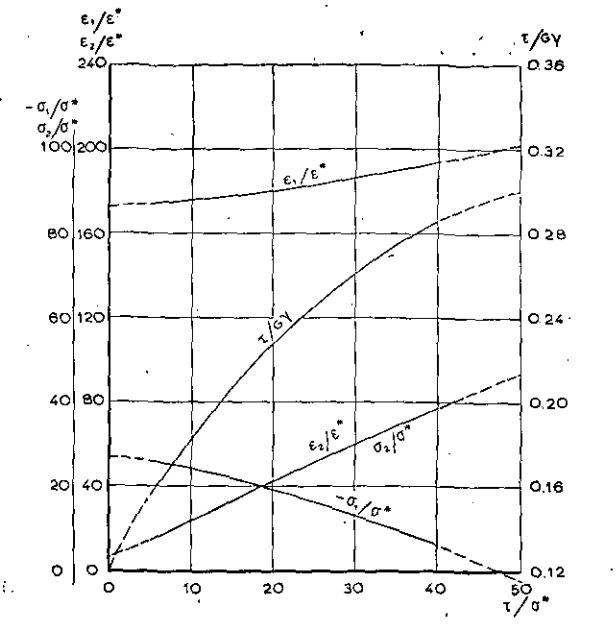

Fig. 3.13. Results for the first example.
$A_a/ah = 0.5$; $A_b/bh = 1$; $\sigma_a/\sigma^* = 0$; $\sigma_b/\sigma^* = -100$.

The numerical results are represented in table 3.1 and fig. 3.13. It is observed that $\tau/\gamma G$ increases with increasing τ/σ^*. This infers that the tangent modulus of rigidity is larger than the secant modulus of rigidity, $d\tau/Gd\gamma > \tau/G\gamma$, which also follows from the formula

$$\{1 - [d(\tau/G\gamma)/d(\tau/\sigma^*)]/[(\tau/G\gamma)/(\tau/\sigma^*)]\} \times d\tau/Gd\gamma = \tau/G\gamma. \quad (3.3)$$

This at first sight rather peculiar behaviour of the construction is caused by the fact that the angle φ between the direction of the buckles in the plate and the X-axis (fig. 2.1), being nearly 90° at small τ/σ^*, decreases with increasing τ/σ^* and ultimately approaches to a limit φ_0 of about 45°.

It is readily observed from ref. 1 or ref. 13, Appendix 1(a) that $\tau/\gamma G$ for a fully developed diagonal tension field tends to a maximum as φ approaches φ_0. Similar results could thus be expected for the partially developed diagonal tension fields considered in this report.

When the construction is loaded in pure shear ($\sigma_a = \sigma_b = 0$) it is found that $d\tau/Gd\gamma < \tau/G\gamma$, because $\tau/\gamma G$ decreases with increasing τ/σ^*.

In the second example the construction is specified by $A_a/ah = 4$ and $A_b/bh = 0.25$. The loading is specified by $\sigma_a/\sigma^* = -100$ and $\sigma_b/\sigma^* = 0$. A constant external compressive load in the lateral direction is thus acting upon the construction. In figs. 3.1 to 3.11 incl. curves $\varepsilon_1/\varepsilon^* = 4\,\sigma_1/\sigma^*$, roughly parallel to the $\varepsilon_2/\varepsilon^*$-axis, and $\varepsilon_2/\varepsilon^* = 125 + 0.25\,\sigma_2/\sigma^*$, roughly parallel to the $\varepsilon_1/\varepsilon^*$-axis, ac-

cording to (3.1) and (3.2) are drawn and $\varepsilon_1/\varepsilon^*$, $\varepsilon_2/\varepsilon^*$, σ_1/σ^*, σ_2/σ^* and $\tau/G\gamma$ are read at the point of intersection of these curves. No results are obtained for $\tau/\sigma^* < 10$ because the diagrams do not extend to $\sigma_2/\sigma^* < 0$. For $\tau/\sigma^* > 40$ an extrapolation had to be carried out. It is, however, unlikely that combinations of so large τ/σ^* and $-\sigma_a/\sigma^*$ will ever occur in actual constructions. The numerical results are represented in table 3.2 and fig. 3.14.

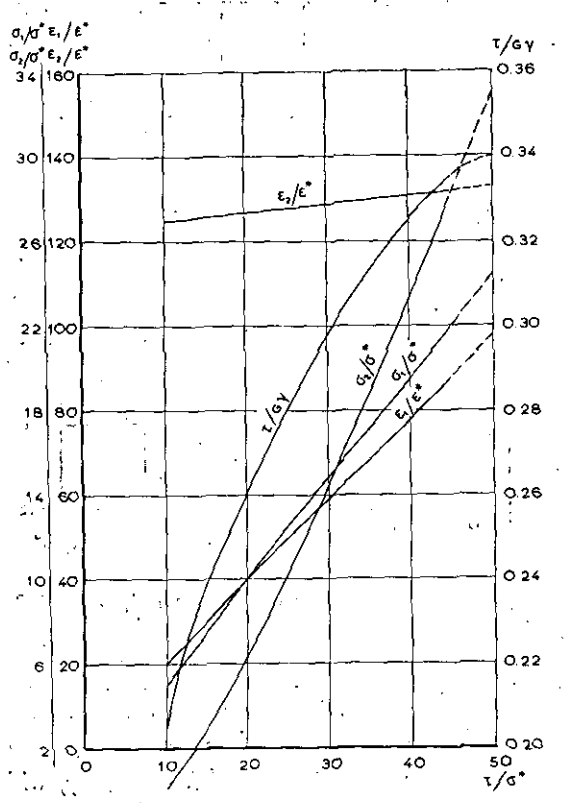

Fig. 3.14. Results for the second example.
$A_a/ah = 4$; $A_b/bh = 0.25$; $\sigma_a/\sigma^* = -100$; $\sigma_b/\sigma^* = 0$.

When the strain in the stiffeners is specified the cross section of the stiffeners can be determined by means of figs. 3.1 to 3.11 incl. This will be demonstrated by two additional examples. In the third example the construction is specified by $A_a/ah = 0.5$, the loading by $\sigma_a/\sigma^* = 0$ and $(1 + A_b/bh)\sigma_b/\sigma^* = -400$ (i. e. a given external longitudinal compression) and the compressive strain in the longitudinal stiffeners, whose cross section A_b has to be determined, by $\varepsilon_1/\varepsilon^* = 100$.

According to (3.1), curves $\varepsilon_2/\varepsilon^* = 2\,\sigma_2/\sigma^*$ are drawn in figs. 3.1 to 3.11 incl., running roughly parallel to the $\varepsilon_1/\varepsilon^*$-axis. At the intersection with $\varepsilon_1/\varepsilon^* = 100$, $\varepsilon_2/\varepsilon^*$, σ_1/σ^*, σ_2/σ^* and $\tau/G\gamma$ are read. The external longitudinal load acting upon the construction being specified by $(1 + A_b/bh)\sigma b/\sigma^*$ and the longitudinal compressive strain of the panel as a whole by $\varepsilon_1/\varepsilon^*$, A_b/bh, and hence the longitudinal stiffener cross section, follows from (3.2). The numerical results are presented in table 3.3 and fig. 3.15.

In the fourth example the construction is specified by $A_b/bh = 0.5$, the loading by $(1 + A_a/ah)\sigma_a/\sigma^* = -400$ (i. e. a given external lateral compression) and $\sigma_b/\sigma^* = 0$ and the compressive strain in the lateral stiffeners, whose cross section A_a has to be determined, by $\varepsilon_2/\varepsilon^* = 100$.

According to (3.2), curves $\varepsilon_1/\varepsilon^* = 2\,\sigma_1/\sigma^*$ are drawn in figs. 3.1 to 3.11 incl., running roughly

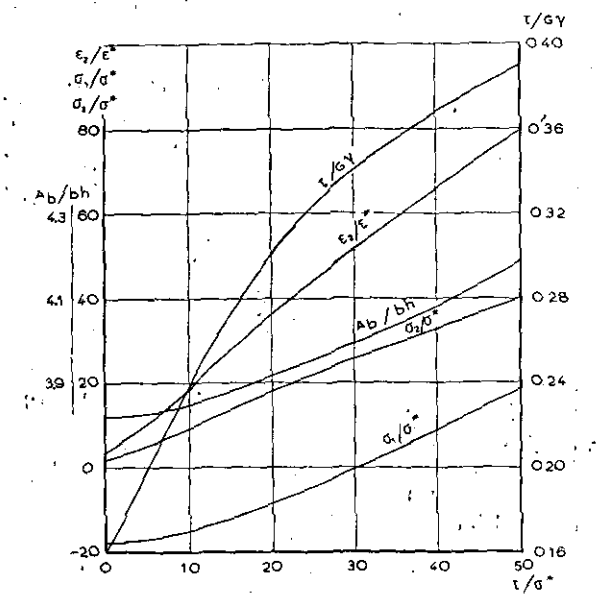

Fig. 3.15. Results for the third example.
$A_a/ah = 0.5$; $\varepsilon_1/\varepsilon^* = 100$; $\sigma_a/\sigma^* = 0$;
$(1 + A_b/bh)\ \sigma_b/\sigma^* = -400$.

parallel to the $\varepsilon_2/\varepsilon^*$-axis. At the intersection with $\varepsilon_2/\varepsilon^* = 100$, $\varepsilon_1/\varepsilon^*$, σ_1/σ^*, σ_2/σ^* and $\tau/G\gamma$ are read. Finally A_a/ah is calculated from (3.1).

No results are obtained for $\tau/\sigma^* < 10$ because the diagrams figs. 3.1 to 3.11 incl. do not extend to $\sigma_2/\sigma^* < 0$.

The numerical results are presented in table 3.4 and fig. 3.16.

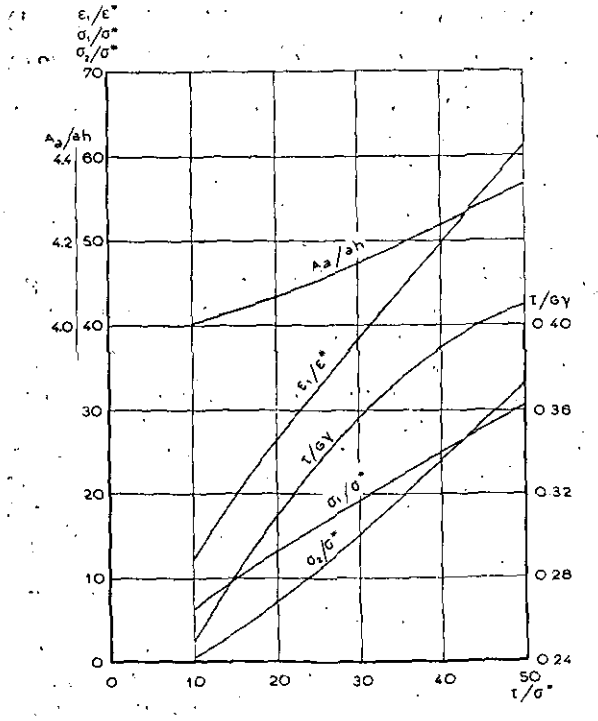

Fig. 3.16. Results for the fourth example.
$A_b/bh = 0.5$; $\varepsilon_2/\varepsilon^* = 100$; $(1 + A_a/ah)\ \sigma_a/\sigma^* = -400$;
$\sigma_b/\sigma^* = 0$.

4 Desirability of additional investigations.

4.1 *Range of the diagrams.*

It is observed from tab. 3.2 and 3.4 or figs. 3.14 and 3.16 that the diagrams figs. 3.1 and 3.2 do not yield a solution for the problems considered in sec. 3.2, second and fourth example. An extension of the range of these diagrams in the direction of negative σ_2/σ^* or positive $\varepsilon_2/\varepsilon^*$ is thus required when the diagrams should be applied to constructions subjected to large lateral compression loads in addition to small shearing loads. Such cases occur in the upper skin of aeroplane wings provided with closely spaced ribs and widely spaced stiffening elements in the spanwise direction. Such an extension must be based upon assumptions for the waveform of the buckles in the plate different from those used hitherto, as discussed in sec. 3.1.

It seems unlikely that large tensile strains in either the longitudinal or the lateral direction will be combined in actual cases with shear strains and compressive strains of such magnitude that buckling occurs. Hence, extension of the diagrams figs. 3.1 to 3.11 incl. in these directions is not considered to be of much practical value. Extension of figs. 3.6 to 3.11 incl. in the direction of negative $\varepsilon_1/\varepsilon^*$ to include the curve $\alpha = 1$, or to $\varepsilon_1/\varepsilon^* = -100$, will soon lead to $m > 2$, even for small $\varepsilon_2/\varepsilon^*$ and is therefore of no practical significance.

It would be convenient to add diagrams for intermediate values of τ/σ^* in the range $\tau/\sigma^* < 10$.

4.2 *The state of stress.*

The diagrams figs. 3.1 to 3.11 incl. are based upon the theory of ref. 3. Hence, they are valid only in so far as the stresses in the material nowhere exceed the proportionality limit. It is thus considered advisable to construct additional diagrams from which the largest strain occurring in the construction can be read for specified $\varepsilon_1/\varepsilon^*$, $\varepsilon_2/\varepsilon^*$ and τ/σ^*. It is advisable to present this effective strain ε_e by the nondimensional ratio $\varepsilon_e/\varepsilon^*$ and to calculate it after the hypothesis of HUBER, VON MISES and HENCKY (refs. 13 to 15 incl.).

Diagrams of the type proposed will show whether the proportionality limit is exceeded or not in a specified construction subjected to specified loading. They will show to which extent this limit is eventually exceeded, but not over which part of the volume of the plate. Hence, it should not be expected that reliable estimations could be made about the behaviour of the construction when the proportionality limit is exceeded in some parts of the plate.

4.3 *The parameters of the waveform.*

When at least one of the parameters in the expressions (A.1) and (A.2) for the waveform of the buckles in the plate is known, the others can easily be calculated from the equations (A.5). It seems advisable therefore to construct diagrams from which one of the parameters can be read, once $\varepsilon_1/\varepsilon^*$, $\varepsilon_2/\varepsilon^*$ and τ/σ^* have been determined. Information about the magnitude of the parameters may be required for aerodynamical investigations (surface roughness of wings). For detailed calculations about the distribution of stresses in the plate, the magnitude of the parameters should also be known. It must be kept in mind, however, that such calculations may lead to erroneous results due to the fact that the assumed waveform (A.1) and (A.2) constitutes only a rough approximation of the actual waveform. Hence, the actual stress distribution may deviate to a considerable extent from the calculated distribution although the elastic energies stored in the plate are only slightly different.

4.4 *The range $\alpha \equiv 1$.*

In figs. 3.1 and 3.2 the range $\alpha \equiv 1$ where (B.4) loses its significance is quite small, when it is specified that $\sigma_2/\sigma^* \geqq 0$. It seems advisable, however, to investigate the range $\alpha \equiv 1$ for figs. 3.3 to 3.5 incl., as this may yield a valuable extension of these diagrams in the direction of the negative $\varepsilon_1/\varepsilon^*$-axis. A similar extension of figs. 3.6 to 3.11 incl. is not considered necessary, because in these diagrams $-\varepsilon_1/\varepsilon^*$ is sufficiently large for $\alpha = 1$ (sec. 4.1).

4.5 *The assumed waveform.*

It is evident from the second and fourth example discussed in sec. 3.2.2 that in certain constructions compressive stresses in the lateral direction will occur in the plate ($\sigma_2/\sigma^* < 0$). It was stated already (sec. 2.2) that the present assumptions (A.1) and (A.2) are considered unreliable when $\sigma_2/\sigma^* < 0$ or $m > 2$. Extension of the investigation to this range using adequate assumptions for the waveform of the buckles is thus advised. It might prove to be difficult to find adequate waveform assumptions.

It also seems advisable to investigate, at least in some representative cases, the influence of the fact that the nodal lines of the buckles after (A.1) and (A.2) fail to intersect the longitudinal edges perpendicularly, e. g. by investigating waveform assumption nr. 2 from ref. 3 in those ranges (secs. 2.1 and 3.1) of the diagrams figs. 3.1 to 3.11 incl. where $m > 2$. It is expected that this procedure will present no mathematical difficulties.

4.6 *Flexible stiffeners.*

In the theory of ref. 3 as well as in the present evaluation it was assumed that the stiffeners (fig. 3.12) remain straight when the plate buckles. In actual constructions it often occurs that a stiffener bends in the plane of the plate as a consequence of the loads exerted by the plate (σ_1 or σ_2). As a rough approximation the flexibility effect of the longitudinal (or lateral) stiffeners can be accounted for in the calculations by introducing a suitable reduction of the cross-sectional area of the lateral (or longitudinal) stiffeners (see ref. 5). It seems advisable, however, to carry out an investigation to cover the case of flexible stiffeners in a more adequate way. An investigation of this kind cannot be based solely upon the theory of ref. 3 but will require additional theoretical work.

5 Conclusions.

5.1 *The theoretical basis of the diagrams.*

The diagrams presented in figs. 3.1 to 3.11 incl. are based upon the theory from ref. 3. In this theory it is assumed that the plate at buckling develops a waveform defined by (A.1) and (A.2) and illustrated schematically by fig. 2.1.

It is observed that this theory does not yield the Euler buckling load for plates loaded in the lateral direction, as should be expected (sec. 2.2). Hence, it is advised not to extend the diagram based upon the present theory to the range $\sigma_2/\sigma^* < 0$, i. e. mean compressive stresses in the lateral direction.

The assumptions of straight nodal lines (fig. 2.1) and hinged support of the longitudinal edges are not in accordance with each other. It is thus advised not to extend the diagrams in the range $m > 2$ (sec. 3.1) unless a different waveform is assumed having nodal lines intersecting the edges perpendicularly.

5.2 *The form of the diagrams.*

The method of representing the results in figs. 3.1 to 3.11 incl. was chosen after a discussion with representatives of the aircraft industry (sec. 2.1). The application of the diagram to some problems of stress calculations and design is shown by a number of numerical examples (sec. 3.2). The results are shown in tables 3.1 to 3.4 incl. and figs. 3.13 to 3.16 incl. It was observed during the evaluation of the numerical examples that the form of the diagrams was very convenient.

5.3 *The range of the diagrams.*

The range covered was chosen as the result of a discussion with representatives of the aircraft industry (sec. 2.2). It was not possible in all cases to cover the full range of parameters chosen, because the waveform assumed in the theory was found inadequate when the average normal stress in the lateral direction acting upon the plate is compressive ($\sigma_2/\sigma^* < 0$).

For $\tau/\sigma^* < 10$ (figs. 3.1 and 3.2) this leads to a considerable reduction of the range covered by the diagrams in the direction of positive $\varepsilon_2/\varepsilon^*$, i. e. compressive strain in the lateral direction. It is evident from the results obtained in two numerical examples, tables 3.2 and 3.4 or figs. 3.14 and 3.16, that the diagrams are not applicable to all constructions and loads for which they were intended.

5.4 *Proposals for additional investigations.*

A number of proposals for investigations intended to improve the usefulness and the range of the diagrams are discussed in sec. 4. Part of these proposals concerns additional numerical evaluations of the theory from ref. 3 (secs. 4.1 to 4.4 incl.). Some small extensions of the range covered by the diagrams are proposed, as well as the construction of diagrams enabling the determination of the maximal effective strain in the plate. It is also considered of interest to construct diagrams representing the magnitude of one or more parameters of the assumed waveform of the buckles.

Finally, proposals are made concerning investigations towards the behaviour of plates in lateral compression and the influence of the flexibility of stiffeners (secs. 4.5 and 4.6). They will require additional theoretical work, because the present theory (ref. 3) is inadequate for these purposes.

6 Notations.

a	length of the plate.
b	width of the (infinitely long) rectangular plate (fig. 2.1).
f	maximum amplitude of the buckles in the plate (fig. 2.1).
h	thickness of the plate.
m	cotangent of the angle between the nodal lines of the buckles and the X-direction (fig. 2.1).
u, v, w	displacements of an arbitrary point (x, y, o) of the median plane $(z = 0)$ of the plate in the X-, Y- and Z-directions, respectively, during buckling (fig. 2.1).
x, y, z	coordinates in the X-, Y- and Z-directions, respectively (fig. 2.1).
A_a, A_b	lateral and longitudinal stiffener cross sections (fig. 3.12).
D	$= b^2/L^2$.
E	modulus of elasticity.
F	$= \pi^2 f^2/4b^2$.
L	half-wave length of the buckles in the plate (fig. 2.1).
V	elastic energy stored in the buckled plate.
X	longitudinal direction of the plate (fig. 2.1).
Y	lateral direction of the plate (fig. 2.1).
Z	direction normal to the plane of the plate (fig. 2.1).
α	ratio between the width of the edge zones and the total width b of the plate (fig. 2.1).
γ	angle of shear of the plate considered as a whole.
$\varepsilon_1, \varepsilon_2$	compressive strains in the longitudinal (X-) and lateral (Y-) directions of the plate considered as a whole.
ε^*	critical compressive strain for pure longitudinal compression, hinged edges, see formula (2.1).
η	$= 2EV/h\sigma^{*2}$.
ν	lateral contraction ratio.
σ_1, σ_2	average tensile stresses in the longitudinal (X-) and lateral (Y-) directions, respectively, in the buckled plate.
σ_a, σ_b	average tensile stresses in the lateral (Y-) and longitudinal (X-) directions, respectively, in the construction consisting of plate and stiffeners (fig. 3.12).
σ^*	$= E\varepsilon^*$, critical compressive stress for pure longitudinal compression, hinged edges, see formula (2.1).
τ	shear stress.

7 References.

1. WAGNER, H.: Ebene Blechwandträger mit sehr dünnem Stegblech. Zeitschrift für Flugtechnik und Motorluftschiffahrt, 1929, p. 200, 227, 256, 279 and 306.
2. KROMM, A. and MARGUERRE, K.: Verhalten eines von Schub- und Druckkräften beanspruchten Plattenstreifens oberhalb der Beulgrenze. Luftfahrtforschung Band 14 (1937), p. 627.
3. KOITER, W. T.: Het schuifplooiveld bij groote overschrijdingen van de knikspanning. Rapport S. 295, Nationaal Luchtvaartlaboratorium, Amsterdam, 1944. With an English abstract: Theoretical Investigation of the Diagonal Tension Field of Flat Plates. Amsterdam, 1946.
4. DENKE, P. H.: Strain Energy Analysis of Incomplete Tension Field Web-Stiffener Combinations. Journal of the Aeronautical Sciences, Vol. 11 (1944), p. 25.
5. DENKE, P. H.: Analysis and Design of Stiffened Shear Webs. Journal of the Aeronautical Sciences, Vol. 17 (1950), p. 217.
6. LEVY, S., FIENUP, K. L. and WOOLLEY, R. M.: Analysis of Square Shear Web above Buckling Load. Technical Note No. 962, NACA, Washington, 1945.
7. LEVY, S., WOOLLEY, R. M. and CORRICK, J. N.: Analysis of Deep Rectangular Shear Web above Buckling Load. Technical Note No. 1009. NACA, Washington, 1946.
8. BERGMAN, S. G. A.: Behaviour of Buckled Rectangular Plates under the Action of Shearing Forces. Diss. Kungl. Tekniska Högskolan, Stockholm, 1948.
9. LAHDE, R. and WAGNER, H.: Versuche zur Ermittlung des Spannungszustandes in Zugfeldern. Luftfahrtforschung Band 13 (1936) p. 262.
10. KUHN, P.: Strength Analysis of Stiffened Beam Webs. Technical Note no. 1364. NACA, Washington, 1947.
11. LEVIN, L. R.: Ultimate Stresses Developed by 24 S-T and Alclad 75 S-T Aluminum-Alloy Sheet in Incomplete Diagonal Tension. Technical Note No. 1756, NACA, Washington, 1948.
12. LEVIN, L. R. and SANDLIN Jr, C. W.: Strength Analysis of Thick Beam Webs. Technical Note No. 1820, NACA, Washington, 1949.
13. VAN DER NEUT, A., FLOOR, W. K. G. and BINKHORST, I.: Experimental Investigation of the Post-Buckling Behaviour of Stiffened, Flat, Rectangular Plates under Combined Shear and Compression. Part I. Report S 300 Nationaal Luchtvaart Laboratorium, Amsterdam, 1947.
14. FLOOR, W. K. G.: Experimental Investigation of the Post-Buckling Behaviour of Stiffened, Flat, Rectangular Plates, under Combined Shear and Compression. Part II. Report S. 328, Nationaal Luchtvaartlaboratorium, Amsterdam, 1947.
15. VAN DER NEUT, A. and FLOOR, W. K. G.: Buckling Behaviour of Flat Plates Loaded in Shear and Compression. Report S. 341, Nationaal Luchtvaartlaboratorium, Amsterdam, 1948.
16. FLOOR, W. K. G.: Experimental Investigation of the Post-Buckling Behaviour of Stiffened, Flat, Rectangular Plates under Combined Shear and Compression. Part III. Report S. 367, Nationaal Luchtvaartlaboratorium, Amsterdam, 1950.
17. MICHIELSEN, H. F.: Berekeningswijze voor plooiveldgrafieken op grond van N. L. L. Rapport S. 295. N.V. Nederlandsche Vliegtuigenfabriek Fokker, Amsterdam, 1949. Appendix 2 to Report S 25 R, Repliek op „Enkele beschouwingen over het plooiveld n. a. v. Fokker-rapport S 25 V", N.V. Koninklijke Nederlandsche Vliegtuigenfabriek Fokker, Amsterdam, 1950. (Unpublished).
18. MICHIELSEN, H. F.: Beoordeling van Stabiliteit van Evenwicht. Rapport S. 58, N.V. Nederlandsche Vliegtuigenfabriek Fokker, Amsterdam, 1949. (Unpublished).
19. FLOOR, W. K. G.: De breuksterkte van verstijfde platen waarin schuifplooiing optreedt. Report S. 378, Nationaal Luchvaartlaboratorium, Amsterdam, 1950.

APPENDIX A.

The assumed waveform and the elastic energy.

It is assumed, that for $0 \leq y \leq ab/2$,

$$
\begin{aligned}
u &= -\varepsilon_1 x + U_0(y) - (\pi f^2/16\,L)(1 - \\
&\quad - \cos 2\pi y/ab)\sin 2\pi(x - my)/L, \\
v &= V_0(y) + (m\pi f^2/16\,L)(1 - \\
&\quad - \cos 2\pi y/ab)\sin 2\pi(x - my)/L + \\
&\quad + (\pi f^2/16\,ab)(\sin 2\pi y/ab)\cos 2\pi(x - my)/L, \\
w &= f(\sin \pi y/ab)\sin \pi(x - my)/L,
\end{aligned}
$$

where

$$
\left.
\begin{aligned}
U_0(y) &= \gamma y - (1-\alpha)(m\pi^2 f^2/4\,L^2)\,y - \\
&\quad - (ab/L)(m\pi f^2/8\,L)\sin 2\pi y/ab, \\
V_0(y) &= -\varepsilon_2 y + (1-\alpha)(\pi^2 f^2/8\,L^2)(\nu + \\
&\quad + m^2 - L^2/\alpha^2 b^2)y + \\
&\quad + (\alpha b/L)(\pi f^2/16\,L)(\nu + m^2 - \\
&\quad - L^2/\alpha^2 b^2)\sin 2\pi y/ab,
\end{aligned}
\right\} \qquad (A.1)
$$

and that, for $\alpha b/2 \leq y \leq (1-\alpha/2)b$,

$$
\begin{aligned}
u &= -\varepsilon_1 x + \overline{U}_0(y) - (\pi f^2/8\,L)\sin 2\pi(x - my)/L, \\
v &= \overline{V}_0(y) + (m\pi f^2/8\,L)\sin 2\pi(x - my)/L, \\
w &= f \sin \pi(x - my)/L,
\end{aligned}
$$

where

$$
\left.
\begin{aligned}
\overline{U}_0(y) &= \gamma y + \alpha(m\pi^2 f^2/4\,L^2)(y - b/2), \\
\overline{V}_0(y) &= -\varepsilon_2 y - \alpha(\pi^2 f^2/8\,L^2)(\nu + m^2 - \\
&\quad - L^2/\alpha^2 b^2)(y - b/2).
\end{aligned}
\right\} \qquad (A.2)
$$

The expressions for $\overline{U}_0$, U_0, $\overline{V}_0$ and V_0 have not been presented explicitly in ref. 3. They were first given in ref. 15 for a coordinate system having its origin at the crest of a buckle, i. e. at $x = mb/2 + L/2$, $y = b/2$.

The expressions (A.1) and (A.2) contain the four parameters for the form of the buckles in the plate mentioned in sec. 2.1, viz. f, L, m and α (fig. 2.1).

Denoting by V the elastic energy stored in the buckled plate and averaged over the surface of the plate and introducing the notations

$$
\begin{aligned}
&\pi^2 f^2/4\,L^2 = F,\ b^2/L^2 = \\
&= D,\ \pi^2 E h^2/3(1-\nu^2)b^2 = \sigma^* = E\varepsilon^*, \qquad (A.3)
\end{aligned}
$$

where h represents the thickness of the plate, it follows from ref. 3 that

$$
\left.
\begin{aligned}
\eta &= 2\,EV/h\sigma^{*2} = (\sigma_1/\sigma^*)^2 - \\
&\quad - 2\nu(\sigma_1/\sigma^*)(\sigma_2/\sigma^*) + (\sigma_2/\sigma^*)^2 + \\
&\quad + 2(1+\nu)(\tau/\sigma^*)^2 + (F/\varepsilon^*)^2\{[2\,A_1 - \\
&\quad - A_3)\alpha - A_1{}^2\alpha^2]D^2 + A_4 m^2 D/\alpha + \\
&\quad + A_5/\alpha^3\} + 0.25(F/\varepsilon^*)\{2\,[1 - A_1\alpha + \\
&\quad + 2(1 - A_2\alpha)m^2 + (1 - A_6\alpha)m^4]D^2 + \\
&\quad + (4\,A_2' + A_7 m^2)D/\alpha + A_8/\alpha^3\}).
\end{aligned}
\right\} \qquad (A.4)
$$

In this expression the stress ratios σ_1/σ^*, σ_2/σ^* and τ/σ^* are, for specified strain ratios $\varepsilon_1/\varepsilon^*$,

$\varepsilon_2/\varepsilon^*$ and γ/ε^*, functions of the parameters F, D, m and α according to

$$\left.\begin{aligned}
&\sigma_1/\sigma^* - \nu\sigma_2/\sigma^* = -\varepsilon_1/\varepsilon^* + (1 - A_1\alpha)DF/\varepsilon^*,\\
&-\nu\sigma_1/\sigma^* + \sigma_2/\sigma^* = -\varepsilon_2/\varepsilon^* +\\
&\quad + (1 - A_2\alpha)m^2DF/\varepsilon^* + (A_2'/\alpha)F/\varepsilon^*,\\
&2(1+\nu)\tau/\sigma^* = \gamma/\varepsilon^* +\\
&\quad - 2(1 - A_0\alpha)mDF/\varepsilon^*.
\end{aligned}\right\} \quad (A.5)$$

Finally, for waveform 1 from ref. 3, assuming $\nu = 0{,}3$,

$$\left.\begin{aligned}
&A_0 = A_1 = A_2 = A_2' = 0.5,\ A_3 = 0.625,\\
&A_4 = 0,\ A_5 = 1/8(1-\nu^2) = 0.13736,\\
&A_6 = 0.5,\ A_7 = 6,\ A_8 = 1.
\end{aligned}\right\} \quad (A.6)$$

APPENDIX B.

Determination of the parameters.

The parameters F, D, m and α must be solved from the equations

$$\left.\begin{aligned}
&\partial\eta/\partial(F/\varepsilon^*) \equiv 2(\sigma_1/\sigma^*)(1 - A_1\alpha)D +\\
&\quad + 2(\sigma_2/\sigma^*)[(1 - A_2\alpha)m^2D + A_2'/\alpha] +\\
&\quad - 4(\tau/\sigma^*)(1 - A_0\alpha)mD + 2(F/\varepsilon^*)\{2A_1 -\\
&\quad - A_3)\alpha - A_1^2\alpha^2]D^2 + A_4m^2D/\alpha +\\
&\quad + A_5/\alpha^3\} + 0.25\{2[(1+m^2)^2 -\\
&\quad - \alpha(A_1 + 2A_2m^2 + A_6m^4)]D^2 +\\
&\quad + (4A_2' + A_7m^2)D/\alpha + A_8/\alpha^3\} = 0,
\end{aligned}\right\} \quad (B.1)$$

$$\left.\begin{aligned}
&D(\partial\eta/\partial D)/(F/\varepsilon^*) \equiv 2(\sigma_1/\sigma^*)(1 - A_1\alpha)D +\\
&\quad + 2(\sigma_2/\sigma^*)(1 - A_2\alpha)m^2D - 4(\tau/\sigma^*)(1 -\\
&\quad - A_0\alpha)mD + (F/\varepsilon^*)\{2[(2A_1 - A_3)\alpha -\\
&\quad - A_1^2\alpha^2]D^2 + A_4m^2D/\alpha\} + 0.25\{4[(1 +\\
&\quad + m^2)^2 - \alpha(A_1 + 2A_2m^2 + A_6m^4)]D^2 +\\
&\quad + (4A_2' + A_7m^2)D/\alpha\} = 0,
\end{aligned}\right\} \quad (B.2)$$

$$\left.\begin{aligned}
&m(\partial\eta/\partial m)/(F/\varepsilon^*) \equiv 4(\sigma_2/\sigma^*)(1 -\\
&\quad - A_2\alpha)m^2D - 4(\tau/\sigma^*)(1 - A_0\alpha)mD +\\
&\quad + 2(F/\varepsilon^*)A_4m^2D/\alpha + 0.25\{[8m^2(1 +\\
&\quad + m^2) - \alpha(8A_2m^2 + 8A_6m^4)]D^2 +\\
&\quad + 2A_7m^2D/\alpha\} = 0,
\end{aligned}\right\} \quad (B.3)$$

$$\left.\begin{aligned}
&(\partial\eta/\partial\alpha)/(F/\varepsilon^*) \equiv -2(\sigma_1/\sigma^*)A_1D -\\
&\quad - 2(\sigma_2/\sigma^*)(A_2m^2D + A_2'/\alpha^2) +\\
&\quad + 4(\tau/\varepsilon^*)A_0mD + (F/\varepsilon^*)\{[(2A_1 -\\
&\quad - A_3) - 2A_1^2\alpha]D^2 - A_4m^2D/\alpha^2 -\\
&\quad - 3A_5/\alpha^4\} + 0.25\{-2(A_1 + 2A_2m^2 +\\
&\quad + A_6m^4)D^2 - (4A_2' + A_7m^2)D/\alpha^2 -\\
&\quad - 3A_8/\alpha^4\} = 0.
\end{aligned}\right\} \quad (B.4)$$

It was found convenient to reduce these equations to the set

$$\left.\begin{aligned}
&\{m(\partial\eta/\partial m)/(F/\varepsilon^*)\}/(2 - \alpha)m^2D \equiv\\
&\quad \sigma_2/\sigma^* - (\tau/\sigma^*)/m + 0.5(1+m^2)D +\\
&\quad + 3/2\,\alpha(2 - \alpha) = 0,
\end{aligned}\right\} \quad (B.5)$$

$$\left.\begin{aligned}
&\{D(\partial\eta/\partial D)/(F/\varepsilon^*) -\\
&\quad - m(\partial\eta/\partial m)/(F/\varepsilon^*)\}/(2 - \alpha)D \equiv\\
&\quad \sigma_1/\sigma^* - m(\tau/\sigma^*) + \{\alpha(3 - 2\alpha)/4(2 -\\
&\quad - \alpha)\}DF/\varepsilon^* + 0.5(1+m^2)D +\\
&\quad + 1/2\,\alpha(2 - \alpha) = 0,
\end{aligned}\right\} \quad (B.6)$$

$$\left.\begin{aligned}
&\{-\partial\eta/\partial(F/\varepsilon^*) + 2D(\partial\eta/\partial D)/(F/\varepsilon^*) -\\
&\quad - \alpha(\partial\eta/\partial\alpha)/(F/\varepsilon^*)\}/2D \equiv\\
&\quad \sigma_1/\sigma^* + m^2(\sigma_2/\sigma^*) - 2m(\tau/\sigma^*) +\\
&\quad + (0.3\alpha D + 0.0686813/\alpha^3D)F/\varepsilon^* +\\
&\quad + 0.25(3 - \alpha)(1+m^2)^2D +\\
&\quad + (1+3m^2)/2\alpha + 1/4\,\alpha^3D = 0,
\end{aligned}\right\} \quad (B.7)$$

$$\left.\begin{aligned}
&\alpha\{\partial\eta/\partial(F/\varepsilon^*) - D(\partial\eta/\partial D)/(F/\varepsilon^*)\} \equiv\\
&\quad \sigma_2\sigma^* + (0.274725/\alpha^2)F/\varepsilon^* -\\
&\quad - 0.25\,\alpha(2 - \alpha)(1+m^2)^2D^2 +\\
&\quad + 0.25/\alpha^2 = 0.
\end{aligned}\right\} \quad (B.8)$$

APPENDIX C.

First method of solution.

Inserting combinations of m and D, τ/σ^* was solved from (B.5) and F/ε^* from (B.8). Improved values for m and D were then obtained from (B.6) and (B.7) by applying NEWTON's method for the case of two variables. This procedure was repeated until the differences between successive approximations were considered practically negligible. It is convenient to write (B.6) and (B.7) in the form $\Phi_i(m, D) = 0$, where $i = 1$ or 2. The n-th approximations m_n and D_n will not exactly satisfy these equations. An expression for $\Phi_i(m_n + \Delta m, D_n + \Delta D)$ is obtained by expansion, Δm and ΔD being small variations of m_n and D_n, respectively. Hence,

$$\Phi_i(m_n + \Delta m, D_n + \Delta D) = \Phi_i(m_n, D_n) + \Delta m\frac{\partial\Phi_i}{\partial m}(m_n, D_n) + \Delta D\frac{\partial\Phi_i}{\partial D}(m_n, D_n) + \ldots\ldots$$

Neglecting all terms containing higher powers of Δm and ΔD the condition that $\Phi_i(m_{n+1}, D_{n+1}) = 0$ yields two linear equations

$$(m_{n+1} - m_n)\frac{\partial\Phi_i}{\partial m}(m_n, D_n) + (D_{n+1} - D_n)\frac{\partial\Phi_i}{\partial D}(m_n, D_n) + \Phi_i(m_n, D_n) = 0, \quad i = 1 \text{ and } 2, \quad (C.1)$$

from which m_{n+1} and D_{n+1} can easily be solved.

A numerical example of the method of evaluation is given in table 2.1. In general, m and D should be estimated to five figures and calculated accurate to four figures in order to avoid serious scatter in the calculated points through which the curves are drawn in the diagrams proposed in sec. 2.1.

Before constructing these diagrams, interpolations towards τ/σ^* have to be carried out. Several methods of interpolation have been used. In the first method for each value of α chosen two diagrams were constructed, one of which represents τ/σ^* as a function of $\varepsilon_1/\varepsilon^*$, the other representing τ/σ^* as a function of $\varepsilon_2/\varepsilon^*$. From these diagrams, containing curves $\sigma_1/\sigma^* =$ constant and $\sigma_2/\sigma^* =$ constant, the coordinates $\varepsilon_1/\varepsilon^*$ and $\varepsilon_2/\varepsilon^*$ of the intersections between the curve $\alpha =$ constant and the curves $\sigma_1/\sigma^* =$ constant and $\sigma_2/\sigma^* =$ constant in the diagrams proposed in sec. 2.1 were obtained.

In the second method, for each combination of σ_1/σ^* and σ_2/σ^* a diagram was constructed containing curves of $\varepsilon_1/\varepsilon^*$, $\varepsilon_2/\varepsilon^*$ and τ/σ^* as functions of α. From these diagrams the coordinates $\varepsilon_1/\varepsilon^*$ and $\varepsilon_2/\varepsilon^*$ of the intersections between the curves of constant σ_1/σ^* and σ_2/σ^* in the final diagrams proposed in sec. 2.1 were obtained by putting $\tau/\sigma^* =$ constant.

A third method consisted of constructing diagrams of τ/σ^* as a function of σ_1/σ^* (or σ_2/σ^*) for constant values of α and σ_2/σ^* (or σ_1/σ^*) from the diagrams determined after the first method. Finally, diagrams were constructed representing σ_1/σ^* (or σ_2/σ^*) as a function of $\varepsilon_1/\varepsilon^*$ or $\varepsilon_2/\varepsilon^*$ for constant values of τ/σ^* and σ_2/σ^* (or σ_1/σ^*). From these diagrams the coordinates $\varepsilon_1/\varepsilon^*$ and $\varepsilon_2/\varepsilon^*$ of the intersections of the curves of constant σ_1/σ^* and σ_2/σ^* in the final diagrams proposed in sec. 2.1 could be read.

In the construction of the final diagrams the curves of constant σ_2/σ^* were determined after the first method of interpolation. The curves of constant σ_1/σ^* were determined partially by the first method of interpolation and partially by the third method, in order to obtain a sufficient number of points to draw the curves.

APPENDIX D.

Second method of solution.

For specified combinations of m and α, D was solved from (B.5) and F/ε^* from (B.8).

Improved values for m and α were then obtained from (B.6) and (B.7) by writing these equations in the form $\psi_i(m, \alpha) = 0$, $i = 1$ or 2 and treating them in a similar way as described in Appendix C for the equations $\Phi_i(m, D) = 0$. Hence, the iteration procedure consists in solving the set of two linear equations

$$(m_{n+1} - m_n)\,\frac{\partial \psi_i}{\partial m}\,(m_n, \alpha_n) + (\alpha_{n+1} - \alpha_n)\,\frac{\partial \psi_i}{\partial \alpha}\,(m_n, \alpha_n) + \psi_i\,(m_n, \alpha_n) = 0, \quad i = 1 \text{ and } 2, \qquad (D.1)$$

for the two unknowns $m_{n+1} - m_n$ and $\alpha_{n+1} - \alpha_n$. In this way, the $(n+1)$-th approximations for m and α are obtained.

A numerical example of the method of evaluation is given in table 2.2. In general, m and α should be estimated to five figures and calculated accurate to four figures for the same reasons as D and α in the first method.

APPENDIX E.

The evaluation for $\tau/\sigma^* = 0$.

Dividing equation (B.3) by mD and inserting A_i from (A.6) the equation

$$[2(2-\alpha)(\sigma_2/\sigma^*) + (2-\alpha)(1+m^2)D + 3/\alpha]\,m - 2(2-\alpha)(\tau/\sigma^*) = 0 \qquad (E.1)$$

is obtained. When τ/σ^* approaches zero, either m or the finite expression in square brackets will also approach zero.

It seemed unlikely that $m = 0$ for τ/σ^*. It was therefore assumed in the numerical evaluation that $m = 0$ for $\tau/\sigma^* = 0$. A further argument in favour of this choice will be discussed at the end of this appendix. The diagram obtained in this way proved to bear a similar character as the diagrams for $\tau/\sigma^* > 0$. For specified sets of values α and D, the corresponding F/ε^* was solved from the equation obtained by eliminating σ_1/σ^* from (B.6) and (B.7). Finally, σ_1/σ^* was calculated from (B.6) or (B.7) and σ_2/σ^* from (B.8).

For each value of α chosen two diagrams were constructed, one representing $\varepsilon_1/\varepsilon^*$ and $\varepsilon_2/\varepsilon^*$ as functions of σ_1/σ^* and the other representing these ratios as functions of σ_2/σ^*. From these diagrams the coordinates $\varepsilon_1/\varepsilon^*$ and $\varepsilon_2/\varepsilon^*$ of the intersections between the curves $\alpha =$ constant and σ_1/σ^* or $\sigma_2/\sigma^* =$ constant in the final diagram of the type proposed in sec. 2.1 could be read.

In order to enable the interpolation of $\tau/\gamma G$ for $0 < \tau/\sigma^* < 5$ curves of constant $\tau/\gamma G$ were also drawn in the diagram for $\tau/\sigma^* = 0$. In this case, $\tau/\gamma G$ should be considered as the limit of the ratio $\tau/\gamma G$ when τ/σ^* approaches zero. It follows from (A.5) that

$$\tau/\gamma G = 2(1+\nu)(\tau/\sigma^*)/\{2(1+\nu)(\tau/\sigma^*) + (2-\alpha)mDF/\varepsilon^*\}.$$

Inserting τ/σ^* from (E.1) it follows that, for $\tau/\sigma^* \to 0$,

$$\tau/\gamma G \to 2(1+\nu)[(\sigma_2/\sigma^*) + 0.5\,D + 1.5/\alpha(2-\alpha)]/\{2(1+\nu)[\sigma_2/\sigma^*) + 0.5\,D + 1.5/\alpha(2-\alpha)] + 0.5\,DF/\varepsilon^*\}. \qquad (E.2)$$

It is interesting to note that the assumption that the expression in square brackets in (E.1) would be zero instead of m would yield the result that $\tau/\gamma G \to 0$ for $\tau/\sigma^* \to 0$, as can be observed by inspection of the expression for $\tau/\gamma G$. This must be considered physically impossible.

TABLE 2.1.

Example of the numerical evaluation after the first method of solution.

$\sigma_1/\sigma^* = 20$			$\sigma_2/\sigma^* = 10$			$\alpha = 0.8$	
n	m_n	D_n	τ/σ^*	F/ε^*	$\Phi_1(m_n, D_n)$	$\Phi_2(m_n, D_n)$	$m_{n+1} - m_n$	$D_{n+1} - D_n$
1	1.382	2.41	20.825	3.2918	— 2.9017	— 1.4551	0.074016	0.32862
2	1.456	2.7386	23.056	16.610	1.8375	1.1357	— 0.011879	— 0.087830
3	1.4441	2.6508	22.603	13.195	0.13084	0.084278	— 0.00063457	— 0.0071416
4	1.4435	2.6437	22.575	12.953	0.00043414	0.00072237	—	—

TABLE 2.2.

Example of the numerical evaluation after the second method of solution.

$\sigma_1/\sigma^* = 10$			$\sigma_2/\sigma^* = 5$			$\tau/\sigma^* = 25$	
n	α_n	m_n	D	F/ε^*	$\psi_1(\alpha_n, m_n)$	$\psi_2(\alpha_n, m_n)$	$\alpha_{n+1} - \alpha_n$	$m_{n+1} - m_n$
1	0.62	1.94	2.5752	37.133	— 12.879	— 7.8229	0.037283	— 0.070772
2	0.65728	1.8692	2.2907	53.062	3.0243	1.9242	— 0.0040184	0.012956
3	0.65326	1.8822	2.8959	50.446	0.093353	0.059599	— 0.00011747	0.00040695
4	0.65314	1.8826	2.8936	50.370	0.0032400	0.0039543	—	—

TABLE 3.1.

Numerical results for the first example.

τ/σ^*	$\varepsilon_1/\varepsilon^*$	$\varepsilon_2/\varepsilon^*$	σ_1/σ^*	σ_2/σ^*	$\tau/G\gamma_*$	Remarks
0	173	6	— 27	3	0.12	extrapolation
5	174	13	— 26	6.5	0.155	
10	176	24	— 24	12	0.18	
15	178	33	— 22	16.5	0.21	
20	181	42	— 19	21	0.23	
25	183	52	— 17	26	0.245	
30	187	60.5	— 13	30.5	0.26	
35	190	69	— 10	34.5	0.275	
40	194	78	— 6	39	0.285	extrapolation
45	198	85	— 2	42.5	0.295	extrapolation
50	202	94	2	47	0.30	extrapolation

$A_a/ah = 0.5$; $A_b/bh = 1$; $\sigma_a/\sigma^* = 0$; $\sigma_b/\sigma^* = -100$.

TABLE 3.2.

Numerical results for the second example.

τ/σ^*	$\varepsilon_1/\varepsilon^*$	$\varepsilon_2/\varepsilon^*$	σ_1/σ^*	σ_2/σ^*	$\tau/G\gamma$	Remarks
0	—	—	—	< 0	—	no results
5	—	—	—	< 0	—	no results
10	20	125	5	0	0.205	
15	30	126	7.5	3	0.24	
20	40.5	126.5	10	6	0.26	
25	49	127.5	12.5	10.5	0.28	
30	59	128.5	14.5	15	0.30	
35	68	129.5	17	18.5	0.31	
40	79	131	19.5	24	0.325	
45	88	132	22	28	0.335	extrapolation
50	98	133	24.5	33	0.34	extrapolation

$A_a/ah = 4$; $A_b/bh = 0.25$; $\sigma_a/\sigma^* = -100$; $\sigma_b/\sigma^* = 0$.

TABLE 3.3.

Numerical results for the third example.

τ/σ^*	$\varepsilon_2/\varepsilon^*$	σ_1/σ^*	σ_2/σ^*	$\tau/G\gamma$	A_b/bh
0	4	-18	2	0.16	3.82
5	10.5	-17.5	5	0.195	3.825
10	19	-14.5	9.5	0.24	3.855
15	28	-12	14	0.27	3.88
20	36	-8.5	18	0.30	3.915
25	44	-5	22	0.325	3.95
30	52	0	26	0.34	4
35	58	4	29	0.355	4.04
40	65	8.5	32.5	0.37	4.085
45	73	13.5	36.5	0.38	4.135
50	80	18.5	40	0.39	4.185

$A_a/ah = 0.5$; $\varepsilon_1/\varepsilon^* = 100$; $\sigma_a/\sigma^* = 0$; $(1 + A_b/bh)\sigma_b/\sigma^* = -400$.

TABLE 3.4.

Numerical results for the fourth example.

τ/σ^*	$\varepsilon_1/\varepsilon^*$	σ_1/σ^*	σ_2/σ^*	$\tau/G\gamma$	A_a/ah
10	12	6	0.5	0.25	4.005
15	20	10	3.5	0.28	4.03
20	26	13	7	0.31	4.07
25	32	16	11	0.335	4.11
30	38	19	15	0.355	4.15
35	43	21.5	19	0.375	4.19
40	50	25	24	0.39	4.24
45	56	28	28.5	0.40	4.285
50	61	30.5	33	0.41	4.33

$A_b/bh = 0.5$; $\varepsilon_2/\varepsilon^* = 100$; $(1 + A_a/ah)\sigma_a/\sigma^* = -400$; $\sigma_b/\sigma^* = 0$.

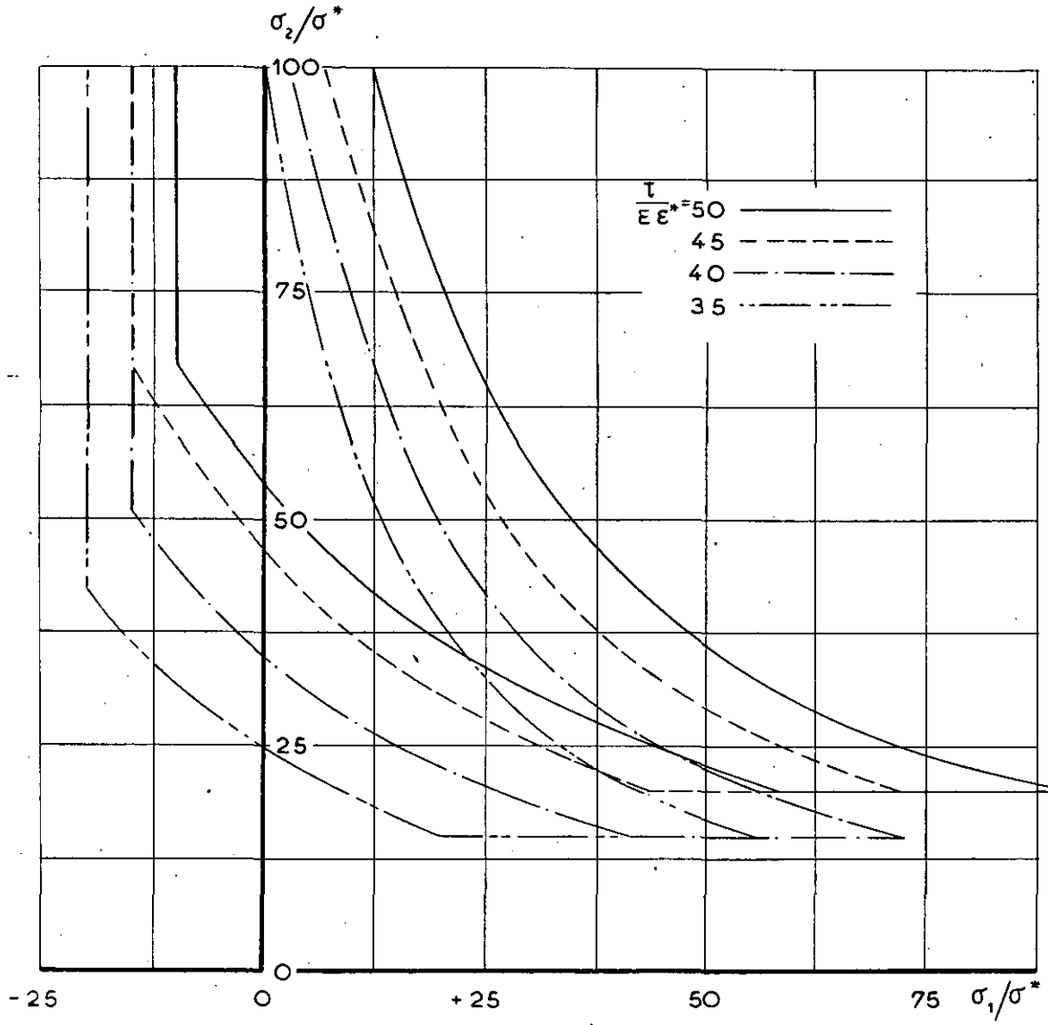

Fig. 2.2.

Range of the investigation for large τ/σ^*.

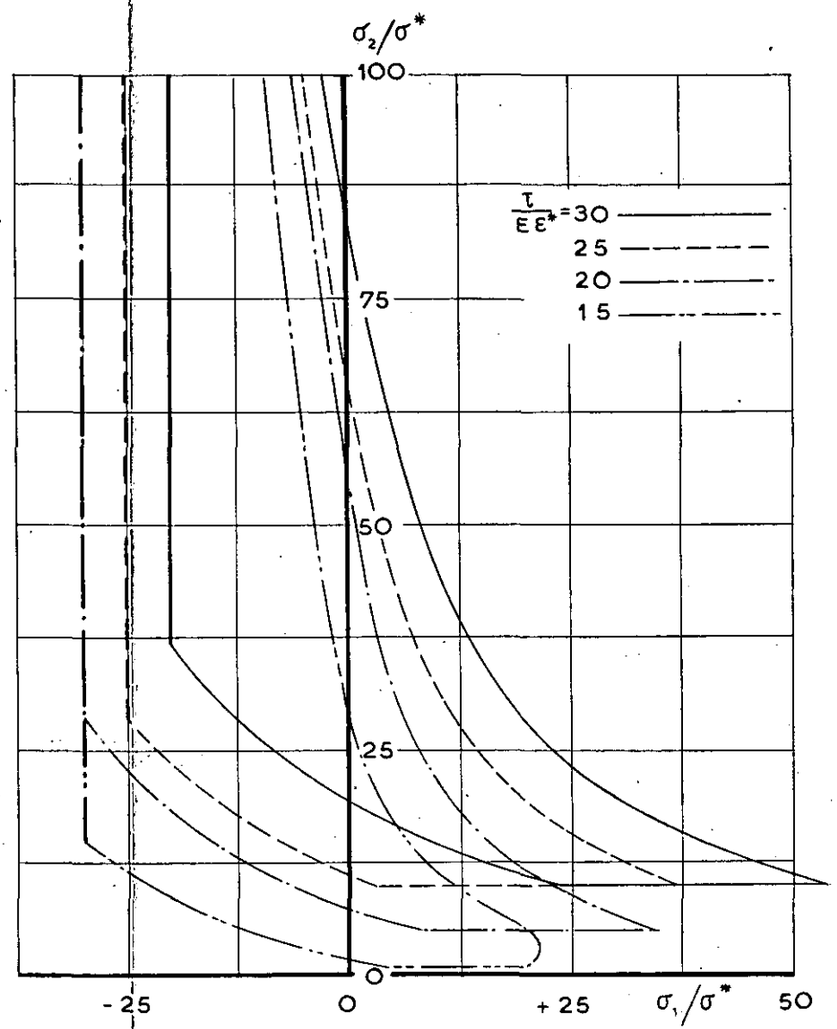

Fig. 2.3.

Range of the investigation for moderate τ/σ^*.

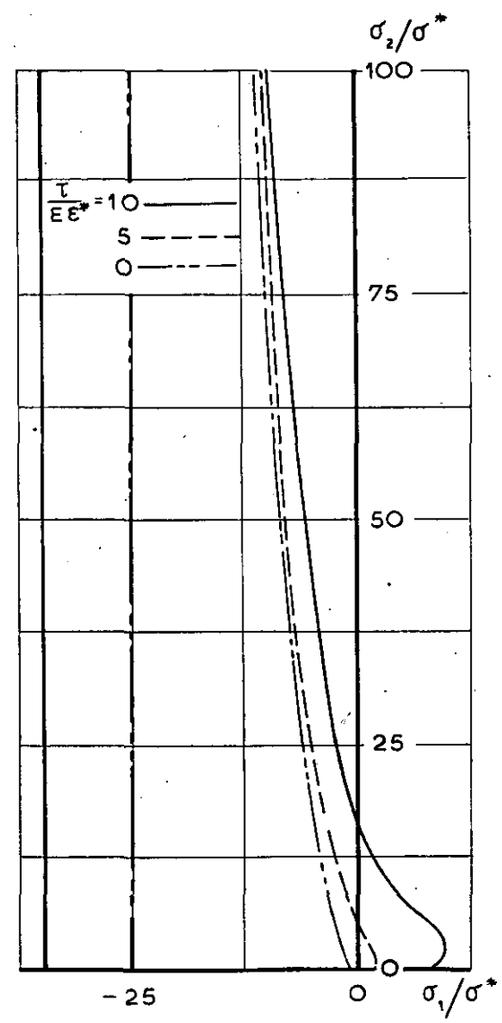

Fig. 2.4.

Range of the investigation for small τ/σ^*.

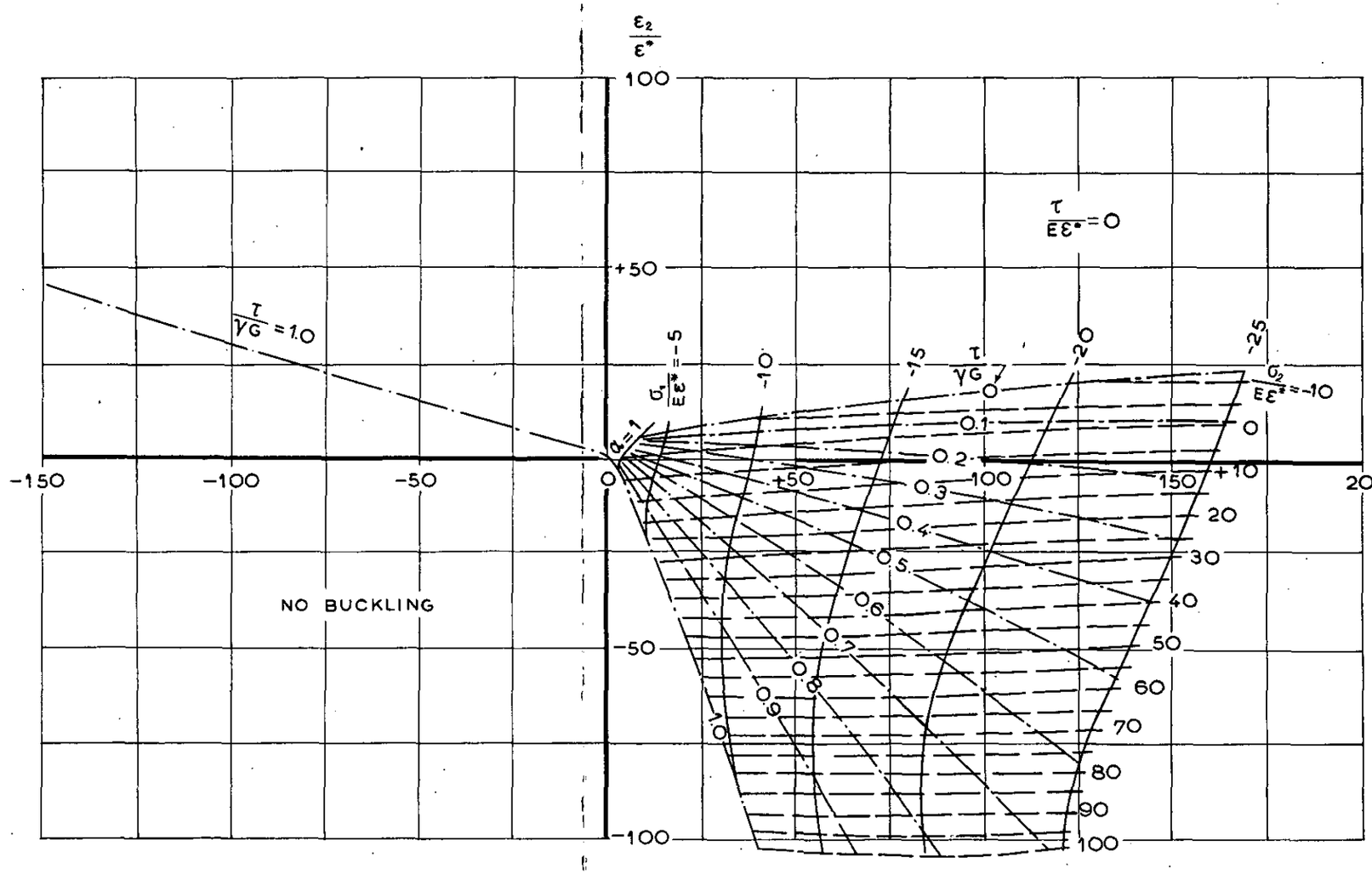
$\frac{\epsilon_2}{\epsilon^*}$
100
+50
−50
−100
−150
−100
−50
0
+50
100
150
200
$\frac{\epsilon_1}{\epsilon^*}$
$\frac{\tau}{\gamma G}=1.0$
$\frac{\tau}{E\epsilon^*}=0$
$\frac{\sigma_1}{E\epsilon^*}=-5$
$\frac{\sigma_2}{E\epsilon^*}=-10$
$\frac{\tau}{\gamma G}$
α=1
-10
-15
-20
-25
0
0.1
0.2
0.3
0.4
0.5
0.6
0.7
0.8
0.9
1.0
+10
20
30
40
50
60
70
80
90
100
NO BUCKLING

Fig. 3.1.

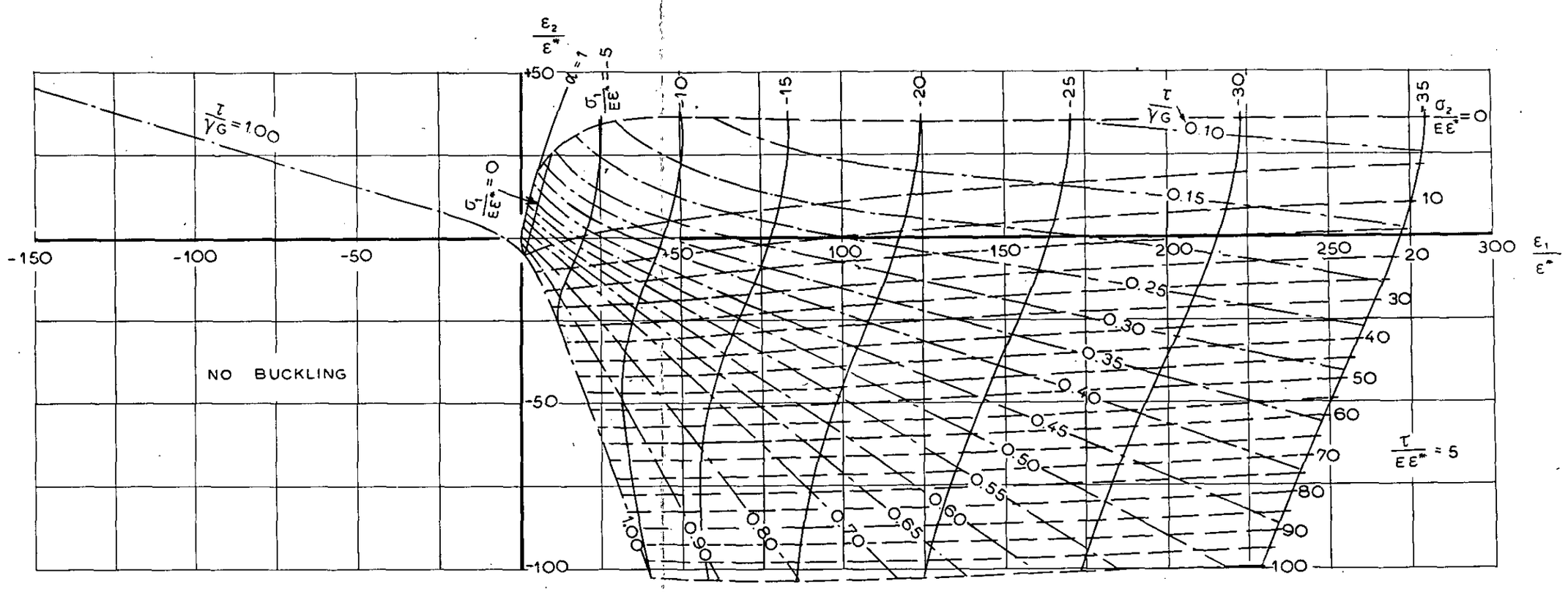
$\frac{\varepsilon_2}{\varepsilon^*}$
$\frac{\tau}{\gamma G}=100$
$\frac{\sigma_1}{E\varepsilon^*}=0$
$\alpha=1$
$\frac{\sigma_1}{E\varepsilon^*}=-5$
$\frac{\tau}{\gamma G}$
$\frac{\sigma_2}{E\varepsilon^*}=0$
$\frac{\tau}{E\varepsilon^*}=5$
NO BUCKLING
-150
-100
-50
+50
100
150
200
250
300
$\frac{\varepsilon_1}{\varepsilon^*}$
+50
-50
-100
-10
-15
-20
-25
-30
+35
0.10
0.15
10
20
0.25
30
0.30
40
0.35
50
0.40
60
0.45
70
0.50
80
0.55
90
0.60
100
0.65
0.70
0.80
0.90
1.00

Fig. 3.2.

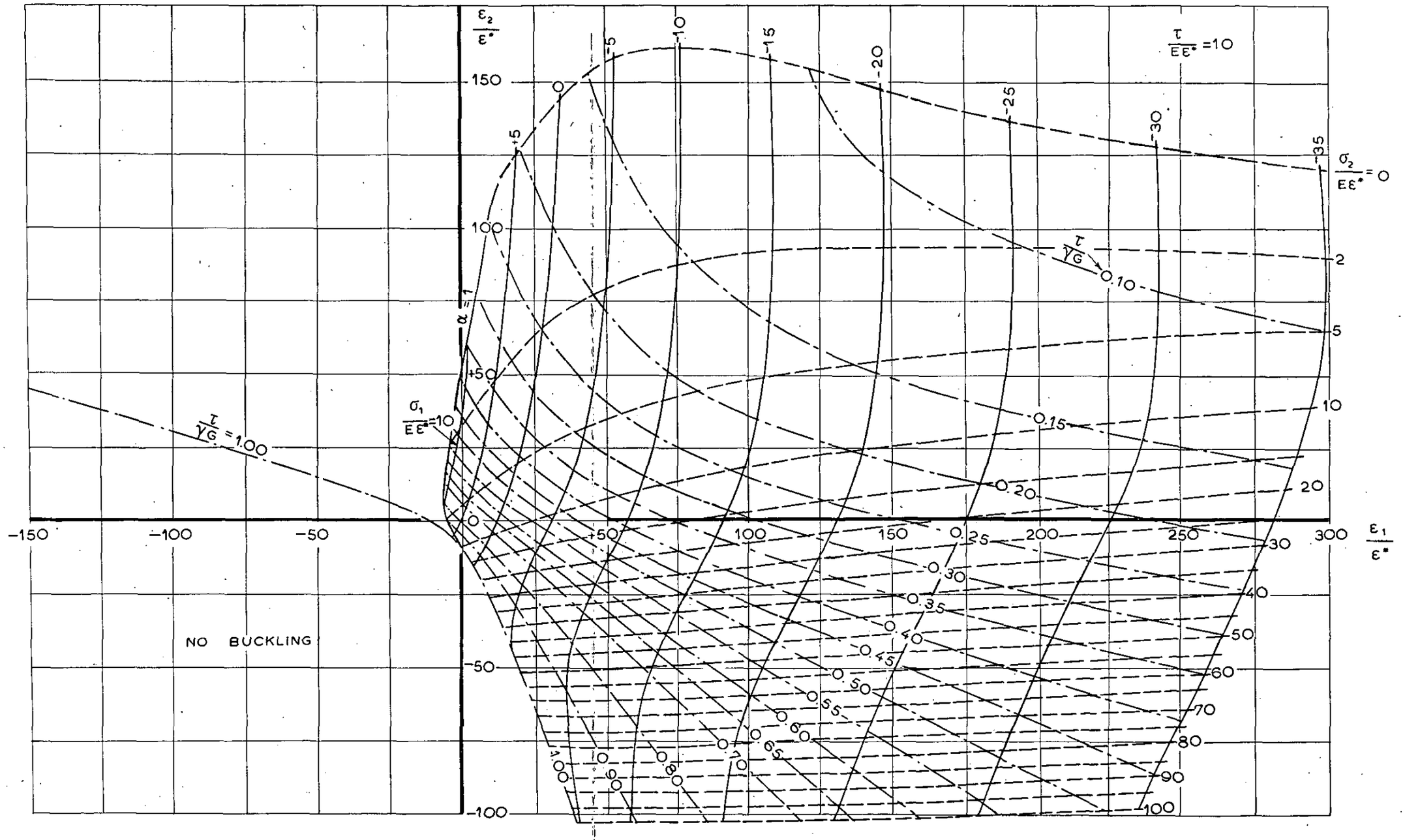
$\frac{\varepsilon_2}{\varepsilon^*}$
$\frac{\tau}{E\varepsilon^*}=10$
$\frac{\sigma_2}{E\varepsilon^*}=0$
$\frac{\tau}{\gamma G}$
$\frac{\sigma_1}{E\varepsilon^*}=10$
$\frac{\tau}{\gamma G}=1.00$
NO BUCKLING
$\frac{\varepsilon_1}{\varepsilon^*}$
$\alpha=1$

Fig. 3.3.

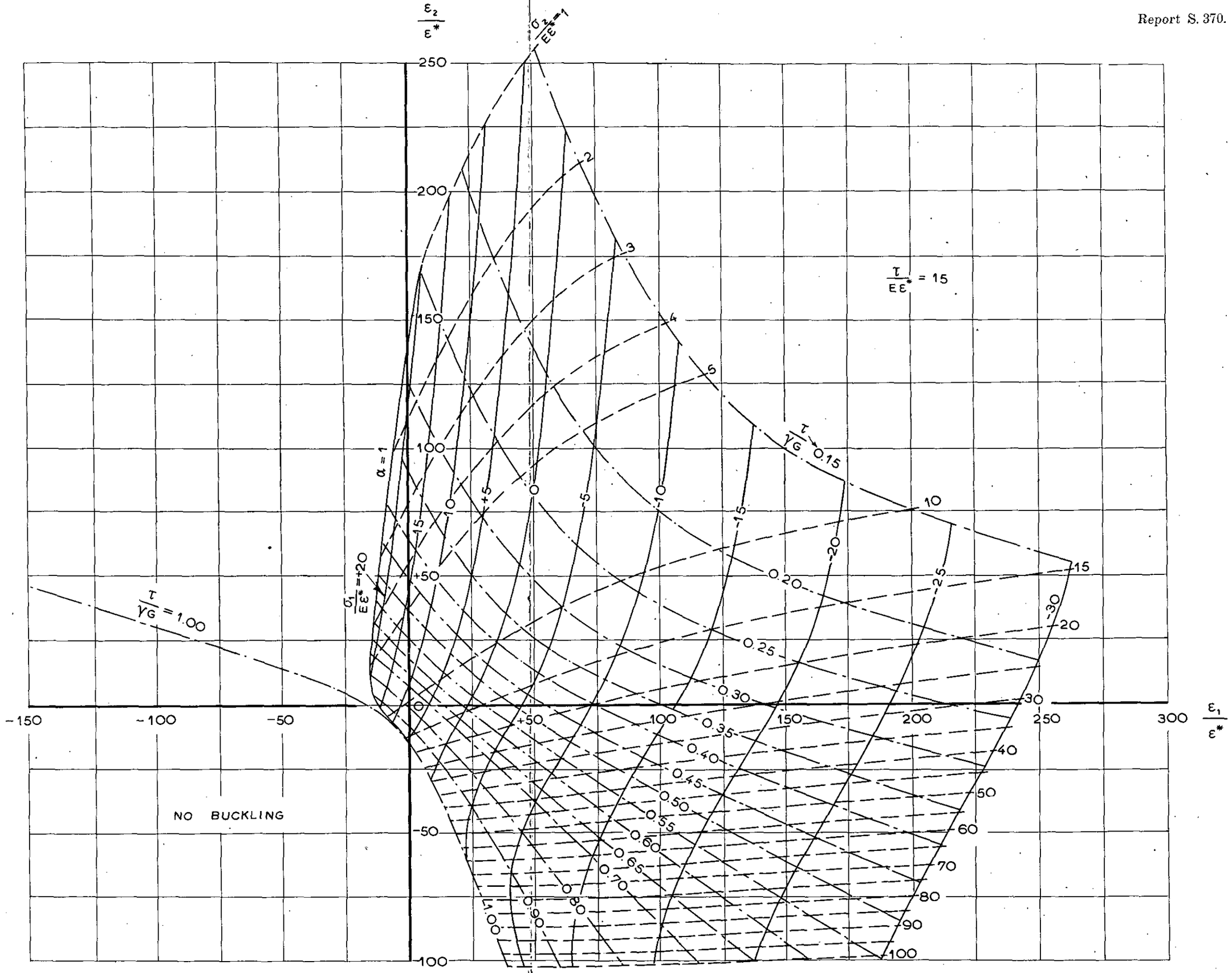
ε₂/ε*
σ₂/Eε* = 1
250
200
150
100
50
0
-50
-100
τ/Eε* = 15
τ/γG → 0.15
α = 1
2
3
4
5
+5
0
-5
-10
-15
10
15
20
25
30
+50
0.20
0.25
0.30
0.35
0.40
0.45
0.50
0.55
0.60
0.65
0.70
0.80
0.90
1.00
σ₁/Eε* = +20
τ/γG = 1.00
-150
-100
-50
+50
100
150
200
250
300
ε₁/ε*
NO BUCKLING

Fig. 3.4.

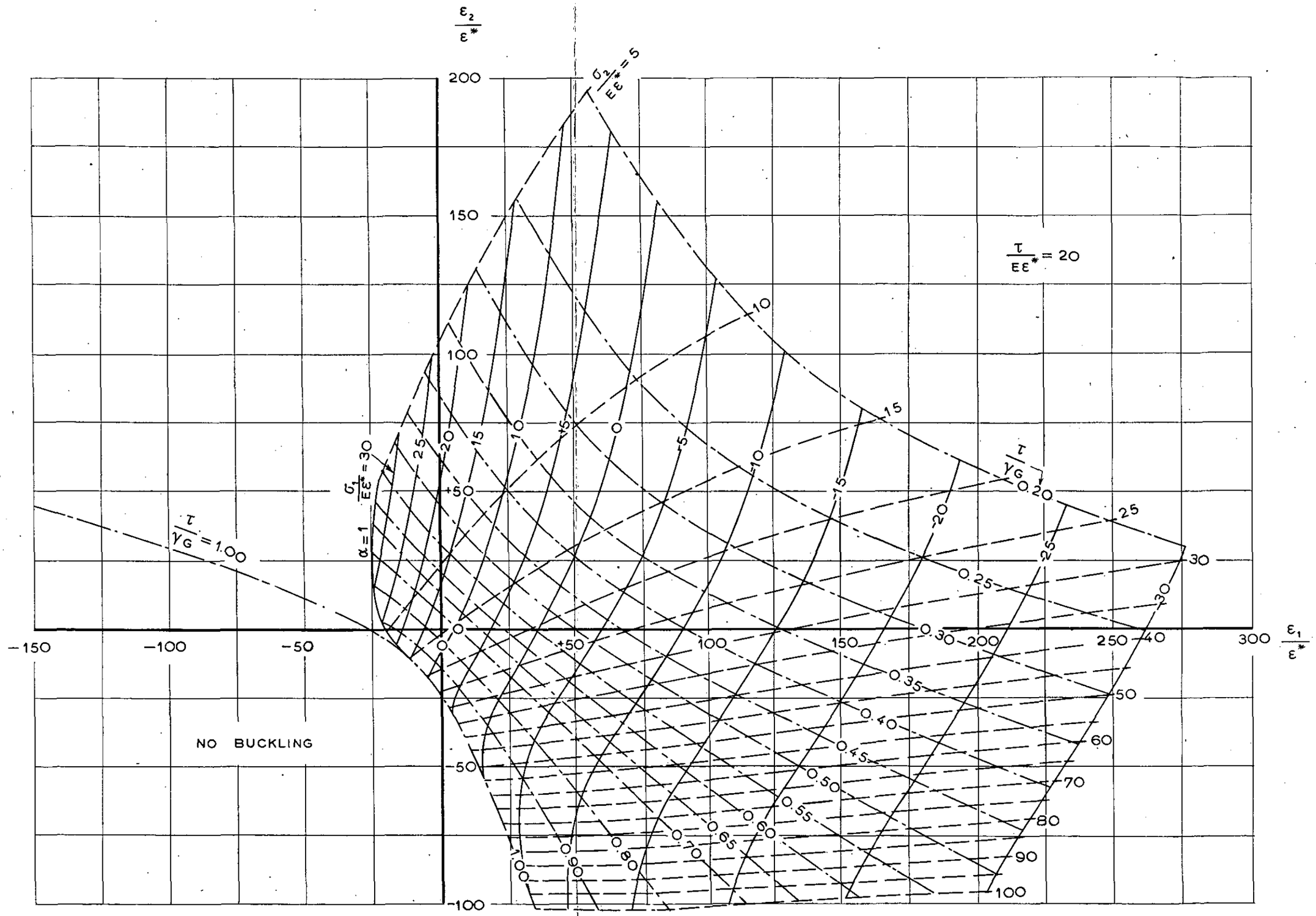
ε2/ε*
σ2/Eε*=5
τ/Eε*=20
τ/γG=1.00
σ1/Eε*=30
α=1
NO BUCKLING
τ/γG
ε1/ε*
200
150
100
50
0
−50
−100
−150
+50
100
150
200
250
300
10
15
0
5
10
15
20
25
30
0.25
0.30
40
0.35
50
0.40
60
0.45
70
0.50
80
0.55
90
0.60
100
0.65
0.70
0.90
1.00

Fig. 3.5.

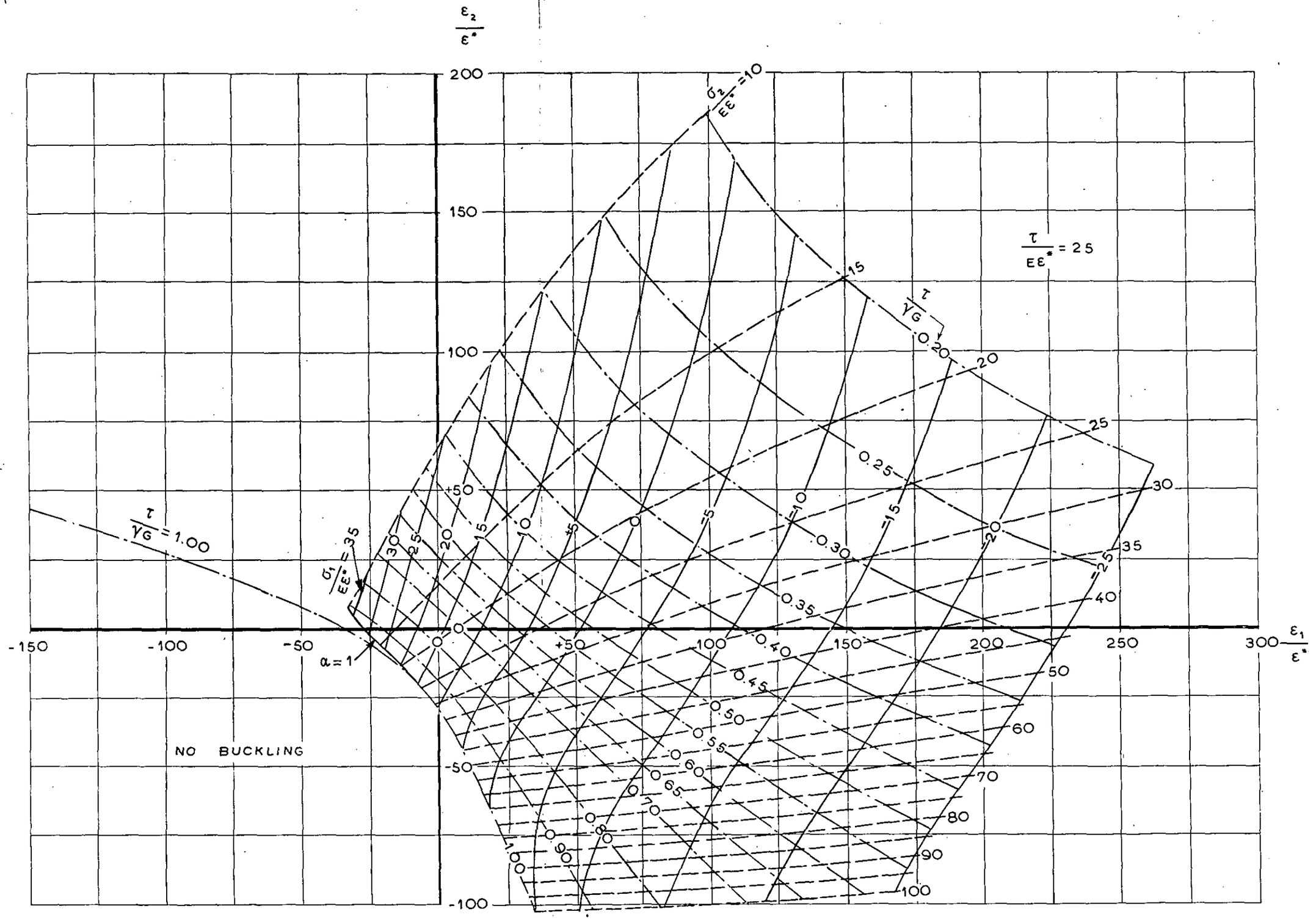
ε₂/ε*
200
150
100
50
-50
-100
-150
-100
-50
+50
100
150
200
250
300
ε₁/ε*
σ₂/Eε* = 10
15
20
25
30
35
40
50
60
70
80
90
100
τ/Eε* = 25
τ/γG
0.20
0.25
0.30
0.35
0.40
0.45
0.50
0.55
0.60
0.65
0.70
0.80
0.90
1.00
τ/γG = 1.00
σ₁/Eε* = 35
α = 1
NO BUCKLING

Fig. 3.6.

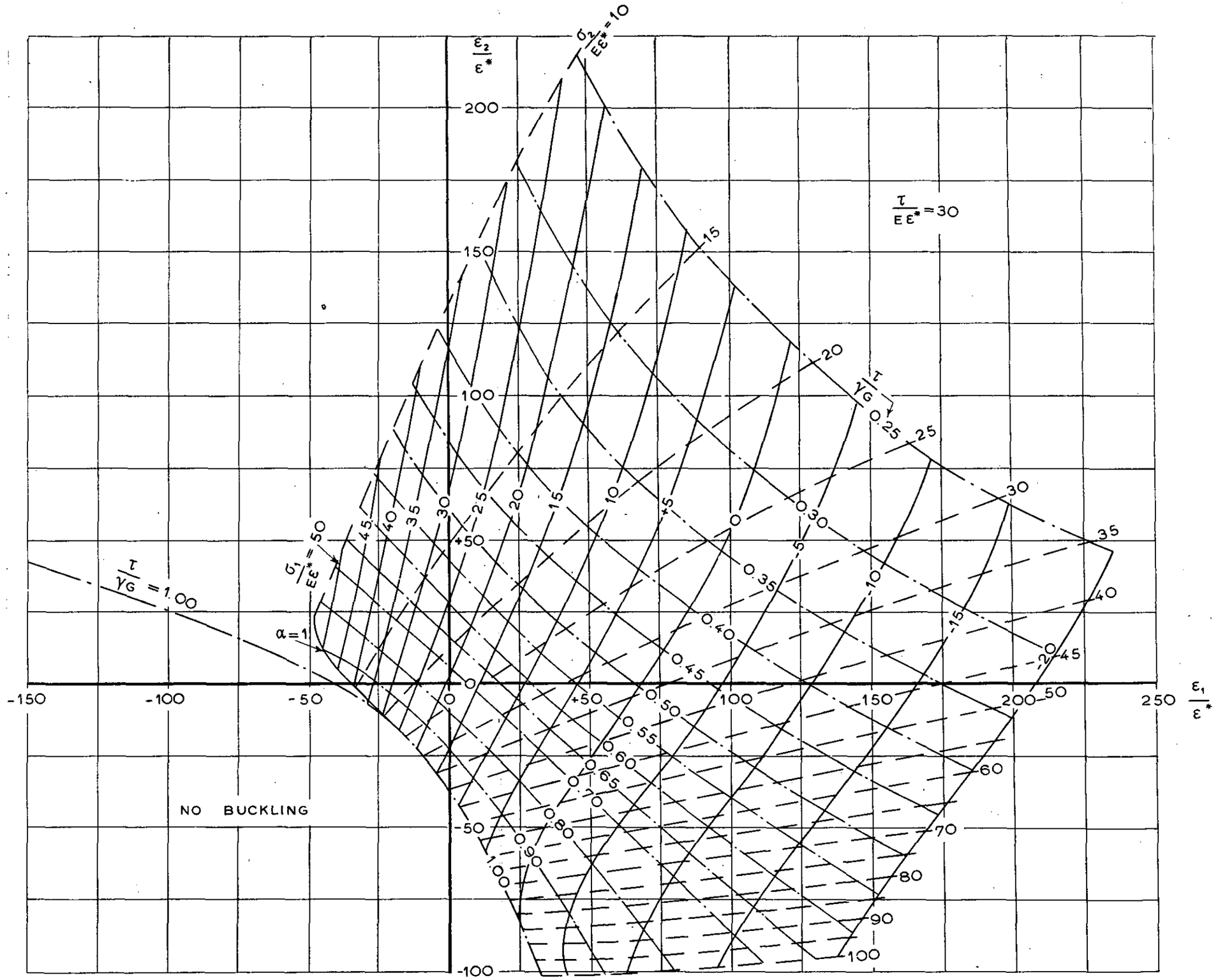
$\frac{\sigma_2}{E\varepsilon^*}=10$
$\frac{\varepsilon_2}{\varepsilon^*}$
200
150
100
$\frac{\tau}{E\varepsilon^*}=30$
15
20
$\frac{\tau}{\gamma_G}$
0·25
25
30
35
40
45
$\frac{\sigma_1}{E\varepsilon^*}=50$
$\frac{\tau}{\gamma_G}=1\cdot00$
$\alpha=1$
NO BUCKLING
-150
-100
-50
0
+50
100
150
200
250
$\frac{\varepsilon_1}{\varepsilon^*}$
+5
-5
-10
-15
-20
-25
-30
-35
-40
-45
-50
0·35
0·40
0·45
0·50
0·55
0·60
0·65
0·70
0·80
0·90
1·00
60
70
80
90
100

Fig. 3.7.

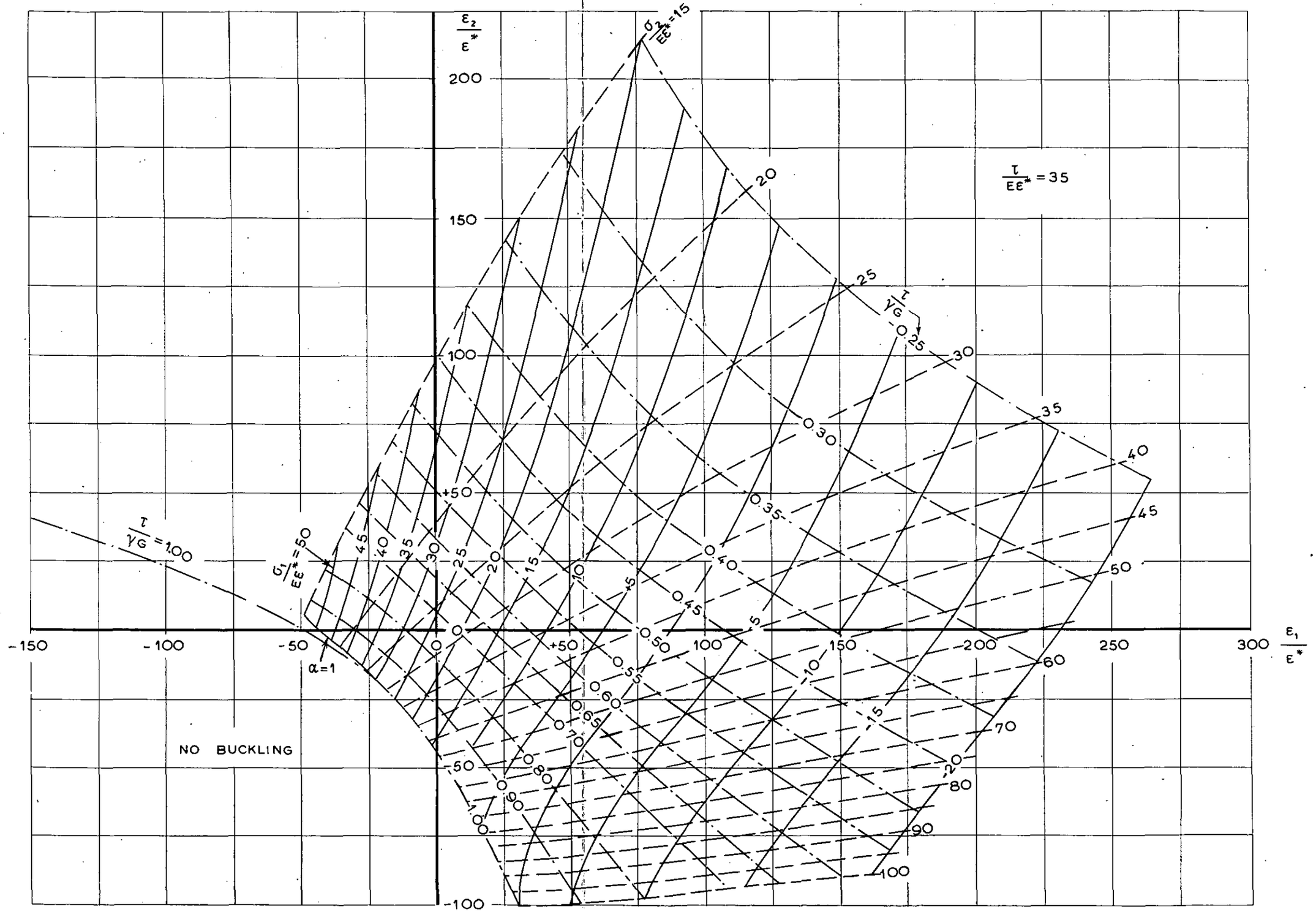
$\frac{\epsilon_2}{\epsilon^*}$
$\frac{\sigma_2}{E\epsilon^*}=15$
$\frac{\tau}{E\epsilon^*}=35$
$\frac{\tau}{\gamma_G}=1.00$
$\frac{\sigma_1}{E\epsilon^*}=50$
$\alpha=1$
NO BUCKLING
$\frac{\epsilon_1}{\epsilon^*}$
200
150
100
+50
0
-50
-100
-150
-200
250
300
20
25
30
35
40
45
50
60
70
80
90
100
+5
+10
+15
-5
-10
-15
-20
0.25
0.30
0.35
0.40
0.45
0.50
0.55
0.60
0.65
0.70
0.80
0.90
1.00

Fig. 3.8.

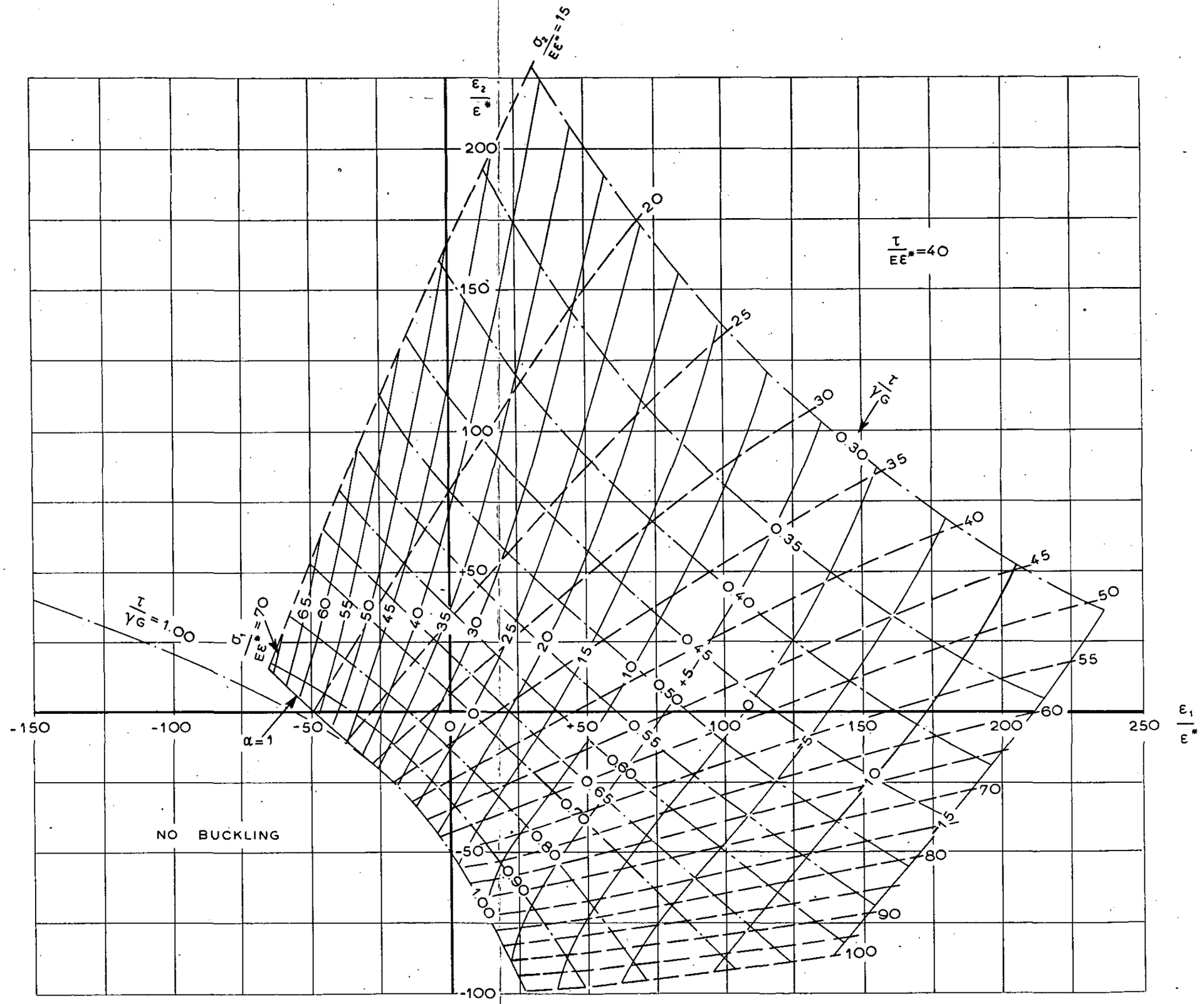
$\frac{\sigma_2}{E\epsilon^*}=15$
$\frac{\epsilon_2}{\epsilon^*}$
200
150
100
20
25
30
35
40
45
50
55
60
$\frac{\tau}{E\epsilon^*}=40$
$\frac{\tau}{\gamma_G}$
0.30
0.35
0.40
+50
+45
+5
0
-5
10
15
70
80
90
100
$\frac{\tau}{\gamma_G}=1.00$
$\frac{\sigma_1}{E\epsilon^*}=70$
65
60
55
50
45
40
35
30
25
20
15
10
0.50
0.55
0.60
0.65
0.70
0.80
0.90
$\alpha=1$
-150
-100
-50
+50
100
150
200
250
$\frac{\epsilon_1}{\epsilon^*}$
-50
-100
NO BUCKLING

Fig. 3.9.

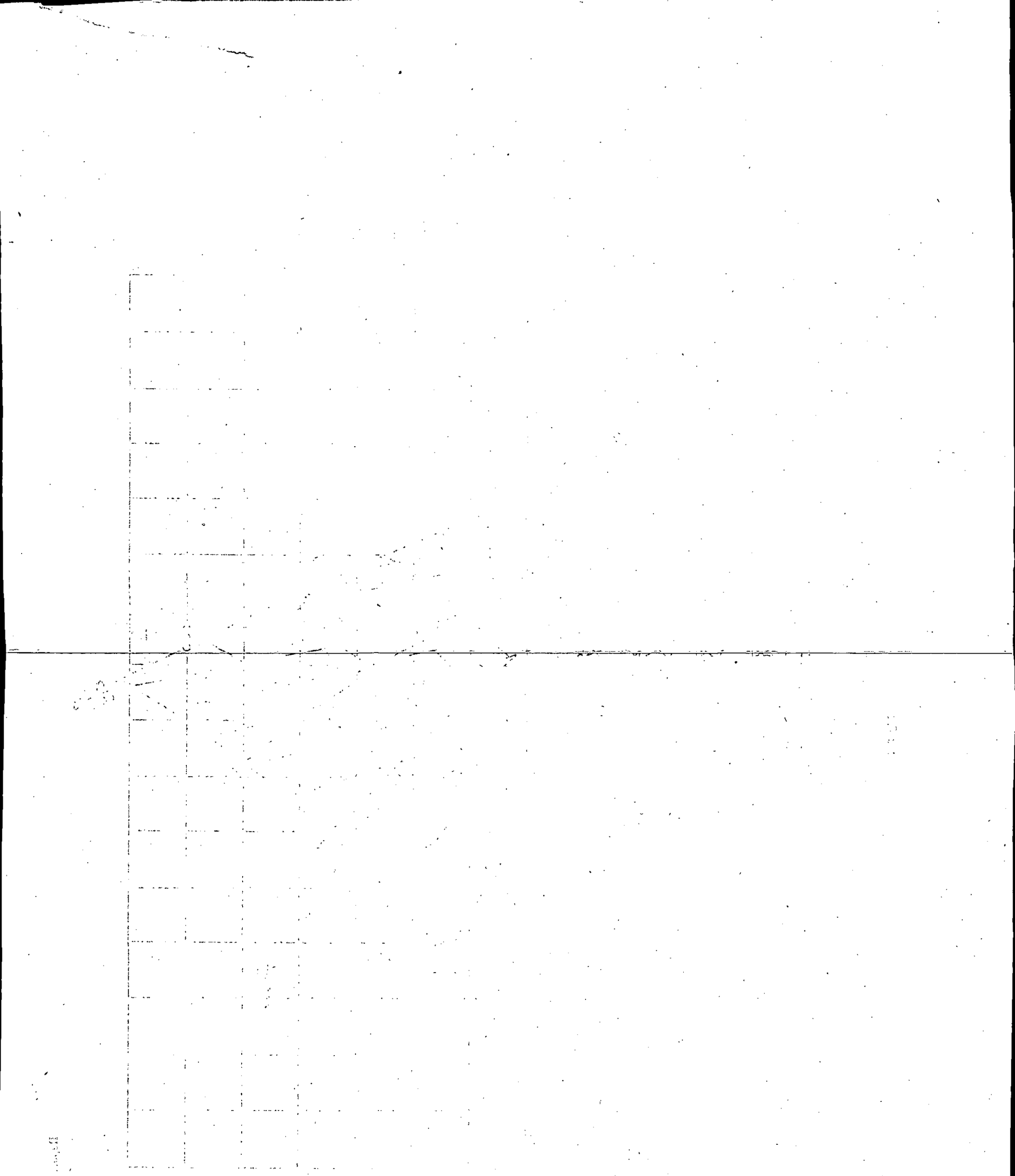

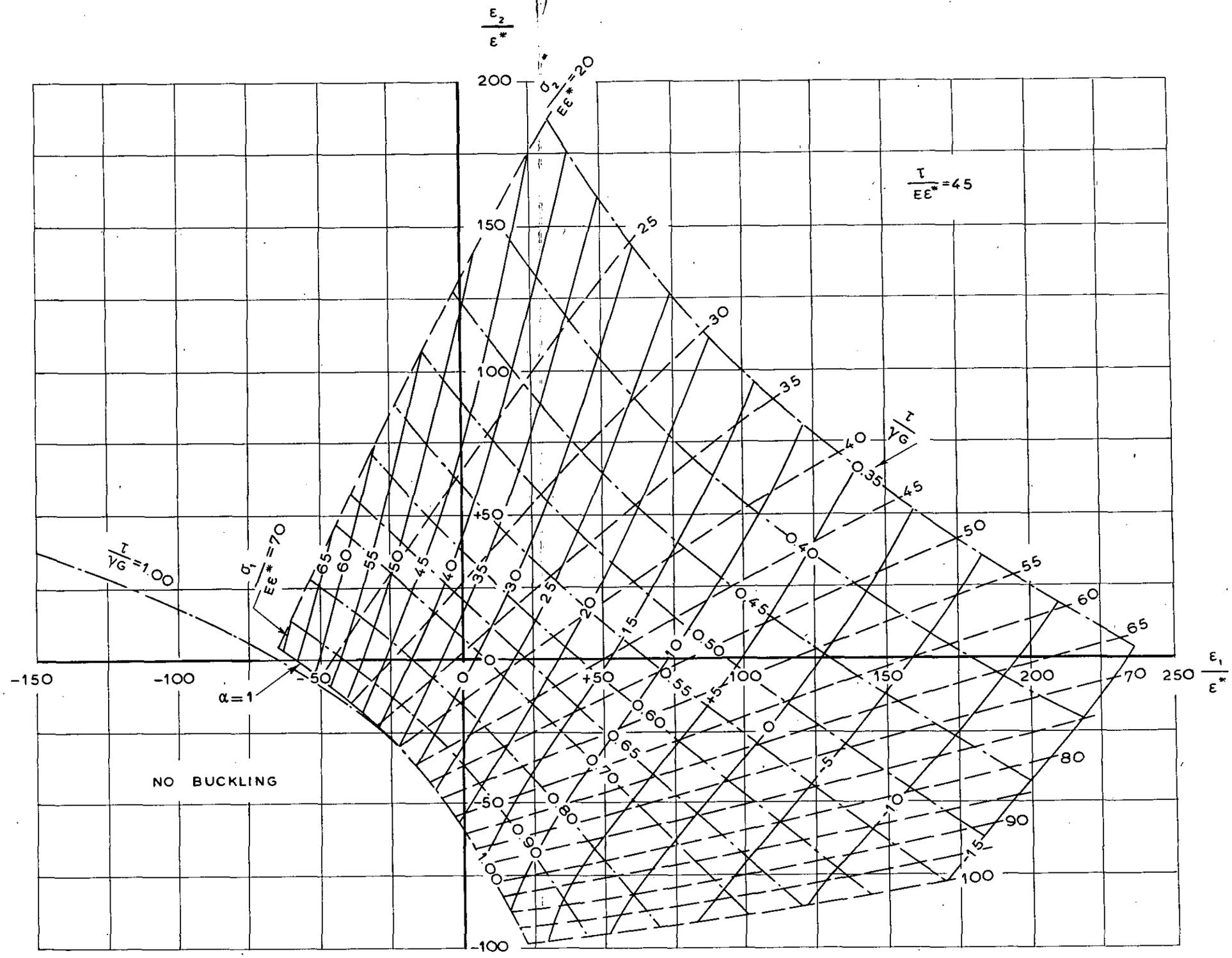
$\frac{\epsilon_2}{\epsilon^*}$
$\frac{\sigma_2}{E\epsilon^*}=20$
$\frac{\tau}{E\epsilon^*}=45$
$\frac{\tau}{\gamma_G}$
$\frac{\tau}{\gamma_G}=1.00$
$\frac{\sigma_1}{E\epsilon^*}=70$
$\alpha=1$
NO BUCKLING
$\frac{\epsilon_1}{\epsilon^*}$

Fig. 3.10.

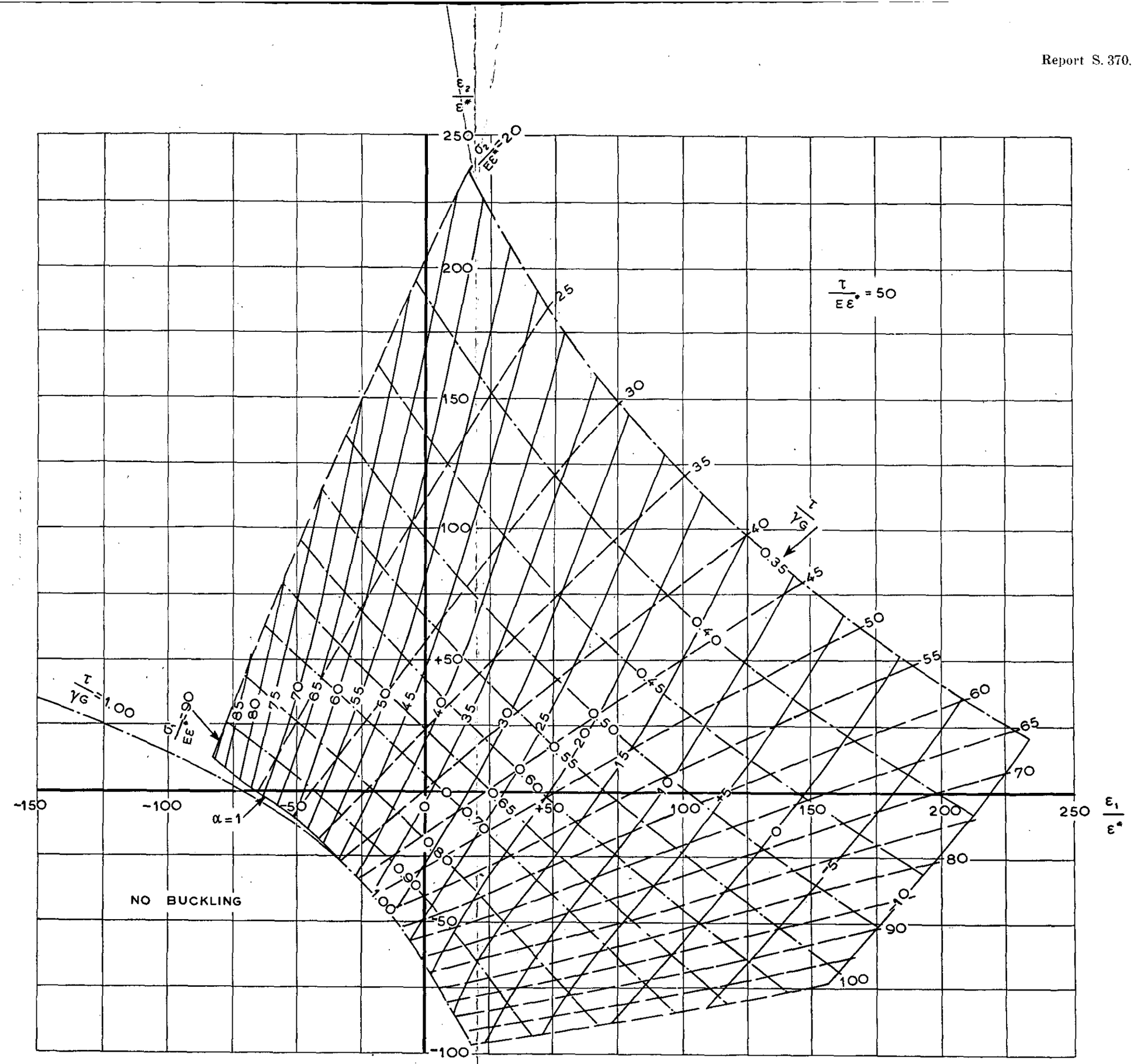
$\frac{\epsilon_2}{\epsilon^*}$
250
$\frac{\sigma_2}{E\epsilon^*}=20$
200
150
100
$\frac{\tau}{E\epsilon^*}=50$
25
30
35
40
$\frac{\tau}{\gamma_G}$
0.35
45
50
55
60
65
70
80
90
100
+50
$\frac{\tau}{\gamma_G}=1.00$
$\frac{\sigma_1}{E\epsilon^*}=-90$
85
80
75
70
65
60
55
50
45
40
35
30
25
20
15
10
5
0
-5
-50
-100
-150
$\alpha=1$
NO BUCKLING
$\frac{\epsilon_1}{\epsilon^*}$

Fig. 3.11.

C.C.L. Class. E 031

REPORT V. 1602

An analysis of the pitching motion of an aeroplane due to sideslip

by

Ir A. J. MARX and Drs J. BUHRMAN

Summary.

The purpose of this report is to establish a criterion for the acceptability of the pitching behaviour of an aeroplane due to sideslip. A computation method to determine the disturbed motion following a sudden rudder deflection or failure of an asymmetrically placed engine from data obtained by means of model tests in the windtunnel or from theoretically calculated data is developed. This method is applied to two aircraft for which also flight-tests results were available. The agreement between theory and experiment appears to be fairly good. On account of the results an appropriate requirement for satisfactory pitching behaviour of an aeroplane in yaw is suggested.

Contents.

1 Introduction.

One of the difficulties in predicting the flying qualities of an aeroplane in the design stage is to determine the dynamic pitching behaviour, when the aeroplane is sideslipped. It may occur that, although windtunnel tests have shown pitching moments due to sideslip which are small enough to meet the wellknown relevant requirement of ref. 1, the dynamic longitudinal response to a rudder-kick is very violent.

Therefore an analysis of the pitching motion due to a sudden yawing motion was carried out during the year 1948 with the object:

a) to establish a method for calculating the pitching response to a sudden rudder deflection or to an engine failure, based on data partially obtained from static model tests in the windtunnel and partially calculated on a theoretical base;

b) to establish a criterion by which the pitching behaviour due to sideslip of the aeroplane can be appreciated.

It is clear that the calculation of the motion of an aeroplane with six degrees of freedom is a rather laborious and uncertain procedure. So means had to be found to simplify the calculations and to obtain a method, which is sufficiently accurate and which enables the designer to make a check on the dynamic behaviour in sideslip in a reasonable time.

2 Method of analysis.

2.1 *Equations of motion.*

The six equations which must be satisfied throughout the motion of the aeroplane can be written (for symbols see par. 6)

$$\left.\begin{aligned} m(\dot{u} - vr + wq) &= X - mg\sin\theta \\ m(\dot{v} - wp + ur) &= Y + mg\cos\theta\sin\psi \\ m(\dot{w} - uq + vp) &= Z + mg\cos\theta\cos\psi \\ A\dot{p} - E\dot{r} - (B - C)\,qr - Epq &= L \\ B\dot{q} - (C - A)\,pr + Ep^2 - Er^2 &= M \\ C\dot{r} - E\dot{p} - (A - B)\,pq + Eqr &= N \end{aligned}\right\} \qquad (2.1)$$

where a dot denotes a differentiation with respect to time.

The equations are referred to axes which are fixed in the aeroplane. The origin O lies on the centre of gravity of the aeroplane; OX lies in the plane of symmetry in the direction of the velocity in steady symmetrical flight. The positive directions of OX, resp. OY and OZ are forward, resp. to starboard and downward.

2.2 *Simplifying assumptions.*

In order to facilitate the computation of the motion it is assumed that the pitching motion as a result of a sudden rudder deflection or engine failure is only affected by the yawing motion and not by the rolling motion. This assumption is supported by results of flight tests, which showed that the character of the pitching motion following a rudder deflection is not influenced by a considerable change in rolling stability (rolling moment due to sideslip). So the rolling motion can be eliminated from the problem by putting $p = \dot{p} = \psi = O$ and omitting the fourth equation (2.1). In other words it is assumed that any rolling moment occurring during the manoeuvre is cancelled by an appropriate aileron deflection.

On account of the short time in which the manoeuvre is performed it is further assumed that the component u of the resultant velocity remains unchanged. As has been found in flight tests this assumption holds with sufficient accuracy; as a result also the first equation (2.1) can be deleted.

Finally it is supposed that the inertia axes of the aeroplane coincide with the chosen axes OX, OY and OZ; so the product of inertia E can be put zero:

Thus the equations of motions can be written:

$$\left.\begin{aligned} m(\dot{v} + ur) &= Y \\ m(\dot{w} - uq) &= Z + mg\cos\theta \\ B\dot{q} &= M \\ C\dot{r} &= N \end{aligned}\right\} \qquad (2.2)$$

2.3 *Evaluation of the aerodynamic forces and moments.*

The aerodynamic forces X, Y, Z and the aerodynamic moments L, M, N are considered to be dependent on the linear and angular velocity components u, v, w, p, q and r and, with one single exception ($M_{\dot{w}}$), independent of their derivatives with respect to time. So it is assumed that the aerodynamic forces depend solely upon the instantaneous motion of the aeroplane and not upon the rate at which the motion is changing since it seems unlikely that instationary effects will influence the manoeuvre considered in this report.

The aerodynamic force X for instance can be represented by the linearized expression:

$$X = X_0 + X_u u + X_v v + X_w w + X_p p + X_q q + X_r r$$

where X_0 = force in the direction of the X-axis in steady symmetrical flight and X_u a.s.o. are partial derivatives.

In many problems in aeromechanics the so-called "cross-derivatives" (X_r, X_p, Y_u etc.), consisting of a "symmetric" and an "asymmetric" symbol, are put zero. In this investigation, however, an exception is made for M_v which is of primary interest to the problem. In view of the symmetry of the aeroplane it cannot be expected that the pitching moment will vary proportionally to the sideslip velocity; it is therefore better to write $M(v)$ instead of $M_v v$.

If further, according to the usual practice, unimportant derivatives such as X_q, Z_q, etc. are omitted the equations (2.2) take the form

$$\left.\begin{aligned} m(\dot{v} + ur) &= Y_v v + Y_\gamma \gamma + Y_0 \\ m(\dot{w} - uq) &= Z_w w + mg\cos(\theta_0 + \Delta\theta) + Z_0 \\ B\dot{q} &= M(v) + M_w w + M_{\dot{w}}\dot{w} + M_q q + M_\beta \Delta\beta + M_0 \\ C\dot{r} &= N_v v + N_r r + N_\gamma \gamma + N_0 \end{aligned}\right\} \qquad (2.3)$$

where $\Delta\beta$ denotes the difference between the instantaneous elevator angle and β_0, the elevator angle in steady flight.

Taking into account that in steady symmetrical flight

$$\left.\begin{aligned} Y_0 &= 0 \\ Z_0 + mg\cos\theta_0 &= 0 \\ M_0 &= 0 \\ N_0 &= 0 \end{aligned}\right\} \qquad (2.4)$$

and putting $\cos\theta = 1$ we obtain

$$\left.\begin{aligned} m(\dot{v} + ur) &= Y_v v + Y_\gamma \gamma \\ m(\dot{w} - uq) &= Z_w w \\ B\dot{q} &= M(v) + M_w w + M_{\dot{w}}\dot{w} + M_q q + M_\beta \Delta\beta \\ C\dot{r} &= N_v v + N_r r + N_\gamma \gamma \end{aligned}\right\} \qquad (2.5)$$

The equations in this form will be used for a numerical analysis of the problem.

If at a given moment $t = t_1$ the value of the velocity components v, w, q and r are known, (2.5) allow the determination of the values of these components at the moment $t = t_1 + \Delta t$ provided all constants and the time histories of β and γ are known. By means of this step-by-step integration it is possible to calculate the manoeuvre resulting from given control deflections.

2.4 *Numerical application.*

When applying the above-described procedure in a special case the quantities Y_v, Y_γ, Z_w, $M(v)$, M_w, M_β, N_v and N_γ can be found from model tests in the windtunnel. The mass m and the moments of inertia B and C can be estimated with a sufficient degree of accuracy. Only $M_{\dot{w}}$, M_q and N_r must be calculated on a theoretical base.

To this end the following well-known approximative formulae are used

$$M_{\dot{w}} = M_{q_{tail}} \frac{1}{V} \frac{d\varepsilon}{d\alpha}. \qquad (2.6)$$

$$M_q = 1{,}2\, M_{q\,tail} =$$

$$= -0{,}6\, \rho V l_H^2 F_H \left(\frac{\partial c_a}{\partial \alpha}\right)_{hor.\ tail} \quad (2.7)$$

$$N_{r_{tail}} = -\tfrac{1}{2}\, \rho V l_v^2 F_v \left(\frac{\partial c_a}{\partial \alpha}\right)_{vert.\ tail} \quad (2.8)$$

For the contribution of the wing in the damping moment in yaw ref. 2 can be consulted.

3 Comparison of theoretical and experimental results.

The above-described computation method was applied to a light single-engined aeroplane for which also flight test results were available.

In order to investigate the pitching behaviour of the aeroplane due to sideslip in flight, a sudden rudder deflection was effected and the resulting motion was recorded by means of an automatic observer. The time history of the rudder angle during a left and right "rudder kick" is given in fig. 1. The pilot was instructed to keep the

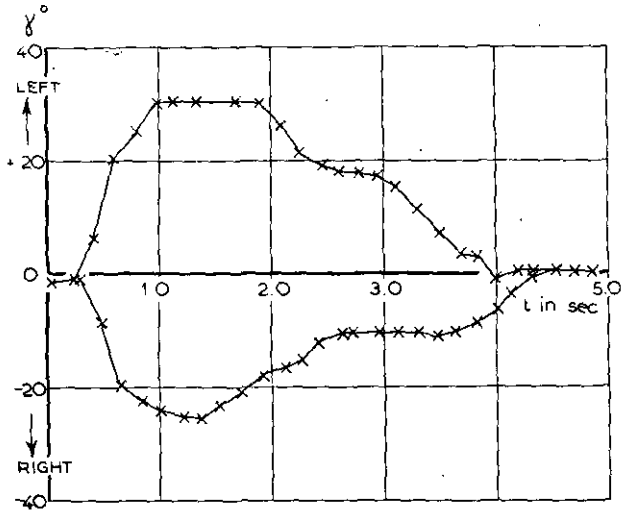

Fig. 1. Rudder angle during right and left rudder kick (single-engined aeroplane).

elevator angle as constant as possible but did not succeed fully in doing so.

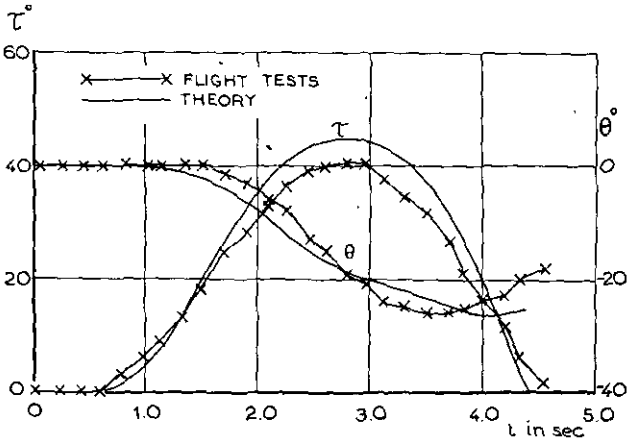

Fig. 2. Angles of sideslip and pitch during left rudder kick (single-engined aeroplane).

The main results are plotted in the figures 2—5 as time histories of the sideslip angle τ, the angle of pitch θ and the lateral and normal components of the acceleration a_y and a_z. The airspeed varied only a few *mph* during the manoeuvre. As may

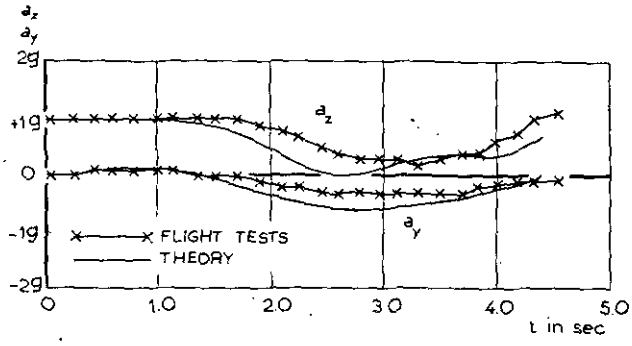

Fig. 3. Normal and lateral accelleration during left rudder kick (single-engined aeroplane).

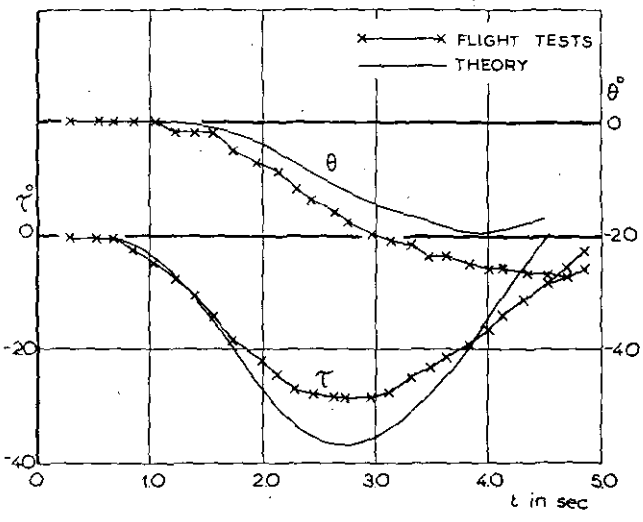

Fig. 4. Angles of sideslip and pitch during right rudder kick (single-engined aeroplane).

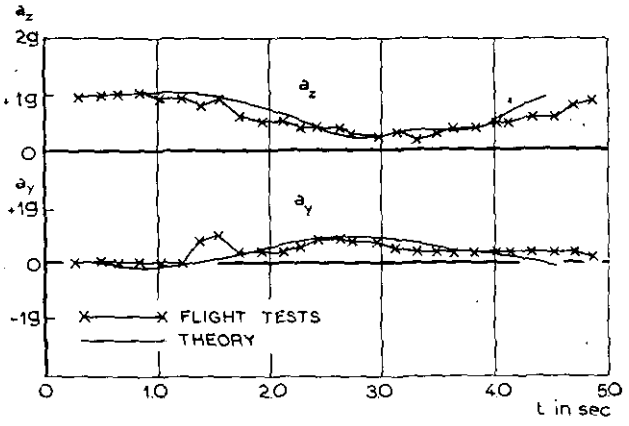

Fig. 5. Normal and lateral acceleration during right rudder kick (single-engined aeroplane).

be seen from the figures the violent response of the aeroplane is unacceptable. Especially the large changes in angle of pitch and normal acceleration are characteristic features of the behaviour of the aeroplane.

The computation of the measured quantities according to the method outlined in par. 2 was based on the measured time history of the rudder deflection. The assumption of constant airspeed seems to be tenable in view of the small variations in airspeed being measured. The data required were partly taken from unpublished results of model tests in the windtunnnel and partly derived from flight tests; the remainder was calculated according to the formulae of par. 2.4. A survey of these data is given in table 1. The small changes in elevator angle $\Delta\beta$ recorded during the manoeuvre were introduced into the equations. The time interval in the step-by-step integration procedure was taken as 0.1 sec.

The results of the calculations together with those of the flight tests are given in the figures 2—5. The agreement between the two sets of curves appears to be fairly good. In both cases the theoretical angle of sideslip is somewhat in excess of the experimental value especially when this angle is large. It is clear that a perfect agreement cannot be expected at those very large sideslip angles because it is unlikely that the assumed linearity holds in this region.

The experimental and theoretical values of the angle of pitch and the normal acceleration are in good agreement. So it can be concluded that the theoretical analysis gives a sufficiently accurate picture of the behaviour of the aeroplane.

Another check on the computation method was made for a twin-engined aeroplane, which, as was proved by flight tests, showed a satisfactory pitching behaviour in sideslip. In fig. 6 and 7 the results of such a "rudder kick" test together with the theoretical results are presented. The character of the manoeuvre following the rudder deflection is much less violent than for the first-mentioned single-engined aeroplane. The changes in angle of pitch and normal acceleration are considerably smaller. Comparison of the curves for the normal acceleration shows that the changes in

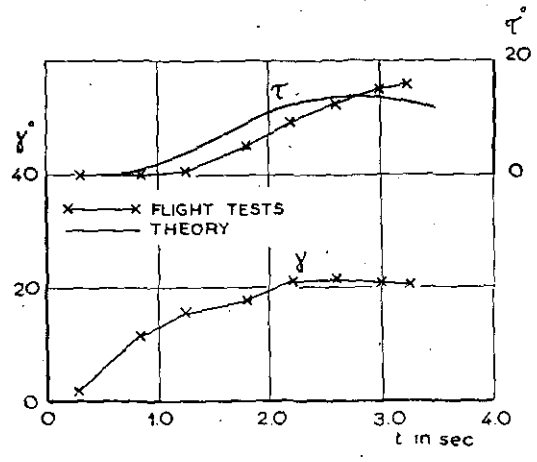

Fig. 6. Rudder angle and angle of sideslip during left rudder kick (twin-engined aeroplane).

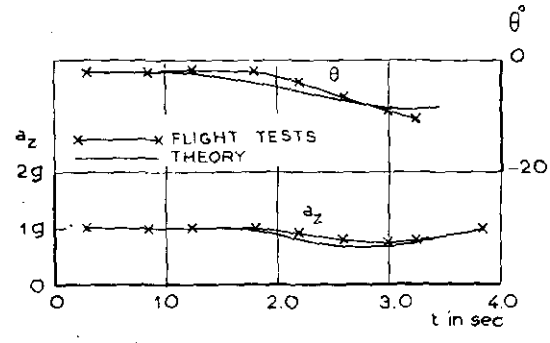

Fig. 7. Angle of pitch and normal acceleration during left rudder kick (twin-engined aeroplane).

TABLE 1.

Data of the single-engined aeroplane.

($V = 42$ m/sec; $\rho = 0.11$ kgm^{-4} sec^2)

m	= 114.5	kgm^{-1}sec^2	M_w	= — 39.2	kg sec *
B	= 180	kgm sec^2	$M_{\dot{w}}$	= — 5.43	kg sec^2
C	= 426	kgm sec^2	M_q	= — 678	kgm sec/rad
Y_v	= — 16.1	kgm^{-1}sec	M_β	= — 55.6	kgm/degr *
Y_γ	= 3.28	kg/degr *	N_v	= 17.4	kg sec
Z_w	= — 197	kgm^{-1}sec *	N_r	= — 930	kgm sec/rad
			N_γ	= — 16.2	kgm/degr *

$$
\begin{aligned}
M(v) &= -7.05\,v && \text{kgm when } 0 < v < 4.16 \text{ m/sec}\\
&= -20.0\,v + 53.9 && \text{" " } 4.16 < v < 10.4 \text{ "}\\
&= 7.05\,v - 227 && \text{" " } 10.4 < v < 14.6 \text{ "}\\
&= -28.4\,v + 289.5 && \text{" " } v > 14.6 \text{ "}
\end{aligned}
$$

Note: All coefficients of v in the expressions for $M(v)$ change sign when v attains negative values.

The quantities marked * are derived from model tests; N_v and Y_v are found from flight tests; all others are estimated.

this quantity are slightly overestimated by theory. Probably this is due to the fact that the computed sideslip angles are somewhat in excess of the measured values.

Although the agreement between theory and experiment is perhaps a little less as in the case of the foregoing example it may be said that the satisfactory behaviour of the aeroplane predicted by theory is verified by the tests. The data used in the computation were derived solely from wind-tunnel tests or estimated according to par. 2.4 (see table 2).

exceed 1 g and not fall below $\frac{2}{3}$ g when stick or wheel is held fixed. The value of γ_{max} is chosen as 20° or as that rudder angle which can be produced with a pedal force of 100 lbs, whichever is the lesser."

The aeroplanes considered in this report always showed a nose-down pitching moment. It is not impossible, however, that a nose-up pitching moment occurs when the aeroplane in sideslipped corresponding with a normal acceleration greater than 1 g, which in the low speed range can cause

TABLE 2.

Data of the twin-engined aeroplane.

($v = 56.5$ m/sec; $\rho = 0.103$ kgm^{-4} sec^2)

m	= 575	kgm^{-1}sec^2	M_w	= — 276	kg sec
B	= 2600	kgm sec^2	$M_{\dot{w}}$	= — 35.6	kg sec^2
C	= 5275	kgm sec^2	M_q	= — 8040	kgm sec/rad
Y_v	= — 87.0	kgm^{-1}sec	M_β	= — 379	kgm/degr
Y_γ	= 17.1	kg/degr	N_v	= 285	kg sec
Z_w	= — 727	kgm^{-1}sec	N_r	= — 3237	kgm sec/rad
			N_γ	= — 139	kgm/degr

$M(v) = -26.0\ v$ kgm when $0 < v < 2.96$ m/sec

$= -98.2\ v + 213$ „ „ $2.96 < v < 22.7$ „

Note: The coefficients of v in the expressions for $M(v)$ change sign when v attains negative values.
All quantities are derived from model tests or estimated.

4 Recommended requirement for the pitching motion due to sideslip.

The violence of the manoeuvre following a sudden rudder deflection can best be appreciated by means of the resulting normal acceleration. The additional normal acceleration (over 1 g) during the manoeuvre of the single-engined aeroplane appeared to be about — 0.8 g (see fig. 3 and 5), which must be considered to be unacceptable. The twin-engined aeroplane showed only — 0.2 g (see fig. 7) corresponding with a satisfactory behaviour.

The relevant requirement mentioned in ref. 1 reads: "As measured in steady sideslip, the pitching moment due to sideslip should be such that not more than 1° elevator movement is required to maintain longitudinal trim at 110 percent of the minimum speed when the rudder is moved 5° right or left from its position for straight flight".

This requirement was met by both aeroplanes and since one of the two showed an intolerable behaviour it seems desirable to introduce another requirement which covers the above-mentioned short-coming. The following proposal is made:

"As a result of a sudden rudder deflection according to fig. 8 in symmetrical flight at 1.3 V_{min} the normal acceleration should not

a dangerous inadvertant stall of the aeroplane. So it looks desirable to require in the first place that the sign of the pitching moment due to side-

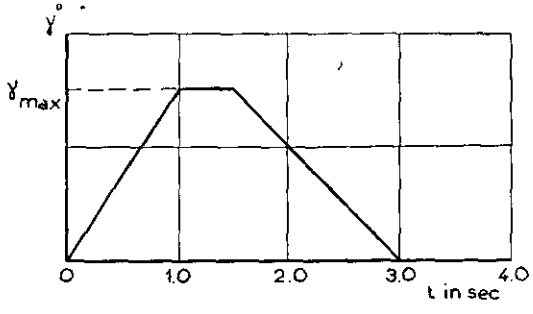

Fig. 8. Idealized rudder kick (par. 4).

slip shall always be negative (nose-down) and further that the above-mentioned decrease of $\frac{1}{3}$ g in the normal acceleration shall not be exceeded.

After completing this study authors became aware of a similar tentative requirement mentioned in ref. 3, which prescribes that the application of a rudder force of 50 lbs should not produce a change in normal acceleration greater than 0.2 g when the elevator is left free.

Although there are a few numerical differences between the two proposals they have the same tendency. An essential difference, however, is the elevator free term in the latter. It is not immediately clear whether this condition makes the requirement more or less severe but according to the experience obtained it is believed the former will be the case. It must be noted that it is rather difficult to apply the requirement of ref. 3 in the design stage of an aeroplane.

5 Conclusions.

An analysis of the pitching motion of an aeroplane due to sideslip given in this report showed that the dynamic response to a sudden rudder kick or, in the case of a multi-engined aeroplane, to an engine failure can be very violent although the well-known relevant requirement of ref. 1 is met. It is concluded that a supplementary requirement as to the change in normal acceleration as the result of a sudden rudder deflection should be added to the existing one. A description of an appropriate proposal is given in par. 4.

In order to be able to predict the pitching behaviour in sideslip in the design stage a computation method is given which was applied to two aeroplanes also tested in flight. The agreement between the theoretical and experimental results is satisfactory. The computations can be carried out in a very reasonable time.

6 List of symbols.

A	moment of inertia about the X axis.
a_x, a_y, a_z	acceleration in the direction of the X, Y, Z axis.
B	moment of inertia about the Y axis.
b	wing span.
C	moment of inertia about the Z axis.
E	product of inertia with respect to X and Z axis.
F	wing area.
F_H	area of horizontal tail.
F_v	area of vertical tail.
G	aeroplane weight.
g	acceleration due to gravity.
l_H	distance of centre of pressure of horizontal tail behind aeroplane c. g.
l_v	distance of centre of pressure of vertical tail behind aeroplane c. g.
L, M, N	moment of aerodynamic forces about X, Y, Z axis (positive when starboard wing downward, nose upward, starboard wing rearward).
m	mass of the aeroplane.
p, q, r	angular velocity about X, Y, Z axis (sign according to L, M, N).
t	time.
u, v, w	linear velocity components in the direction of the X, Y, Z axis (positive when forward, to starboard, downward).
V	resultant velocity.
X, Y, Z	aerodynamic forces in the direction of the X, Y, Z axis (sign according to u, v, w).
α	angle of incidence.
β	elevator angle (positive when downward).
γ	rudder angle (positive when to port).
ε	angle of downwash.
θ	angle of pitch (positive when nose up).
ψ	angle of bank (positive when starboard wing down).
τ	sideslip angle (positive when starboard wing leading).
ρ	air density.

Symbols consisting of a big character and a small index such as Y_v, N_r a. s. o. denote partial derivatives of Y, N with respect to v, r.

7 References.

1 Gilruth, R. R. Requirements for Satisfactory Flying Qualities of Airplanes, NACA T. Rep. Nr. 755, 1943.

2 Pearson, H. A. and Jones, R. T. Theoretical Stability and Control Characteristics of Wings with Various Amounts of Taper and Twist, NACA T. Rep. Nr. 635, 1938.

3 Phillips, W. H. Appreciation and Prediction of Flying Qualities, NACA T. N. Nr. 1670, 1948.

Completed: March 1952.

C.C.L. Class. E 004

REPORT V. 1625

The Static Longitudinal Stability and Control of an Aeroplane as affected by the Compressibility of the Air

by

Drs J. BUHRMAN and Ir C. M. KALKMAN.

Summary.

A computation method is given for the effect of the compressibility of the air on the static longitudinal stability and control characteristics of an aeroplane. The derived formulae are based on the Prandtl rule.

Their applicability is limited to Mach numbers below the critical Mach number since the linear theory holds no longer beyond this limit.

In order to illustrate the magnitude of the influence of the Mach number on static and manoeuvre margins and trim changes the results of a numerical application of the formulae are included in the report.

For a more detailed summary of the conclusions see sec. 5.

Contents.

1 Introduction.

There are two main causes for the change in the flying characteristics of an aeroplane when the speed increases to high subsonic values, the first of which is the distortion of the various parts of the aeroplane and the second the compressibility of the air.

In ref. 1 GATES and LYON give an extension of the theory of longitudinal stability and control by abandoning the usual assumption of the speed independence of the aerodynamic coefficients. Their theory is of a very general character and comprises the two mentioned high speed effects as well as the slipstream effects at low speeds.

As it seems desirable to gain an insight in the separate effects a computation method for the influence of the air compressibility alone on the static longitudinal stability and control characteristics is given in this report. So the aeroplane will be considered to be perfectly rigid. The range of speeds to which the formulae derived are applicable lies below the critical Mach number since the linearized theory on which the computations are based holds no longer beyond this limit.

2 Mach number effects on the aerodynamic coefficients of a three-dimensional aerofoil.

In order to be able to predict the changes in the stability and control characteristics of an aeroplane occurring when speed is increased to high subsonic values it is necessary to know how the basic aerodynamic parameters of a three-dimensional aerofoil are affected by Mach number.

To this end a brief survey of the changes in the following parameters with Mach number will be given in this paragraph:

Lift curve slope of wing or tailplane (a; a_1).
Rate of increase of lift with elevator or tab angle (a_2; a_3).
Downwash angle behind aerofoil (ε).
Rate of change of hinge moment with angle of incidence, elevator or tab angle (b_1; b_2; b_3).
Wing pitching moment at zero lift (c_{m_0}).

In ref. 2 GÖTHERT gives the following extension of the well-known PRANDTL rule: The field of streamlines of a compressible flow around an aerofoil (undisturbed flow in the direction of the X-axis of the aerofoil) can be compared with the field of streamlines in an incompressible flow, which is obtained by contracting the first one (aerofoil contours included) in a ratio $\sqrt{1-M^2}$ in all directions normal to that of the undisturbed flow. Then the non-dimensional pressures $(\Delta p/\frac{1}{2}\rho v_0^2)$ and perturbation velocities $(\Delta v_x/v_0)$ for the compressible flow are $1/(1-M^2)$ times as

large as in corresponding points of the incompressible flow.

The application of this rule to the lift curve slope of an elliptic wing with aspect ratio λ gives

$$\frac{A}{a} = \frac{a_0 + \pi\lambda}{a_0 + \pi\lambda\sqrt{1-M^2}}, \qquad (2.1)$$

where according to ref. 1 small characters resp. capitals refer to the incompressible resp. compressible case.

For other than elliptic wing plan forms matters are more complicated. In an incompressible fluid the following formula can be given for the lift curve slope

$$a = \frac{1}{\frac{1}{a_0} + \frac{1+\tau}{\pi\lambda}},$$

where τ depends on the plan form of the wing.

It is shown in ref. 3 that for a compressible fluid

$$A = \frac{1}{\frac{\sqrt{1-M^2}}{a_0} + \frac{1+\tau}{\pi\lambda}}.$$

In this formula the value of τ must be taken from the incompressible theory for a wing with an aspect ratio of $\lambda\sqrt{1-M^2}$. It would be possible to express τ in terms of Mach number but this would result in a rather complicated form. The computations in the next part of the report will therefore be confined to the case of the elliptic lift distribution along the span of wing and tail surfaces which is believed to give a satisfactory impression of the trend of stability characteristics with increasing Mach number. Eventually further refinements can be made in special practical cases.

Similar formulae hold for the effect of Mach number on the rates of increases of tail plane lift with elevator and tab angle.

The relations to be used are (see sec. 6 for notation)

$$\frac{A_2}{a_2} = \frac{A_3}{a_3} = \frac{a_{10} + \pi\lambda_H}{a_{10} + \pi\lambda_H\sqrt{1-M^2}} = \frac{A_1}{a_1}. \qquad (2.2)$$

Another aerodynamic parameter affecting the longitudinal stability of an aeroplane is the downwash behind the wing. If allowance is made for the rolling-up of the vortex-sheet and the distance between the rolled-up vortices is denoted by $2s'$. then the downwash angle ε at a point in the plane of symmetry at a distance l behind the aerofoil can be represented by (ref. 3)

$$\varepsilon = \frac{A\alpha}{2\pi\lambda}\left(\frac{s}{s'}\right)^2\left\{1 + \left(1 + \frac{s'^2(1-M^2)}{l^2}\right)^{\frac{1}{2}}\right\}. \qquad (2.3)$$

For an elliptic load grading (2.3) reduces to

$$\varepsilon = \frac{8A\alpha}{\pi^3\lambda}\left\{1 + \left(1 + \frac{\pi^2 s^2(1-M^2)}{16\,l^2}\right)^{\frac{1}{2}}\right\}. \qquad (2.4)$$

Again, it must be remembered that when applying formula (2.3) the value of s' can be taken from the theory of incompressible flow for a wing of an aspect ratio $\lambda\sqrt{1-M^2}$.

Not very much is known about the influence of Mach number on the hinge moment coefficients for controls on aerofoils of finite span. Use will be made of the formulae derived by YOUNG and OWEN in ref. 4, which read

$$\frac{B_1}{b_1} = \frac{a_{10} + \pi\lambda}{a_{10} + \pi\lambda\sqrt{1-M^2}}, \qquad (2.5)$$

$$\frac{B_2}{b_2} = \frac{a_{10} + \pi\lambda}{a_{10}\sqrt{1-M^2} + \pi\lambda(1-M^2)} \times \frac{\pi\lambda b_{20}\sqrt{1-M^2} + (a_{10}b_{20} - b_{10}a_{20})}{\pi\lambda b_{20} + (a_{10}b_{20} - b_{10}a_{20})} \qquad (2.6)$$

and

$$\frac{B_3}{b_3} = \frac{a_{10} + \pi\lambda}{a_{10}\sqrt{1-M^2} + \pi\lambda(1-M^2)} \times \frac{\pi\lambda b_{30}\sqrt{1-M^2} + (a_{10}b_{30} - b_{10}a_{30})}{\pi\lambda b_{30} + (a_{10}b_{30} - b_{10}a_{30})}. \qquad (2.7)$$

Since the formulae (2.6) and (2.7) are too complicated for the purpose of this report the following approximation is made. In the right hand sides of (2.6) and (2.7) the terms $b_{10}a_{i0}$ are omitted, which implies only a rather small loss in accuracy in most cases, so that

$$\frac{B_2}{b_2} = \frac{B_3}{b_3} = \frac{1}{\sqrt{1-M^2}}. \qquad (2.8)$$

It must be noted that the coefficients b_i are related to the stick forces and the stick free stability characteristics of the aeroplane, which even in the low speed case are much more difficult to predict than the control deflections and the stick fixed stability characteristics. From this point of view the approximation (2.8) seems to be sufficiently accurate.

An important parameter with respect to longitudinal stability is the wing pitching moment at zero lift (c_{m_0}). As a first approximation the following formula will be used (ref. 5)

$$c_{m_0} = \frac{f}{t},$$

where f represents the maximum camber of the aerofoil section.

With the aid of the above-mentioned rule governing compressibility effects it is easy to show that

$$c_{M_0} = \frac{1}{\sqrt{1-M^2}}\,c_{m_0}. \qquad (2.9)$$

For more accurate approximations ref. 6 can be consulted. It is allowed to assume as a first approximation that the position of the aerodynamic centre of the wing is not affected by compressibility below the critical Mach number since this position is given by the derivative of pitching moment coefficient with respect to lift coefficient. As these coefficients are changed in the same ratio by compressibility the a. c. position remains unchanged.

3 Static longitudinal stability.

3.1 *General.*

When the assumption that the aerodynamic parameters are independent of speed is no longer true, the theory of longitudinal stability takes a more complex form. In ref. 1 it is shown that the derivative dc_m/dc_r can be taken as a measure of static longitudinal stability. For the not too steep glides to be considered in this report c_r is approximately equal to c_a. Then dc_m/dc_r passes into the usual dc_m/dc_a which now can be represented by

$$\frac{dc_m}{dc_a} = \left(\frac{\partial c_m}{\partial c_a}\right)_M + \left(\frac{\partial c_m}{\partial M}\right)_{c_a} \frac{dM}{dc_a} . \qquad (3.1)$$

Since in a steady glide

$$G = \tfrac{1}{2}\rho V^2 F c_r \approx \tfrac{1}{2}\rho V^2 F c_a \qquad (3.2)$$

(3.1) can also be written

$$\frac{dc_m}{dc_a} = \left(\frac{\partial c_m}{\partial c_a}\right)_M - \left(\frac{\partial c_m}{\partial M}\right)_{c_a} \frac{M}{2\,c_a} . \qquad (3.3)$$

In low speed theory only the first term on the right hand side has to be taken into account since the partial derivative $\partial c_m/\partial M$ may then be assumed to be zero. In the next sections the value of $\partial c_m/\partial M$ will be computed for both the stick fixed and the stick free case.

3.2 *Stick fixed.*

The pitching moment coefficient of an aeroplane about the centre of gravity at a distance ht behind the wing leading edge can be given by (see sec. 6 for notation)

$$c_M = c_{M_0} + (h - h_0)A\alpha + c_{m_{fus}} - \frac{l - (h - h_0)t}{t} \frac{F_H}{F} c_{a_H} . \qquad (3.4)$$

Since the total lift coefficient of the aeroplane can be written

$$c_a = A\alpha + c_{a_H} = A\alpha + \frac{F_H}{F}\left\{A\alpha\left(\frac{1}{A} - \varepsilon_0\right)A_1 + A_1\sigma + A_2\beta + A_3\beta'\right\} \qquad (3.5)$$

elimination of $A\alpha$ and c_{aH} from (3.4) and (3.5) yields

$$c_M = c_{M_0} + (h - h_0)c_a + c_{m_{fus}} - \overline{V}\,\frac{c_a A_1\left(\frac{1}{A} - \varepsilon_0\right) + A_1\sigma + A_2\beta + A_3\beta'}{1 + \frac{F_H}{F} A_1\left(\frac{1}{A} - \varepsilon_0\right)} . \qquad (3.6)$$

The fuselage contribution in the pitching moment $c_{m\,fus}$ is assumed to be linearly dependent on the angle of incidence and can thus be represented by $c_{m'fus}(\alpha + \delta)$ in which expression δ denotes the angle between the fuselage axis and the zero lift line of the wing.

Application of the extended PRANDTL rule shows that the effect of compressibility on the fuselage moment is very small (ref. 5); so it will be neglected in this report.

It must be noticed that the application of formula (3.3) involves the appearance of a term containing the partial derivative $\left(\frac{\partial \alpha}{\partial M}\right)_{c_a}$, since the term $c_{m\,fus}$ contains α. In order to evaluate this derivative we differentiate (3.5) and obtain from

$$dc_a = \left(\frac{\partial c_a}{\partial \alpha}\right)_M d\alpha + \left(\frac{\partial c_a}{\partial M}\right)_\alpha dM = 0$$

the following expression for $\left(\frac{\partial \alpha}{\partial M}\right)_{c_a}$:

$$A\left\{1 + \frac{F_H}{F}\left(\frac{1}{A} - \varepsilon_0\right)A_1\right\}\left(\frac{\partial \alpha}{\partial M}\right)_{c_a} = -\frac{M}{\sqrt{1 - M^2}}\left\{\frac{A^2}{a_0}\alpha + \frac{A_1}{a_{10}}(c_a - A\alpha)\right\} + \frac{F_H}{F}\left\{\frac{A^2}{a_0}A_1\alpha\varepsilon_0\frac{M}{\sqrt{1 - M^2}} + A_1 A\alpha\frac{\partial \varepsilon_0}{\partial M}\right\} . \qquad (3.7)$$

From an estimation of the different terms in (3.7) it followed that an adequate approximation is given by

$$\left(\frac{\partial \alpha}{\partial M}\right)_{c_a} = -\frac{\{A^2 a_{10}\alpha + A_1 a_0(c_a - A\alpha)\}M}{A a_{10} a_0\left\{1 + \frac{F_H}{F}\left(\frac{1}{A} - \varepsilon_0\right)A_1\right\}\sqrt{1 - M^2}} . \qquad (3.8)$$

From the formulae (3.3) and (3.6) an expression for the static margin stick fixed K_n, defined as $-dc_m/dc_a$ can now easily be found when the data of sec. 2 are borne in mind.

When moreover the elevator angle β is eliminated by means of $c_M = 0$ the formula reads

$$K_n = \frac{1}{A}\,\frac{-c'_{m_{fus}} + \overline{V}A_1 A\left(\frac{1}{A} - \varepsilon_0\right)}{1 + \frac{F_H}{F}A_1\left(\frac{1}{A} - \varepsilon_0\right)} - (h - h_0) + \frac{M^2}{\sqrt{1 - M^2}}\,\frac{1}{2\,c_a\left\{1 + \frac{F_H}{F}A_1\left(\frac{1}{A} - \varepsilon_0\right)\right\}} \times \left[\frac{c_{M_0}}{\sqrt{1 - M^2}}\left\{\frac{A_1}{\pi\lambda_H} + \frac{F_H}{F}A_1\left(\frac{1}{A} - \varepsilon_0\right)\right\} - \left\{\frac{A\alpha}{a_0} + \frac{A_1 c_a}{A a_{10}} + \frac{A_1}{a_{10}}\delta\right\}c'_{m_{fus}} - \frac{A_1}{a_{10}}(h - h_0)c_a - \overline{V}A_1 A\alpha\left\{-\frac{1}{a_0} + \frac{\sqrt{1 - M^2}}{2\pi\lambda}\,\frac{s^2}{l^2}\,\frac{1}{\sqrt{1 + (1 - M^2)\left(\frac{\pi s}{4\,l}\right)^2}}\right\}\right] . \qquad (3.9)$$

The first two terms of (3.9) are originated with $(\partial c_m/\partial c_a)_M$, whereas the third term is connected with $(\partial c_m/\partial M)c_a$.

The formula (3.9) being rather complicated its right hand side was evaluated for the particular case of a single-engined fighter in gliding flight, the data of which are given in table 1. A few results are given in fig. 1.

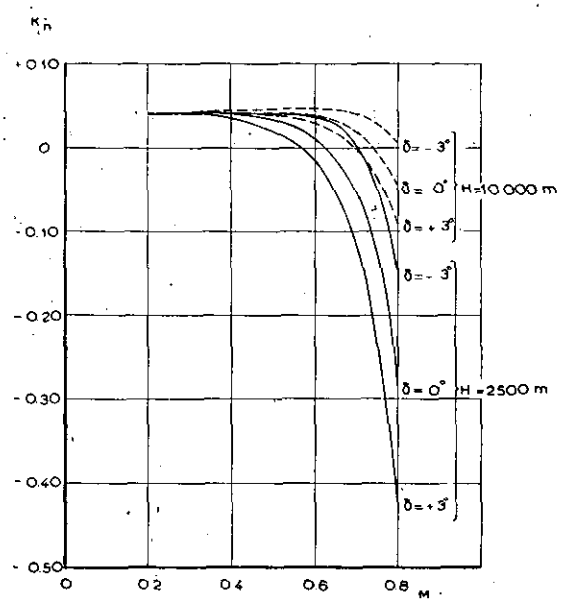

Fig. 1. Mach number effect on static margin stick fixed.

In order to show the trend of K_n with Mach number more clearly the curves in this and the following figures are given for Mach numbers up to $M = 0.8$, although this value will be well above the critical Mach number.

It is seen that as distinct from the incompressible case altitude has an important effect on the changes of K_n with Mach number. These changes are smaller at high altitudes. Furthermore the plot reveals the influence of δ, the angle between the fuselage axis and the non-lift line of the wing, in the compressible case. It appears to be possible to modify the stability changes with M by means of the wing setting relative to the fuselage.

From the computations it was further concluded that the wing pitching moment c_{m_0} has a very important influence on the changes of K_n. In the example of fig. 1 a negative value of c_{m_0} (— 0.02) was assumed according to an average profile camber. It would also be possible to effect positive changes in K_n by application of a reversed wing camber.

The large decrements in the static margin which according to (3.9) can occur do not always imply a deterioration of the longitudinal flying qualities of the aeroplane. It is pointed out in ref. 1 that rather large negative static margins can be accepted if only the manoeuvre margins remain positive.

In order to find the effect of compressibility on the trim curves, the change of the elevator angle with increasing Mach number and at constant lift coefficient must be computed. This can be done by using equation (3.6). Putting $c_M = 0$ gives the following relation for the elevator angle in the compressible case

$$(\beta_{tr})_c = \frac{1 + \frac{F_H}{F} A_1 \left(\frac{1}{A} - \varepsilon_0\right)}{\overline{V} A_2} \times$$

$$\times \left[c_{M_0} + c'_{m_{fus}} (\alpha + \delta) + (h - h_0) c_a\right] -$$

$$- \frac{1}{A_2} \left\{ c_a A_1 \left(\frac{1}{A} - \varepsilon_0\right) + A_1 \sigma + A_3 \beta' \right\} \quad (3.10)$$

whilst in the incompressible case

$$(\beta_{tr})_i = \frac{1 + \frac{F_H}{F} a_1 \left(\frac{1}{a} - \varepsilon_0\right)}{\overline{V} a_2} \times$$

$$\times \left\{ c_{m_0} + c'_{m_{fus}} (\alpha_0 + \delta) + (h - h_0) c_a \right\} -$$

$$- \frac{1}{a_2} \left\{ c_a a_1 \left(\frac{1}{a} - \varepsilon_0\right) + a_1 \sigma + a_3 \beta' \right\} \quad (3.11)$$

where α_0 denotes the angle of incidence in the incompressible case. The difference $\Delta\alpha = \alpha - \alpha_0$ can be approximated by equating the wing lift in both cases

$$a\alpha_0 = A\alpha$$

from which by means of (2.1) and putting $\sqrt{1 - M^2} \approx 1 - \frac{1}{2} M^2$ we find

$$\Delta\alpha = - \frac{M^2}{2} \frac{c_a}{a_0}. \quad (3.12)$$

When taking for the downwash factor ε_0 the low speed value in both cases, which according to the computations involves only a slight error, subtraction of (3.11) from (3.10) gives for the change in elevator angle to trim due to compressibility at constant lift coefficient the following approximative expression:

$$\Delta\beta = \tfrac{1}{2} c_{m_0} \frac{M^2}{\sqrt{1 - M^2}} \frac{t a_1}{l a_2} \left(\frac{F}{F_H} \frac{1}{\pi \lambda_H} + \frac{1}{\pi\lambda} - \varepsilon_0\right) - c'_{m_{fus}} \frac{t a_1}{l a_2} \frac{M^2}{2} \left(\frac{F}{F_H} \frac{1}{a_{10}} + \frac{1}{a_0}\right) \delta -$$

$$- \frac{M^2 c_a}{2} \frac{t a_1}{l a_2} \left[\frac{c'_{m_{fus}}}{a} \left\{ \frac{F}{F_H} \left(\frac{1}{a_{10}} + \frac{a}{a_1} \frac{1}{a_0}\right) + \frac{2}{a_0} - \frac{a}{a_0} \varepsilon_0 \right\} + (h - h_0) \left\{ \frac{F}{F_H} \frac{1}{a_{10}} + \frac{1}{a_0} \right\} - \frac{l}{t a_0} \right]. \quad (3.13)$$

A numerical evaluation is given in fig. 2, where the trim changes due to compressibility are plotted against Mach number. It is seen from the graph that these changes are rather small even for high values of M and never exceed half a degree.

As can be seen from (3.13) immediately the

curves for different altitudes are parallel since the last term on the right hand side contains $M^2 c_a$ which is a constant for a given altitude.

An important parameter in (3.13) is c_{m_0} which is normally negative (in the example $c_{m_0} = -0.02$). It has a predominant influence on the trend of $\Delta\beta$ with increasing M. Thus in most cases $\Delta\beta$ will become negative at high Mach numbers indicating a nose down pitching moment due to compressibility.

Although δ has also a rather important influence on $\Delta\beta$ (see fig. 2) it does not affect the trend of $\Delta\beta$ with M in the same way as c_{m_0} since the factor $M^2/\sqrt{1-M^2}$ has a stronger influence than $M^2/2$ (see (3.13)).

It can be noted that according to (3.13) the expression for $\Delta\beta$ at a given lift coefficient tends to zero for very low Mach numbers. For a given altitude, however, one part of $\Delta\beta$, i. e. the term containing $M^2 c_a$ in (3.13), does not disappear when M decreases. So even at very low Mach numbers a small compressibility effect is left as a result of the corresponding high lift coefficient.

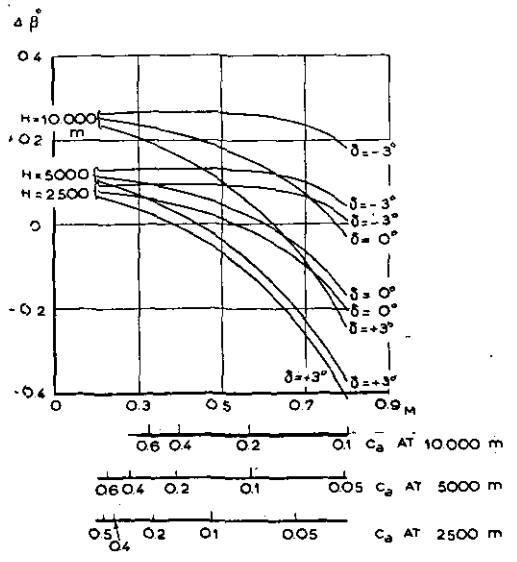

Fig. 2. Elevator trim change due to compressibility as a function of Mach number.

3.3 *Stick free.*

If the elevator weight moment is neglected the hinge moment coefficient can be written

$$c_H = B_1\alpha_H + B_2\beta + B_3\beta'. \qquad (3.14)$$

Eliminating β from (3.4) and (3.14) yields the stick free pitching moment coefficient

$$c_M = c_{M_0} + c'_{m_{fus}}(\alpha+\delta) + (h-h_0)c_a - \frac{\overline{V}}{1+\frac{F_H}{F}\left(\frac{1}{A}-\varepsilon_0\right)\overline{A}_1}\left[c_a\overline{A}_1\left(\frac{1}{A}-\varepsilon_0\right) + \overline{A}_1\sigma + \overline{A}_3\beta'\right]. \qquad (3.15)$$

In a similar way to the stick fixed case a formula for the static margin stick free K'_n can be given with the aid of formula (3.3).

The result is

$$K'_n = \frac{1}{A}\,\frac{-c'_{m_{fus}} + \overline{V}\overline{A}_1 A\left(\frac{1}{A}-\varepsilon_0\right)}{1+\frac{F}{F_H}\overline{A}_1\left(\frac{1}{A}-\varepsilon_0\right)} - (h-h_0) + \frac{M^2}{\sqrt{1-M^2}}\,\frac{1}{2\,c_a\left\{1+\frac{F_H}{F}\overline{A}_1\left(\frac{1}{A}-\varepsilon_0\right)\right\}}\times$$

$$\times\left[\frac{c_{M_0}}{\sqrt{1-M^2}}\left\{\frac{A_1}{\pi\lambda_H}+\frac{F_H}{F}\overline{A}_1\left(\frac{1}{A}-\varepsilon_0\right)\right\} - \left(\frac{A}{a_0}\alpha+\frac{A_1 c_a}{A a_{10}}+\frac{A_1}{a_{10}}\delta\right)c'_{m_{fus}} - \right.$$

$$-\frac{A_1}{a_{10}}(h-h_0)c_a - \overline{V}\overline{A}_1 A\alpha\left\{-\frac{1}{a_0}+\frac{\sqrt{1-M^2}}{2\pi\lambda}\,\frac{s^2}{l^2}\,\frac{1}{\sqrt{1+(1-M^2)\left(\frac{\pi s}{4l}\right)^2}}\right\} -$$

$$\left. -\frac{\overline{V}A_1A_2B_1}{\pi\lambda_H B_2\sqrt{1-M^2}}(\alpha+\sigma-\alpha A\varepsilon_0)\right]. \qquad (3.16)$$

Although formula (3.9) for the stick fixed static margin resembles (3.16) very much there is one remarkable difference between the two. The last term on the right hand side of (3.16) between the square brackets is the only one which has no corresponding term in (3.9). It contains the tail-plane setting σ. For positive values of the ratio B_1/B_2 increasing σ decreases K'_n. Since K'_n is a measure for the trimmer movement for steady flight at various speeds with zero stick force or the stick force required to change speed at constant trimmer setting, adjusting the incidence of the tail plane can improve the characteristics of the longitudinal control. In ref. 7 flight tests with a Firefly Mk I aircraft are described, the results of which can be considered as a confirmation of the above-mentioned conclusion. It must be remembered, however, that aero-elastic deformations, which are neglected here can also have affected the flight test results.

In fig. 3 the effect of altitude on the variation of K'_n with Mach number is given for the same aeroplane as the one of sec. 3.2. The curves show the same trend as those for the stick fixed static margin. Especially at low altitudes rather large decreases of K'_n can occur. Again, it was found

from the computations that c_{m_0} has a dominant influence on the changes in K'_n; small values of c_{m_0} imply small changes in static margins.

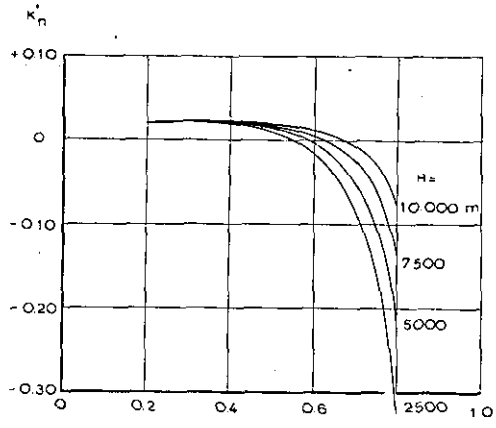

Fig. 3. Effect of altitude on the variation of static margin stick free with Mach number $\delta = \sigma = 0°$.

The influence of wing and tail setting (δ and σ) in the compressible case are illustrated in fig. 4, from which it appears that the changes due to δ and σ are of the same order for the chosen example. It must be noted that these effects are absent in the incompressible case.

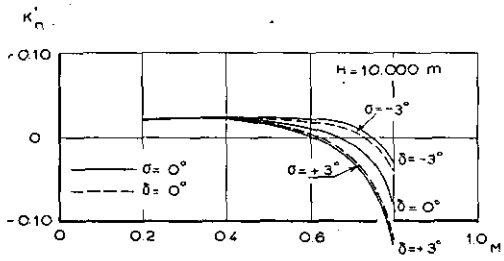

Fig. 4. Effect of wing and tail setting (δ and σ) on the variation of K'_n with Mach number.

Similar to the stick fixed case it can be said that rather large negative margins at high speeds are acceptable provided the manoeuvre margin stick free remains positive since the divergence associated with it becomes small at high speeds.

The changes in trim tab angle due to compressibility can be computed along the same lines as the elevator trim changes in sec. 3.2. The trim tab angle at a given lift coefficient c_a can be found in the compressible case from equation (3.15) by putting $c'_M = 0$

$$(\beta'_{tr})_c = \frac{1 + \frac{F_H}{F}\,\bar{A}_1\left(\frac{1}{A} - \varepsilon_0\right)}{\bar{V}\bar{A}_3} \times$$

$$\times \left[c_{M_0} + c'_{m_{fus}}(\alpha + \delta) + (h - h_0)c_a\right] -$$

$$- \frac{1}{\bar{A}_2}\left\{c_a\bar{A}_1\left(\frac{1}{A} - \varepsilon_0\right) + \bar{A}_1\sigma\right\}. \quad (3.17)$$

whereas in the incompressible case at the same lift coefficient

$$(\beta'_{tr})_i = \frac{1 + \frac{F_H}{F}\,\bar{a}_1\left(\frac{1}{a} - \varepsilon_0\right)}{\bar{V}\bar{a}_3} \times$$

$$\times \left[c_{m_0} + c'_{m_{fus}}(\alpha_0 + \delta) + (h - h_0)c_a\right] -$$

$$- \frac{1}{\bar{a}_3}\left[c_a\bar{a}_1\left(\frac{1}{a} - \varepsilon_0\right) + \bar{a}_1\sigma\right]. \quad (3.18)$$

Similar to (3.13) the change in elevator tab angle due to compressibility at a given lift coefficient can be derived by subtraction of (3.18) from (3.17) in the following approximative form

$$\Delta\beta' = \tfrac{1}{2}\,c_{m_0}\frac{M^2}{\sqrt{1-M^2}}\;\frac{t}{l\,\bar{a}_3}\left[\frac{F}{F_H}\;\frac{a_1}{\pi\lambda_H} + \frac{\bar{a}_1}{\pi\lambda} - \bar{a}_1\varepsilon_0\right] - c'_{m_{fus}}\frac{t}{l\,\bar{a}_3}\left(\frac{Fa_1}{F_H a_{10}} + \frac{\bar{a}_1}{a_0}\right)\delta -$$

$$- \frac{M^2 c_a}{2}\;\frac{t}{l\,\bar{a}_3}\left[\frac{c'_{m_{fus}}}{a}\left\{\frac{F}{F_H}\left(\frac{a_1}{a_{10}} + \frac{a}{a_0}\right) + 2\,\frac{\bar{a}_1}{a_0} - \frac{\bar{a}_1 a\varepsilon_0}{a_0}\right\} + (h - h_0)\left\{\frac{F}{F_H}\;\frac{a_1}{a_{10}} + \frac{\bar{a}_1}{a_0}\right\} - \frac{l}{t}\;\frac{\bar{a}_1}{a_0}\right] -$$

$$- \frac{M^2}{2}\;\frac{a_2}{b_2}\;\frac{b_1}{a_3}\;\frac{A_1}{\pi\lambda_H}\,\sigma. \quad (3.19)$$

In order to illustrate the magnitude of $\Delta\beta'$ this quantity has been plotted against Mach number in fig. 5 for four different altitudes.

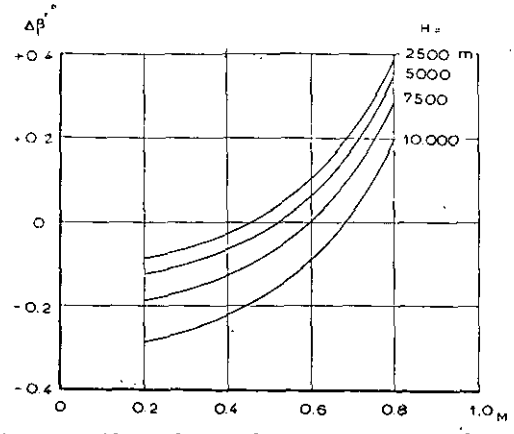

Fig. 5. Effect of altitude on elevator tab change, due to compressibility as a function of Mach number.

It is seen that a change in altitude results in a parallel displacement of the curves. Although $\Delta\beta'$ appears not to be large for the chosen example it is about twice as large as the elevator changes.

The first term on the right hand side of (3.19) containing c_{m_0} forms an important part of $\Delta\beta'$ and can be considered as a means of modifying the trim

tab angle changes at high speeds. The influences of wing and tail setting (δ and σ) are shown in fig. 6 from which it appears that these are relat-

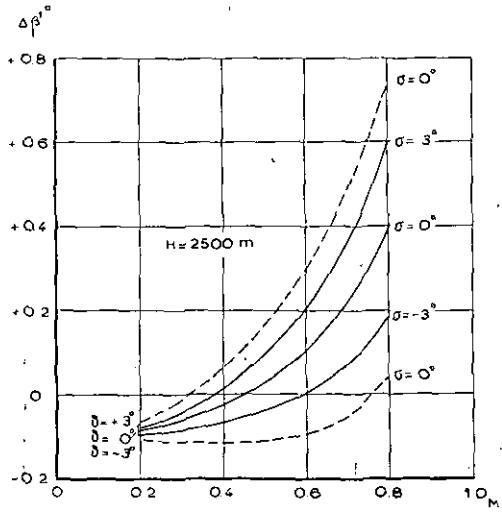

Fig. 6. Effect of tail and wing setting (τ and δ) on elevator tab change due to compressibility as a function of Mach number.

ively important. The contribution of σ, which is determined by the last term on the right hand side of (3.19), contains the factor b_1/b_2, which can vary between rather wide boundaries; normally it lies in the region 1 to -1.

It is clear from the foregoing analysis that the changes in β' due to compressibility are dependent on many parameters. It would carry too far to investigate the influence of each single parameter in this report. In general, however, it may be concluded that the trend of $\Delta\beta'$ with increasing Mach number lies in the positive direction corresponding to the decrease of the static margin found before.

Finally it may be observed that similar to $\Delta\beta$ the expression for $\Delta\beta'$ tends to zero for low Mach numbers at a given lift coefficient but contains a finite part for constant altitude.

4 Manoeuvrability.

4.1 *General.*

The criteria for the manoeuvrability of the longitudinal motion commonly used are the elevator actions necessary to produce a given normal acceleration in a pull-out, i. e. the well-known stick travel and stick force per g. Since a circular motion in a vertical plane cannot be perfectly steady because of changes in the position of the aeroplane with respect to the vertical, the manoeuvrability theory can only be an approximate one, in which the assumptions are made that the duration of the manoeuvre is so small, that the variations of speed and of the normal component of gravity may be neglected.

The position of the centre of gravity for which the elevator action per g (stick travel resp. stick force) is zero, is known as the manoeuvre point (stick fixed resp. stick free), whilst the manoeuvre margins are defined as the distances of the manoeuvre points to the centre of gravity.

The assumption that speed is constant during the manoeuvre simplifies the computation of the effect of compressibility on the manoeuvrability characteristics considerably since partial derivatives with respect to Mach number as appearing in the static stability theory do not occur. As a result of this the formulae in the next two sections resemble those of the basic theory for a good deal.

4.2 *Stick fixed.*

The elevator angle to trim in steady symmetric flight at a given speed (or c_a) is determined by (see 3.6)

$$c_{M_0} + c'_{m_{fus}}(\alpha+\delta) + (h-h_0)c_a - \overline{V}\,\frac{c_a A_1\left(\frac{1}{A}-\varepsilon_0\right) + A_1\sigma + A_2\beta + A_3\beta'}{1+\frac{F_H}{F}A_1\left(\frac{1}{A}-\varepsilon_0\right)} = 0. \tag{4.1}$$

In the steady pull-out with a normal acceleration of $(n+1)$ g at the same speed and trimmer setting the following relation describes the equilibrium of pitching moments

$$c_{M_0} + c'_{m_{fus}}(\alpha+\Delta\alpha+\delta) + (h-h_0)(c_a+\Delta c_a) - \overline{V}\,\frac{(c_a+\Delta c_a)A_1\left(\frac{1}{A}-\varepsilon_0\right) + A_1(\sigma+\Delta\alpha_H) + A_2(\beta+\Delta\beta) + A_3\beta'}{1+\frac{F_H}{F}A_1\left(\frac{1}{A}-\varepsilon_0\right)} = 0, \tag{4.2}$$

where $\Delta c_a = n c_a$.

The increment in angle of incidence of the horizontal tail $\Delta\alpha_H$ is due to the rotation of the aeroplane about its lateral axis and can be equated to

$$\Delta\alpha_H = \frac{n c_a}{2\mu_1},$$

where μ_1 denotes the relative density of the aeroplane $= \dfrac{m}{\rho F l}$.

In order to eliminate $\Delta\alpha$ from the equations it must be remembered that

$$c_a+\Delta c_a = A(\alpha+\Delta\alpha) + \frac{F_H}{F}\left\{A_1(\alpha+\Delta\alpha)A\left(\frac{1}{A}-\varepsilon_0\right) + A_1(\sigma+\Delta\alpha_H) + A_2(\beta+\Delta\beta) + A_3\beta'\right\}. \tag{4.3}$$

Elimination of β and $\Delta\alpha$ from (4.1), (4.2) and (4.3) and omitting very small quantities results in

$$\overline{V}A_2\frac{\Delta\beta}{n c_a} = \frac{c'_{m_{fus}}}{A} - \overline{V}A_1\left(\frac{1}{A}-\varepsilon_0+\frac{1}{2\mu_1}\right) + (h-h_0)\left\{1+\frac{F_H}{F}A_1\left(\frac{1}{A}-\varepsilon_0\right)\right\}, \tag{4.4}$$

from which an expression for the manoeuvre margin stick fixed H_m is easily derived

$$H_m = h_m - h = h_0 - h + \frac{\overline{V} A_1 A \left(\frac{1}{A} - \varepsilon_0 + \frac{1}{2\mu_1} \right) - c'_{m_{fus}}}{A \left\{ 1 + \frac{F_H}{F} A_1 \left(\frac{1}{A} - \varepsilon_0 \right) \right\}} \quad (4.5)$$

An illustration of the variation of H_m with M is given in fig. 7 for the aircraft mentioned in

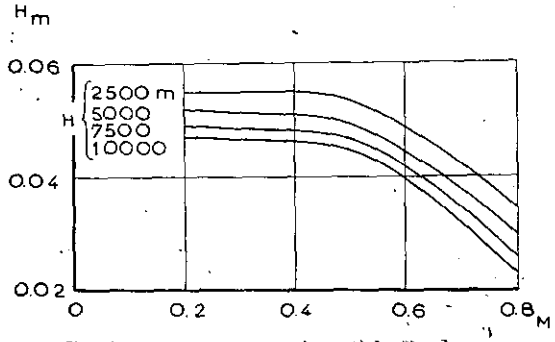

Fig. 7. Manoeuvre margins stick fixed as a function of Mach number.

the preceding sections. Compared with the static margin the changes in H_m appear to be rather small and even at $M = 0.8$ amount to no more than a few per cent of the mean aerodynamic chord. The quantity μ_1 contains σ and so introduces an altitude effect on the manoeuvre margin; the margin decreases with increasing altitude. This effect increases slightly with Mach number.

It may be observed, that the distance between the neutral and the manoeuvre point can become very large, the former travelling far ahead of the latter. This situation does not necessary give rise to a deterioration of the flying qualities since as said before a negative static margin combined with a positive manoeuvre margin can be quite acceptable at high speeds.

Further, it is also possible that the variation of the static margin is so small that the manoeuvre point comes in front of the neutral point, a situation that does not occur at low speeds. This will be the case, for instance, when the value of c_{m_0} is only slightly negative or even positive.

Although the variations of H_m with M in fig. 7 correspond to one special aeroplane the curves have a much more general significance than those of the figures concerning the static margins, because the parameters in (4.5) which are responsible for the variation of H_m do not vary very much from one aeroplane to another.

Finally the elevator movement per g, β_g, is plotted against Mach number for two different altitudes in fig. 8 according to the following formula

$$\beta_g = - \left\{ 1 + \frac{F_H}{F} A_1 \left(\frac{1}{A} - \varepsilon_0 \right) \right\} \frac{c_a}{\overline{V} A_2} H_m . \quad (4.6)$$

In order to illustrate the Mach number effect more clearly β_g is also given for the case in which all compressibility effects are neglected (dotted lines). It is seen that below the critical Mach number (say 0.7) the compressibility effect on β_g is small.

4.3 *Stick free.*

The effect of Mach number on the manoeuvre margin stick free and the corresponding manoeuvre point can be found along similar lines as in the pre-

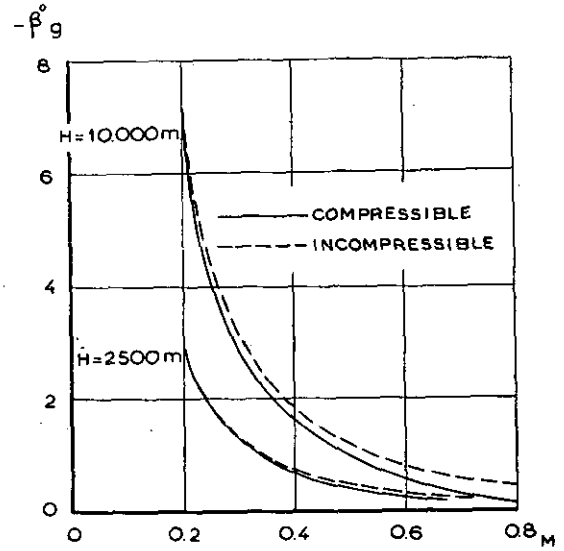

Fig. 8. Effect of Mach number on elevator angle per g.

ceding section. Starting from trimmed flight (stick force zero) at a given speed (or c_a) the hinge moment coefficient c_H in a pull-out with a normal acceleration of $(n+1)$ g at the same speed and trimmer setting can be derived from the same equations as in par. 4.2 and

$$\Delta c_H = A \left(\frac{1}{A} - \varepsilon_0 \right) \Delta\alpha B_1 + \frac{\Delta c_a}{2\mu_1} B_1 + \Delta\beta B_2 , \quad (4.7)$$

which follows from (3.14).

Similar to (4.4) it is found

$$\frac{\overline{V}}{B_2} \frac{A_2}{n c_a} \frac{\Delta c_H}{} = \frac{c'_{m_{fus}}}{A} - \overline{V} \overline{A}_1 \left(\frac{1}{A} - \varepsilon_0 + \frac{1}{2\mu_1} \right) + (h - h_0) \left\{ 1 + \frac{F_H}{F} \overline{A}_1 \left(\frac{1}{A} - \varepsilon_0 \right) \right\} , \quad (4.8)$$

whereas the formula for the manoeuvre margin stick free reads

$$H'_m = h'_m - h = h_0 - h + \frac{\overline{V} A \overline{A}_1 \left(\frac{1}{A} - \varepsilon_0 + \frac{1}{2\mu_1} \right) - c'_{m_{fus}}}{A \left\{ 1 + \frac{F_H}{F} \overline{A}_1 \left(\frac{1}{A} - \varepsilon_0 \right) \right\}} . \quad (4.9)$$

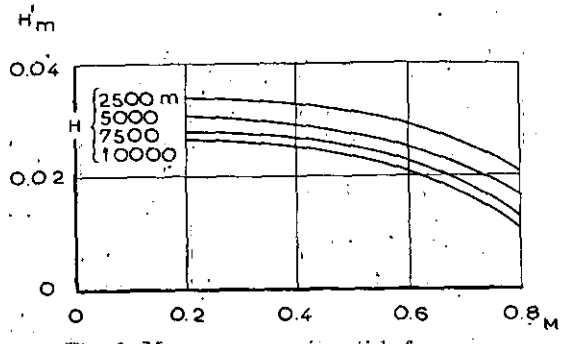

Fig. 9. Manoeuvre margins stick free as a function of Mach number.

In fig. 9 H'_m is plotted against Mach number which shows the same picture as H_m in the preceding section. The decrease in H'_m at $M = 0.7$ amounts to about one per cent of the mean aerodynamic chord. As distinct from the stick fixed case the parameters in (4.9) can vary much more than those in (4.5) from one aeroplane to the other; therefore the variation of H'_m in fig. 9 is less representative than that of H_m.

The stick force per g can be computed from

$$P'_g = -m_\beta \left\{1 + \frac{F_H}{F} \bar{A}_1 \left(\frac{1}{A} - \varepsilon_0\right)\right\} \times \times \frac{B_2}{\overline{V}\overline{A}_2} \frac{G}{F} F_\beta t_\beta H'_m . \qquad (4.10)$$

The results for the chosen example are given in fig. 10, which shows a moderate reduction of the stick force per g with increasing Mach number.

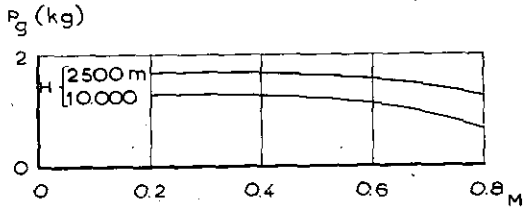

Fig. 10. Effect of Mach number on stick force per g.

5 Summary and conclusions.

In this report the effect of the compressibility of the air on the static longitudinal stability and control of an aeroplane is investigated. Formulae are derived from which the changes in the stability criteria (static margins stick fixed and free) with Mach number can be found. These changes appear to be dependent on altitude, being smaller at high altitudes.

In general both static margins decrease with increasing Mach number and occasionally assume large negative values, which, however, need not give rise to unacceptable flying qualities of the aeroplane. An important parameter in the relations is c_{m_0}, the pitching moment coefficient at zero wing lift, which has a dominant effect on the changes in the stability margins. To a lesser extent these changes are affected by the wing setting relative to the fuselage. Especially c_{m_0} can be considered as a means to modify the stability changes due to compressibility since the decrement in stability with increasing Mach number is reduced by decreasing the value of $-c_{m_0}$.

The changes of elevator angle and elevator tab angle due to compressibility are rather small and for the example chosen in the report never exceed one degree. According to the above-mentioned decrease of the static margins the elevator angle tends to negative and the tab angle to positive values with increasing Mach number indicating a nose-down pitching moment.

The stick free stability appears to be affected also by the tail setting σ. Generally an increase of σ results in a decrement of the stick free static margin. As the changes of stick force with speed at constant trimmer setting or the trimmer movements at various speeds with zero stick force are proportional to this margin, adjusting the tail plane setting can be considered as a means to alter the control characteristics of the aeroplane at high speeds.

The changes in manoeuvrability due to compressibility are mostly considerably smaller than those of the static margins. In most cases a slight decrease of the manoeuvre margins (stick fixed and free) occurs with increasing Mach number. The distances between the neutral and the manoeuvre points generally increase, the former travelling ahead of the latter. Nevertheless it is also possible that the manoeuvre points come in front of the neutral points at high speeds for instance when c_{m_0} is only slightly negative or even positive. At low speeds on the other hand the manoeuvre margins are always greater than the static margins.

Since no rapid divergence from the equilibrium condition occurs as long as the manoeuvre margins remain positive the effect of compressibility generally does not give rise to unacceptable flying qualities of the aeroplane at high speeds although the static margins can attain rather large negative values.

6 List of symbols.

$A = \frac{\partial c_a}{\partial \alpha}$ of aeroplane without tail.

$A_1 = \frac{\partial c_{aH}}{\partial \alpha_H}$

$A_2 = \frac{\partial c_{aH}}{\partial \beta}$

$A_3 = \frac{\partial c_{aH}}{\partial \beta'}$

a, a_1, a_2, a_3 = low speed values of A, A_1, A_2, A_3

a_0, a_{10}, a_{20}, a_{30} = values of a, a_1, a_2, a_3 for aerofoils of infinite span.

$\bar{A}_1 = A_1 - \frac{A_2 B_1}{B_2}$.

$\bar{A}_3 = A_3 - \frac{A_2 B_3}{B_2}$

$\bar{a}_1$, $\bar{a}_3$ = low speed values of $\bar{A}_1$, $\bar{A}_3$

$B_1 = \frac{\partial c_H}{\partial \alpha_H}$

$B_2 = \frac{\partial c_H}{\partial \beta}$

$B_3 = \frac{\partial c_H}{\partial \beta'}$

b = wing span.

b_1, b_2, b_3 = low speed values of B_1, B_2, B_3.

b_{10}, b_{20}, b_{30} = values of b_1, b_2, b_3 for aerofoils of infinite span.

c_a = lift coefficient of complete aeroplane (positive when upward).

c_{aH} = lift coefficient of horizontal tail surfaces.

c_H = (elevator hinge moment)/$\frac{1}{2} \rho V^2 F_\beta t_\beta$ (positive when tailheavy).

c_M = pitching moment coefficient (positive when tailheavy).

$c_{M_0} = c_{M_{wing}}$ when wing lift is zero.

c_m, c_{m_0} = low speed value of c_M, c_{M_0}.

$c_{m\,fus}$ = fuselage pitching moment coefficient.
$c'_{m\,fus}$ = $\frac{\partial c_{m\,fus}}{\partial \alpha}$
c_r = coefficient of resultant aerodynamic force on complete aircraft.
F = wing area.
F_H = area of horizontal tail surface.
F_β = area of elevator.
f = maximum wing camber.
G = aeroplane weight.
g = acceleration due to gravity.
ht = distance of centre of gravity aft of leading edge of mean aerodynamic chord.
$h_0 t$ = distance of aerodynamic centre of aeroplane without tail aft of leading edge of mean aerodynamic chord.
$h_m t$ = distance of manoeuvre point stick fixed aft of leading edge of mean aerodynamic chord.
$h'_m t$ = distance of manoeuvre point stick free aft of leading edge of mean aerodynamic chord.
H_m = $h_m - h$.
H'_m = $h'_m - h$.
K_n = static margin stick fixed.
K'_n = static margin stick free.
l = distance of aerodynamic centre of tail aft of aerodynamic centre of aeroplane without tail.
M = Mach number.
m = aeroplane mass.
m_β = stick-elevator gear ratio.
ng = additional normal acceleration.
P_g = stick force per g.
s = semi wing span.
s' = semi span of rolled-up vortex-sheet behind wing at horizontal tail.
t = mean aerodynamic chord.
t_β = elevator chord.
V = forward speed.
$\overline{V}$ = tail volume (lF_H/Ft).
α = angle of incidence of zero lift line of aeroplane without tail.
α_H = angle of incidence of horizontal tailplane.
β = elevator angle (positive when downward).
β' = elevator tab angle (positive when downward).
β_g = elevator movement per g.
δ = wing setting relative to fuselage (positive when fuselage nose high).
ε = downwash angle at tail.
ε_0 = $\frac{1}{A}\frac{d\varepsilon}{d\alpha}$
λ = aspect ratio of wing.
λ_H = aspect ratio of horizontal tailplane.
μ_1 = relative density of aeroplane ($m/\rho Fl$).
ρ = air density.
σ = tail setting relative to zero lift line of aeroplane without tail (positive in tail heavy sense).

7 References.

1. Gates, S. B. and Lyon, H. M., A Continuation of Longitudinal Stability and Control Analysis. Part I, General Theory, R. and M. No. 2027, 1944.
2. Göthert, B., Ebene und räumliche Strömung bei hohen Unterschallgeschwindigkeiten. (Erweiterung der Prandtl'schen Regel), Forschungsbericht Nr. 1275 der Deutschen Luftfahrtforschung, 1940.
3. Goldstein, F. R. S. and Young, A. D., The Linear Perturbation Theory of Compressible Flow, with Application to Wind-Tunnel Interference, R. and M., No. 1909, 1943.
4. Morgan, M. B. and Thomas, H. H. B. M., Control Surface Design in Theory and Practice, J. of the Royal Aeronautical Society, Aug. 1945.
5. Bader, W., Ueber den Einflusz hoher Fluggeschwindigkeiten auf die Flugzeug-Langsbewegung, Bericht der Deutschen Versuchsanstalt für Luftfahrt, 1942.
6. Hilton, W. F., Empirical Laws for the Effect of Compressibility on Quarter-chord Moment Coefficient, and for the Choice of an Aerofoil with small Compressibility Effects on Centre of Pressure, R. and M., No. 2195, 1943.
7. Dickinson, D. R. H., Elevator Control on Firefly Mk I and N. F. Mk II Aircraft, R. and M. 2202, 1947.

TABLE 1.

Data used in example (Fig. 1—10).

G	= 2950 kg	a_0	= 6,0
F	= 22,5 m²	a	= 4,48
F_H	= 3,1 m²	a_{10}	= 4,8
F_β	= 1,25 m²	a_1	= 3,18
l	= 5,5 m	a_2	= 1,78
b	= 11,3 m	a_3	= 0,15
t	= 2,0 m	b_1	= −0,05
t_β	= 0,4 m	b_2	= −0,18
$\overline{V}$	= 0,375	b_3	= −0,12
m_β	= 2,66 rad/m	ε_0	= 0,104
λ	= 5,7	c_{m_0}	= −0,02
λ_H	= 3,0	$c_{m'fus}$	= 0,2
$h - h_0$	= −0,05		